

# OSO-7

# ORBITING SOLAR OBSERVATORY

## FINAL REPORT

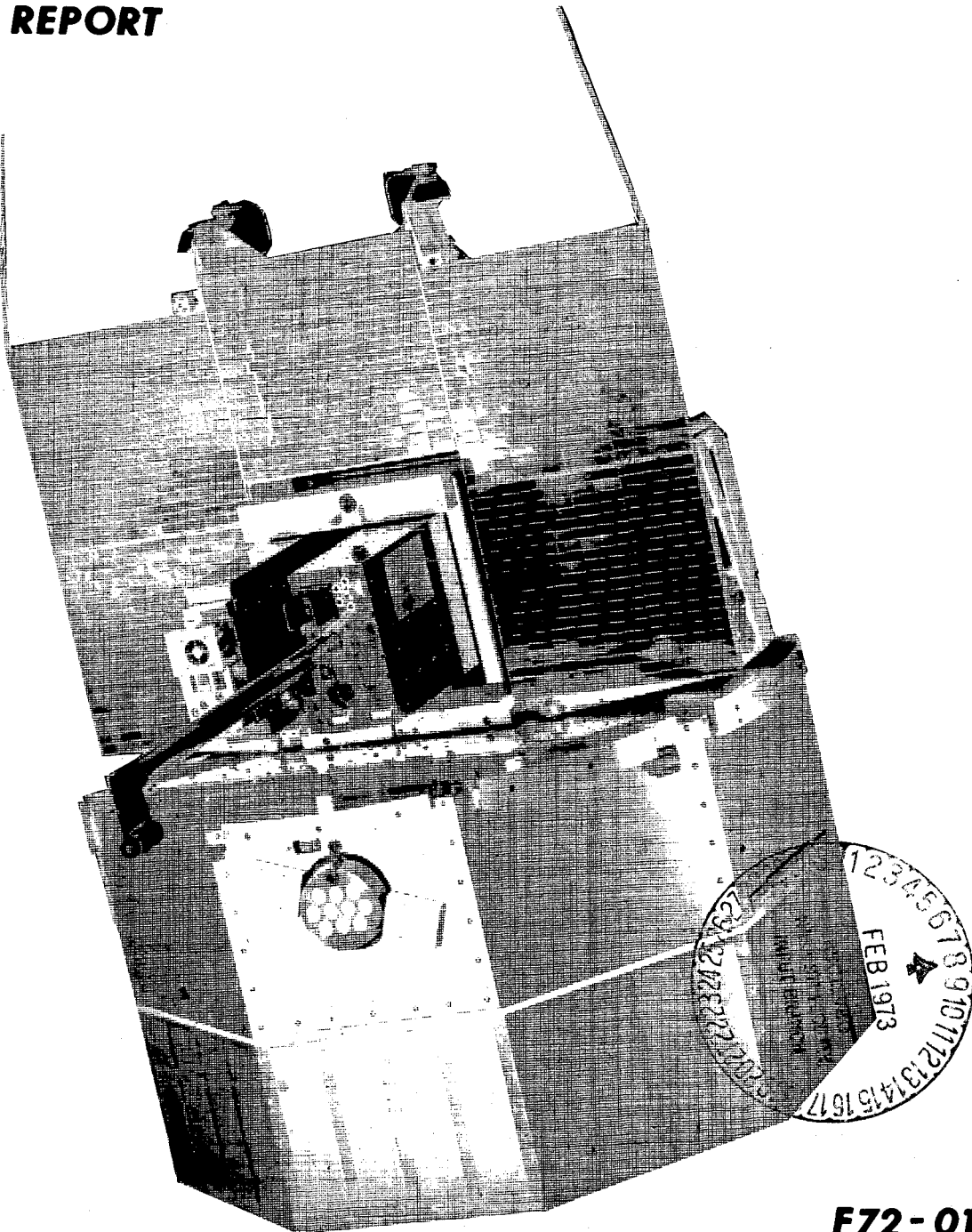
N73-20879

Unclas  
53694

G3/31

CSSL 22B

(NASA-CR-130157) OSO-7 ORBITING SOLAR  
OBSERVATORY PROGRAM Final Report (Ball  
Bros. Research Corp.) - 280 p HC \$16.00



F72-01



**BALL BROTHERS RESEARCH CORPORATION**

SUBSIDIARY OF BALL CORPORATION

BOULDER, COLORADO

OSO-7

ORBITING SOLAR OBSERVATORY  
PROGRAM FINAL REPORT

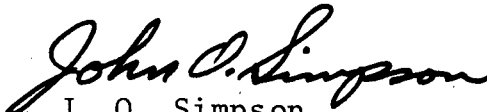
F72-01

December 31, 1972

PREPARED BY

OSO Program Staff

APPROVED BY

  
J. O. Simpson  
Director, OSO Programs

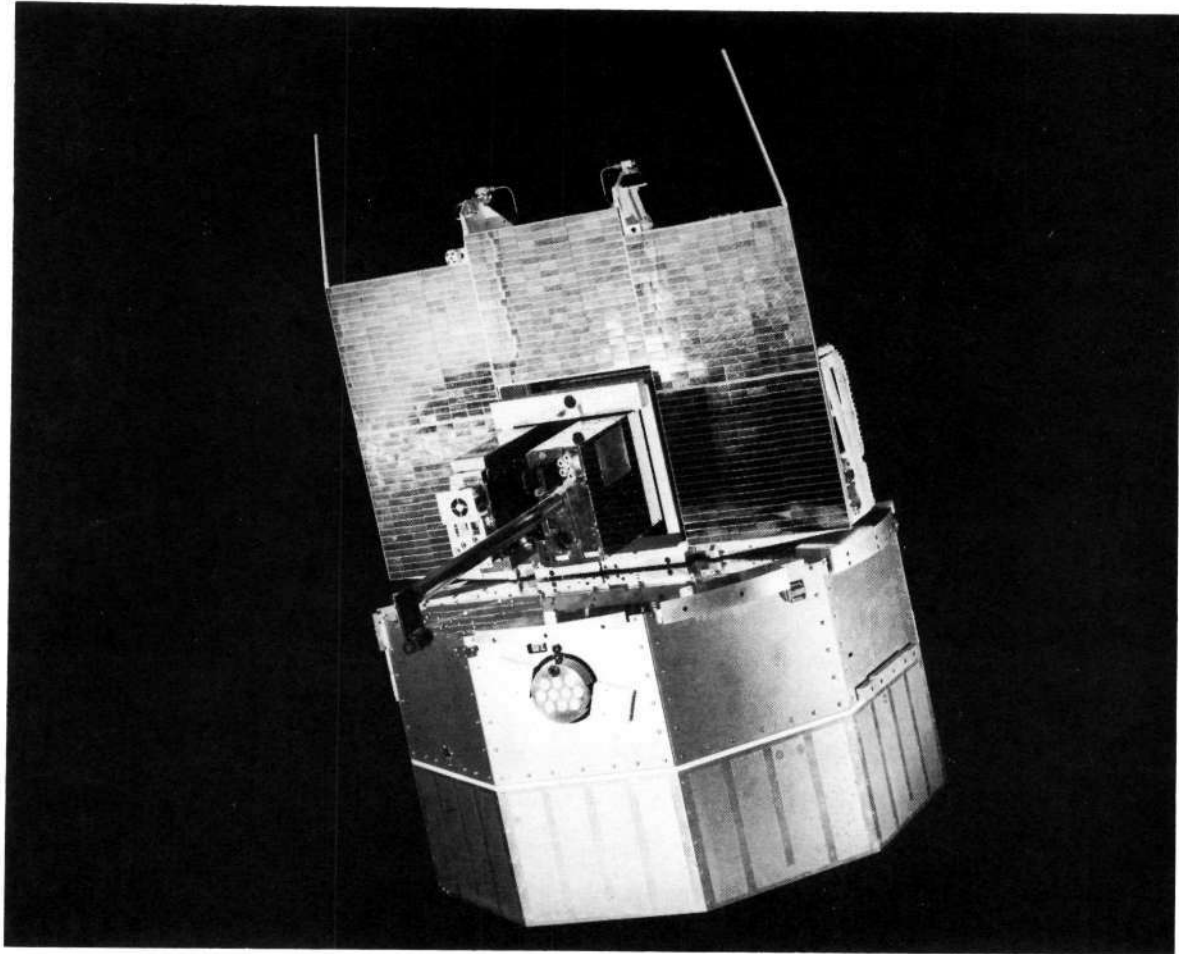


**BALL BROTHERS RESEARCH CORPORATION**  
SUBSIDIARY OF BALL CORPORATION  
BOULDER, COLORADO

*J*



F72-01





F72-01

PREFACE

During the 1950's rapid progress was made in solar physics and in instrument and space hardware technology, using rocket and balloon flights that, although of brief duration, provided a view of the sun free from the obscuring atmosphere. The significance of data from these flights confirmed the often-asserted value of long-term observations from a spacecraft in advancing our knowledge of the sun's behavior.

Thus, the first of NASA's space platforms designed for long-term observations of the universe from above the atmosphere was planned, and the Orbiting Solar Observatory program started in 1959. Solar physics data return began with the launch of OSO-1 in March of 1962. OSO-2 and OSO-3 were launched in 1965, OSO-4 and OSO-5 in 1967, OSO-6 in 1969, and the most recent, OSO-7, was launched on September 29, 1971.

All seven OSO's have been highly successful both in scientific data return and in performance of the engineering systems. The gain to date in scientific knowledge amply justifies the foresight of the early planners. OSO lifetimes have been several years, allowing long-term observations of solar and other galactic and extra-galactic events as planned. This report describes OSO-7, the seventh of the continuing series of Orbiting Solar Observatories.



F72-01

CONTENTS

Section		Page
	PREFACE	iii
1	PROGRAM SUMMARY	1-1
	1.1 Overall Orbiting Solar Observatory Program Objectives	1-1
	1.2 OSO-7 Program Activity Summary	1-2
	1.3 Observatory Description	1-6
	1.4 Mission Performance	1-15
2	HARDWARE PERFORMANCE	2-1
	2.1 In-Orbit Performance	2-1
	2.2 Launch Phase Performance	2-14
3	DESIGN, INTEGRATION, AND TEST PROGRAM SUMMARY	3-1
	3.1 Subassembly Qualification	3-1
	3.2 Observatory Qualification Model Testing	3-1
	3.3 Flight Model Test History	3-2
4	DYNAMICS	4-1
	4.1 Rotational Dynamics of OSO	4-1
	4.2 Ballasting for Proper Moment of Inertia	4-10
	4.3 Stability and Dynamics During Initial Acquisition	4-11
5	OBSERVATORY ASPECT MONITORS	5-1
	5.1 General Description	5-1
	5.2 Fine Pitch Monitor	5-2
	5.3 Large-Angle Pitch Monitor	5-4
	5.4 Coarse Aspect Monitor (SORE)	5-7
	5.5 Fine Aspect Monitor (ASA)	5-13
6	CONTROL SYSTEMS	6-1
	6.1 Introduction	6-1
	6.2 Pneumatic Pitch-Attitude Control	6-2
	6.3 Pneumatic Roll-Attitude Control	6-5
	6.4 Pneumatic Spin-Rate Control	6-5
	6.5 Magnetic Roll, Pitch and Spin Control	6-12
	6.6 Pointing Control	6-14
	6.7 Launch-Sequence Control	6-45
	6.8 Nutation Control	6-50
7	POWER SYSTEM	7-1
	7.1 General Description	7-1
	7.2 Observatory Power Budget	7-1
	7.3 Power Source	7-3
	7.4 Energy Storage	7-7
	7.5 Power Control	7-9
	7.6 Power Distribution	7-12
8	TELEMETRY SYSTEM	8-1
	8.1 Introduction	8-1
	8.2 Data Handling Subsystem	8-4
	8.3 Spacecraft Housekeeping Data Acquisition	8-32
	8.4 RF Subsystem	8-33
	8.5 Telemetry Link Analysis	8-42



F72-01

CONTENTS (Cont.)

Section		Page
9	COMMAND SYSTEM	9-1
	9.1 General Description	9-1
	9.2 Command and Address Formats	9-4
	9.3 Decoder Description	9-6
	9.4 Command Receivers	9-17
	9.5 System Performance Requirements	9-18
10	STRUCTURAL, PNEUMATIC AND THERMAL CONTROL DESCRIPTION	10-1
	10.1 Development History of OSO-7	10-1
	10.2 Observatory Structure	10-5
	10.3 Pneumatic Systems	10-9
	10.4 Structural Analysis Summary	10-10
	10.5 Mass Properties	10-16
	10.6 OSO-7 Thermal System Description	10-19
Appendix		Page
A	SORE AND ASA SOFTWARE AND ASPECT COORDINATE SYSTEMS	A-1
B	THERMAL ANALYSIS METHODS	B-1



F72-01

## ILLUSTRATIONS

Figure		Page
1-1	OSO-7 Program Activities Summary	1-7
1-2	OSO-7 Configuration	1-8
1-3	OSO-7 Dimensions	1-9
1-4	Spacecraft Structural Breakdown	1-10
1-5	Azimuth Drive Assembly	1-11
1-6	Pointing Modes	1-12
2-1	Attitude History, Spacecraft Spin Axis	2-2
2-2	Wheel Spin Rate and Spin Gas Pressure History	2-2
2-3	Pitch Attitude, Pitch Coil Status, and Pitch Gas Pressure History	2-3
2-4	Spacecraft Bus Voltage, Load Current, and Solar Array Current History	2-3
2-5	Solar Array Energy Developed During Orbit Revolution Nos. 225, 274, 665, 892, 1905	2-4
2-6	Elevation and Azimuth Motor Torque History	2-5
2-7	Solar Array Temperature History	2-5
2-8	Spin-Axis (Pitch) Motion After Dawn Acquisition (Gyro Control During Night-Orbit Revolution No. 968)	2-6
2-9	Pitch Motion During Changes in Pointing Modes - Orbit Revolution No. 846	2-7
2-10	Pointing Control Performance Read-Out Sensor Output - Orbit Revolution No. 75	2-8
2-11	Typical Gyro Azimuth Drift (Orbit Revolution No. 225) Measured Relative to Stars Observed by Star Scanner	2-9
2-12	Star Scanner Sensitivity	2-10
2-13	Star Sensor Performance During Orbit Revolution No. 271. Comparison of Results Using Original and Improved Data Reduction	2-11
2-14	Power System Parameters - Normal Profiles (Pars 318) and Overcharge Condition (Pars 76)	2-12
2-15	Wheel Experiment Temperature, Orbit Revolution 77	2-15
2-16	OSO-7 Wheel Temperatures, Orbit Revolution 77	2-16
2-17	OSO-7 Pointed Experiment Temperature, Orbit Revolution 77	2-17
2-18	OSO-7 Sail Temperatures, Orbit Revolution 77	2-18
2-19	Nominal and Actual OSO-7 Launch Sequence	2-20
2-20	Pitch Attitude and Spin Rate Data	2-22
2-21	Pitch Attitude Sensor Geometry	2-23
2-22	Permissible Pitch Attitude Readout-Momentum Vector 19 Degrees from Line of Sight to Sun	2-23
2-23	Telemetry Data, Modes, and Corrective Commands - OSO-7 Recovery	2-24
3-1	Qualification Model Test History	3-3
3-2	Spacecraft Test History	3-5
3-3	Observatory Test History	3-7
4-1	Motion of $\bar{H}$ and $\bar{S}$ During Pitch Precession	4-3
4-2	Residual Nutation of $\bar{S}$ After Constant Torquing Stops	4-6
4-3	Dusk Transient	4-7
4-4	Dawn Transient	4-8
4-5	Time Required to Enter Dynamically Stable Region During Launch Sequence	4-13
4-6	Worst Case Expected Nutation Decay During First Solar Acquisition	4-14



F72-01

ILLUSTRATIONS (Cont.)

Figure		Page
5-1	Location of Aspect Sensors and Reference Axes	5-3
5-2	Diagram of Pitch Readout Sensor	5-4
5-3	Pitch Readout Sensor Output Curve	5-5
5-4	Principle of Large-Angle Pitch Monitor	5-6
5-5	Flux-Gate Magnetometer	5-8
5-6	Azimuth Encoder (Blipper) Operation	5-9
5-7	SORE Functional Block Diagram	5-10
5-8	Aspect Sensor Assembly	5-14
5-9	ASA Optics	5-15
5-10	ASA Data Words	5-16
5-11	ASA Timing Relationships	5-17
6-1	Pneumatic Pitch Control Block Diagram	6-3
6-2	Pitch Control Sensors	6-4
6-3	Typical Pitch Control Sensor Response	6-4
6-4	Pneumatic Spin Control Block Diagram	6-6
6-5	Spin-Down-Loop Timing Diagram	6-8
6-6	Spin-Up Loop Timing Diagram	6-9
6-7	Day/Night Sensing and Timing	6-11
6-8	Pitch and Roll Coils Functional Diagram	6-13
6-9	Servo Loops Functional Interfacing	6-15
6-10	OSO-7 Pointing Control Block Diagram	6-18
6-11	Coarse Sensor Assemblies	6-19
6-12	Coarse Sensor Signal	6-20
6-13	Rate Signal Compensation	6-21
6-14	Net Despin Drive Efficiency	6-23
6-15	Coarse-Azimuth Preamp/AC Amplifier Response	6-24
6-16	Typical PWM/Power Switch Response	6-25
6-17	Fine Control Eyes and Response Curve	6-28
6-18	Offset-Mode Patterns	6-32
6-19	Offset Mode Block Diagram	6-33
6-20	OIRU Configuration and Dimensions	6-36
6-21	Night-Pointing Control Functional Diagram	6-39
6-22	Rate-Integrating Gyro	6-44
6-23	Launch Sequence Control Block Diagram	6-47
6-24	Time-Delay Relay Driver	6-49
6-25	Nutation Damper	6-51
6-26	Nutation Damper Effectiveness	6-54
7-1	Simplified OSO-7 Power System Schematic	7-2
7-2	OSO-7 Power Load Tree	7-4
7-3	OSO-7 Solar Panel Layout and Module Dimensions	7-6
7-4	Solar Cell and Interconnect	7-7
7-5	OSO-7 Seven-Cell Battery Pack	7-8
7-6	Dummy Load System Simplified Schematic	7-10
7-7	Dummy Load Locations	7-11





F72-01

ILLUSTRATIONS (Cont.)

Figure		Page
7-8	Simplified Power Distribution	7-13
7-9	Flex Cable	7-13
7-10	Flex Cable Mounting Configuration	7-14
8-1	Telemetry System Block Diagram	8-2
8-2	Data-Handling System Functional Block Diagram	8-9
8-3	Digital Multiplexer and Encoder Logic Diagram	8-11
8-4	DME Timing Chart	8-14
8-5	ASC Functional Block Diagram	8-17
8-6	Analog Subcommutator Logic Diagram	8-18
8-7	ASC Timing Chart	8-19
8-8	ASC Block Diagram	8-21
8-9	PCM Junction Box Functional Block Diagram	8-23
8-10	PCM Junction Box Power Switching	8-24
8-11	Frame Counter and Digital Submultiplexer Functional Block Diagram	8-25
8-12	Tape Recorder Block Diagram	8-27
8-13	Tape Recorder Switching Diagram	8-30
8-14	Tape Recorder Timer	8-31
8-15	ASSC Synchronization Circuit	8-33
8-16	Telemetry System (PSK-600A) Block Diagram	8-34
8-17	Turnstile Slot Antenna	8-36
8-18	Progressive Phase Feed Layout	8-37
8-19	Progressive Phase Feed Block Diagram	8-38
8-20	Feed Network Schematic	8-39
8-21	Telemetry Frequency Radiation Pattern (RHC Polarized)	8-40
8-22	Telemetry Frequency Radiation Pattern (LHC Polarized)	8-40
8-23	Telemetry Frequency Radiation Pattern (Combined RHC and LHC)	8-41
8-24	Vehicle/Antenna Coordinate System	8-42
8-25	Command Frequency Radiation Pattern (RHC Polarized)	8-43
9-1	OSO-7 Command System Block Diagram	9-1
9-2	Command and Address Word Format	9-5
9-3	Command Frame Timing Formats	9-7
9-4	Command Decoder Functional Diagram	9-11
9-5	Decoder Timing Diagram	9-14
9-6	Output Switch Configuration	9-17
9-7	VHF Command Receiver Block Diagram	9-18
10-1	Wheel Structural Components	10-6
10-2	Beam and Frame Assemblies	10-8
10-3	Azimuth Drive Assembly	10-9
10-4	Spin Pneumatic System	10-11
10-5	Pitch Pneumatic System	10-13
10-6	Sail Structure Idealization	10-16



F72-01

ILLUSTRATIONS (Cont.)

Figure		Page
10-7	Basic Wheel Structure Idealization	10-17
10-8	Geometry of Maximum $\beta$ Angle with Time of Year	10-21
10-9	Expected Typical Wheel Hub Temperature Variation	10-22
10-10	Wheel Exterior and Interior Thermal Control Surfaces	10-24
10-11	Forward Sail Thermal Control Surfaces	10-25
10-12	Aft Sail Thermal Control Surfaces	10-26

TABLES

Table		Page
1-1	OSO Program Flight Summary	1-3
1-2	OSO Program Experiments Summary	1-4
1-3	OSO Spacecraft Parameters	1-14
1-4	OSO-6/7 Weight Breakdown (KG)	1-14
2-1	Pointing Alignment Raster	2-8
2-2	Predicted Flight Temperatures and Orbit No. 77 Flight Data	2-13
2-3	Spacecraft Prelaunch Status	2-19
2-4	Launch Events	2-21
2-5	On-Orbit Spacecraft Checkout	2-28
2-6	Experiment High-Voltage Turn-On	2-30
4-1	OSO-7 Mass Properties	4-12
5-1	Gray-to-Binary Conversion	5-6
5-2	SORE Modes	5-11
6-1	Magnetic Attitude Control Dipoles	6-14
7-1	OSO-7 Power Loads and Duty Cycles	7-5
7-2	Adhesives Used on the OSO-7 Solar Array Cell Assembly	7-8
8-1	OSO-7 Telemetry Chart	8-6
8-2	Specifications for the PSK-600A Telemetry Transmitter	8-34
8-3	OSO-7 Telemetry Link Analysis	8-43
9-1	OSO-7 Command Chart	9-2
9-2	Address and Command Enable Codes	9-6
9-3	Output Characteristics	9-8
9-4	Performance Characteristics	9-8
9-5	Receiver Electrical Characteristics	9-19
9-6	OSO-7 Command Link Analysis	9-20
10-1	Spin Pneumatic Parameters	10-12
10-2	Pitch Pneumatic Parameters	10-14
10-3	Primary Modes of OSO-7	10-15
10-4	Minimum Margin of Safety Summary - OSO-7 Spacecraft	10-17
10-5	OSO-7 Launch Mass Properties	10-18
10-6	OSO-7 Weight Breakdown by Subsystem	10-19
10-7	Surface Finishes	10-23
10-8	OSO-7 Predicted Temperatures	10-27



F72-01

Section 1  
PROGRAM SUMMARY

This report describes the seventh Orbiting Solar Observatory (OSO-7, frontispiece) in the continuing series designed to gather solar and celestial data that cannot be obtained from the earth's surface. OSO-7 was launched September 29, 1971. It has been highly successful in returning scientific data giving new and important information about solar flare development, coronal temperature variations, streamer dynamics of plasma flow, and solar nuclear processes. OSO-7 is expected to have sufficient lifetime to permit data comparisons with the Skylab A mission during 1973.

The OSO-7 is a second generation observatory. It is about twice as large and heavy as its predecessors, giving it considerably greater capability for scientific measurements.

This section reviews mission objectives, flight history, and scientific experiments; describes the observatory; briefly compares OSO-7 with the first six OSO's; and summarizes the performance of OSO-7.

1.1 OVERALL ORBITING SOLAR OBSERVATORY PROGRAM OBJECTIVES

The general objectives of the OSO program are to make observations and measurements contributing to:

- Determination of details of the sun's atmospheric structure, composition and physical state and the process of energy transport radially outward and inward.
- Determination of origin, energy supply, and solar/terrestrial consequences of transient solar phenomena such as sun spots, flares, radio bursts, and particle bursts.
- Prediction of transient solar events and their consequences by combining data with those from other spacecraft, rockets, balloons, and ground-based observations.
- Secondary objectives including study of the earth and celestial objects.

1.1.1 OSO Program Flight Summary

Seven OSO's have been launched successfully: the first in March 1962, and the latest, OSO-7, in September 1971. All have met mission objectives and have been considered highly successful. Many improvements have been made since the initial design, with a major capability increase on OSO-7. OSO-7 is a considerably larger spacecraft than the earlier OSO's. Improvements include a 300 percent increase in experiment payload capability, a 250 percent increase in power, a 200 percent increase in pitch gas supply, and a 300 percent increase in spin gas supply. Most of the improvements were in size and weight; the basic



F72-01

spacecraft operation and most of the electronics remained the same. Thus the scientific capability was substantially increased with no significant reduction in performance confidence. Its excellent orbital performance has shown that this approach was sound. Table 1-1 summarizes these observations and their orbit performance to date.

#### 1.1.2 OSO Program Scientific Experiments Summary

Sixty solar and celestial scientific experiments have been flown to date. Measurements have covered the spectrum from 1000 MeV through the X-ray, XUV, EUV, UV, photographic, and IR to  $30\mu$ . Proton, electron and neutron experiments have also been flown. The OSO wheel provides short term celestial scan, solar scan, and earth scan; the roll precession of the spacecraft rotates the scan plane thus allowing complete celestial sphere coverage in a few months. Table 1-2 lists organizations, principal investigators, spectral range, and OSO mission on which experiment was flown.

#### 1.1.3 OSO-7 Program Objectives

The OSO-7 instruments monitor X-rays, gamma rays, ultraviolet radiation, outer corona-white light, and other emanations from the sun along with X-rays and high-energy charged particles from the entire celestial sphere. Specific mission objectives are to:

- Obtain extreme ultraviolet spectroheliograms between  $170 \text{ \AA}$  and  $400 \text{ \AA}$ , spectroheliograms in the  $1.7 \text{ \AA}$  to  $2.5 \text{ \AA}$  and  $8 \text{ \AA}$  to  $15 \text{ \AA}$  regions, and to determine polarization of flare X-rays from 20 to 40 keV.
- Study, sequentially, the solar disc and inner corona in the extreme ultraviolet ( $170 \text{ \AA}$  to  $550 \text{ \AA}$ ) and outer corona in white light ( $3900 \text{ \AA}$  to  $6500 \text{ \AA}$ ).
- Survey the entire celestial sphere for sources of cosmic X-rays in the energy range from 1 to 60 keV with an angular resolution of about  $0.1^\circ$ , and to perform spectral analysis in five broad energy bands.
- Perform a celestial sphere scan to determine the intensity, position, and spectrum of cosmic X-ray sources in the 10 to 550 keV range, with an angular resolution of  $0.2^\circ$ .
- Study solar X-ray bursts in the energy range of about 1.4 to 300 keV.
- Monitor intensity and line structure of solar gamma ray flux in the energy range of 0.3 to 9.1 MeV.

#### 1.2 OSO-7 PROGRAM ACTIVITY SUMMARY

The OSO-7 program hardware consists of a qualification model observatory, a flight model observatory, and the necessary flight spares. Many of the spares were carried over from the OSO-6 program. The program started in February 1969 and the observatory was launched on September 29, 1971.



F72-01

Table 1-1  
OSO PROGRAM FLIGHT SUMMARY

DESIGNATION	LAUNCH	INITIAL ORBIT (1)	LAUNCH VEHICLE	OPERATIONAL STATUS (2)	MISSION LIFE Months	WEIGHT KG	EXPERIMENT WEIGHT KG	SPACECRAFT SIZE CM	MAJOR MODIFICATIONS
OSO-1 1962 Z1	3/7/62 ETR	553 x 633 32.9°/96.2	DELTA DM-19	Turned off 5/63. Solar array degraded by "Starfish". Tape recorder failed 3 mo. Obtained data on 75 flares.	15	208	82	Dia - 112 Height - 94 (Dia. arms ex- tended - 234)	(First dual-spin spacecraft. First NASA observatory satellite)
OSO-2 1965 7A	2/3/65 ETR	550 x 633 32.9°/96.5	DELTA-C	Turned off 11/65. Pitch control gas used up due to large dipole moment.	9	248	98	Dia - 112 Height - 94 (Dia. arms ex- tended - 234)	Added-Manual spin con- trol, raster scan of disk, magnetometer roll readout. Changed-Telemetry from FM/PM to PCM, P/N to N/P solar cells, tape re- corder redesigned. Incorporated-PAM/AM/AM command system.
OSO-3 1967 20A	3/8/67 ETR	541 x 570 32.9°/95.8	DELTA-C	Tape recorder failed- 18 mo. Turned off 12/71	58	288	112	Dia - 112 Height - 94 (Dia. arms ex- tended - 234)	Added-Fitch dipole coil, automatic spindown con- trol, belt drive on tape recorders. Decreased sun acquisi- tion time. Increased-pointing accuracy; Command capability.
OSO-4 1967 100A	10/18/67 ETR	553 x 555 32.9°/95.7	DELTA-C	Tape recorder failed- 7 mo. Turned off 12/71. First extreme UV pictures of sun.	51	275	110	Dia - 112 Height - 94 (Dia. arms ex- tended - 234)	Added dummy load battery charge control. Increased command capacity.
OSO-5 1969 6A	1/22/69 ETR	541 x 567 33.0°/95.7	DELTA-C	Operating (2)	47(2)	291	116	Dia - 112 Height - 94 (Dia. arms ex- tended - 234)	Changed from shingled to flat mount solar cell array. Increased transmitter power; doubled data rate. Variable telemetry for- mat for U. Minn. experi- ment.
OSO-6 1969 68A	8/9/69 ETR	495 x 559 33.0°/95.2	Long Tank TAD Delta-N	Operating (2)	40(2)	288	100	Dia - 112 Height - 94 (Dia. arms ex- tended - 234)	Added-Roll dipole coils, small aster scan, off- set pointing. Added premod filtering to transmitter. Incorporated word gate generator
OSO-7 1971 83A	9/29/71 ETR	329 x 575 33.1°/93.6	Long Tank TAD Delta-N	Operating (2) (Launch vehicle mal- function gave lower than desired orbit. Spacecraft operating successfully. Scientific data be- ing obtained.)	15(2)	640	208	Dia - 144 Height - 180	Increased-Number commands experiment weight, experi- ment power, data storage capability to two orbits. Improved-pointing accu- racy and stability, anten- na pattern. Added-Star scanner for high accuracy attitude determination, night pointing, all attitude control, pneumatic roll control. Removed deployable arms.

(1) Perigee x Apogee (KM); Inclination (DEG)/Period (MIN).

(2) As of December 1972.



F72-01

Table 1-2  
OSO PROGRAM EXPERIMENTS SUMMARY

HIGH ENERGY (<1Å, >10 KEV)		X-RAY (1Å-300Å)		XUV-EUV (300Å-1500Å)					
GSFC	Frost	20-100Kev	GSFC	1.8Å	OSO-1	GSFC	Hallam	1100-1250Å	OSO-1
GSFC	Frost	0.2-1.5Mev	GSFC	50-400Å	OSO-1	NRL	Tousey	304-1216Å	OSO-2
GSFC	White	0.2-1.5Mev	NRL	2-60Å	OSO-2	HCO	Goldberg	500-1500Å	OSO-2
U.Minn	Winckler/Peterson	50Kev-5Mev	GSFC	1-400Å	OSO-3	AFCLR	Hinteregger	225-1300Å	OSO-3
U.Roch	Fazio	100-500Mev	U.Mich	8-14Å	OSO-3	NRL	Mange	1050-1350Å	OSO-4
GSFC	Frost	0.15-0.55Mev	NRL	1-8Å	OSO-4	HCO	Goldberg	300-1300Å	OSO-4
U.NM	Leavitt	50-1200Mev	NRL	0.5-60Å	OSO-4	U.Col Lond	Boyd	304Å	OSO-4
UCSD	Peterson	7-190Kev	AS&E	0.1-510Å	OSO-4	NRL	Purcell	304-1216Å	OSO-5
U.Roch	Kaplon	>100Mev	AS&E			U.Colo	Rense	280-1030Å	OSO-5
MIT	Kraushaar/Clark	>100Mev				U.Paris	Blamont	1216Å	OSO-5
GSFC	Frost	14-250Kev	U.Col Lond/	3-70Å	OSO-4	HCO	Goldberg	285-1370Å	OSO-6
U.Bologna	Brini	20-200Kev	U.Leicester			NRL	Boyd	171-922Å	OSO-6
GSFC	Neupert	20-40Kev	GSFC	1.2-75Å	OSO-4	NRL	Tousey	170-550Å	OSO-7
UCSD	Peterson	1-300Kev	NRL	1-400Å	OSO-5	GSFC	Neupert	140-400Å	OSO-7
UCSD	Peterson	10-550Kev	NRL	0.5-60Å	OSO-5				
MIT	Clark	1-60Kev	NRL						
			U.Col Lond/	0.6-28Å	OSO-6				
U.NH	Chupp	0.3-9.1Mev	U.Leicester	3-18Å	OSO-5				
			Los Alamos	16-40Å	OSO-6				
			GSFC	1.7-15Å	OSO-7				
UV (1500Å-3000Å)		PHOTOGRAPHIC (3000Å-9000Å)		PARTICLES/OTHER					
GSFC	Hallam	1500-3300Å	GSFC	3800-4800Å	OSO-1	GSFC	Alexander/McCracken	Interplanetary Dust	OSO-1
			U.Minn	Ney	Zodiacal	OSO-2	U.Calif.	Hess	Neutrons
			NRL	Tousey	Wh.Lt. Corona-graph	OSO-2	U.Calif.	Schrader	Prot. >2Mev; Elect. >60Mev
			ARC	Neel	3200-7800Å		ARC	Neel	Emissivity
			U.Minn	Ney	Albedo Zodiacal	OSO-3	ARC	Neel	Emissivity
			Rutg.	Rouy/Carroll	Zodiacal Lt.	OSO-6	ARC	Neel	1-30μ IR
			NRL	Tousey	3900-6500Å		Lawr Rad Lab	Waggoner	Prot. 2-3 Mev;
					Wh.Lt. Corona-graph	OSO-7	U.NM	Leavitt	Kev-5Mev Neutrons
							GSFC	Maag	20-30Mev Thermal Coating



F72-01

The qualification model was mechanically complete with active pneumatics and attitude control systems, and a functional antenna. All other equipment was modeled to reproduce the mass properties of the flight observatory. It was tested to prototype vibration levels and underwent static load testing. Tests were also performed in the Launch Phase Simulator at Goddard Space Flight Center. The upper structure was used as the test model for thermal simulation verification testing, and served as a test bed for pointing control tests.

Testing of the qualification model resulted in cost savings over using a full prototype observatory. That the tests were adequate was demonstrated when the booster malfunction occurred. The observatory structure was exposed to 8 g's as it tumbled at 55 rpm. This unexpected stress did no apparent harm, since the observatory performance has been excellent.

The flight model observatory was fabricated, assembled, integrated with the experiments and tested in the standard manner. The only significant problem encountered, an improper surface treatment of the oriented section that produced poor adherence of the temperature control paint, was solved by using the qualification model upper section structure (built to flight standards) after it underwent proper treatment.

During the launch on September 29, 1971, the booster lost pitch steering control during the injection burn. The resulting final orbit, although elliptical rather than circular, was adequate. However, the spacecraft was required to recover from the severe tumbling motion imparted by the booster. After the observatory stabilized, its spin axis was nearly along the sun line, rather than perpendicular to the sun line as planned.

Fortunately, this possibility had been considered in the design, which allowed for acquisition from any attitude. Furthermore, a comprehensive contingency plan had been prepared and practice runs had been made to prepare for potential launch anomalies. After eight hours of data analysis and command control reactions, the observatory spin axis was precessed toward the proper solar orientation so the automatic control systems could take over. The observatory batteries were nearly discharged during this recovery operation, and it was feared that power would be exhausted before recovery. However, all spacecraft systems except one inoperative tape recorder functioned normally. On this recorder, the loop of tape passing over the record head (the only part of the tape not contained in the reel) may have been thrown from its guides.

After the observatory was operating properly in its automatic control mode, the experiment turn-on sequence was initiated. Experiment operations were verified; all performed as anticipated. The only effects of the launch anomaly were the loss of one tape recorder and the unexpected depletion of control gas used to orient the observatory. About one-third of the pitch control gas was used, and about one-half of the spin control gas. However, the spacecraft has magnetic torquing coils for pitch and spin control as well as a conservatively sized gas supply, so no serious reduction of in-orbit life is anticipated. The 319 by 571 km final orbit (inclined 33.1 degrees to the equator) is predicted to last through 1974.

Experiment data acquisition, begun according to plan, showed immediate scientific results practically from the first operational orbit. The data acquisition program has continued with good results to date.



F72-01

Figure 1-1 shows the time phasing of the program activities from start until launch.

### 1.3 OBSERVATORY DESCRIPTION

#### 1.3.1 General Arrangement

OSO-7 is a spin-stabilized "dual-spin" spacecraft with a solar-oriented despun platform for sun-pointed instruments and the solar array. A rotating wheel stores angular momentum and contains those instruments which do not require sun pointing. The solar-oriented section or sail, is connected to the wheel by a despin drive unit called the azimuth drive assembly. Figures 1-2 and 1-3 show the principal components and dimensions of the OSO-7 observatory. Figure 1-4 shows the sail and wheel interfaced with the drive assembly.

The wheel structure is a cylinder divided into nine wedge-shaped compartments arranged around an 18-inch center tube. The center tube contains the azimuth drive assembly and the nitrogen spin gas supply vessel. This center tube mounts to the booster 18-inch attach fitting. Four of the wheel compartments mount spacecraft components and five compartments house wheel experiments. The slot antenna and its ground-plane skirt extend below the wheel.

The azimuth drive assembly, Figure 1-5, has two low-friction bearing assemblies, a drive motor, and slip rings for transferring power and signals between the wheel and the sail.

The sail assembly consists of the elevation frame, beam assembly, and an open framework which mounts 5 solar cell array panels. Also included are the electronic, mechanical and pneumatic components necessary for operation and orientation of the sail and pointed experiments.

#### 1.3.2 Scientific Instruments

The OSO-7 orbited six scientific instruments and one engineering experiment. Most of the instruments consisted of equipment for more than one experiment. The pointed instruments are from Goddard Space Flight Center and the Naval Research Laboratories. Wheel instruments are from the Massachusetts Institute of Technology, The University of California at San Diego, and the University of New Hampshire. The engineering experiment is from Goddard Space Flight Center.

#### 1.3.3 Control Systems

The OSO-7 has two basic control systems. The first system keeps the spin axis of the observatory in a plane normal to the sun line and controls the spin axis position in that plane. These motions are called pitch and roll. The second system biaxially orients the pointed instruments relative to the center of the sun. These motions are called azimuth and elevation. An additional system maintains spin rate, and another reduces nutational coning motion of the spin axis.





F72-01

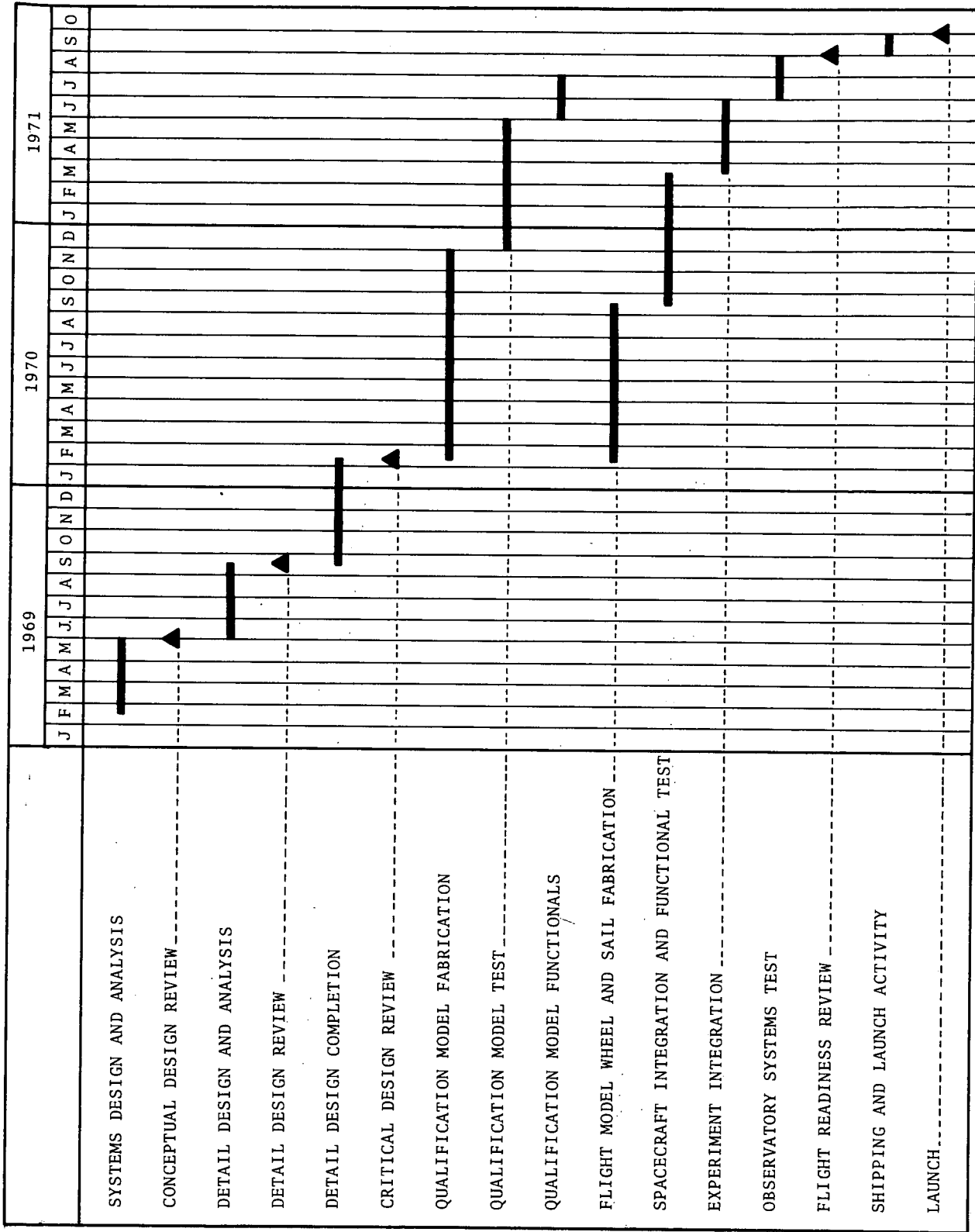


Figure 1-1 OSO-7 Program Activities Summary



F72-01

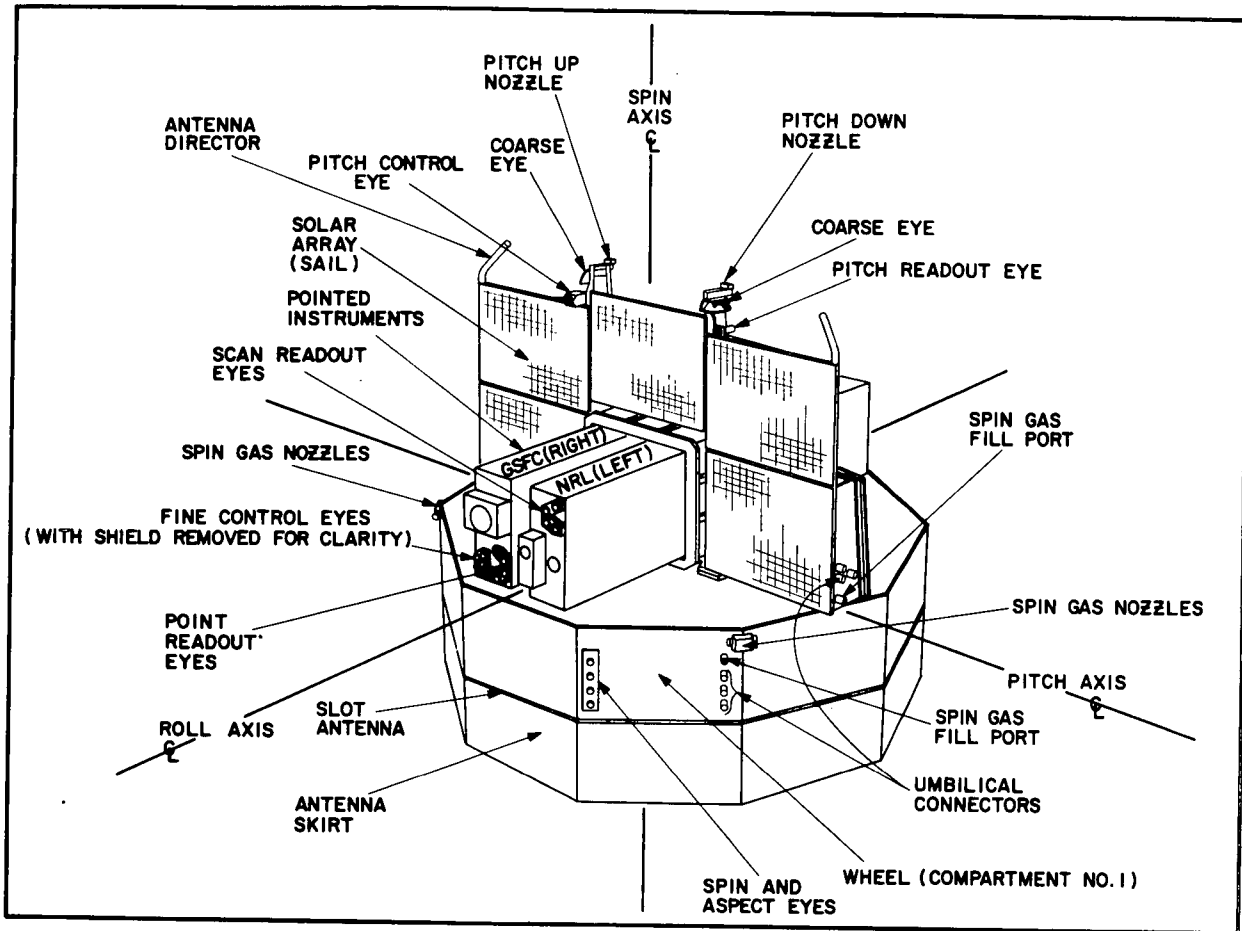


Figure 1-2 OSO-7 Configuration

Spin Axis Orientation. The spinning wheel stores angular momentum. The pitch control gas system moves the spin axis by expelling gas. This precession of the spacecraft is similar to the motion of a gyroscope. Sun sensors measure the angular difference between a line normal to the spin axis and the sun direction. When this angle becomes greater than 3 degrees, gas is expelled to precess the spin axis through 4 degrees to overcorrect the error. The system can be manually operated.

The pitch attitude system can be used to roll the spacecraft about the sun line, aligning the plane of the wheel in celestial coordinates so that a specific celestial target can be scanned by the wheel experiments. To roll the spacecraft, the sail pointing control system is switched from solar orientation to a gyroscope (inertial reference unit) which maintains the despun position of the sail. The gyroscope is commanded to rotate the sail 90 degrees and hold it there. Pitch gas expulsion by command now causes precession about the sun line which results in spacecraft roll.



F72-01

The observatory also has pitch and roll magnetic torquing capability. By ground command, current level through coils mounted along and normal to the spin axis is adjusted to cause slow precession of the spin axis. This system allows adjustment without using the expendable gas.

A nutation damper (a tuned pendulum bob in a fluid-filled case) removes the coning energy of nutation caused by the biaxial pointed instrument control system reaction torques on the observatory. A gas system maintains the spin rate of the wheel to assure that the tuned damper will operate near its maximum efficiency in removing nutational energy. Spin rate is not critical, so this system reacts within a 15 percent wide dead band. The system spins up the wheel at one edge of the dead band and spins it down at the other edge.

The dipole moment reactions of the pitch and roll coils against earth's magnetic field

will cause spin rate changes as well as pitch and roll changes. The coils can therefore be used as a backup to the gas spin rate controller as well as the gas pitch system.

Pointing Control System. The pointed experiments are biaxially oriented to the center of the sun by azimuth and elevation servo controllers. They use sun sensors for error sensing and dc torque motors for positioning. The instruments can be made to point as much as 30 arc-minutes of angle away from the center of the sun on each axis. This is done by current generator which adds simulated error signals into the control loops.

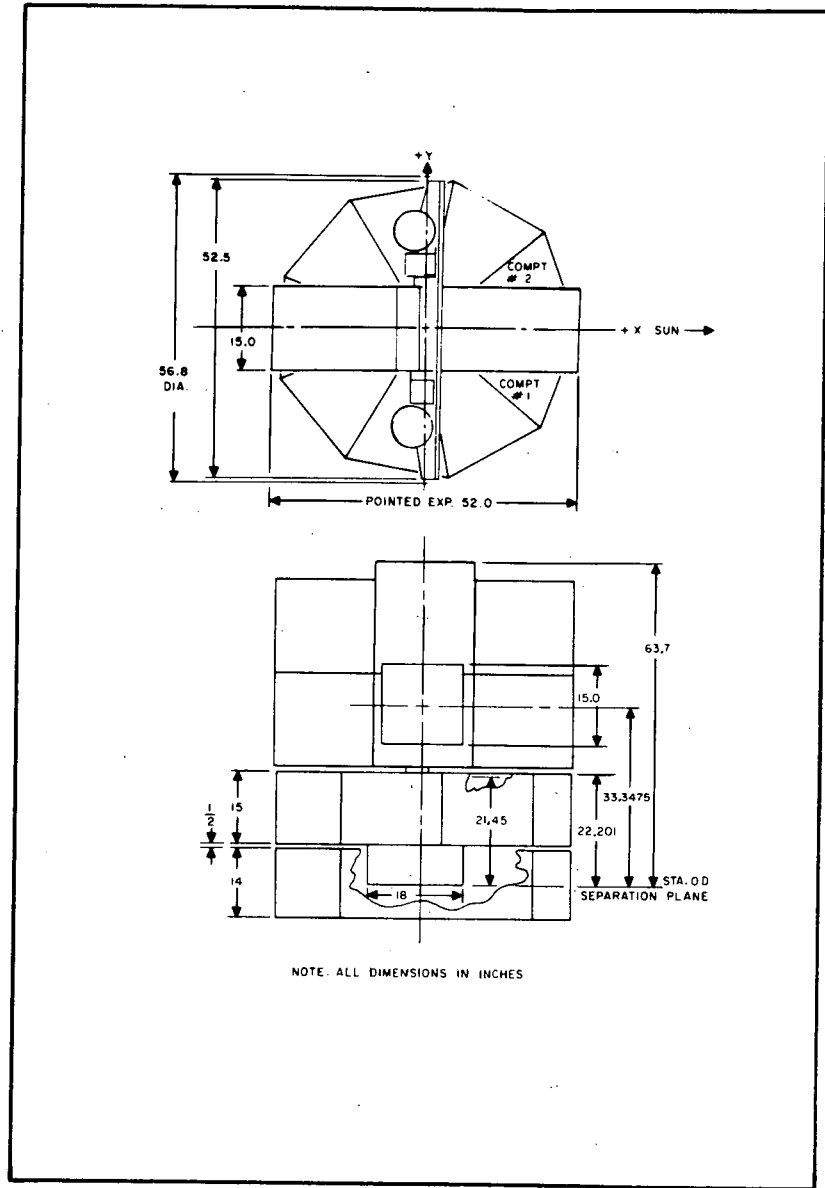


Figure 1-3 OSO-7 Dimensions



F72-01

Either a fixed "offset point" mode or a "raster scan" mode can be used. In the "large raster" mode, a 60 x 60 arc min raster of 64 lines is produced every 8 minutes. In the "small raster" mode, a 5 x 5 arc min raster of 16 lines can be produced about any offset point every minute. The offset point capability provides a grid of 128 x 128 points over the 60 arc min square centered on the sun making it possible to point to any of 16,384 selected positions within 15 arc sec. The pointing modes and pointing positions illustrated in Figure 1-6 are selected by ground command in response to experiment data evaluation.

The gyro (inertial reference unit) orients the sail in azimuth to within about one-third of a degree of a desired direction. Torquing signals applied to the gyro can be used to slew the sail at one-third of a degree per second, and step the sail position in 3 arc-minute increments.

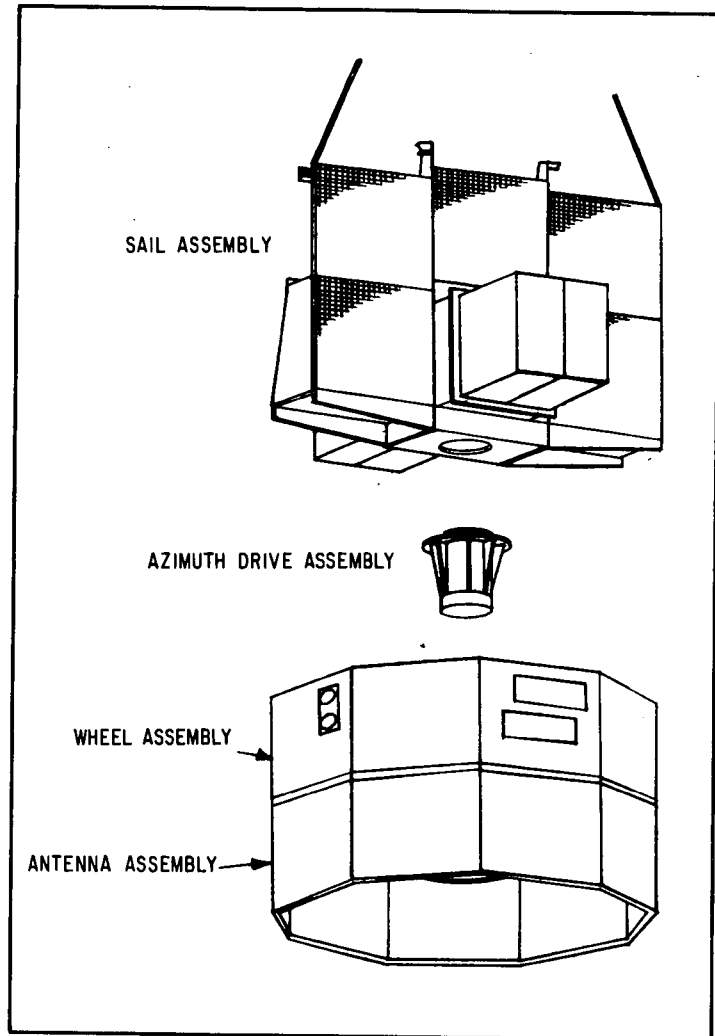


Figure 1-4 Spacecraft Structural Breakdown

#### 1.3.4 Attitude Determination

A number of aspect monitors are used to determine the attitude of the spin axis. The pitch angle is monitored with a large-angle digital aspect sun sensor which has 1 degree resolution over 180 degrees. This sensor is primarily for large angle initial acquisition data. The pitch angle is also monitored by a fine sun sensor which has about 2 arc-minute resolution over 11 degrees.

A magnetometer and sun blipper sensor, each rotating in the wheel, generate data from which the wheel plane angle (a plane normal to the spin axis) is determined to about 2 degrees accuracy. The same sensors provide blip data from which spin rate is determined. A star scanner, rotating in the wheel, generates star location data which is compared to a star map giving spin axis celestial orientation to about 3 arc-minute accuracy. Instantaneous wheel experiment look angle information is also generated.



F72-01

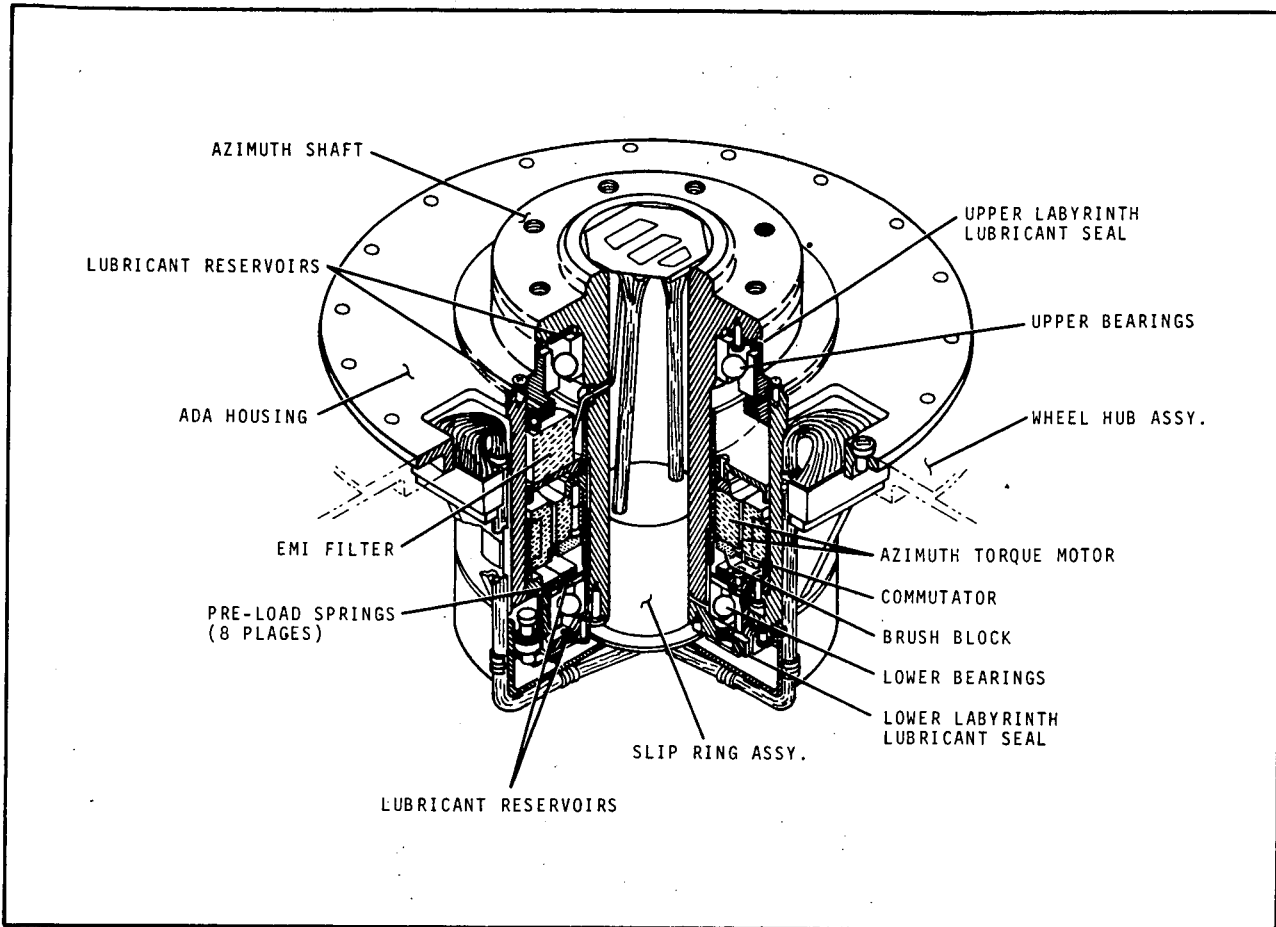


Figure 1-5 Azimuth Drive Assembly

The pointed position, relative to sun center, of the sun-pointed experiments is measured by sun sensors. These sun sensors are separate from the control sensors but are mounted in the same location. These sensors monitor azimuth and elevation pointing position with about 1/2 arc-second resolution.

### 1.3.5 Communications System

The OSO-7 telemetry system samples, encodes, and telemeters spacecraft and experiment data to the GSFC Satellite Tracking and Data Acquisition Network (STADAN) by means of a PCM/PM telemetry system. This consists of a data handling system and an rf system.



F72-01

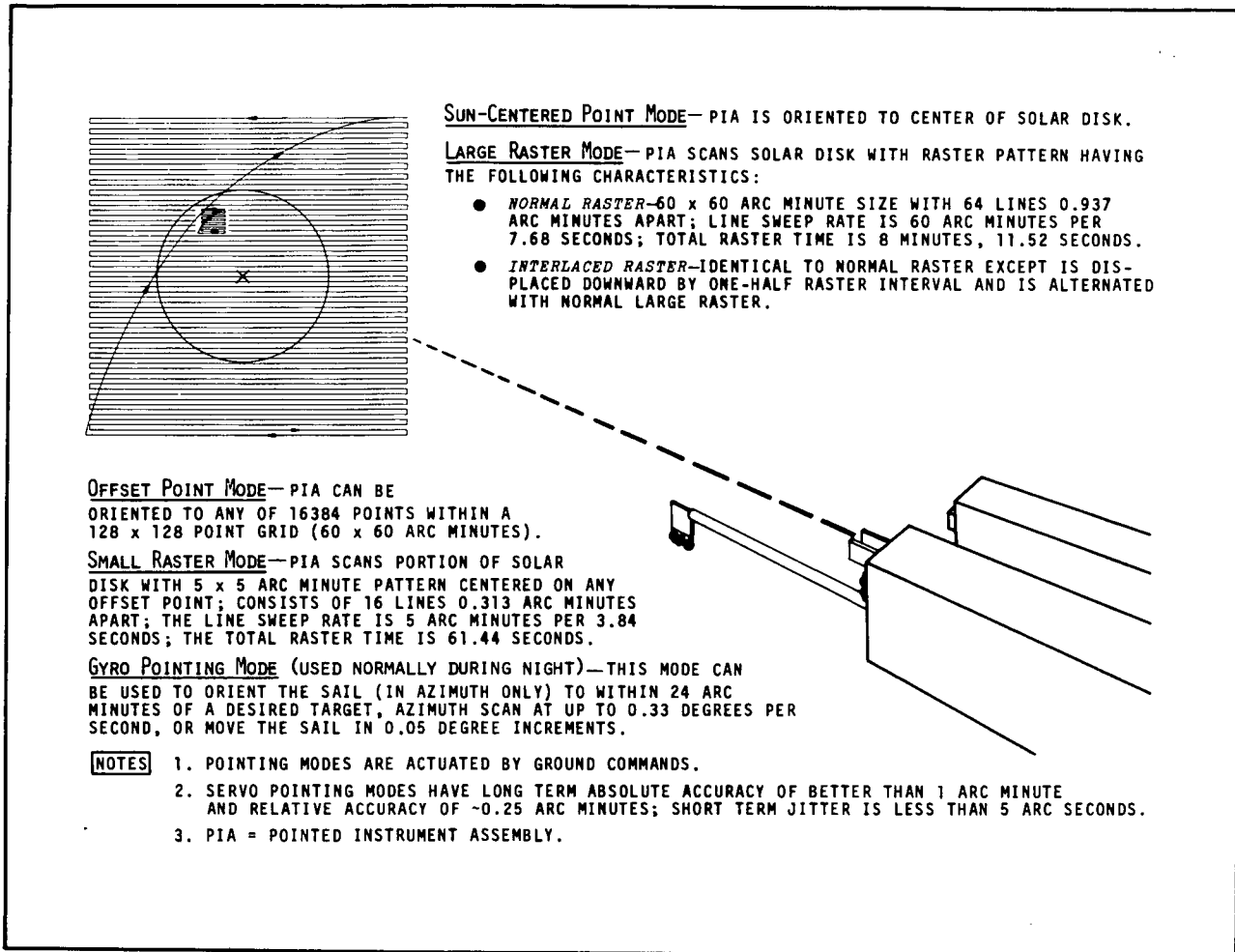


Figure 1-6 Pointing Modes

The data handling system is built around a 32-channel, 8-bit word digital multiplexer, operating at 800 bits per second. It takes 27 channels of direct digital data, two from two 48-channel analog subcommutators, and one from a 48-channel digital subcommutator. Two channels are used for synchronization. There are also three 24-channel analog subcommutators. The digital multiplexer handles 270 total telemetry channels, 70 digital words, 32 single bit monitors, 153 analog monitors, and 15 synchronization channels. The data system also produces gating pulses to shift data out of experiment shift registers and provides timing signals.

The data from the digital multiplexers are stored on tape recorders which are played back by ground command over the STADAN ground stations. The tape recorders store data for 108 minutes and can be used serially, redundantly, or one at a time.

The data from the digital multiplexers are also transmitted in real time using 136.5 Hz, 700 mw transmitters. These transmitters feed a turnstile slot antenna having a gain of greater than -8 dB for all aspect angles. The telemetry link margin is +12 dB in playback and +24 dB for real-time transmissions.



F72-01

The command system uses the same antenna as the telemeter, with a diplexer permitting simultaneous operation. By means of a hybrid circulator, two command receivers operate on the same frequency and feed tone-digital commands to seven 70-command decoders. The 490 available commands are largely redundant; 282 commands are actually used. OSO-7 has never accepted a spurious command signal. This security results from a command enable timer which will allow command access for only 1.5 seconds after a proper address followed by a command-enable command. The command system link margin is +11.5 dB for 95 percent coverage and +2.5 dB for 99.7 percent coverage.

#### 1.3.6 Power System

The power system for OSO-7 consists of a solar array, a nickel-cadmium battery, and power control and distribution circuits. The solar array is made up of five identical panels, each about 16 x 18 inches and containing 180 2 x 5 cm N on P solar cells. A single panel produces approximately 20 watts so that the total array output is 100 watts. The battery is made up of four 14-cell strings. Each string stores 4 ampere-hours for a total capacity of 16 ampere-hours. The cells are in eight packs of seven cells each.

Power control is provided by an undervoltage switch, a set of dummy loads for charge control, and various power switches that provide for day/night switching and on/off switching of spacecraft equipment and experiments. The power distribution system provides continuous, launch, day, night, and 15-volt regulated buses for the observatory. The distribution harness separates noisy and quiet lines, and provides single point grounds in the wheel and the sail. Array output and observatory load currents are monitored to determine the dummy loads required for battery charge current limitation.

#### 1.3.7 Thermal Control

The OSO-7 observatory uses passive surface treatment for thermal control. In all, 17 different surface preparations are used for temperature control. However, four surface treatments are used on the majority of the surfaces. These are a white paint with absorptivity of 0.26 and emissivity of 0.82; a flaked aluminum pigment paint with absorptivity of 0.42 and emissivity of 0.47; gold plate; and aluminum tape. An acid etch finish on the aluminum structural parts is the principal interior finish throughout the observatory wheel. The passive treatment keeps the observatory components within an acceptable temperature range as the geometry of the spacecraft, earth, and sun changes, as the spacecraft passes through its orbit day/night cycles, and as electrical power dissipation changes.

#### 1.3.8 OSO-7 Comparison with Previous OSO's

To put the capability demonstrated by OSO-7 in perspective with the capability demonstrated by earlier OSO's, Table 1-3 compares a number of the more important parameters.

Table 1-4 compares the weight distribution of OSO-7 and OSO-6.



F72-01

Table 1-3  
OSO SPACECRAFT PARAMETERS

POINTING MODES	SUN CENTER POINTING (1)		WOBBLE + NUTATION Arc-Min	SOLAR ARRAY (4)		EXPERIMENT POWER W-Hrs/Orbit	DATA RATE (BPS)		DATA STORAGE Megabits	TRANSMITTER		NO. COMMANDS (Freq. -148MHz)			
	5 Min	1 Hr		1 Year	SIZE CM		NO. CELLS	REAL-TIME		PLAYBACK	POWER Watts		FREQ MHz	TOTAL	EXPERIM
OSO-1 Sun Center	20	40	120	10	1x2	1872	28	9	100 (3)	1530 (3)	0.6	0.2	136	10	4
OSO-2 Sun Center Large Raster (40x40) (2)	10	10	12	6	1x2	1966	36	11	400	7200	2.4	0.5	136	70	36
OSO-3 Sun Center	5	7	20	10	1x2	2016	40	13	400	7200	2.4	0.5	136	94	56
OSO-4 Sun Center Large Raster (39x40)	4	5	10	3	1x2	2016	40	13	400	7200	2.4	0.5	136	140	106
OSO-5 Sun Center Large Raster (40x42)	3	18	30	3	2x2	960	40	13	800	14400	4.8	0.7	136	155	112
OSO-6 Sun Center Large Raster (45x44) Offset Point Small Raster (7x7)	2	3	6	12	2x2	960	40	15	800	14400	4.8	0.7	136	206	108
OSO-7 Sun Center Large Raster (60x60) Offset Point Small Raster (5x5) Az Night Point	1.5	2.0-3.0	3	3	2x5	900	97	30	800	14400	5.2	0.7	136	282	166

(1) Accuracy in Arc Sec (2) Raster scan in Arc Min (3) Equivalent BPS (OSO-1 has FM system) (4) P/N OSO-1; N/P All Others

Table 1-4  
OSO-6/7 WEIGHT BREAKDOWN (KG)

	STRUCTURE	EXPERIMENTS	ELECTRICAL POWER	STABILITY AND CONTROL	BALANCE WTS AND MAGNETS	TELEMETRY AND COMMAND	EXPENDABLES	WIRING HARNESS	SPACECRAFT TOTAL
OSO-6	57.5 Wheel - 46.2 Sail - 11.3	100 Wheel - 60 Sail - 40	20.0	38.3	17.5	26	3.7 (N <sub>2</sub> )	25	288
OSO-7	124.4 Wheel - 79.2 Sail - 45.2	208 Wheel - 124 Sail - 84	31.2	80	105	52	8.6 (N <sub>2</sub> )	30.8	640





F72-01

#### 1.4 MISSION PERFORMANCE

After one year in orbit, all spacecraft systems are operating normally except for one of the redundant tape recorders which was damaged during the launch sequence. This section gives brief descriptions of the performance of spacecraft subsystems.

##### 1.4.1 Spin Axis Orientation

The observatory spin axis was initially oriented near the south ecliptic pole for several weeks. The spacecraft was then rolled with the magnetic torquing coils to move the spin axis direction to the north galactic pole by mid-December. For the next few months, the spin axis remained in the north ecliptic hemisphere.

##### 1.4.2 Control System Performance

The spin control system has operated normally. After the initial launch sequence, the spin gas supply pressure was 1540 psi. (About half of the initial quantity of gas was used in recovery from the tumbling orbit injection.) The pressure declined 450 psi while compensating the spin rate changes caused by the roll maneuver to the North Galactic Pole. Spin rate adjustments have been made both by the on-board control system and manually with the command system link. Both systems functioned properly.

The pitch control system has operated normally. After the initial launch sequence, the pitch gas supply pressure was 2200 psi. (About one-third of the initial quantity of gas was used in recovery from the tumbling injection.) The spin axis roll maneuver to the North Galactic Pole dropped the pressure to about 1950 psi. Since that time, pitch corrections have been made almost entirely with the magnetic torquing system. Both manual and automatic pitch bursts were used, both systems functioning properly.

The sum of nutation and wobble motions of the spin axis is less than 3 arc-minutes. Nutation amplitude declines to less than 1 arc-minute in a few minutes after raster mode changes cause as much as 18 arc-minute amplitudes. Therefore, the accuracy of the pre-launch balance process and the effectiveness of the passive nutation damper are excellent.

The biaxial solar pointing control system is working well. The combined jitter and one-orbit drift have been within one to two arc seconds. The effects of earth light disturbance on the sun sensors at dawn and dusk is clearly discernible, but amounts to little more than the random drift and jitter effects during the orbit. No changes in shaft torques have been noted, indicating that bearings, slip rings, and torque motors are not degrading. The large raster, small raster, and offset pointing modes are all working well.

A minor difficulty has been experienced with the vernier bit in the raster offset system. This feature offsets alternate large raster patterns to effectively double the raster resolution. Occasionally the raster offset intended does not occur, producing the effect of reducing the offset indexing resolution from 0.3 arc-minute to 0.6 arc-minute.



F72-01

The gyro system, which orients the despun solar platform inertially, has performed in a satisfactory manner. After on-orbit determination and command adjustment of the proper setting for the gyro internal heater and corresponding gain setting, the gyro offset and drift was calculated using the star scanner data. After command adjustment of drift compensation, the drift was less than 0.1 degree per hour. The star scanner, used to determine the observatory spin axis attitude and instantaneous position of the rotating wheel, has performed well, attitude determinations being made to about 3 arc-minute accuracies. The South American anomaly region radiation causes errors in the star scanner, but does not damage the device and recovery is rapid, taking only a few seconds after leaving the region.

#### 1.4.3 Power System

The power system has performed as expected with no measurable degradation. Operational methods were developed for command adjustments to keep dummy loads trimmed to limit battery charge rate at a level which prevents battery cell string unbalance; a level just sufficient to allow full charge to be reached at the end of the orbit day. Battery voltage is kept between 17.3 and 19.8 volts by this procedure. Solar array output and operating temperatures agree closely with predicted values. No array temperatures over 60°C have been observed, and the orbit noon temperatures have consistently been less than 55°C.

#### 1.4.4 Communications System

The data handling and telemetry system functions normally. The surviving tape recorder has been operated continuously with no evidence of degradation. The most probable end of continuous scientific data acquisition will be due to loss of the remaining recorder. The recorder has operated beyond the one year in orbit design criteria, and it is probable that considerable further life will be realized. Much useful data can still be received after the tape recorder dies, since real-time data can be acquired at all the STADAN ground stations.

The command system has performed well with 99.1 percent of all intended commands being executed. One reason for some of the lost commands is attempts at commanding when the observatory is below 10 degrees elevation angle. However, some commands have been lost with the observatory in very favorable position. Even though this loss is small, it has caused inconvenience to experimenters requiring sequences to set up experiment modes.

Of equal significance to the high intentional command success ratio is the fact that the command system has not allowed or created a single unintentional or spurious command. The improvements made on OSO-7 in command security have been 100 percent successful. Command and telemetry signal strengths have been nominally as expected, and there have been no problems with data acquisition.



F72-01

#### 1.4.5 Thermal Control

The passive thermal control techniques used on all previous OSO's were continued on OSO-7. Almost all monitored temperatures have been within predicted ranges. A few minor variations from prediction have been measured, but all operating temperatures have been within the temperature ranges used for testing. One of the most important temperatures, relative to orbit operation, is that of the solar array. The solar array output is a quite critical function of temperature. Therefore, accurate pre-launch prediction of array operating temperature is essential. The temperature of the solar array has been as predicted, providing power output within about 1 percent of the predicted value.

#### 1.4.6 Launch Sequence

Ordinarily, the launch sequence "system" is of little interest after launch for the Delta vehicle due to its excellent performance record. For the OSO-7 observatory launch, however, the booster system misbehaved and created an interesting situation for the spacecraft. During the normal launch sequence, the solid motors are jettisoned, and the second stage separates and ignites. Then the fairing is jettisoned and the OSO sail section is spun up to provide angular momentum for stabilization when the observatory is later separated in orbit. After second stage engine shutdown, the second stage and observatory coast to orbit altitude.

When orbit altitude is reached, the second stage engine is restarted to give the observatory the necessary orbit injection velocity. After second stage engine cutoff, the observatory is separated. After separation, the spinning sail begins to slow down as it acquires the sun, transferring the sail stored angular momentum to the wheel. At the same time, the spin gas system adds angular momentum to the wheel so that the wheel spin rate reaches that desired for orbital operation.

If the sail or the wheel does not spin up automatically, recovery from either of these anomalies can be made by ground command. The observatory can be made to acquire the sun from any angle to the sun and from any initial spin rate.

The OSO-7 launch was completely normal up to and including second stage restart. After second stage restart, the booster lost steering control and tumbled end over end at about 55 rpm. The centrifugal force on the spacecraft bearings increased bearing friction and the spinning sail quickly slowed and stopped. The observatory was then separated in this condition, but fortunately with sufficient velocity and in a direction to achieve a useful orbit. The angular momentum vector with the spacecraft tumbling was perpendicular to the normal spacecraft spin axis.

The details of recovery from this situation are given in Section 2. In summary, the spacecraft stabilized itself initially in about an hour and was then spinning about its proper spin axis at about 56 rpm with the spin axis about 71 degrees away from perpendicular to the sun line. The spacecraft sail was stopped by using the gyro, which allowed the pitch system to be used to precess the spin axis to the sun. This took several orbits, due to the limited real-time access to the spacecraft data and command link over ground stations.



F72-01

The stored battery energy was very nearly depleted just as the pitch maneuvers got the spin axis close enough to perpendicular to the sunline so that automatic control could be assumed by the observatory and battery charging could be started. If a quite comprehensive contingency plan had not been prepared and practiced prior to launch, it is unlikely that the observatory could have been extricated from the difficulties caused by the tumbling orbit injection.



F72-01

Section 2  
HARDWARE PERFORMANCE

2.1 IN-ORBIT OPERATION

The status of the OSO-7 spacecraft after 9 months in orbit is as follows: All spacecraft subsystems are operative except the redundant tape recorder which was damaged by the tumbling vehicle. Minor difficulties have been encountered with the vernier offset bit in the raster offset system, evidenced by a small shift in the indexing of the raster and offset point grids. These defects have been eliminated by avoiding the use of the vernier bit. This limits the resolution of the commandable offset indexing to about 0.6 arc-minutes instead of 0.3 arc-minutes.

2.1.1 General Long-Term Performance

The spin axis of the spacecraft was pointing almost directly at the south ecliptic pole after the initial launch acquisition, somewhat different than would have been the attitude with a normal launch sequence.

As shown in Figure 2-1, the spin axis remained pointed near the south ecliptic pole for several weeks. Then the spacecraft was caused to drift in roll so the spin axis was oriented to the north galactic pole by December 18th. This roll maneuver was achieved by using the roll magnetic torquing coils. The use of these coils also applied spin torques and spin gas was consumed in maintaining the wheel spin rate within the automatic control limits.

The wheel spin rate and the spin gas pressure history are shown in Figure 2-2. At the end of the initial launch sequence, the spin gas pressure was about 1540 psi. Another 450 psi of gas was used in the roll maneuver to the north galactic pole. Virtually no spin gas has been used since this maneuver was completed.

Spin rate corrections were made using both manual spin control via the command system and by the automatic on-board spin rate control system. Both systems function properly.

The pitch attitude of the spacecraft has been controlled almost exclusively by magnetic torquing using the pitch coil. The coil status, the corresponding pitch angle, and the pitch gas pressure are shown in Figure 2-3. Both manual and automatic pitch bursts were used to keep the pitch angle within  $\pm 3$  degrees. Use of the pitch coil was somewhat restricted during the roll maneuvers, since it also exerts roll torques, and to increase the rate of roll correction, pitch gas was used instead of magnetic torquing.

Figure 2-4 shows the spacecraft bus voltage, load current, and solar array current. The points on these plots, as are all the long-term data points, are taken at noon in each orbit. Variations in the loading, solar intensity, solar array temperature, and battery state-of-charge cause scatter in the power system data.



F72-01

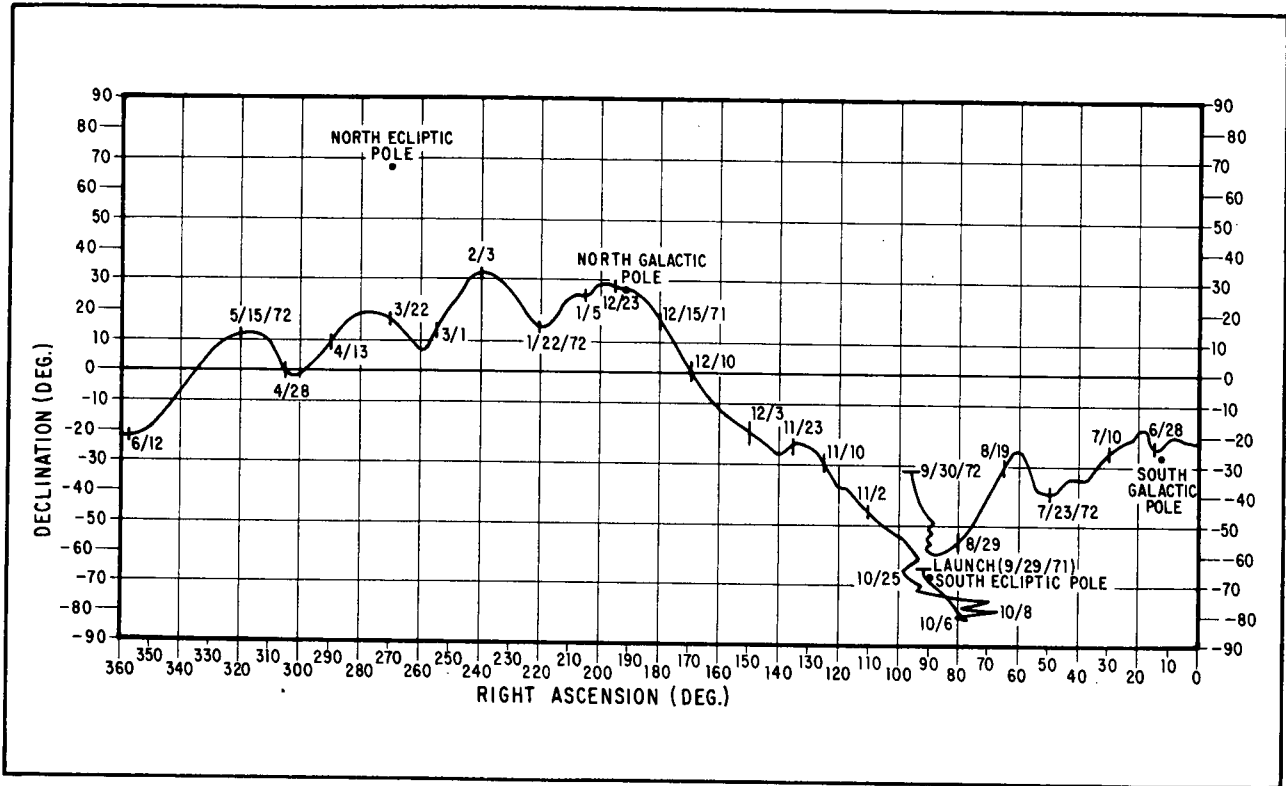


Figure 2-1 Attitude History, Spacecraft Spin Axis

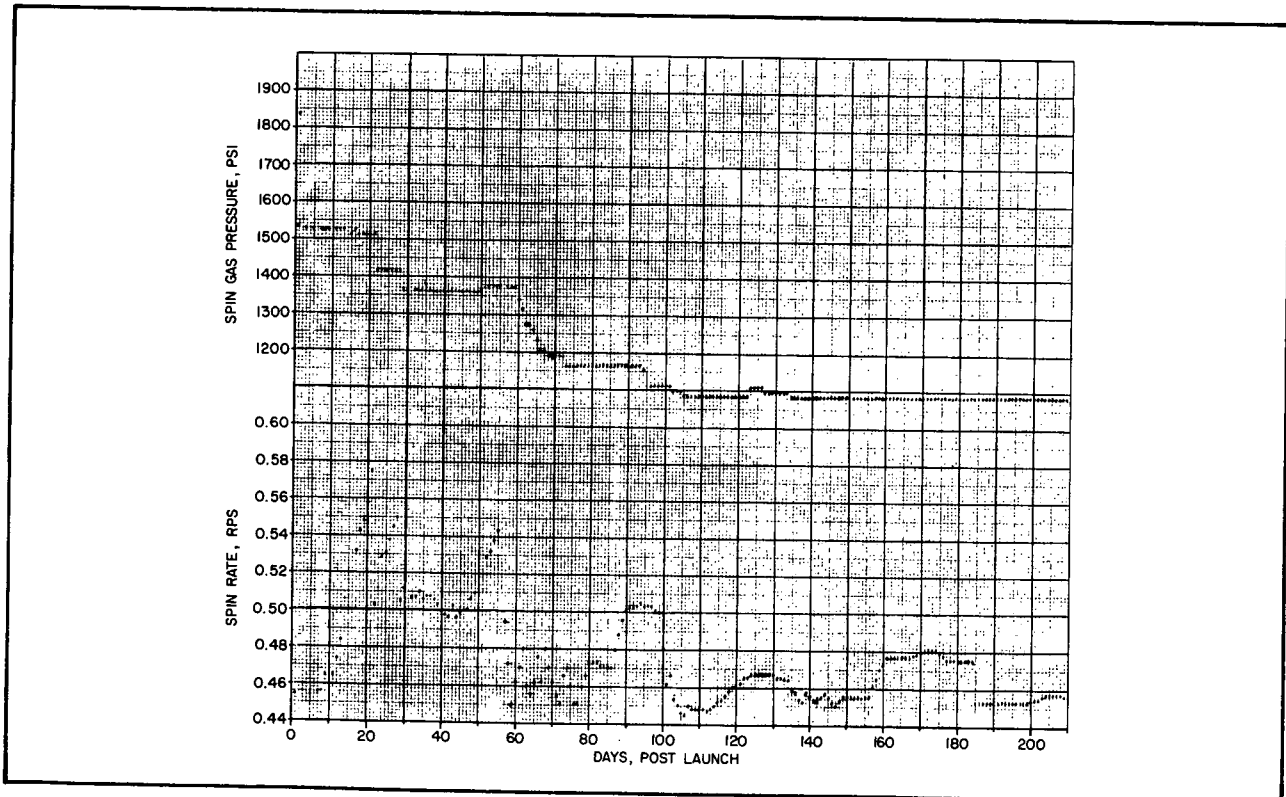


Figure 2-2 Wheel Spin Rate and Spin Gas Pressure History



F72-01

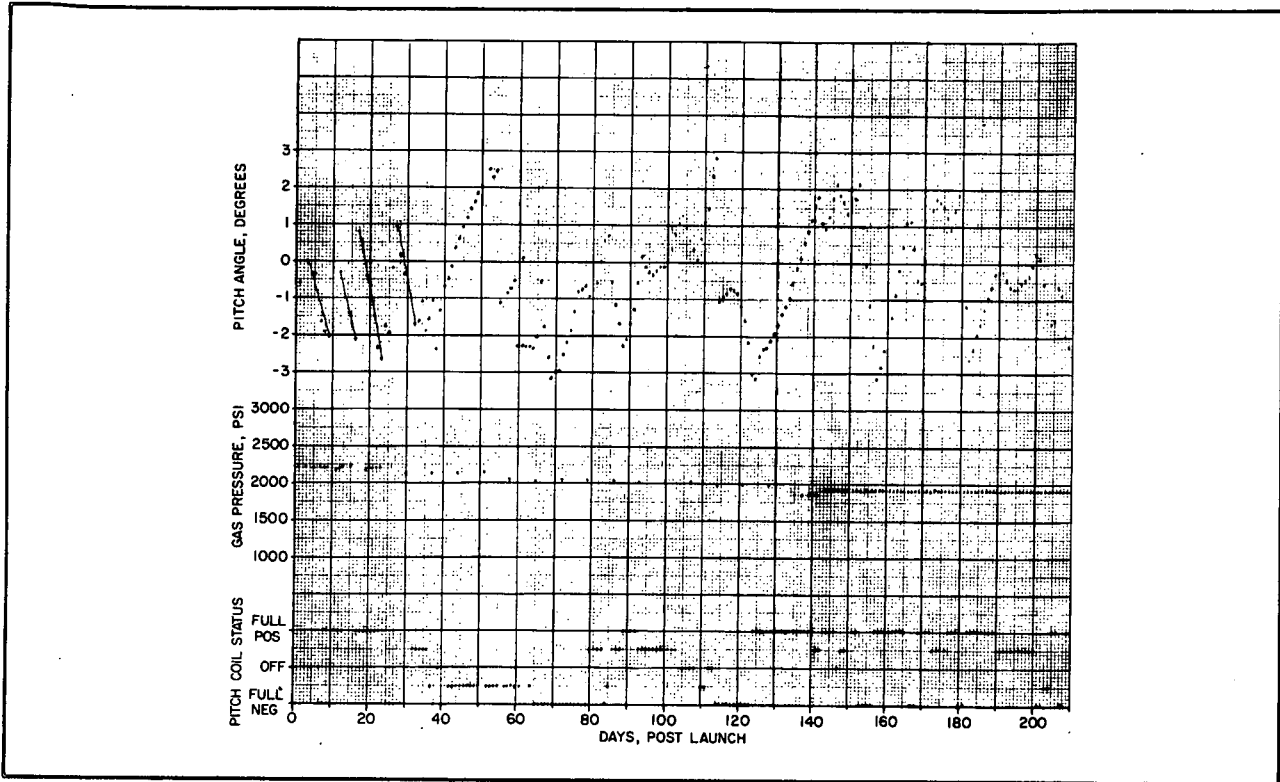


Figure 2-3 Pitch Attitude, Pitch Coil Status, and Pitch Gas Pressure History

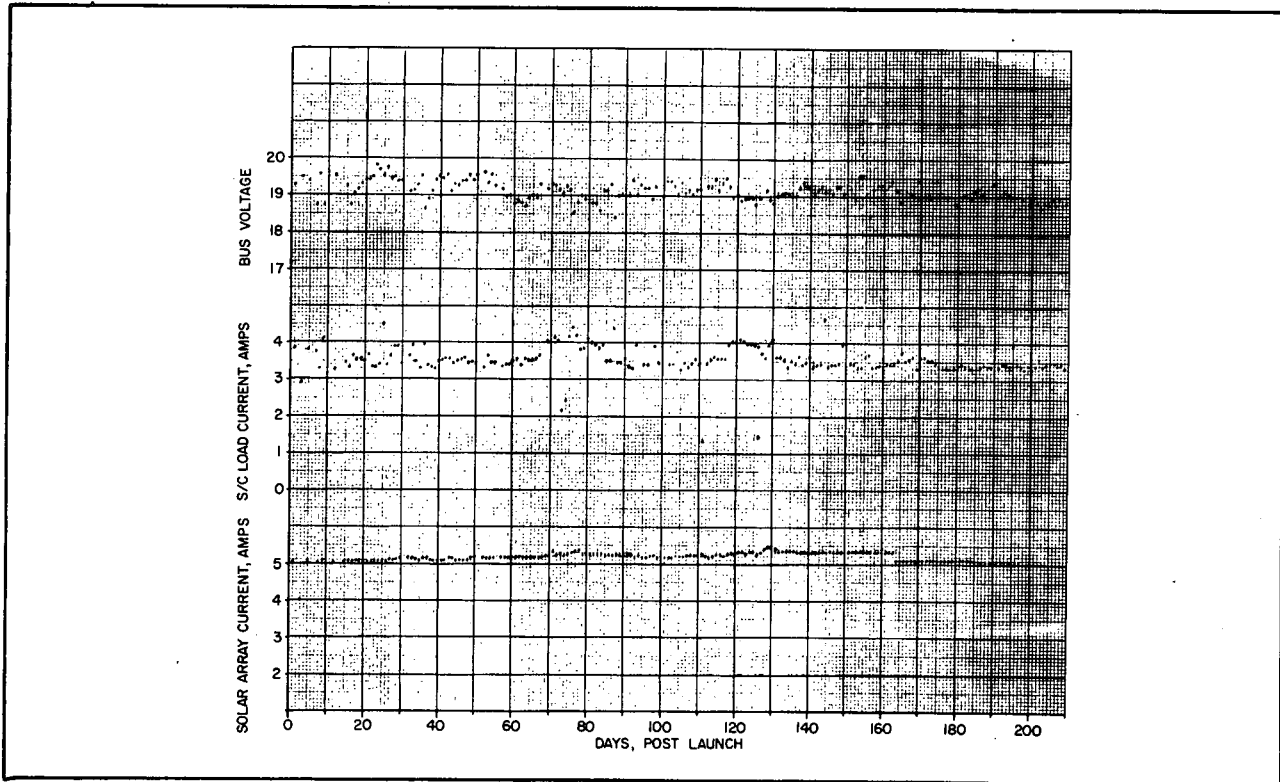


Figure 2-4 Spacecraft Bus Voltage, Load Current, and Solar Array Current History



F72-01

There has been no perceptible degradation in the power system performance over six months in-orbit. Figure 2-5 shows the integrated solar array power for five orbits during the first six months of orbital life. The output of the array, over 75% of the daylight portion of the orbit, is about 97 1/2 watts. These plots have been adjusted for the effects of solar intensity, and the data was taken at times when the roll position of the spacecraft was similar, so that the array temperatures were about the same.

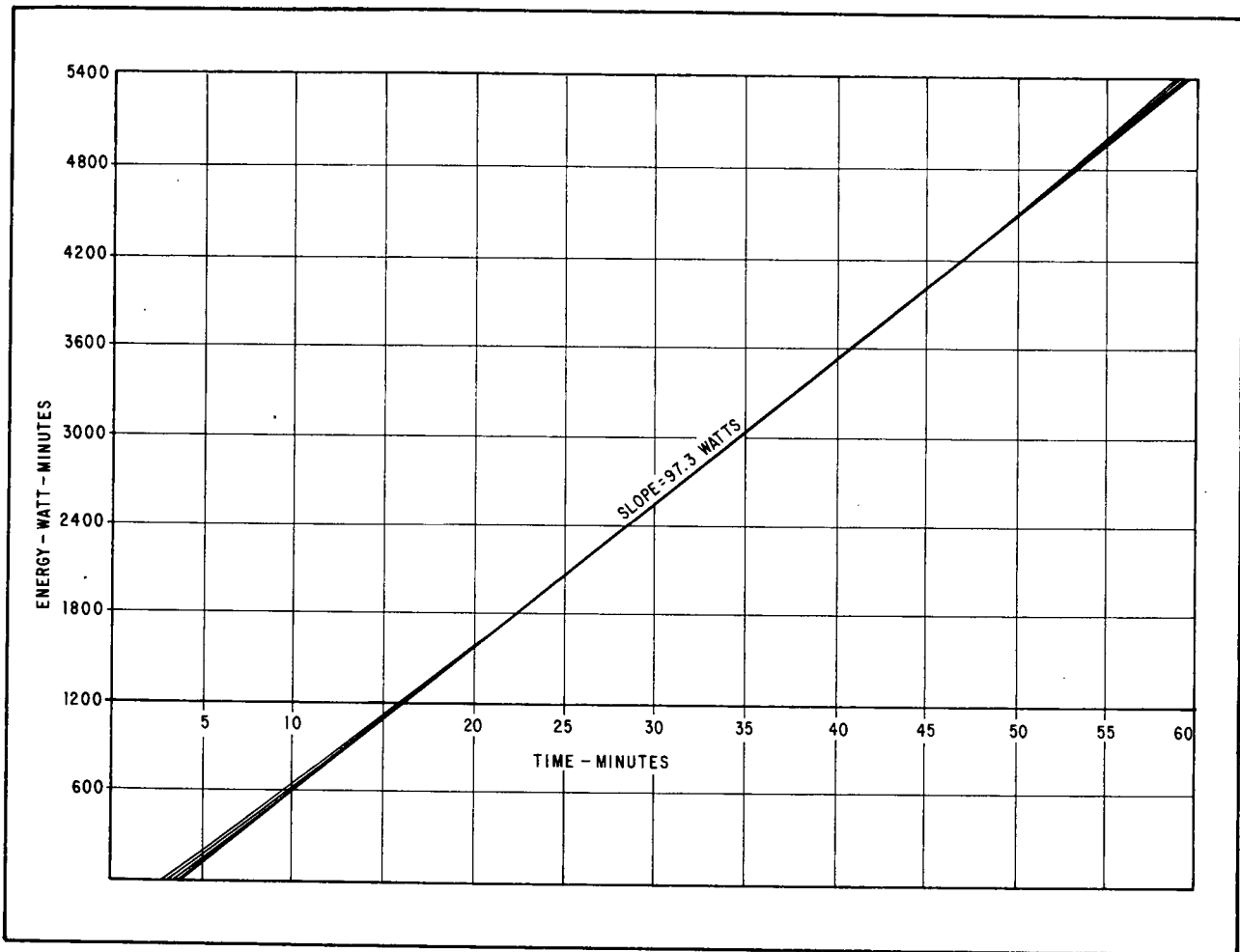


Figure 2-5 Solar Array Energy Developed During Orbit Revolution Nos. 225, 274, 665, 892, 1905

The motor torques on the elevation and azimuth axes have shown little change over the life of the spacecraft as indicated by the noon-time values shown in Figure 2-6.

The solar array temperatures shown in Figure 2-7 are influenced by many factors. The temperature data is scattered because of the length of the orbital day, the roll attitude of the spacecraft, the solar intensity, and the position of the spacecraft relative to earth as affected by the orientation of the orbital plane. No solar array temperatures over 60°C have been observed. The noon-time temperature of the array panels at the point of monitoring is consistently less than 55°C. Temperature profile data is given in Section 2.1.7.





F72-01

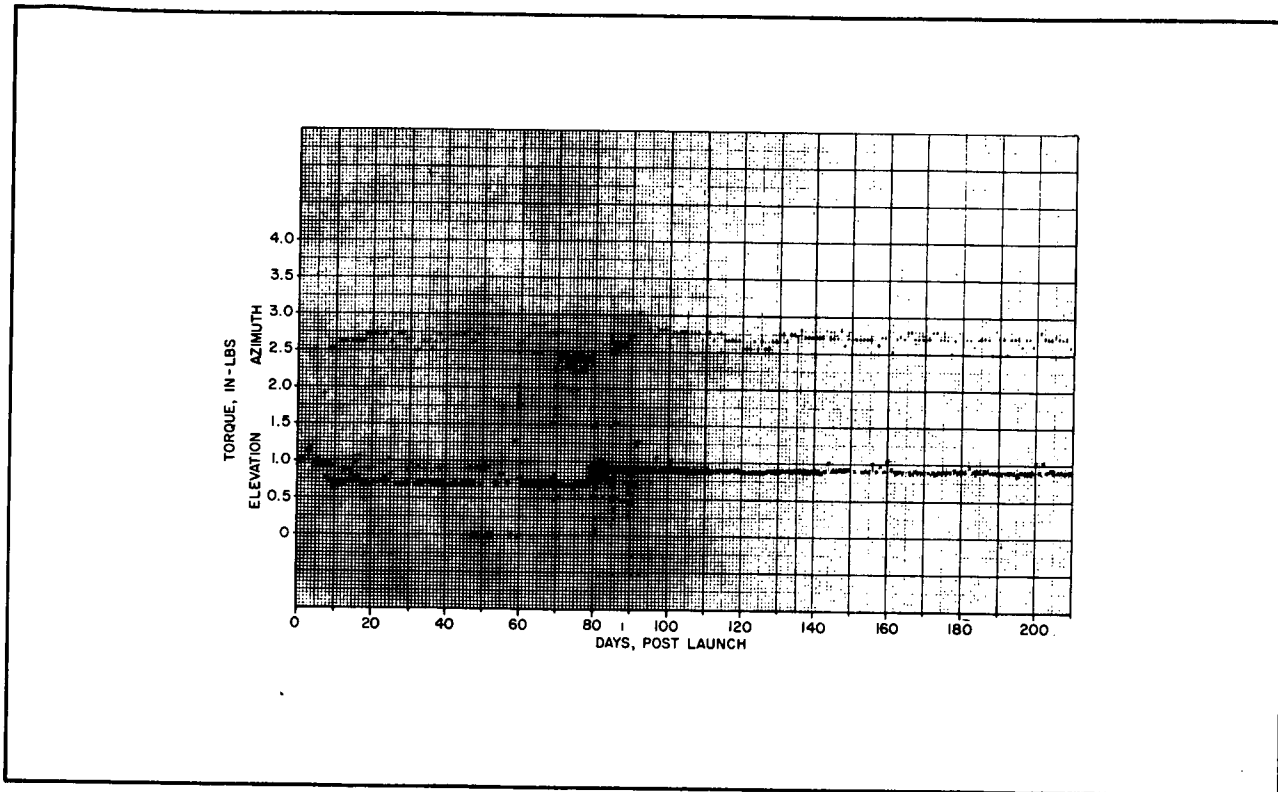


Figure 2-6 Elevation and Azimuth Motor Torque History

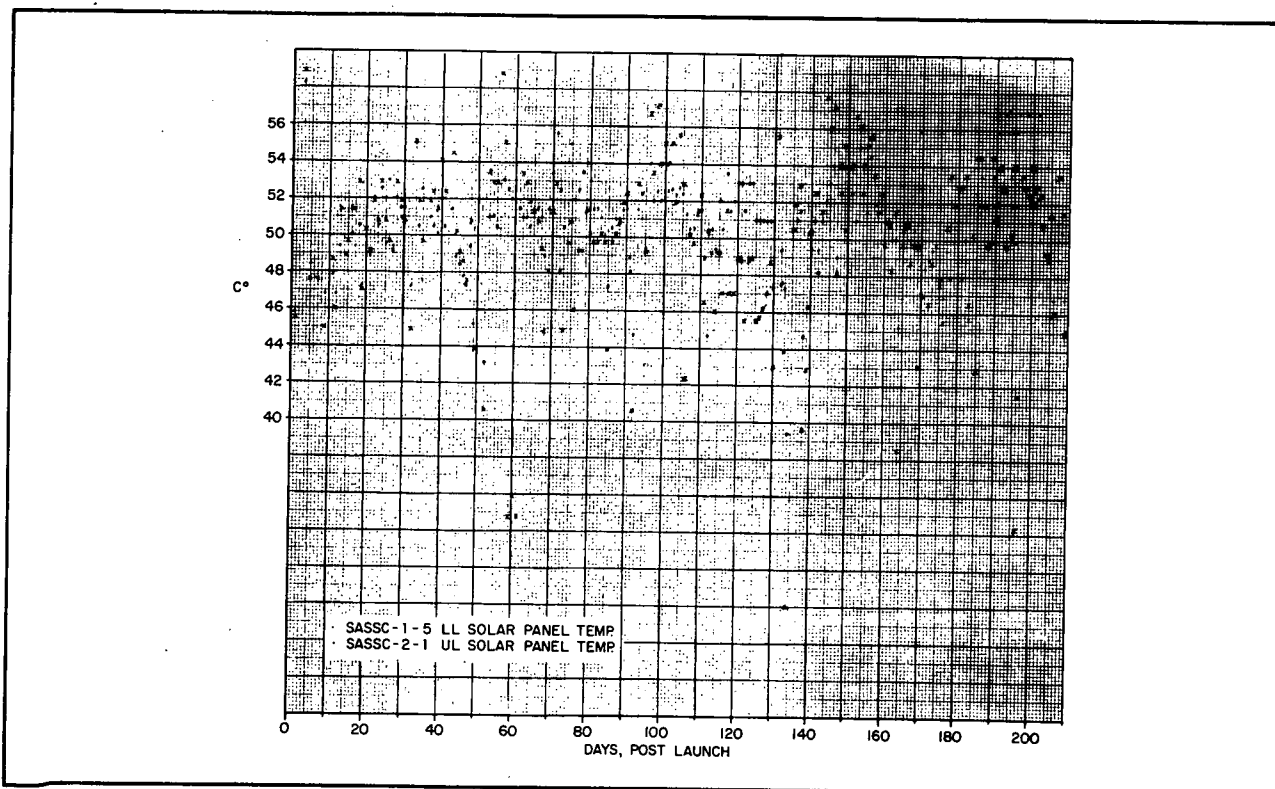


Figure 2-7 Solar Array Temperature History



F72-01

2.1.2 Attitude Control System

Figure 2-8 indicates the behavior of the spin axis as the spacecraft comes into orbit day, and acquires in elevation. During this orbit the spacecraft was in the small raster mode, and the nutation of approximately 0.8 degree peak-to-peak at the beginning of orbit day is caused by the momentum disturbance as the elevation drive moves the pointed instrument assembly off its snubber, overcoming the bias spring, and into pointing position.

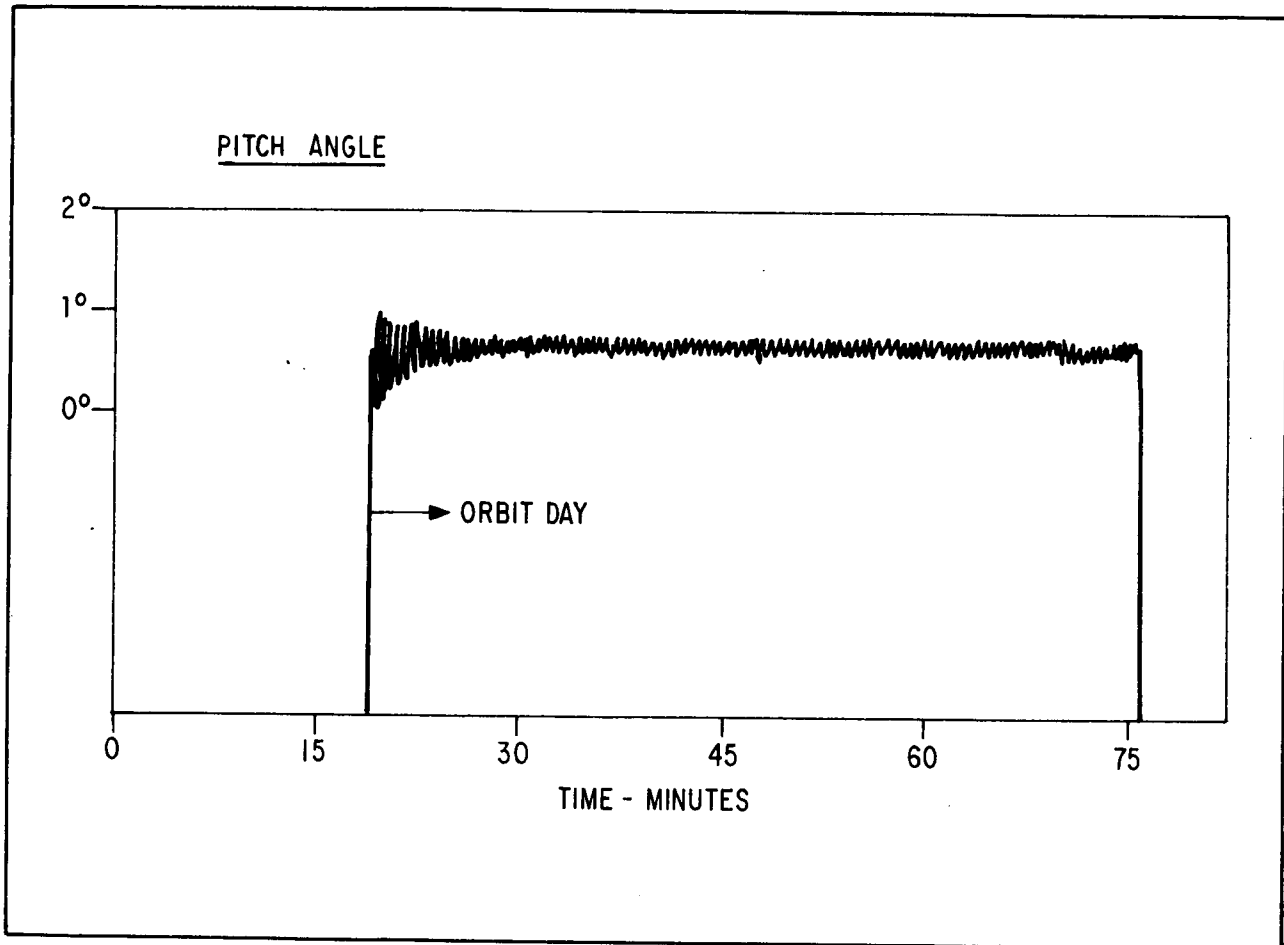


Figure 2-8 Spin-Axis (Pitch) Motion After Dawn Acquisition (Gyro Control During Night-Orbit Revolution No. 968)

In Figure 2-9 the spacecraft was in the small raster mode for approximately 1/4th of the orbit, then changed to a large raster mode. This caused an increase in the nutational amplitude as the instrument was reindexed to begin the large raster.

The remaining part of the orbit with the spacecraft in the large raster mode, demonstrates that the movement accompanying large raster retrace has negligible effect on the nutation amplitude. The residual spin axis motion of about 0.1 degree peak-to-peak is caused by misalignment of about 3 arc-minutes between the inertial axis of the wheel and the azimuth bearing axis. This is an indication of the accuracy with which the spacecraft was aligned and dynamically balanced.



F72-01

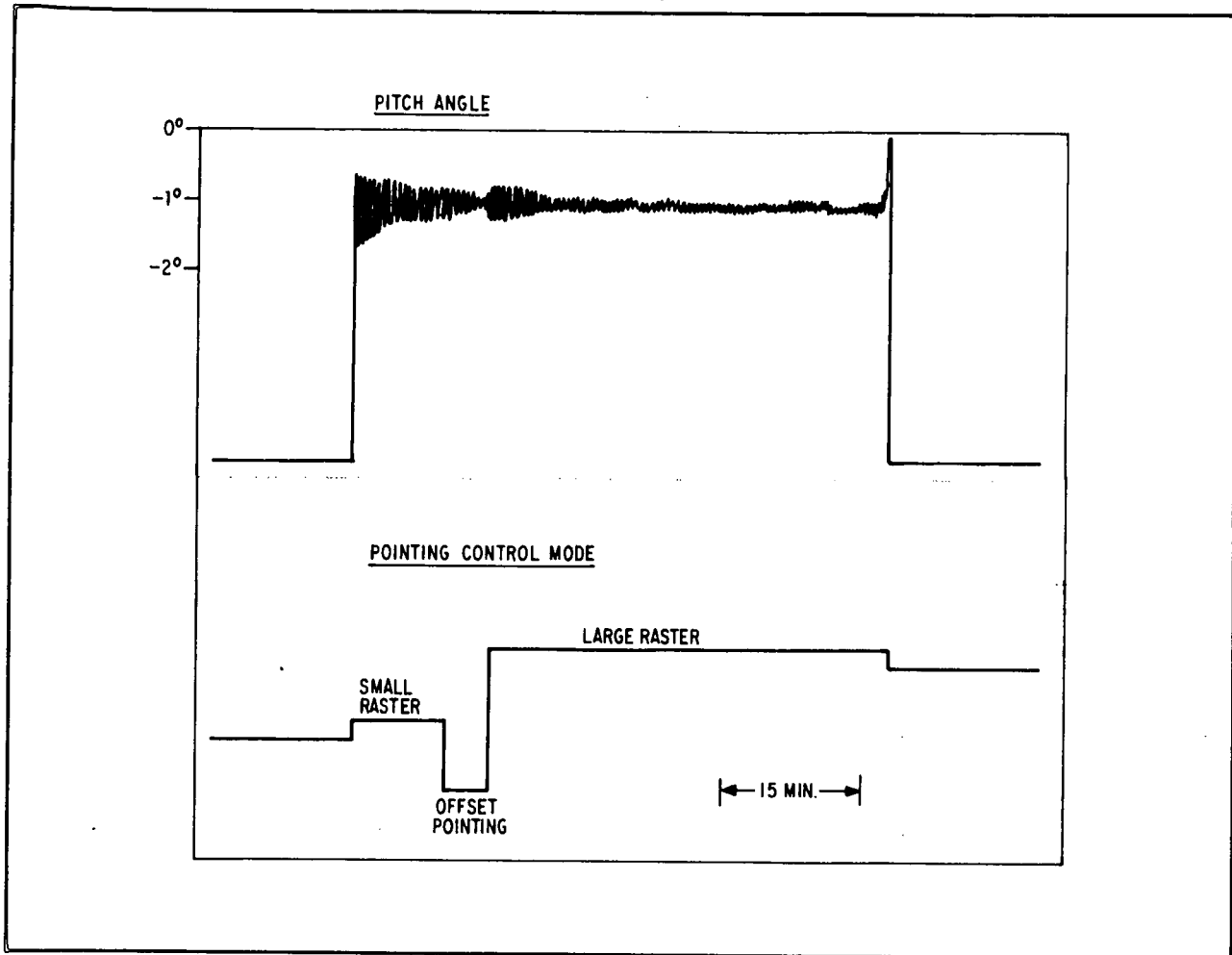


Figure 2-9 Pitch Motion During Changes in Pointing Modes - Orbit Revolution No. 846

### 2.1.3 Solar Pointing Control System

Figure 2-10 shows telemetry records of the azimuth and elevation fine point sensors. The telemetry system resolution is about 1 1/2 arc-seconds. The jitter amplitude is less than 1 1/2 arc-seconds peak-to-peak.

The pointing control stability in the sun centered mode is about 3 arc-seconds peak-to-peak, including medium-term drift over 90% of the orbit day. For a few minutes at the beginning and end of an orbit day, there is about 6 arc-seconds of shift, as scattered light from the earth enters the control eyes.

Table 2-1 lists the misalignment of the readout eyes and the pointed instruments relative to the control system null points. The pointed instrument axes were determined by examination of in-orbit data generated by the instrument detectors, as the pointing control scanned features of the sun. Instrument alignment errors were essentially removed by the data reduction process which reconstructs the instrument raster in coordinates referenced to the limb of the sun.



F72-01

The spacecraft has been operated in the center point mode very little, and therefore, the offset indexing and raster data reduction has been done principally with respect to the optical axes of the pointed instruments.

2.1.4 Gyro Performance

The gain and drift of the gyro is dependent on the temperature of the gyro. This temperature is automatically controlled by an internal heater with command-selectable threshold levels. The gain of the gyro may be adjusted by ground command to achieve the proper system gain for the overall azimuth control loop.

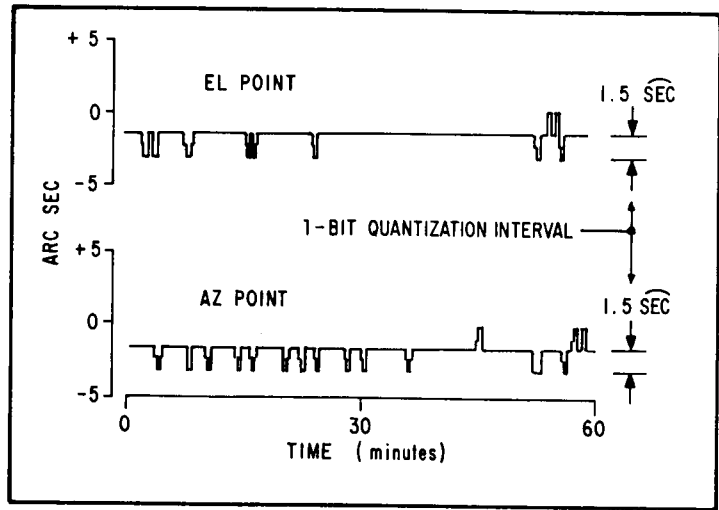


Figure 2-10 Pointing Control Performance Read-Out Sensor Output - Orbit Revolution No. 75

Table 2-1  
POINTING ALIGNMENT RASTER

	<u>Control Eyes</u>	<u>Fine Readout Eyes</u>	<u>Raster Readout Eyes</u>	<u>NRL</u>	<u>GSFC</u>
Azimuth	0	+(L)13 arc-sec	-(R)0.9 arc-min		+(R)0.5 arc-min
Elevation	0	-(D)12 arc-sec	-0.1 arc-min		+(U)0.1 arc-min

The initial on-orbit checkout of the gyro system was directed at determining the proper setting for the internal heater and the corresponding gain setting for the gyro to achieve drift-free and accurate control by the gyro. The gyro is also equipped with drift and offset compensation to permit the removal of steady-state bias errors or to buck out the drift components.

The heater set point was determined experimentally during Orbit 24 and again in Orbits 135, 142 and 155. This was done by observing the temperature range of the gyro at different set points of the heater. From this data, a gyro temperature was selected for which the performance was predictable and satisfactory.

Initial in-orbit adjustments in the gyro drift and offset compensation were made by observing the readout of the scan readout eyes with the gyro operating during the day. Later, the gyro offset and drift was calculated by comparing the inertial position of the pointed instruments relative to the stars as measured by the azimuth shaft blipper and the star scanner.

Figure 2-11 shows early gyro drift data obtained over a 30 minute period during Orbit 225. The drift was about 0.23°/hr. Subsequently, command adjustment of the drift compensation reduced drift to less than 0.1°/hr.



F72-01

2.1.5 Attitude Determination-  
Star Scanner Performance

The star scanner permits determination of the spacecraft spin axis attitude and the instantaneous look angle of the rotating wheel experiments to within  $0.1^\circ$  in inertial space. This is made possible by statistically processing the star scanner intercept data and comparison with a catalog of known star locations.

The principal on-orbit adjustment of the star scanner involved the experimental determination of a gain setting for the star scanner which yielded a sufficient number of intercepts, but was low enough so that false triggering did not occur. Figure 2-12

shows the results of in-orbit operations compared with the predicted values for sensitivity to various star magnitudes.

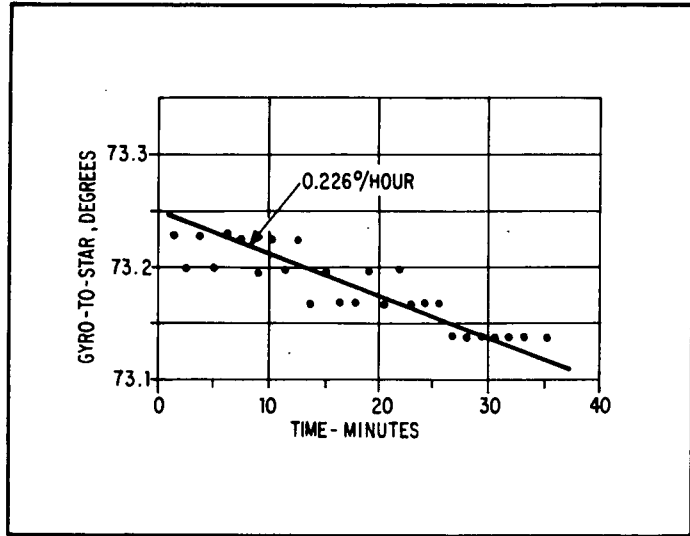


Figure 2-11 Typical Gyro Azimuth Drift (Orbit Revolution No. 225) Measured Relative to Stars Observed by Star Scanner

During the early weeks of operation, various improvements were made in the data reduction program to increase the accuracy and accommodate the data generated by the star scanner in-orbit. Figure 2-13 shows the data processing statistics for a typical orbit. The same data was processed first by the data processing routine developed before launch and again by an improved routine.

The roll covariance plotted in the bottom chart of Figure 2-13 is indicative of the residual error in the attitude, calculated by matching the star sighting data with the star catalog. This residual error does not include random errors introduced by the hardware or other portions of the data reduction. These may add several hundredths of a degree. The overall accuracy of the attitude determination is better than  $0.1$  degree.

Other tests were conducted to determine whether the radiation levels present in the South Atlantic anomaly had any serious effect on the star scanner. While the South Atlantic anomaly evidently causes increased hardware errors while the spacecraft is in the region of high radiation, no apparent permanent damage is done and the recovery is quite rapid after leaving the anomaly.

The star scanner was also operated during the daylight portion of the orbit. Star crossings were observed and the software was able to calculate the vehicle attitude based on a limited number of sightings of brighter stars in the presence of sunlight. The star scanner was not intended to be used during the daylight portion of the orbit and its discrimination may not be adequate for routine operation under these conditions.



F72-01

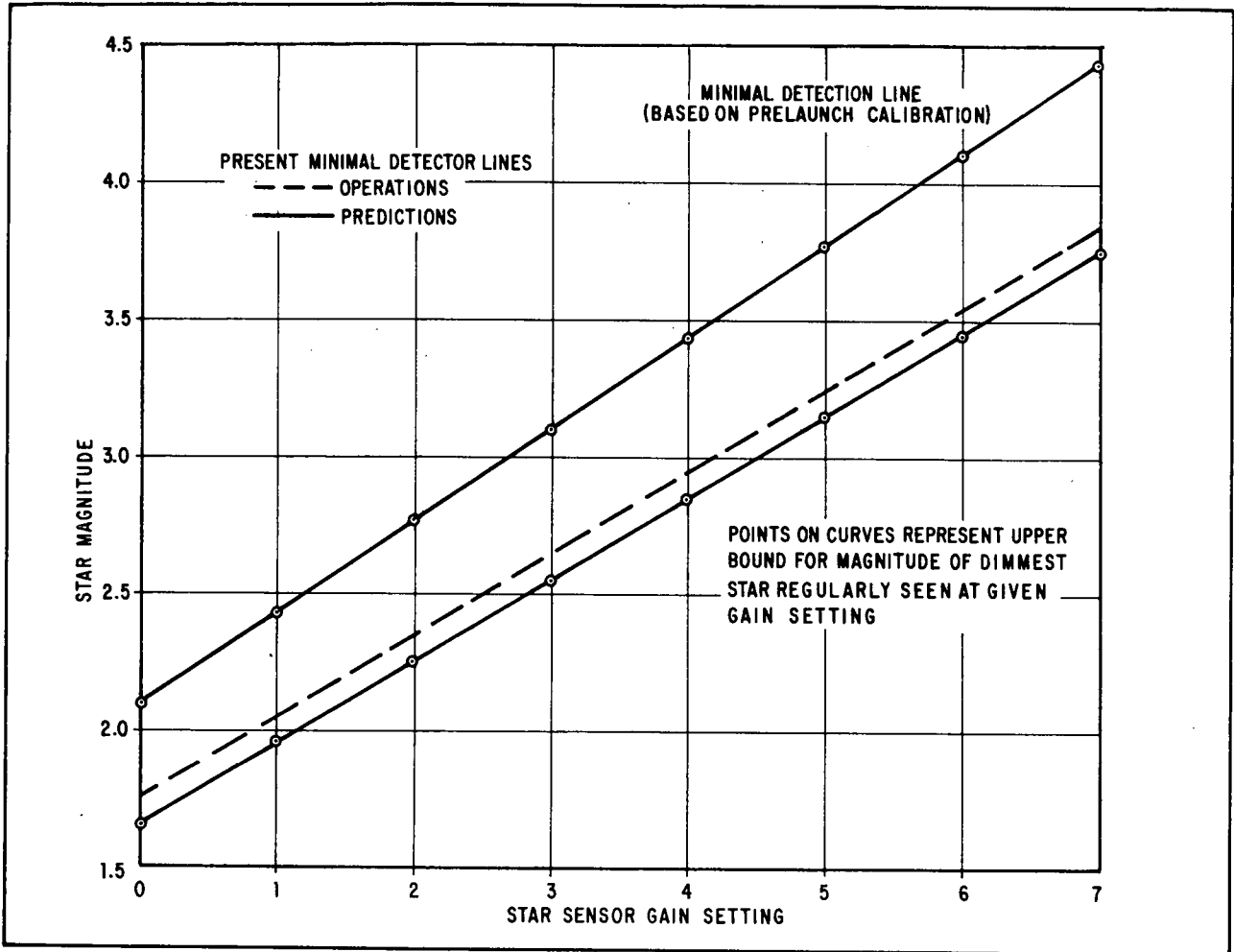


Figure 2-12 Star Scanner Sensitivity

#### 2.1.6 Electrical Power System

During orbital operations, battery charge is controlled by adjusting the dummy loads in the spacecraft or turning off solar array panels by command so that the energy provided to the batteries is just sufficient to enable them to reach full charge at the end of orbit day.

Figure 2-14 shows the battery current and bus voltage for two early orbits. During orbit 76, the batteries became overcharged before the end of orbit day, as indicated by the bus voltage increase. During orbit 318, the battery charge was held normal by disconnecting a solar panel, producing a sharp drop in charge current. Bus voltage remained under 20 at the end of orbit day and above 17.5 through orbit night.

After a few days of orbital operation, methods were developed for trimming the dummy loads so that the bus voltage remained between 17.3 and 19.8 volts. Subsequent operation was satisfactory, as long as major changes in electrical loads were compensated for by adjusting the appropriate dummy loads.



F72-01

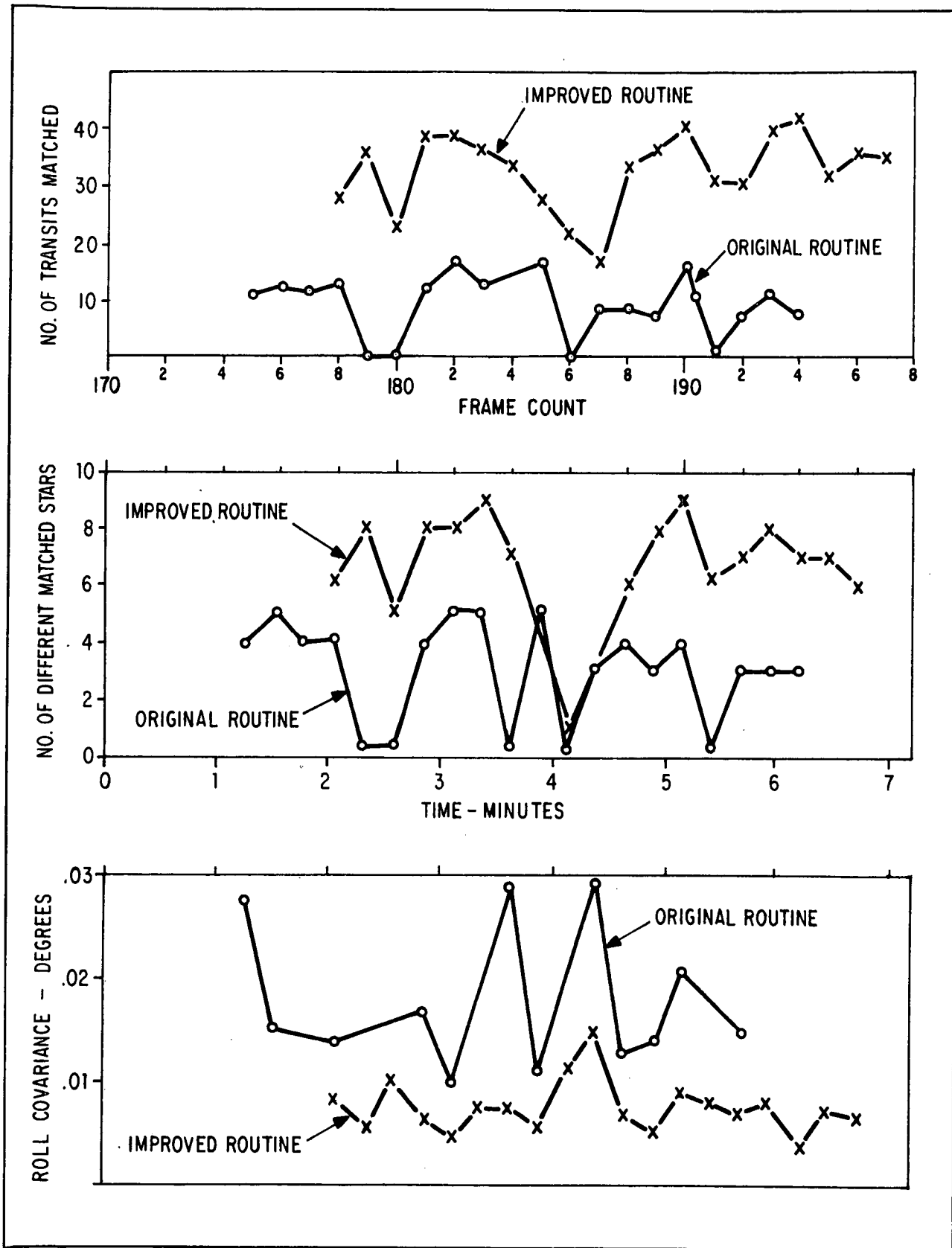


Figure 2-13 Star Sensor Performance During Orbit Revolution No. 271. Comparison of Results Using Original and Improved Data Reduction



F72-01

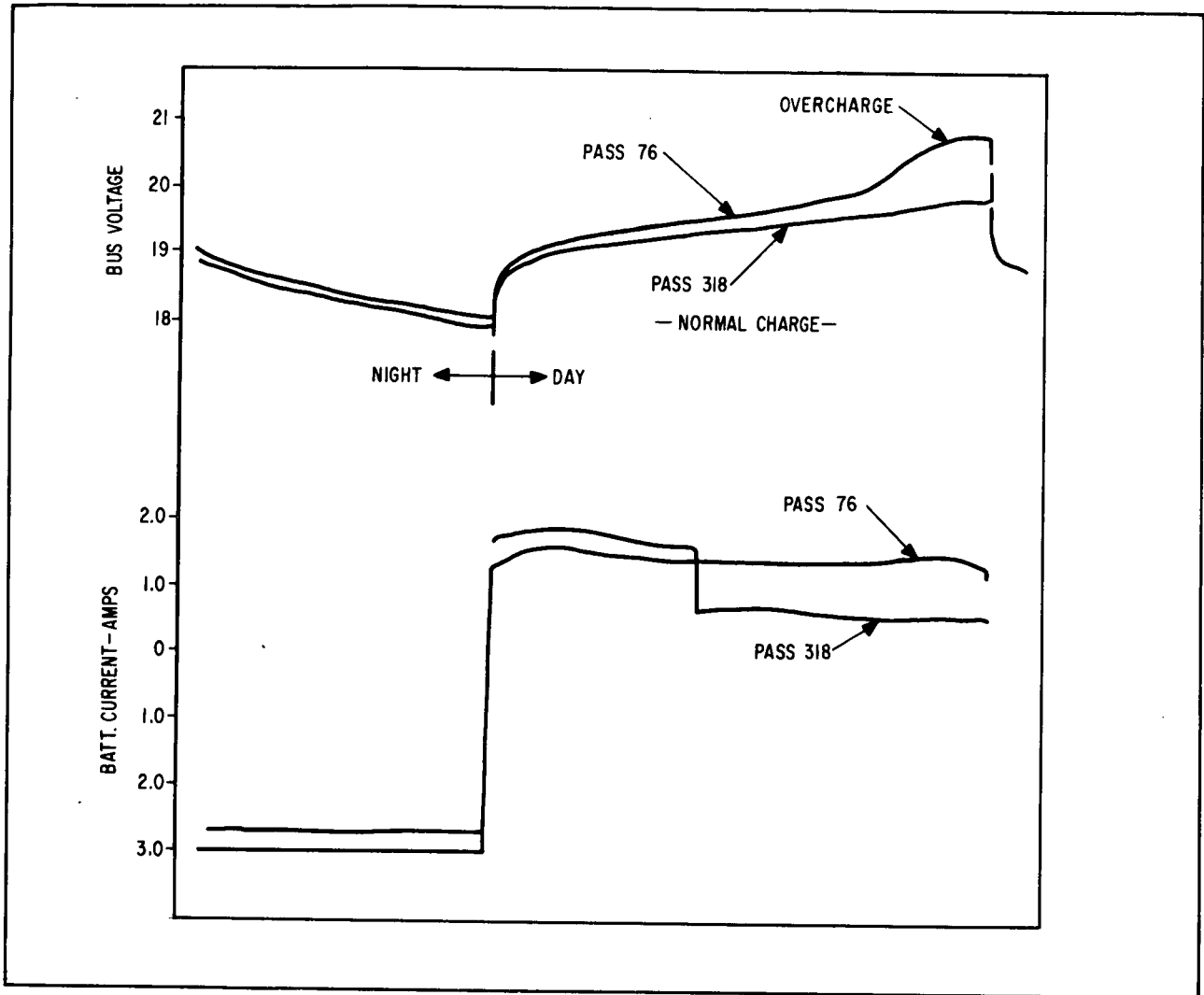


Figure 2-14 Power System Parameters - Normal Profiles (Pars 318) and Overcharge Condition (Pars 76)

One other effect which became apparent during and after periods of overcharge was that the cell balance monitor indicated some unbalance in the strings of battery cells. Usually this effect was not permanent and when the power system was returned to normal operation, the monitors again indicated a balanced condition.

Some unbalance still remained in battery string No. 4. Therefore, this battery string was removed from the system for several weeks, and only reconnected for periodic charging. Subsequently, its unbalance decreased and it was returned to service with no ill effects.

#### 2.1.7 Thermal Control System

Table 2-2 compares the flight temperatures for Orbit No. 77 with the analytical predictions. The average temperatures of all observatory wheel components are within 5°C of the predicted values.





F72-01

Table 2-2  
 PREDICTED FLIGHT TEMPERATURES AND ORBIT NO. 77 FLIGHT DATA

Node	Name	Temperature, °C					
		Prediction			Flight Data		
		Max	Nom	Min	Max	Nom	Min
1	Despin Drive	17.3	17.1	17.0	18.5	18.4	18.0
	Despin Drive	17.3	17.1	17.0	16.2	16.2	16.2
4	Wheel Hub	13.3	12.9	12.6	12.5	12.2	11.3
27	Spin Gas Bottle	12.3	12.3	12.2	13.2	11.7	12.5
78	Rib Comp No. 7	12.9	12.2	11.5	14.1	12.5	10.9
103	Upper Left Solar Panel	67.8	38.4	-28.3	52.9	28.9	-21.3
105	Lower Left Solar Panel	63.8	43.5	1.2	57.2	36.8	3.7
112	Left Trunnion	20.6	19.8	19.0	20.4	19.4	18.1
134	Sail Analog Subcommutator	8.9	2.6	-4.8	13.0	8.4	1.5
135	Power Amplifier	16.8	15.5	14.0	31.0	29.2	27.0
136	Servo Amplifier	21.4	20.2	18.4	19.6	18.7	17.7
139	NRL (Fore)	18.9	18.1	17.1	---	---	---
	NRL	18.9	18.1	17.1	14.5	13.3	10.8
140	NRL (Mid)	17.6	17.3	16.9	---	---	---
	NRL	17.6	17.3	16.9	---	---	---
	NRL	17.6	17.3	16.9	9.4	9.1	8.2
142	NRL (Eyeblock)	22.7	20.1	16.5	15.0	11.9	8.0
143	GSFC (Fore)	30.0	29.2	28.3	19.0	17.6	15.9
	GSFC	30.0	29.2	28.3	19.0	17.7	16.3
144	GSFC (UV) Slit	28.2	27.9	27.6	16.7	16.3	15.9
	GSFC (Mid)	28.2	27.9	27.6	15.6	15.3	14.8
145	GSFC (Aft)	28.5	28.0	27.6	17.8	15.5	12.9
150	Sail Analog Sub-Subcommutator (Left)	24.5	21.0	17.2	24.9	21.4	17.9
162	GSFC - Thermal Monitor	23.4	21.0	18.3	17.5	15.1	9.2
	GSFC - Thermal Monitor	23.4	21.0	18.3	17.1	13.1	11.3
331	Pitch Gas Bottle (Right Aft)	19.2	15.3	11.2	6.7	3.0	-0.7
505	OIRU (TG Temperature)	44.1	39.5	34.5	43.4	38.7	31.7
506	OIRU Mounting Flange	31.9	25.7	17.1	39.5	32.4	24.2
601	Antenna	12.6	10.6	8.6	15.2	10.6	3.5
1012	Batteries Comp No. 1	14.3	13.8	13.5	15.7	14.9	13.6
3010	MIT (Power Converter)	17.5	16.5	15.6	20.0	20.0	20.0
	MIT (Base Plate)	17.5	16.5	15.6	14.3	13.5	13.0
	MIT (Cal. Actuator)	17.5	16.5	15.6	18.2	16.8	15.2
	MIT (Memory)	17.5	16.5	15.6	20.2	20.2	20.2
	MIT (Lower Detector)	17.5	16.5	15.6	16.8	15.8	15.4
	MIT (Upper Detector)	17.5	16.5	15.6	17.8	17.4	16.7
4000	Deck Compartment No. 4	16.8	16.3	16.0	14.4	14.4	14.4
4001	Cover Compartment No. 4	13.4	12.4	11.6	16.9	12.4	10.2
7000	Deck Compartment No. 7	13.7	13.4	13.1	13.7	13.6	13.0
7003	Rim Compartment No. 7	17.3	11.8	4.5	17.0	13.2	8.2
8010	UCSD-S	10.7	10.3	9.9	14.5	14.1	13.5
9010	UNH (Electronics)	13.8	13.6	13.4	17.4	17.2	16.7
	UNH (Detector)	13.8	13.6	13.4	14.5	14.1	13.8



F72-01

The average temperatures of all but four spacecraft sail components (excluding instruments) are within 5°C of the predicted values.

Other flight data from the hottest orbit No. 1178, with a sun-line to orbit plane angle ( $\beta$ ) of 56.5 degrees shows only two temperature-sensitive components, the sail analog sub-commutator (SASC) and sub-subcommutator (SASSC), that are hotter than their analytically predicted acceptance temperatures (SASC too hot by 5.7°C and SASSC too hot by 2°C). All components perform within their qualification temperature limits as predicted by analysis and Thermal Balance Test.

Figures 2-15 through 2-18 are profile plots of the component temperatures observed during Orbit No. 77. For this orbit, the  $\beta$  was 29° and the solar constant was near the mean value.

#### 2.1.8 Communications System

The data handling and telemetry system continues to function normally after 12 months in-orbit. The single surviving tape recorder has been operated continuously, with no evidence of degradation.

Command Execution. As of 1 October 1972, after twelve months in orbit, 120,503 commands had been transmitted. The length-of-pass time for sending commands is somewhat reduced when orbital perigee occurs over a ground station; in some cases, to lengthen the pass time, commands have been transmitted at elevation angles less than 10 degrees.

Of the 120,503 commands transmitted, all but 1210, or 99.0 percent were executed. A total of 156 of the 1210 missed commands occurred at low elevation angles. At normal elevation angles, 99.1 percent of the commands were successfully executed. There has been no evidence of commands executed which were not transmitted (spurious command response).

Data Recovery. During the first year of orbital operation, all but about 2.3 percent (190 hours) of the data were recovered. The main cause of lost data was the absence of the Lima, Peru station which left a gap in the data recovery pattern. If both spacecraft tape recorders had been operable, this difficulty would have been circumvented by using the recorders in the serial record mode.

About 13 hours of data (0.1 percent) were lost due to communications difficulties, operator errors, and conflict with higher priority activities.

#### 2.2 LAUNCH PHASE PERFORMANCE

Final prelaunch preparations took place on the morning of September 28, 1971, and the vehicle was prepared for a liftoff at 0945 GMT. Data from the spacecraft was received at the Orbiting Solar Observatory Operation Control Center (OSO OCC) prior to liftoff; the status of the spacecraft was as listed in Table 2-3.



F72-01

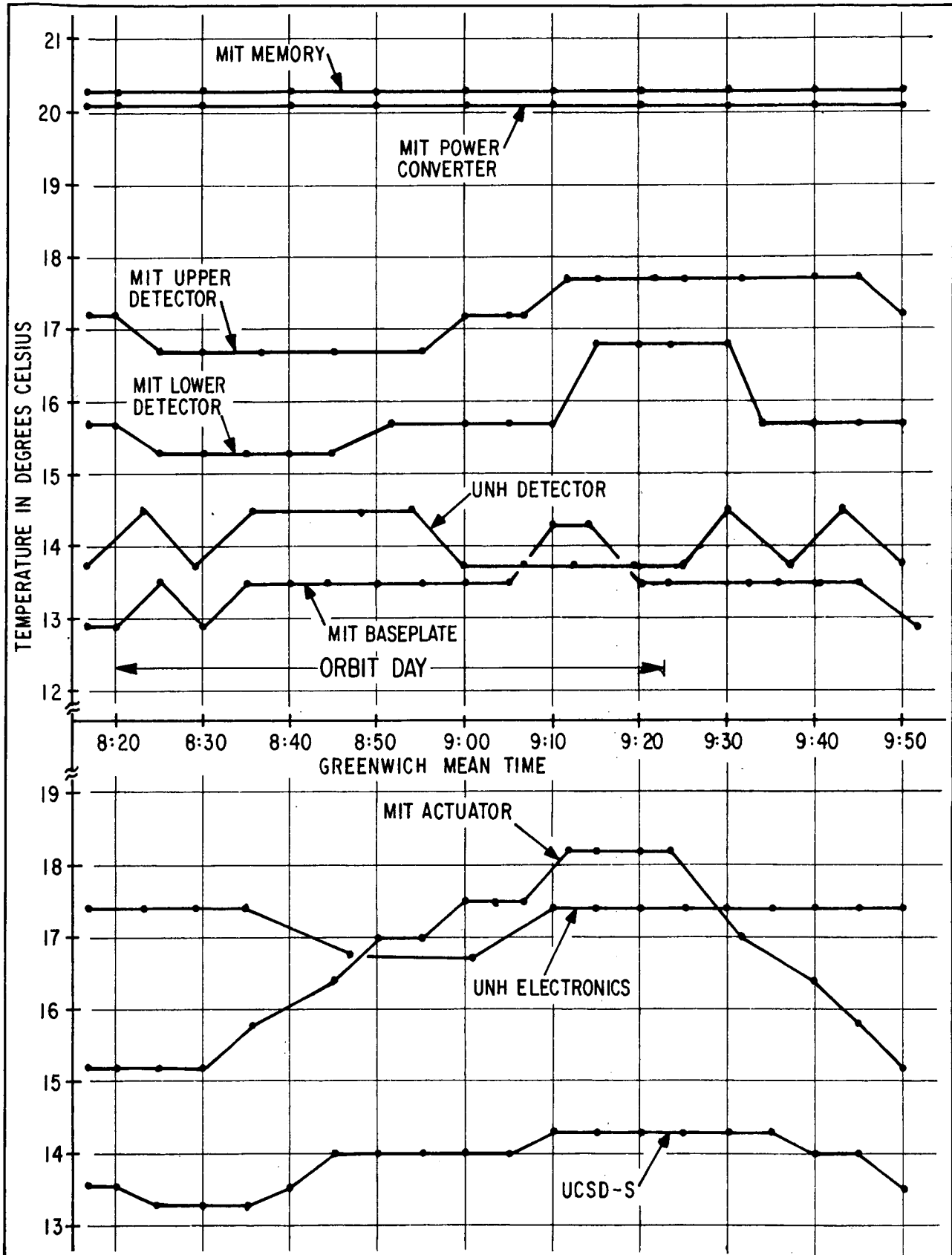


Figure 2-15 Wheel Experiment Temperature, Orbit Revolution 77



F72-01

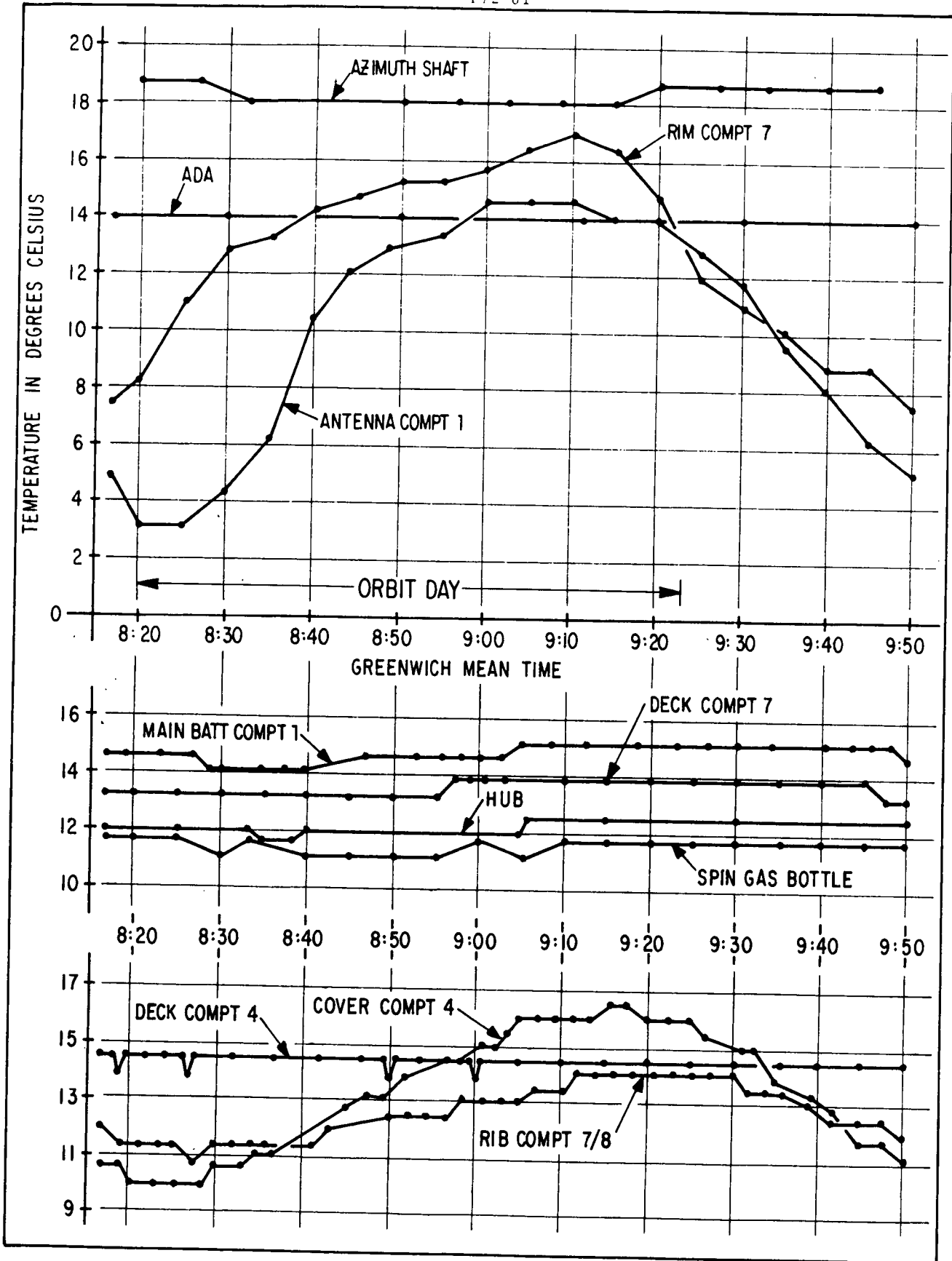


Figure 2-16 OSO-7 Wheel Temperatures, Orbit Revolution 77



F72-01

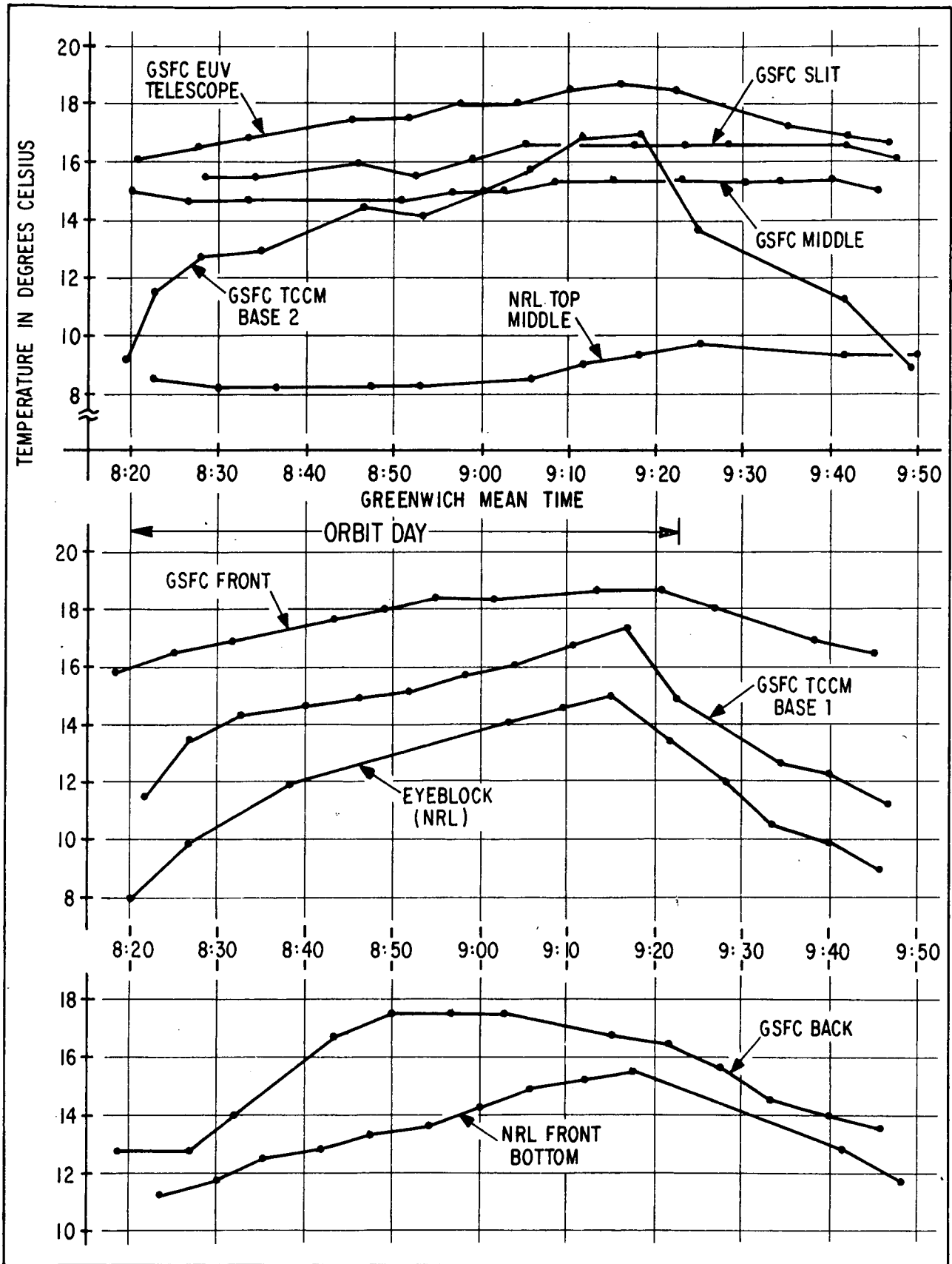


Figure 2-17 OSO-7 Pointed Experiment Temperature, Orbit Revolution 77



F72-01

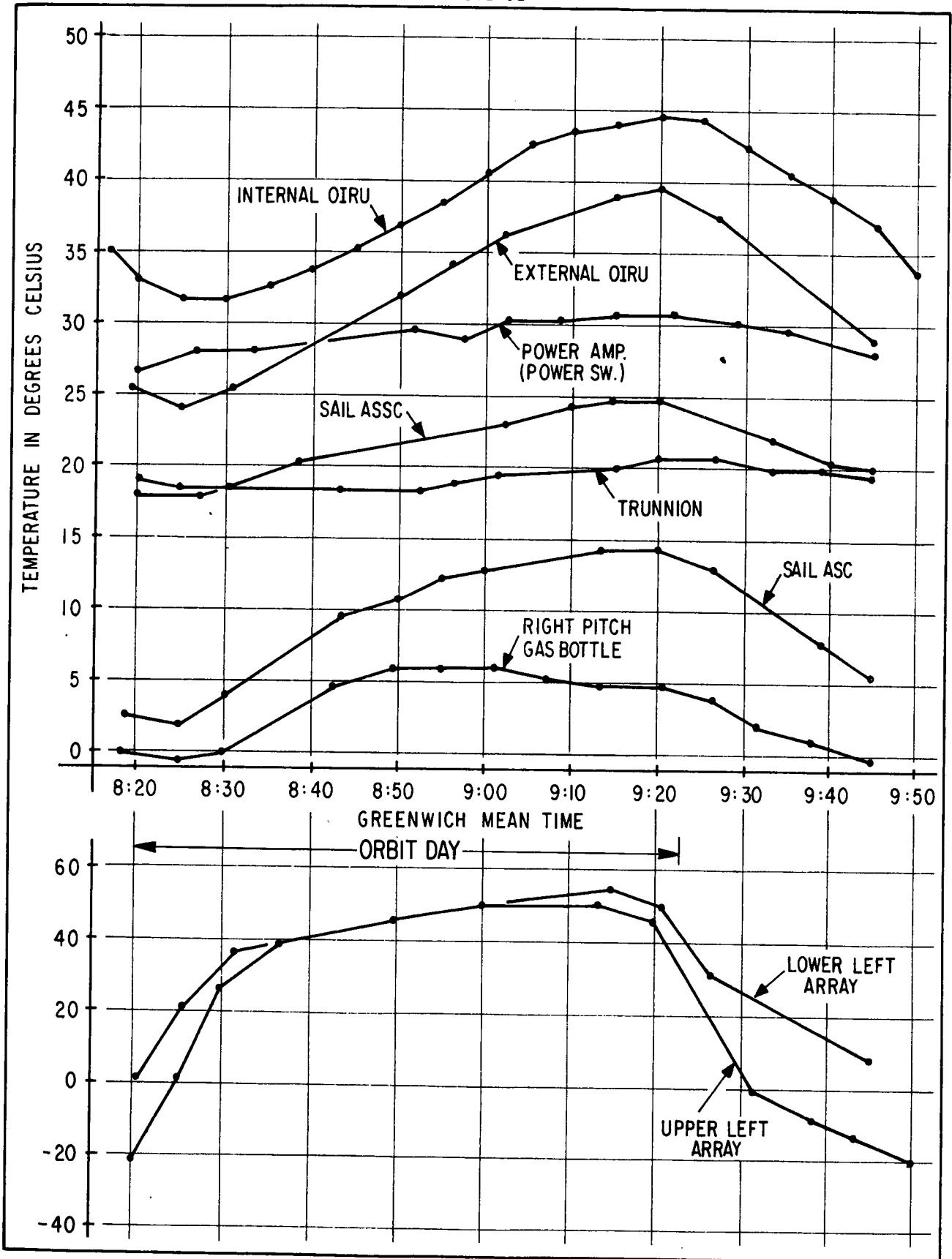


Figure 2-18 OSO-7 Sail Temperatures, Orbit Revolution 77



F72-01

Table 2-3  
SPACECRAFT PRELAUNCH STATUS

Spin Gas Pressure - 2952 psi  
Pitch Gas Pressure - 2931 psi  
Battery Voltage - 19.1 vdc  
Spacecraft Load Current - 0.76 amps  
Tape Recorders - Both on and recording in manual mode  
Temperatures - Between 21.6°C (despin drive) and 24.8°C (compartment no. 4 deck)  
Gyro Power - OFF  
Spin - Manual  
Pitch - Manual  
Solar Panels - Enabled  
Dummy Loads - OFF  
Undervoltage Turn-On Disabled  
SORE Alternate - Encoder Enabled

#### 2.2.1 Launch Sequence

The intended spacecraft launch sequence events are shown in the upper trace of Figure 2-19. When the vehicle fairing is ejected, the spacecraft azimuth servo is energized and placed in a mode which spins up the sail to about 40 rpm. The sail continues to spin through the coast phase, second stage restart, and orbit injection.

After the second-stage burn is terminated, the spacecraft is separated from the launch vehicle. The angular momentum of the spinning sail stabilizes the spacecraft against normal tip-off rates occurring during separation.

When the spacecraft is separated from the launch vehicle, the injection attitude is controlled so that the spin axis is perpendicular to the line of sight of the sun within 10 degrees. The azimuth servo is automatically switched to the sun-pointing mode and the sail begins to despin under control of the coarse azimuth solar sensors. Gas is also released from spin-up jets on the wheel for about 180 seconds to bring the wheel up to its normal operating spin rate of about 30 rpm. In the meantime, the sail has despun and acquired in azimuth and if the pitch axis is more than three degrees from perpendicular to the line-of-sight to the sun, the automatic pitch system precesses the spacecraft to reduce the pitch error.

Upon acquiring the sun in azimuth an on-target signal from a solar sensor releases the bob of the fluid-filled nutation damper and unlocks the elevation gimbal so that the pointed instruments are free to move under the control of the elevation servo.



F72-01

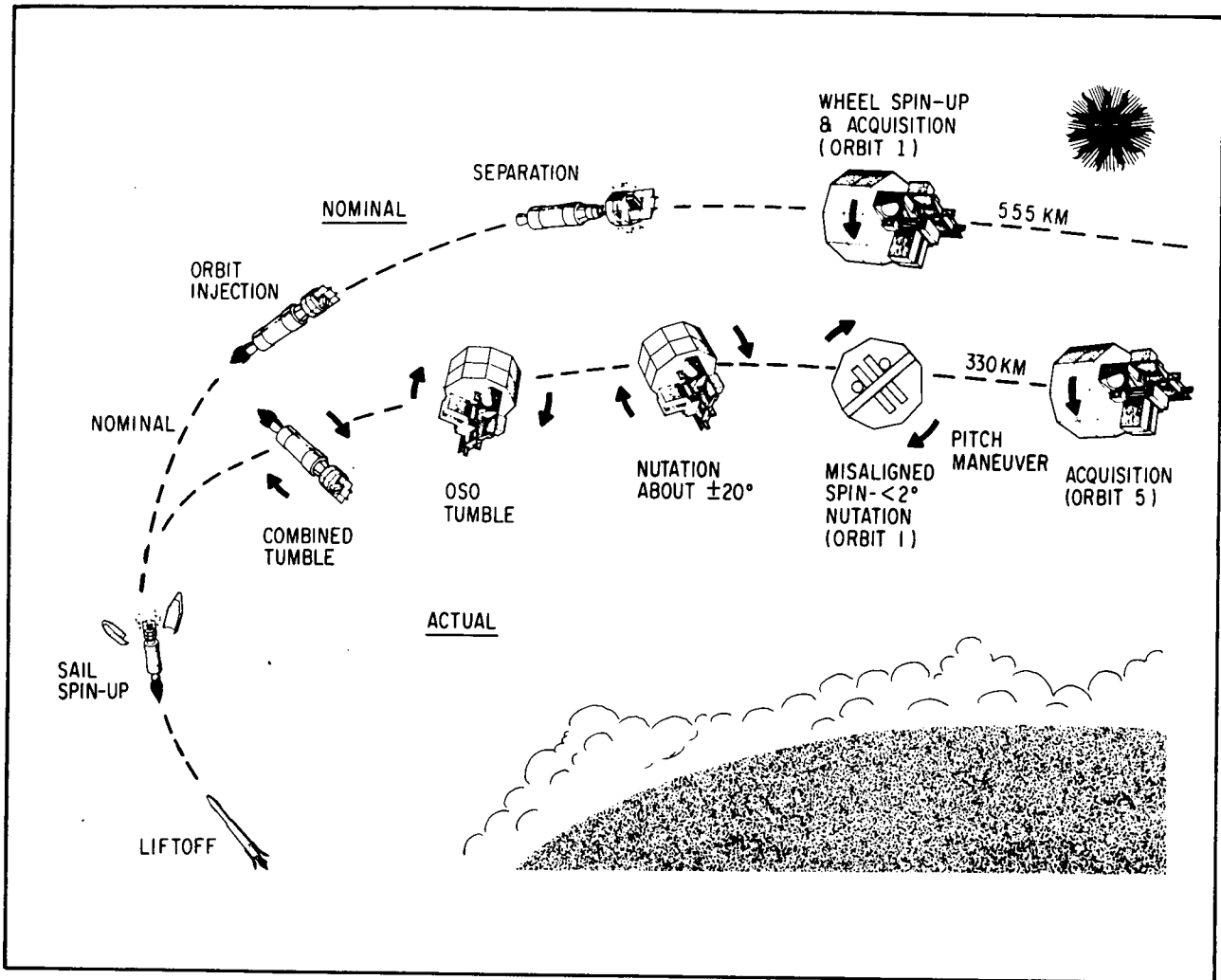


Figure 2-19 Nominal and Actual OSO-7 Launch Sequence

Actual OSO-7 Launch Sequence. The actual launch sequence events for OSO-7 are shown in the lower trace of Figure 2-19 and tabulated in Table 2-4. Lift-off was followed by completely normal vehicle and spacecraft behavior through the boost phase, fairing ejection, sail spin-up, and the coast phase.

Soon after the second-stage engine was reignited to provide thrust to achieve orbital velocity, a vehicle malfunction caused the second stage to begin tumbling. At the completion of the second-stage burn, the tumble rate was about 55 rpm.

The longitudinal acceleration at the spacecraft due to the tumbling motion was about 8 g's, increasing the axial thrust loading on the spacecraft azimuth shaft bearing to about 3600 pounds. The spinning sail, constrained from precessing by the much larger angular momentum of the vehicle, came to a stop within a few seconds. The sail spinup circuits delivered full drive current to the azimuth motor in an attempt to increase the sail-to-wheel spin rate to a normal value.





F72-01

Table 2-4  
LAUNCH EVENTS

ORBIT "O"

094500.86Z	Lift Off. OSO-OCC receiving data from Ft. Myers.
094855.5Z	Fairing ejection and sail spin-up. The sail spin rate increased to 24.3 rpm.
095003Z	Antigua AOS. Data was of poor quality and the OSO-OCC could not obtain PCM lock throughout the pass.
095515Z	Ft. Myers LOS
100226Z	Antigua LOS
100330Z	Ascension AOS. Data received indicated the sail spin rate had increased to 42.9 rpm.
101330.4Z	Telemetry detection of second stage restart. After second stage burn was completed, the relative spin rate between the wheel and sail decreased to $\emptyset$ rpm. Azimuth motor current increased from 0.2 amps to 0.78 amps, indicating motor was attempting to increase sail spin rate.
101602Z	Joburg AOS
101716Z	Ascension LOS
101822.4Z	Telemetry detection of separation from the launch vehicle. Spin rate could not be determined from telemetry data. AGC reading at ground station indicated wheel spin rate was approximately 63 rpm.
102025.3Z	First reading of large-angle pitch readout. Readout indicated $+71^\circ$ pitch.
102111.4Z	Spin gas stopped depleting. 500 psi of gas was used. The pitch readout continued to increase until a reading of $+85^\circ$ with nutation nulls of $26^\circ$ peak-to-peak was detected.

After completion of the second stage burn, the roll control system on the booster continued to function and maintained the vehicle roll (motion about the longitudinal axis) rate near zero. Therefore, the spacecraft-vehicle rotated about a vehicle transverse axis with very little nutation.

Separation Dynamics. The dynamic motion of the spacecraft immediately following separation from the vehicle occurred in two phases. During the first phase, the spacecraft began tumbling about a transverse axis through its center of mass. Simultaneously, gas was automatically released from the spinup jets on the wheel, changing the momentum of the



F72-01

system and partially erecting the spacecraft. In the second phase, spinup torques were no longer present, and the orientation of the total angular momentum vector remained essentially constant. The elevation caging was released and the nutation began to decay as energy was dissipated by the elevation gimbal suspension.

Spin torques applied about the axis of the wheel produce widely varying attitude motion depending on the orientation of the original tumble axis relative to the transverse principal inertial axes, and the relative difference (asymmetry) between the transverse moments of inertia.

While spinup torques are applied, the wheel does not rotate appreciably about its axis of maximum moment of inertia (spin axis). Instead, it oscillates through a fraction of a revolution. This explains the absence of data from the pitch angle solar sensor during most of the wheel spinup period, as shown in Figure 2-20.

When spinup torques ceased, the spacecraft motion approximated that of a disk-shaped body, rotating with large nutation. Data from the pitch attitude sensor are shown on the upper right of Figure 2-20. By the next station pass, about 1-1/2 hours later, the spacecraft was spinning about its normal spin axis and the nutation half-angle was about 1 degree. The pitch attitude relative to the sun was 71 degrees, indicating that the angular momentum vector was about 19 degrees from the antisolar direction.

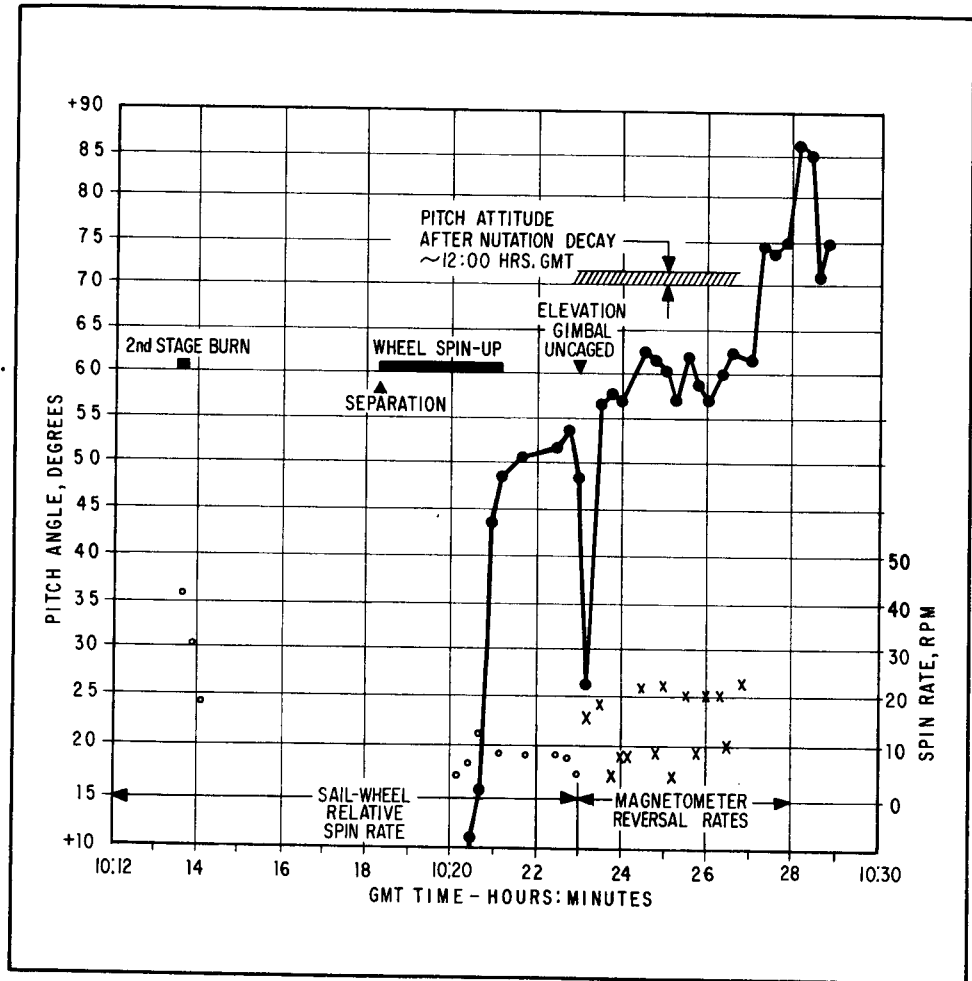


Figure 2-20 Pitch Attitude and Spin Rate Data

Assuming the orientation of the momentum vector relative to the sun did not change after spinup gas termination, the geometry affecting pitch attitude readout is that shown in Figure 2-21. When the spacecraft is in a pure tumble about a transverse axis, the line of sight to the sun traces out a cone,



F72-01

with half-angle of 19 degrees, centered about the tumble axis. As the nutation angle decreases, the sun cone intersects the sensor readout plane at different pitch angles. The pitch readout sensor will generate data only when the wheel azimuth position is such that the sensor field-of-view plane intersects the sun cone; this occurs when  $|\phi| < 19$  degrees. The attitude sensor geometry and the relationship between the angular momentum vector and the line of sight to the sun restrict the pitch readout angles to those shown in Figure 2-22.

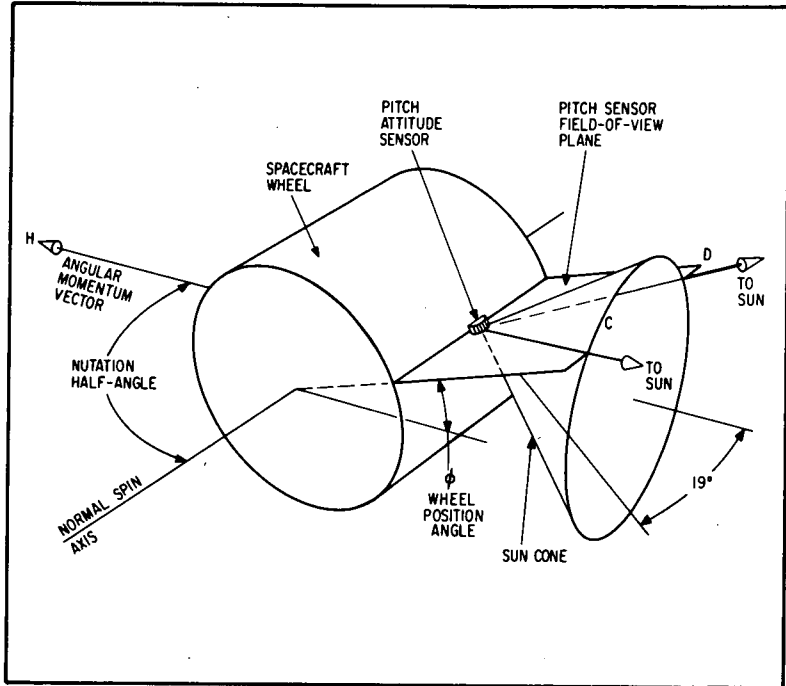


Figure 2-21 Pitch Attitude Sensor Geometry

Using this graph to interpret the pitch-angle data in the upper right part of Figure 2-20, reveals that the spacecraft became partially erected during the few minutes following separation, and the nutation half-angle was reduced to less than 20 degrees.

2.2.2 Recovery  
Operation

The telemetry data, spacecraft modes and the command groups transmitted during the recovery operation are indicated on Figure 2-23. Two additional orbital revolutions, for which data are not shown, were used to return the spin rate to normal and place the spacecraft in a normal operating mode.

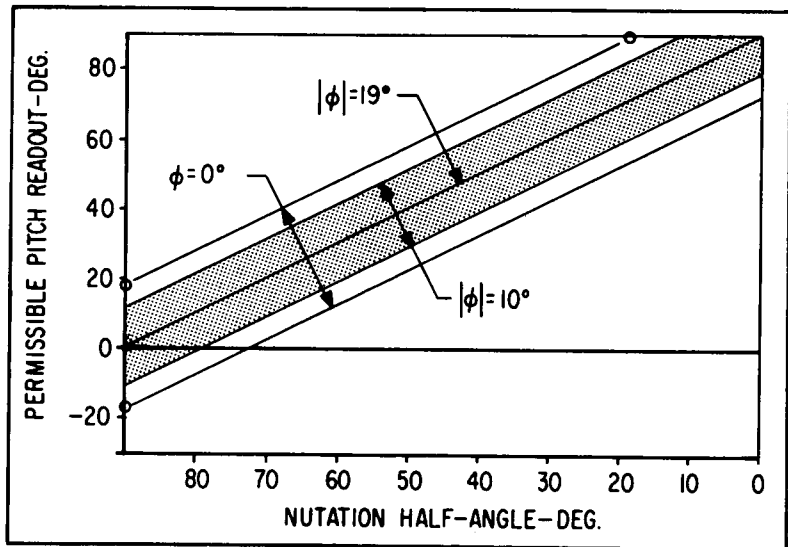


Figure 2-22 Permissible Pitch Attitude Readout-Momentum Vector 19 Degrees from Line of Sight to Sun



F72-01

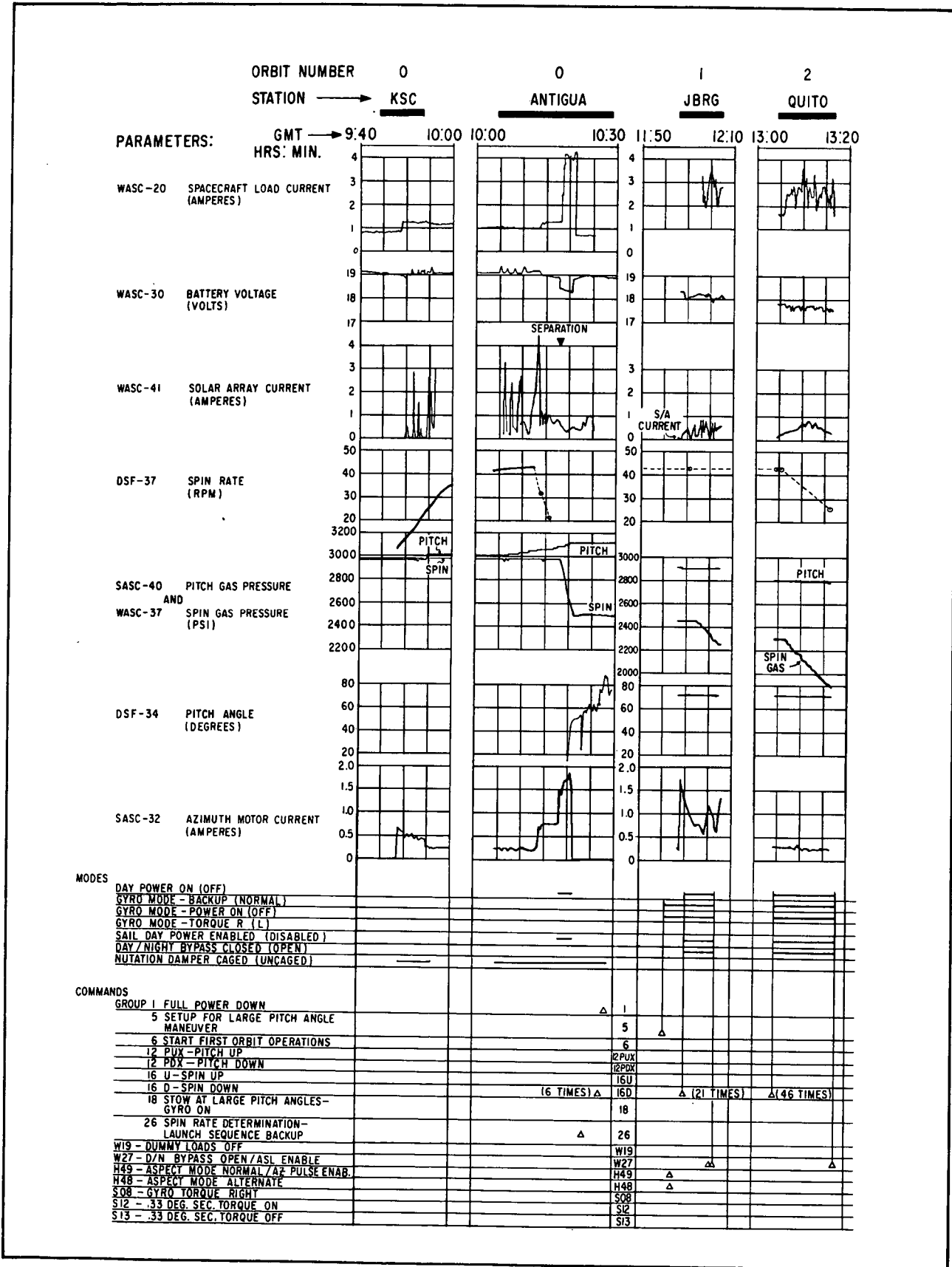


Figure 2-23 Telemetry Data, Modes, and Corrective Commands - OSO-7 Recovery (1 of 2)



F72-01

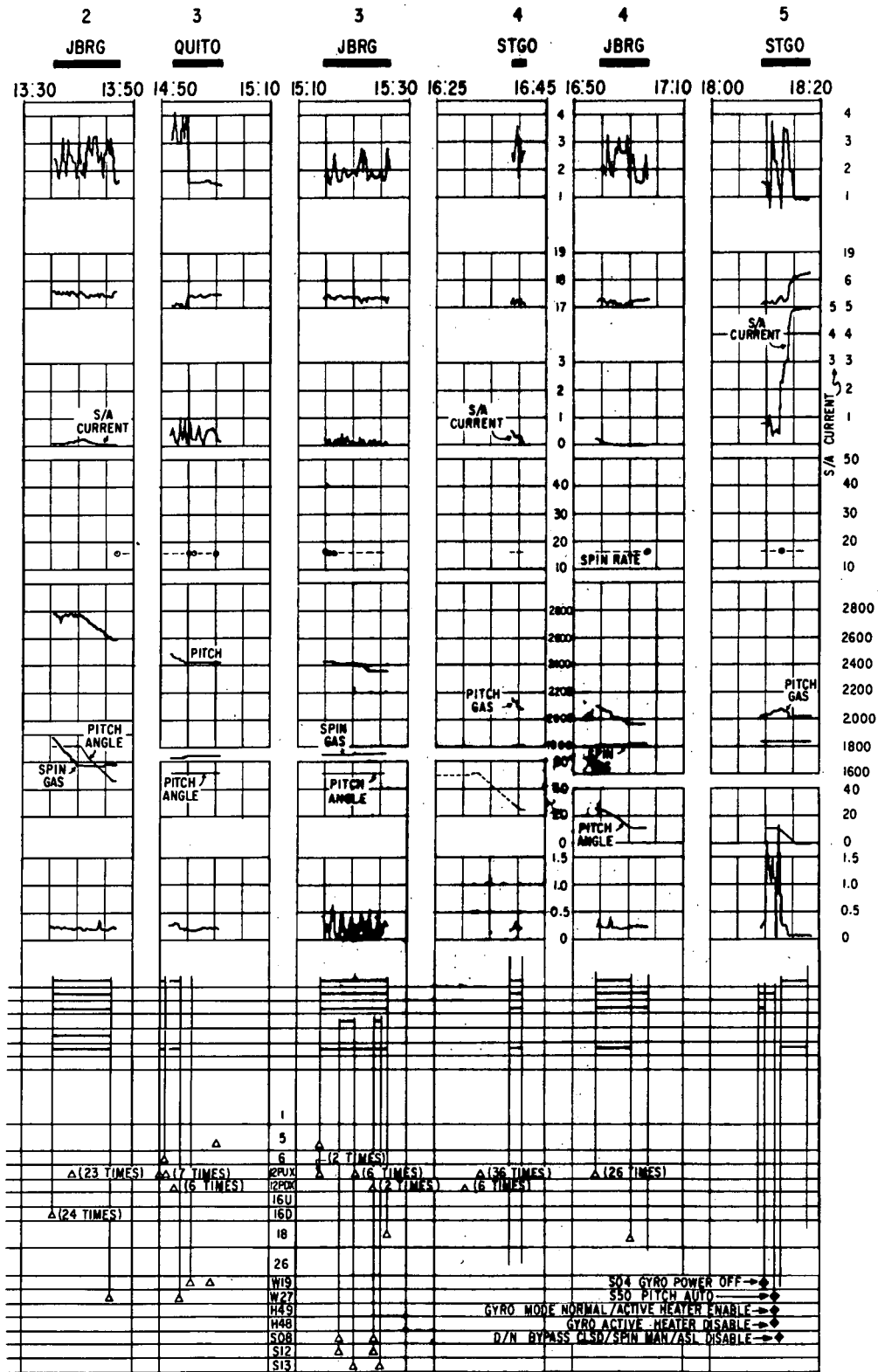


Figure 2-23 Telemetry Data, Modes, and Corrective Commands - OSO-7 Recovery (2 of 2)



F72-01

As shown in Figure 2-22, the spacecraft load current reflects the additional current drawn by the azimuth servo during sail spinup and initial attempts at acquisition after separation while the spin axis was still broadside to the sun. Other fluctuations in the load current are due to bus voltage variations caused by current developed by the array as it occasionally viewed the sun or earth and by solenoid energizing current during gas expulsion.

The state of battery charge is indicated roughly by the bus voltage, which had declined to about 17 volts by orbit 4. This corresponds to about 75 percent discharge of the battery. While sufficient energy remained for one or two more orbital revolutions, operation below 16.8 volts could have resulted in undervoltage disconnect during current surges such as that accompanying azimuth acquisition.

The azimuth motor current, shown in the lower trace of Figure 2-23, reflects the action of the azimuth drive servo. The decaying current, during orbit Revolution 0, reflects the decrease in motor current as the sail came up to terminal velocity. The increased drive current during Revolution 1 accompanied sail despin under gyro control. With the sail stopped, the normal level of azimuth motor current is shown in Revolutions 2, 3 and 4 (gyro control) and in Revolution 5 after normal solar acquisition.

The other traces on Figure 2-23 display the spin and pitch gas supply pressures which varied slightly from changes in reservoir temperatures and declined from an initial pressure of about 3000 psi as acquisition maneuvers were executed. At the beginning of normal orbital operations the spin and pitch gas pressures were 1540 and 2200 psi respectively.

The incidence of the sun on the underneath side of the wheel introduced a substantial temperature gradient along the spin axis of the spacecraft. The temperature of the antenna skirt, located on the lower rim of the wheel, rose above 78°C compared with a normal temperature of about 25°C. The case temperature of the azimuth gyro, located in the sail, fell below -15°C, compared to a normal minimum temperature of 0°C. These temperatures caused no permanent damage; however, the gyro gain was reduced to the point where azimuth acquisition was slowed.

A summary of recovery operations is as follows.

Revolution 0 - *Johannesburg* - Sent commands in accordance with contingency logic to (1) release elevation axis and nutation damper caging, providing mechanisms to damp nutation if present, (2) enable determination of spin rate from magnetometer data, (3) begin despin toward 9 rpm, (4) power-down spacecraft.

Revolution 1 - *Guam* - Readout housekeeping data. Spin rate tentatively determined to be 43.5 rpm. (Data not shown on Figure 2-23.)



F72-01

*Ft. Myers* - Repeated commands to (1) release nutation damper and elevation caging, (2) spinup (4 bursts) spacecraft slightly to observe and confirm spin rate, (3) stow spacecraft in power-down condition. Pitch angle read out +71 degrees. (Data not shown in Figure 2-23.)

*Johannesburg* - Sent commands to (1) set up for large angle pitch maneuver (turn on gyro), (2) sent 21 spindown bursts to make pitch maneuvers easier. Spin rate with sail stopped reduced from 60 rpm to 46 rpm.

Revolution 2 - *Santiago* - Sent 47 more spindown bursts, reducing spin rate to 26.6 rpm.

*Johannesburg* - Sent 24 spindown bursts, reducing spin rate to about 15 rpm. Sent 22 pitch-up bursts reducing pitch angle from 71 degrees to 47 degrees.

Revolution 3 - *Quito* - Sent 5 pitch-up bursts. Pitch angle increased to 53 degrees because gyro had drifted so sail was in wrong position. Erroneously sent command group placing spacecraft in sun-pointing mode, which allowed sail to rotate. Sent a pitch-up and 12 pitchdown bursts. No net effect on pitch angle because sail was rotating.

*Santiago* - Sent commands to place gyro in control.

*Johannesburg* - Sent 3 pitch-up bursts to test for direction and sail position. Slewed 60 degrees right. Sent 6 pitch-up bursts. No appreciable effect. Slewed 40 degrees right to improve sail position. Sent 2 pitchdown bursts to confirm sail position and direction. Stowed spacecraft with gyro on.

Revolution 4 - *Santiago* - Sent 6 pitchdown bursts increasing pitch angle. Sent 36 pitch-up bursts decreasing pitch angle to 26 degrees.

*Johannesburg* - Sent 26 pitch-up bursts, reducing pitch angle to 12 degrees. Stowed spacecraft in minimum power configuration (gyro on).

Revolution 5 - *Santiago* - Enabled sun-pointing mode by turning gyro off. Enabled auto-pitch mode. Pitch angle reduced to -1 degree automatically. Pointing system acquired sun.

Revolution 6 - *Santiago* - Sent 18 spin-up bursts, increasing spin rate from 15.6 to 24 rpm. Opened day/night bypass. Fired experiment deployment squibs. High and low dummy loads ON.

On subsequent revolutions, spin control was switched to the automatic system and the wheel rate increased in a normal fashion to 26 rpm. When attempts were made to play back the onboard tape recorders and retrieve stored data, only one of the two redundant recorders responded. It is assumed the second recorder was damaged by the accelerations experienced during the launch sequence.



F72-01

Orbital operation has continued for 14 months (as of November 29, 1972). The vehicle malfunction resulted in an orbit with apogee altitude of 310 nautical miles and perigee altitude of 178 nautical miles instead of the 300 nautical mile circular orbit normally used. This has had no effect on the performance of the spacecraft.

2.2.3 Early Orbit Spacecraft Checkout and Experiment Turn-on

Orbital revolutions 7 through 49 were used for initial on-orbit checkout of the spacecraft and to turn on experiments. Additional spacecraft tests to optimize the set points for the gyro and star scanner sensitivity were continued on selected orbits through revolution 155.

The basic spacecraft checkout activities are summarized in Table 2-5.

Table 2-5  
ON-ORBIT SPACECRAFT CHECKOUT

<u>Activity</u>	<u>Pass No.</u>	<u>Results</u>
TR1 playback attempt no. 1	GAGO 7	Unsuccessful - clear carrier
TR1 playback attempt no. 2	GQUI 8	Unsuccessful - clear carrier
TR2 placed in record mode	GBUR 17	-----
Operational checkout of pointed control system	GBUR 17	Function normal
TR2 playback attempt	GAGO 19	Normal playback
Pointed control system accuracy	GQUI 24	
Gyro heater performance	GQUI 24	Obtained preliminary temperature profiles
Verification of offset bits	GYRS 27	Function normal
Gyro drift test no. 1	GBUR 29	Preliminary drift data
Gyro offset compensation test no. 1	GBUR 30	Preliminary offset data
Comparison of offset pointed accuracy and sun-centered pointed accuracy	GYRS 42	-----
Gyro drift test no. 2	GYRS 44	
Gyro offset compensation test no. 2	GBUR 45	
ASA turn-on	GYRS 57	

In addition to the spacecraft checkout activities, the following further tests were conducted.

Gyro Heater Performance Test No. 2 (GROS 135 through GAGO 155). This test was repeated for four reasons: to check the gyro temperature profiles as the orbit days became longer; up-to-date temperature data was needed to predict when the gyro temperature would reach 104°F (this data was needed for a subsequent gyro offset compensation conducted during Orbit 170); to check the effect, if any, of gyro gain on the star scanner gain-setting;





F72-01

and to determine the set-point most nearly corresponding to the gyro end-of-day temperature. The results of this test are described below:

- Temperature profiles:

<u>Mode</u>	<u>Temp. Range</u>	<u>Notes</u>	<u>Playback Pass</u>
116°F/Htr. Enabled	93°F to 120°F	116°F 5 min before night	GYRS 135
116°F/Htr. Disabled	85°F to 111°F	-----	GAGO 142
104°F/Htr. Enabled	90°F to 115°F	104°F 20 min before night	GAGO 155

- Temperature prediction: The 104°F/Htr. Enabled mode was chosen for gyro offset compensation test no. 3. Using this mode, it was predicted that the gyro temperature would be 104°F about one minute before GBUR 170 LOS. Thus, the gyro temperature would be very close to ideal during this pass.
- Effect of gyro gain on ASA: It was thought that if the gyro was oscillating slightly, the resulting noise on the power bus might be causing the ASA gain-setting circuits to behave abnormally. Since the gyro gain is directly proportional to its temperature and indirectly proportional to its gain setting, the gyro was operated at various combinations of gain setting and heater modes. There were no conclusive results of this test.
- Best set-point for normal operation: It was determined that the 116°F set-point with the heater enabled was the best operating mode. In this mode, the gyro temperature at the end-of-day would be about 120°F which is the closest match of set-point and operating temperature.

Gyro Offset Compensation Test No. 3 (GBUR 170). Previous tests were run using the offset position (1,2) only. This last test used offset positions (128,2), (1,2) and sun-center. Since the gyro temperature was predicted to be much closer to the set-point (i.e., 104°F), it was expected that the offset error would be less than that observed during the first two tests (i.e., 25 and 30 arc-minutes, respectively). The results of this last test are shown below:

<u>Sail Position to be Compensated for</u>	<u>Gyro Temp. (°F)</u>	<u>Offset Comp. Error (arc-min)</u>
Far right (128,2)	98	16 Left
Far left (1,2)	103	12 Right
Sun-Center	104	1.2 Left

Gyro Long-Term Drift Test No. 3 (GAGO 171 to GAGO 172). The gyro was left in the backup mode for an entire orbit. The actual drift was about 0.1 degree per hour to the left, which was very close to the nominal capabilities of the gyro.



F72-01

Spacecraft Anomalies. There were four spacecraft anomalies discovered during the checkout phase:

- When in the backup mode, the gyro offset the sail to the left about 0.5 degree during the night-day transition. This, however, has no effect on normal observatory operation since the sail always goes through a coarse acquisition every dawn anyway.
- The star scanner gain setting changed for no apparent reason and the gain setting had to be re-commanded periodically. This difficulty disappeared after a few weeks in-orbit.
- Tape Recorder No. 1 had failed during the launch phase. Tape Recorder No. 2, however, operated normally. The effect of this failure was the loss of the series-record capability.
- The spacecraft azimuth vernier bit caused the pointed instrument assembly to be shifted about 4 arc-minutes to the right instead of 0.472. This problem has been overcome by avoiding the use of the azimuth vernier bit.

Experiment Turn-On and Checkout. The first experiment turn-on activities began during Orbit No. 21. The typical checkout sequence consisted of first verifying the operation of the low-voltage functions. Then the high voltage functions were momentarily energized and their operation checked. If the high voltage function seemed normal, the experiment high voltage detectors were re-energized and left on.

All experiment functions and modes would then be checked. Upon the successful completion of this last check, routine experiment operations began.

Table 2-6 shows when the experiment high voltages were first checked out and when they were finally turned on and left on continuous operation.

Table 2-6  
EXPERIMENT HIGH-VOLTAGE TURN-ON

<u>Instrument</u>	<u>Momentary HV Turn-on Tests Began</u>	<u>HV Left On</u>
GSFC (Pointed):		
X-Ray	GBUR 46	GBUR 46
UV	GBUR 59	GYRS 61
Polar	GBUR 46	GBUR 46
H-alpha	GBUR 47	GAGO 50
NRL (Pointed):		
XUV	GQUI 63	GAGO 65
WL	GYRS 59	GYRS 74
UCSD-Solar (Wheel):	GYRS 46	GBUR 47
UCSD-Cosmic (Wheel):	GBUR 46	GAGO 49
UNH (Wheel):	GYRS 58	GBUR 61
MIT (Wheel):	GBUR 46	GBUR 49



F72-01

### Section 3 DESIGN, INTEGRATION, AND TEST PROGRAM SUMMARY

OSO-7 design, integration, and test activities spanned about two and one-half years from the beginning of systems design in early 1969 until launch on September 29, 1972. Both flight and qualification model spacecraft were constructed and tested. This section summarizes the program with flow charts showing the integration and testing history of the observatory program.

#### 3.1 SUBASSEMBLY QUALIFICATION

Many subassembly designs (including OSO-6 spares) were directly usable on OSO-7 without further qualification testing. Some components were subjected to partial qualification tests, mainly temperature and vibration, where the qualification levels on OSO-7 exceeded those for which the components had been previously tested.

Components involving a substantial amount of new design were subjected to a complete qualification test sequence. A formal qualification program was conducted for the following components either as separate subassemblies or as part of the observatory qualification model:

Stabilized Section Assembly	Gyro
Azimuth Drive	Gyro Electronics
Sail Structure	Star Scanner
Solar Array	SORE Package
Electrical Distribution Box	Separation Switch
Time Delay Relay	Command Decoder
Spin Pneumatics System	Antenna Assembly
Pitch Pneumatic System	Antenna Matching Assembly
Elevation Torque Motor	Tape Recorder Assembly

#### 3.2 OBSERVATORY QUALIFICATION MODEL TESTING

The observatory qualification model included flight-equivalent parts for the basic structure, high pressure gas systems, and the control system. Mass models were used to simulate experiment instruments. The data-handling system was sufficiently complete to generate PCM signals; the antenna and RF system were not used; however, the antenna was functional and subjected to survival tests.

Details of the qualification test operation are shown on Figures 3-1 and 3-2. The sail pointing control system was completely functional and extensive tests were conducted in the sun and in the thermal-vacuum chamber.

The spacecraft with functional and mass model components was balanced and ballast was added to achieve the proper moments of inertia ratio.



F72-01

### 3.3 FLIGHT MODEL TEST HISTORY

Details of the spacecraft integration, testing and experiment integration are shown in Figure 3-2. The observatory test sequence is shown in Figure 3-3.

In most cases, testing on the flight model was done with test methods and equipment similar to those employed for previous OSO's. The integration of spacecraft, scientific experiments, acceptance testing, and prelaunch operations covered a period of about twelve and one-half months.



F72-01

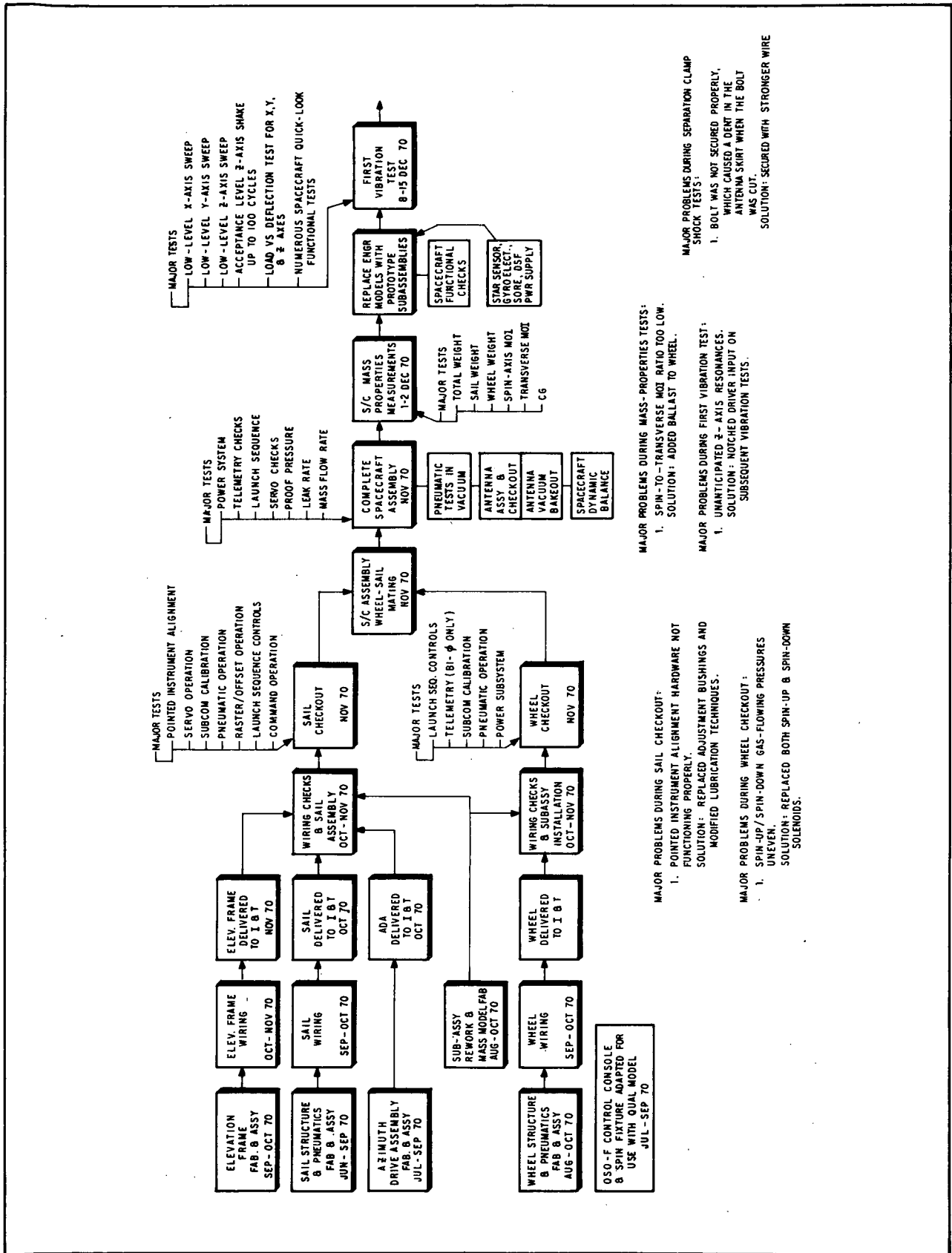


Figure 3-1 Qualification Model Test History (Sheet 1 of 2)



F72-01

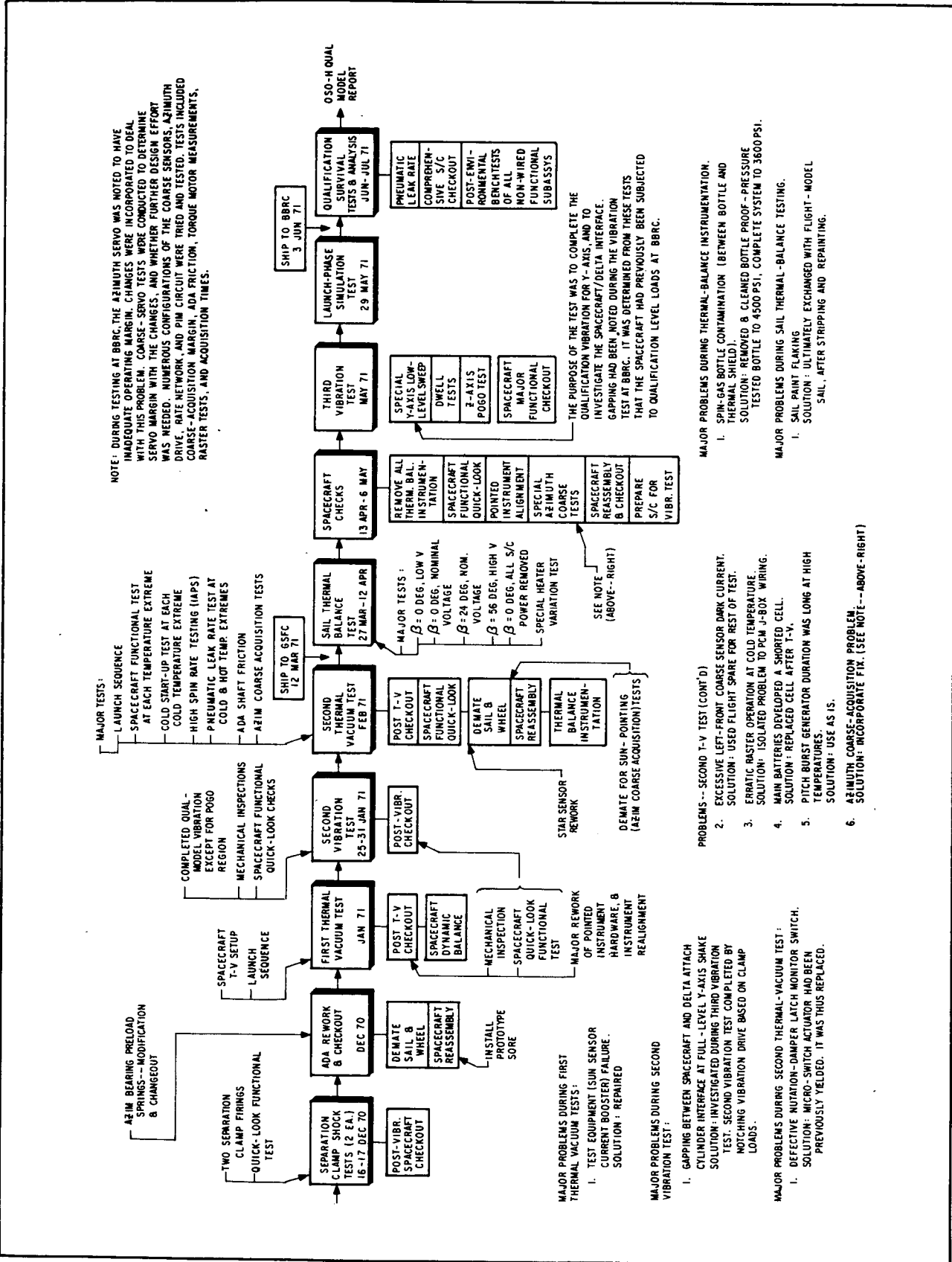


Figure 3-1 Qualification Model Test History (Sheet 2 of 2)



F72-01

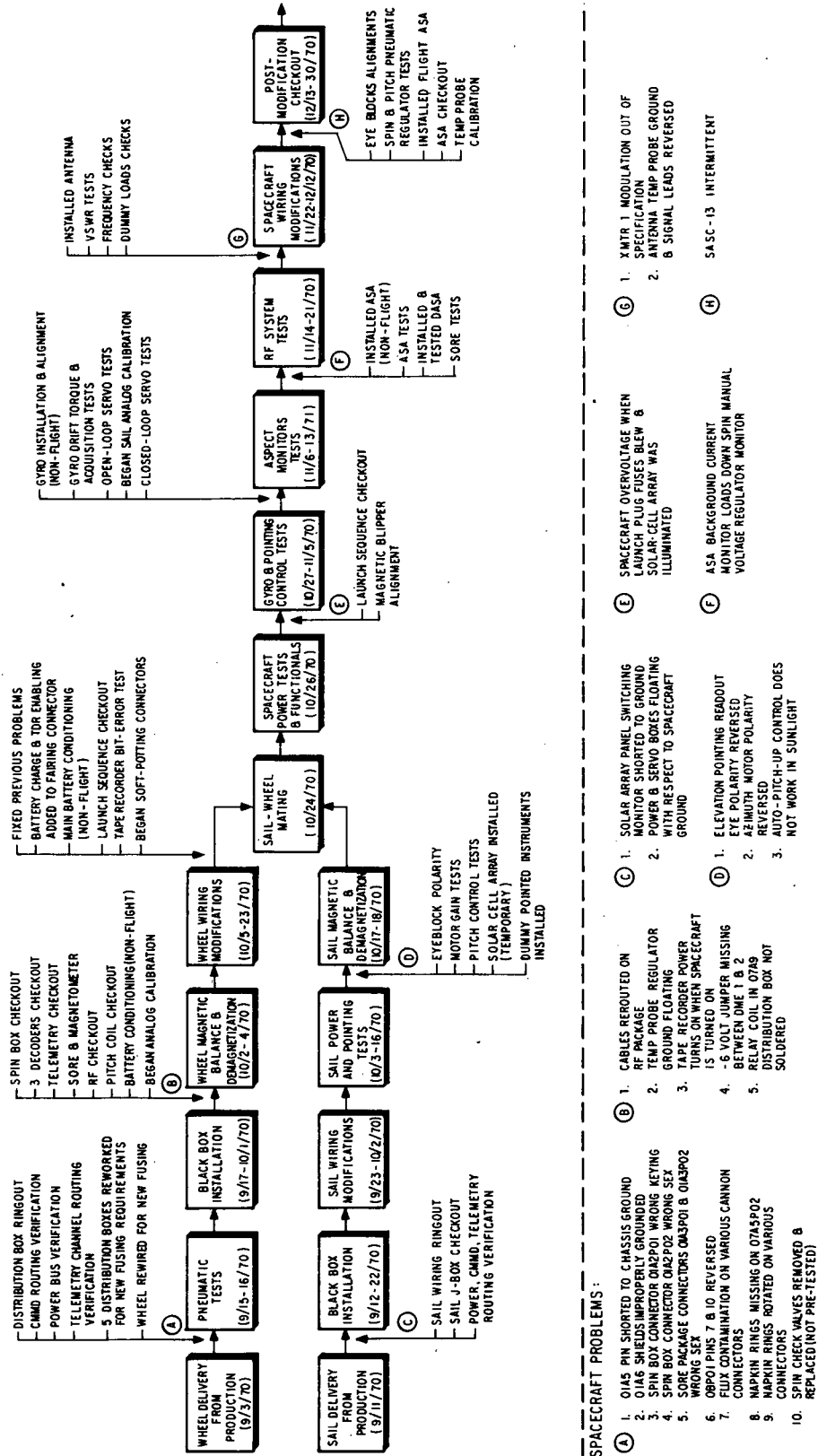


Figure 3-2 Spacecraft Test History (Sheet 1 of 2)

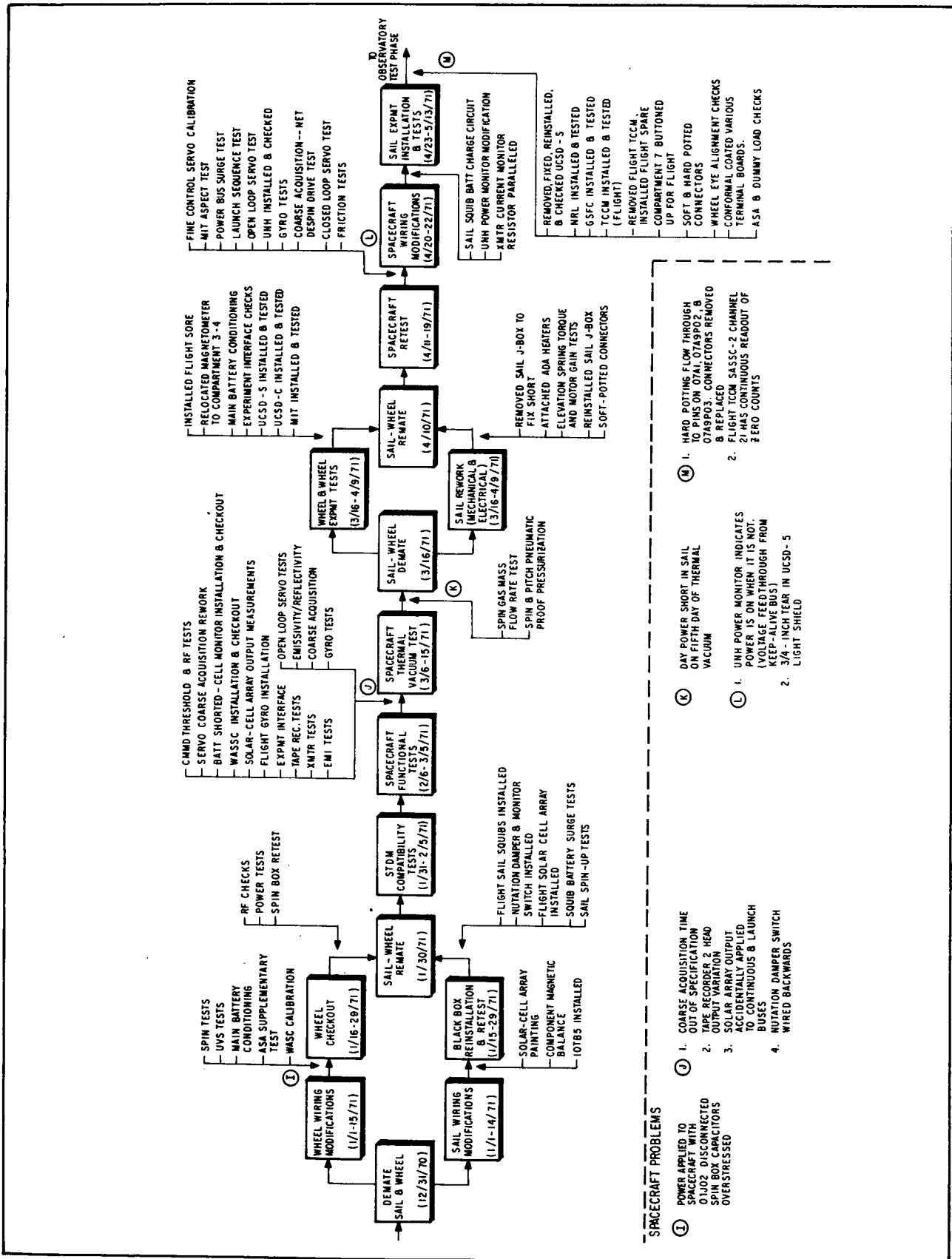


Figure 3-2 Spacecraft Test History (Sheet 2 of 2)





F72-01

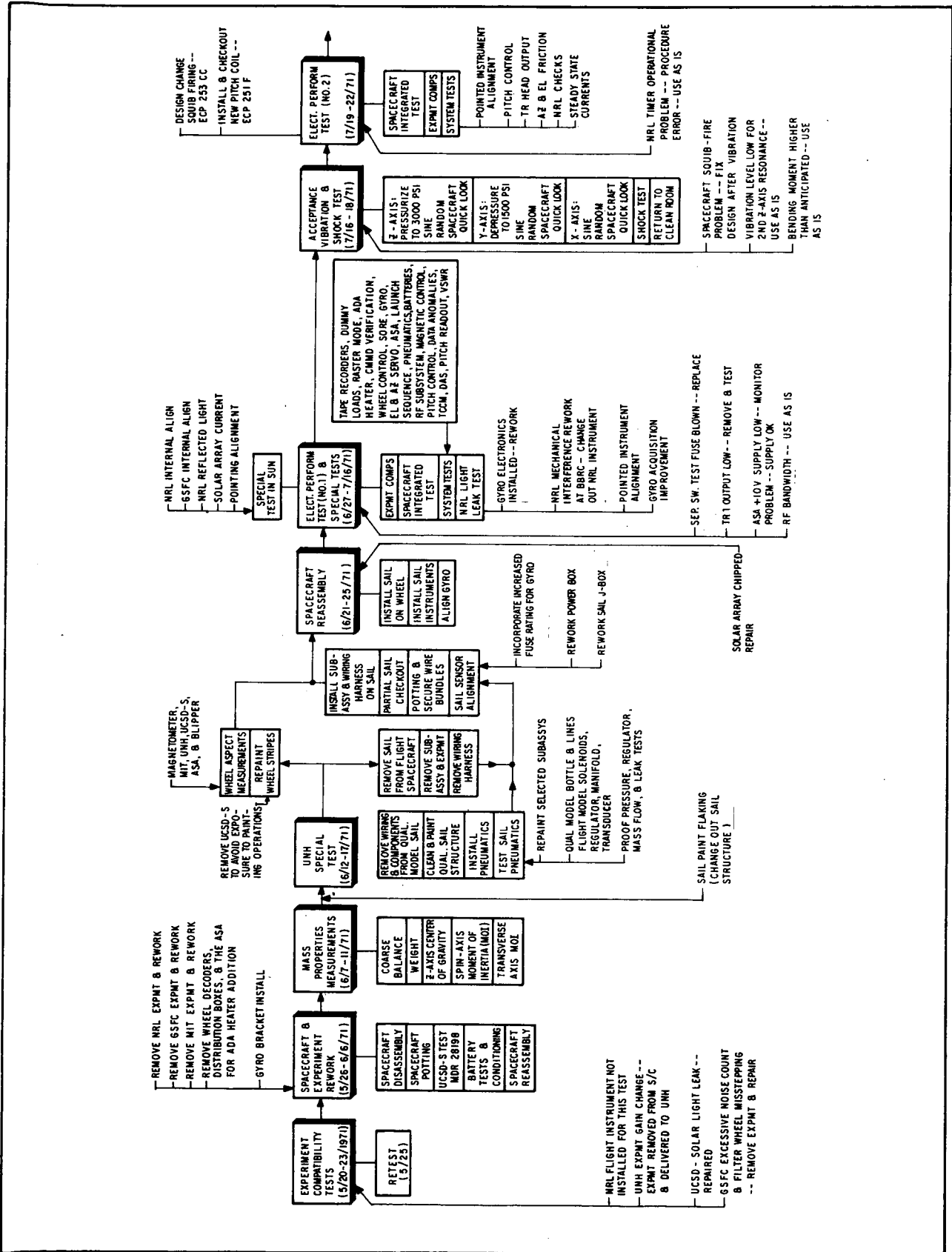


Figure 3-3 Observatory Test History (Sheet 1 of 2)



F72-01

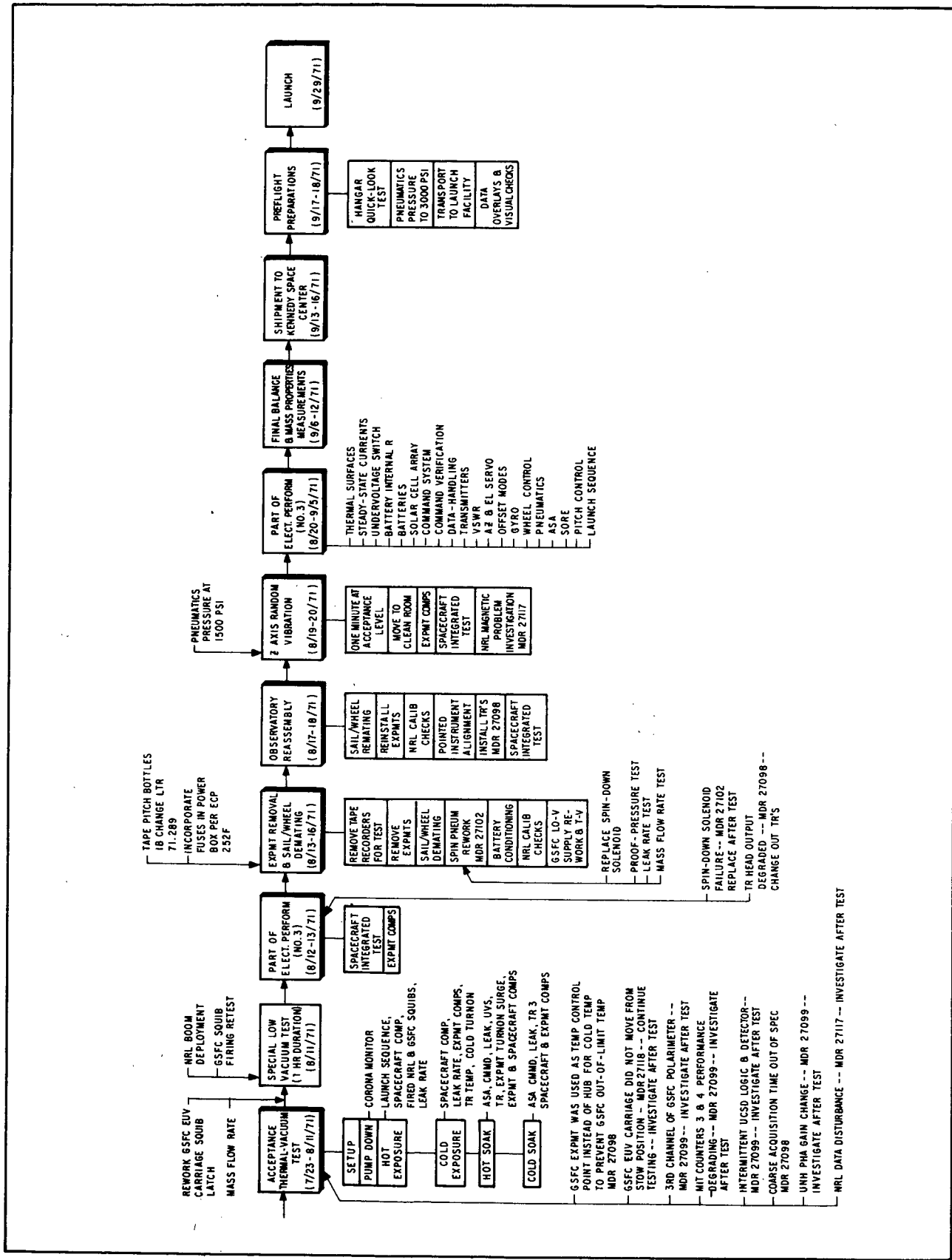


Figure 3-3 Observatory Test History (Sheet 2 of 2)



F72-01

## Section 4 DYNAMICS

Both internal and external torques act on the OSO, causing changes in the position of the spin axis and the spin rate of the wheel. Some of these torques also produce nutation which must be damped. The following is a discussion of the sources of these torques, their influence on OSO, and how their effects are controlled.

### 4.1 ROTATIONAL DYNAMICS OF OSO

The OSO behaves much like a simple, single-body gyroscope, in that they both display "gyroscopic rigidity". This characteristic is due to the rotation of a body about an axis (called the spin axis) which itself may or may not be rotating about some other axis. Because of the angular momentum stored in the wheel, OSO behaves according to basic gyroscopic principles. There are, however, some significant differences that make its motion much more complicated than that of the simple gyro, and the simplified analysis does not accurately describe this complex motion. Some of the more important differences are:

- The simple gyroscope is usually considered to be a rigid body (i.e., not consisting of flexible parts); OSO is semi-rigid.
- The spin rate of the simple gyroscope is normally assumed to be thousands of times greater than the cross-spin rates; with OSO pointing control reactions produce cross-spin rates as large as 0.1 times the spin rate.
- The simple gyroscope consists of a single rotating body; OSO consists of two bodies one of which is constantly spinning (the wheel), while the other (the sail) is normally de-spun. Also, movements of the pointed instruments give the moments of inertia (MOI) of the sail a time-varying character.
- The simple gyroscope is acted upon only by external torques; OSO is acted upon by both external and internal torques. The internal torques come from the elevation and azimuth servos, the nutation damper, and other non-rigid components.

#### 4.2.1 Rotational Dynamics of OSO

In early 1965, BBRC began a thorough analysis of the short-term dynamic properties of OSO. This work was performed under NASA contract NAS5-3695. It was completed in late 1965 and is documented in BBRC Document No. F66-06, OSO Dynamic Analysis. Much of this discussion of OSO dynamic properties was derived from that report. Other sources were the BBRC Document No. F63-3, S-16 Final Report, and analysis and tests of OSO-7.



F72-01

Definition of Nutation, Precession and Wobble. The OSO is a spin-stabilized satellite with a biaxial pointing system. The satellite "precesses" and "nutates" when external and interbody (internal) torques are applied and "wobbles" when the spinning part is not perfectly balanced. Nutation and wobble contribute to short-term pointing instability (jitter) of the pointed instruments.

The coning motion of a balanced, symmetrical satellite that is slightly disturbed from a condition of "pure spin" about its symmetry axis we refer to as "nutation". The term "precession" is used to describe the motion of the angular momentum vector during application of external torques. Both precession and nutation occur during application of external torques. Interbody torques only cause nutation.

The term "wobble" is used to describe the "steady state" motion which results from imperfect balance of the wheel. Wobble and nutation are usually present simultaneously.

Motion of OSO's Spin Axis During Pitch Precession. To adjust OSO pitch attitude, control torques are applied about the X-axis (roll axis) by means of gas jets. These torques cause precessional motion about the Y-axis (pitch axis). The pitch control circuits and gas system, are designed to keep the spin axis aligned to within 3 degrees of normal to the sun line. The spacecraft dynamics associated with this system are discussed here. In this analysis, we will first present the gyroscopic motion of a rigid, symmetrical OSO being constantly torqued, the motions of the same OSO after the external torquing has been removed, and finally a nonsymmetrical OSO being torqued.

For sufficiently small torques the spin axis and angular momentum vector rotate at approximately the same constant rate. This is the only important motion of the typical simple gyro. For larger torques the spin axis ( $\bar{S}$ ) nods or nutates with respect to the smoothly precessing momentum vector ( $\bar{H}$ ).  $\bar{S}$  traces a cycloid while  $\bar{H}$  follows a great circle path. During OSO pitch precession the maximum separation between  $\bar{S}$  and  $\bar{H}$  is about 0.05 degree. This motion is depicted in Figure 4-1\*. In this figure, the X, Y and Z axes are shown as they would appear before the pitch thrust (F) is applied to the spin axis. After the pitch jet is activated, the product of F and its distance from the center of gravity of the spacecraft results in a torque ( $M_x$ ) about the roll axis. This causes the spin axis to rotate (precess) toward the roll axis since it adds momentum along that axis. The paths of  $\bar{H}$  and  $\bar{S}$  during precession are shown as vectors with the precession angles in the XZ plane represented by  $\alpha_H$  and  $\alpha_S$ , respectively. Because the  $\bar{H}$  vector moves only in the XZ plane, it always makes an angle of  $\theta_H = \frac{\pi}{2}$  radians with the pitch axis. The  $\bar{S}$  vector, however, moves in both the XZ and YZ planes and makes an angle of  $\theta_S$  with the pitch axis.

---

\*Figure 4-1 was drawn with the spin axis in the horizontal plane so that an edge view could be obtained of the pitch plane, in order to illustrate the motion of  $\bar{H}$  and  $\bar{S}$  more clearly.



F72-01

Motion Equations of  $\bar{H}$  and  $\bar{S}$  During Precession (Symmetrical OSO). The motion of  $\bar{H}$  and  $\bar{S}$  during precession can be described by a series of equations, that were derived in BBRC Document No. F63-3. These equations are discussed below:

The position of  $\bar{H}$  after  $t$  seconds of precession is identical to that for the typical simple gyro, thus:

$$\alpha_H \approx \frac{\Delta H_X}{H_S} = \frac{M_X t}{I_S \omega_S} \text{ (Rad)} \quad (1)$$

where  $I_S$  is the wheel spin MOI and  $\omega_S$  is the wheel spin rate.

The rate at which  $\bar{H}$  precesses in the XZ plane is:

$$\dot{\alpha}_H \approx \frac{M_X}{I_S \omega_S} \text{ (Rad/sec)} \quad (2)$$

The roll axis torque does not add pitch axis momentum, so  $\theta_H$  is constant at  $\frac{\pi}{2}$  radians =  $90^\circ$ .

The position of the  $\bar{S}$  projection in the XZ plane at any time during precession is given by:

$$\alpha_S = \frac{M_X t}{I_S \omega_S} - \frac{M_X \sin Pt}{I_S \omega_S P} \text{ (Rad)} \quad (3)$$

where "P" is the nutation frequency of the OSO, given by:

$$P = \frac{I_S \omega_S}{I_t} \text{ (Rad/sec)}, \quad (4)$$

where  $I_t$  is the transverse MOI of the entire spacecraft.

Thus, it can be seen from Equation 3 that  $\bar{S}$  leads or lags  $\bar{H}$  by the amount:

$$\left[ \frac{M_X \sin Pt}{I_S \omega_S P} \right]$$

and in Figure 4-1 we have shown that  $\alpha_S$  lags  $\alpha_H$  during the first half-cycle of nutation, leads  $\alpha_H$  during the last half cycle, and coincides with  $\alpha_H$  at the end of each nutation cycle ( $t = \frac{2\pi}{P}$ ).

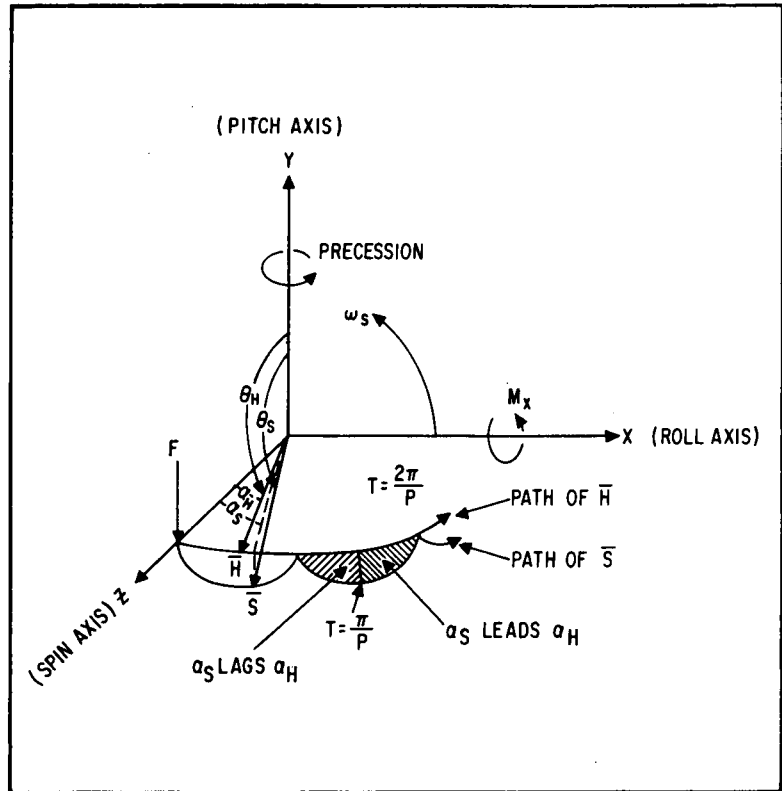


Figure 4-1 Motion of  $\bar{H}$  and  $\bar{S}$  During Pitch Precession



F72-01

The rate at which  $\bar{S}$  moves in the XZ direction is given by:

$$\dot{\alpha}_S = \frac{M_x}{I_s \omega_s} - \frac{M_x \cos Pt}{I_s \omega_s} \quad (\text{Rad/sec}) \quad (5)$$

Thus,  $\dot{\alpha}_S = 0$  at the end of each nutation cycle ( $t = \frac{2\pi}{P}$ ) and is equal to twice the  $\alpha_H$  rate (i.e.,  $\dot{\alpha}_S = 2\dot{\alpha}_H$ ) at the half-cycle point ( $t = \frac{\pi}{P}$ ).

The position of  $\bar{S}$  in the YZ direction is given by:

$$\theta_S = \frac{\pi}{2} + \frac{M_x(1 - \cos Pt)}{I_s \omega_s P} \quad (\text{Rad}) \quad (6)$$

From this it is seen that  $\theta_S = \frac{\pi}{2}$  (the same as  $\theta_H$ ) at the end of each nutation period ( $t = \frac{2\pi}{P}$ ) and equals  $\frac{\pi}{2} + \frac{2M_x}{I_s \omega_s P}$  at the half cycle point ( $t = \frac{\pi}{P}$ ). The term  $\frac{2M_x}{I_s \omega_s P}$  is, therefore, the maximum nutation amplitude of  $\bar{S}$  in the YZ plane and is denoted by:

$$A_n = \frac{2M_x}{I_s \omega_s P} \quad (\text{Rad}) \quad (7)$$

The rate at which  $\bar{S}$  moves in the YZ plane is given by:

$$\dot{\theta}_S = \frac{M_x \sin Pt}{I_s \omega_s} \quad (\text{Rad/sec}) \quad (8)$$

Clearly at both  $\frac{2\pi}{P}$  and  $\frac{\pi}{P}$ ,  $\dot{\theta}_S = 0$ .

The residual nutation amplitude at any time is given by the following equation:

$$r = \frac{1}{P} \sqrt{\dot{\alpha}_S^2 + \dot{\theta}_S^2} \quad (\text{Rad}) \quad (9)$$

where "r" is the half angle of the circular nutational motion (assuming that the transverse MOIs are equal) and  $\dot{\alpha}_S$  and  $\dot{\theta}_S$  are the velocity components of  $\bar{S}$  at the time the torque is removed. Thus, the amount of residual nutation left after a pitch correction depends on when the pitch torque is removed. This residual nutation is damped by the OSO nutation damper.

Motion Equations of  $\bar{S}$  During Precession (Unsymmetrical Body). The equations of motion given above apply to a single-body, symmetrical OSO under constant torque. However, the actual OSO consists of both a rotating "wheel" and a normally stationary "sail" and it is, therefore, necessary to determine the effects of this stationary sail and the pointed instrument assembly (PIA) on the motion of  $\bar{S}$ .



F72-01

If the total\* transverse MOIs of OSO are unequal (i.e.,  $I_x \neq I_y$ ) after the effects of the sail and PIA are accounted for, the OSO is said to be asymmetric. The nutation frequency becomes:

$$P = \frac{I_s \omega_s}{\sqrt{I_x I_y}} \quad (\text{Rad/sec}) \quad (10)$$

However, as shown in BBRC Document No. F63-3, the  $\alpha_s$  equation remains the same as in the symmetric case but the  $\theta_s$  equation changes to:

$$\theta_s = \frac{\pi}{2} + \frac{M_x I_y (1 - \cos Pt)}{I_s^2 \omega_s^2} \quad (11)$$

Thus, for a composite OSO (wheel + sail + PIA) with unequal total MOIs about the transverse axes, both the frequency and amplitude of nutation are different than for a symmetrical OSO.

Residual Motion of  $\bar{S}$  After Pitch Correction Has Been Completed. It was shown in the preceding section that the angular momentum vector,  $\bar{H}$ , remains in the XZ plane ( $\theta_H = \pi/2$ ) at all times during torquing. When torquing of the gyroscopic body is stopped, the residual motion is a nearly circular motion of the spin vector about the angular momentum vector. From Equation 6 it is seen that the amplitude of this motion is dependent upon the position of  $\bar{S}$  on the cycloidal path at the time torquing is stopped. Thus, a maximum residual amplitude of  $2M_x/I_s \omega_s P$  will remain if  $t = (2n + 1) \pi/p$ ; and no residual motion is present if torquing stops when  $t = 2n \pi/p$ , or when the spin vector is coincident with the angular momentum vector. This motion is illustrated in Figure 4-2. Asymmetries of the sail and PIA make the spin axis cone slightly elliptical.

#### Values of Some OSO-7 Dynamic Parameters

Spin MOI of Wheel:  $I_s = 92.8 \text{ slug-ft}^2$ .

Spin MOI of Sail:  $I_s = 19.6 \text{ slug-ft}^2$ .

Transverse MOI of Wheel and Sail with Pointed PIA (geometric mean value):  
 $I_t = 84.35 \text{ slug-ft}^2$ .

MOI Ratio (orbit day condition):  $\frac{I_s}{I_t} = 1.1$

Pitch Torque:  $M_x = 0.356 \text{ ft-lb}$ .

Nutation Frequency:  $P = \frac{I_s \omega_s}{I_t} = 3.46 \text{ Rad/sec}$ .

\*The "total" transverse MOI of OSO takes into account, in addition to the transverse MOI of the wheel, the MOI of the sail about the X and Y axes and the MOI of the PIA about the X and Y axes. Thus,  $I_x$  and  $I_y$  refer to the total (wheel + sail + PIA) transverse MOI of OSO about the X and Y axes. When the PIA is pointed or "free wheeling" the OSO moves as if the X axis MOI of the PIA was absent.



Maximum Nutation Amplitude  
During Pitch Precession:

$$A_{\eta} = \frac{2M_x}{I_s \omega_s^2 P} = 0.685 \times 10^{-3} \text{ Rad}$$

Angular Velocity of  $\bar{H}$  During  
Pitch Precession:

$$\dot{\alpha}_H = \frac{M_x}{I_s \omega_s} = 1.22 \times 10^{-3} \text{ Rad/sec.}$$

4.1.2 Interactions  
Between the  
Pointing Control  
System and  
Nutation

The coupling between the azimuth and elevation servos is complex. Some conclusions obtained from computer analysis regarding these couplings are summarized in the following paragraphs:

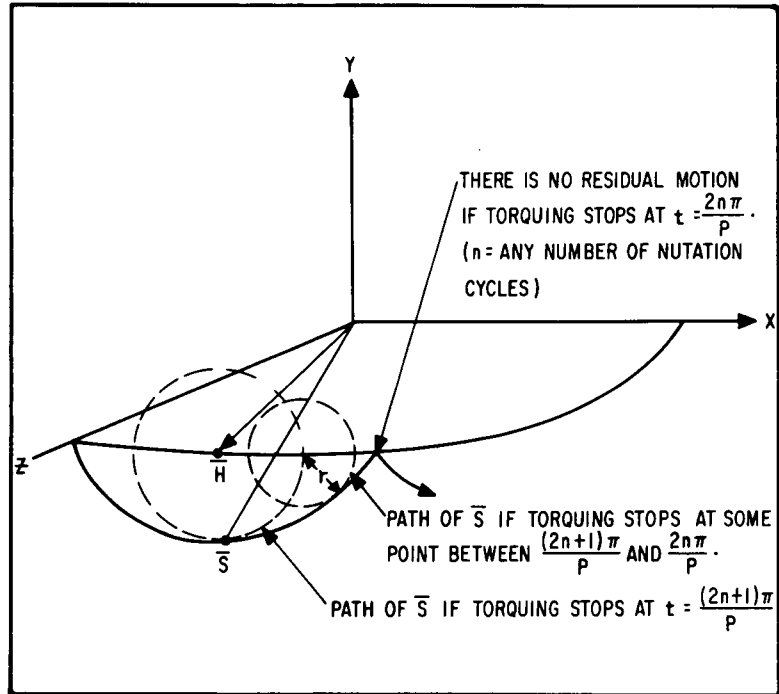


Figure 4-2 Residual Nutation of  $\bar{S}$  After Constant Torquing Stops

Effects of the Azimuth and Elevation Servos in Nutation on the Pointing Mode. The azimuth and elevation control servos form a biaxial pointing control system. When the sail is accelerated in azimuth by the azimuth servo, the reaction torque (acting about the spin axis) causes a small change in the wheel spin rate ( $\omega$ ). This torque has little effect on OSO nutation. On the other hand, when the PIA is accelerated in elevation by the elevation servo, the reaction torque is in the "cross-spin" direction (perpendicular to the spin axis) and thus directly affects the nutational motion of the spin axis.

During the normal pointing mode, i.e., after coarse acquisition has occurred, any spin axis nutation causes a periodic disturbing torque to be applied to the PIA about the elevation bearing axis. This disturbance, caused by friction in the elevation bearings, causes periodic changes in the elevation pointing error (jitter). The elevation servo generates corrective torques proportional to the magnitude and rate of change of the elevation pointing error.

Torques from the elevation servo have a slight tendency to increase nutation. In OSO-7, this tendency is very small and is nearly damped out by the nutation damper. The effect is a small residual nutation, on the order of 1 arc-second, the result of a balance between the tendency of the servo to increase nutation and the damper's tendency to squelch it.

Effect on Nutation of Dusk Transient. When the spacecraft passes into the shadow of the earth the solar reference is lost. When this happens the PIA is pulled over to the negative stop position by the elevation axis spring. This causes nutation as illustrated in Figure 4-3.





F72-01

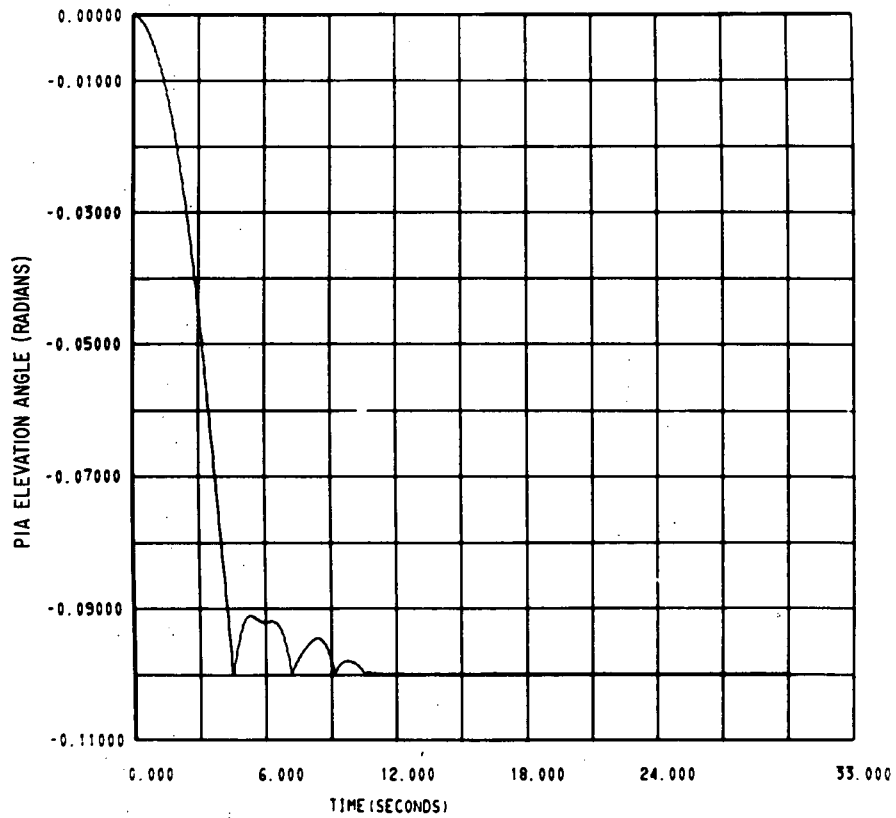
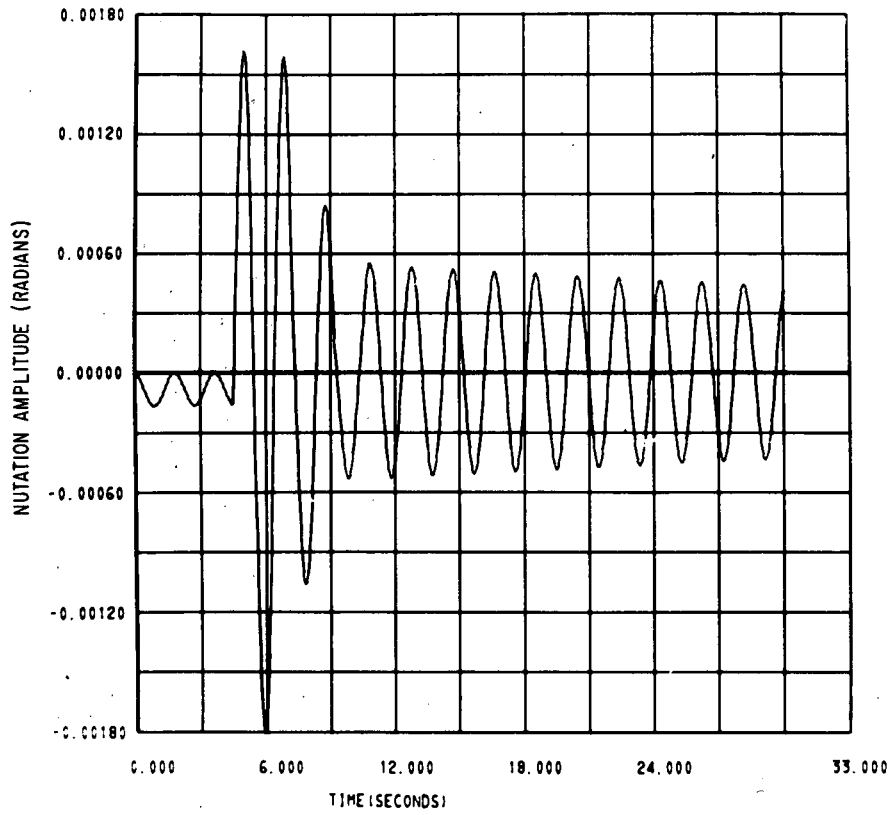


Figure 4-3 Dusk Transient



F72-01

The first trace shows the elevation angle of the PIA as it moves over to and bounces on the stop. The second trace shows the resulting nutation. Notice that the initial motion of the PIA before contact with the stop causes only a small amount of nutation, about 30 seconds of arc peak-to-peak. The contact causes nutation to increase to just under 0.1 degree. The damper then rapidly reduces nutation.

Effect on Nutation of Dawn Acquisition. When the spacecraft emerges from the dark side of the earth into sunlight at orbit dawn, the azimuth and elevation servos point the PIA at the sun. Because the gyro holds the sail position at night the azimuth transient is very small. There is, however, a large elevation transient.

Figure 4-4 shows the nutation caused by such a transient. The spacecraft is in a 3 degree pitched down position, and the PIA is at the negative stop, because of the spring. This is a worst case, i.e., the pitch angle is at its limit and of a polarity to cause maximum PIA motion at acquisition. During the PIA transient, which lasts 10 seconds, nutation reaches a maximum amplitude of 1.0 degree. It then begins to decrease due to damper action.

Nutation Damper Action.

The damper used on the OSO consists of a bob of dense material attached to the end of a length of piano wire. This bob is immersed in a viscous fluid which applies retarding forces to the bob. The bob and damping fluid are contained in a compact case. This damper dissipates the kinetic energy associated with nutation by converting it into heat.

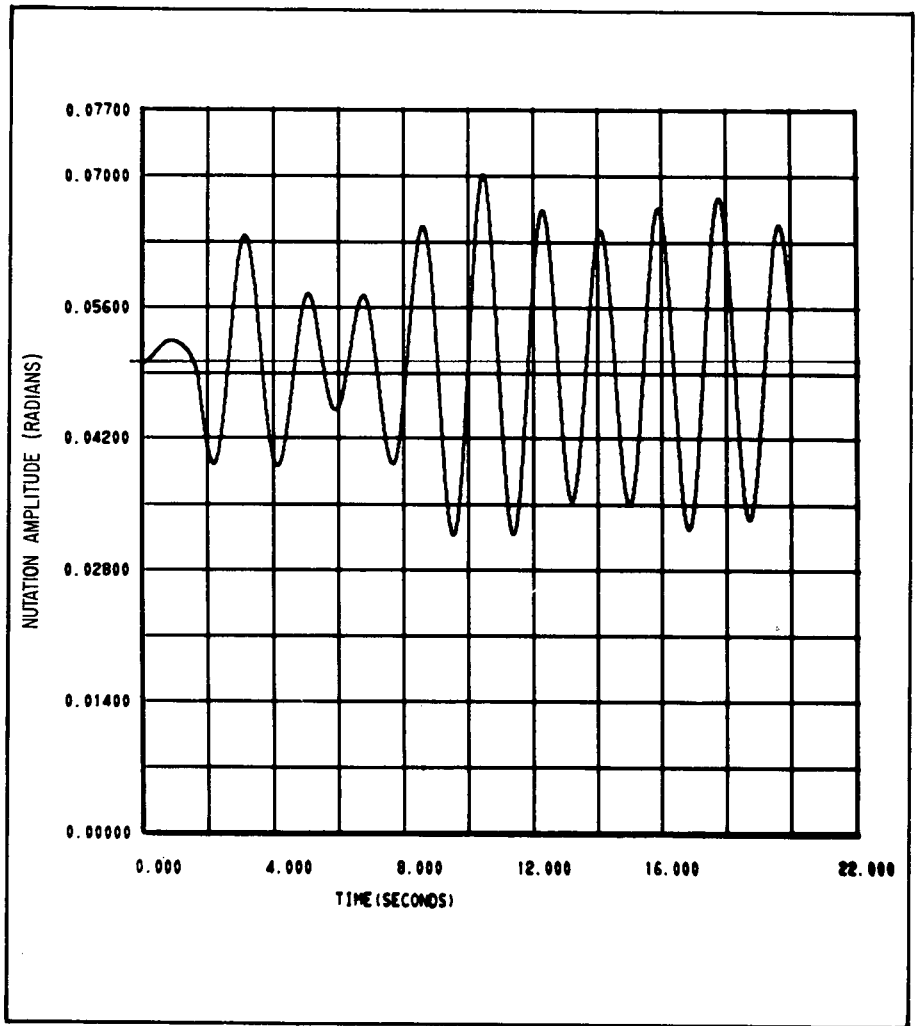


Figure 4-4 Dawn Transient



F72-01

The total rotational kinetic energy of a nutating OSO can be expressed as the vector sum of the spin kinetic energy ( $T_s = 1/2 I_s \omega_s^2$ ) and the cross-spin kinetic energy ( $T_t = 1/2 I_t \omega_t^2$ ). Thus, the total kinetic energy is:

$$T = 1/2 I_s \omega_s^2 + 1/2 I_t \omega_t^2 \quad (12)$$

The cross-spin kinetic energy is associated only with the coning motion (nutation) of the spin axis about the spin angular momentum vector ( $\bar{H}_s$ ), and must decay to zero if the nutation cone is to collapse onto the angular momentum vector. It can also be said that the total angular momentum ( $\bar{H}$ ) is the sum of its spin and cross-spin components, or

$$\bar{H} = \bar{H}_s + \bar{H}_t \quad (13)$$

If it is assumed that the nutation cone collapses strictly as the result of dissipation of energy by the nutation damper, then the total kinetic energy of the spacecraft must change; but its angular momentum remains constant (since no external torque is involved). Because the angular momentum vector is constant, the final spin rate of the wheel (after dissipating the nutation energy) can be calculated as follows. Initially,

$$H^2 = (I_s \omega_s)^2 + (I_t \omega_t)^2 \quad (\text{from Pythagoras' theorem for right triangles})$$

The  $(I_t \omega_t)^2$  term in the above equation is reduced to zero as the cross-spin component is dissipated by the nutation damper. Using \* to denote final values we write the fluid momentum as

$$H^{*2} = (I_s \omega_s^*)^2 \quad (14)$$

However, since  $H^* = H$ ,  $\omega_s$  must increase and the final spin rate ( $\omega_s^*$ ) can be calculated as follows:

$$H^{*2} = (I_s \omega_s^*)^2 = (I_s \omega_s)^2 + (I_t \omega_t)^2$$

or

$$\omega_s^{*2} = \omega_s^2 + \left(\frac{I_t}{I_s}\right)^2 \omega_t^2 \quad (15)$$

The final kinetic energy of OSO after dissipation of the nutation energy is:

$$T^* = T_s^* = 1/2 I_s \omega_s^{*2} = 1/2 I_s \omega_s^2 + 1/2 \left(\frac{I_t^2}{I_s}\right) \omega_t^2 \quad (16)$$

The net change in kinetic energy ( $\Delta T$ ) during collapse of the nutation cone is the difference between the kinetic energy expressions in Equations 12 and 16, thus

$$\Delta T = T - T^* = 1/2 I_t \left(1 - \frac{I_t}{I_s}\right) \omega_t^2 \quad (17)$$

or

$$\Delta T = \left(1 - \frac{I_t}{I_s}\right) T_t$$



F72-01

The conclusions that can be drawn from the above are that:

- $H_t$  and  $T_t$  have decayed to zero
- $T_s$  has grown to  $T_s^*$
- The total kinetic energy of OSO must decrease if  $I_s > I_t$ .

The increase in wheel spin rate is caused by a damper spin axis torque which the azimuth servo transmits to the wheel. Thus, as the damper dissipates the cross-spin energy the azimuth servo increases the spin kinetic energy (this energy is actually supplied by the solar array).

OSO Nutation Damper Performance. The OSO nutation damper (with a seismic mass of 1/1800 of the spacecraft mass) causes a nutation amplitude of less than 1/3 degree to decay to about 1/3 of its initial value in about 2 minutes (larger amplitudes force the damper bob against the case).

#### 4.2 BALLASTING FOR PROPER MOMENT OF INERTIA

OSO-7 is inertially "disk-shaped" in the sense that the wheel spin moment of inertia (MOI) is greater than the overall transverse MOI. Location of wheel equipment and wheel rim ballast weight is carefully arranged to meet this requirement. The reason for making the spacecraft inertially "disk-shaped" is to assure nutational stability. We thus ensure that the nutation cone collapses rather than expands following a disturbance. If this MOI relationship was not achieved, stability would be dependent on the relative energy dissipation rates on the sail and wheel. OSO's disk-shaped design assures that the spacecraft is unconditionally stable and avoids the expensive testing and analysis of potentially destabilizing mechanisms on the wheel.

Ballasting also affects wobble. If spin and transverse inertias are close to one another, dynamic imbalance will produce a large wobble coning motion. For this reason, a margin must be allowed between spin and transverse inertias. With the sail despun the wobble angle is proportional to the imbalance and inversely proportional to the difference between the wheel spin MOI and the mean of the overall transverse MOIs.

Stability Criterion. If the spinning and non-spinning sections of the spacecraft were symmetrical, so that the transverse MOIs were the same about X and Y axes, then the stability criterion would be:

$$I_{s(\text{wheel})} - I_{T(\text{overall})} > 0 \quad (18)$$

For the real case of an OSO-7 with both sail and wheel that are asymmetric, we use the criterion that spin MOI must exceed the geometric mean of the overall transverse principal MOI's where the largest transverse principal MOI of the wheel is used in both axes (care is taken to ballast for nearly equal wheel transverse MOI's). Since measurement of MOIs cannot be made exactly, we add a margin of 2 slug-ft<sup>2</sup> to the requirement. The final ballasting requirement for stability is



F72-01

$$I_{s(\text{wheel})} - \sqrt{(I_x)(I_y)} > 2 \text{ slug-ft}^2 \quad (19)$$

since the transverse principal axes are approximately along the X and Y axes.

Wobble Criterion. The ballasting requirement from a wobble standpoint is slightly different. An asymmetrical spacecraft will have a nearly (but not exactly) circular wobble cone that is approximately defined by:

$$\theta_{\text{wobble}} \approx \frac{U}{I_s - I_T} \quad (20)$$

where U is the dynamic imbalance and  $I_T$  is the average of the transverse MOIs. We can dynamically balance the spacecraft to about 250 oz-in<sup>2</sup>. We would like to hold  $\theta_{\text{wobble}}$  to 3 arc-min (a total wobble cone angle of 6 arc-min or 0.1 degree) to control "blur" at the sun's limb. To meet this criterion, the ballasting requirement is:

$$I_{s(\text{wheel})} - \sqrt{(I_x)(I_y)} > 4 \text{ slug-ft}^2 \quad (21)$$

Note that the wobble criterion is based on a daytime pointing requirement. At night, wobble can be larger since no pointing is taking place. Larger wobble is expected at night because a spring pulls the pointed-instrument assembly against one of the stops. This effectively increases the transverse moment of inertia.

Summary. The OSO-7 spacecraft is ballasted so that both of the requirements (Equations 19 and 21) are met. For OSO-7, the wobble requirement sets the ballast size.

OSO-7 Mass Properties. The more important OSO-7 mass properties are given in Table 4-1

#### 4.3 STABILITY AND DYNAMICS DURING INITIAL ACQUISITION

As discussed in Section 7, the sail is spun up to about 33 rpm prior to separation from the launch-vehicle. Since the spin MOI of the sail is smaller than the overall transfer MOI, the observatory has "rod-like" stability properties. As the sail despins and the wheel spins up, the unconditional stability region is entered. It is possible to calculate the angular velocity of the sail and wheel for which this occurs. The "energy-sink" stability condition for symmetric dual-spin spacecraft is:

$$\frac{\lambda_o}{I_t} \left( \frac{\dot{T}_1}{\lambda_1} + \frac{\dot{T}_2}{\lambda_2} \right) < 0 \quad (22)$$

where:

- $\lambda_o = (CW_s + I_s W_w) / I_t$
- $\lambda_1 = \lambda_o - W_s$
- $\lambda_2 = \lambda_o - W_w$
- $I_t =$  transverse moment of inertia
- $\dot{T}_1 =$  energy dissipation rate in the sail



F72-01

- $\dot{T}_2$  = energy dissipation rate in the wheel
- $W_s$  = angular velocity of the sail
- $W_w$  = angular velocity of the wheel
- $C$  = spin moment of inertia of the sail
- $I_s$  = spin moment of inertia of the wheel

Table 4-1  
OSO-7 MASS PROPERTIES

<u>PARAMETER</u>	<u>VALUE</u>
<u>Spin MOI</u>	
Wheel Only	92.8 slug-ft <sup>2</sup>
Wheel and Sail	112.2 slug-ft <sup>2</sup>
<u>"Night" Transverse MOI (with PIA locked)</u>	
	$I_x^N = 89.65 \text{ slug-ft}^2$
	$I_y = 87.55 \text{ slug-ft}^2$
<u>"Day" Transverse MOI (with PIA "floating")</u>	
	$I_y = 87.55 \text{ slug-ft}^2$
	$I_x^D = 81.15 \text{ slug-ft}^2$
<u>Total Weight (at liftoff)</u>	1415.5 lbs
<u>Ballast Weight</u>	225.2 lbs
<u>Ballast-Stability and Wobble</u>	

$$\text{"Night" } I_{S(\text{wheel})} - \sqrt{(I_x^N)(I_y)} = 4.2 \text{ slug-ft}^2$$

$$\text{"Day" } I_{S(\text{wheel})} - \sqrt{(I_x^D)(I_y)} = 8.45 \text{ slug-ft}^2$$

During the launch sequence, the worst case is when energy is dissipated in the sail but not in the wheel. Since  $\lambda_o$  and  $I_t$  are positive and  $\dot{T}_1$  is negative, the stability boundary for this case is defined by:

$$\lambda_1 > 0$$

or

$$CW_s + I_s W_w - I_t W_s > 0 \tag{23}$$



F72-01

This can be rearranged slightly to give:

$$(C - I_t) + \left(\frac{W_w}{W_s}\right) I_s > 0 \quad (24)$$

At a ratio of wheel to sail angular velocity of 0.7, the spacecraft enters the unconditionally stable region. Acquisition is programmed by the launch-sequence subsystem (with the wheel being spun-up by the jets and the sail being despun by the motor). Unconditional stability is attained at about 29 seconds, as shown in Figure 4-5.

During these 29 seconds energy dissipation on the sail tends to make nutation grow. This tendency is small because little sail dissipation is expected with the damper caged and PIA locked. Figure 4-6 shows that even with the damper uncaged to dissipate energy, the spin-up jet control torque adds spin momentum fast enough to cancel the damper's destabilizing tendency.

To further assure that OSO is stable during the launch sequence, we examined the case in which the pointed instruments were prematurely unlocked. Our examination showed that nutation build-up could be prevented by keeping the initial sail spin rate below about 50 rpm. This influenced our choice of a nominal sail spin rate of 33 rpm.

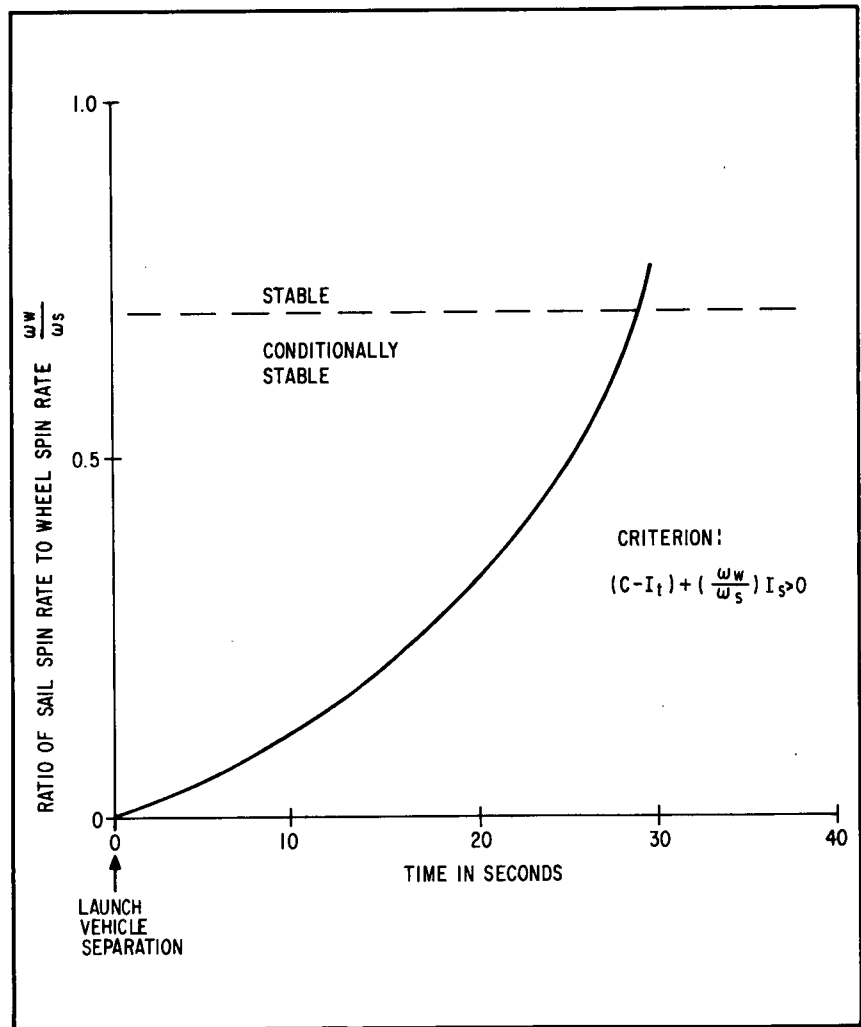


Figure 4-5 Time Required to Enter Dynamically Stable Region During Launch Sequence



F72-01

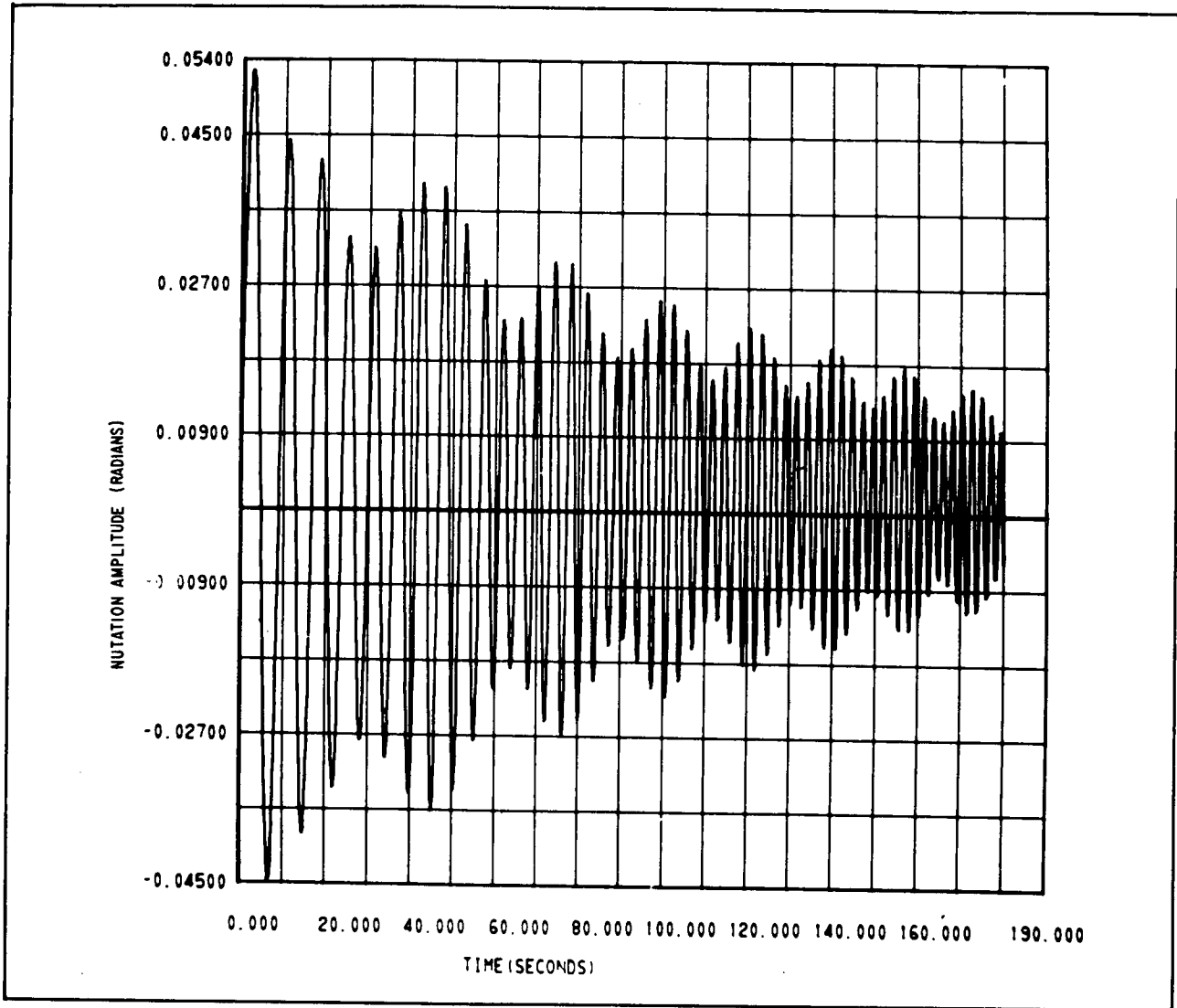


Figure 4-6 Worst Case Expected Nutation Decay During First Solar Acquisition





F72-01

Section 5  
OBSERVATORY ASPECT MONITORS

5.1 GENERAL DESCRIPTION

The aspect monitors generate information from which the spacecraft attitude and the instantaneous viewing direction of each experiment instrument may be determined. The measurements are made using four independent monitoring schemes, each of which is discussed below. Telemetry data reduction and aspect coordinate systems are discussed in Appendix A.

Fine Pitch Monitor. The fine pitch monitor is similar to that flown on earlier OSO missions. It indicates the observatory pitch attitude when the spacecraft upper structure is aimed within seven degrees of the sun. Pitch angle is defined as zero when the OSO spin axis is perpendicular to the sun line. The pitch angle is normally within 3 degrees of zero.

The fine pitch solar sensor generates an analog voltage (0 to 5 volts) corresponding to pitch angles within its range. This voltage is encoded by the data-handling system and entered in the sail analog subcommutator frame every 15.36 seconds. Four successive channels, 0.32 second apart, are used, so that short-term changes such as from nutation or wobble can be observed.

Pitch attitude data are used together with data from the Spin Orientation and Rate Electronics (SORE) package in the calculation of spacecraft roll attitude and aspect.

Large Angle Pitch Monitor. The large angle pitch monitor, usually referred to as the Digital Aspect Sensor (DAS), measures the angle between the wheel plane and the sun line for any spacecraft orientation with an accuracy of about 1 degree. The DAS is a new component on OSO-7.

The sensor, located in a wheel compartment, views the sun once each revolution. The pitch angle is encoded using Gray code and stored in a buffer. Every 15.36 seconds it is read out through channel 34 of the digital subframe.

The DAS indicates spacecraft pitch attitude outside the range of the fine pitch readout sensor. It does not require orientation of the pointed instruments toward the sun for its operation.

Coarse Aspect Monitor. The coarse aspect monitor consists of the Spin Orientation and Rate Electronics (SORE) and associated equipment, roughly similar to that flown on earlier OSO missions. The OSO-7 SORE incorporates new operating modes which expand the capability of the monitor.

A solar sensor, or spin eye, mounted on the rim of the wheel, generates a pulse every wheel revolution as its sensitive axis passes the sun. The magnetometer sensor is mounted on the rim of the wheel at the lower edge of the antenna skirt. Electronic



F72-01

circuits in the SORE package generate one pulse every wheel revolution at the positive-going zero crossing of the magnetometer output signal. If there is relative motion between the wheel and sail, one pulse is generated each revolution by an azimuth encoder (blipper) located in the despin drive assembly.

The outputs from these three sensors are combined with a data-gate time reference in the SORE to provide time-interval information. The telemetered counts correspond to the number of 800 bps spacecraft clock pulses that occur between the signals generated by the sensors and the data system timing reference. The desired counting mode may be selected by ground command.

Fine Aspect Monitor. The fine aspect monitor, usually called the Aspect Sensor Assembly (ASA) or, more simply, the star sensor, is a new component on OSO-7. It generates information from which the spacecraft and experiment aspect is calculated more accurately (to about 0.1 degree) than with the SORE. The ASA provides data only during orbit night.

The star sensor, mounted in a wheel compartment and aimed downward at an angle of 37 degrees from the wheel plane, measures the intervals between observations of bright stars as the wheel rotates. The ASA registers crossings of stars in an elevation band about ten degrees high. The images enter one vertical and one skewed slit spaced in azimuth so that the time interval between the observations of a star by the two slits is dependent on the elevation position of the star. The detection threshold of the star sensor may be adjusted by ground command.

The location of the aspect sensors is shown in relation to the payload instruments in Figure 5-1. The angles indicated on the figure are design nominal values rather than the result of calibration measurements.

## 5.2 FINE PITCH MONITOR

The pitch readout sensor is identical to the one used on all earlier OSO's. The sensor consists of an analog sun-sensing unit and electronic signal-conditioning circuits all contained in a common housing. It is mounted on the sail with its optical axis parallel to the spacecraft roll axis.

The sensing unit consists of a filter/reticle and a pair of silicon photovoltaic cells arranged as shown in Figure 5-2. The beam of sunlight that goes through the slit in the reticle falls equally on the two cells at null. As the angle between the sun line and the sensor axis increases, the energy increases on one cell and decreases on the other.

The cells are connected in parallel opposition. The resulting output is linear to approximately  $\pm 6.5$  degrees (where the light beam no longer falls on one of the cells). Beyond 6.5 degrees, the output continues to increase slightly until the entire beam of light is on one cell. The output then stays constant until the light beam begins to move off the cell. The total field of view of the sensor is about  $\pm 25$  degrees. The electronics serve to limit the output of the sensor at an angle corresponding to about  $\pm 5.5$  degrees, resulting in the overall output-versus-angle characteristic shown in Figure 5-3.



F72-01

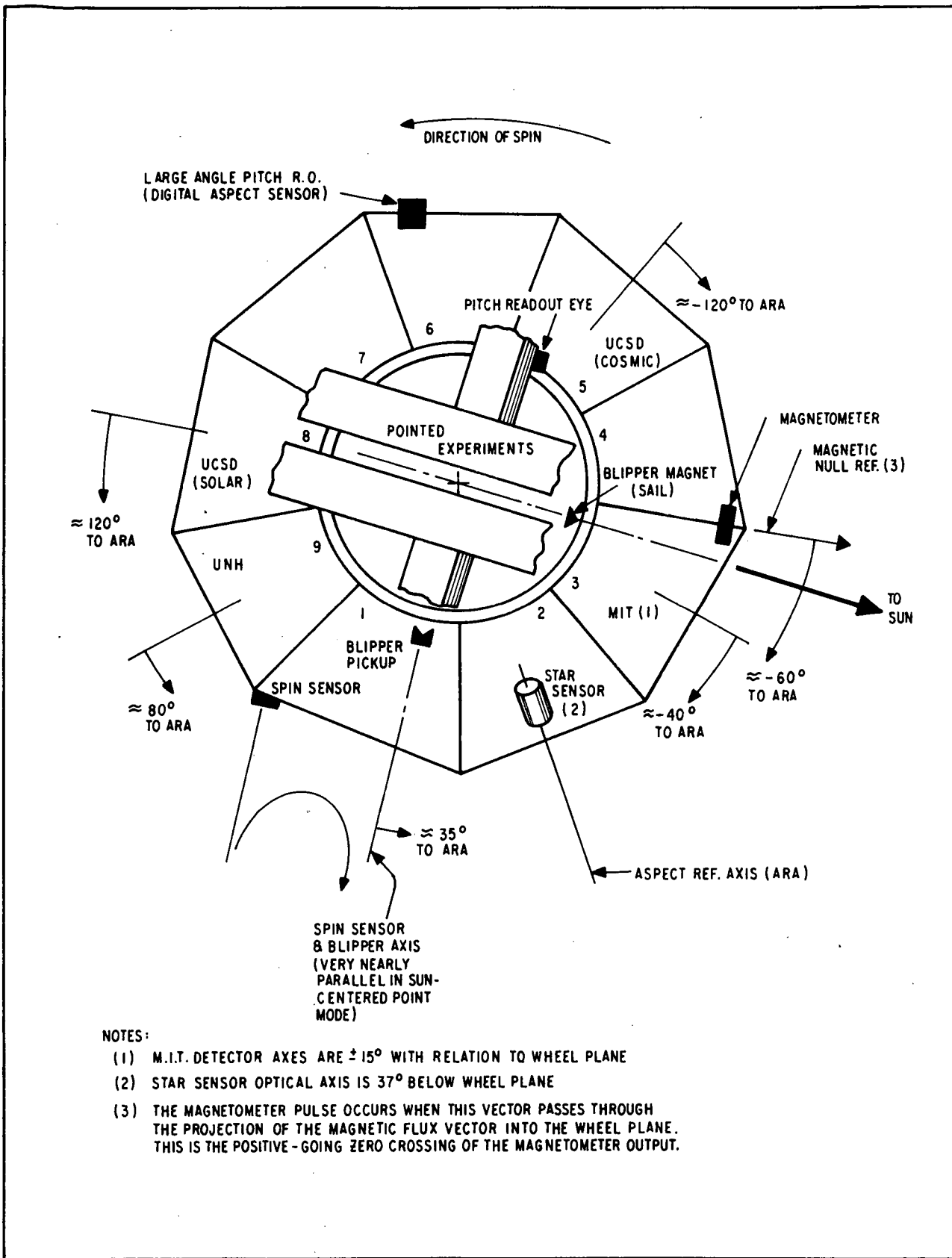


Figure 5-1 Location of Aspect Sensors and Reference Axes



F72-01

The output of the fine pitch monitor is sampled by four consecutive channels of the sail analog sub-commutator. Since the periods of nutation and wobble are roughly 2 seconds, the four consecutive readings cover about one-half of a period in each sample interval. This provides a better means of evaluating nutation and wobble than was available on earlier OSO flights.

The angle between the spacecraft roll axis and the sun line may be reconstructed from the telemetered data using the relation:

$$\text{Pitch Angle (degrees)} = (\text{count} - 130) \times 0.0368$$

The negative sign in this angle occurs when the roll axis is below (in spacecraft coordinates) the sun line.

### 5.3 LARGE-ANGLE PITCH MONITOR

The large-angle pitch monitor consists of the Digital Aspect Sensor (DAS) and supporting electronic circuits. The DAS provides a telemetry readout representing the angle between the observatory wheel plane and the sun line. This angle (pitch angle) is measured to an accuracy of  $\pm 1$  degree for any spacecraft attitude. The DAS uses two sets of sensors, each having a 90 degree vertical field of view, and a 1.5 degree horizontal field of view. One set is used to read negative pitch angles, and the other is used when pitch angle is positive.

As the wheel rotates, the sky is scanned by the DAS once each revolution. When the sun is in the field of view, the pitch angle is encoded and stored until read by telemetry (DSF word 34). The unit may be turned on or off by ground command.

The main purpose of the DAS is to determine the pitch angle when the fine pitch sensor is not usable. The DAS consists of a sensor assembly, and an electronics assembly. The sensor assembly consists of two separate sets of sensors, each of which operates over a 90° field of view. The two sets are arranged symmetrically about the wheel plane, thus providing the full 180° of coverage. Each set of sensors consists of two sensors, one "command eye", and one coded eye, as shown in Figure 5-4.

Figure 5-4 illustrates the principle of operation of a set of sensors. When the sun's rays strike the reticles of a set of sensors, the command eye output causes the coded eye output to be read into the storage register. The register stores the digital output until the next command-eye pulse or until it is cleared by the telemetry readout.

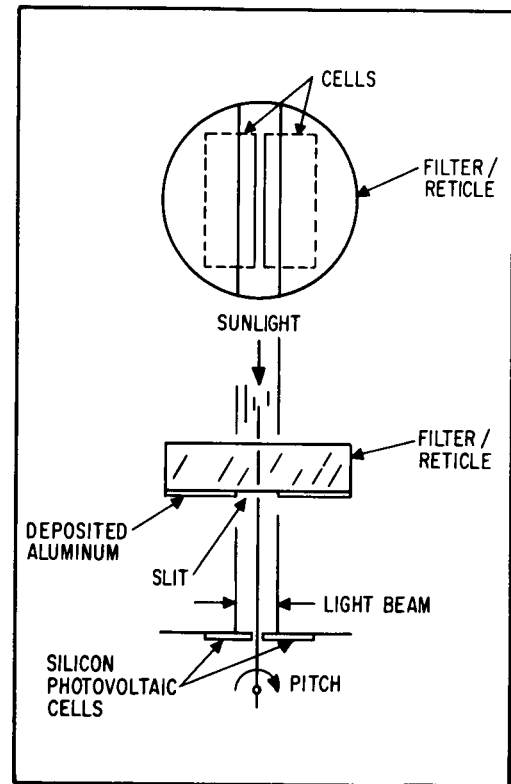


Figure 5-2 Diagram of Pitch Readout Sensor



F72-01

The output of the DAS is contained in a single eight-bit DSF telemetry word. As seen in Figure 5-4, the most-significant bit indicates which set of sensors is illuminated, and thus establishes the sign of the pitch angle. The other seven bits contain the coded data representing the magnitude of the angle. Note that the seven digit bits of the two coded eyes are operated in parallel. The 7-bit code is accommodated in a single 8-bit word, because only one coded reticle is illuminated at one time. The eighth bit indicates which reticle is illuminated.

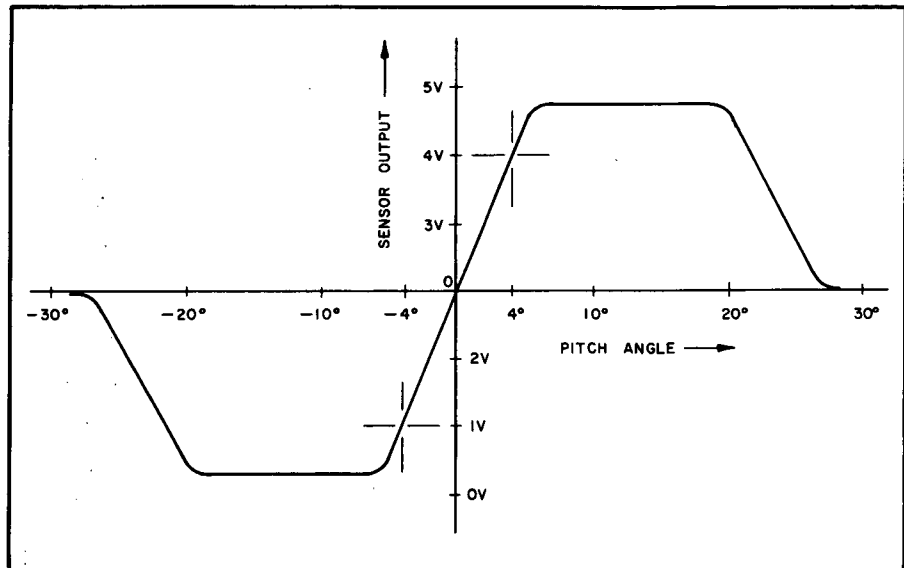


Figure 5-3 Pitch Readout Sensor Output Curve

Readout occurs when the "word gate" signal is present. This signal is such that it overlaps eight clock pulses. The gate signal allows the clock to step the contents of the storage register into the telemetry frame. It also inhibits the command eye pulse in order to prevent invalidation of a reading by a bit being read into the register during the shift period.

The outputs of the photocells are conditioned by the bit amplifiers. The output of each bit amplifier is 0 volts or +5 volts, indicating whether a photocell is illuminated or not. The change of state occurs at about 0.75 of mean solar intensity, to avoid the possibility of having the register loaded by earthshine.

Gray Code. Any angle encoder, whether optical or mechanical, must provide some means of avoiding certain ambiguities which arise if a natural binary-code pattern is used. The origin of these ambiguities can be seen by examining the natural binary numbers of Table 5-1. Consider the case where the angle is changing from 4 to 3. If the third binary digit from the right were to change before the first two, the angle would change to 0 instead of 3. Since no mechanical or optical encoder can be perfect, this sort of error can always occur. To eliminate this difficulty, so-called unit-distant codes, which permit only one digit at a time to change, have been designed. Such a code, named cyclic binary, reflected binary, or Gray code, is used on the OSO-7 DAS.

Two methods are available to decode the data: look up each number in a calibration table, or use a mathematical relation suitably programmed into a computerized data-reduction procedure.



F72-01

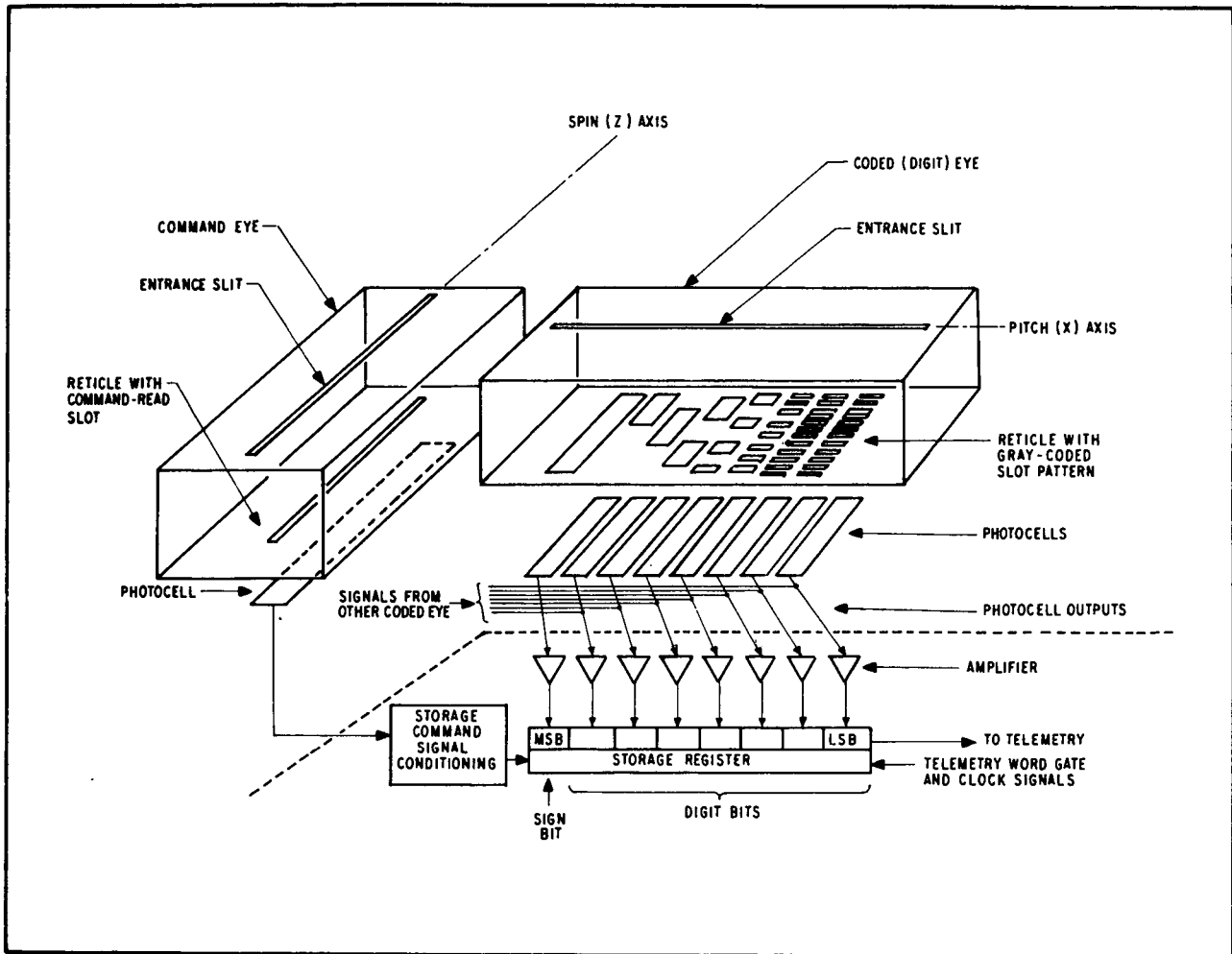


Figure 5-4 Principle of Large-Angle Pitch Monitor

Table 5-1  
GRAY-TO-BINARY CONVERSION

- (1) The most significant bit is the same in either code.
- (2) Each succeeding binary bit is the complement of the corresponding Gray bit if the preceding binary bit is a "one" or is the same as the corresponding Gray bit if the preceding binary bit is a "zero".

<u>Decimal</u>	<u>Binary</u>	<u>Gray</u>
0	00000000	00000000
1	00000001	00000001
2	00000010	00000011
3	00000011	00000010
4	00000100	00000110
5	00000101	00000111



F72-01

#### 5.4 COARSE ASPECT MONITOR (SORE)

The coarse and fine pitch monitors measure the angle between the spin axis (or wheel plane) and the direction line to the sun. This does not, however, provide a total attitude picture; it only defines a locus of possible spin-axis orientations. In order to fully define the great circle of the sky being scanned by the rotating instruments, or the portion of the sun being observed by the pointed instruments when operating in the offset mode, the orientation of the spacecraft spin axis in the celestial sphere must be fully defined. To establish the spin axis direction, it is necessary to find another reference independent of the sun. The one used by the SORE is the earth's magnetic field.

The main function of the SORE, is to fully define spin axis direction at any time in the flight. It does this by telemetering the wheel plane angle between the solar vector and the earth's magnetic field. Mathematical computations, described in Appendix A, relate this angle to the known directions of the solar and field vector, and yield the spacecraft roll orientation, referenced to the celestial north pole.

In addition to providing spin-axis direction, the SORE also provides information from which the instantaneous position of a rotating instrument's optical axis may be calculated. This information is time-related to the telemetry frame. Thus, an experimenter can relate observed cosmic events to their particular direction of origin.

In both of the measurements defined above, observatory spin rate is a necessary parameter. Spin rate may be calculated to within  $\pm 10^{-4}$  rps using SORE data. Another potentially useful function provided by the SORE is information from which sail spin rate with respect to the wheel may be calculated.

##### 5.4.1 SORE Signal Inputs

Magnetometer Signal. The magnetometer signal input to the SORE is generated in a flux-gate magnetometer which produces a voltage proportional to the magnetic field along its sensitive axis. Since the magnetometer rotates with the wheel, its output is an ac voltage phased with wheel rotation. A detector in the SORE produces a pulse when the positive-going zero crossing of the magnetometer signal is sensed. The zero crossing of the signal is sensed rather than its peak since the greater slope of the signal at its crossing makes the crossing the most easily sensed point on the signal over a wide range of field magnitudes.

The magnetometer consists of an oscillator, sensor, signal amplifier, and demodulator (Figure 5-5). The oscillator provides an alternating current large enough to cyclically drive the core into magnetic saturation. If there is no external magnetic field acting on the core, the core saturates equally on both the positive and negative portions of the cycle, and the flux generated in the core has a symmetrical pattern. If there is a magnetic field acting on the core, the core remains saturated longer on one half of the cycle than on the other. The flux generated in the core then has an asymmetrical waveform containing even-order harmonics of the excitation frequency, not present in the symmetrical flux pattern. For weak magnetic fields such as that of the earth, the even harmonics are proportional in magnitude to the intensity of the applied magnetic field.



F72-01

The amplifier signal from the oscillator excites the primary winding on the sensor. The signal from the sensor secondary passes through an amplifier tuned to the second harmonic of the oscillator frequency. The amplitude of this harmonic signal is proportional to the strength of the magnetic field at the sensor. Using a second-harmonic reference voltage (derived from the same transformer that drives the sensor), the signal is demodulated, thus producing a dc output

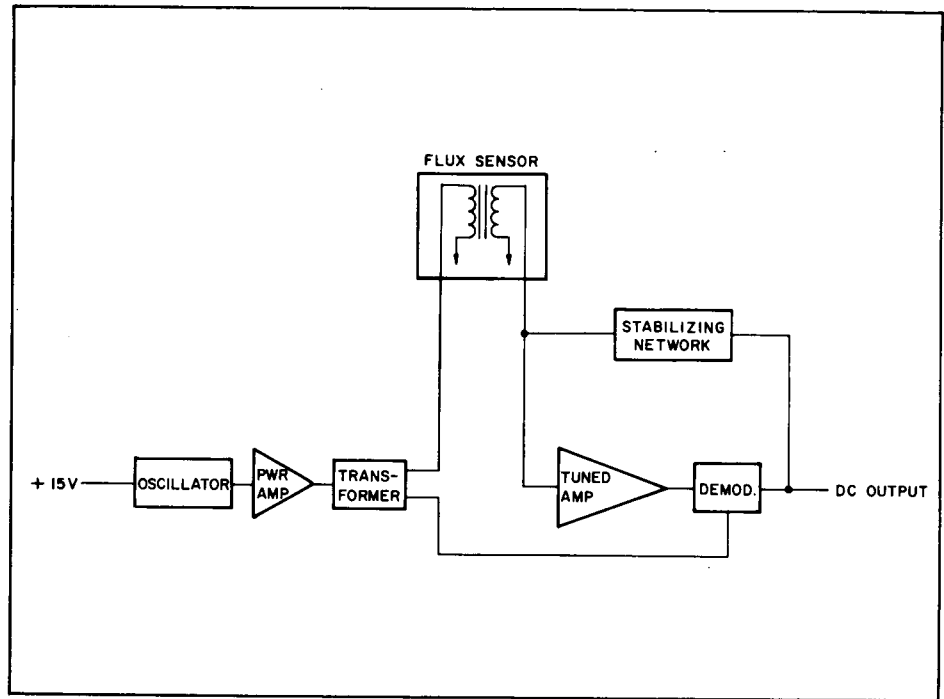


Figure 5-5 Flux-Gate Magnetometer

voltage proportional to the strength of the earth's magnetic field. A negative feedback network from the output to the sensor secondary is used to temperature-stabilize the circuit and to provide automatic gain control.

Aspect Spin Eye Signal. The aspect spin eye is part of the spin sensor assembly and is identical to that used on earlier OSO's. The spin sensor assembly is an array of four solar sensors on an aluminum block, mounted on the rim of the wheel, with their sensing planes parallel to the spin axis.

Each of the four eyes consists of a housing, lens, aperture plate, filter, and a silicon photovoltaic cell. The copper-foil aperture plate is located in the focal plane of the lens, and the slit in the aperture plate defines a long, narrow field of view,  $26 \pm 2$  degrees in elevation and  $2.5 \pm 0.5$  degree in azimuth. The eyes are mounted so that the fields of view of two of them are symmetrical about the wheel plane, while the other two are canted up 3 degrees and down 3 degrees, respectively. The outputs of the two canted eyes go to the automatic spin control system. The other two eyes provide outputs for the SORE and the auto-spin limiter in the spin control assembly.

The aspect spin eye pulse is squared and amplified in the SORE package. It is used to indicate the time when the aspect spin eye reference crosses the solar vector in each wheel revolution.



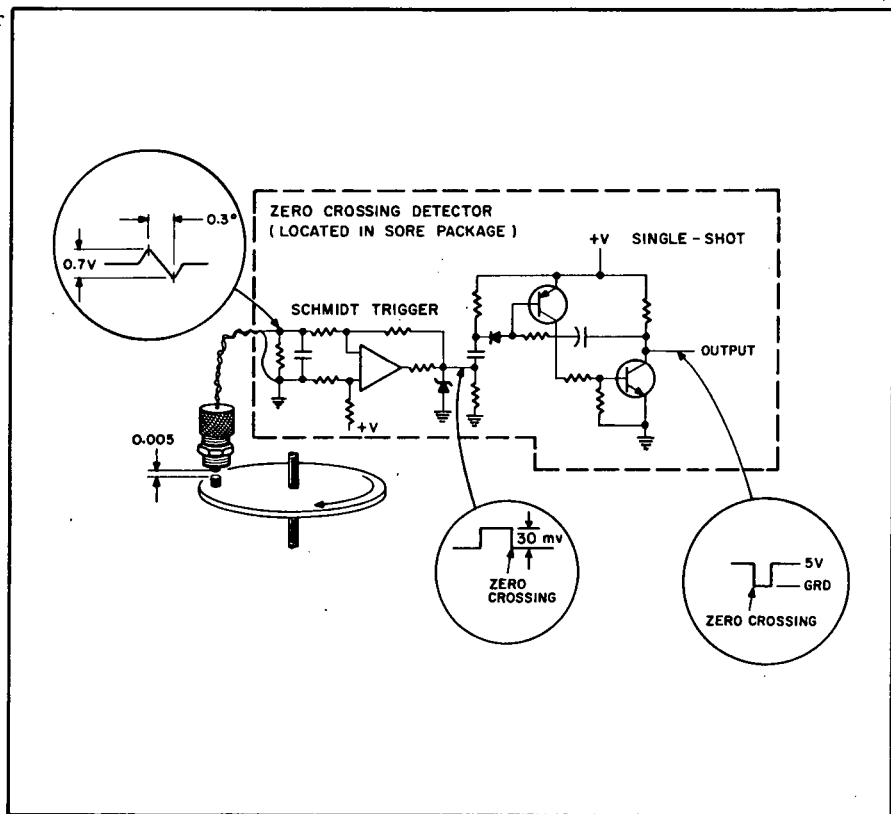


F72-01

Azimuth Encoder (Blipper) Signal. The blipper generates one pulse each revolution of the wheel relative to the sail. When the sail is pointed at the sun, the blipper pulse occurs within  $\pm 0.1$  degree of the aspect spin eye pulse. Thus, if the sail is held in its sun-pointing position at night (by using the gyro for azimuth control), the blipper pulse can be used as a night-time equivalent of the sun pulse. The blipper pulse is used as a reference by the SORE and by the ASA.

The blipper sensor consists of a magnet attached to the azimuth shaft and a magnetic pickup attached to the hub (Figure 5-6). When there is relative rotation between the sail and the wheel, a pulse is produced each time the pickup passes under the magnet. This pulse is coupled to the zero-crossing detector.

The zero-crossing detector consists of a modified Schmidt trigger and a single-shot multivibrator. The Schmidt trigger circuit converts the roughly sinusoidal wave output of the magnetic pickup into a square wave. The trailing edge of this square wave represents the zero crossing of the magnet's field and, therefore, corresponds to the actual center of the magnet. This pulse is amplified and inverted, and the trailing edge is converted to the leading edge by the single-shot, which serves as an amplifier.



Other Signals. In addition to the sensor signals described above, the SORE unit receives and uses the following inputs:

Figure 5-6 Azimuth Encoder (Blipper) Operation

- DSF Word Gate 2, for SORE timing reference
- 800 Hz telemetry clock signal, to be counted for measuring time intervals
- DSF word gates for gating data out of the counters



F72-01

- Day-Night indicator which selects either daytime (sun) pulses or night-time pulses (Mag or Enc).
- Command signals for ground control of SORE operating modes.

5.4.2 The SORE Unit

Figure 5-7 shows the basic functional parts of the SORE unit. Intervals are measured by gating the counters, driven by the 800 Hz telemetry clock signal, in response to the various pulses described in Paragraph 5.4.1. Table 5-2 shows the counting intervals provided by the SORE in each of its operating modes, and the telemetry monitor points which indicate modes. The A counter alternates between the A1 and A2 interval each digital subframe.

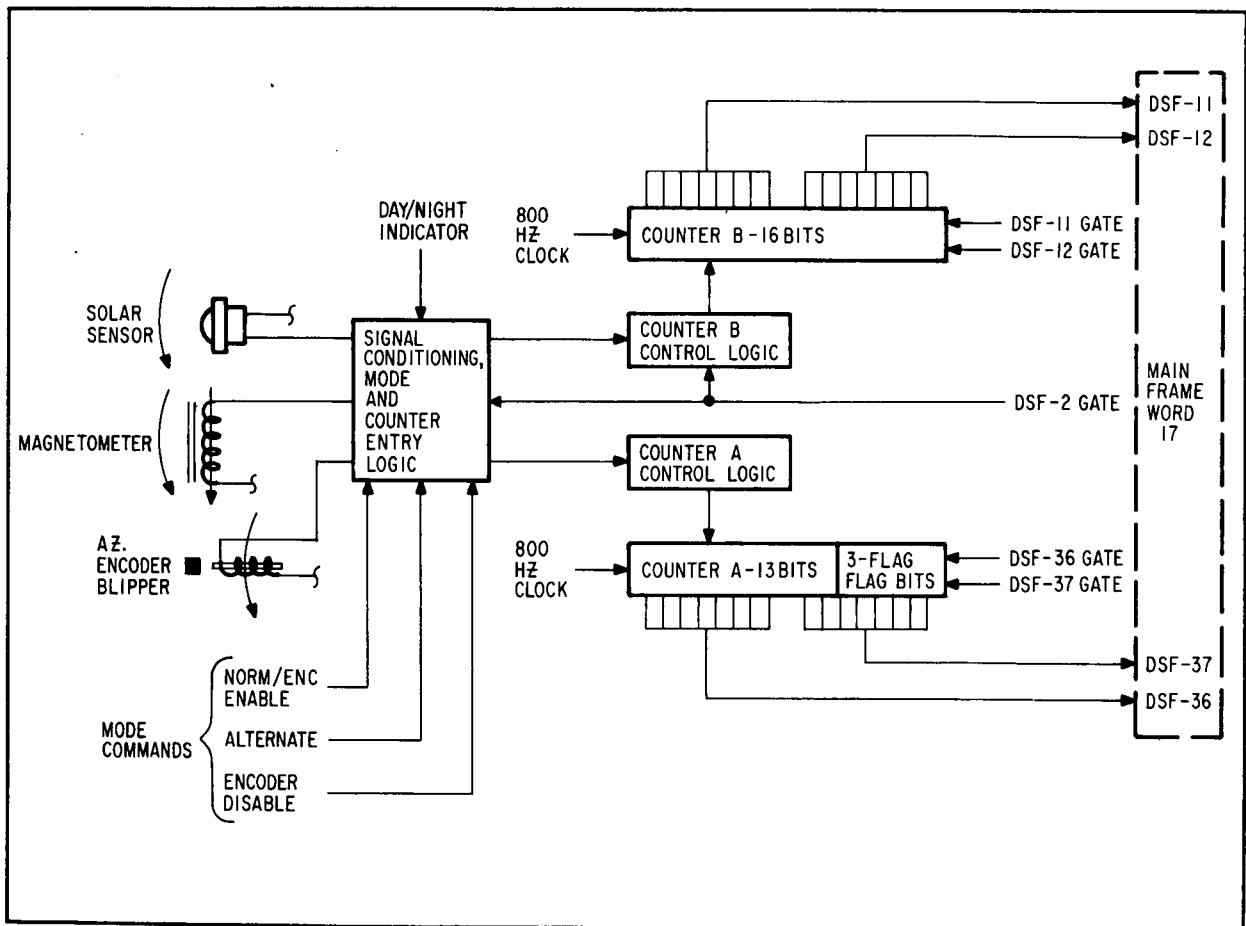


Figure 5-7 SORE Functional Block Diagram



F72-01

Table 5-2  
SORE MODES

SORE MODE NAME	DSF-37, Bit 2			DAY OR NIGHT	DSF-11/12 (Count B)	DSF-37, Bit 1 (MSB)	
	DSF-37, Bit 2	DSF-37, Bit 3	DSF-31, Bit 2			DSF-37, Bit 1 (MSB)	DSF-36/37 (Count A)
Normal/Enc Enab	0	1	1	Day	DSF-2 to Sun	1	A1/Sun to Sun
			0	Night		1	A2/Mag to Sun
	0	0	1	Day	DSF-2 to Enc (1)	1	A1/Enc to Enc(1)
			0	Night		0	A2/Mag to Enc(1)
Normal/Enc Disab	0	0	1	Day	DSF-2 to Sun	1	A1/Sun to Sun
			0	Night		1	A2/Mag to Sun
	0	0	1	Day	DSF-2 to Mag	1	A1/Mag to Mag
			0	Night		0	A2/Mag to Mag
Alternate/Enc Enab	1	1	1	Day	DSF-2 to Sun	1	A1/Sun to Sun
			0	Night		1	A2/Enc to Sun(1)
	1	0	1	Day	DSF-2 to Enc (1)	1	A1/Enc to Enc(1)
			0	Night		0	A2/Enc to Enc(1)
Alternate/Enc Disab	1	0	1	Day	DSF-2 to Sun	1	A1/Sun to Sun
			0	Night		1	A2/Mag to Sun
	1	0	1	Day	DSF-2 to Mag	1	A1/Mag to Mag
			0	Night		0	A2/Mag to Mag

(1) Meaningless unless sail rotation is stopped (gyro on or day mode after solar acquisition)



F72-01

Table 5-2 shows that DSF-11/12 always represents intervals between the fall of the DSF-2 word gate and the rise of a sensor (Sun, Mag, or Enc) pulse. This composite word ties the timing of the telemetry frame to the phasing of wheel rotation.

The A1 counting interval is the time for one revolution of the wheel, either with respect to the sun line (Sun to Sun), the magnetic flux vector (Mag to Mag), or the Sail (Enc to Enc). What is telemetered by the A1 count is simply the spin period.

The basic count telemetered by the A2 count is the Mag-to-Sun interval, which is used in the calculation of spacecraft roll attitude. In the normal mode, provided that the blipper is enabled and the gyro is on, the encoder pulse serves as a night-time equivalent of the sun pulse. The Enc-to-Sun count available in the Alternative/Enc-Enab mode provides a means of checking (1) coalignment of the blipper with the spin eye in the sun-centered point mode (2) position of the sail in the offset point mode; or (3) position of the sail when slewed away from the sun in the gyro-controlled point mode.

The other intervals available in the A2 count duplicate those in the A1 count, in the same modes.

The basic principles involved in the OSO-7 SORE are the same as those in earlier OSO's. The major differences are:

- Separate counters for the A and B counting intervals
- The blipper for use with the gyro in providing night-time aspect information
- The expansion of the counters to accept higher counts, thus providing data over a wider range of spin rates
- Mode-selection commands to provide ground control of the counting interval selection, and telemetry monitors of these modes

The operation of the SORE will be explained by going through a typical frame sequence and discussing the timing of signals. The mode selected for discussion is the SORE Normal/Enc-Enab Day mode. Any of the other modes would be similar, but simpler.

The sequence starts with the fall of DSF word gate 2, which starts counter B by ungrounding B's clock pulse input. Word gate 2 also enables a flip-flop circuit which will later unground the input to counter A.

The first sun pulse after DSF-2 stops counter B, and starts counter A. The count is held in counter B for later readout. The second sun pulse after DSF-2 stops counter A and inhibits counter A from being further gated open until it has been again enabled by the next DSF-2 gate.



F72-01

The count, representing the time from DSF-2 to the ensuing sun pulse, remains in the B counter until DSF-11, when the 8 least-significant bits are read out into the digital subframe. The 8 most-significant bits are then read out by DSF-12, the trailing edge of which clears the counter. The counter then is idle until the next DSF-2 gate.

The count in counter A, the A1 count representing the spin period (Sun to Sun), remains intact until DSF-36. The 8 least-significant bits are then read into the telemetry frame. The remaining 5 bits are then shifted, along with the 3 status bits, into DSF-37, the trailing edge of which clears the counter. The counter then is idle until it is again enabled by DSF-2.

When DSF-2 occurs, counter B is again started and counter A again enabled, but this time it may be started by a magnetometer pulse instead of a sun pulse. The DSF-2 pulse causes this alternating action each time it is sensed by the SORE, and the A1 or A2 condition of the counter is indicated in the telemetry frame by the most-significant bit of DSF-37.

The B counter does not alternate, so its loading and readout sequence are the same in this subframe as in the last. The A counter, however, is now started by the first magnetometer pulse after DSF-2. The A counter is then stopped by the ensuing sun pulse, as before. This time the count read out on DSF-36/37 represents the time for wheel rotation between the magnetometer pulse and the ensuing sun pulse. This is the A2 count.

During orbit night, when the sun cannot be seen, the encoder pulse is substituted for the sun pulse. For this to be a valid substitution, the sail must be held in its daytime position (that is, pointed at the sun) by the servo operating in the gyro mode.

#### 5.5 FINE ASPECT MONITOR (ASA)

The fine aspect monitor, sometimes called the star sensor or the Aspect Sensor Assembly (ASA), operates only during orbit night. The monitor consists of two major elements:

- An on-board star sensor (hardware) shown in Figure 5-8
- A ground-based computer and program (software) used to reduce the data.

The star sensor is mounted in Compartment 2 of the wheel section and rotates constantly about the observatory spin axis. The star sensor generates a pair of pulses each time its field of view sweeps past a star brighter than a preselected level. The sensor circuits encode azimuth and elevation position data for the star, and multiplex this information into the telemetry frame for transmission to ground receivers.

The software decodes the data and identifies the stars by comparing the telemetered data with known star positions. From these data, it calculates the orientation of the OSO spin axis and the instantaneous azimuth position of any reference line in the wheel at any time in the telemetry frame.

The concepts used by the ASA provide considerably higher accuracy than the SORE. Stars make excellent targets for attitude reference, due to their large number and wide distribution. In addition, their angular positions are well known.



F72-01

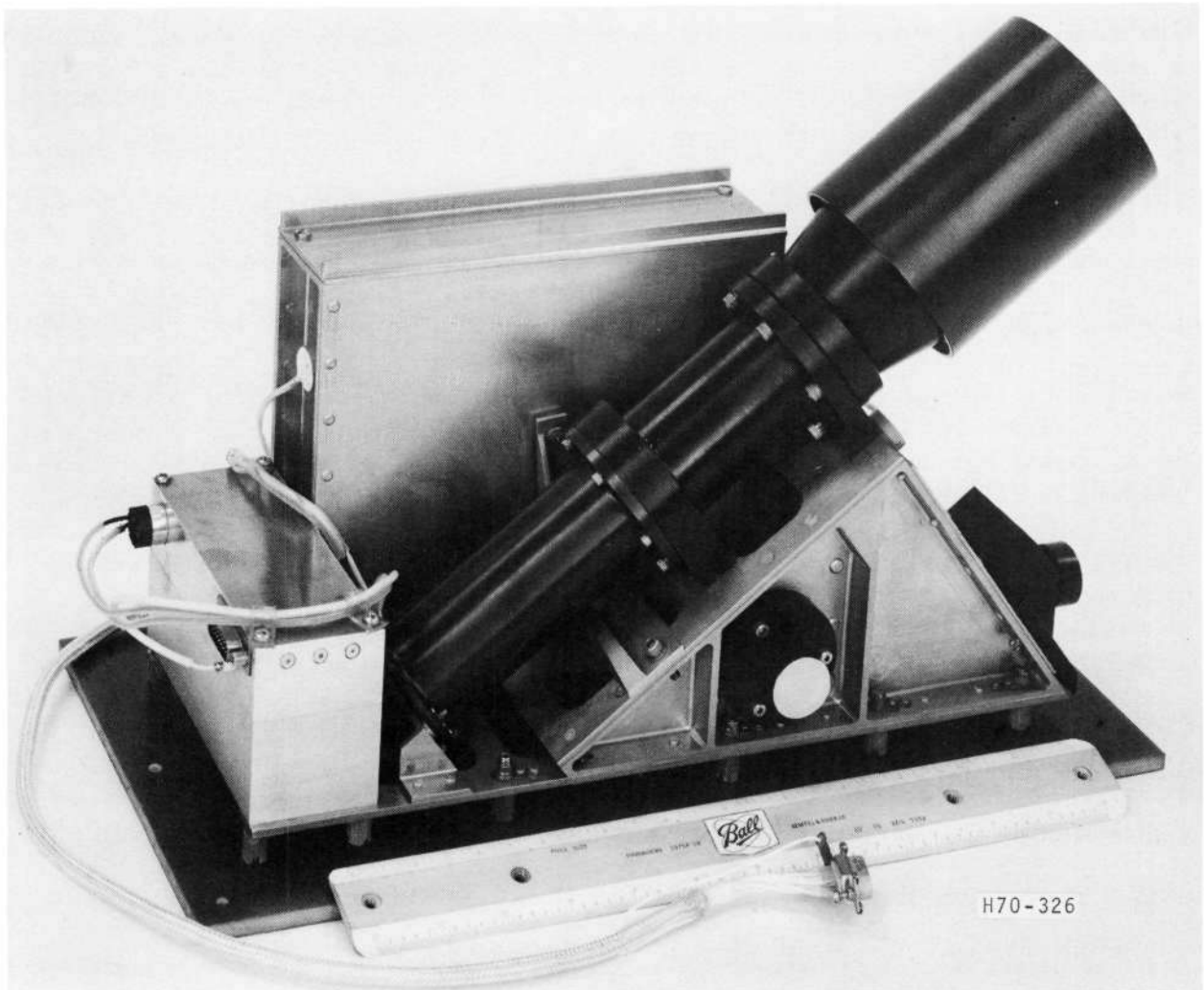


Figure 5-8 Aspect Sensor Assembly

#### 5.5.1 ASA Operating Principles

The star sensor hardware consists of the electro-optical components, electronic processing circuits, and the power supply. The electro-optical components are a sun shield, the lens assembly, the reticle, and the photomultiplier. Electronic processing circuits include a preamplifier, a video amplifier, a level detector, logic circuits, the data encoder, and telemetry-interface circuits. The power supply includes a voltage regulator, a low-voltage converter, and a high-voltage converter.

Figure 5-9 is a diagram of the ASA optical components. As the lens assembly scans the sky, the photomultiplier produces a pulse as each leg of the "V" slit crosses a star. The pulse from the crossing of the first (vertical) leg of the "V" is the azimuth reference for the star. It is time-referenced to the telemetry frame by the electronic processing circuits. The night azimuth pulse (blipper or magnetometer) from the SORE also is reported once per major frame in the ASA data. This provides a rough azimuth reference, which is refined by the software using the star data.



F72-01

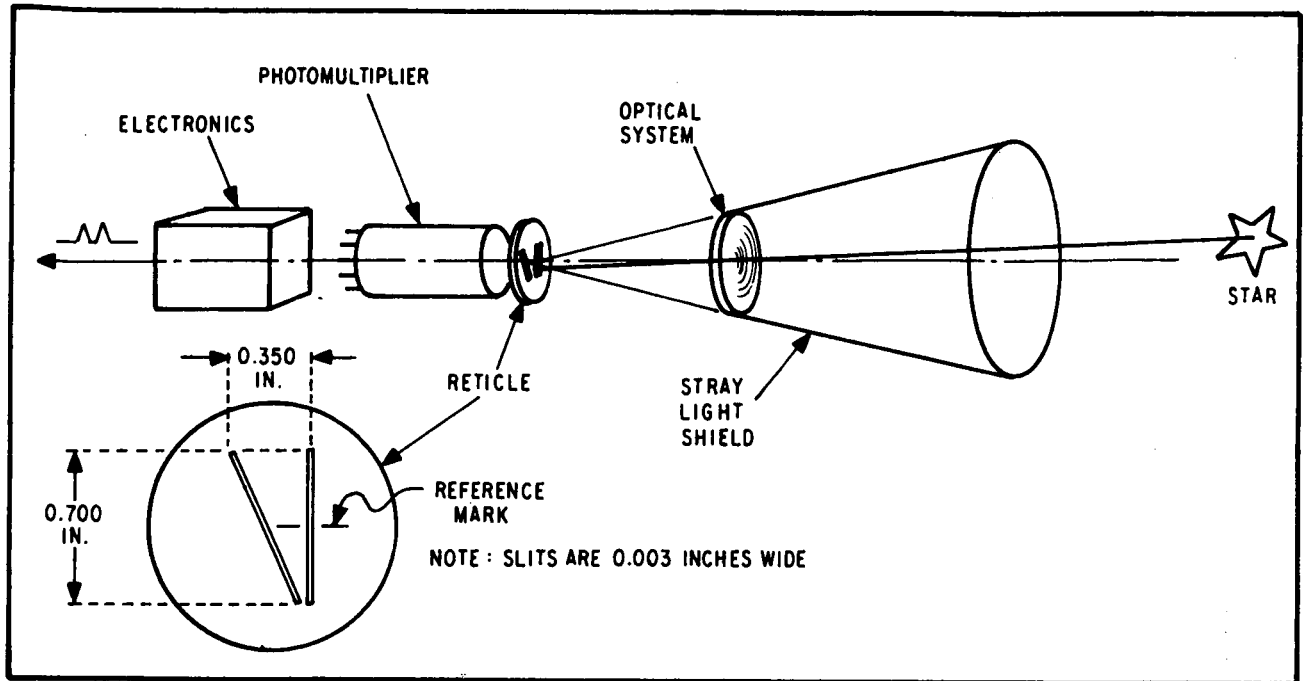


Figure 5-9 ASA Optics

The elapsed time between the crossing of the first leg and the second (slanted) leg is determined by the star's declination (or elevation) angle in spacecraft coordinates. Thus, each star produces a characteristic "signature" dependent on its position in spacecraft coordinates. The signature consists of its azimuth position at a particular time in the telemetry frame, and its elevation position above or below the wheel plane.

The level detector receives the star pulses and excludes those that are below certain magnitudes (dim stars). This prevents overloading of the data-handling system due to clusters of dim stars or background noise. The level-detector threshold is normally set for +3 magnitude stars, but it can be changed to any of eight detecting thresholds by ground commands. This permits data reduction in the densely-populated areas of the sky.

In each minor telemetry frame (320 milliseconds), the electronic processing circuits generate two 24-bit words. Each of these words may report a single star. The words are read out in the telemetry frame on groups of three 8-bit words in the night allocation. The first report appears in minor frame words 2, 3, and 4, and the second in 18, 19, and 20, as shown in Figure 5-10. The counts are generated by gating a 6400 Hz clock signal with the DSF-48 word gate, star pulses, and the SORE night azimuth pulse.

At a nominal spin rate of 0.5 rps, there are about six minor frames of data during each spin period. Thus, a maximum of 12 stars may be reported for each revolution of the wheel. Different stars may be reported in succeeding revolutions, but a star must be reported at least twice in a telemetry major frame for the software to recognize it as a valid star and not noise.



F72-01

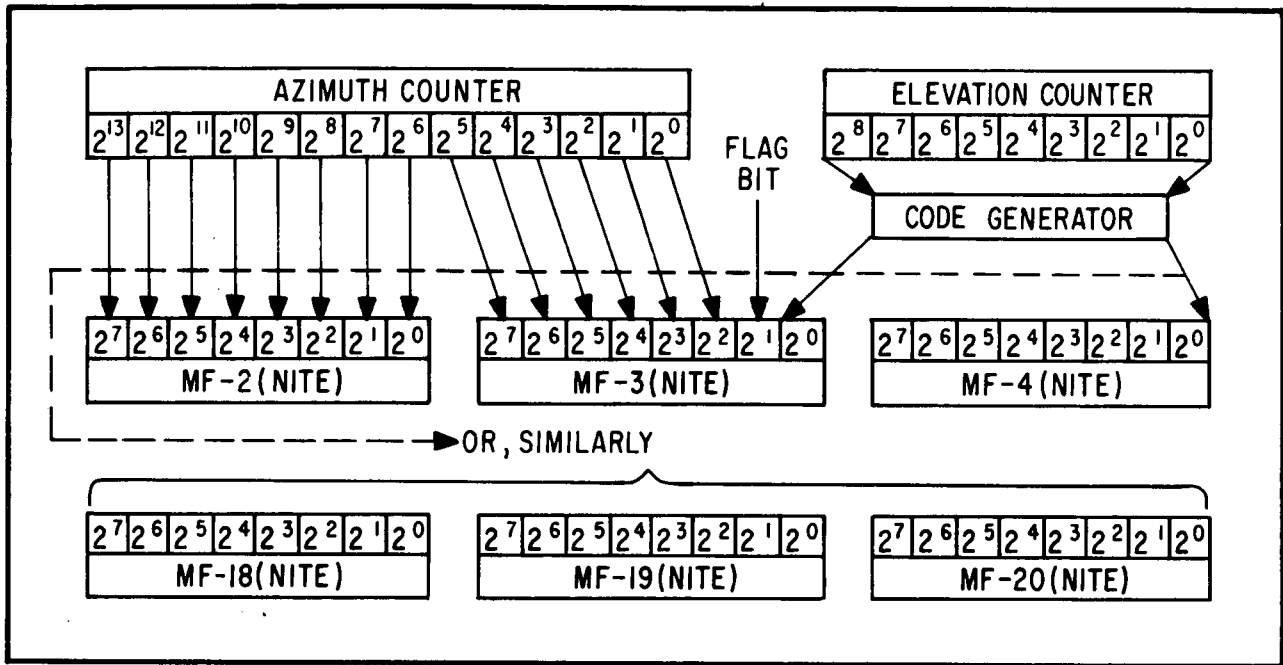


Figure 5-10 ASA Data Words

The 24-bit word for each star is composed of 14 bits of azimuth information, one flag bit, and a 9-bit word containing elevation information. The azimuth count is the number of cycles of 6400 Hz clock signal from the time DSF-48 occurs to the time the vertical slit crosses the star. The flag bit identifies the data as "questionable" when more than two crossings are sensed during a 50-millisecond gate pulse triggered by the first star pulse. The elevation count is the number of cycles of 6400 Hz clock signal between the two slit crossings of the star. This counting interval is determined by the spin rate and the elevation position of the star in spacecraft coordinates.

The DSF-48 word gate synchronizes the azimuth counter at zero every 15.36 seconds. The azimuth counter, having a count capacity of 16,384 ( $2^{14}$ ), starts at zero every 2.56 seconds. The timing relationships involved are shown in Figure 5-11. Fortunately, 15.36 is an integral multiple of 2.56, so once the counter is synchronized with the telemetry frame, it stays synchronized. The 6400 Hz ASA clock is synchronized with the 800 Hz telemetry clock. The ground-based computer keeps track of the resets to zero and adds the lost counts back into the azimuth count for each star sighted.

The occurrence of the first night-time SORE reference pulse (Enc or Mag) after DSF-48 is reported as a star with no elevation count. If the SORE pulse occurs during readout of the 24-bit word, the word is invalidated and the pulse is reported on the next 24-bit word. Thus the SORE pulses are used by the ASA to provide data for spin-period calculation in almost the same manner as in Paragraph 5.4.3. The instantaneous angular position of OSO





F72-01

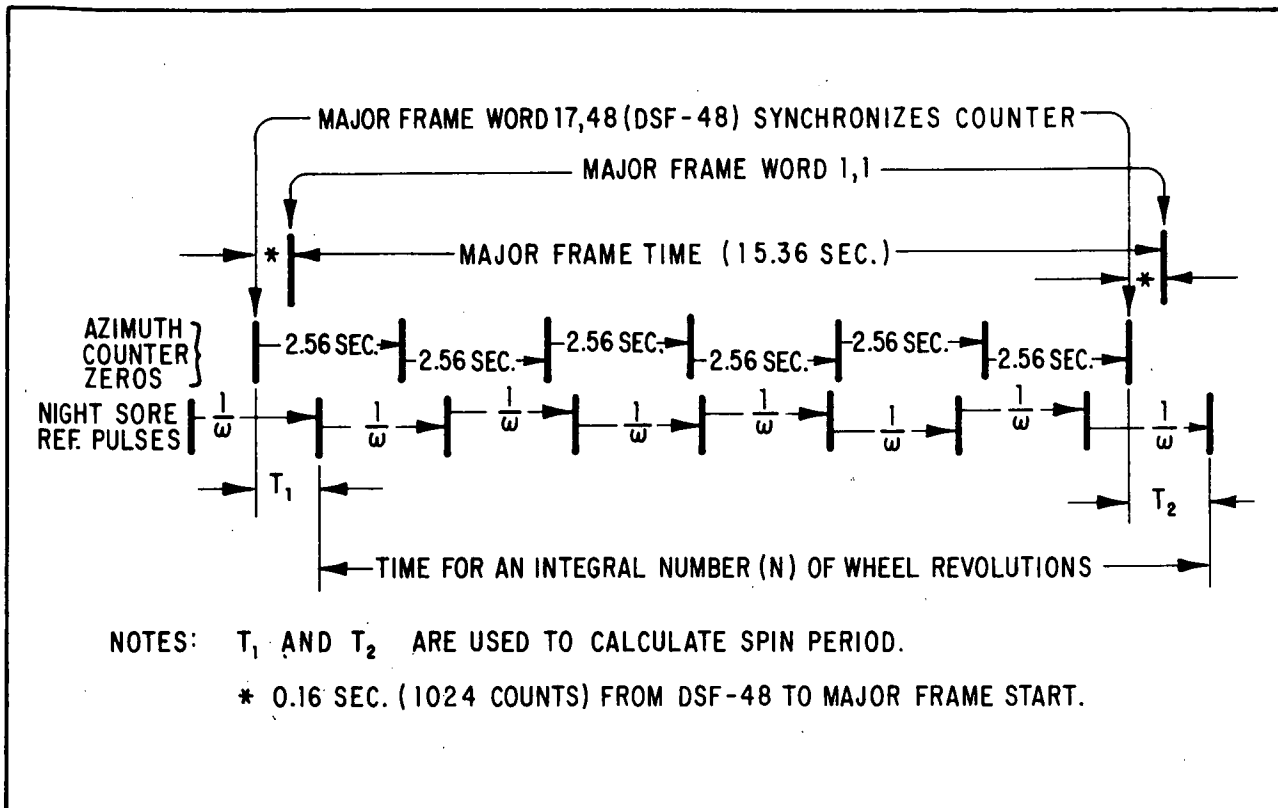


Figure 5-11 ASA Timing Relationships

about its spin axis is calculated by relating the time of occurrence of major frame word 1,1 to the time of the SORE pulse, very much as is done in the SORE. The star data, however, is used to refine both the pitch and roll angle and the orientation of OSO about its spin axis to an accuracy of about  $\pm 0.1$  degree.

The star sensor nominal characteristics are:

- Vertical field of view =  $\pm 5$  degrees
- Azimuth field of view =  $\pm 2.5$  degrees
- Width of each slit leg = 0.036 degrees
- Angle from sensor axis to wheel plane = 37 degrees
- Detectable star range = -4.5 to +4.0 magnitude (selectable gain thresholds +2.0 to +4.0 in 0.33 magnitude steps)
- Maximum equivalent background = +3.5 magnitude
- Total power consumption = 1.25 watts



F72-01

- Weight = 10 pounds
- Capable of determining roll, pitch, and yaw position of OSO to  $\pm 0.1$  degree

#### 5.5.2 Additional Features

Since the point is missing from the bottom of the "V" slit, the elevation count cannot be zero for a real star, as it is for the night azimuth reference pulse. At the nominal (0.5 rps) spin rate, the elevation count for real stars falls between 16 and 218.

The flag bit lags the azimuth and elevation data by one star word, since the third pulse would always occur after that data had been shifted into the readout register.

The star sensor electronic processing circuits include features for excluding moon and earth sightings from the output data. The sun is never seen by the ASA optics, because of the stray-light shield and the 37-degree offset of the viewing axis from the wheel plane.

The star magnitude threshold settings are retained from orbit to orbit by keeping power on the threshold circuits through the orbit day. Threshold status is monitored by telemetry.

A single pulse may enter the digital processing circuits, due to noise, a star of threshold magnitude where only one crossing pulse exceeds the discriminator threshold, or some other cause. In such an event, overflow of the elevation counter automatically resets the elevation counter gates.

The housekeeping data provided by the ASA include:

- Threshold gain setting -- three DSF single-bit monitor channels
- Voltage of the +10, -10, and -2800-volt supplies through WASC channels
- Photomultiplier background current through a WASC channel
- ASA Enable/Disable and On/Off status through a WASC channel.

The star sensor logic circuits include a feature which prevents a 24-bit data word from being shifted into the telemetry frame before the elevation counter is stopped. Thus, only complete words are transmitted.



F72-01

Section 6  
CONTROL SYSTEMS

6.1 INTRODUCTION

This section presents detailed functional descriptions of the OSO-7 control systems. The seven basic systems are:

Pneumatic Pitch-Attitude Control. This system provides automatic pitch control of OSO to maintain its spin axis normal to the sun line within 3 degrees. It automatically switches to the manual mode in case of malfunction. Pitch attitude can be controlled manually by ground station command when necessary.

Pneumatic Spin-Rate Control. This system automatically corrects the wheel spin rate to within the nominal limits of 0.448 and 0.662 rps. In case of a malfunction in which the spin rate goes outside the range of 0.391 to 0.699 rps, it automatically switches to manual spin-rate control by ground station command.

Pneumatic Roll-Attitude Control. This system uses the pneumatic pitch control hardware to make "fast reaction" roll maneuvers. Using the gyro mode (see pointing control), the sail is rotated 90 degrees, then manual pitch bursts are commanded.

Magnetic Attitude Control. An alternate method of attitude and spin rate control, using commandable pitch and roll coils. On ground commands, these coils change the magnetic dipole moment of the spacecraft.

Pointing Control. The pointing control system provides:

- Automatic solar acquisition of pointed-instrument assembly (PIA), each orbit morning
- Pointing of PIA at sun-center within 1 arc minute
- Pointing of PIA to any point within a 128-128 grid centered on the sun
- Small rastering of PIA about any of these points
- Large rastering of PIA about sun-center
- Gyro control of sail (in azimuth) during day or night.

Gyro control will be selected automatically every orbit-night, if desired.

Launch-Sequence Control. This system automatically changes OSO from the launch to the orbit condition by executing certain control functions at prescribed times. The launch-sequence events are time-referenced to the jettisoning of the fairing and the separation of OSO from the launch vehicle.



F72-01

Nutation Control System. This system damps nutational motion acquired during launch and while in orbit.

## 6.2 PNEUMATIC PITCH-ATTITUDE CONTROL

The pneumatic pitch control is normally used as a backup for the magnetic attitude control for long-term attitude control. It also serves as the primary control system for "fast-reaction" pitch and roll maneuvers.

The pneumatic pitch control consists of pitch angle sensors located on the front of the sail, electronic control circuits contained in the power-amplifier box located on the back of the sail, and a nitrogen-gas pneumatic system located on the back of the sail. Figure 6-1 is a block diagram of the pitch pneumatic control including related commands and telemetered monitor points.

The OSO-7 pitch pneumatic control is nearly identical to that used on previous OSO's. The only differences are replacing the auto pitch limiter (APL) timer with a coincidence circuit; resizing the pneumatic components to make them compatible with the heavier spacecraft; and relocating the pitch gas storage bottles (two instead of one) from the wheel hub to the back of the sail.

### 6.2.1 Automatic Pitch Control

The pneumatic pitch control, operating in the automatic mode, is controlled by signals from the pitch-control sensors, shown in Figure 6-2. The vertical fields of view of the sensors are shown in Figure 6-1, and in Figure 6-3. The azimuth field is about 13 degrees wide. The sensor block is mounted to the front of the sail at the top, so that it is pointed at the sun in azimuth by the pointing control.

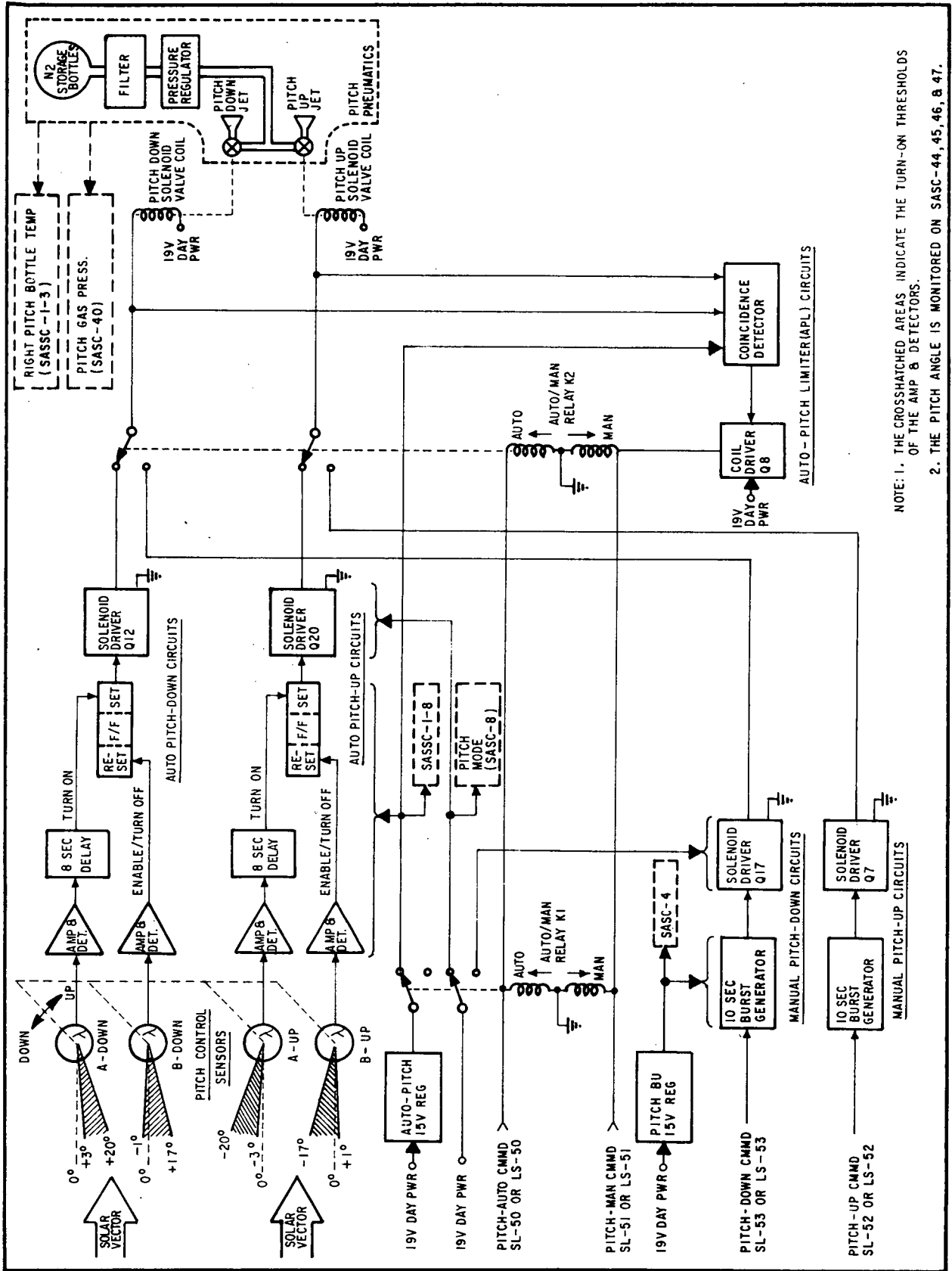
When the tilt of the spin axis has drifted so that both "up" eyes are illuminated by the sun for more than eight seconds, the pitch-up circuits activate the pitch-up solenoid valve. This releases nitrogen gas from the pitch-up thruster mounted at the top of the sail, causing the spin axis to precess toward zero pitch angle. Gas flow continues until illumination is removed from the B-up eye, at about one degree past the zero pitch angle. The B eye enables the flip-flop circuit, the A eye triggers the gas flow, and removal of illumination from the B eye ends the gas flow.

The logic for the automatic pitch-down operation is similar to that of the pitch-up, except that the thruster faces the other side of the sail.

The automatic mode may be selected by ground command. The manual mode may be selected either by ground command or by operation of the coincidence circuit shown in Figure 6-1. The coincidence circuit senses the simultaneous activation of the pitch-up and pitch-down valves and throws the auto-manual relays to the manual state. This feature prevents pitch gas depletion if the automatic pitch control circuits fail. A status monitor in the sail analog subcommutator frame is used to telemeter pitch mode to ground-based operators.



F72-01



NOTE: 1. THE CROSSHATCHED AREAS INDICATE THE TURN-ON THRESHOLDS OF THE AMP & DETECTORS.  
 2. THE PITCH ANGLE IS MONITORED ON SASSC-44, 45, 46, & 47.

Figure 6-1: Pneumatic Pitch Control Block Diagram



F72-01

### 6.2.2 Manual Pitch Control

With manual control selected, ground stations can command either pitch-down or pitch-up as required. Each manual pitch command triggers a 10-second monostable multivibrator, called a burst generator. The monostable output signal controls the appropriate pitch valve through a solenoid driver. The pitch-correction increment for each 10-second burst is about  $0.65^\circ$  when the wheel spin rate is 15 rps.

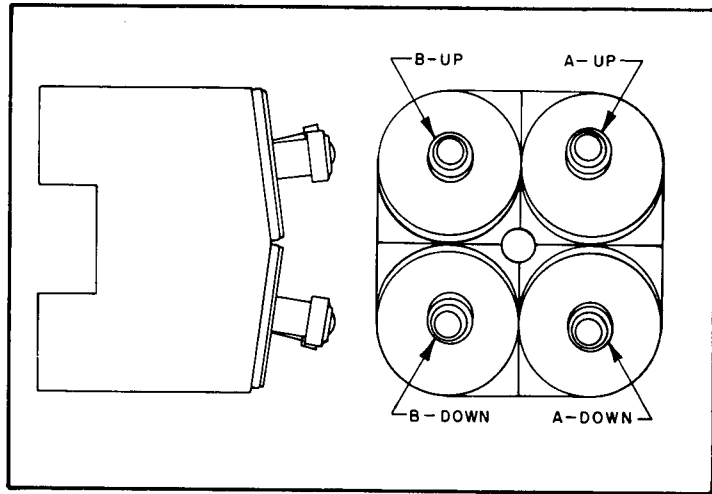


Figure 6-2 Pitch Control Sensors

### 6.2.3 Operation During Launch

During the launch, the pitch control is in the manual mode. This prevents a pitch correction from occurring while the wheel is spinning at a low rate, and the subsequent excessive nutation that could be generated. The automatic mode is selected by ground command after the correct spin rate is verified.

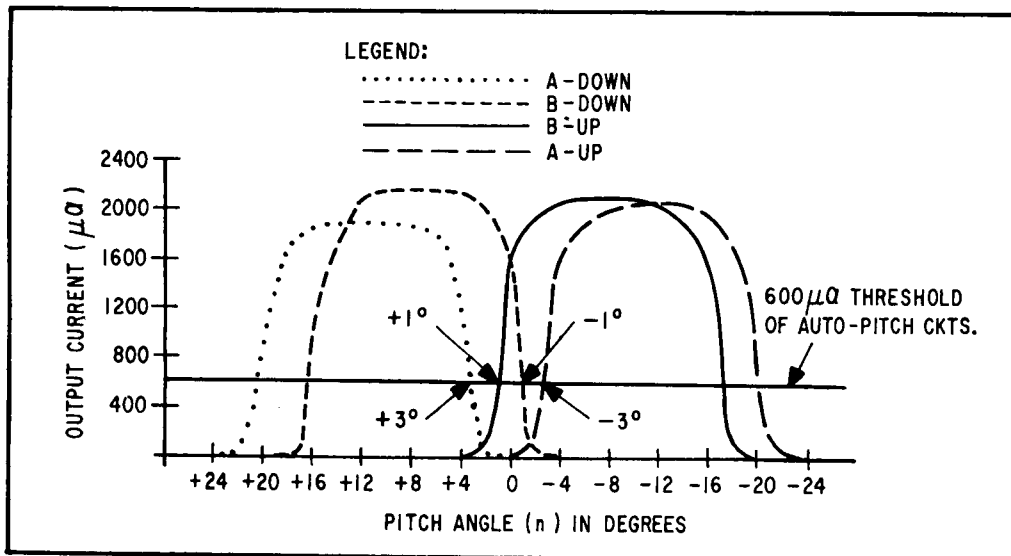


Figure 6-3 Typical Pitch Control Sensor Response

After being commanded to automatic mode, providing that the OSO is injected into orbit at the proper attitude, the pitch control automatically makes any required initial pitch corrections. The criteria for proper injection attitude are that the sun must lie within the field of view of the spin-control, pitch-control, and servo azimuth coarse sensors.



F72-01

### 6.3 PNEUMATIC ROLL-ATTITUDE CONTROL

Roll control for large maneuvers, or for small rapid angular adjustments, is performed by using the pitch control gas jets, located on the top of the sail. To do so, the sail is rotated 90° from the sun, using the gyro. Slow roll rates are generated by magnetic torquing coils.

Pneumatic roll control is accomplished by ground commands, using aspect data collected on the ground to determine roll attitude and then commanding the pitch control system to torque the spacecraft to the desired attitude.

### 6.4 PNEUMATIC SPIN-RATE CONTROL

The pneumatic spin control, like the pneumatic pitch control, may be operated in either the automatic or manual (command) modes. The manual mode is normally considered as a backup for the automatic system. It may also be used, however, to adjust the spin rate to a specific value between the automatic-control limits. A block diagram of the spin control system is shown in Figure 6-4.

The OSO-7 pneumatic spin control is similar to that of earlier OSO's. The primary differences are increased spin torques, compatible with the increased size and spin moment of inertia; replacing the three spin gas bottles previously located on the tips of the arms with one bottle located in the hub; and the added input from the launch-sequence control circuits for initial spin-up during launch.

#### 6.4.1 Automatic Spin Control

The automatic-spin circuits measure the period of revolution of the wheel. When this period increases (wheel slows) to the spin-up threshold (0.448 rps), a four-second burst is discharged from the spinup nozzles, increasing spin rate by about 0.0075 rps. Similarly, if the spin period decreases (wheel speeds up) to the spin-down threshold (0.662 rps), a four-second burst is discharged from the spin-down nozzles, decreasing spin rate by a similar increment.

Spin Sensors and Amplifiers. The auto-spin control mode uses two identical and redundant solar sensors (Spin Eyes 1 and 2), mounted on the perimeter of the spacecraft wheel. As these sensors sweep past the sun, each produces 20-millisecond current pulses of approximately square waveform. The two pulses are fed to two voltage amplifiers and the outputs of the amplifiers are mixed on the way to a level detector.

Level Detector. The level detector has two modes of operation, high level (low sensitivity), and low level (high sensitivity). The high-level mode is used during orbit dawn when the spin eyes first see the sun, and the light intensity varies. When the instantaneous output level of the spin eyes is sufficient to overcome the high-level detecting threshold, spin pulses pass through the pulse shaper circuit to the day-night turn-on circuits. These circuits then cause day power to be applied to the spacecraft. The day-power relay applies



F72-01

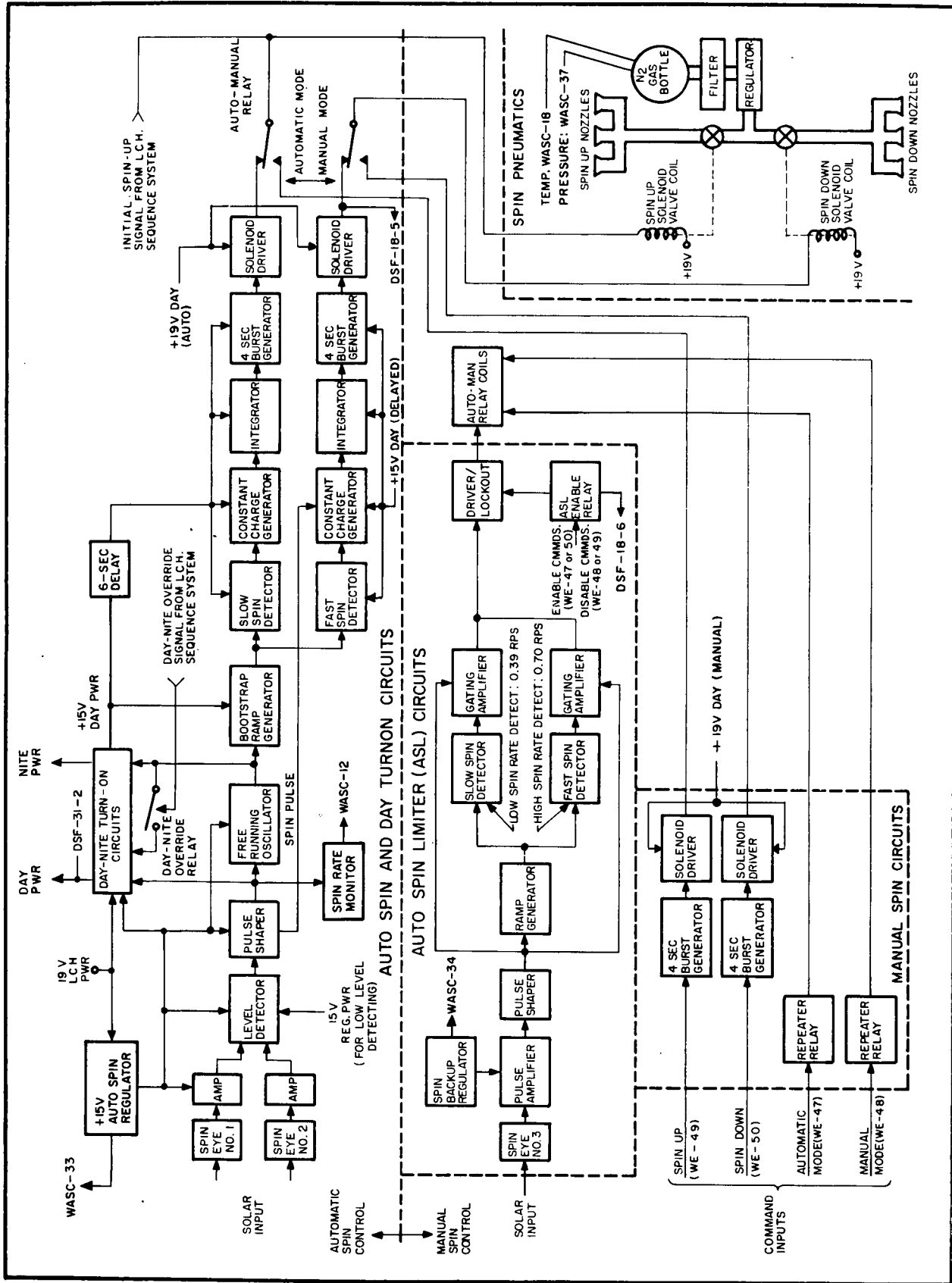


Figure 6-4 Pneumatic Spin Control Block Diagram





F72-01

the output of the spin box 15-volt regulator to the level-detector bias network, causing the detector to operate in its low-level mode. This action effectively "latches" the detector on, once its high-detecting threshold is overcome. Variations in light intensity are thereby prevented from causing intermittent application (chattering) of day power.

Pulse Shaper. As mentioned above, the output of the level detector is fed to a pulse shaper circuit. Here the pulses are given a constant width, squared, and inverted twice. After the first inversion, the positive-going trailing edge (originally negative going) is used to turn on day power. It is also used to synchronize a free-running oscillator. After the second inversion, the positive spin pulses are fed through an inhibiting network to the constant-charge generator in the over-spin loop. Thus, the free-running oscillator is synchronized by the trailing edge of the spin pulses and when not inhibited, the constant-charge generator is triggered by the leading edge of the spin pulse.

Free-Running Oscillator. The free-running oscillator has a natural frequency of about 0.345 rps, much slower than the normal wheel spin rate. The trailing edge of the spin pulse is used to synchronize the oscillator, raising its frequency to match the spin rate. The oscillator output is fed to the day-power turn-on circuits, and to a bootstrap ramp generator.

Bootstrap Ramp Generator. The ramp generator develops a sawtooth voltage waveform that increases linearly with time. The period of this sawtooth (or ramp) is identical to the spin period of the wheel since the ramp generator is controlled by the oscillator, which in turn is synchronized by the trailing edge of the spin pulses. The peak voltage reached by the ramp is thus directly proportional to the spin period: the slower the spin rate, the higher this peak voltage. The ramp voltage is fed to an overspin detector and an underspin detector.

Overspin Detector. When the spin rate is below the spin-down threshold, the overspin detector operates as an overvoltage detector. When the ramp generator output climbs above the overvoltage threshold before being reset by the trailing edge of the spin pulse, the detector pulses a storage capacitor, thus creating a bias voltage which inhibits the action of the constant-charge generator. When the spin period is less than 1.52 seconds (0.66 rps), no overvoltage pulses are generated, and the constant-charge generator is not inhibited.

Overspin Constant-Charge Generator. When the inhibiting voltage from the overspin detector is not present (overspin condition) the constant-charge generator amplifies the spin pulses to a fixed voltage. These amplified pulses then contain a fixed amount of energy which is supplied to the integrator network.

When the spin rate is normal (below the spin-down threshold), the spin pulses are inhibited by the bias developed in the overspin detector.

The timing relationships between the spin pulses, ramp, overvoltage pulses, and constant-charge generator outputs are shown in Figure 6-5 for both the normal and overspin conditions.



F72-01

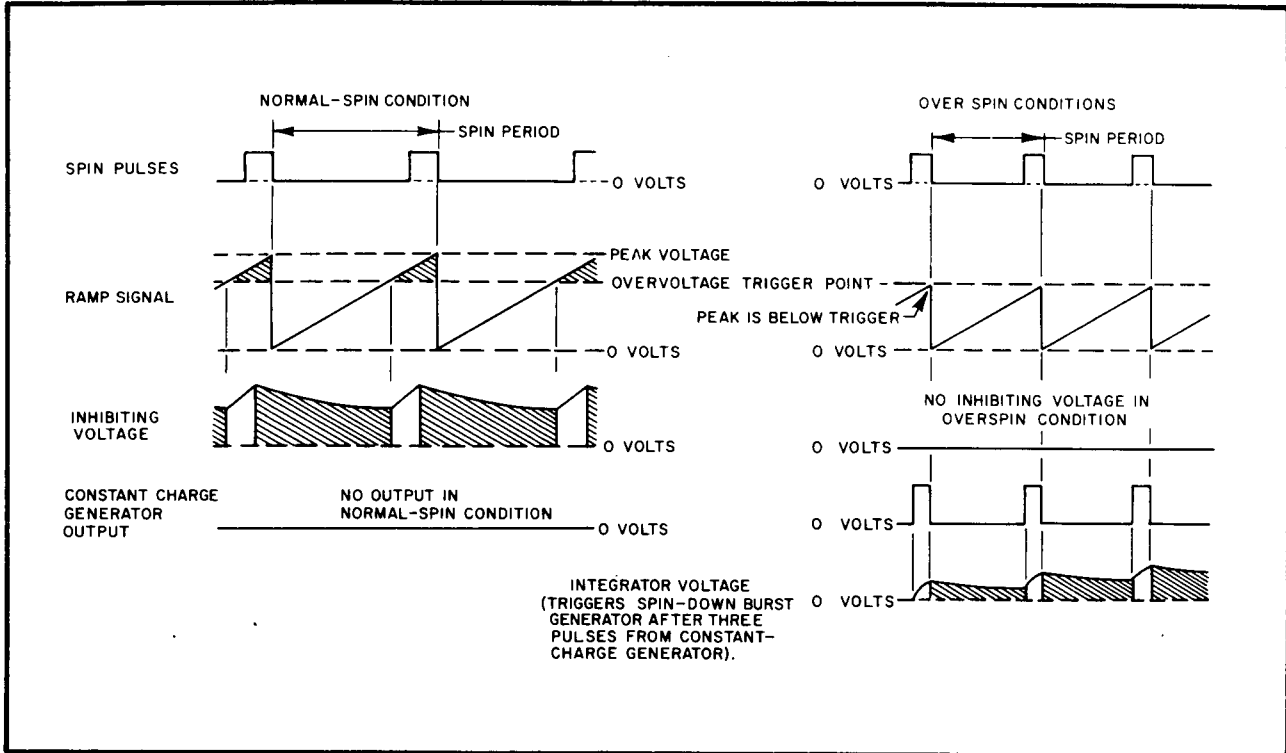


Figure 6-5 Spin-Down-Loop Timing Diagram

Integrator, Spin-Down Burst Generator, and Solenoid Driver. The output pulses from the constant-charge generator are fed to an integrator circuit where they are stored in a capacitor. Three consecutive constant-charge pulses will cause the storage voltage to be high enough to trigger a unijunction switch. The output pulse from the unijunction switch then triggers the spindown burst generator.

The burst generator is a monostable multivibrator. Each time it is triggered, it generates a four-second pulse, activating a solenoid-driver circuit which provides a ground path for the spin-down solenoid. A four-second burst of gas is then released from the spin-down nozzles.

Underspin Loop. The bootstrap ramp generator output is fed to the underspin detector, which operates as an overvoltage detector. As the spin rate decreases, the peak voltage reached by the ramp increases, ultimately reaching the triggering threshold of the detector. The threshold corresponds to a spin rate of about 0.45 rps.

The output of the underspin detector triggers a constant-charge generator. This generator differs from the one in the overspin loop in that it is a monostable multivibrator, whereas the underspin constant-charge generator is simply an amplifier. The width of the constant-charge pulses is set by the characteristics of the multivibrator.



F72-01

As in the overspin loop, the output of the constant-charge generator is stored by a capacitor in the integrator circuit. When three consecutive pulses are so stored, the integrator voltage triggers the spin-up burst generator, which provides a four-second pulse to the spin-up solenoid driver. The driver then provides a four-second ground closure for the spin-up solenoid, which releases a burst of gas through the spin-up nozzles.

The signal-timing relationships of the underspin-loop circuits are shown in Figure 6-6.

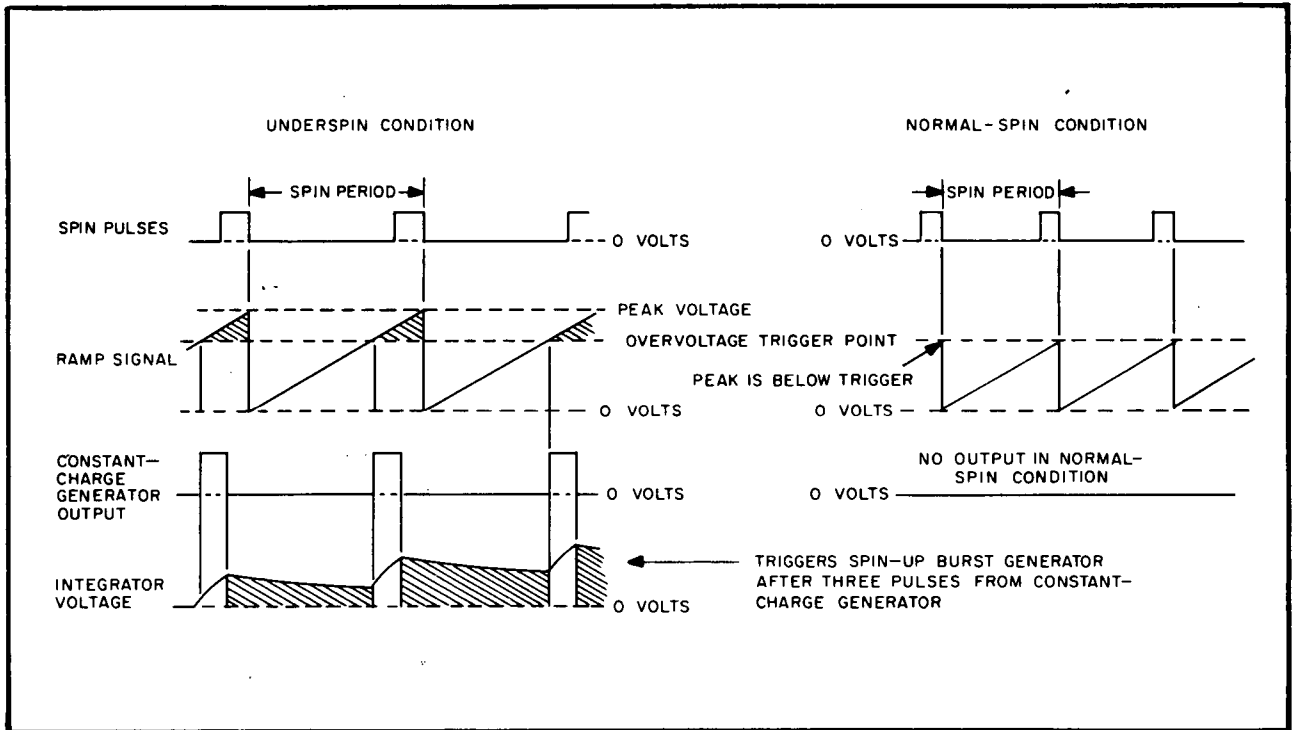


Figure 6-6 Spin-Up Loop Timing Diagram

#### 6.4.2 Manual Spin Control

Manual spin control serves as a backup for the automatic control system. In the manual mode, the spin rate can be corrected by ground-control commands.

The manual-spin mode is automatically selected when the automatic-spin limiter (ASL) circuits detect spin rates outside the range of 0.39 to 0.70 rps. When either limit is reached, a failure in the automatic-spin circuits is indicated so they are disabled by the ASL. Manual control can also be selected by ground-station command. The manual-mode circuits are shown at the bottom of Figure 6-4.



F72-01

ASL Operation. Detection of the ASL overspin and underspin rates is similar to that in the automatic spin control. Spin Eye 3 provides a spin pulse once each wheel revolution. The pulse-amplifier output is fed through a pulse shaper to a ramp generator whose output rises linearly with time. The ramp reaches a peak level which is a measure of the spin period, and is reset by the trailing edge of the spin pulse. Overspin and underspin detectors are then used to sense spin rates outside the acceptable range.

The overspin detector is very similar to the one used in the automatic spindown circuits. When the spin rate exceeds 0.70 rps, the detector's output falls toward zero, thus removing the inhibiting bias from the gating amplifier. The next spin pulse after this pulses the driver/lockout circuit, latching the auto-manual relay to the manual position.

The underspin detector responds to the high ramp voltages occurring with wheel spin rates of 0.39 rps or less. It then puts out a pulse which also switches the system to the manual mode. This action is gated by the spin pulse itself, to prevent such switching between the final spin pulse of an orbit day and the removal of day power from the ASL circuits.

Command Operation. When the manual control mode is selected, ground station commands may be sent to initiate four-second spinup or spin-down bursts. Repeater relays drive their respective burst generators and solenoid drivers when commanded. The required command functions for selecting the manual or automatic modes are also shown in Figure 6-4. Also shown are the commands for ASL enabling and disabling and the various telemetry monitor channels related to the spin-control circuits.

The spin-gas supply for OSO-7 was calculated to be sufficient for about 1.4 years of orbital operations under the worst-case conditions of leakage, aerodynamic drag, eddy-current drag, magnetic effects, and roll-coil interaction. A more realistic estimate of these factors leads us to conclude that the gas supply is adequate for several years.

#### 6.4.3 Day Power Turn-On

The spin pulses are also used to turn day power on and off at sunrise and sunset. For this reason, operation of the day-night switching circuits is discussed here rather than with the power and distribution systems in Section 7. A block diagram of the circuits is shown in Figure 6-7, along with the signal timing relationships used for day-night sensing.

In the night condition, there are no spin pulses to synchronize the free-running oscillator or to inhibit its output. The first oscillator pulse after darkness occurs switches the day-night flip-flop to its "night" state. This removes power from the night relay coil, thus conserving battery power. The free-running period of the oscillator is about three seconds, the interval necessary to turn off day power after the last spin pulse.

During orbit day, the spin pulses synchronize the oscillator with the wheel spin rate. Spin pulses also trigger the monostable multivibrator which generates pulses used to set the flip-flop to the day state and inhibit the oscillator from resetting the flip-flop. Power is then removed from the day coil to conserve power.



F72-01

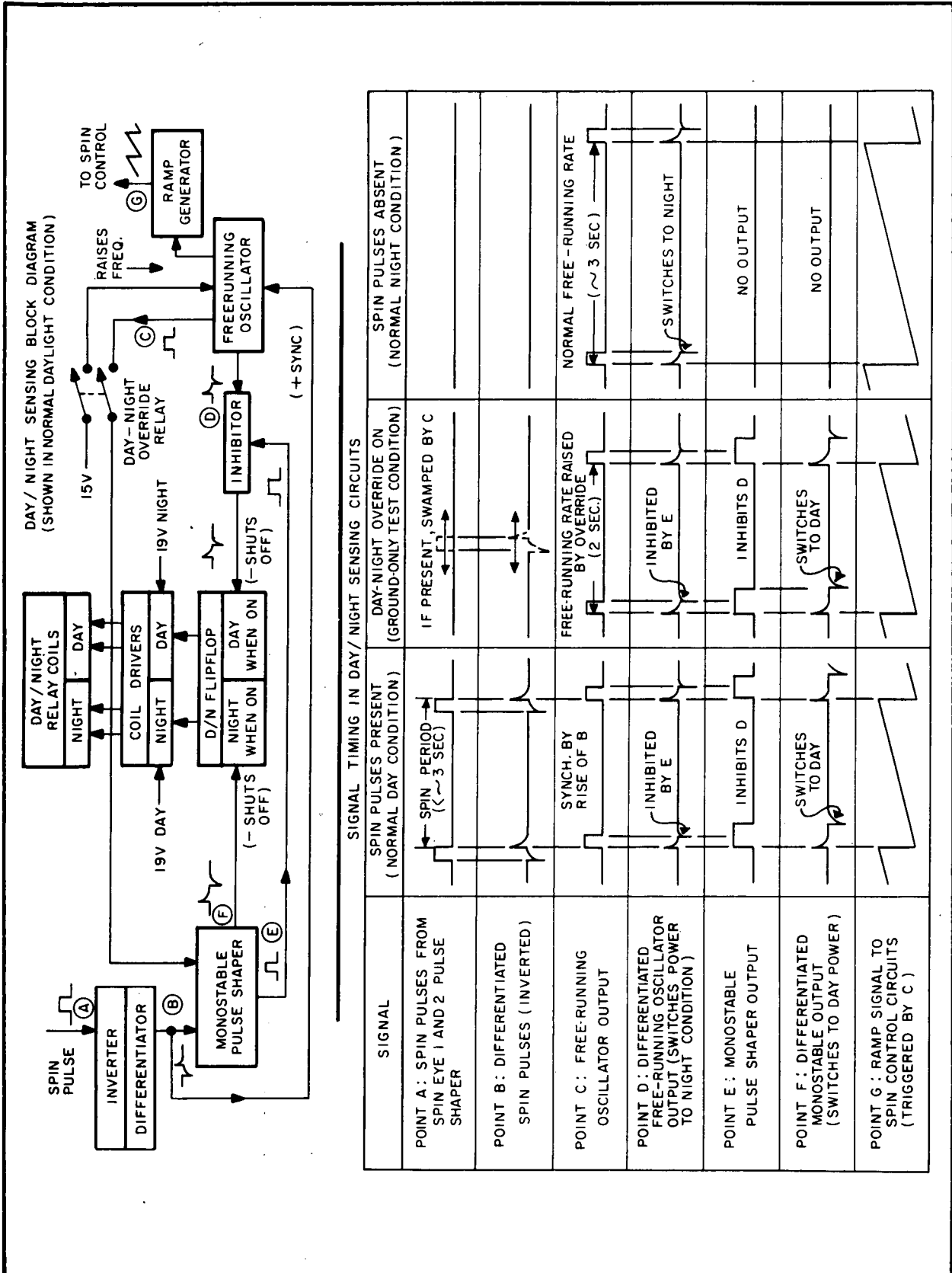


Figure 6-7 Day/Night Sensing and Timing



F72-01

During ground-test operations, day power can be turned on by closing the day-night eye override relay. This raises the free-running rate of the oscillator to the nominal spin rate and applies its output to the monostable circuit. The other circuits then act as though spin pulses were present. The day-night eye override circuit is also used during the launch sequence. The override is used only during ground testing and the launch sequence, because the relay cannot be operated by command control. Another relay, however, can be used to bypass the day-night relay in flight, by ground-station command.

#### 6.4.4 Analog Spin-Rate Monitor

The analog spin-rate monitor, shown as part of Figure 6-4, is read out through the Wheel Analog Subcommutator (WASC). It consists of a binary counter and a summing network. The binary counter is stepped by spin-eye pulses, and thus steps one count for each revolution of the wheel in sunlight. Spin Eyes 1 and 2 are used when the spin control is in the automatic mode, and Spin Eye 3 is used in the manual mode.

The five multivibrator stages of the binary counter feed currents to the summing network, producing analog voltage steps roughly proportional to the binary count. Samples of this voltage are identified with particular steps using the subcommutator data-conversion tables. There are 32 such steps in a counting cycle, and 32 discrete levels of analog output associated with the steps. The counter recycles to 1 after each 32 revolutions of the wheel.

Successive samples of the monitor are separated in time by the ASC frame period (15.36 seconds). Spin rate is calculated from the number of steps taken by the counter over a sample period, some whole-number multiple of 15.36 seconds. Dividing the sample period by this number of steps yields the spin period. Accuracy is increased by increasing the sample period.

#### 6.5 MAGNETIC ROLL, PITCH AND SPIN CONTROL

Occasionally, the attitude or the spin rate of OSO must be changed quickly. The pneumatic controls, discussed earlier, provide the torques for such changes. Normally, however, only slow changes are needed, so that smaller torques are adequate. Such torques can be produced by magnetic dipoles reacting with the earth's magnetic field. Using magnetic dipoles for long-term attitude and spin control conserves the pneumatic control gas supply.

A dipole along the spin axis such as that produced by the pitch coil produces torque about the roll axis, causing precession about the pitch axis. It also produces torque about the pitch axis, which causes motion about the roll axis. Figure 6-8 shows the switching arrangement and Table 6-1 lists the dipole strengths for various command settings.

The roll coils, mounted in the sail, create a dipole along the roll axis. They produce torques about the pitch axis, causing precession about the roll axis and torques about the spin axis that tend to alter the spacecraft spin rate. The roll coils are powered only during orbit day, when the sail is pointed at the sun. Their orientation is such that their dipoles lie along the spacecraft roll axis, within 4 degrees of the sun line.



F72-01

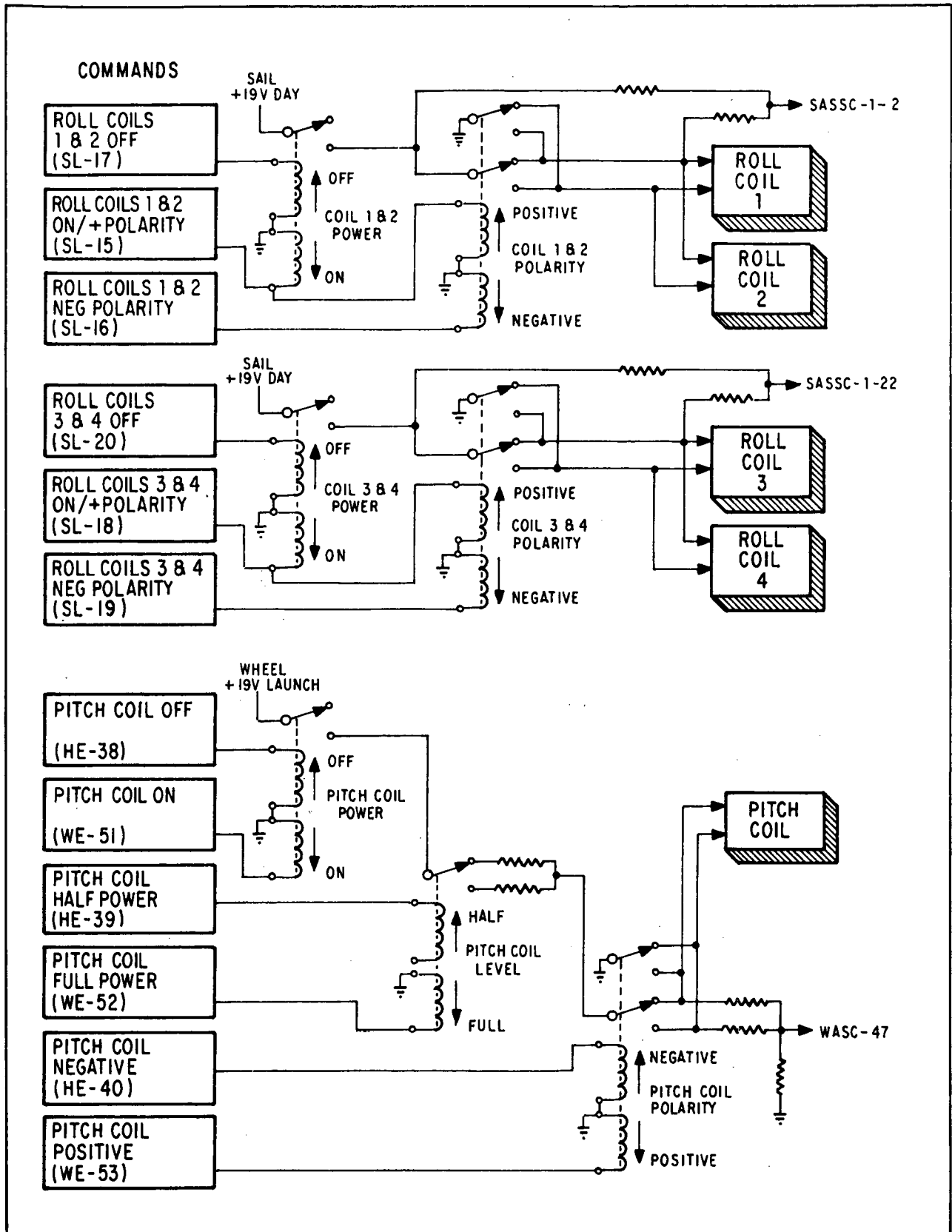


Figure 6-8 Pitch and Roll Coils Functional Diagram



F72-01

Table 6-1  
MAGNETIC ATTITUDE CONTROL DIPOLES

<u>PITCH COIL STATE</u>		<u>NOMINAL DIPOLE</u>
On-Full-Positive		+6000
On-Half-Positive		+2250
Off (No Residual)		0
On-Half-Negative		-2250
On-Full-Negative		-6000

<u>Roll Coils 1 and 2</u>	<u>Roll Coils 3 and 4</u>	<u>Total Dipole</u>
On/+5000	On/+5000	+10000
On/+5000	Off/+600	+5600
Off/+600	On/+5000	+5600
Off/-600	On/+5000	+4400
On/+5000	Off/-600	+4400
Off/+600	Off/+600	+1200
Off/+600	Off/-600	0
Off/-600	Off/+600	0
Off/-600	Off/-600	-1200
Off/+600	On/-5000	-4400
On/-5000	Off/+600	-4400
On/-5000	Off/-600	-5600
Off/-600	On/-5000	-5600
On/-5000	On/-5000	-10000

All dipole levels are given in gauss-cm<sup>3</sup>.

Figure 6-8 shows how OSO's roll coils are controlled to provide nine different dipoles as listed in Table 6-1. Note that the residual dipoles in the roll coils' iron cores are 300 gauss-cm<sup>3</sup> per coil, whereas the pitch coil has no ferromagnetic core.

Thus, dipoles along only two axes can produce control torques about all three axes. With selective programming of these dipoles in orbit, they usually can produce desired torques without excessive torque in an undesirable direction. By using the orbit-average fields and switching coil states every few days as required, gas need be used only for fast maneuvers.

## 6.6 POINTING CONTROL

The pointing control provides automatic solar acquisition each orbit morning, points the sail and the pointed-instrument assembly (PIA) at the sun during orbit day, and can point the sail and PIA at desired targets in azimuth during orbit night.

The pointing control uses four servo loops: azimuth-coarse, azimuth-fine; elevation-fine; and azimuth-gyro. These servo loops consist of control eyes mounted on the sail and the PIA, electronic circuits contained in the servo amplifier and power amplifier assemblies on the back of the sail, azimuth and elevation torque motors, and an azimuth reference gyro. Figure 6-9 illustrates the functional interfacing of the four servo loops.





F72-01

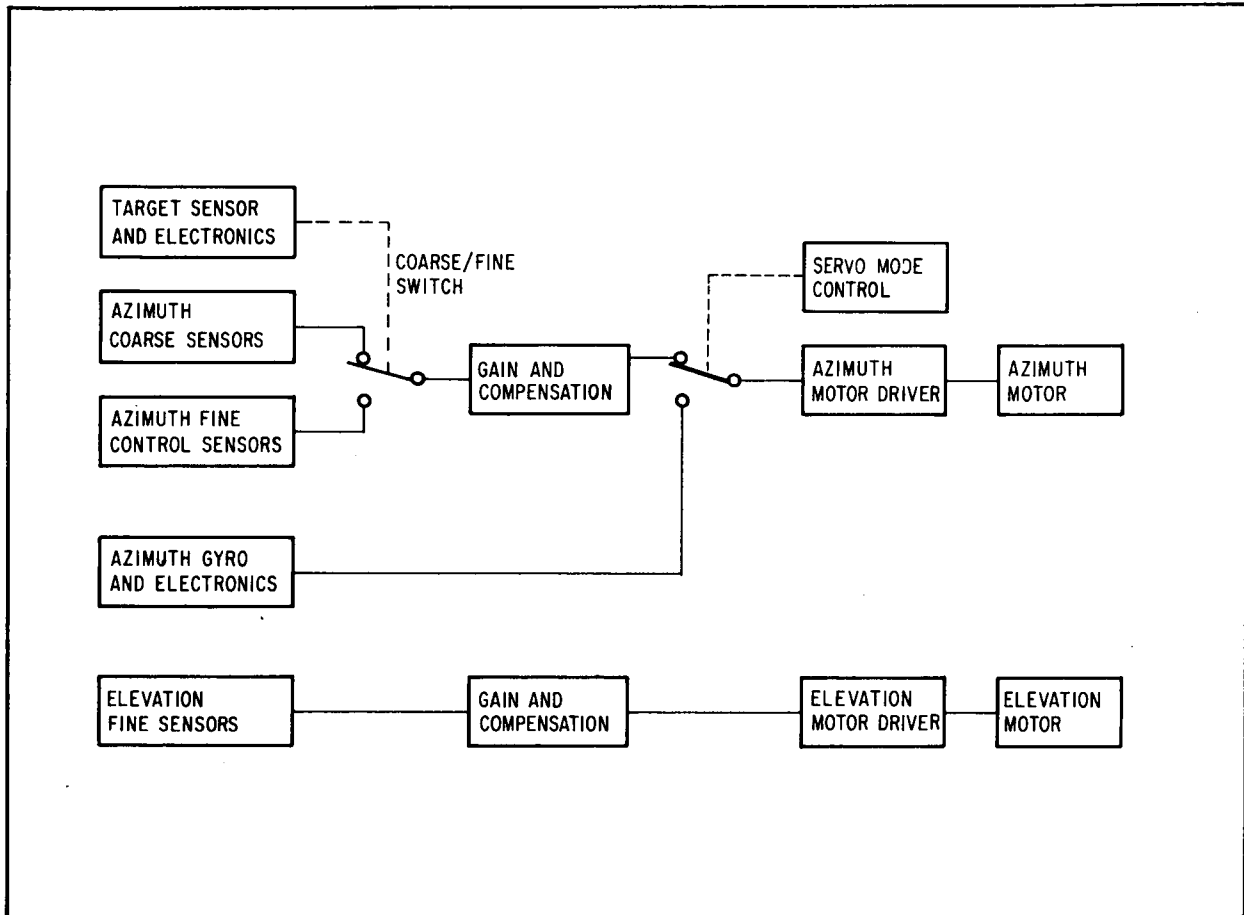


Figure 6-9 Servo Loops Functional Interfacing

Improvements Over Past OSO's. The control concept is basically the same as that used on OSO-6. The major improvements are: an azimuth night-pointing mode has been added; larger pointed instruments can be handled (up to 20 slug-ft<sup>2</sup>), and, because of this improvement, larger azimuth and elevation motors are used; the elevation motor is brushless, giving an increase in reliability; the raster "reset" motion is now exponential, providing a reset which produces little nutation; and coarse azimuth acquisition is improved.

Modes of Operation. The pointing control has six operating modes: coarse-acquisition; sun-centered-point; large-raster; offset-point; small-raster; and night-pointing. The mode of operation is selected by ground command and verified by telemetry.

In the sun-centered-point mode, the optical axis of the PIA points at the center of the sun. In the large-raster mode, the PIA scans the sun with either a 64-line or a 128-line raster pattern centered on the sun. The 128-line pattern consists of two interlaced and alternating 64-line patterns. The size of the large raster is 60 x 60 arc-minutes. In the offset-point mode, the PIA can be pointed at any one of 16,384 points (128 x 128 grid) within the large-raster pattern. In the small-raster mode, the PIA can trace a 5 x 5 arc-minute raster



F72-01

pattern about any of these offset points. The number of lines in the small raster is 16. In the night-point mode, the PIA can be held stationary in azimuth or allowed to slew in azimuth at 0.33 degree per second.

Coarse Acquisition. Solar acquisition is initiated each orbit morning by the day turn-on sensors (spin eyes) located on the rim of the wheel. These eyes detect the sun as it rises above the horizon and activate the pointing control circuits. The azimuth-coarse eyes then produce drive signals for the azimuth-coarse servo, and the sail is brought to within  $\pm 3$  degrees of stationary azimuth pointing. At this time, the target eye sees the sun and after a delay of about 8 seconds a coarse/fine control relay transfers control to the azimuth-fine servo. The azimuth-fine and elevation-fine circuits then complete the acquisition, and provide accurate pointing of the PIA in the selected mode.

Control Sensors. The coarse-sensor assemblies ("coarse eyes") are mounted on the top of the sail, one on the right and the other on the left. Each assembly contains two coarse eyes. Together, the four eyes provide full 360-degree coverage in azimuth, and  $\pm 15$  degrees in elevation. The four sensor outputs are combined and the composite signal is used to control the azimuth servo during acquisition.

The target sensor ("target eye"), on the front of the PIA, senses when the sun is within the field of view of the fine-control eyes. The target eye is the same as used on previous OSO's, and has a field of view of  $\pm 3$  degrees in azimuth and  $\pm 6$  degrees in elevation.

The fine-control sensors ("fine eyes") are mounted on the front of the right-hand pointed instrument. The long-term absolute accuracy of these sensors is better than 30 arc-seconds while the short-term null drift is  $\pm 2$  arc-seconds for 5 minutes and  $\pm 4$  arc-seconds for one complete orbit. These sensors achieve a long-term fine-pointing accuracy of  $\pm 10$  arc-seconds. Short-term stability is  $\pm 3$  arc-seconds, including jitter and drift.

Sun-Centered Pointing. In the sun-centered-pointing mode, the fine eye outputs are at null when the PIA is pointed at the center of the sun. The outputs of the fine eyes are processed through dc amplifiers, pulse width modulators (PWM), and power switches to produce drive signals to the elevation and azimuth torque motors. Since the servo drives directly to the sensor null in this mode, rather than to the null of some composite signal, changes in gain, temperature, or other circuit parameters have little effect on pointing accuracy. Hence, this is the most accurate of the OSO pointing modes.

The sun-centered-pointing mode is not considered the primary operating mode of the OSO-7 servo, even though it is the most accurate and stable. The new generation of pointed instruments, flown on OSO-7, are able to view and resolve a field subtending an angle of a few arc-seconds. These new instruments do not view the entire sun in one glance. Thus, the raster and offset-point modes are more useful, since they provide the means for seeking and selectively viewing interesting areas of the sun's surface.



F72-01

Offset Point and Raster. The offset mode circuits provide azimuth and elevation bias signals to the servo loops for constructing the large and small rasters, and for pointing the PIA at selected coordinates on the offset-point grid. Offset pointing and rastering is accomplished by summing these bias signals with the respective feedback signals from the elevation and azimuth fine-control eyes. The effect of the bias signals is to shift the null position of the control eyes, thus causing the servo to drive the PIA to the desired position, or in the desired raster pattern.

Offset pointing is accomplished by sending two 7-bit "location commands" to the offset generator. These two commands (one for elevation and one for azimuth) are binary words representing the desired point on the 128 x 128 offset-point grid. The commands are decoded by a digital-to-analog converter. The resulting analog signals are summed with the outputs of the fine control eyes and cause the PIA to point at the desired location.

Rastering is accomplished by generating separate raster control signals for elevation and azimuth. The elevation raster signal is a "staircase" waveform that is reset at the end of each raster frame. This waveform controls the elevation position of each line in the raster pattern. The azimuth signal is a "sawtooth" waveform which controls how fast the PIA moves in azimuth and the angle at which the scanning direction reverses. As with offset pointing, both the elevation and azimuth raster signals are summed with the outputs of the fine control eyes to produce the raster pattern.

Night Pointing. During orbit night, the gyro may be used as a reference to keep the sail and PIA pointed (in azimuth) in the direction of the sun. The sail can also be offset from this position in increments of 0.05 degree. In addition, it can be slewed at a constant rate of 0.33 degree per second. The 0.05-degree steps are obtained by torquing the gyro in 150 millisecond steps using an on-board pulse generator. A constant rate of rotation is obtained by applying a constant input to the gyro torque generator. Switchover to gyro control at day-to-night transition results in a pointing-direction change of less than 15 arc-seconds. Maximum drift rate of the sail at night is 0.5 degree per hour.

#### 6.6.1 Azimuth-Coarse Servo

Because of their functional similarities, we present a detailed discussion of the azimuth servo, and only a brief discussion of the elevation servo. Also, because many components in the azimuth coarse servo are shared with the fine servo, a detailed discussion of one loop explains a large portion of the other. Figure 6-10 is a block diagram of the entire pointing control system.

Coarse Sensors. The four azimuth coarse eyes are mounted on pedestals on top of the sail. Each eye consists of a silicon photoelectric sensor mounted in an aluminum block (Figure 6-11) and covered by a Corning No. 2600 red glass filter. The eye assembly is then covered by a 0.1-inch quartz cover slip that protects the sensor from radiation damage.



F72-01

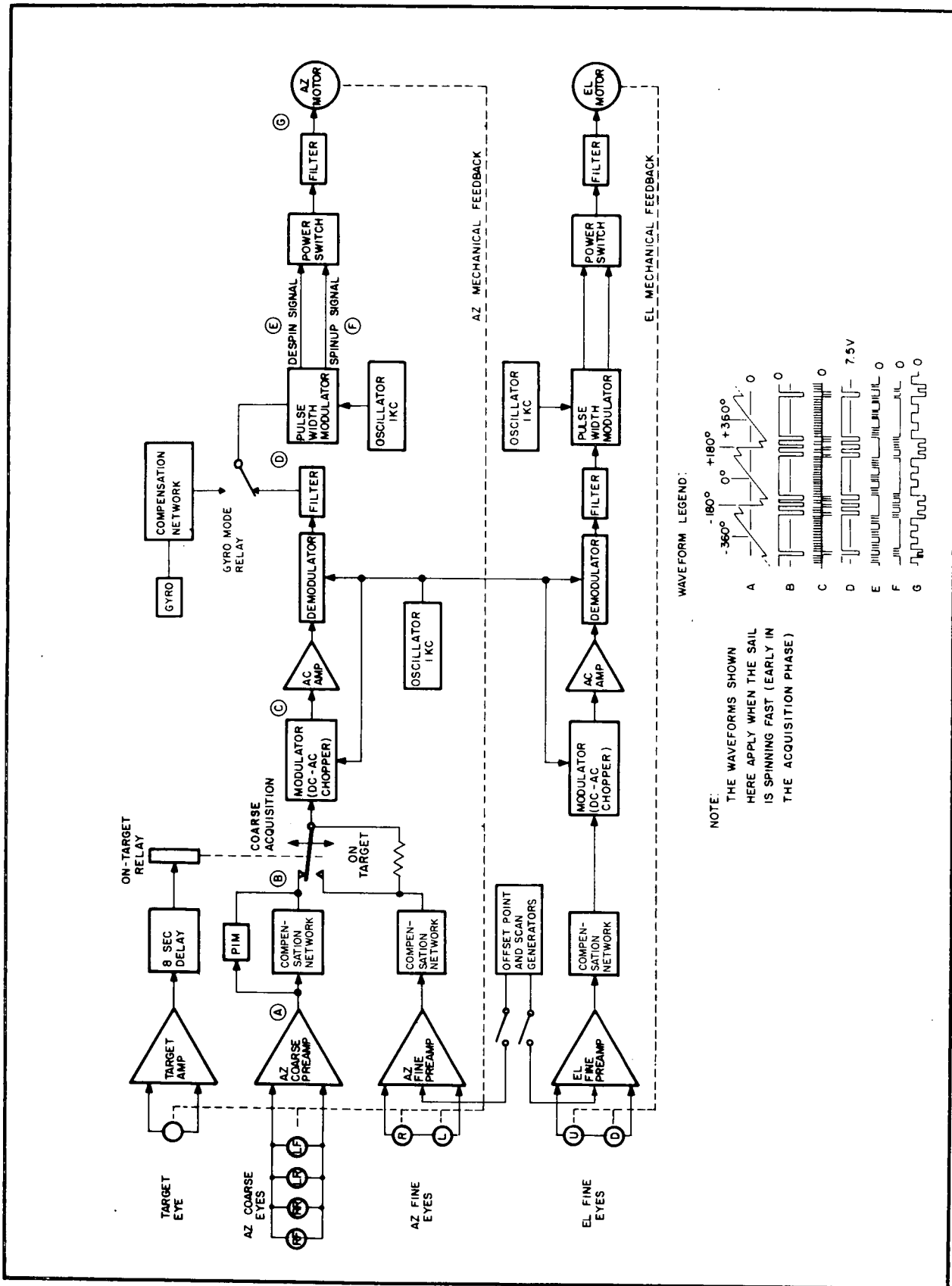


Figure 6-10 OSO-7 Pointing Control Block Diagram



F72-01

The vertical field of view for the eyes is from 15 degrees above to 15 degrees below the wheel plane. This restricted field of view shields the eyes from light reflected from the top of the wheel and from earth albedo. It also prevents their sensing the sun if the spin axis is not within 15 degrees of perpendicular to the solar vector. The composite field of the eyes is 360 degrees in azimuth. The view angle, however, is about 110 degrees for each front eye, and about 95 degrees for each rear eye. (See Figure 6-12.)

As the sail rotates, the coarse eyes produce a current waveform (error signal) as shown in Figure 6-12. The figure shows the field of view of each eye and the output waveform of each as the sail rotates. The four individual outputs are summed to form the input signal for the azimuth-coarse preamplifier.

The composite signal from the coarse eyes has two important terms: a position term and a time-rate-of-change term. The position term is the instantaneous amplitude of the signal. The rate term reflects the rate at which the position term changes. Each of these terms plays an important role in the coarse-acquisition function.

The polarity of the position term is such that the positive area of the signal (shown on Figure 6-12) causes the sail to be driven in the despin direction. This portion of the signal is produced by the right-front (RF) and right-rear (RR) eyes. The negative area of the signal causes the sail to be driven in the spinup direction. This portion of the signal is produced by the left-rear (LR) and left-front (LF) eyes.

The drive produced by signals in the region of the unstable null (③ on the curve) are away from the null, while those near the stable null (① on the curve) are toward the null. This assures that the sail will stop only at the stable null.

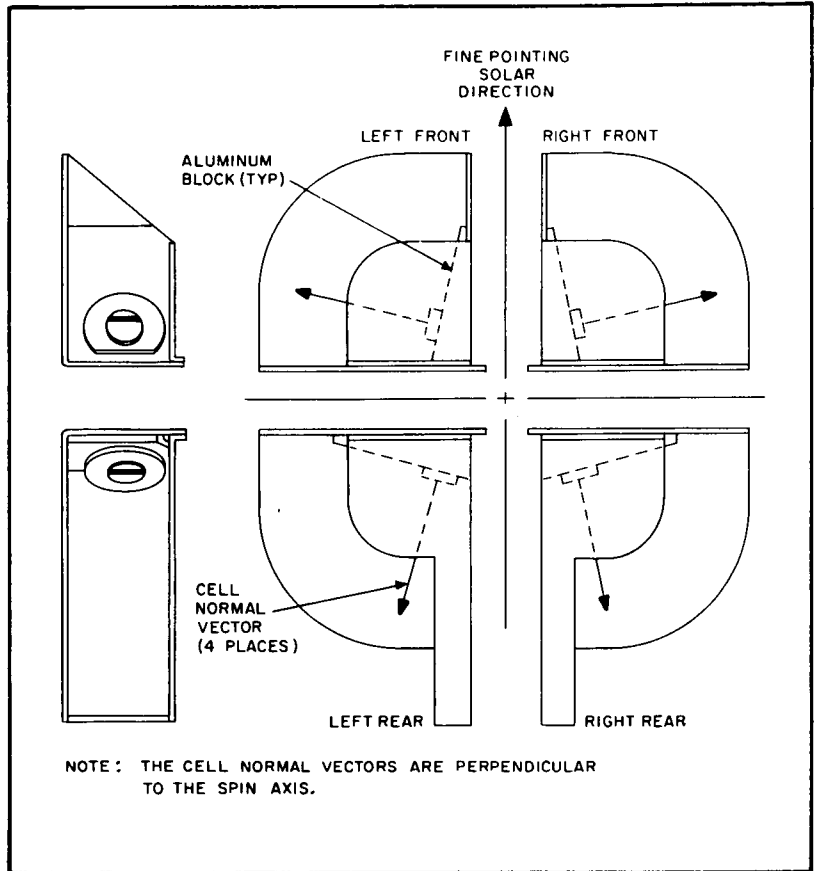


Figure 6-11 Coarse Sensor Assemblies



F72-01

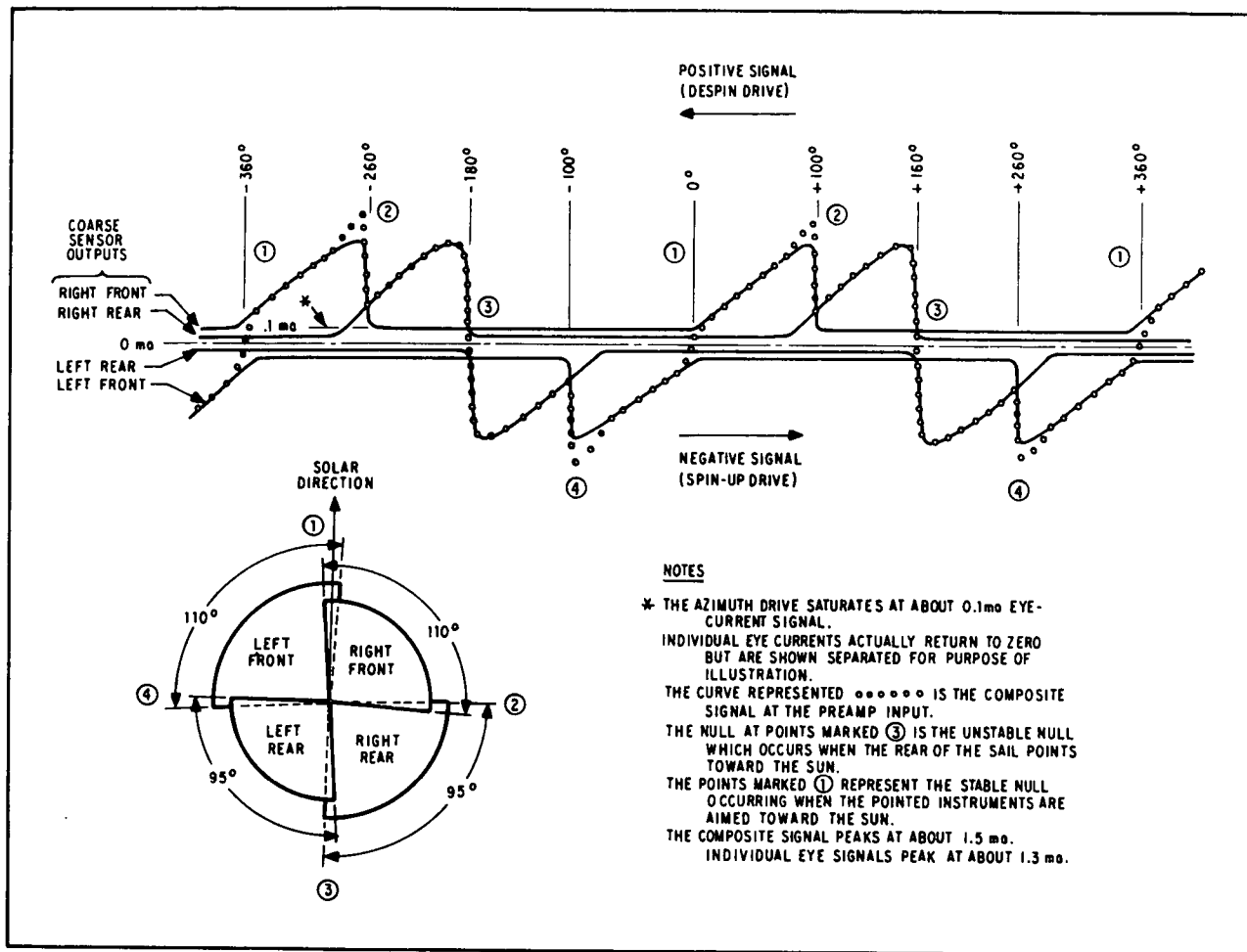


Figure 6-12 Coarse Sensor Signal

The rate term dominates while the sail rotates quickly. A rate network and pulse-inverter circuit convert most of the negative (spinup) signal into a positive signal. This action continues until the spin rate is reduced to about 0.07 rps. The position term then becomes dominant and remains so throughout the rest of the acquisition. Thus, the rate term is dominant at high spin rates and the position term at slow spin rates.

The coarse preamplifier (see Figure 6-10) converts the coarse-eye output (Figure 6-12) from a current waveform to a voltage waveform. The preamp is a differential, low-drift amplifier with circuits for automatic compensation of changes in its own gain. It provides a low-impedance load for the eyes and a low-impedance output to the rate network. The preamp is designed for unsaturated operation between  $\pm 1.5$  ma of input eye current.

The output of the azimuth coarse preamp is fed into a compensating network and a pulse-inverter module (PIM) as shown in Figure 6-10. Rate sensing and the conversion of spinup signals are accomplished in these circuits.



F72-01

The compensation network consists of a resistor-capacitor coupling arrangement which provides dc coupling for low-spin-rate eye signals and predominantly-despin signals for higher spin rates. This network provides a positive (despin) drive signal when the eye signal is positive-going and spin rate is greater than about 0.07 rps. Traces A and B of Figure 6-13 show the relationship between the eye signal and the ideal output of the compensating network. Notice how this compensation turns the symmetrical waveform into a predominantly positive signal.

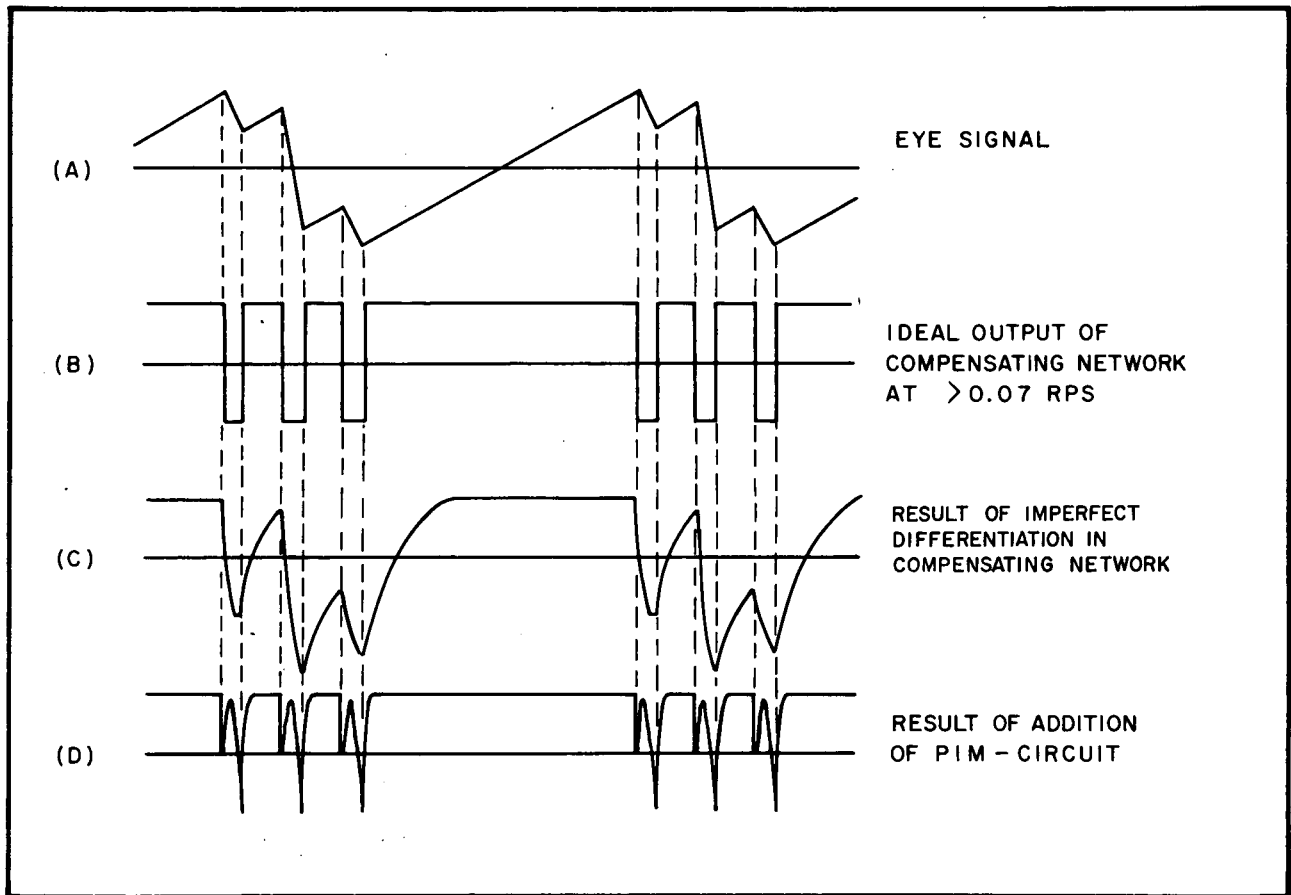


Figure 6-13 Rate Signal Compensation

Part of the despin signal is lost, however, due to imperfect differentiation of the output. The resultant waveform is shown in Figure 6-13, trace C. The negative portion of this waveform represents spin-up drive and therefore decreases net despin efficiency. The effect of the negative signal is substantially reduced by the addition of the PIM circuit.



F72-01

The *pulse-inverter module* (PIM) tends to superimpose a positive signal on the negative output of the compensating network. It does this through a time constant which prevents it from interfering with spin-up drive in the final phase of solar acquisition. The PIM also peaks up the leading edge of the positive output of the compensation network. Both of these actions increase net despin drive efficiency, as shown in Figure 6-13, trace D.

When the sail rotation is reduced to about 0.07 rps, the compensation network and PIM yield to direct dc coupling of the eye signal to the modulator (Figure 6-10). The position term of the error signal then becomes dominant and controls the final stages of coarse azimuth acquisition.

The net efficiency of the azimuth coarse servo is expressed in a term known as net despin drive. It is found by subtracting the percent of time the drive is negative (spin-up) from the percent of time drive is positive (despin) during a revolution of the sail. Net despin drive is expressed as a percent and plotted as a function of sail spin rate in Figure 6-14.

The output of the coarse-servo circuits is fed through the on-target relay to the circuits which are common to the azimuth servo in both the coarse-acquisition and fine-pointing modes.

The *modulator* is a dc-to-ac chopper, which samples the differential output of the coarse preamplifier and rate network at about a 1 kHz rate. The output of the modulator is a square wave with a peak-to-peak amplitude equal to the differential input signal. This output is fed to the azimuth ac amplifier.

The *ac amplifier* saturates with an input corresponding to coarse-eye currents of about  $\pm 0.1$  ma. Thus, during acquisition, this amplifier is saturated most of the time, providing a clipped output. This output goes to the demodulator.

The *demodulator* is driven by the same oscillator that drives the modulator. It converts the output of the ac amplifier to a dc signal. The output of the demodulator is an amplified and clipped reconstruction of the error signal, referenced to a 7.5 v bias level, and has 1 kHz transients in it. The response curve for the coarse-preamp/ac-amplifier combination is shown in Figure 6-15. The output voltage is clipped on the spin-up side. This improves coarse azimuth acquisition by minimizing spin-up drive signals.

The output of the demodulator is fed through a filter which removes the 1,000 Hz transients and any other system noise down to about 50 Hz. This filtered signal then goes to the PWM circuit.

The *pulse-width modulator* (PWM) converts the amplitude-modulated error signal into a constant-amplitude 2500 Hz waveform in which pulse width (or duration) is proportional to the amplitude of the dc error signal. The principal reason for using a PWM design is to reduce power dissipation in the power switch.





F72-01

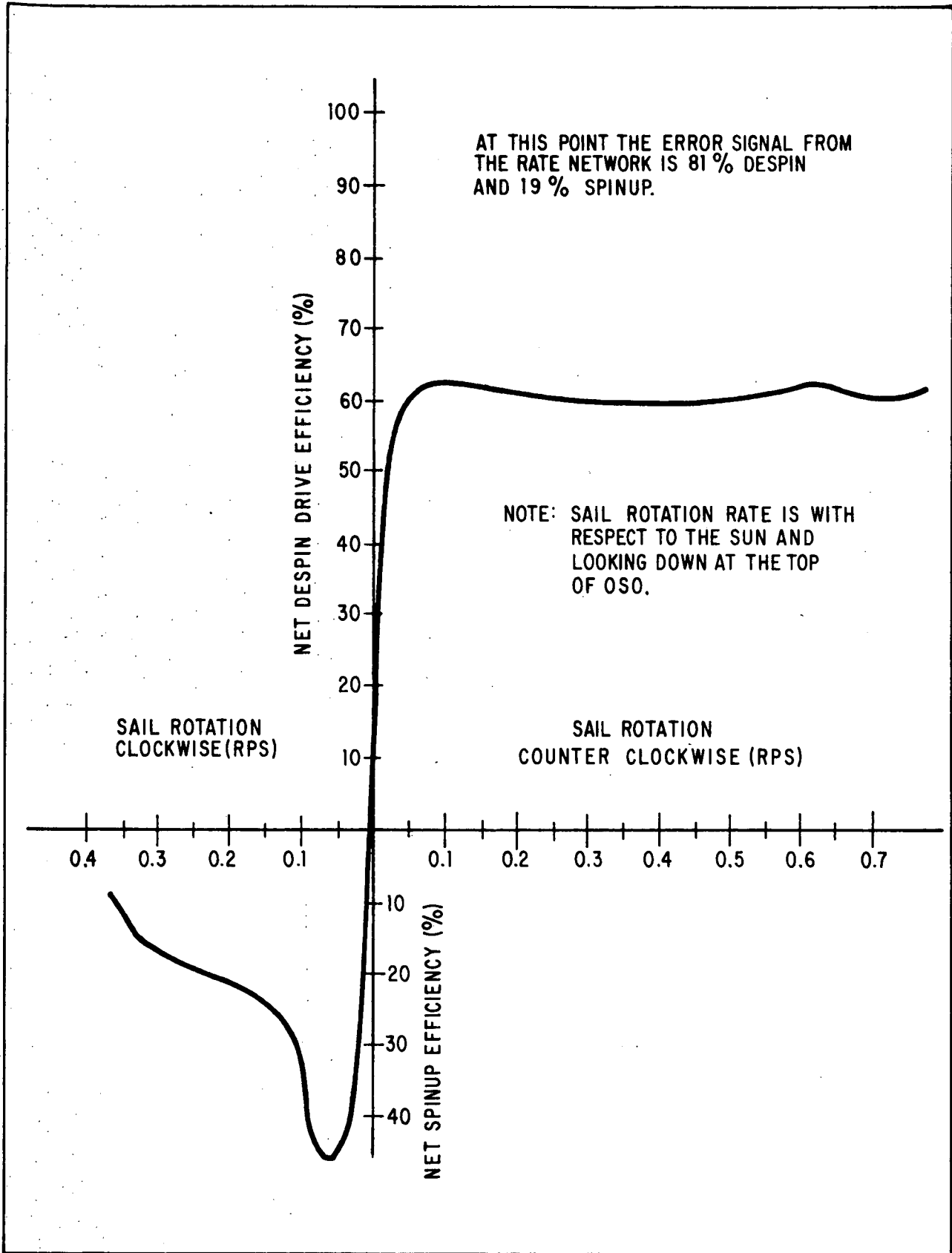


Figure 6-14 Net Despin Drive Efficiency



F72-01

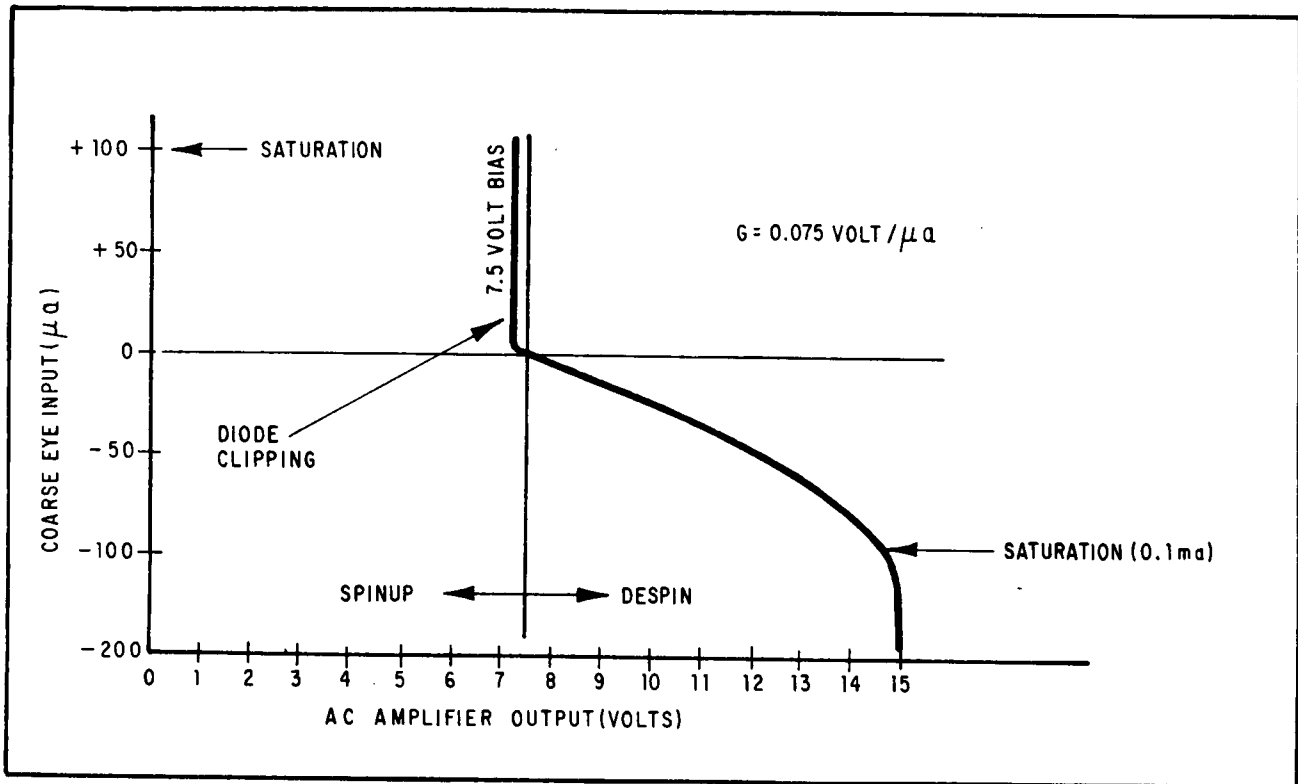


Figure 6-15 Coarse-Azimuth Preamp/AC Amplifier Response

The PWM is designed to produce an output only when the input varies above or below the 7.5 v bias level. This variation is typically between about +7 and +13 v as the sail rotates. The PWM has a dead zone (no output) at about  $7.5 \pm 0.25$  v. The dead zone has no effect on the operation of the azimuth loop since the wheel always spins in the same direction, holding azimuth-loop operation on one side of the dead zone except during acquisition. The PWM dead zone is shown in Figure 6-16.

The PWM actually consists of two separate modulators that work together. One converts despin signals ( $>7.5$  v) into pulse-width waveform and the other converts spin-up signals ( $<7.5$  v). Outputs of both PWM circuits are positive. Each output is fed to one side of the power switch for power amplification.

The *power switch* consists of two pairs of saturable-transistor switches. One pair of transistors is controlled by the despin PWM and drives the azimuth torque motor in the despin direction. The other pair is controlled by the spinup PWM and drives the motor in the spinup direction. The outputs from the power switch are filtered before being applied to the torque motor to reduce power losses in the motor windings. The drive current is averaged by the filter. Operation of the power switches in the region of saturation and cut-off avoids the heat dissipation and power waste inherent in other areas of the transistor load line. Figure 6-16 shows a typical overall response of the PWM and power-switch circuits to inputs from the demodulator.



F72-01

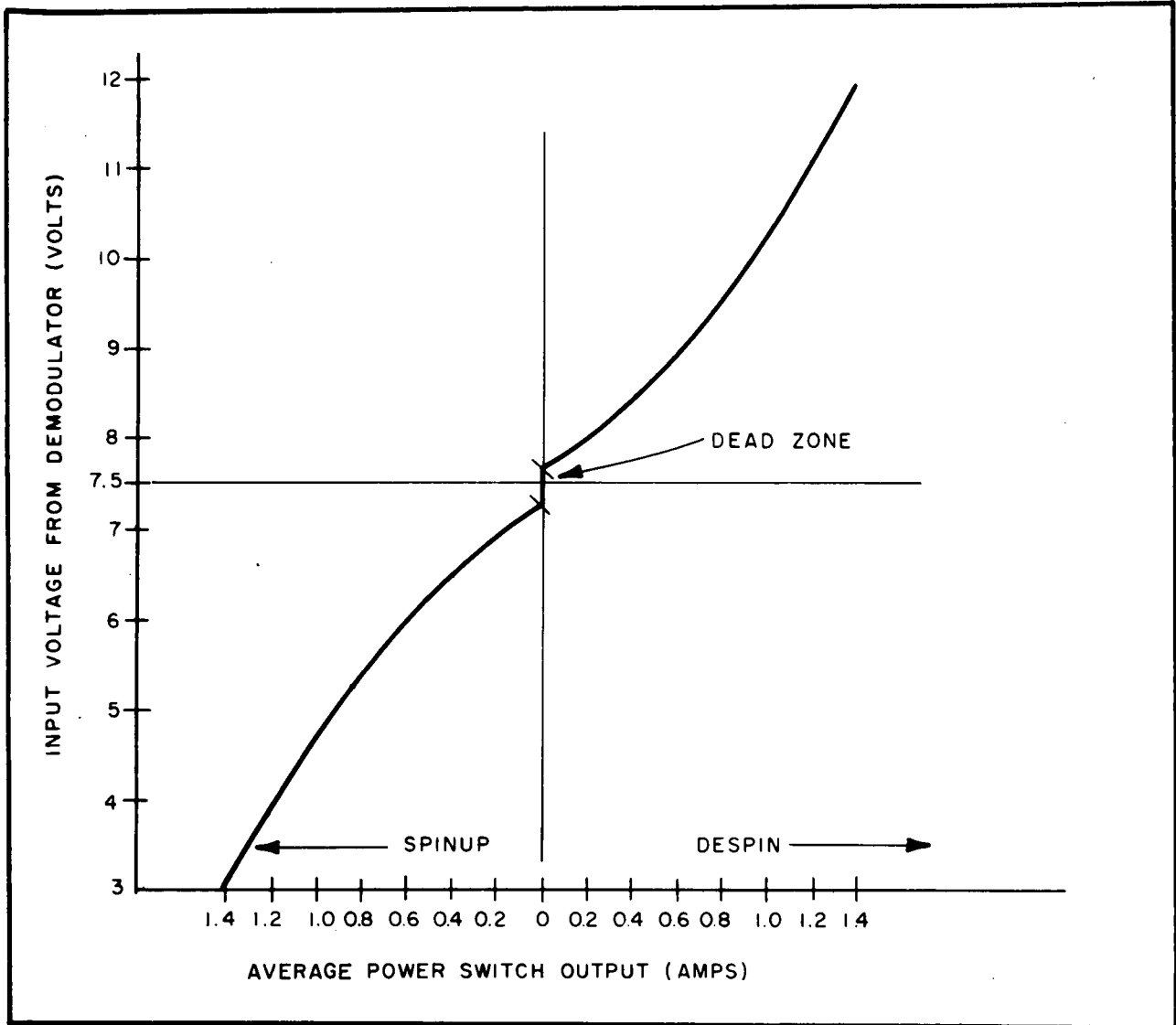


Figure 6-16 Typical PWM/Power Switch Response.



F72-01

The *azimuth torque motor* is a frameless dc permanent-magnet-type motor unit. The windings and commutator bars are on the outer member, which is fixed to the wheel (rotating section) of the spacecraft inside the azimuth despin assembly (ADA) in the upper end of the wheel hub assembly. The permanent magnets and brush ring are on the inner member, which is fixed to the azimuth shaft. The motor has a nominal torque sensitivity of 0.785 pound-feet/ampere and develops back emf at about 1.06 volts/radian/second. The dc resistance is about 7.7 ohms.

Total acquisition Time. The total acquisition time, between 75 and 100 seconds, is dependent on many factors:

- Motor torque constant
- Back-emf function
- Bearing friction
- Armature resistance
- Saturation drive voltage
- Sail moment of inertia
- Sail initial spin rate
- Net despin drive efficiency
- The uncertainty in the direction of approach of the sail to its final pointing position.

#### 6.6.2 Target Eye and Coarse/Fine Switch

The target eye and coarse/fine switch are the link between the azimuth coarse and fine servo loops. When the coarse loop has brought the pointed instruments within 3 degrees of the solar direction, the target-eye senses the sun. After about an eight-second delay, coarse/fine switching occurs. The input to the azimuth ac amplifier is then developed in the fine-mode sensors and circuits.

The target eye, mounted in the fine-control-eye block, produces about a 2 ma current when the pointed instruments are aimed within the capability of the coarse pointing control. The elevation field-of-view of the target eye is about  $\pm 6$  degrees, making operation of the elevation servo unnecessary for coarse/fine switching. The field of view of the azimuth fine-control eyes is greater than  $\pm 12$  degrees, providing the necessary overlap for smooth coarse/fine transition. The output of the target eye is fed through the target-eye amplifier to the coarse/fine relay driver and a telemetered target-intensity monitor.



F72-01

The *azimuth coarse/fine switch* is called the "on-target relay". After the target-eye has been illuminated for the 8-second delay period, the on-target switch is released to the "fine" position. The switch is a momentary-operation relay and is energized in the coarse mode. The relay also generates an "on-target" signal which is monitored by telemetry.

The *target-intensity monitor* is a telemetry sampling of the output of the target-eye amplifier. The linear characteristic of this amplifier permits in-flight evaluation of target intensity and sensor degradation.

### 6.6.3 Fine Azimuth and Elevation Servo Loops

Fine azimuth and elevation servo control begins at the completion of coarse acquisition (coarse-fine switching). These servo loops function very much like the coarse azimuth servo loop, with the following exceptions:

- The error signals are produced by the azimuth and elevation fine eyes.
- A different preamplifier is used.
- The rate-sensing and PIM circuits are replaced by compensation networks designed to adjust servo stability and response characteristics to other servo parameters such as static gain and structural resonances.
- The elevation torque motor produces slightly less torque than the azimuth motor.

The fine control eyes for the azimuth and elevation servos consist of pairs of BBRC FE-5 fine sensors. Each FE-5 sensor has a focusing lens, a red-glass filter, and a silicon solar cell. One half of each red filter disc is masked by a thin aluminum film. The output of each cell is a function of the direction it is pointing, as shown in Figure 6-17.

The electrical leads from each sensor are connected in opposing polarity to the other half of the sensor pair. The sensors of each pair point slightly away from each other so that, on point, each sensor produces about ten percent of its maximum output. The two opposing currents produce a stable null in the on-point direction.

An azimuth or elevation error signal results when the sensor assembly is rotated from the on-point position. Figure 6-17 shows the output curve for a typical fine-eye pair. It also shows the front view of the eyeblock (including the target eye), the aluminum shield orientation, and the behavior of individual eye outputs near the null region.

The fine azimuth and elevation servo loops seek a precise null position, and maintain pointing accuracy. As can be seen in Figure 6-10, the fine-servo loops differ from the azimuth coarse loop primarily in the development of the sensor signals. The fine azimuth and elevation preamplifiers convert the current signal from the eyes to a voltage signal for the ac amplifiers. In the region of the null, the eye/preamp gain is very stable.



F72-01

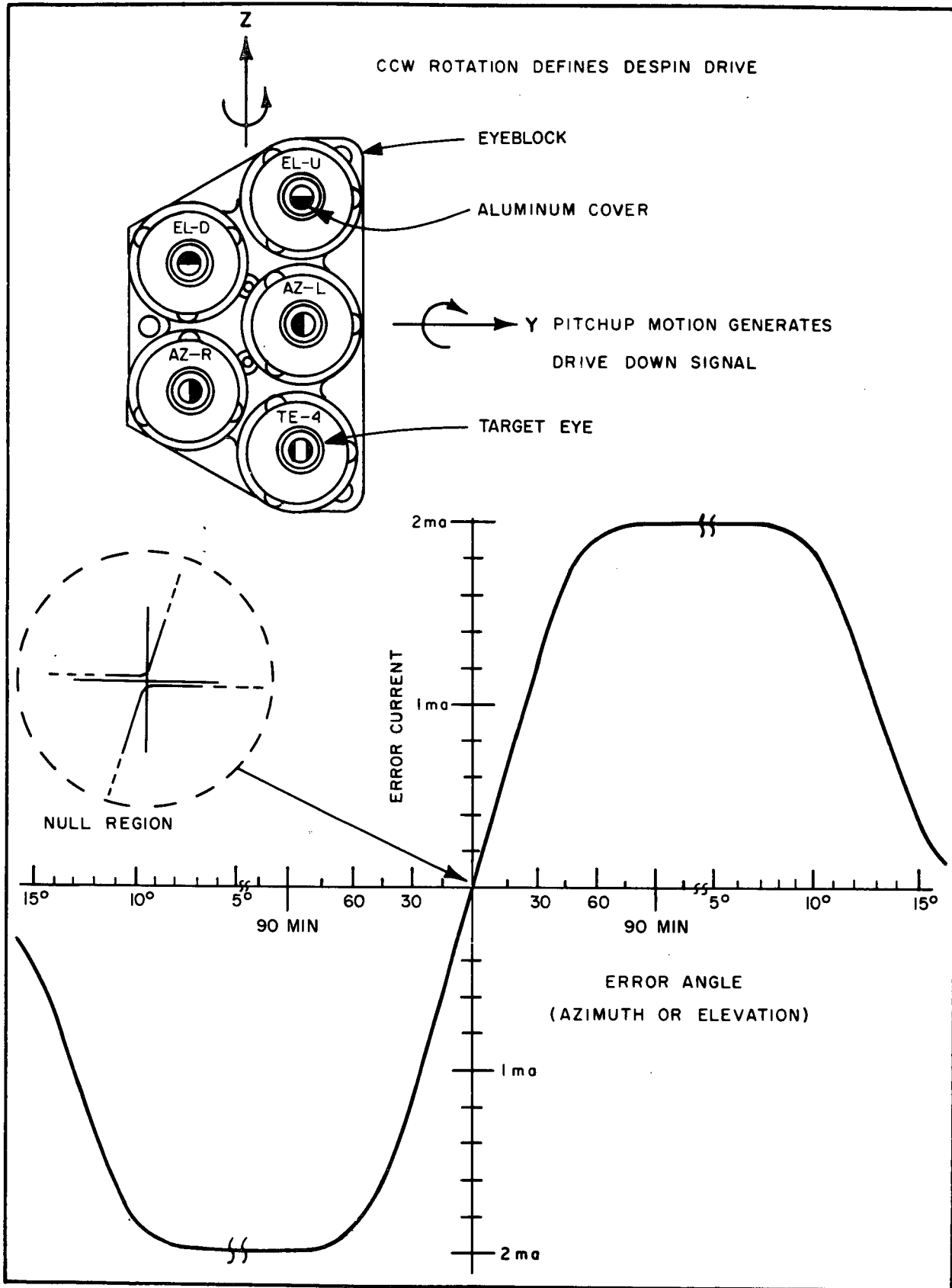


Figure 6-17 Fine Control Eyes and Response Curve



F72-01

After the preamp stage, the circuits of the azimuth fine control loop are common to the coarse loop. The elevation loop has its own modulator, ac amplifier, demodulator, PWM, power switch, and torque motor, similar to those for the azimuth loop. The base frequency of the elevation PWM is 500 Hz below that of the azimuth, to prevent frequency beating of the two signals. The overall loop gain of the azimuth-fine servo is about 31 inch-pounds per arc-minute. The gain of the elevation servo is about 28 inch-pounds per arc-minute.

Sensor Accuracy. By careful control of the alignment procedure, initial null offsets are held to less than five arc-seconds. Null shifts during environmental testing are below ten arc-seconds and the initial null offset at launch is less than fifteen arc-seconds.

Tests on the fine sensor assembly in a thermally changing atmosphere indicate that the null drift coefficient is less than  $\pm 0.5$  arc seconds per  $^{\circ}\text{C}$ . Since the expected temperature change over one orbit is expected to be about  $4^{\circ}\text{C}$  maximum, this results in a  $\pm 2$  arc-second null shift. Over five minutes, the shift is much less than this. The sensors are linear to better than  $\pm 0.4$  arc-minute over a  $\pm 30$  arc-minute linear angle. Their output can be predicted to an accuracy of better than  $\pm 2$  percent (that is,  $\pm 0.6$  arc-minute on the raster size).

Gain change with temperature is due to the cell's output changing with temperature. Since the output (near null) of the fine sensor is strictly a function of one cell alone, any change in cell output has a direct effect on gain even if the cells in a pair are precisely matched. When the cells are used in the short-circuit current mode, (as they are on OSO) the main cause of gain change is a shift in the spectral response curve of the cell with temperature.

When the cells are used with a red filter, they have a gain coefficient of  $\pm 0.2$  percent per  $^{\circ}\text{C}$ . This results in a change of  $\pm 0.8$  percent over the 4-degree orbital temperature range. This is equivalent to a pointing shift of 7.6 arc-seconds at the maximum offset point.

Azimuth Servo Errors. There are two major sources of fine azimuth pointing errors (other than the sensor): azimuth shaft friction, and back emf of the azimuth torque motor. They can cause a total error or "hang off" of 0.18 arc-minute.

Elevation Servo Errors. Pointing errors in the fine elevation servo loop can be caused by elevation motor shaft friction, and electronic and mechanical alignment drift. The spin-rate/back-emf changes that can cause pointing errors in azimuth servo do not apply to the elevation servo. The friction errors are related to wobble or nutation of the spin axis. These motions tend to drive the elevation gimbal above and below its average pointing position and the pointing error appears as an approximate squarewave. This pointing anomaly, called "jitter", is of most concern and it is desirable to minimize it. If nutation causes the jitter, the frequency is about 0.525 Hz for a wheel spin rate of 0.5 rps. When wobble causes the jitter, the jitter frequency is identical to the wheel spin rate.



F72-01

Jitter has been minimized by minimizing the friction and by using a bias torque offsetting the elevation position slightly. This bias torque moves the operating point out of the dead zone region, preventing motion through the dead zone. The elevation position is offset to one side of the dead zone by light spring tension against the pointed instruments.

The cumulative total of the sources of pointing error is such that steady-state azimuth and elevation pointing error is well within  $\pm 1$  arc-minute.

Elevation Motor. The elevation motor is quite different from the azimuth motor. The limited angular traverse of the PIA (about  $\pm 5$  degrees) allows the use of a motor having limited rotation capability.

The motor is a frameless, limited-rotation, brushless, permanent-magnet type manufactured by Aeroflex Laboratories, Inc. The windings, on the outer member or stator, are fixed to the sail trunnion. The inner member, or rotor, holds the permanent magnets and is fixed to the elevation frame of the PIA. The travel of the motor is greater than  $\pm 7$  degrees. Torque constant is about 0.7 inch-pounds per ampere, and winding resistance is nominally 9 ohms. Torque constant is uniform to within 5 percent of its center-position value over the full range of rotation.

Pointing Position Monitors. A sensor block, containing two fine-eye pairs similar to the fine-control eyes, is mounted to the front of the right-hand pointed instrument, next to the fine-control eyes. The signals from these fine-eye pairs are used to develop telemetered azimuth and elevation position monitor information. Eye and preamp gains are such as to provide an accurate readout of position in a range just over  $\pm 2$  arc minutes in both azimuth and elevation. These fine-point-position data appear on Words 1 (E1) and 2 (Az) of the sail analog subframe.

A similar sensor block, adjusted to telemeter the range of azimuth and elevation positions generated in the offset-point modes, is mounted to the front of the left-hand pointed instrument. Comparison of data from these two sensor blocks provides a means of evaluating misalignment between the two pointed instruments. Such misalignment may result from vibration during the launch, or thermal warpage in orbit.

#### 6.6.4 Offset Pointing and Raster

The offset pointing and raster operating modes permit on-board pointed instruments to locate and examine relatively small areas of the sun's surface, by aiming the pointed instrument assembly. The modes and offset positions are selected by ground command and monitored by telemetry. Either a large-raster, small raster, or offset point mode may be selected.

Large-Raster Mode. In the large-raster mode, the PIA scans the area of and around the sun in a square, 64-line raster pattern. Each line takes 24 telemetry minor frames, or  $0.32 \text{ sec/MF} \times 24 \text{ MF} = 7.68$  seconds. The period for a complete large-raster pattern is  $7.68 \text{ sec/line} \times 64 \text{ lines} = 491.52$  seconds or about 8.2 minutes. The nominal size of the large raster is 60 by 60 arc minutes, meaning that line separation, ideally, is 0.937 arc minutes. The size of the large raster is affected by changes in solar intensity due to the elliptic orbit of the earth. This variation is about 6 percent over a period of one year.





F72-01

Figure 6-18 illustrates the OSO-7 raster patterns together with the offset-point grid coordinates. Point A represents the on-point position (center of the sun). The large raster centers about this point.

When the large raster mode is selected, a start-of-raster (SOR) pulse is generated by the raster-synchronizing generator, causing the raster generator to begin the large raster at the center of line 1. Thereafter, a SOR pulse is generated each time a new raster pattern begins (each 8.2 min). Also, a start-of-line (SOL) pulse is generated each time a new line begins (every 7.68 sec). The SOR and SOL pulses are available for indexing functions in the scientific-instrument payload.

Small-Raster Mode. Point B of Figure 6-18 illustrates the small-raster mode. The size of this 16-line raster is 5 by 5 arc minutes. Ideally, line separation is 0.313 arc minutes. Each line takes 3.84 seconds, making the raster frame period 61.44 seconds. The small raster is always centered about whatever offset-point coordinate is programmed into the offset-point generator.

Offset Point Mode. By means of the offset-point mode, the PIA can be pointed at any one of 16,384 points within a square pattern the size of the large raster. In Figure 6-18, the numbers 1 through 64 (in both azimuth and elevation) define the offset-pointing grid (excluding the vernier offset). Any coordinate point on this grid can be selected by sending the proper combination of offset commands.

In addition, the 64 by 64 offset-point grid can be expanded to 128 by 128 by using the azimuth and elevation vernier offset commands (Bits 1). The azimuth vernier command moves the PIA an additional one half step (or 1/2 bit) to the right. The elevation vernier command moves the instruments 1/2 bit up.

Interlaced-Raster Feature. An optional function in the large-raster mode is the raster interlace. When this function is commanded on, every other raster is automatically shifted up by one half of the line separation. This feature is not provided in the small raster.

Offset-Mode Circuits. Figure 6-19 is a block diagram of the offset-mode circuits. The mode switching logic and timing sequence generator processes the mode commands. These commands select the proper timing relationships, scaling amplifier settings, and logic to perform a desired function. Shaping the start-of-line (SOL) pulses and generating the offset status monitor signals are also functions of these circuits.

An azimuth-scan generator and scaling amplifier generate the azimuth-scan triangular waveform. The amplitude of this waveform is adjusted by field-effect-transistor switches and a scaling amplifier. The elevation staircase waveform is produced by an elevation scan generator.

Azimuth and elevation current generators then convert the scan voltage waveforms into differential current waveforms. These are then summed with the fine-sensor error signals before being fed to the fine-control servos.



F72-01

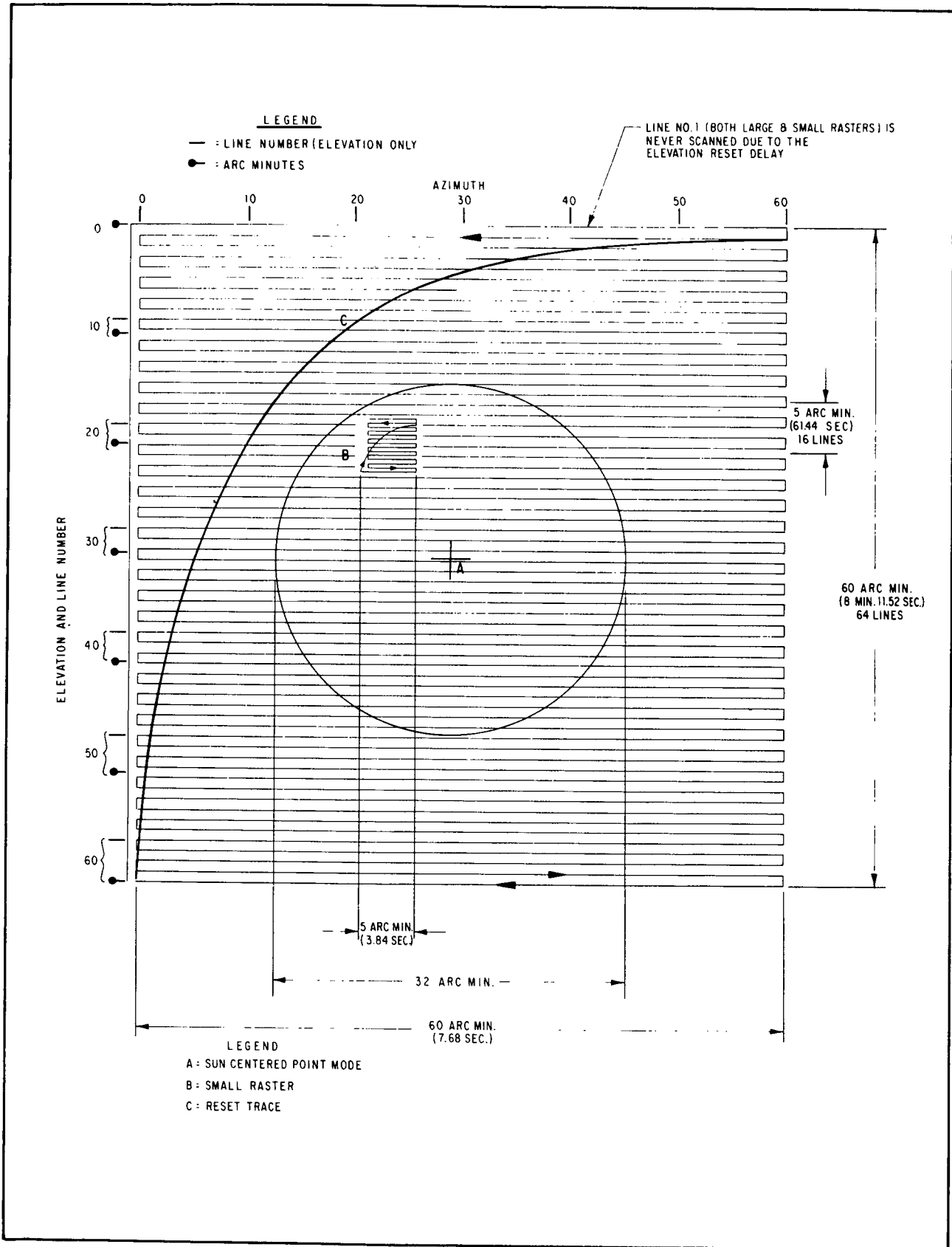


Figure 6-18 Offset-Mode Patterns



F72-01

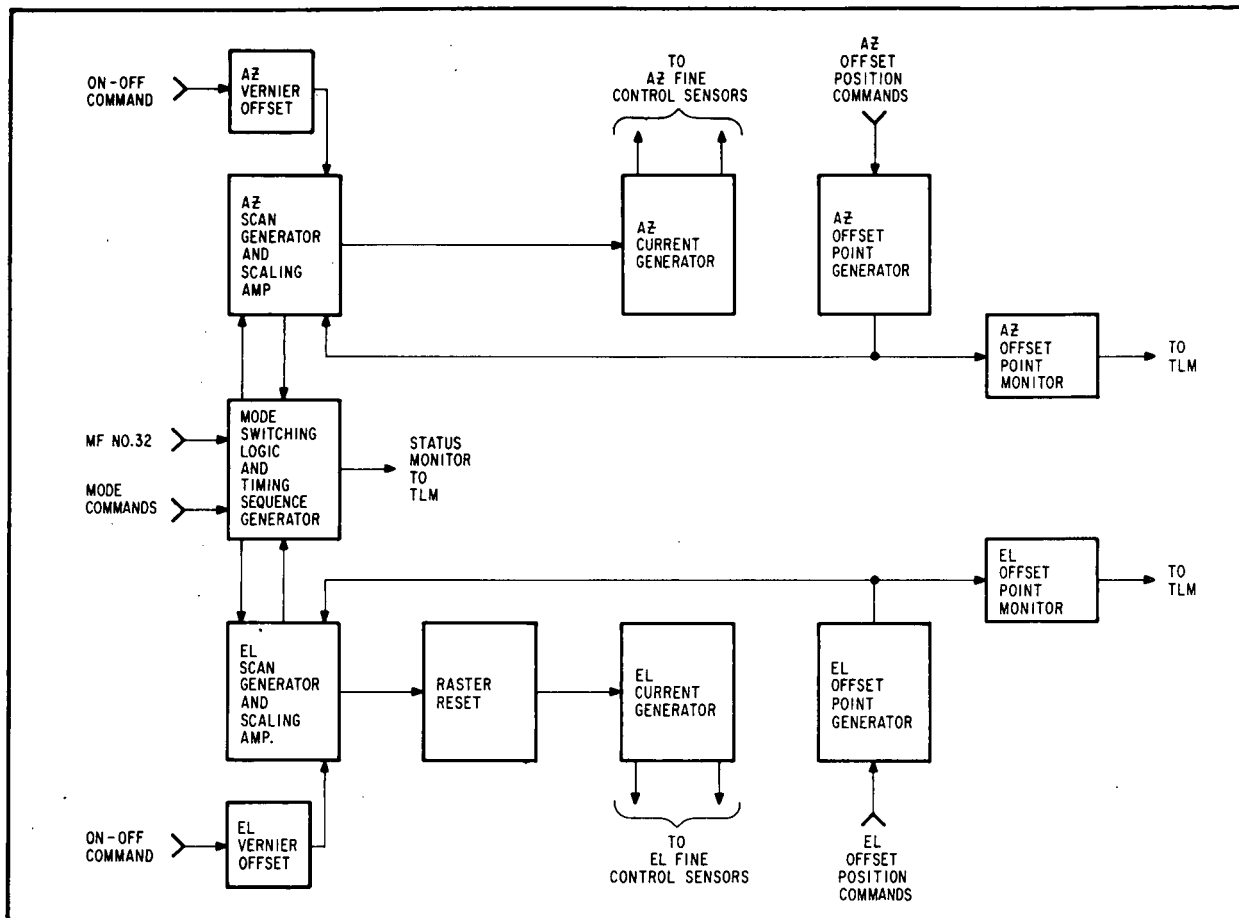


Figure 6-19 Offset Mode Block Diagram

The elevation and azimuth offset-point generators are essentially digital-to-analog converters which generate the discrete voltage levels required to position the pointed instruments within the offset grid pattern. The generator outputs are summed with the scan-generator outputs in the scaling amplifiers.

Two precision +15 vdc regulators and a +7.5 vdc reference regulator provide the regulated voltages for the offset-mode circuits.

Identical elevation and azimuth offset-point monitor circuits convert the offset-point generator outputs (3.5 to 11.5 vdc) to 0 to 5 vdc for use as telemetry signals to indicate the commanded offset position.

The raster reset circuit provides an exponential reset of the pointed instruments in the elevation axis to avoid a mechanical transient which could cause nutation of the satellite. The entire period of the first line of the new raster is devoted to resetting of the elevation axis, as shown in Figure 6-18.



F72-01

Raster Position Monitors. A sensor block, containing two fine-eye pairs similar to the fine-control eyes and the pointing position monitors, is mounted to the front of the left-hand pointed instrument. Eye and preamp gains are adjusted to provide an accurate readout of azimuth and elevation position over the range provided by the offset modes. The actual range of the sensors is  $\pm 35$  arc minutes from the sun-centered-point position. The raster position monitors appear in Words 3, 15, 25, and 39 (E1) and 7, 11, 33, 37, and 41 (Az) of the sail analog subframe.

Offset Circuit Packaging. The offset-point and scan circuits are packaged on four printed circuit boards. Three of the boards are in the power amplifier assembly and one is in the servo amplifier assembly. The board titles and circuit arrangements are as follows:

Power Amplifier Assembly:

- Line Sync Generator - mode switching logic, timing sequence generator, offset status monitor, and SOR and SOL monostables
- Scan Signal Generator - elevation and azimuth scan signal generators and scaling amplifiers
- Auto Pitch and Scan Current Generator - azimuth and elevation scan current generators

Servo Assembly:

- Offset-Point Generator - azimuth and elevation offset-point generators

The offset-point monitors are packaged in a small assembly mounted on the side of the servo amplifier assembly.

Provisions for many different scan and offset point options have been included in the design of the circuit boards. These options can usually be realized by the addition or removal of jumper wires.

6.6.5 Night-Pointing (Gyro) Control

An inertial reference unit was added to OSO-7 so that the azimuth position of the sail could be controlled during the night portion of the orbit. This night-pointing mode provides some of the rotating instruments with an inertial reference-pulse when collecting their data. When the gyro signal is used to prevent sail rotation at night, a night-time inertial reference-pulse is generated by the azimuth blipper.

In addition, the gyro provides a second means for controlling sail position. It can be used to move the sail, during either night or day, to positions other than the solar orientation, and to hold the sail at such positions. This permits the use of the pneumatic pitch control to make "fast reaction" roll maneuvers, if desired. It also provides a somewhat effective backup pointing control in the event of a failure of the primary solar-oriented pointing control.



F72-01

During the day portion of the orbit, the gyro null is driven to the sun's direction, thus establishing the reference for night-time pointing. This process is referred to as "electronic caging". At night, when the sun becomes occulted, the gyro is "uncaged" and its output is switched into the pointing control servo in place of the signal from the solar sensors. This switching takes place at the input to the pulse-width modulator (PWM).

Gyro caging is actuated by a level detector which senses the output of the target intensity monitor. The gyro is caged when the intensity is greater than 85 percent of mean solar intensity, and is uncaged at other times. Switching in and out of the gyro mode is controlled by the presence or absence of day power, or by external command.

#### 6.6.5.1 Night-Pointing Control Hardware

The night-pointing control consists of two separate assemblies: the orbiting inertial reference unit (OIRU); and an additional circuit package, often called "gyro electronics".

OIRU. The OIRU is manufactured by the Bendix Navigation and Control Corporation. It contains the rate-integrating gyro and nine boards of electronic components, all packaged in a single assembly. Figure 6-20 is a cut-away drawing of the assembly. The OIRU weighs about 7 pounds. It uses about 14 watts of power from the 19-volt supply, not including the heater which uses a maximum of 5 watts.

The gyro used for the OIRU is a model 25IRIG and is identical to those produced by Bendix for the Poseidon missile program. It has the following performance characteristics:

- An angular momentum of 430,000 gram-centimeters<sup>2</sup> per second
- A damping constant at 135°F of  $1.14 \times 10^6$  dyne-centimeters per radian per second
- A float inertia of 720.1 gram-centimeters<sup>2</sup>
- A signal generator scale factor of 31.7 volts per radian
- An elastic restraint constant of 0.1 dyne-centimeters per milliradian.

When this gyro is combined with the electronic control circuits to make up the total OIRU the overall performance specifications are:

- Gyro drift rate less than 0.1° per hour at null and 0.35° per hour at a 50-millivolt (1.5 arc-minute) offset.
- An output signal of 2 volts per degree (±10%)
- Input power 13.4 watts (non-slewing) and 14.7 watts (at maximum slew rate)
- Input angle ±1.5°



F72-01

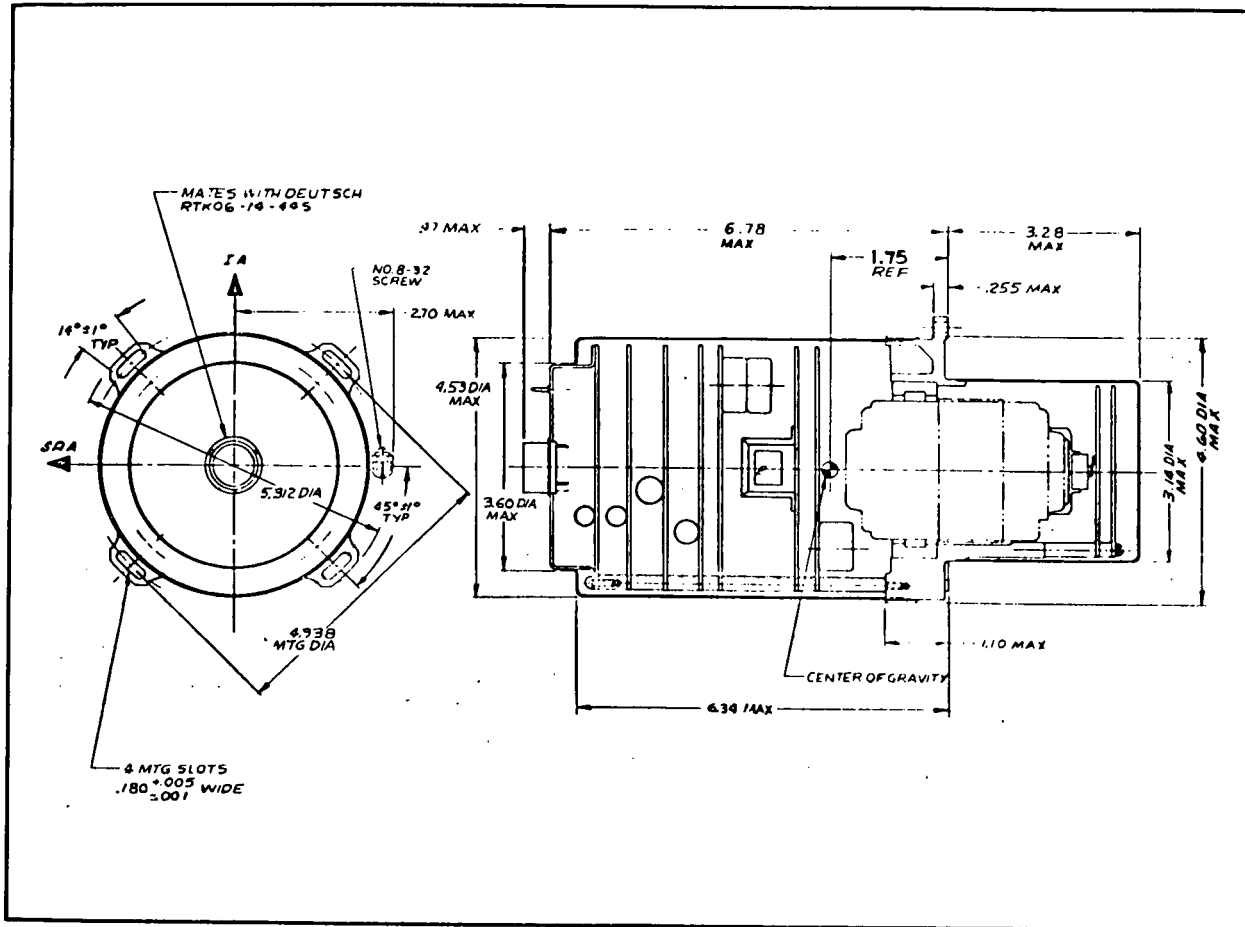


Figure 6-20 OIRU Configuration and Dimensions

- Torque rates: High rate =  $\pm 1/3$  of a degree per second; Low rate =  $0.1^\circ$  per hour per increment

The functions of the electronic circuits in the OIRU are:

- Generation of ac and dc voltages required for operation of the gyro and its circuits
- Sensing of gyro temperature and control the heater to maintain the gyro at a specific temperature
- Conversion of the ac gyro output to a dc error signal
- Generation of the proper ac torquing signals for input into the gyro torquer
- Providing the amplifiers and switches necessary to cage the gyro upon command



F72-01

- In-orbit compensation of the gyro drift by conversion of commanded low-torque-rate bits into analog signals for input into the gyro torquer

External Circuits Package. The external circuits package contains the additional circuits required for control of the night-pointing control. This package consists of three printed wiring boards inside an aluminum box (not illustrated). The circuits in this box are:

- The error-signal amplifier and compensation network that form the link between the OIRU output and the pulse-width modulator (PWM)
- The 15-volt and 7.5-volt regulators that supply power to the gyro control circuits
- A level detector and switching logic that actuate the caging function
- A relay register that stores the in-orbit-compensation digital word
- The relays that store the gyro operational and torquing modes and perform the required switching.

The external circuits package weighs about 1.6 pounds and draws about 30 milliamperes from the 19-volt supply.

#### 6.6.6.2 Gyro Operating Modes

Normal Mode. In this mode the gyro is caged during the day. This caging is actuated when the output from the target eye intensity monitor indicates that the solar intensity is above 85 percent of the mean. If the spacecraft is in the sun-centered point mode, the gyro stores this reference position. If the sail is either in the scan or offset-point mode, a compensating signal may be fed into the gyro caging loop. This compensating signal shifts the null in the opposite direction to compensate for the offset position of the sail, so that the gyro reference position remains solar oriented regardless of the daytime pointing-control mode.

As OSO approaches dusk, solar intensity falls off. When it reaches about 85 percent (which amounts to a pointing error of about 6 arc minutes due to solar refraction) the gyro is uncaged. From this time on, if the sail moves due to the refraction of the sun's rays through the earth's atmosphere, the gyro will hold the "true" solar orientation.

When the sun intensity has fallen sufficiently to cause switching to the night mode, day power goes off and azimuth control of the sail switches to the gyro output. The gyro remains in control throughout the night, holding the sail stable except for the slight gyro drift. At dawn, when the day power comes back on, the gyro is removed from control of the sail. When target intensity reaches 85 percent again, the gyro is recaged for a repeat of the cycle.

The gyro pointing control may have a maximum pointing error of 24 arc minutes over a single orbit.



F72-01

Gyro Backup Mode. The gyro pointing control can be put in a backup mode by ground command. In this mode, the gyro is uncaged, regardless of sun intensity, and always controls the azimuth position of the sail. The position of the sail will be held wherever the gyro was when the command was received.

This mode can be used to keep the pointed instruments relatively well solar oriented in case of failure in the primary solar-pointing control. Of course, in this mode the gyro drift makes it necessary to periodically reorient the sail to keep it towards the sun.

Another use for the backup mode is to allow the sail to be pointed away from the sun during the day (as for torquing the sail 90 degrees and using the pneumatic pitch control for roll maneuvers).

High-Torque Mode. On a command from the ground, the gyro system can be placed in a mode in which it rotates the sail either left or right at 1/3 degree per second. This is done by torquing the gyro. The procedure is to send a command (SL-12) to start the movement and another command (SL-13) to stop the movement. The angle of rotation is determined by the time between the start and stop commands. In addition, the gyro control moves the sail 0.05 degree in the selected direction each time the SL-13 command is received.

Low-Torque Mode. The low-torque mode provides a means for trimming out gyro drift while in orbit. A ground-based operator commands an appropriate 5-bit word into storage relays in the gyro control circuits. This word is converted to an analog signal in the gyro circuits, and fed into the gyro torque generator to compensate for drift.

The compensation range is  $\pm 1.5$  degrees per hour in increments of 0.1 degree. Once a new torque-rate command word is set and stored in the spacecraft, the gyro is torqued at the selected rate whenever it is uncaged. The compensating torque is enabled by command SL-14, and disabled by command SL-04.

#### 6.6.5.3 Gyro Circuits

A functional diagram of the entire night-pointing control is presented in Figure 6-21. The circuits to the left of the dotted line are those which are peculiar to the night-pointing control. Those to the right are common to the gyro and sun-sensor pointing modes. All components marked with an asterisk (\*) are located in the separate gyro-circuits assembly. Those unmarked components to the left of the line are located in the OIRU assembly.

Power Circuits. The gyro power circuits are shown in the upper-left corner of Figure 6-21. The gyro circuits are turned on by means of a ground-commanded latching relay (K1). This relay applies power to both the OIRU and the separate circuits package.

In the circuits package, the 19-volt power is reduced to 15 volts by a 15-volt regulator. This regulator is followed by a resistor divider and operational amplifier with a buffered output stage which generates a precise 7.5-volt signal reference. In the gyro circuits, only the relays are powered by raw 19 volts. All other circuits are powered by a 15-volt regulator.





F72-01

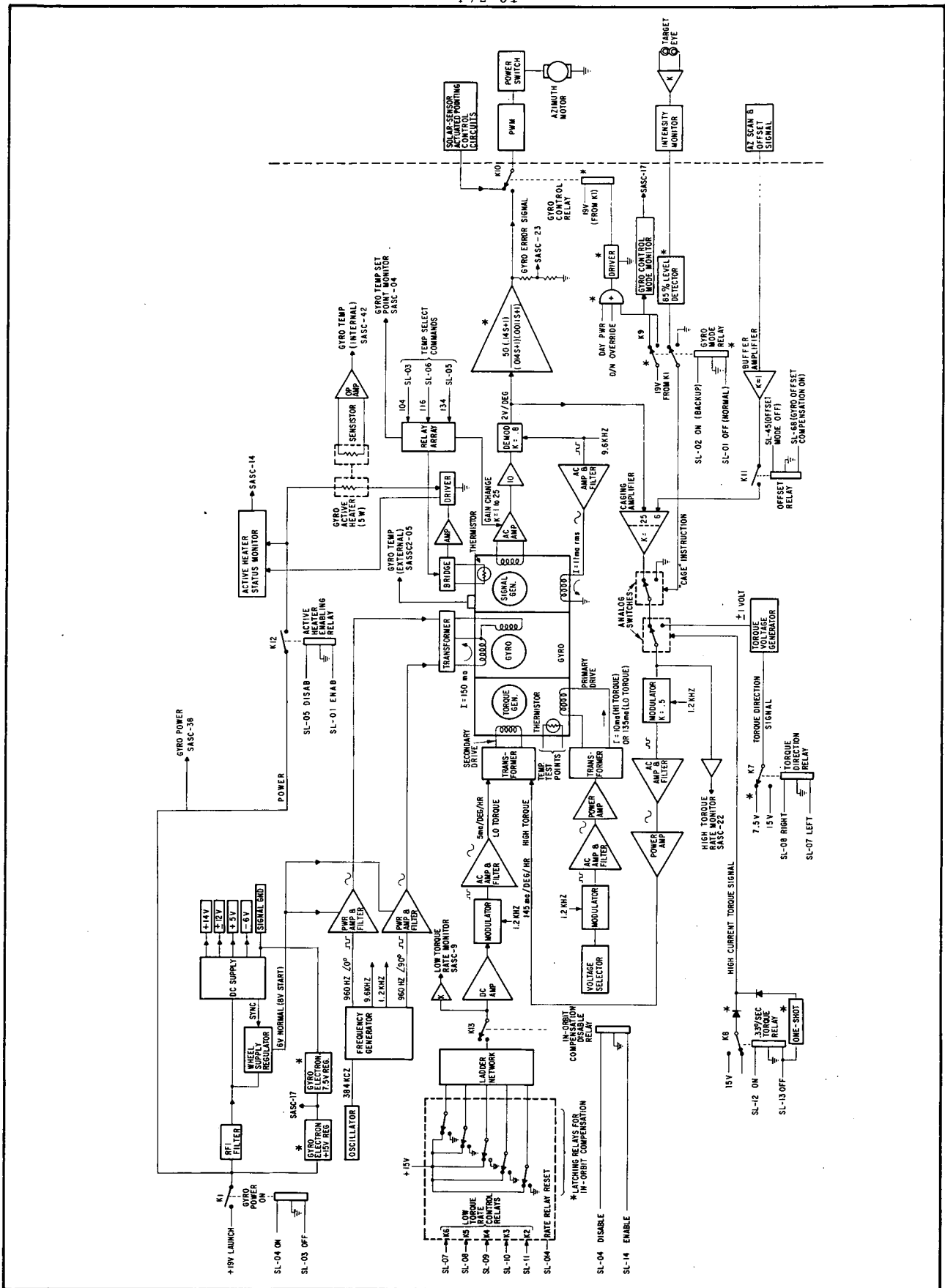


Figure 6-21 Night-Pointing Control Functional Diagram



F72-01

In the OIRU, the 19 volts first goes through a high-frequency RFI noise filter and then a low-frequency filter. This latter filter prevents the high current requirements of the OIRU power supplies from causing excessive noise on the spacecraft power bus.

The 19 volts in the OIRU is used by two power supplies -- a dc supply and a gyro supply. The dc supply consists of a switching pre-regulator, which generates a regulated 14-volt dc, followed by a free-running converter which generates filtered voltages of  $\pm 12$ , +5 and -6 vdc. The free-running converter operates at about 20 kHz. The gyro supply consists of a switching pre-regulator that generates two regulated voltages - one is about 6 volts for normal gyro operation and the other is about 8 volts for the high-torque starting requirement of the gyro. The switching from starting to normal voltage is controlled by a 20-second time delay. Both the pre-regulator in the dc supply and the ac gyro supply are synchronized with the 20 kHz frequency of the converter in the dc supply.

The output of the 7.5-volt regulator is tied to the signal ground return line of the dc supply in the OIRU. This is necessary because of the conversions between the PWM power reference and the OIRU signal reference. In addition, the signal ground and the power ground in the OIRU are well isolated.

Frequency Generation. The OIRU requires several different frequencies for its operation. All derive these frequencies from a single crystal-controlled oscillator, consisting of a McCoy 384-kHz crystal and a  $\mu$ A-710 integrated circuit. The 384-kHz signal from this oscillator is counted down by a series of flip-flops to produce the following frequencies: 9.6 kHz for the signal generator, 1.2 kHz for the torque generator, 960 Hz ( $0^\circ$  and  $90^\circ$ ) for the two-phase gyro motor. The frequency-generator block in Figure 6-21 performs this count-down and, in addition, switches these frequencies to the proper components according to mode.

Gyro Motor Drive. Each phase of the two-phase gyro motor is driven by a two-stage transformer-coupled power amplifier. The power amplifier is supplied by the 6-volt/8-volt regulated voltage from the wheel supply. It amplifies the 960 Hz ( $0^\circ$  and  $90^\circ$ ) square waves to drive the gyro rotor at 24,000 RPM. About 5 to 6 watts of the total power consumed in the OIRU is used in these circuits.

Signal Generation. The output error signal of the gyro is a function of the angular rotation of the signal generator attached to the gyro float. The excitation for this signal generator is a 9.6 kHz sine wave, which is developed from the 9.6 kHz square wave by an ac amplifier and filter assembly.

The output of the signal generator is an ac signal with an amplitude of about 2.7 volts per degree of input rotation at a gyro temperature of 134 degrees F. The scale factor varies greatly with temperature so that at the lowest expected operating temperature, 104 degrees F, the scale factor is about 0.034 volts per degree.

This ac signal is amplified by the ac amplifier with a gain between 1 and 25. The gain is selected by the temperature-control circuit. This stage is followed by an ac amplifier with a gain of 10. The signal is then demodulated by the same 9.6 kHz square wave used to excite the signal generator.



F72-01

This processing results in a signal that has a scale factor of 2 volts per degree when the gyro is at any of its three temperature-select points (104, 116, and 134 degrees F).

The gain selection is performed by latching relays located in the OIRU that also select the control temperature.

The output of the demodulator is further amplified by a combination operational amplifier and non-saturable rate network. The output of this amplifier then goes through the gyro mode transfer relay (when the gyro is in control) and is fed into the azimuth pulse-width modulator.

Gyro Torquing. The gyro torque generator is similar to the signal generator. It requires an excitation on the primary winding and torque is generated by applying an in-phase current on the secondary winding. The operating frequency of the torque generator is 1.2 kHz.

The primary excitation current has two values, depending upon the mode selected. In the low torque mode, when only the in-orbit compensation, or low torque, is applied, the excitation is about 10 ma. In the high-torque mode, the excitation is increased to 135 ma. Primary excitation is selected by a voltage selector which applies a different voltage (for each mode) to the modulator. The voltage square wave output of the modulator is amplified and filtered to produce a sine-wave signal. The sine wave is further amplified by a power amplifier before being applied, through a transformer, to the primary of the torque generator.

The reason for the two levels of current is the large difference in the two torquing rates. The high-torque requirement is 1/3 degree per second while the low-torque requirement is 1/10 degree per hour.

The secondary drive of the torque generator is also supplied through a transformer. This transformer has two input windings, a high-sensitivity and a low-sensitivity winding. The low-sensitivity winding is used for the in-orbit compensation and the high sensitivity winding is used for the high-torque rate and caging.

A series of five latching relays are, by ground command, thrown into the proper state to represent the "ones" and "zeros" of the desired drift-compensation word. This word (which has 15-volt and 0-volt levels) is sent to a ladder network (digital-to-analog converter), the output of which is an analog voltage proportional to the binary value of the commanded word. This voltage is amplified by a dc amplifier and modulated at the 1.2 kHz torque-generator frequency. It is then further amplified and converted to a sine wave before being applied to the torque-generator transformer. The sensitivity at this point is about 1 degree per hour per milliampere. The high-torque transformer winding is driven by a power amplifier and an ac amplifier and filter similar to that used elsewhere in the gyro circuits.

Upon ground command, a latching relay in the gyro circuits package stores the desired high-torquing direction: left or right. This relay controls the polarity of the output from the torque-voltage generator. The output is then gated into the torque generator by the high-torque-on command, or the high-torque-off command (0.05-degree increment). This secondary



F72-01

excitation of the torque generator is conditioned on its way to the generator by modulator, an ac amplifier and filter, and a power amplifier. The square-wave output of these circuits torques the gyro in the desired direction at 1/3 degree per second.

When the "High-Torque Off" (SL-13) command is received, the 43-degree-per-second torquing stops. This command, however, also triggers a one-shot multivibrator which issues a 150-millisecond pulse, causing an additional torquing of 0.05 degree. Further 0.05-degree increments may be executed by repeating the SL-13 command.

Caging Circuits. The output of the gyro, (the 2-volt-per-degree signal) is applied at all times to a caging amplifier with a gain of about 25. Here it is summed with an offset compensation signal which has a scale factor of 8 volts per degree. The compensation-signal channel of the cage amplifier has a gain of about 6.25. Thus, the scale factor of the amplifier output is the same for both inputs in terms of degrees ( $2 \times 25 = 8 \times 6.25$ ). Since the actual output of the scan generator is not exactly 8 volts per degree, a buffer amplifier (located in the gyro electronics) is used to scale up the scan-generator output to produce the proper 8-volt-per-degree output.

The output of the caging amplifier is applied through an analog switch (FET) to the input of the high-torque modulator. Thus, the output of the gyro signal generator, when in the "caging" mode, applies the high-torque signal to the torquer to null the gyro output signal. With the gyro mode relay in the "normal" position, as shown in Figure 6-21, the caging signal is switched on and off by the target-intensity level detector. When intensity is greater than 85 percent, a 15-volt signal from the detector gates the caging signal into the high-torque circuits. When intensity falls below 85 percent, the detector output (zero volts) removes the output of the caging amplifier from the high-torque circuits.

When the gyro mode relay is in the "backup" position, the gyro is always uncaged, regardless of target intensity. In this mode, the output of the caging amplifier never reaches the high-torque circuits.

Gyro Control Switching. The gyro control relay, in the gyro circuits package, switches the gyro error signal into the pulse-width monitor, as shown in Figure 6-21. The power for this relay is only available when the gyro is on, so that with the gyro off, the PWM is always connected to the solar-sensor-actuated error signals. The circuit is designed so that a failure in the relay or its drive circuit causes the relay to de-energize, putting the azimuth servo in its solar-pointing mode. This feature was incorporated so that the addition of the gyro would not compromise the reliability of OSO-7's solar-pointing control.

The gyro control relay driver can be actuated by any of three conditions:

- When the day-power bus voltage drops to zero volt (night condition)
- When the day-night-bypass-open signal is absent (when D-N Byp is closed)
- When the gyro backup mode is selected



F72-01

Any of these conditions, when gyro power is on, puts the gyro in control of azimuth pointing.

Temperature Control. The sensor for temperature control is a thermistor located in the floatation fluid inside the gyro. This thermistor forms one leg of a bridge circuit, the output of which is amplified by an operational amplifier and used to drive the 5-watt gyro heater. The heater is wrapped around the outside of the gyro.

The three control temperatures are selected by switching shunt resistors across the thermistor, thereby changing the bridge null point. This switching is done by relays that are controlled by ground command. These relays also control the gain of the signal-generator ac amplifier so that, regardless of the temperature selected, the nominal scale of the OIRU output is 2 volts per degree.

There are three temperature monitors associated with the OIRU. The first is located within the heater blanket wrapped around the gyro. Its output, telemetered in SASC-42, is generally called, "gyro internal temperature". The second monitor is located on the outside of the gyro case. Telemetered in SASSC2-05, its output is called "gyro external temperature". The third monitor is located at the opposite end of the gyro in the gyro fluid and its leads are brought out through the OIRU connector. This monitor is used during preflight testing of the OIRU but not used in orbit.

Survival Heater. In the early stages of OIRU design, it appeared that the gyro might be damaged by low temperatures which could be reached in orbit. A survival heater was therefore incorporated into the gyro hardware, to keep the gyro temperature above the danger point regardless of OSO's operating mode. Subsequent analysis, after the hardware was developed, showed that no such danger of damage existed. The gyro was therefore flown without electrical connection to the survival heater.

#### 6.6.5.4 Operating Considerations

The most significant operating constraints on the night-pointing control are the effect of temperature changes on the gyro gain, which require that the correct temperature control points are commanded; and proper use of the day-night bypass and torquing modes. The temperature constraint is particularly important, and merits some detailed explanation.

Temperature Effect on Gyro Operation. The OIRU, containing the gyro, is mounted on the sail with the gyro input axis parallel to the spacecraft spin axis, as shown in Figure 6-22. The output of the gyro operates through the azimuth servo, to oppose rotation of the sail. Rotation of the sail about the gyro input axis applies a torque to the gyro floated assembly about the output axis. This torque is equal to the product of the input rate ( $\omega$ ) and the rotor angular momentum ( $H$ ). It acts to drive the rotor momentum vector toward the input vector ( $\omega$ ).



F72-01

Rotation of the floated assembly is opposed by the viscosity of the fluid in which it is immersed. The resulting drag produces an opposing torque equal to the product of the fluid damping constant (B) and the rotation rate of the floated assembly about the output axis ( $\dot{\zeta}$ ). A balance is obtained when:

$$\dot{\zeta} B = \omega H$$

Which can be rewritten as:

$$\zeta = \frac{H}{B} \int \omega dt$$

i.e., the gyro float rotation is proportional to the integral of the sail rate; and thus the name, rate integrating gyro. The term H/B is the gyro gain.

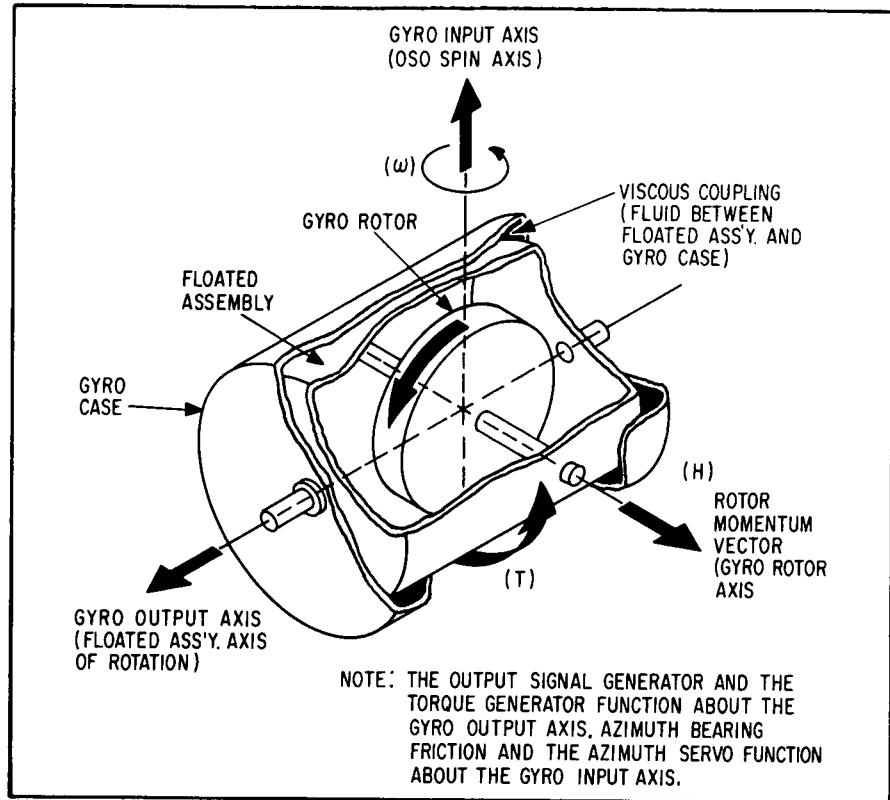


Figure 6-22 Rate-Integrating Gyro

This brings us to the crux of the temperature problem. In the gain figure H/B, the angular momentum (H) is constant. It is a function of gyro rotor moment of inertia and speed of rotation. The viscosity, or damping term (B), however, varies by a factor of two for a temperature change of 11°F. Thus, to keep gyro gain constant, gyro fluid temperature must be kept constant.

Gain change also adversely affects raster and offset mode compensation. The gains of the caging amplifier are selected so that the gyro output and offset compensation amplifier signals have equal weight, so that the compensation signal can correct the position of the sail when the system switches to night pointing. Gyro gain variations would introduce substantial night-pointing errors if the sail was not at the zero position when the night condition occurred.

Ideally, the gyro should be kept at a constant temperature, which would mean heating it above the highest anticipated temperature. This would require a heater that could raise the gyro temperature by as much as 50°F and the power requirement for such a heater is prohibitive.



F72-01

To keep gyro gain constant under varying orbit conditions with reasonable heater power, the gain of the gyro output amplifier is adjusted to compensate for temperature within the expected gyro temperature range (83 to 104 degrees F). Three temperature control points (104, 116 and 134°F) were chosen. Thus the heater need only bring the gyro temperature up to a control point. The ground commands which select these control points also adjust the gain of the gyro output ac amplifier, so that overall gyro gain is the same at any of these three temperatures.

In orbit, a control temperature must be selected which is next above the unheated operating temperature. If the heater was not working or if it was desirable to leave it off because of a power-budget problem, selecting the control point closest to the average gyro temperature would keep the gyro gain within acceptable limits. In this way, the error introduced by offset compensation would be kept under 0.5 degrees of arc.

Day-Night Bypass Mode. A special operating constraint exists when the day-night bypass relay is commanded closed. In this condition, the system is always in the gyro mode to prevent spin-up of the sail when the day power bus is energized during orbit night. During the day, however, in the gyro "normal" mode, the gyro cages when the target eye senses sun intensity greater than 85%. When the gyro is both caged and in control, the sail drifts rapidly away from null. Eventually the target eye senses sun intensity less than 85 percent; at that point the gyro uncages and pointing is stabilized 3 degrees off null. Thus, when the day-night bypass is closed, and the system is operating in the gyro "normal" mode, the PIA cannot be pointed at the sun.

One could solve this problem by commanding the "gyro backup" mode, wherein the gyro never cages. However, this requires that the sail position be monitored and corrected to ensure that the spacecraft batteries receive sufficient charge from the solar-cell array. Unless the night-pointing mode is specifically required, it is best to turn off the gyro when the Day-Night Bypass is closed. Then the pointing control will operate as it has on previous OSOs (that is, the sail will be solar-oriented during day and will spin at the wheel spin rate at night).

Torquing Modes. The 1/3 degree-per-second torquing is started and stopped by command. If the observatory goes out of range of a control station before the "stop" command is sent, the gyro will continue torquing and the daytime "caging" function will be disabled.

If the gyro is in the "backup" mode when this happens, pointing control will not revert to the solar sensors during orbit day, and the spacecraft batteries will not be recharged by the solar-cell array.

## 6.7 LAUNCH-SEQUENCE CONTROL

The launch-sequence control automatically changes the observatory from the launch configuration to orbit configuration. It performs its control functions at prescribed times and in a particular sequence.



F72-01

A feature of the OSO-7 launch sequence is that the launch vehicle did not spin up the spacecraft before separation. Equipment on the satellite brought it to its normal (solar-oriented) position, even though it was tumbling at separation. The sequence that follows is for a normal launch and separation. Backup procedures also are summarized.

All of the timed functions are controlled by two vehicle events (fairing jettison and payload separation) and by a time-delay relay in the launch-sequence control circuits.

#### 6.7.1 Launch-Sequence Events

The major events that occur during the launch sequence are summarized in the following paragraphs:

Fairing Jettison (T+227 Sec). When the fairing is jettisoned, it pulls a jumpered electrical connector from the wheel, with a lanyard. The sail then begins to spin-up. The final sail spin rate is about 33 rpm.

Spacecraft Separation (T+1996 Sec). Spacecraft separation from the launch vehicle causes the following:

- Day power is applied to the observatory.
- Sail spin-up drive is removed, and the pointing control starts operating in the normal coarse-acquisition mode.
- A 180-second wheel spin-up gas burst starts.

Solar Acquisition, Elevation Frame and Nutation Damper Release (T = ~2030 Sec). The sail completes solar acquisition and the subsequent "on target" signal causes the elevation latch mechanism and the nutation damper cage mechanism to release. These are squib-actuated functions.

Wheel Spin-up Complete (T = ~2176 Sec). The transfer of momentum from the sail to the wheel plus the 180-second wheel spin-up gas burst causes a final wheel spin rate of about 29 rpm.

Experiment Squib Fire (not a timed function). The sail squib batteries furnish electrical power for the NRL and GSFC experiment squibs. The NRL squib causes the occulting disc boom to extend. The GSFC squib unlatches the spectrometer grating. These functions are performed when desired by command from a STADAN station.

#### 6.7.2 Launch Sequence Operation

Liftoff Condition. Figure 6-23 shows the state of all relays and the separation switches when in the "liftoff" condition. Launch power is present at all points indicated on this diagram; day power is not on at liftoff.





F72-01

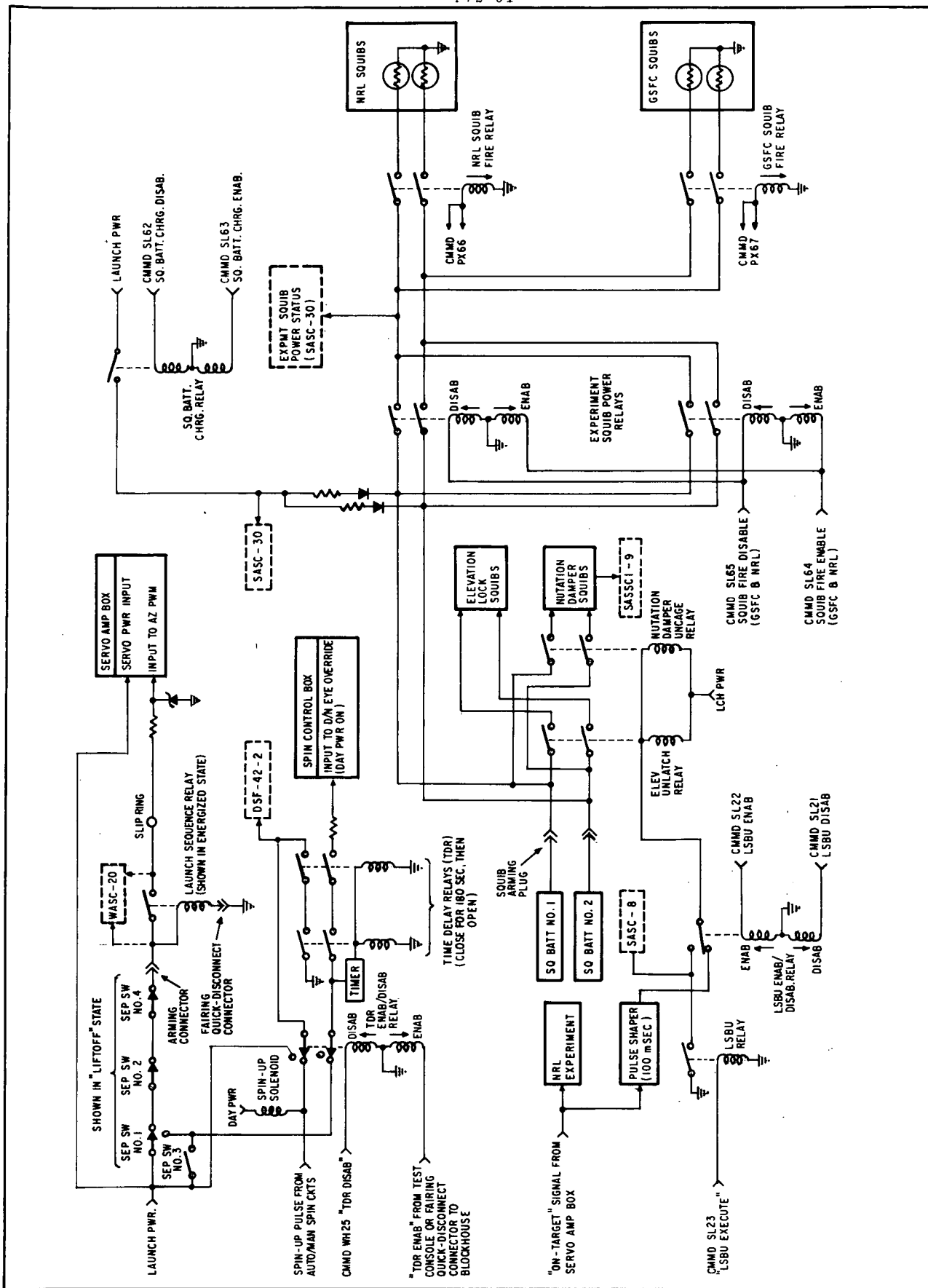


Figure 6-23 Launch Sequence Control Block Diagram



F72-01

The liftoff state is verified on the following telemetry channels:

WASC-20. This channel indicates that separation switches 1, 2, and 4 are in the positions shown in Figure 6-23.

DSF Word 42, Bit 2. This bit reads "0", indicating that the time-delay relay is "enabled".

SASC-8. This channel verifies the "disabled" state of the launch-sequence backup relay.

SASC-30. This channel verifies the "disabled" state of the experiment squib power relays.

Liftoff does not cause any change in these telemetry indications. These conditions exist until the fairing is jettisoned.

Normal Circuit Operation. At fairing jettison (T = 227 seconds), the fairing quick-disconnect connector is pulled, allowing the launch-sequence relay to de-energize (see Figure 6-23). This applies spin-up drive to the azimuth servo. At this time WASC-20 indicates the closure of the launch-sequence relay. The sail continues to spin-up until about 40 rpm is reached, then its spin rate is held constant until separation from the launch vehicle. Unlike earlier OSOs, the OSO-7 pointing control is powered from the launch-power bus, rather than day power. This is due primarily to the addition of the night-time pointing capability.

When the spacecraft is separated from the launch vehicle at T=1996 seconds, several events occur. First, the separation switches all transfer to the positions opposite those shown in Figure 6-23. This removes the drive signal from the servo. WASC-20 indicates this function. Second, when separation switches 1 and 2 operate they supply power to the 180-second time-delay relays. A schematic diagram of the time-delay relay driver is shown in Figure 6-24. When these relays are energized two more events occur:

- The spin-up solenoid is grounded, starting pneumatic spin-up of the wheel.
- Day power is turned on by the day-night override relay in the spin control box.

With day power applied, the pointing control starts solar acquisition by despinning the sail. Sail coarse acquisition is completed at about T=2030 seconds and, after an 8-second delay, the "on-target" signal switches the servo system to the fine pointing mode. The "on-target" signal is also fed through an ac-coupled circuit to a pulse-shaping transistor switch. This switch applies a ground to the nutation-damper squib-firing relay and the elevation-unlatch squib-firing relay. With the elevation latch released, the elevation servo points the pointed instruments at the center of the sun. The nutation damper eliminates any nutation that might be present.



F72-01

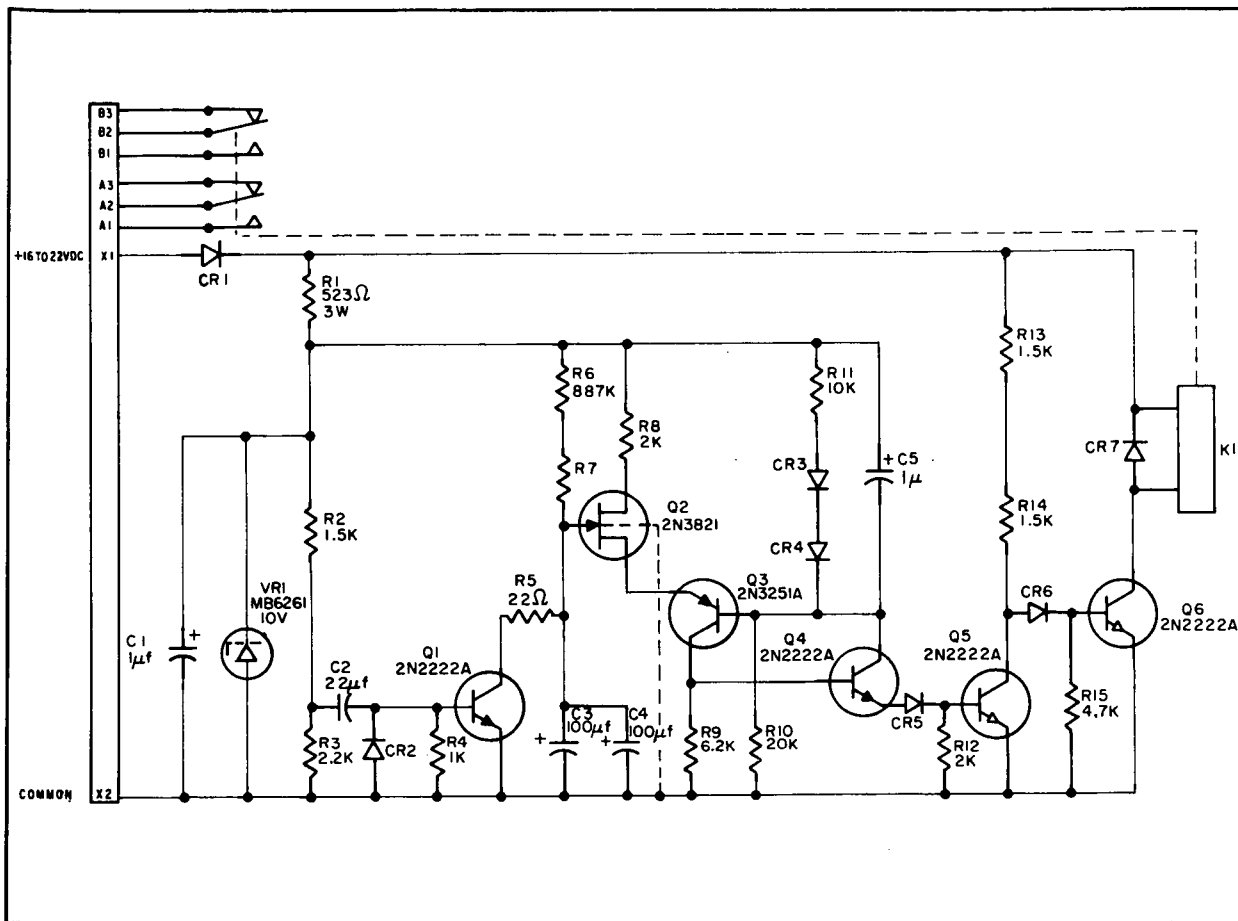


Figure 6-24 Time-Delay Relay Driver

The 180-second time delay relays complete their functions at about  $T = 2176$  seconds. At this time the relay contacts open and the spin-up valve closes. Also, the day-night eye override signal line is de-energized. Now the wheel spin rate is about 29 rpm. The automatic day-power circuits, therefore, operate normally, keeping day power on. (The threshold of this circuit is 20.2 rpm.)

Launch-Sequence Backup. If the normal sequence does not release the elevation unlatch and nutation uncage mechanisms, they are released by command as shown in Figure 6-23. The command-operated launch-sequence backup operates in parallel with the circuits described above.

Experiment Squib Operations. After a proper orbit is verified, the experiment squibs are fired by ground command.



F72-01

Correction of Excessive Pitch Error at Injection. If, for some reason, the injection error puts the wheel plane greater than  $15^\circ$  from the sun, backup operation can be implemented. In this operation, the gyro is used to despun the sail and orient it properly for correcting pitch. The digital aspect sensor provides readings of the pitch angle. By observing pitch angle changes brought about by bursts of pitch gas, an operator can deduce the orientation of the sail and which command (up or down) will bring pitch angle toward zero. The spacecraft is then pitched manually until day power comes on, indicating that the sun is within  $15^\circ$  of the wheel plane. The presence of day power causes the servo control to switch to its coarse-solar acquisition mode, thus pointing the sail at the sun. Further pitch correction is then made either by more manual-pitch commands, or by commanding pitch control to the automatic mode.

## 6.8 NUTATION CONTROL

Because the primary mission of the spacecraft is to provide a stable platform from which the pointed experiments can operate and also to allow the wheel experiments to sweep the celestial sphere uniformly, a nutation damper is used. The principal sources of nutation are:

- Launch sequence operations: separation, initial solar acquisition of the pointed experiments, and initial pitch corrections.
- Normal orbit-morning solar acquisition, due to elevation motor torque during sun acquisition.
- Normal pitch corrections, due to pitch jet activation.

### 6.8.1 Description and Operation

The nutation damper is mounted on the sail. It consists basically of a bob supported by a wire and immersed in a bath of silicone oil (Figure 6-25). This type of damper is passive because it requires no energy input (other than the undesired nutational cross-spin energy).

The damper pendulum is a 0.8-pound spherical bob suspended by a steel wire with a length of 2.98 inches and a diameter of 0.020 inches. The main body of the nutation damper and the bellows contains silicone oil. The bellows accommodates volume changes of the oil due to temperature variations, and maintains the oil under positive pressure.

The bob is caged with the squib-actuated caging plunger which holds it against a caging seat during the test, transportation, and launch phases. The bob is uncaged at about  $T = 2030$  seconds by firing squibs in the latch assembly. The spring forces the caging plunger to the down position and frees the bob. The bob is then able to move in the oil bath with about a 2-degree amplitude.

The nutation damper dissipates cross-spin energy by converting it to heat caused by fluid friction as the bob moves in the oil bath. Nutation damper performance is evaluated by analyzing pitch readout data.



F72-01

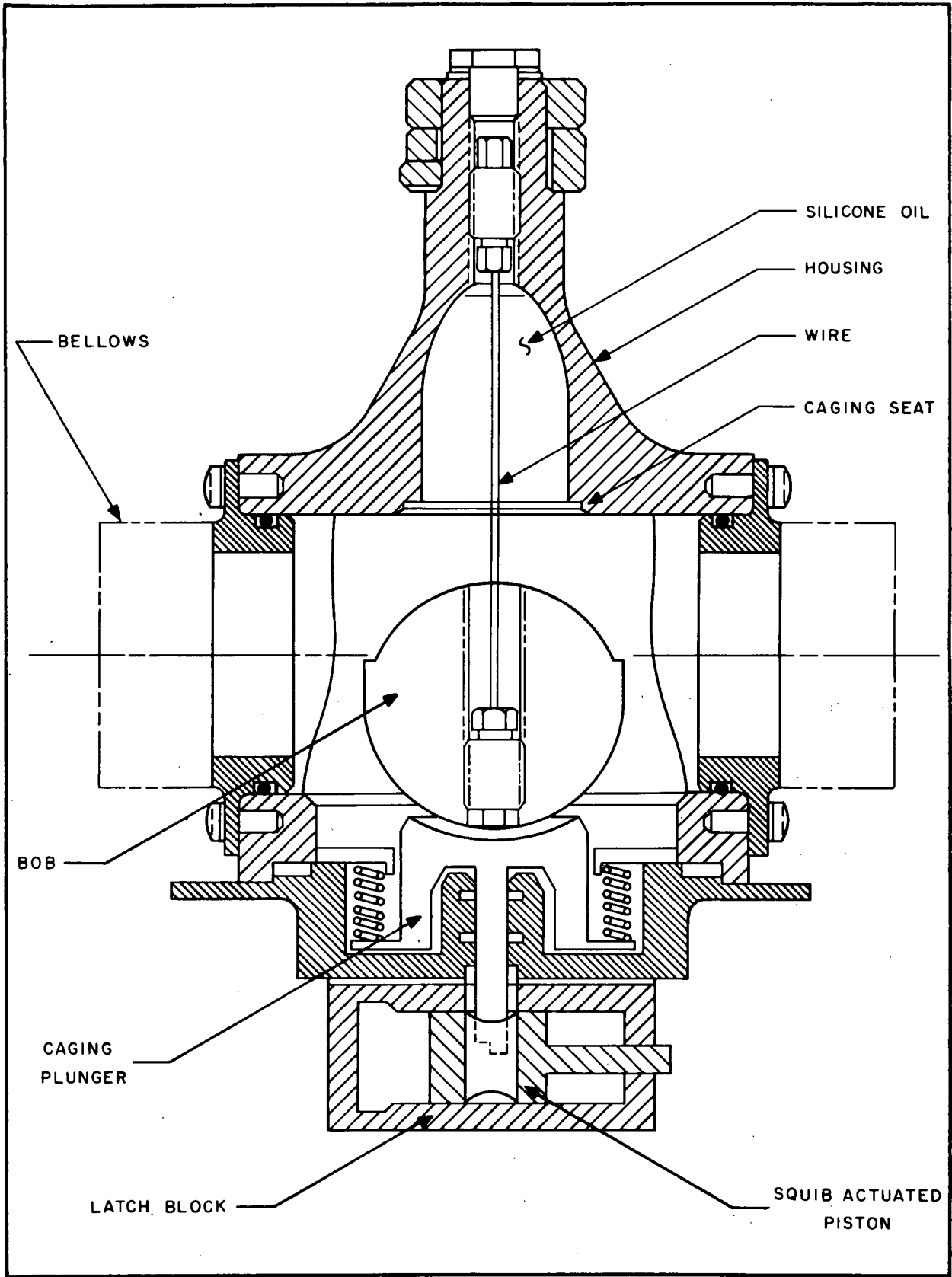


Figure 6-25 Nutation Damper



F72-01

The nutation damper is designed for spin rates from about 0.43 to 0.68 rps, and is most effective near the center of this range.

6.8.2 Design Requirements

General Design Requirements. The general design requirements for the OSO-7 nutation damper were as follows:

- Damping rate: time constant of 1 to 3 minutes for the exponential decay of the nutation amplitude, for initial values of less than 20 minutes of arc.
- Undamped natural frequency: tunable for a moment of inertia ratio from 1.0 to 1.2 and a spin rate of 0.5 rps.
- Maximum anticipated external torque: 1 lb-ft (reaction of the elevation servo motor upon the oriented section of the platform during the initial acquisition of the pointed experiments).
- Minimum allowable residual nutational amplitude: less than 1 arc minute.
- Temperature range: -10 to 50°C

Spacecraft Nutational Frequency. When the observatory is in the oriented condition, the frequency of nutation (P) is given by:

$$P = \frac{I\omega}{\sqrt{I_a I_b}}$$

- where:
- I = Wheel spin moment-of-inertia (MOI)
  - I<sub>a</sub> and I<sub>b</sub> = Principal transverse MOIs
  - ω = Wheel spin rate (rps)

Damper Frequency. The formula for the natural undamped frequency of the nutation damper in a gravity field is as follows:

$$P' = 34.4 \left[ \frac{EI_w \pm 0.405W_e L^2}{WL(L^2 + 2.467\rho^2)} \right]^{1/2}$$

- where:
- P' = natural undamped frequency of damper in gravity field
  - E = modulus of elasticity of the spring wire
  - I<sub>w</sub> = moment of inertia of wire = πd<sub>w</sub><sup>4</sup>/64 for circular wire and d<sub>w</sub> = wire diameter
  - W = weight of pendulum bob
  - W<sub>e</sub> = effective weight of the pendulum bob immersed in the damping fluid (actual weight minus the weight of the displaced fluid)



F72-01

L = length of pendulum arm (wire)

$\rho$  = radius of gyration of pendulum bob about its transverse axis

The double-signed term in the above equation takes into account the effect of mounting the pendulum in either an upright or inverted position in the gravity field; that is, the (+) is for upright and (-) for inverted. In the gravity-free environment of orbital flight, the double-signed term becomes zero and the equation becomes:

$$P'' = 1.745 \left[ \frac{EI_w}{ML(L^2 + 2.467\rho^2)} \right]^{1/2}$$

where:  $P''$  = natural undamped frequency of damper in zero gravity field

M = mass of pendulum bob

Damper Tuning and Effect of Spin Rate Variation. The tuned natural frequency of the damper should be equal to the spacecraft nutation frequency for maximum effectiveness. However, the spin rate and thus the nutation frequency will vary in flight up to 20 percent from nominal. The effectiveness of the damper with changing nutation frequency is shown in Figure 6-26. The worst-case requirement for the damper is to reduce the nutation following a maximum offset step to 0.1 degree in less than 120 seconds. An analysis shows that this requires a time constant of about one minute. This requirement is met for spin rates of 0.5 to 0.56 rps.

The effectiveness of the damper will vary with temperature and other parameters. In general, decreased temperature (i.e., increased viscosity) will increase the damping time constant. Other parameter variations also will cause slight shifts about the nominal curve. Therefore, the nominal tuning frequency was selected off center in order to compensate for the skew of the curves and to produce about equal damping constants at the two extremes of spin rate.



F72-01

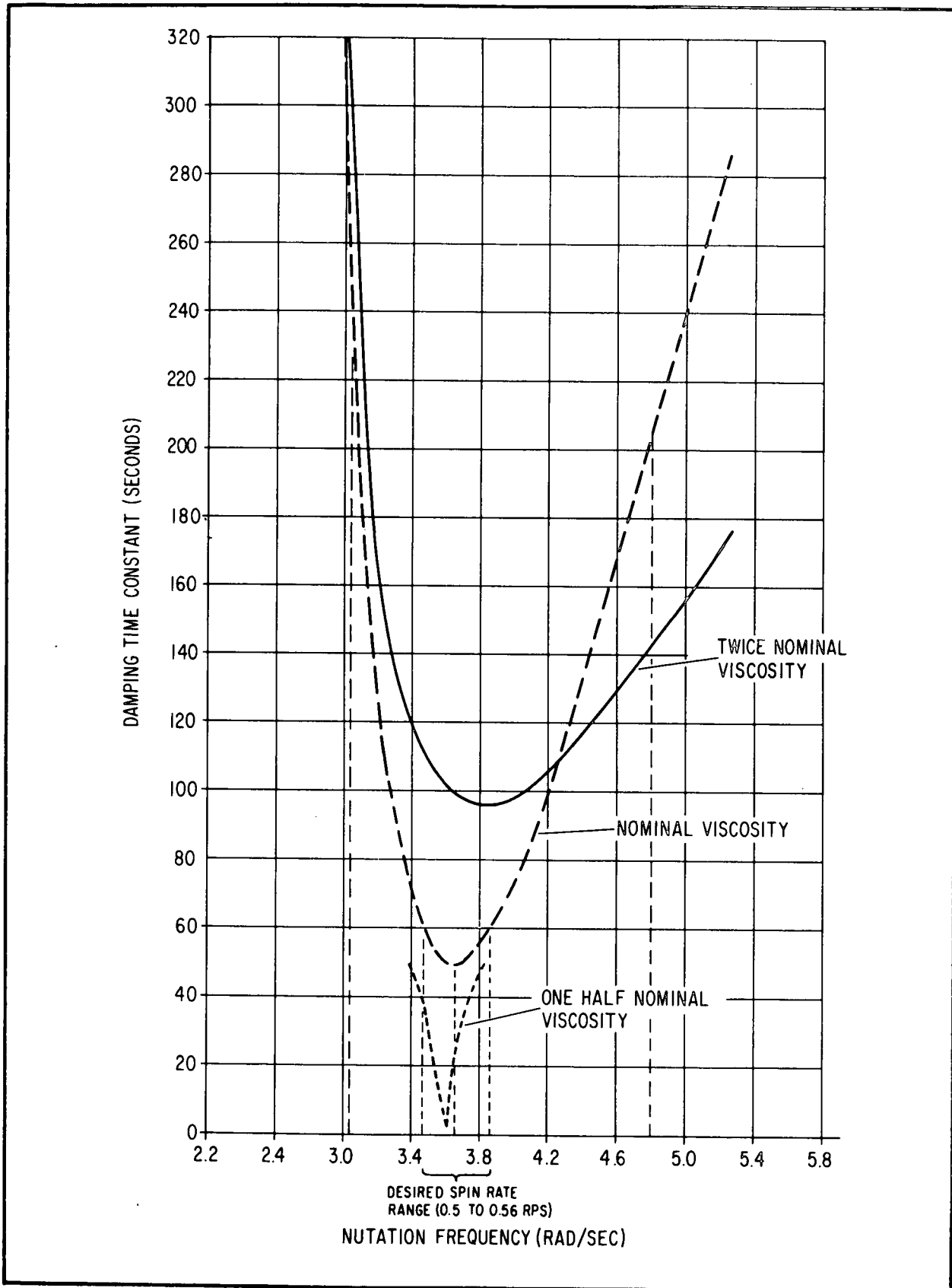


Figure 6-26 Nutation Damper Effectiveness





F72-01

## Section 7 POWER SYSTEM

### 7.1 GENERAL DESCRIPTION

A simplified schematic of the power system is shown in Figure 7-1. Five identical solar array panels with a total area of about 10.3 square feet produce about 97 watts of electrical power during the unocculted portion of the orbit. The array panels are connected through isolation diodes directly to the continuous (battery) bus.

Electrical energy is stored in four strings of cylindrical nickel-cadmium cells, each string consisting of 14 four ampere-hour cells. The charging path of up to two strings of cells may be interrupted by ground command. All of the cell strings are able to deliver current via bypass diodes to the continuous bus, regardless of the position of the command relay. Each string of battery cells is equipped with a cell balance (shorted cell) monitor which indicates the deviation of the potential of the midpoint in the cell string from half of the string terminal voltage.

Solar array and spacecraft currents are monitored by telemetry. Power through the continuous bus is supplied to essential loads such as the command receiver and wheel decoders. The balance of the observatory power passes through the undervoltage relay which protects against unforeseen heavy current drains and discharge of the battery below 16.2 volts. Day and night power is switched by a relay controlled by the spin control electronics, using signals from the spin solar sensors.

Dummy loads are selectable by command to regulate the battery charge rate when observatory loads are less than nominal. The dummy loads draw power only during the day. Any interruption in the launch power (such as an undervoltage condition) allows the dummy-load hold-in relays to open, automatically disconnecting the dummy loads until they are again enabled by command.

Each experiment is controlled by a separate turn-on command relay; the sail experiment power also passes through the sail day-power command relay which provides protection against inadvertent turn-on of the experiments.

Each experiment is equipped with a dummy load. When the experiment is off, the load consumes about the same amount of power as if the experiment were on. The experiment dummy loads can be disabled by ground command.

### 7.2 OBSERVATORY POWER BUDGET

The power budget section is covered in three parts: the solar array output calculations, the observatory loads, and the power margin.



F72-01

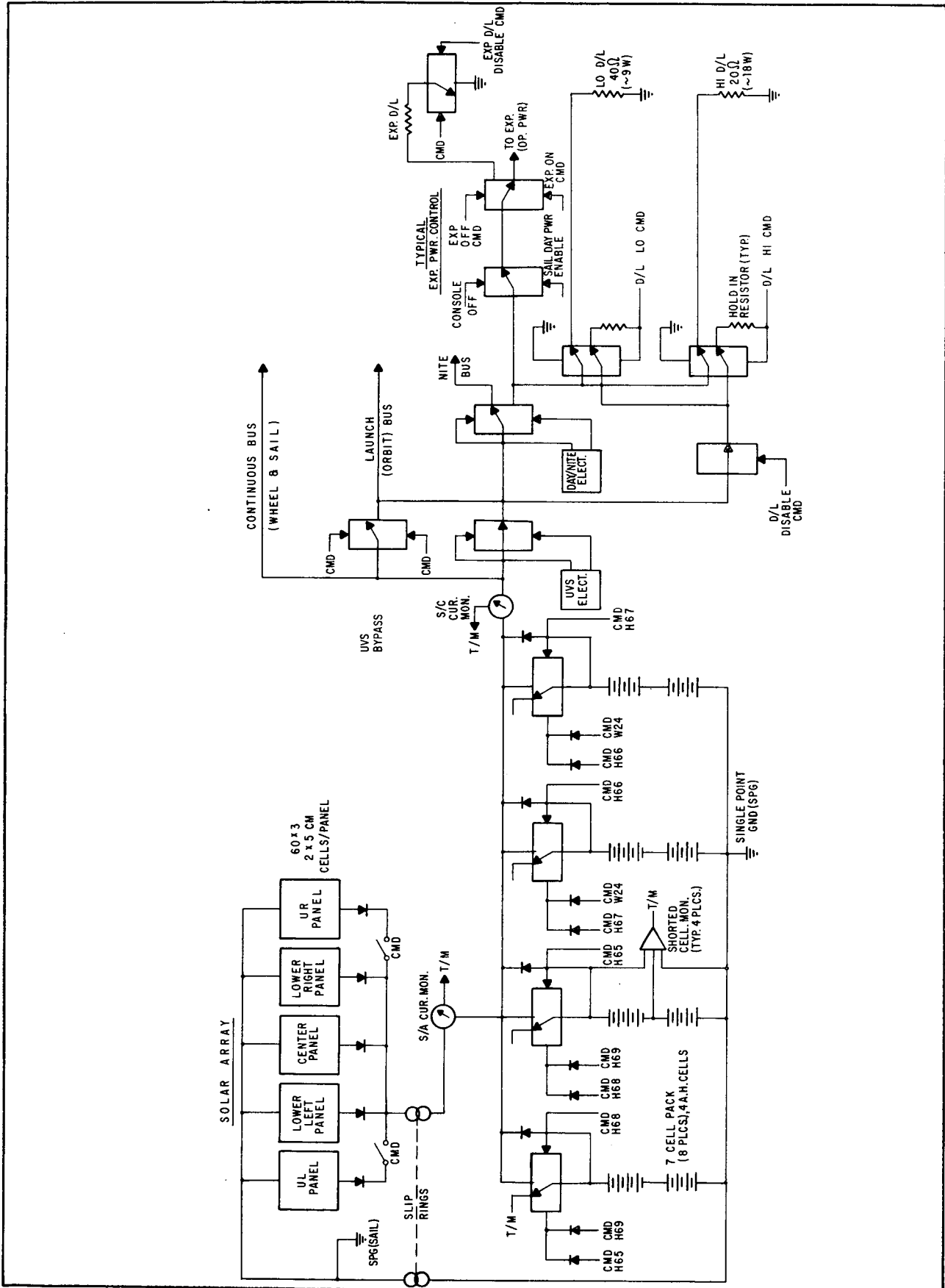


Figure 7-1 Simplified OSO-7 Power System Schematic



F72-01

### 7.2.1 Solar Array Output

Output calculations for the solar array were made two ways:

- The basic calculations were made by a computer simulation program
- The basic calculations were checked by simple two-zone integration of solar array temperatures and the battery charge voltages.

In both sets of calculations, outputs from the actual solar array, measured by Spectrolab Division of Textron Electronics, Sylamar, California, were used. The results from the computer simulation are:

- Nominal sun, 65-minute day = 101.4 watt-hours
- Minimal sun, 61-minute day = 95.5 watt-hours

These calculations include a 1 percent radiation degradation.

### 7.2.2 Observatory Power Loads

The observatory power loads are given in the "load tree" (Figure 7-2) and in a listing of the individual loads with their duty cycles (Table 7-1). The total observatory nominal load is equal to 95.7 watt-hours. All of the load values given in Figure 7-2 and Table 7-1 were calculated at 19 volts.

### 7.2.3 Power Margin

The calculations include allowance for 1 percent measurement error, deducted from Spectrolab's actual recorded data.

For the nominal case with an average sun and an average day, the power margin is about 5.7 watts. Through much of the life of the spacecraft there is excess power and the dummy loads and/or solar array switching will be necessary to prevent battery overcharge.

## 7.3 POWER SOURCE

The OSO-7 power source is a silicon N on P solar cell array. The array consists of five panels that are electrically identical. The panels are fabricated by Spectrolab.

### 7.3.1 Configuration

Each of the five panels consists of three modules of solar cells, as shown in Figure 7-3. Each module is made up of 20 submodules in series. Each submodule consists of three solar cells connected in parallel. Therefore, each panel has 3 x 60 or a total of 180 cells.

Figure 7-3 also shows the panel layout of these modules. The three modules are connected in series, with the return wiring going diagonally across the back to minimize the area of the current loop.



F72-01

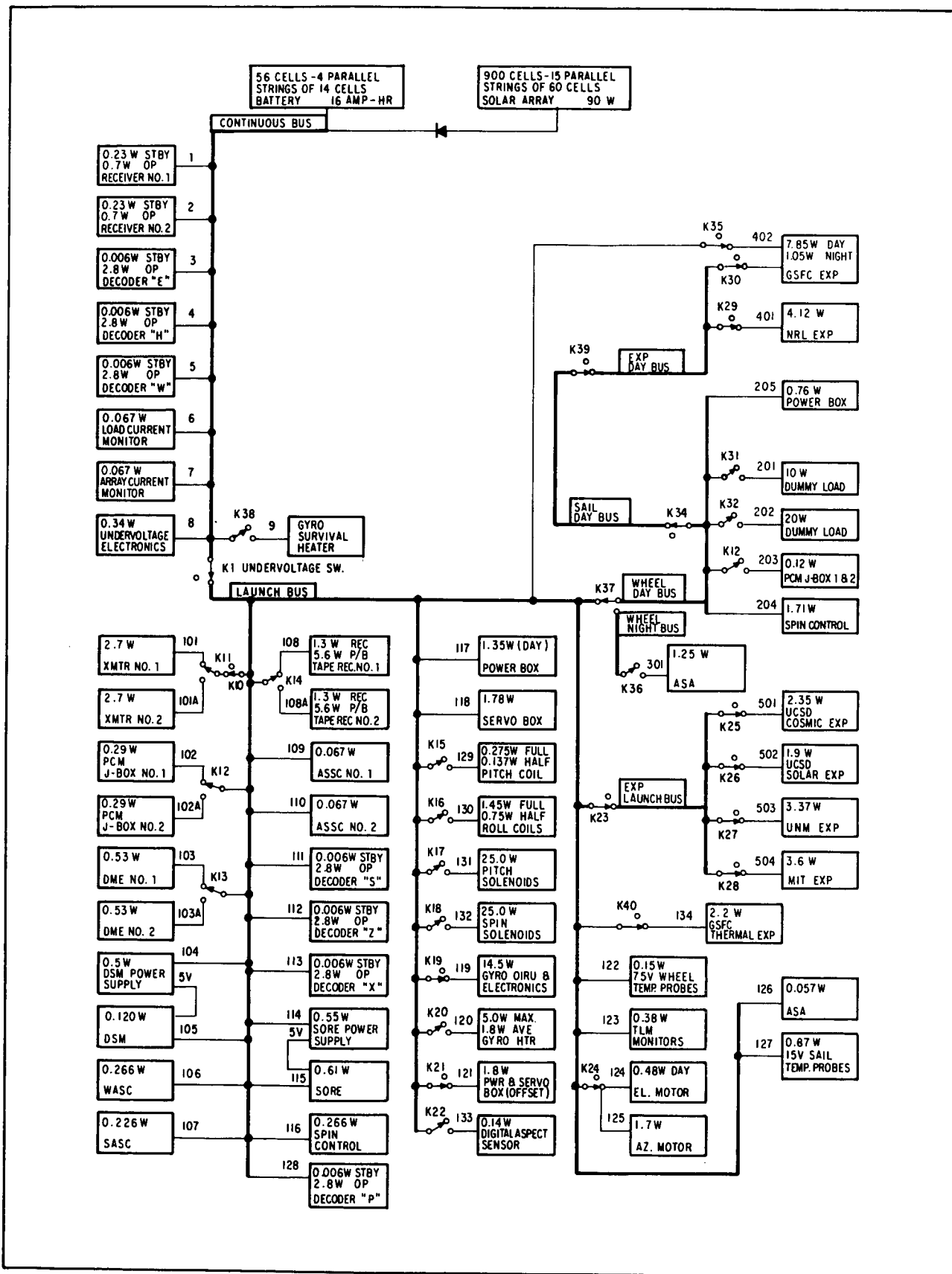


Figure 7-2 OSO-7 Power Load Tree



F72-01

Table 7-1  
OSO-7 POWER LOADS AND DUTY CYCLES

LOAD NO.	FUNCTION	LOAD (MILLIWATTS)	LOAD (MILLIAMPS)			DUTY CYCLE (%)	COMMENTS
			DAY/NIGHT	NIGHT (ONLY)	DAY (ONLY)		
1	Receiver 1	230 Standby 700 Operate	12.1 18.3 36.8 Ave			25	
2	Receiver 2	230 Standby 700 Operate	12.1 18.3 36.8 Ave			25	
3	Decoder "E"	6 Standby 2800 Operate	0.3 147.5			Negligible	
4	Decoder "H"	6 Standby 2800 Operate	0.3 147.5			Negligible	
5	Decoder "W"	6 Standby 2800 Operate	0.3 147.5			Negligible	
6	Load Current Monitor	67	3.5			100	
7	Array Current Monitor	67	3.5			100	
8	Undervoltage Electronics	340	17.9			100	
9	Gyro Survival Heater					0	
SUB-TOTAL	Loads 1-9		62.4 Ave				Use Not Anticipated Current is Averaged Over 1 Orbit
101-101A	VHF Transmitter 10R2	2700	142.0			100	
102-102A	PCM J-Box 10R2	290	15.3			100	
103-103A	DME 1 or 2	530	28.0			100	
104	DSM Power Supply	500	26.3			100	
105	DSM	120	6.3			100	
106	WASC	266	14.0			100	
107	SASC	266	14.0			100	
108-109A	Tape Recorder 1 or 2	1300 Record 5600 Playback	70.0 290.0	48.3 (Ave)		100	26 Min Playback is Assumed at Night
109	ASSC 1	67	3.5			100	
110	ASSC 2	67	3.5			100	
111	Decoder "S"	6 Standby 2800 Operate	0.3 147.5			Negligible	
112	Decoder "L"	6 Standby 2800 Operate	0.3 147.5			Negligible	
113	Decoder "X"	6 Standby 2800 Operate	0.3 147.5			Negligible	
114	SORE Power Supply	550	28.9			100	
115	SORE	610	32.1			100	
116	Spin Control	450	23.7			100	
117	Power Box	1350			71.0	100	
118	Servo Box	1700	89.5			100	
119	Gyro & Gyro Electronics	14500	763.2			100	
120	Gyro Heater	5000	263.2			50	
			131.6 Ave				
121	Power & Servo Offset	1000	52.6			100	
122	15V Wheel Temp Probes	246	13.0			100	
123	Telemetry Monitors	380	20.0			100	
124	Elevation Motor	480			25.3	100	
125	Azimuth Motor	1700	89.5			100	
126	ASA	57.0	3.0			100	
127	15V Sail Temp Probes	870	45.8			100	
128	Decoder "P"	6 Standby 2800 Operate	0.3 147.5			Negligible	
SUB-TOTAL	(Loads 101-128)		1617.4	48.3	96.3		
129	Pitch Coil	275	14.5			0	Not Included in Pwr Budget, "Intermittent Use"
130	Roll Coils	1450	76.3			0	Not Included in Pwr Budget, "Intermittent Use"
131	Pitch Solenoid	25000	1315.8			0	Not Included in Pwr Budget, "Intermittent Use"
132	Spin Solenoid	25000	1315.8			0	Not Included in Pwr Budget, "Intermittent Use"
133	Digital Solar Aspect	190			10.0	0	Not Included in Pwr Budget, "Intermittent Use"
134	GSFC Thermal Monitor	2200			115.8	0	Not Included in Pwr Budget, "Intermittent Use"
SUB-TOTAL	(Loads 129-134)		2722.4		125.8		Not Included in Pwr Budget, "Intermittent Use"
201	Low Dummy Load	10000			526.3		Used Only for Excess Power
202	High Dummy Load	20000			1052.6		Used Only for Excess Power
203	PCM J-Box 1 or 2	120			6.3		
204	Spin Control	1710			90.0		
205	Power Box	760		40.0			
SUB-TOTAL	(Loads 203-205)			40.0	96.3		
301	ASA	1259		66.0			
401	NRL Pointed Experiment	4120			217.0		
402	GSFC Pointed Experiment	7850 Day 1050 Night		55.3	413.2		
SUB-TOTAL	(Loads 401-402)			55.3	630.2		
501	UCSD Cosmic Experiment	2350	124.0				
502	UCSD Solar Experiment	1900	100.0				
503	UNH Experiment	3370	178.0				
504	MIT Experiment	3600	190.0				
SUB-TOTAL	(Loads 501-504)		592.0				
TOTAL	Observatory (All Loads Averaged at 19 VDC)		2360.1	209.6	726.5		



F72-01

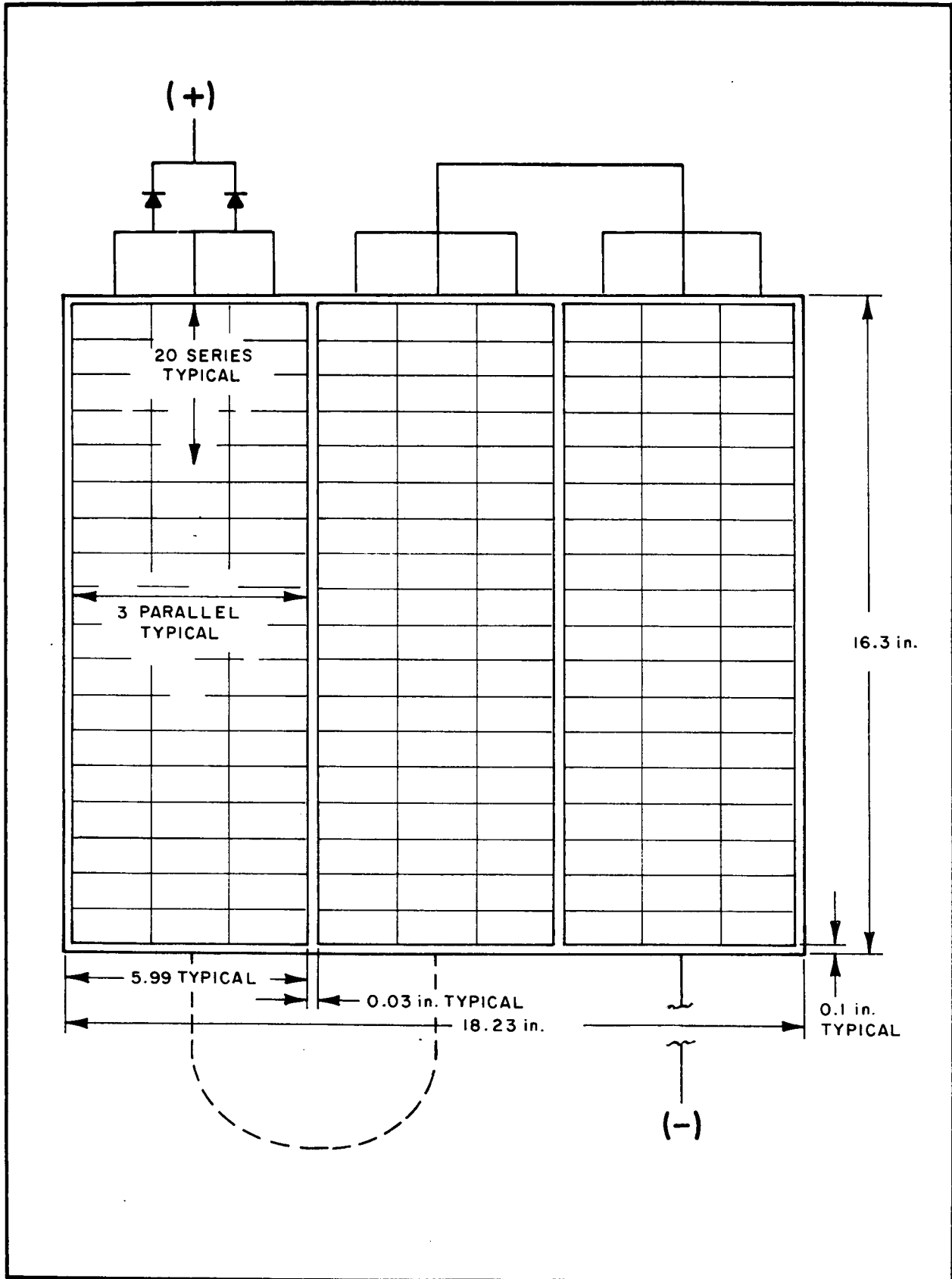


Figure 7-3 OSO-7 Solar Panel Layout and Module Dimensions



F72-01

### 7.3.2 Operating Environment

The panels will operate for more than one year in a temperature environment ranging from  $-40^{\circ}\text{C}$  to  $+80^{\circ}\text{C}$ . They have a power output of 0.95 amps at 19 volts (18.05 watts) at their maximum operating temperature of  $70^{\circ}\text{C}$ . The time-average temperature during the day is about  $52^{\circ}\text{C}$ . At that temperature the array will provide 4.95 amps for a load voltage of 19.5 volts. This is the expected nominal array output for an average sun.

The expected radiation degradation is less than 1 percent after one year exposure to in-orbit radiation. This conclusion is based on OSO-3 flight data which showed a total degradation from all causes of less than 1 percent.

### 7.3.3 Solar Cells

An OSO-7 solar cell and interconnecting strip are shown in Figure 7-4. The interconnection strip is made of 0.002 inch silver-plated copper. The cells, manufactured by Heliotek, are N-on-P silicon (10 ohms per centimeter) and measure 2 x 5 centimeters.

### 7.3.4 Solar Cell Coverglass

The solar cells are protected with fused silica coverglass 30 mils thick. These coverslips have a filter coating with a cutoff wavelength of  $410 \pm 15$  microns.

### 7.3.5 Adhesives

All of the adhesives considered for use on the solar array were tested before the final selection was made. The final choice of adhesives is shown in Table 7-2. The 0.004 inch thick insulation sheet is an epoxy-filled glass cloth material called Micaply.

## 7.4 ENERGY STORAGE

Energy is stored in a main battery of nickel-cadmium.

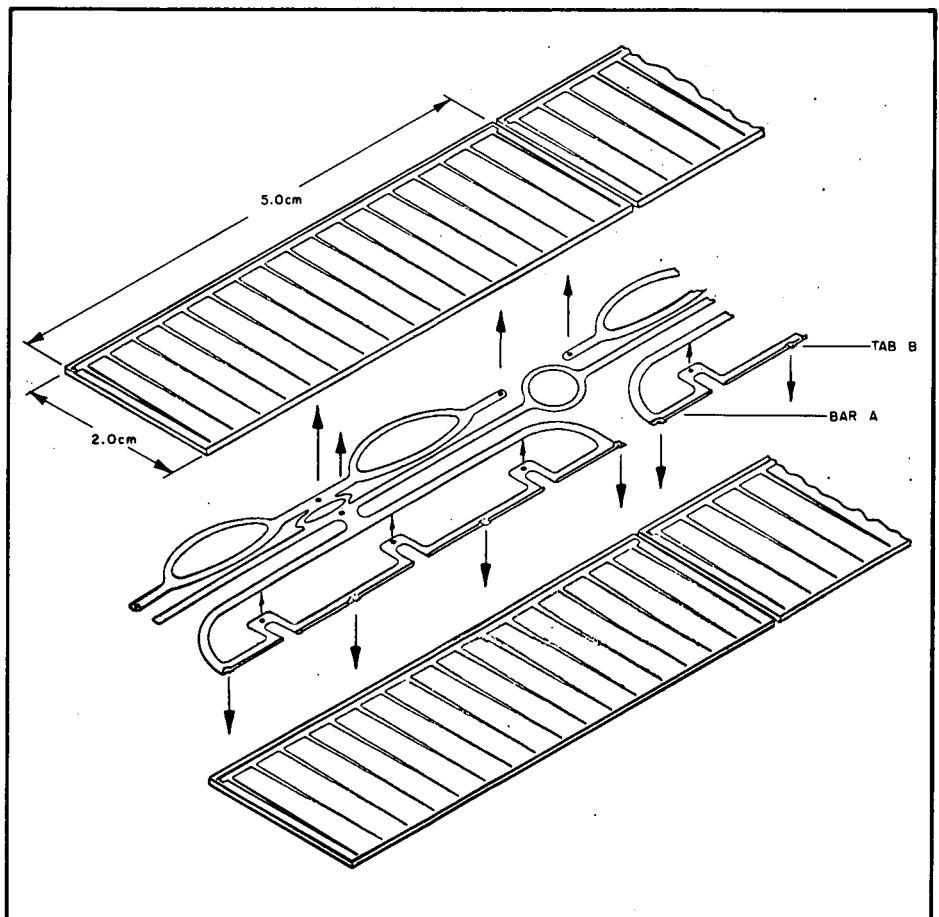


Figure 7-4 Solar Cell and Interconnect



F72-01

cells purchased from General Electric. This battery is used to supply the night and surge power requirements of the observatory. In addition, a separate set of squib batteries is used for firing the various pressure cartridges (squibs) in the spacecraft and experiment systems.

Table 7-2  
ADHESIVES USED ON THE OSO-7 SOLAR ARRAY CELL ASSEMBLY

<u>Application</u>	<u>Adhesive</u>
Cover Slip to Cell	Dow 93-500
Cell Modules to Insulation	RTV-566
Insulation to Panel	Epibond 101

7.4.1 Main Battery

The main battery consists of four strings of 14 cells each for a total capacity of 16 ampere-hours. There are two packs of seven cells in each string. Figure 7-5 shows one of these seven-cell packs and a sketch of how the individual cells are potted into the housing.

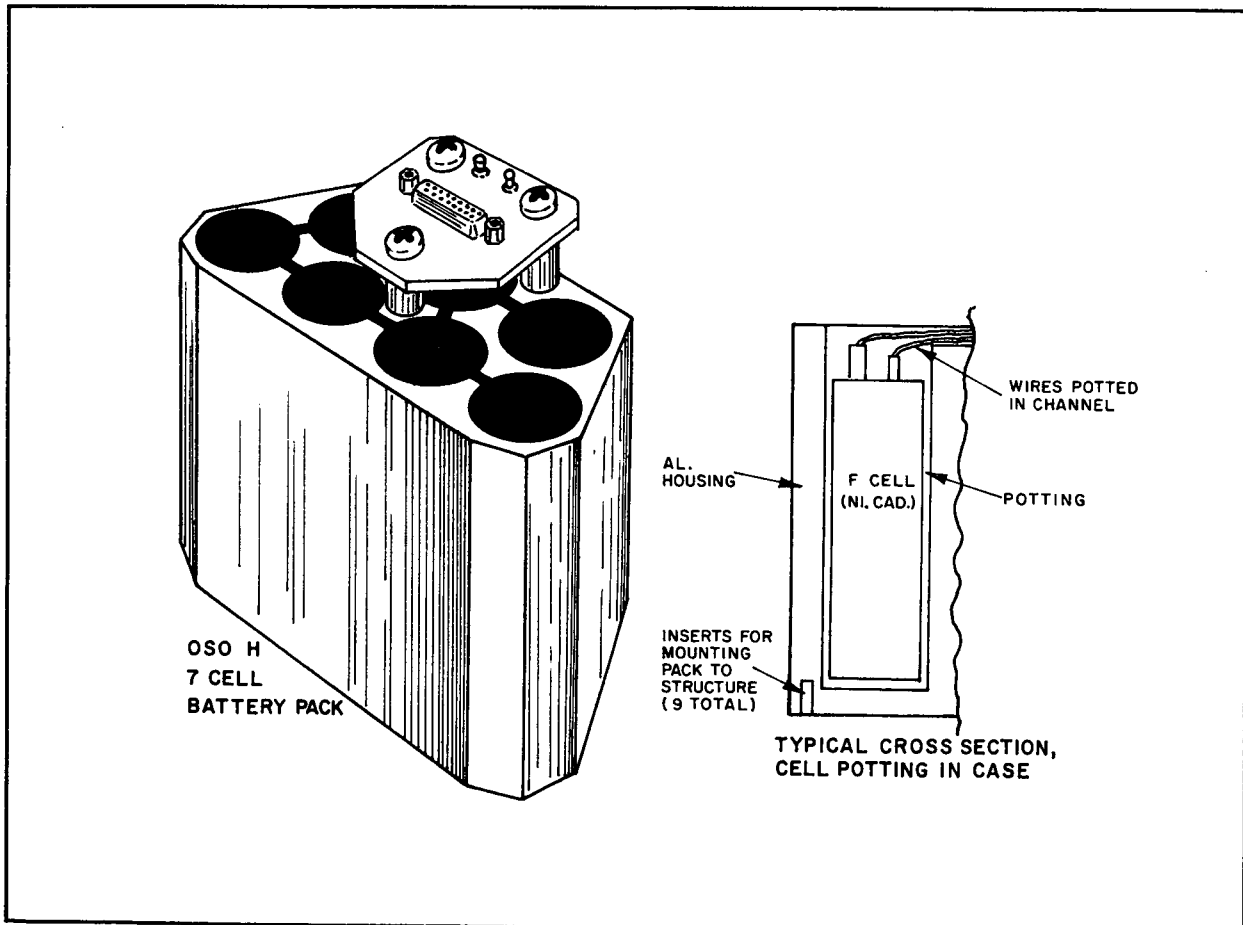


Figure 7-5 OSO-7 Seven-Cell Battery Pack





F72-01

Each string of battery cells is connected to the main continuous bus by diodes. Diode bypass switches are connected across these diodes to eliminate discharge losses and to provide a charge path for each battery string. Opening one of these switches removes the string from the charge line.

Each cell must have a minimum capacity of 3.35 ampere-hours when discharged to 1.2 volts at 0° to 35°C. Nominal capacity is 4.2 ampere hours at 24°C. Both of these capacities were measured during acceptance testing, at a discharge rate of 0.84 amperes.

The cells have a maximum continuous charge voltage of 1.48 volts in a temperature range of 21°C to 35°C when charged at 0.45 amperes. The spacecraft loads require a normal charge rate of about 0.4 amperes and an average discharge rate of 0.6 amperes per cell. Therefore, each cell operates well within the range of the charge and discharge rates at which they are tested.

#### 7.4.2 Sail Squib Batteries

The OSO-7 sail squib batteries are the same as those used on OSO-6 and OSO-5. Two squib battery assemblies (three cells each) using Sonotone 1/2 C cells are used redundantly to fire four spacecraft squibs (pressure cartridges) and four experiment squibs. The squib batteries are tested to ensure that they can remain above 2.5 volts for two seconds with a 0.25-ohm load.

#### 7.5 POWER CONTROL

Power is controlled by the undervoltage switch, the dummy load system, and power switches (relays) that provide day-night power and on/off functions to the spacecraft equipment and the experiments.

##### 7.5.1 Undervoltage Switch (UVS)

The undervoltage switch prevents excessive power consumption from depleting the batteries to the point where it would be impossible to execute corrective commands.

When the spacecraft is in the undervoltage state, the sail can no longer be solar-oriented, and therefore, the solar array charges the batteries at about 25 percent of the normal rate until the voltage rises to about 19.1 volts. At this time, power is reapplied to the observatory, and normal functions can be resumed.

The undervoltage switch consists of a voltage sensing circuit that automatically opens the relay when the battery voltage drops to 16.2 volts. The control circuit closes the relay again when the voltage rises above 19.1 volts, if the auto-reset function has been enabled by command. A bypass relay can be commanded to bypass the UVS circuits.



F72-01

### 7.5.2 Dummy Load System

The dummy load system consists of two sets of dummy loads, as shown in Figure 7-6. The first set of dummy loads permits adjustment of the spacecraft load by 10, 20 or 30 watts using a combination of two different dummy loads. The other part of the dummy load system consists of simulated loads for each experiment that are connected only when the experiment is disconnected.

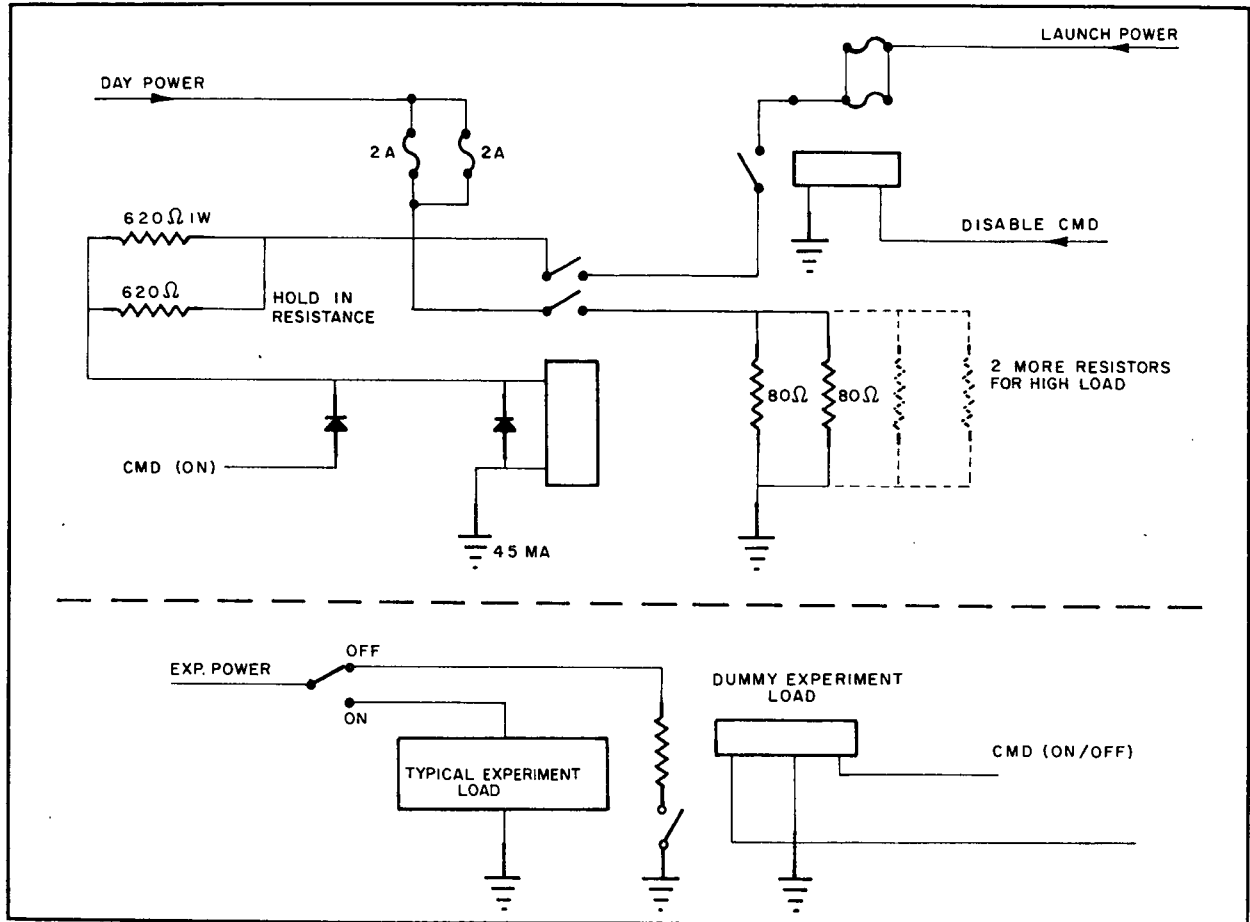


Figure 7-6 Dummy Load System Simplified Schematic

The dummy load resistors are etched from nickel chromium foil and encapsulated between two Kapton sheets. Figure 7-7 shows how these resistors are connected and where they are located on the spacecraft. By locating the resistors on the antenna skirt, their heat is easily radiated into space.

The dummy load resistors in the experiments are "Daleohm" power resistors. With one exception these are located in the experiment chassis to simulate the thermal load. The GSFC experiment load resistor is located on the elevation frame rather than on the experiment chassis.



F72-01

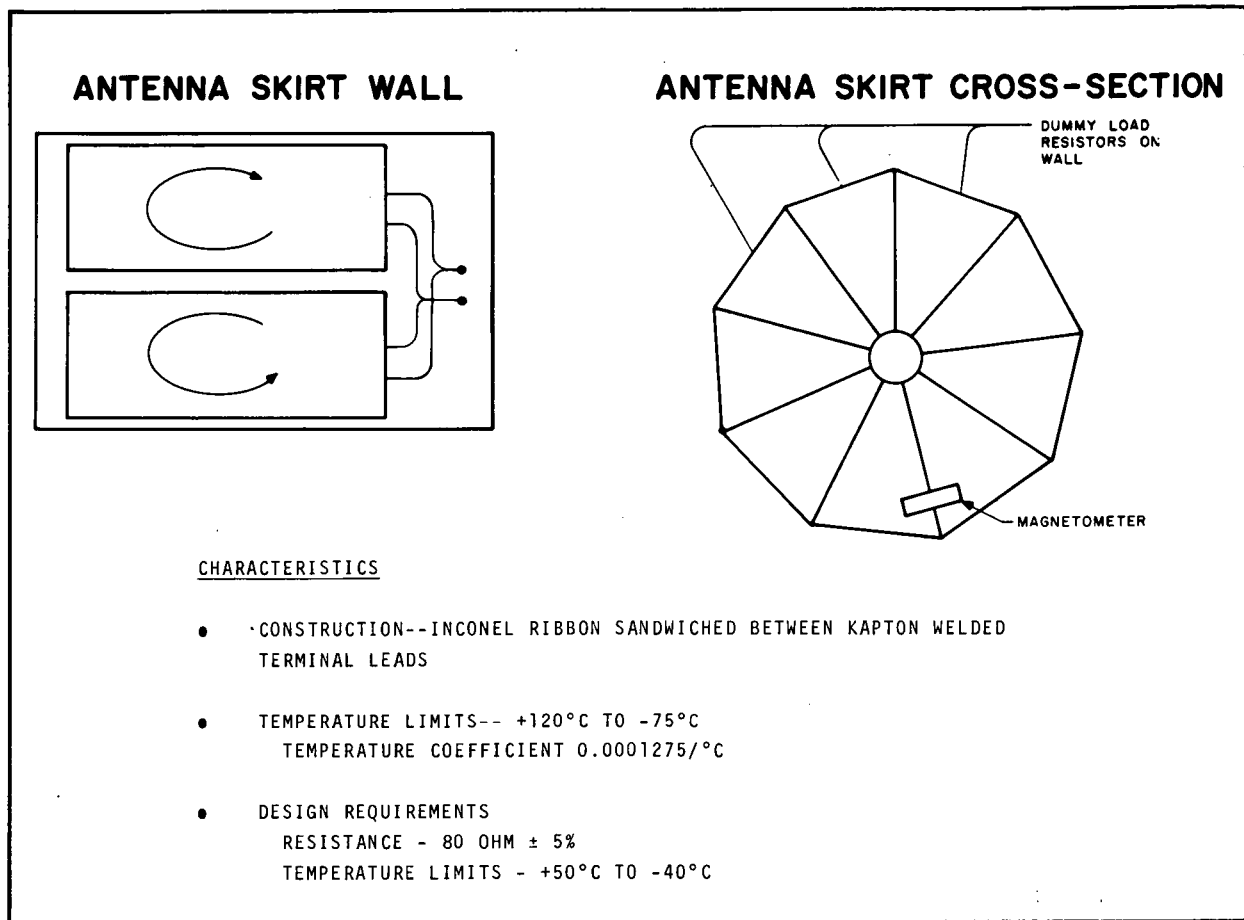


Figure 7-7 Dummy Load Locations

### 7.5.3 Power Switching

The major power switches in the spacecraft are:

- Day-Night Switch - A 10-ampere relay with six contacts, for switching power to the day and night buses from the launch bus. This power control is used by the spacecraft equipment and the experiments.
- Experiment Wheel and Sail Enable Switches - These are 3-ampere relays with two contacts each, used for enabling either the wheel or the sail experiment power lines. They are followed by individual on/off switches for each experiment.
- Solar Array Switches - Two of the solar array panels have disconnect switches to reduce the power generated by the array.



F72-01

- Battery Diode Bypass Switches - These switches are used to take the battery strings off the charge line. A logic network prevents switching off more than two packs at one time. This switching is shown on the simplified power system block diagram (Figure 7-1).

#### 7.5.4 Regulated Power Supplies

The DSM and SORE are provided with regulated +5 vdc from separate, identical, regulated power supplies.

These power supplies provide  $5.0 \pm 0.1$  vdc at a ripple voltage of less than 15 millivolts and are capable of delivering 30 to 75 milliamperes into a resistive load at an efficiency of 40 percent or greater.

#### 7.6 POWER DISTRIBUTION

The power distribution system provides continuous, launch, day, night, and +15-volt regulated buses to the observatory. The night bus is available only in the wheel. All the buses except the continuous bus are isolated from the battery by the undervoltage switch (UVS). There are two current monitors on the spacecraft, one for the solar array output current and one for observatory loads. A simplified schematic of the power distribution system is shown in Figure 7-8.

Grounding System. Single-point grounds are provided in the wheel and sail. These ground points are connected by four slip ring circuits for minimum difference in potential. Separate power and signal returns are provided for each component where practical. These returns are individually returned to the sail or wheel single-point ground.

Torque Motor Power and Return Isolation and Decoupling. The torque motor power and power return is isolated and decoupled from sail power and sail chassis to prevent the pulse width modulator (PWM) pulses from interfering with susceptible sail systems or appearing across the wheel/sail slip ring data interface. These returns are shown on Figure 7-8. Separate slip rings are provided for the torque motor power and the power return is shared with the solar array return.

Gyro Power and Return Isolation. The launch power for the gyro is supplied from the torque motor power bus and the return is tied to the solar array return (battery ground) to prevent the low frequency gyro noise from interfering with susceptible sail systems.

##### 7.6.1 Flex Cables

The OSO-7 flex cable is shown in Figure 7-9. None of the wires are twisted pairs, to reduce the torque in the flex cable. Four flex cables are used, two mounted on each side of the elevation housing as shown in Figure 7-10. The flex cables use standard Cannon "D" connectors with a solder cup design. The flex cables generate a torque of less than 2 inch-ounces over a 10 degree arc.



F72-01

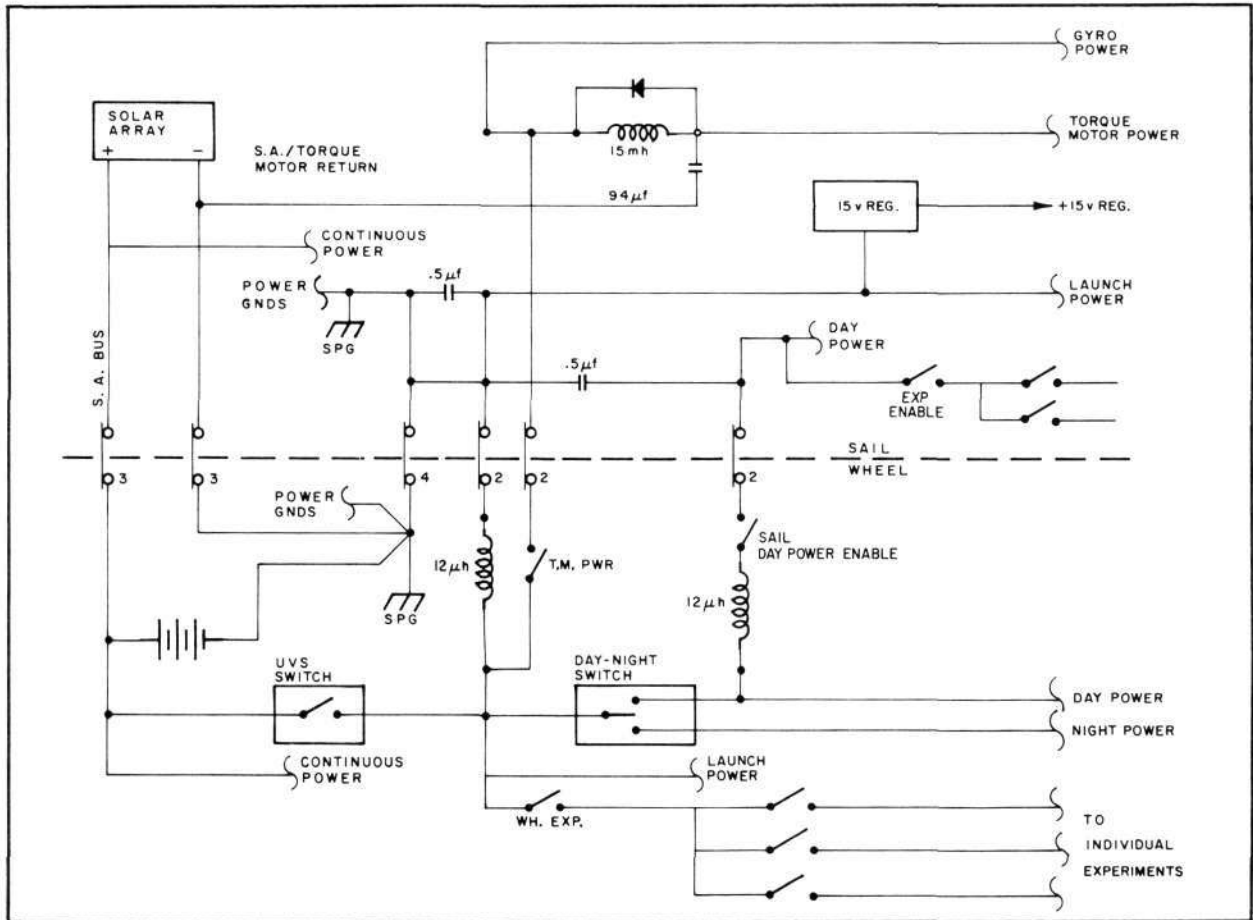
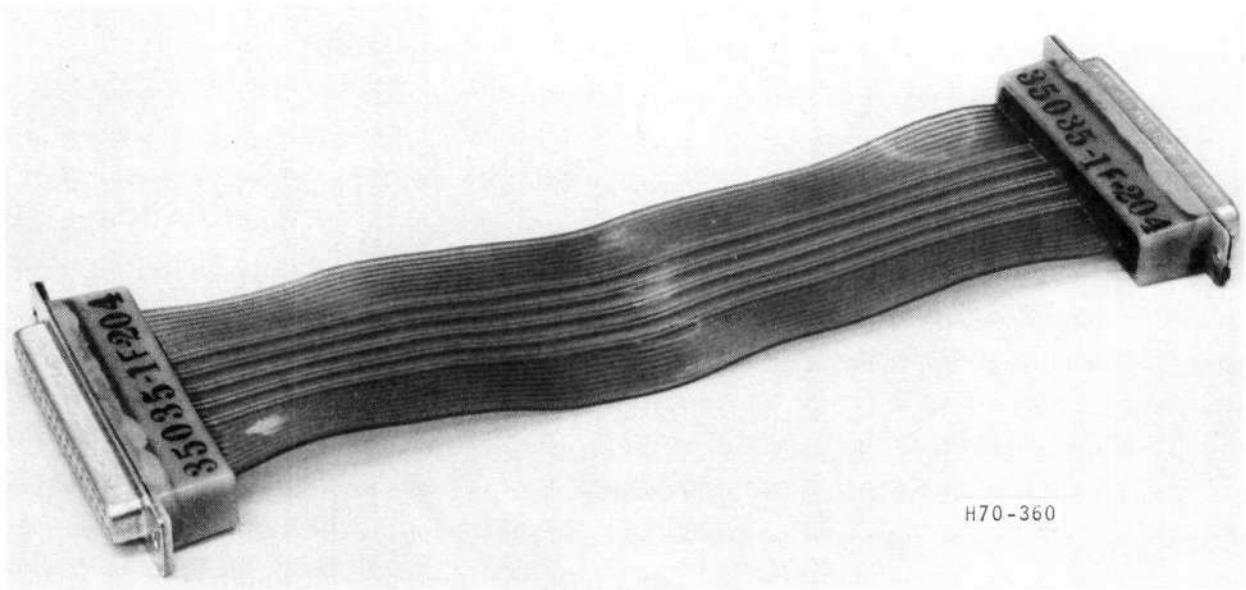


Figure 7-8 Simplified Power Distribution



H70-360

Figure 7-9 Flex Cable



F72-01

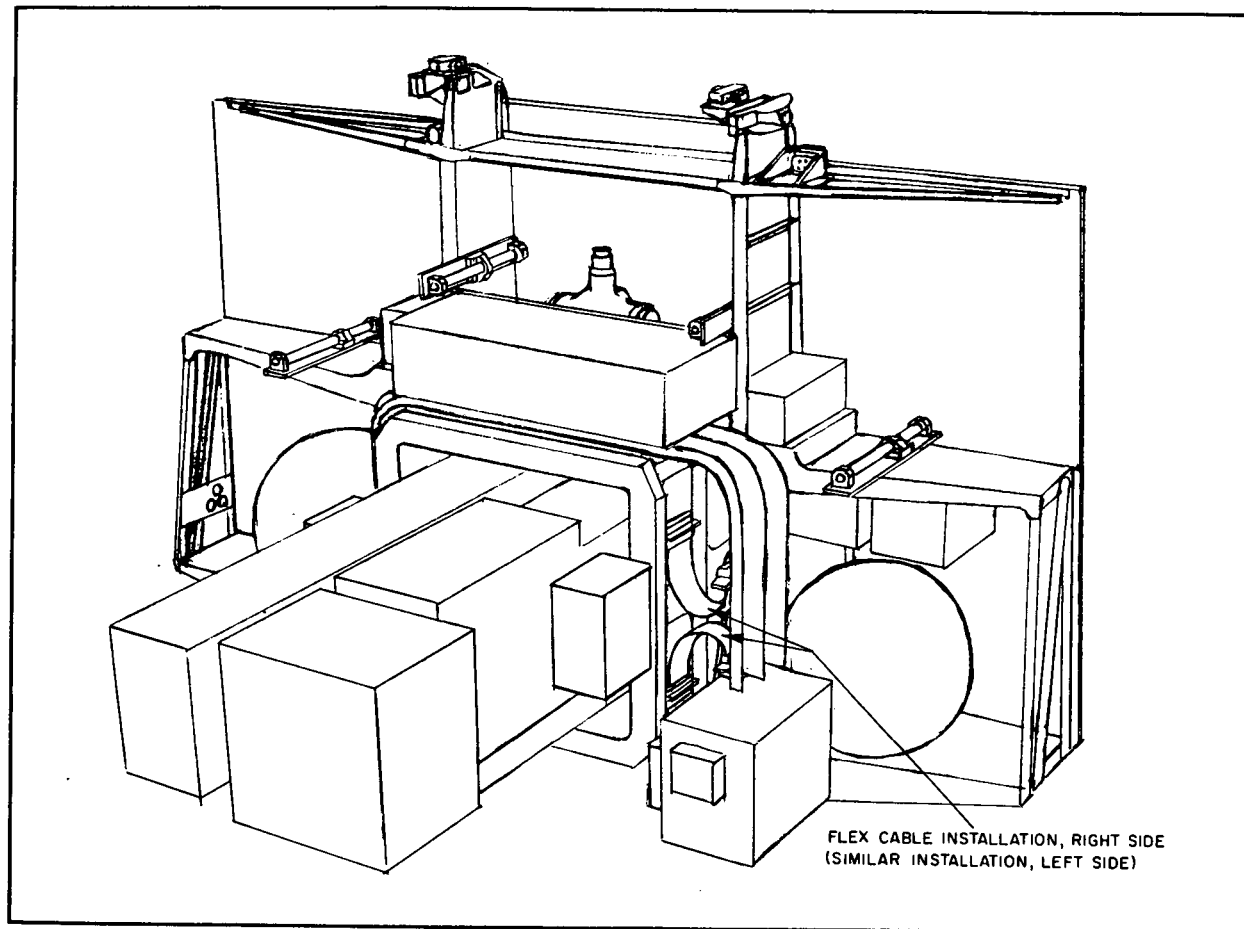


Figure 7-10 Flex Cable Mounting Configuration



F72-01

Section 8  
TELEMETRY SYSTEM

8.1 INTRODUCTION

The spacecraft and experiment data are sampled, encoded, and telemetered to the GSFC Satellite Tracking and Data Acquisition Network (STADAN) by means of an on-board pulse code modulation/phase modulation (PCM/PM) telemetry system. This system consists of a data handling subsystem and an RF subsystem (Figure 8-1). The data handling subsystem provides commutation (sampling), multiplexing (time sharing), encoding, and on-board storage of the observatory data. The RF subsystem provides RF transmission of both real-time and stored data to the STADAN stations.

The OSO-7 telemetry system is similar to OSO-6. The main differences are:

- Deletion of the word gate generator in the sail, made possible by a new 40-circuit slip-ring assembly.
- Addition of a redundant PCM J-box in the wheel.
- Addition of a ninth stage to the frame counter. This increases the frame count cycle time from 65.5 minutes to 131 minutes.
- Addition of a second analog sub-subcommutator in the sail to increase telemetry capacity.
- Addition to an analog sub-subcommutator in the wheel to increase telemetry capacity.
- Modifications to the analog sub-subcommutator, to withstand the lower "back sail" temperature requirements.
- The tape recorder capacity was increased from 100 minutes to 108 minutes.
- The tape recorder control circuitry was redesigned to provide three operating modes:
  - a) Continuous operation of either recorder in the normal record playback cycle.
  - b) Alternating recorder operation each orbit, to allow recording of data on one recorder during playback of the other recorder.
  - c) A mode for automatic serial recording of two consecutive orbits (that is, filling one recorder with about 10 minutes of data and automatically switching the other recorder to record. The stored data on the first recorder are played back several orbits later).



F72-01

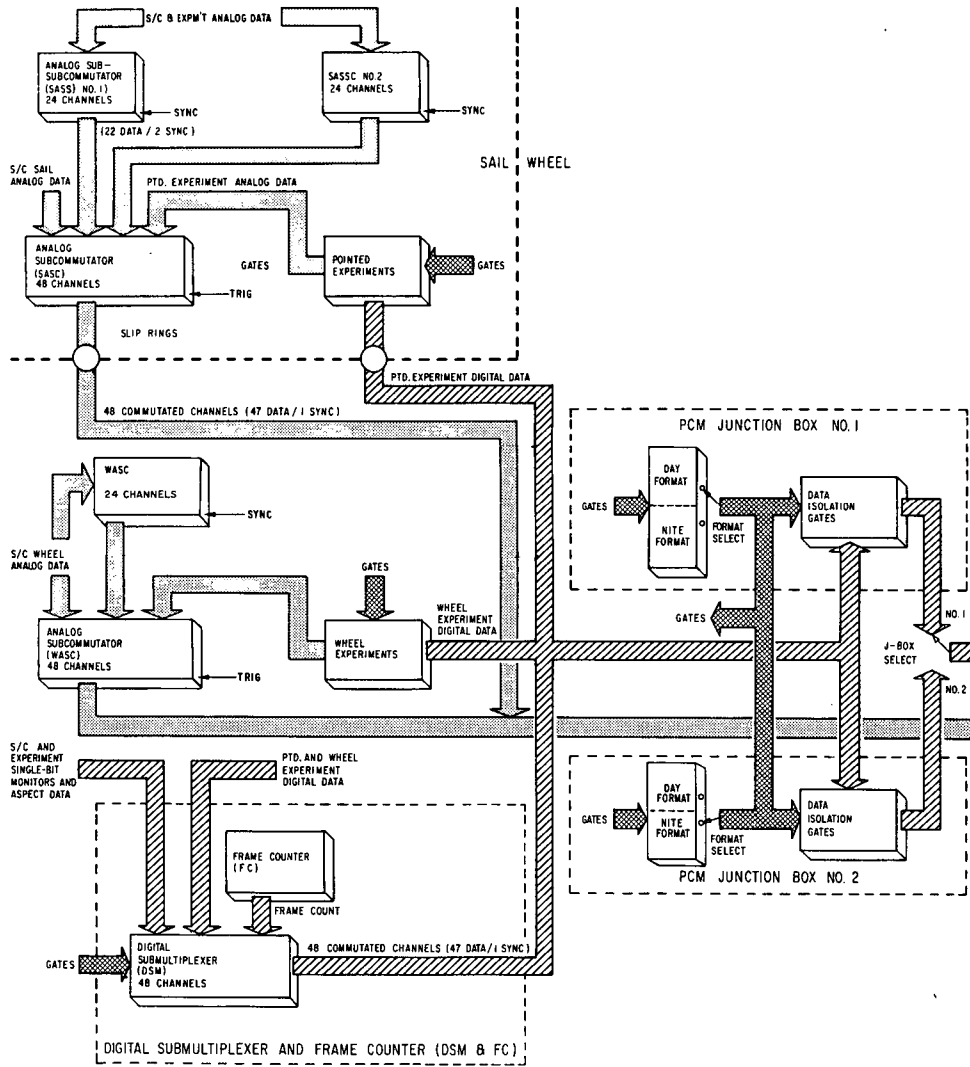


Figure 8-1 Telemetry System Block Diagram (1 of 2)





F72-01

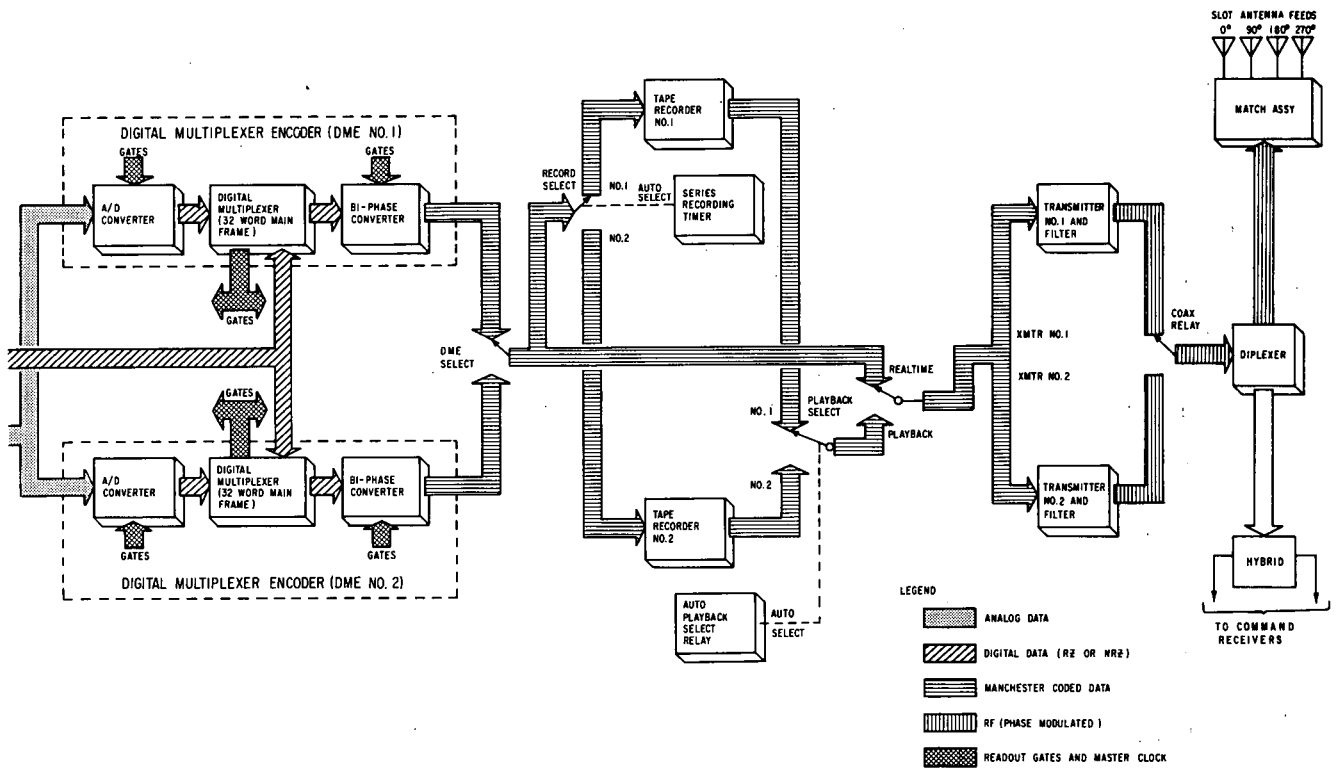


Figure 8-1 Telemetry System Block Diagram (2 of 2)



F72-01

- The antenna configuration was changed to a turnstile slot which has low spin modulation and improves telemetry link performance.
- The TMG (time mark generator) circuits were deleted to increase reliability. Data gaps due to tape recorder coast time will be used for time marks in case of a frame counter failure.

## 8.2 DATA HANDLING SUBSYSTEM

The data handling subsystem provides the interface between all observatory data sources and the RF subsystem. Its primary function is to assemble the observatory data into a form suitable for transmission and to store these data for playback when the observatory is over a selected STADAN station.

The data-handling subsystem uses time multiplexing techniques wherein each data source is assigned a time interval (channel) for transmission of the parameter being measured. These source data can be in either digital or analog form.

The OSO-7 telemetry system provides 27 channels of a 32-channel main-frame format for experiment prime (digital) data. Most of the spacecraft status and performance data are in analog form, and the system provides 47 data channels in each of the two 48-channel analog subcommutators (ASC's) and 22 data channels in each of the three 24-channel analog sub-subcommutators (ASSC) for this type of data. Some of the analog channels are used for experiment performance data. A 48-channel digital sub-multiplexer (DSM) provides additional digital channels for aspect, spacecraft housekeeping and experiment data. There are 270 telemetry channels (70 digital word, 32 single-bit monitors, 153 analog monitors and 15 sync) available. Additional sub-multiplexing is done internally in some of the experimenters' instruments.

The multiplexed PCM signal has a bit rate of 800 bps. Each of the 32 main-frame channels (or words) contains eight bits. Two words (16 bits) are used for a main frame synchronization code, one word is assigned to each of the two ASC's, one word is assigned to the DSM, and the remaining 27 words are assigned to the experiment instruments. The two ASC's, the three ASSC's, and the DSM subframes contain their own synchronization codes.

Telemetry Timing. The telemetry timing breakdown is as follows:

- Bit rate = 800 bps = 100 words/sec at 8 bits per word
- $32 \text{ words/MF} \times \frac{\text{sec}}{100 \text{ words}} = 0.32 \text{ sec/MF}$
- $0.32 \text{ sec/MF} \times 48 \text{ MF/ASC cycle} = 15.36 \text{ sec/ASC cycle or DSF cycle}$
- $15.36 \text{ sec/ASC cycle} \times 24 \text{ ASC cycles/ASSC cycle} = 368.64 \text{ sec/ASSC cycle}$   
 $= 6.144 \text{ min/ASSC cycle}$



F72-01

All signals into the two redundant digital multiplexer encoders (DME) are connected in parallel, and the internal circuit design is such that failure in one will not affect the other. The redundant DME output is selected by the same ground station commands that control DME power switching.

The experiments have self-contained storage shift registers for their digital data. The spacecraft data handling subsystem provides gate pulses to shift the stored data into the telemeter at the assigned time interval.

Data are stored by redundant, continuous-loop, magnetic tape recorders which have the capacity to record data for  $108 \pm 2$  minutes. Either of the two recorders is selectively powered in response to ground station command and, upon receiving a "playback command", the selected recorder reproduces the recorded data at 18 times the realtime rate (14,400 bps). The recorder automatically reverts to the record mode at the end of the playback.

A serial recording timer will automatically switch to the standby tape recorder after 103 minutes when ground station commands are not available. This extends the total record capacity to 211 minutes. Automatic controls are also provided for selection of the recorder to be played back. A single playback command, in this automatic mode, will cause the latest recorded data to be played back first.

The telemetry data channels have the following characteristics:

Analog Data (153 Channels)

- Levels: 0 to +5 volts
- Input resistance: 100 K ohms

Single Bit Data (Type A) (3 Channels: word 42, bit 7; word 42, bit 8; and word 31, bit 8.)

- Logic one: +15 to +22 volts
- Logic zero: 0 to +0.5 volts
- Input impedance: 100 K ohms

Single Bit Data (Type B) (29 Channels)

- Logic one: +15 to +22 volts
- Logic zero: 0 to +0.5 volts
- Input impedance: 5 K ohms

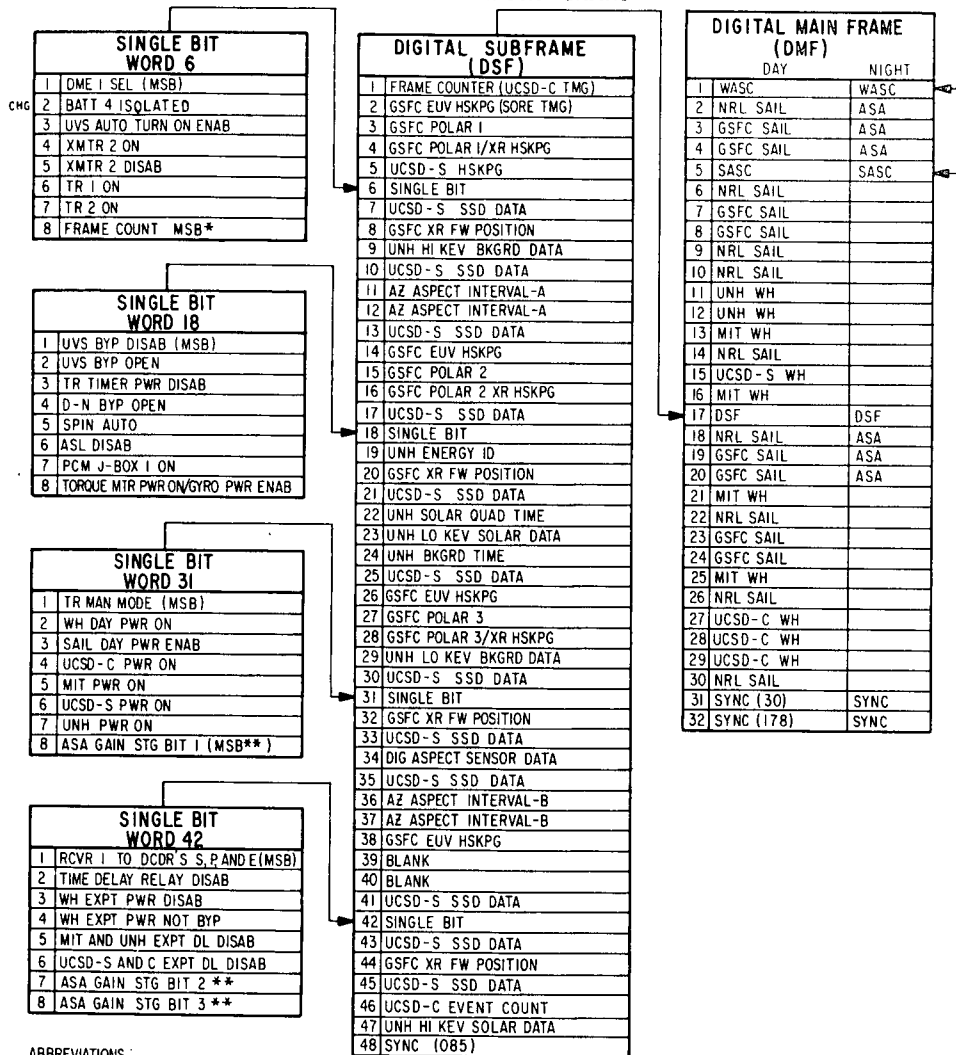
Parallel Digital Data (1 Channel)

- Logic one: 2.5 to +5 volts
- Logic zero: 0 to +0.5 volts
- Input impedance: 1 K ohms



F72-01

Table 8-1  
OSO-7 TELEMETRY CHART



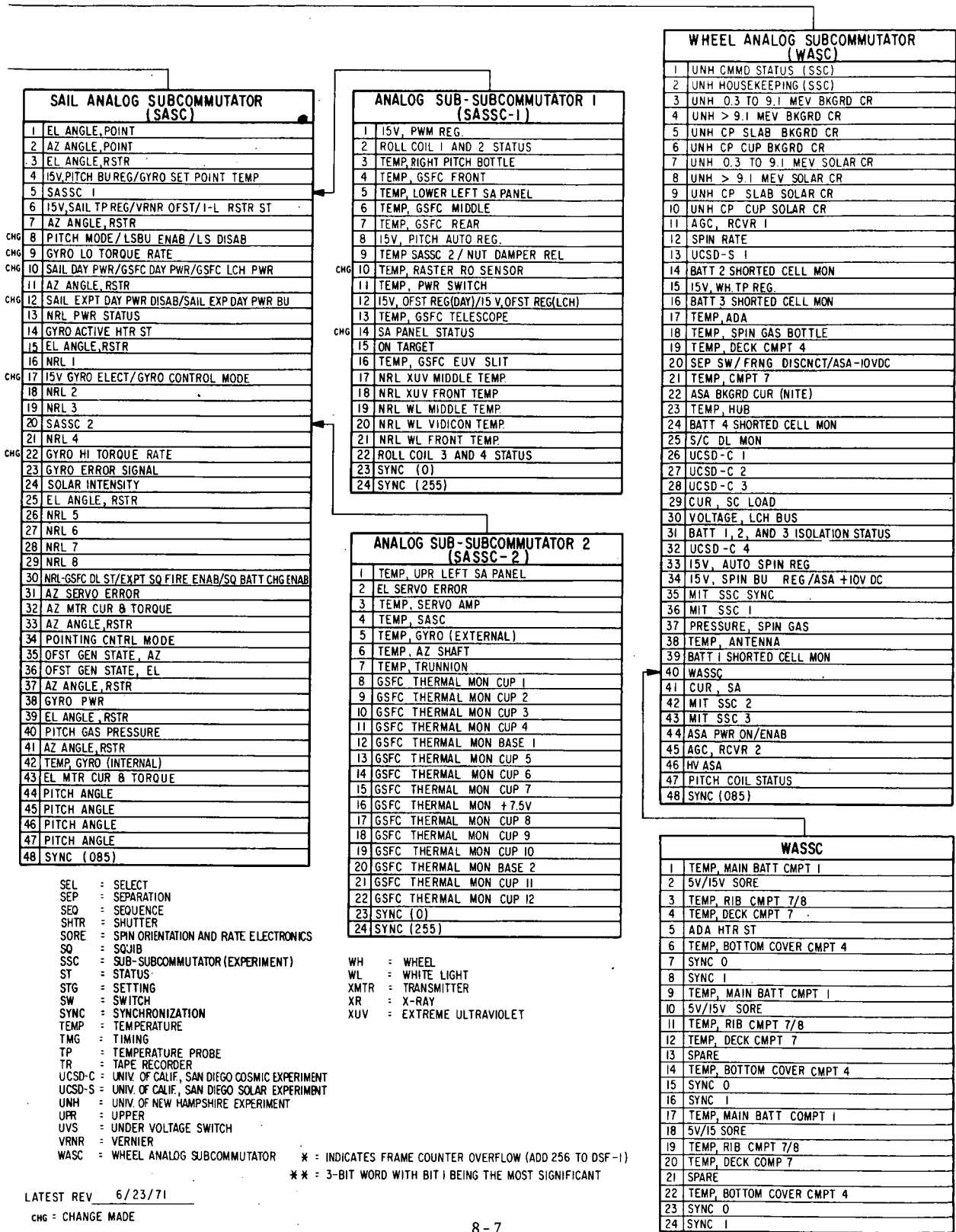
ABBREVIATIONS:

- |                                       |   |  |
|---------------------------------------|---|--|
| ADA = AZ DRIVE ASSEMBLY               | DSF = DIGITAL SUBFRAME                  | MIT = MASSACHUSETTS INSTITUTE OF TECHNOLOGY EXPERIMENT |
| AGC = AUTOMATIC GAIN CONTROL          | ELECT = ELECTRONICS                     | MON = MONITOR  |
| ASA = ASPECT SENSOR ASSEMBLY          | EL = ELEVATION                          | MSB = MOST SIGNIFICANT BIT                             |
| ASL = AUTOMATIC SPIN LIMITER          | ENAB = ENABLE                           | MSP = MISPOINT   |
| ASSC = ANALOG SUB-SUBCOMMUTATOR       | ENCDR = ENCODER                         | MTR = MOTOR  |
| AUTO = AUTOMATIC                      | EUV = EXTREME ULTRA VIOLET              | NEG = NEGATIVE   |
| AZ = AZIMUTH                          | EXCT = EXECUTE                          | NRL = NAVAL RESEARCH LABORATORY EXPT                   |
| BATT = BATTERY                        | EXP = EXPOSURE                          | NUT = NUTATION   |
| BKGRD = BACKGROUND                    | EXPT = EXPERIMENT                       | OFST = OFFSET  |
| BU = BACKUP                           | FIL = FILAMENT                          | OPER = OPERATION                                       |
| BYP = BYPASS (BYPASSED)               | FOC = FOCUS                             | O-R = OVERRIDE   |
| CALIB = CALIBRATE                     | FRNG = FAIRING                          | PCM = PULSE CODE MODULATOR                             |
| CD = CENTRAL DETECTOR                 | FW = FILTER WHEEL                       | PBK = PLAYBACK   |
| CKT = CIRCUIT                         | GEN = GENERATOR                         | POLAR = POLARIMETER                                    |
| CLK = CLOCK                           | GSFC = GODDARD SPACE FLIGHT CENTER EXPT | POS = POSITIVE   |
| CMMD = COMMAND                        | HI = HIGH                               | PT = POINT   |
| CMPT = COMPARTMENT                    | HSKPG = HOUSEKEEPING                    | PWM = PULSE WIDTH MODULATOR                            |
| CNTRL = CONTROL                       | HTR = HEATER                            | PWR = POWER  |
| CP = CHARGED PARTICLES                | HV = HIGH VOLTAGE                       | RCVR = RECEIVER  |
| CR = COUNT RATE                       | HVPS = HIGH VOLTAGE POWER SUPPLY        | REG = REGULATOR  |
| CTR = COUNTER                         | ID = IDENTIFICATION                     | REL = RELEASE  |
| CUR = CURRENT                         | I-L = INTERLACED                        | RO = READOUT   |
| DCDR = DECODER                        | LCH = LAUNCH                            | RST = RESET  |
| DDP = DIGITAL DATA PROCESSOR          | LG = LARGE                              | RSTR = RASTER  |
| DEG/SEC = DEGREE PER SECOND           | LO = LOW                                | SA = SOLAR ARRAY                                       |
| DIG = DIGITAL                         | LSBU = LAUNCH SEQUENCE BACKUP           | SASC = SAIL ANALOG SUBCOMMUTATOR                       |
| DISAB = DISABLE                       | LV = LOW VOLTAGE                        | SC = SPACECRAFT  |
| DISONCT = DISCONNECT                  | LVPS = LOW VOLTAGE POWER SUPPLY         | SECT = SECTOR  |
| DL = DUMMY LOAD                       | LWR = LOWER                             |  |
| DME = DIGITAL MULTIPLEXER AND ENCODER | MAG = MAGNETOMETER                      |  |
| DMF = DIGITAL MAIN FRAME              | MAN = MANUAL                            |  |
| D-N = DAY-NIGHT                       |   |  |



F72-01

Table 8-1 (Cont.)



SAIL ANALOG SUBCOMMUTATOR (SASC)	
1	EL ANGLE, POINT
2	AZ ANGLE, POINT
3	EL ANGLE, RSTR
4	15V, PITCH BUREG/GYRO SET POINT TEMP
5	SASSC 1
6	15V, SAIL TP REG/VRNR OFST/1-L RSTR ST
7	AZ ANGLE, RSTR
8	PITCH MODE/LSBU ENAB/LS DISAB
9	GYRO LO TORQUE RATE
10	SAIL DAY PWR/GSFC DAY PWR/GSFC LCH PWR
11	AZ ANGLE, RSTR
12	SAIL EXPT DAY PWR DISAB/SAIL EXP DAY PWR BU
13	NRL PWR STATUS
14	GYRO ACTIVE HTR ST
15	EL ANGLE, RSTR
16	NRL 1
17	15V GYRO ELECT/GYRO CONTROL MODE
18	NRL 2
19	NRL 3
20	SASSC 2
21	NRL 4
22	GYRO HI TORQUE RATE
23	GYRO ERROR SIGNAL
24	SOLAR INTENSITY
25	EL ANGLE, RSTR
26	NRL 5
27	NRL 6
28	NRL 7
29	NRL 8
30	NRL-GSFC DL ST/EXPT SQ FIRE ENAB/SQ BATT CHG ENAB
31	AZ SERVO ERROR
32	AZ MTR CUR & TORQUE
33	AZ ANGLE, RSTR
34	POINTING CNTRL MODE
35	OFST GEN STATE, AZ
36	OFST GEN STATE, EL
37	AZ ANGLE, RSTR
38	GYRO PWR
39	EL ANGLE, RSTR
40	PITCH GAS PRESSURE
41	AZ ANGLE, RSTR
42	TEMP, GYRO (INTERNAL)
43	EL MTR CUR & TORQUE
44	PITCH ANGLE
45	PITCH ANGLE
46	PITCH ANGLE
47	PITCH ANGLE
48	SYNC (085)

ANALOG SUB-SUBCOMMUTATOR 1 (SASSC-1)	
1	15V, PWM REG.
2	ROLL COIL 1 AND 2 STATUS
3	TEMP, RIGHT PITCH BOTTLE
4	TEMP, GSFC FRONT
5	TEMP, LOWER LEFT SA PANEL
6	TEMP, GSFC MIDDLE
7	TEMP, GSFC REAR
8	15V, PITCH AUTO REG.
9	TEMP SASSC 2/ NUT DAMPER REL
10	TEMP, RASTER RO SENSOR
11	TEMP, PWR SWITCH
12	15V, OFST REG(DAY)/15 V, OFST REG(LCH)
13	TEMP, GSFC TELESCOPE
14	SA PANEL STATUS
15	ON TARGET
16	TEMP, GSFC EUV SLIT
17	NRL XUV MIDDLE TEMP
18	NRL XUV FRONT TEMP
19	NRL WL MIDDLE TEMP
20	NRL WL VIDICON TEMP
21	NRL WL FRONT TEMP
22	ROLL COIL 3 AND 4 STATUS
23	SYNC (0)
24	SYNC (255)

ANALOG SUB-SUBCOMMUTATOR 2 (SASSC-2)	
1	TEMP, UPR LEFT SA PANEL
2	EL SERVO ERROR
3	TEMP, SERVO AMP
4	TEMP, SASC
5	TEMP, GYRO (EXTERNAL)
6	TEMP, AZ SHAFT
7	TEMP, TRUNNION
8	GSFC THERMAL MON CUP 1
9	GSFC THERMAL MON CUP 2
10	GSFC THERMAL MON CUP 3
11	GSFC THERMAL MON CUP 4
12	GSFC THERMAL MON BASE 1
13	GSFC THERMAL MON CUP 5
14	GSFC THERMAL MON CUP 6
15	GSFC THERMAL MON CUP 7
16	GSFC THERMAL MON +7.5V
17	GSFC THERMAL MON CUP 8
18	GSFC THERMAL MON CUP 9
19	GSFC THERMAL MON CUP 10
20	GSFC THERMAL MON BASE 2
21	GSFC THERMAL MON CUP 11
22	GSFC THERMAL MON CUP 12
23	SYNC (0)
24	SYNC (255)

WHEEL ANALOG SUBCOMMUTATOR (WASC)	
1	UNH CMMD STATUS (SSC)
2	UNH HOUSEKEEPING (SSC)
3	UNH 0.3 TO 9.1 MEV BKGRD CR
4	UNH > 9.1 MEV BKGRD CR
5	UNH CP SLAB BKGRD CR
6	UNH CP CUP BKGRD CR
7	UNH 0.3 TO 9.1 MEV SOLAR CR
8	UNH > 9.1 MEV SOLAR CR
9	UNH CP SLAB SOLAR CR
10	UNH CP CUP SOLAR CR
11	AGC, RCVR 1
12	SPIN RATE
13	UCSD-S 1
14	BATT 2 SHORTED CELL MON
15	15V, WH TP REG.
16	BATT 3 SHORTED CELL MON
17	TEMP, ADA
18	TEMP, SPIN GAS BOTTLE
19	TEMP, DECK CMPT 4
20	SEP SW/FRNG DISCNCT/ASA-10VDC
21	TEMP, CMPT 7
22	ASA BKGRD CUR (NITE)
23	TEMP, HUB
24	BATT 4 SHORTED CELL MON
25	S/C DL MON
26	UCSD-C 1
27	UCSD-C 2
28	UCSD-C 3
29	CUR, SC LOAD
30	VOLTAGE, LCH BUS
31	BATT 1, 2, AND 3 ISOLATION STATUS
32	UCSD-C 4
33	15V, AUTO SPIN REG
34	15V, SPIN BU REG/ASA +10V DC
35	MIT SSC SYNC
36	MIT SSC 1
37	PRESSURE, SPIN GAS
38	TEMP, ANTENNA
39	BATT 1 SHORTED CELL MON
40	WASSC
41	CUR, SA
42	MIT SSC 2
43	MIT SSC 3
44	ASA PWR ON/ENAB
45	AGC, RCVR 2
46	HV ASA
47	PITCH COIL STATUS
48	SYNC (085)

WASSC	
1	TEMP, MAIN BATT CMPT 1
2	5V/15V SORE
3	TEMP, RIB CMPT 7/8
4	TEMP, DECK CMPT 7
5	ADA HTR ST
6	TEMP, BOTTOM COVER CMPT 4
7	SYNC 0
8	SYNC 1
9	TEMP, MAIN BATT CMPT 1
10	5V/15V SORE
11	TEMP, RIB CMPT 7/8
12	TEMP, DECK CMPT 7
13	SPARE
14	TEMP, BOTTOM COVER CMPT 4
15	SYNC 0
16	SYNC 1
17	TEMP, MAIN BATT CMPT 1
18	5V/15V SORE
19	TEMP, RIB CMPT 7/8
20	TEMP, DECK CMPT 7
21	SPARE
22	TEMP, BOTTOM COVER CMPT 4
23	SYNC 0
24	SYNC 1

SEL = SELECT  
 SEP = SEPARATION  
 SEQ = SEQUENCE  
 SHTR = SHUTTER  
 SORE = SPIN ORIENTATION AND RATE ELECTRONICS  
 SQ = SQJIB  
 SSC = SUB-SUBCOMMUTATOR (EXPERIMENT)  
 ST = STATUS  
 STG = SETTING  
 SW = SWITCH  
 SYNC = SYNCHRONIZATION  
 TEMP = TEMPERATURE  
 TMG = TIMING  
 TP = TEMPERATURE PROBE  
 TR = TAPE RECORDER  
 UCSD-C = UNIV. OF CALIF., SAN DIEGO COSMIC EXPERIMENT  
 UCSD-S = UNIV. OF CALIF., SAN DIEGO SOLAR EXPERIMENT  
 UNH = UNIV. OF NEW HAMPSHIRE EXPERIMENT  
 UPR = UPPER  
 UVS = UNDER VOLTAGE SWITCH  
 VRNR = VERNIER  
 WASC = WHEEL ANALOG SUBCOMMUTATOR

WH = WHEEL  
 WL = WHITE LIGHT  
 XMTR = TRANSMITTER  
 XR = X-RAY  
 XUV = EXTREME ULTRAVIOLET

\* = INDICATES FRAME COUNTER OVERFLOW (ADD 256 TO DSF-1)  
 \*\* = 3-BIT WORD WITH BIT 1 BEING THE MOST SIGNIFICANT

LATEST REV 6/23/71  
 CHG = CHANGE MADE



F72-01

Serial Digital Data (69 Channels)

- Logic one: 2 to 22 volts
- Logic zero:  $0 \pm 0.5$  volts
- Input impedance: 10 K ohms

Digital Data Gates

DMF

DSF

- |                          |               |                   |
|--------------------------|---------------|-------------------|
| • Logic one (gate ON):   | 3.2 $\pm$ 0.5 | 2.4 to 4.5 volts  |
| • Logic zero (gate OFF): | 0 $\pm$ 0.5   | 0 $\pm$ 0.5 volts |
| • Impedance:             | 2 K ohms      | 20 K ohms         |

The assignment of words on OSO-7 for both digital and analog channels is shown in Table 8-1. These assignments include two sampling formats, one for orbit day and one for orbit night. Format selection is controlled by the spacecraft day/nite switch. The day format includes data from pointed experiments, while the night format replaces pointed experiment data with star scanner data.

8.2.1 Digital Multiplexer and Encoder

The digital multiplexer and encoder (DME) assembly provides the following five basic functions:

- Generates telemetry master clock (800 Hz)
- Generates gate pulse signals for multiplexing digital and analog signals
- Generates sync codes for main frame and ASC subframes
- Encodes the analog data into eight-bit digital words
- Provides signal conditioning to convert the multiplexed digital data into a biphasic (Manchester) code.

Functional block diagrams of the data handling subsystem and logic diagram of the DME are shown in Figures 8-2 and 8-3, respectively.

The basic timing-signal generator is a crystal-controlled oscillator operating at 102.4 kHz. This frequency is divided down through a binary divider consisting of five flip-flops. The output of the 6.4 kHz flip-flop is fed to another binary counter in the bi-phase modulator. The 800 Hz (master clock) output of this divider provides all of the necessary timing signals in the system. The master clock is also brought out to be used as shift pulses in the experiment and spacecraft shift registers.





F72-01

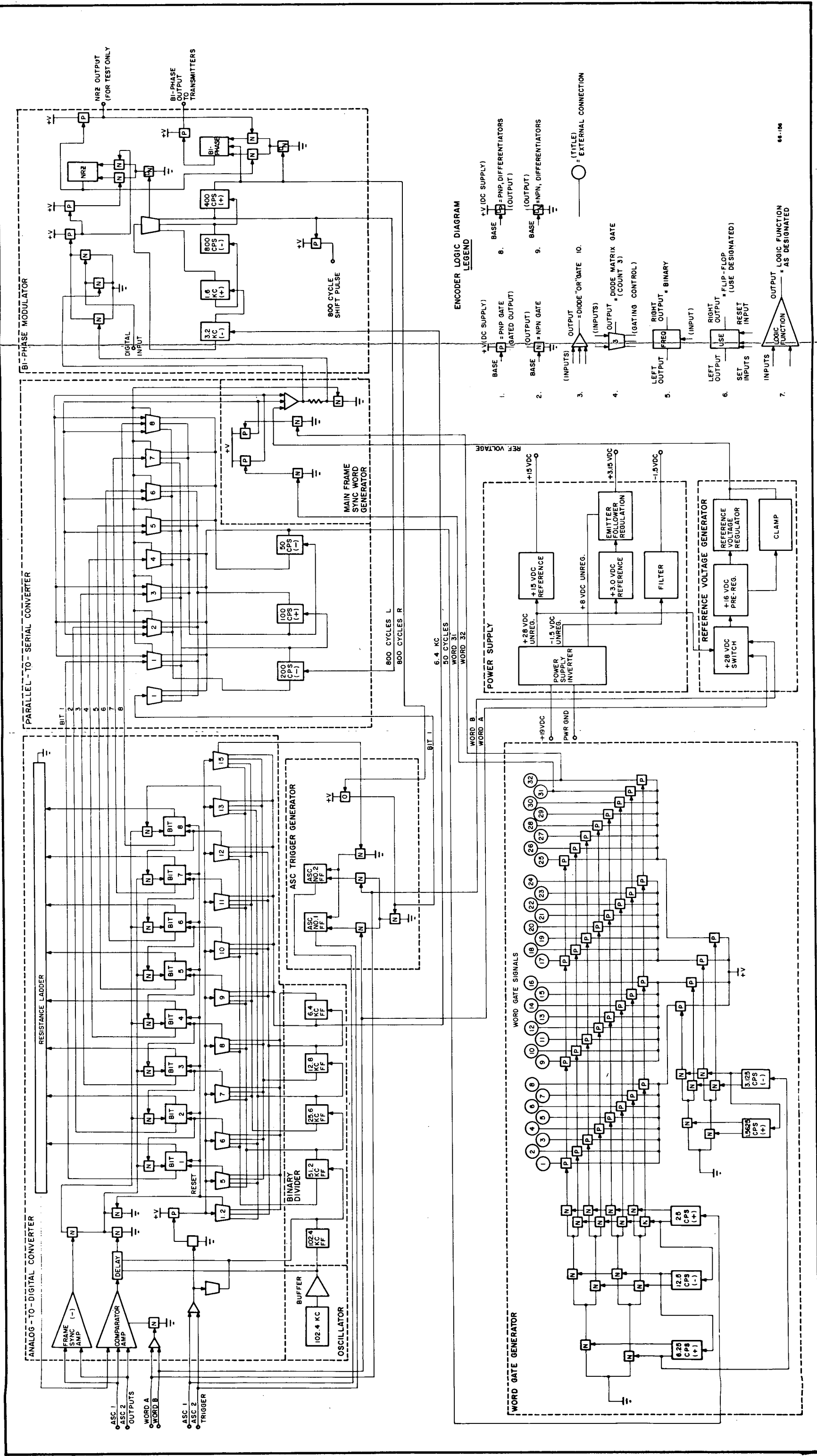


Figure 8-3 Digital Multiplexer and Encoder Logic Diagram

8-11/8-12

FOLDOUT FRAME 2

FOLDOUT FRAME

66-106





F72-01

The main-frame word-gate signals are generated by the word-gate generator consisting of a matrix of AND gates. This circuit is essentially a sequential pulse generator that produces 32 sequential pulses. The timing is such that each pulse is one word-length in duration (10 msec). These 32 pulses are referred to as "word gates". Word gates 31 and 32 are connected internally to the main frame sync-code-generation circuits. During the time of word 31 and 32, a pseudo-random code, "00011110/10110010" (which corresponds to a count of 30 and 178 respectively), is multiplexed into the output for main-frame identification and ground equipment synchronization.

Twenty-eight of the remaining word gates are routed outside the DME to the PCM junction box patch panel where they are interconnected to make up the desired multiplex format for the wheel and pointed experiments and the Digital Sub-Multiplexer (DSM). Two of the word gates are connected back into the DME at the inputs designated "word A" and "word B" for generation of the analog subcommutator timing signals. These two inputs activate trigger generation circuitry that develops two gates, 156  $\mu$ sec wide. These gates are routed outside the DME as ASC-1 trigger and ASC-2 trigger.

The "word A" and "word B" inputs also operate a power switch that applies power to the analog-to-digital converter (ADC) portion of the DME. Although the circuitry required to do the analog-to-digital conversion takes appreciable power, a significant power savings is accomplished by switching the ADC on only when it is required to operate. (See Figure 8-4 for the DME timing diagram.)

The redundant PCM junction boxes also provide gate pulses to the DSM to generate the 48 DSM words, and to the individual experiment instruments to shift out their data at the proper time.

Analog-to-Digital Encoding. The analog-to-digital encoding is accomplished by a successive-approximation method. The analog input from each ASC is fed to a comparator in the DME where it is compared against a series of reference voltages and the result of each comparison is stored in a flip-flop. For example, during the first comparison interval, a voltage is applied to the resistance ladder network to develop a one-half-scale voltage reference at the comparator. When the input voltage is more than half scale, a "one" will be set into the first flip-flop and if it is less than half scale, a "zero" is set into the first flip-flop. During the second comparison interval a voltage is applied to the resistance ladder network to develop a one-quarter-scale reference voltage. If a "one" is set into the first storage flip-flop during the first interval, the half-scale reference will remain and is added to the one-quarter-scale reference. If a "zero" is set, only the one-quarter-scale reference will be retained.

The result of the second comparison is then set into the second storage flip-flop. This process continues through eight successive comparisons, in each of which the reference voltage is changed by one-half of its previous incremental change. During the last comparison, the reference voltage will have a difference from the input voltage within one part in 256 of the full-scale voltage and a binary code equivalent of the analog input will thus be stored in the eight AND gates. The complete encoding process takes place during each sample interval of the analog subcommutator, which is approximately 156  $\mu$ sec.



F72-01

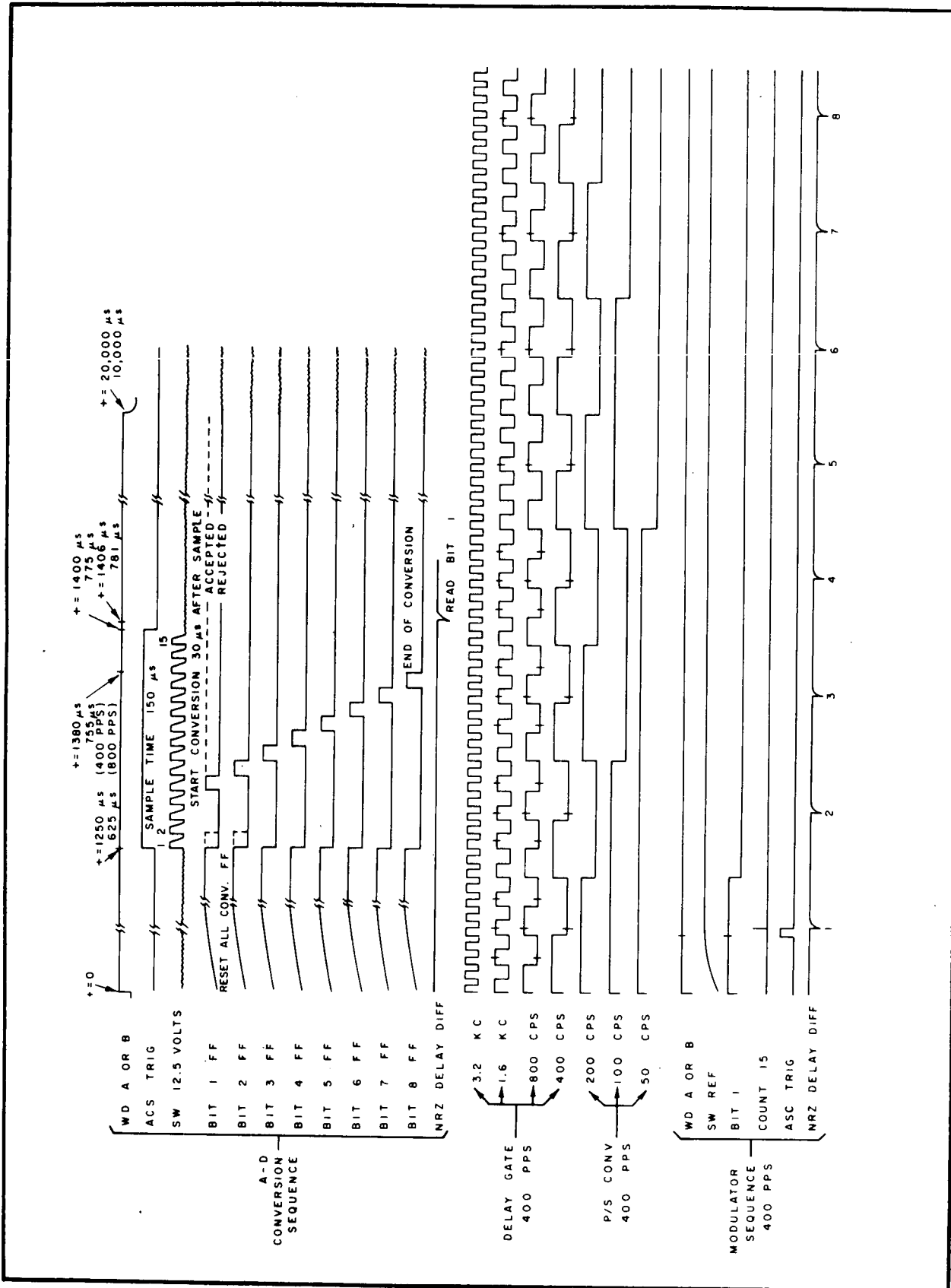


Figure 8-4 DME Timing Chart



F72-01

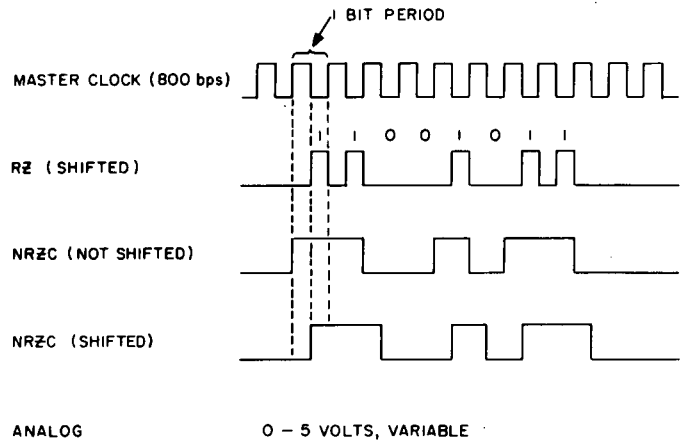
The output of each of the flip-flop storage units is applied to the eight AND gates. These AND gates are then sequentially enabled at the 800-Hz bit rate, and the output is a serial pulse train of eight bits which represents the coded analog signal for that particular ASC channel. These serial data are then applied through OR logic, where they are time-multiplexed with the digital data from the experiments and DSM. The complete data train is then applied to the biphase modulator to develop the Biphase coded output signal.

Input and Output Data Formats. The DME will accept four types of data formats:

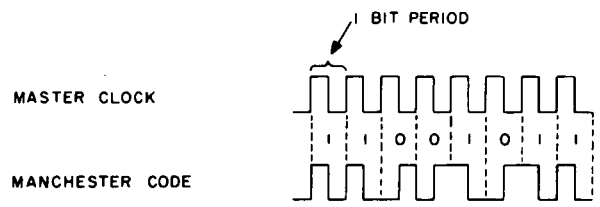
- 0 to 5 v analog
- RZ (shifted)
- NRZC (not shifted)
- NRZC (shifted).

In the RZ (return-to-zero) format, the presence of a bit signifies a binary "one" and the absence of a bit signifies a zero. In the NRZC (non-return-to-zero, change) format, the data train changes state for every change in binary value. The timing relationships of these formats and the biphase (Manchester) format are as illustrated:

DME INPUT TIMING



DME OUTPUT





F72-01

ASC Sync-Code Generation. The input from the sail or wheel ASC is a positive-going pulse (ASC channel 48 only), rather than the normal negative-going pulse. It is detected by the frame sync amplifier in the DME, the normal action of the ADC is inhibited, and a "one" is set into every other storage flip-flop. This alternate "one-zero" code is the synchronization code for the subcommutator, and is read out as encoded data with a count value of 085. The value 085 is unique in that all other ASC channels are inhibited from having this count.

Main Frame Sync Generation. Main frame synchronization is determined by noting that the proper number of main frame words exist between the main frame sync words. These words consist of words 31 and 32 into which a 16-bit pseudo-random code of 30/178 is inserted.

The main-frame sync code is generated by applying pulses to the appropriate AND gates that are used for sampling the encoder storage units. This process of sequentially enabling these AND gates during main-frame words 31 and 32 generates the synchronization (or ID) code.

ASC Synchronization. The wheel and sail ASCs are mutually synchronized within the 32-word main frame by using the unique sync code contained in the 48th word of each ASC. This synchronization is accomplished automatically by circuitry in the DME in the following manner:

The sync circuits in the DME expect to see both of the ASC sync words at their assigned times within the ASC subframe. The sail ASC sync word is used as the synchronization reference, or "master", and the wheel ASC is "slaved" to this reference.

The presence of the sail sync word and the absence of the wheel sync word in the same main frame results in a synchronization error decision by the sync circuits in the DME. The sync circuits then generate trigger pulses at 1,024 times the normal ASC trigger rate. These trigger pulses are used to advance the wheel ASC during main-frame words 31 and 32 until the wheel ASC sync word appears. The wheel ASC is then mutually synchronized with the sail ASC again. Since the ASC sync words are assigned to channel 48, the next time the ASC's are read out, channel one will be present because the ASC's will have been recycled.

External Digital Multiplexing. External digital signals (experiment prime data) are time-multiplexed in the PCM junction boxes and are fed to the DME's in serial form. These data are then multiplexed with the converted analog data by OR logic circuits, and converted to biphasic PCM code.

DME Redundancy. Except for some of the logic in the analog-to-digital converter, all circuitry within the DME is quad-redundant. That is, each logic function is both series and parallel redundant and multiple component failures must occur before the logic function fails. Assembly failures caused by component failures are greatly reduced by this design, but at the sacrifice of some simplicity in fabrication.



F72-01

### 8.2.2 Analog Subcommutator

The purpose of the wheel and sail analog subcommutators (ASC-1 and ASC-2) is to time-multiplex 47 wheel and sail analog input signals varying in amplitude from zero to +5 v and to provide an ID synchronization signal (word 48) to facilitate data reduction. A block diagram of the ASC is shown in Figure 8-5 and a logic diagram in Figure 8-6.

The input timing signal consists of the ASC trigger pulse from the DME. This trigger is applied to a divide-by-48 counter that recycles at the end of 48 counts. The counter consists of binary stages two through seven on the logic diagram. A seventh binary (number one on the logic diagram) is triggered "on" by the leading edge of the trigger pulse and "off" by the trailing edge of the trigger pulse. (See Figure 8-7 for ASC timing chart.)

The outputs of each stage of the binary counter are applied to decoding gates that are interconnected to form two matrices. One matrix has an eight-line output and the other has a six-line output. Each line of the eight-line matrix is connected to six analog gates, which are referred to as first tier gates, and each line of the six-line matrix is connected to a single analog gate which is referred to as a second tier gate.

The second tier gates sequence at one-eighth the rate of the first tier gates and, therefore, only one input is connected to the output at any one time.

The type of analog gate used is characterized by high input impedance in the "off" condition and very low impedance in the "on" condition. The input impedance in the "on" condition is essentially the input impedance (100 K ohm) of the buffer amplifier which provides impedance matching. As shown in the logic diagram, there are six groups of eight analog gates where the outputs of each group are connected. The six common lines are then connected through the second tier analog gates. The second tier gates sequence at one-eighth the rate of the first tier gates and, therefore, only one input is connected to the output at any one time.

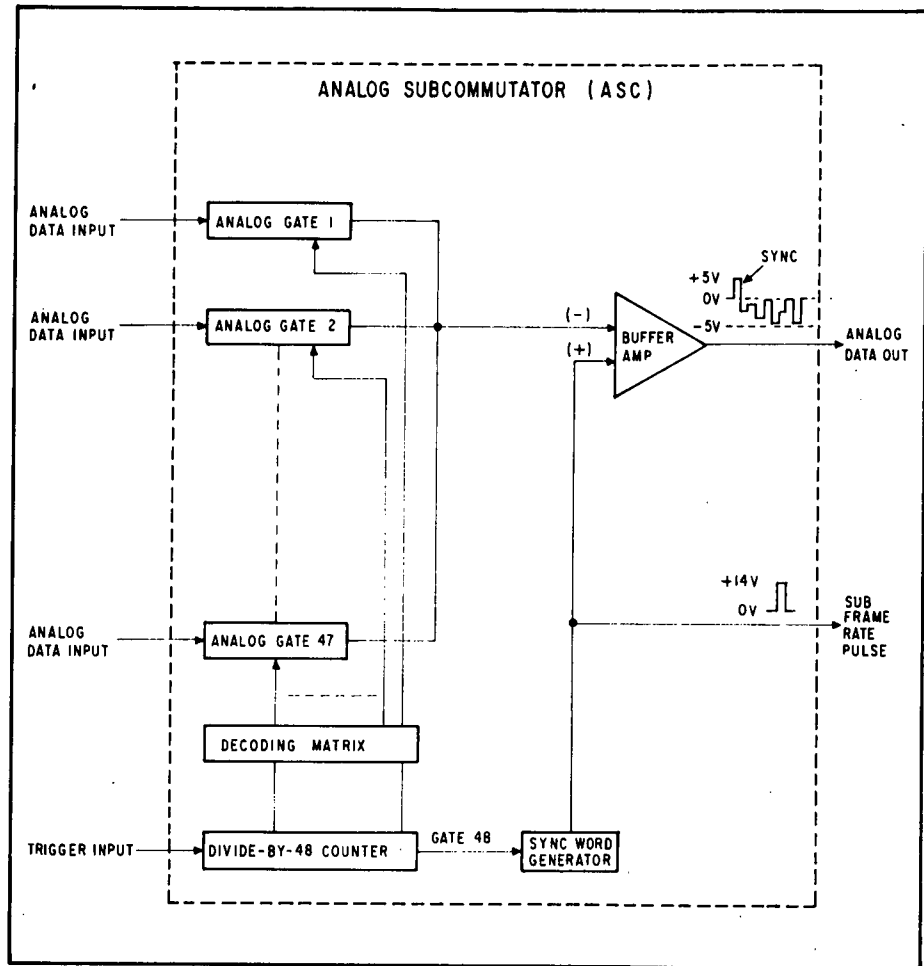


Figure 8-5 ASC Functional Block Diagram



F72-01

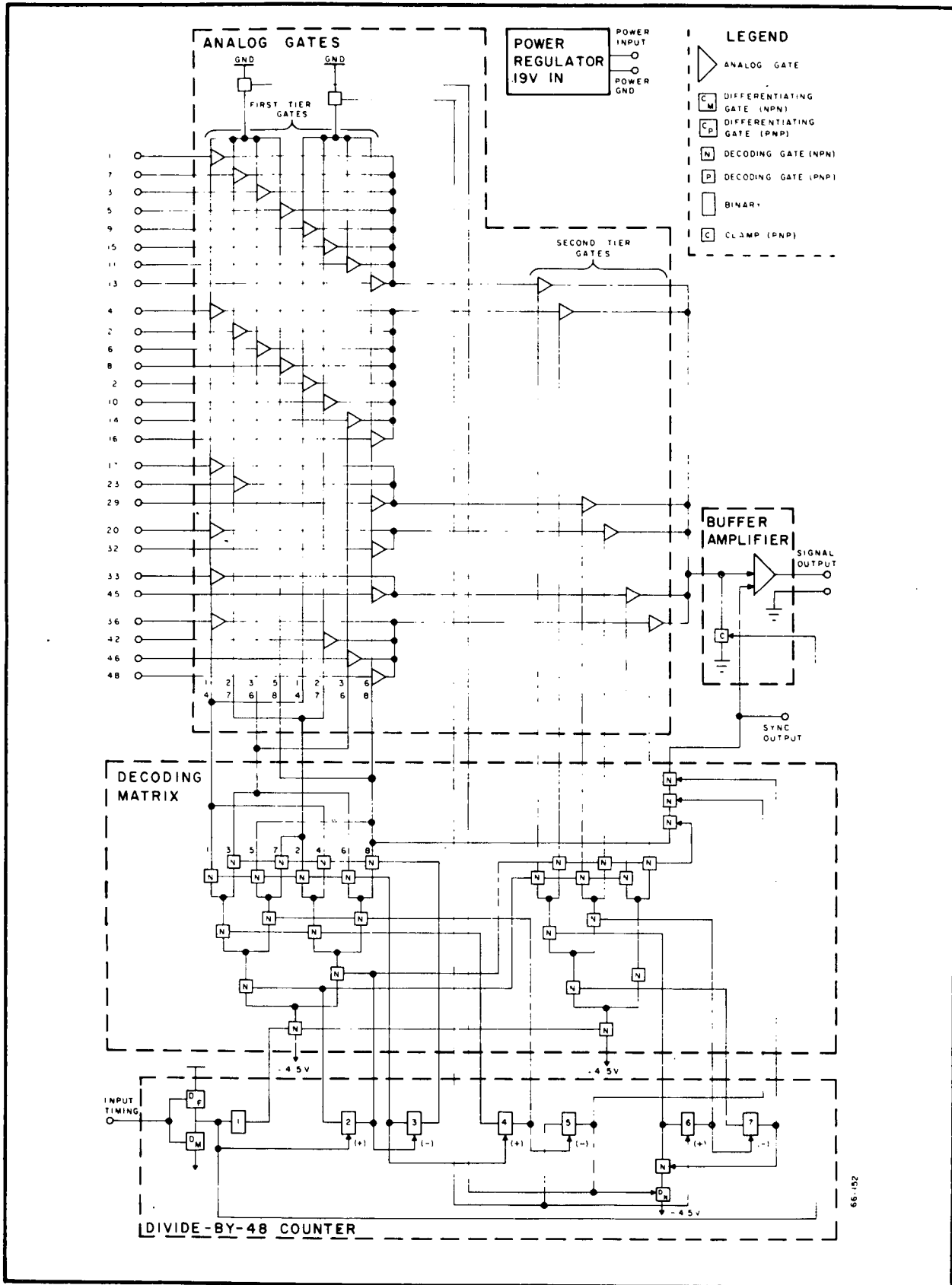


Figure 8-6 Analog Subcommutator Logic Diagram



F72-01

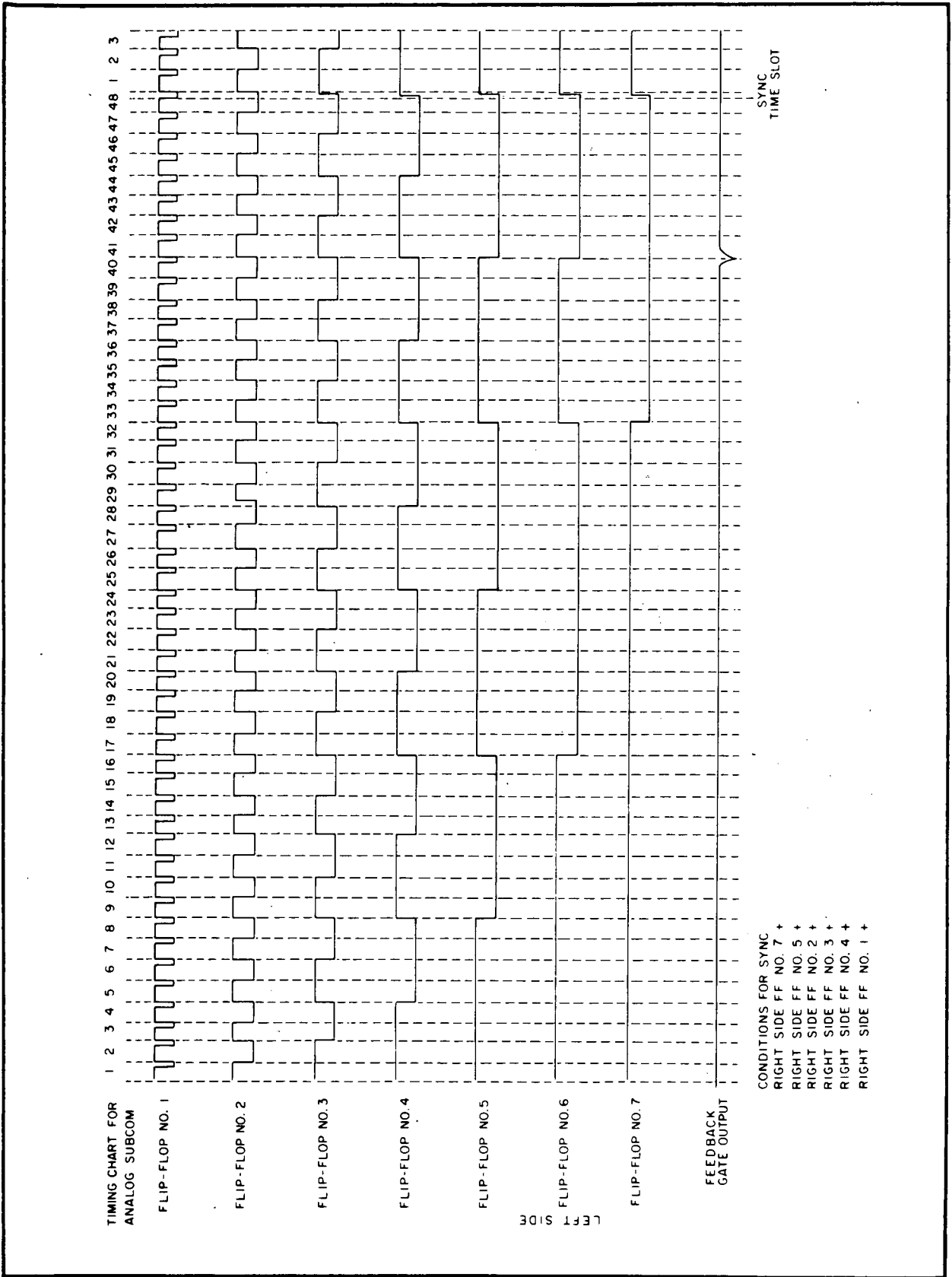


Figure 8-7 ASC Timing Chart



F72-01

The common connection of the second tier gates is connected to a buffer amplifier. The purpose of the buffer amplifier is to provide a constant input impedance for all channels and provide a low output impedance for the signal going to the encoder in the DME. The buffer also inverts the input signal and inserts a dc reference of +8 volts. The output signal is a negative-going pulse that is amplitude modulated over a range of five volts, and has a zero reference of +8 volts.

When the binary counter reaches the forty-eighth count, it activates logic circuitry which applies a negative voltage to the input of the buffer. Since the buffer inverts, this results in a positive-going pulse being generated for the forty-eighth channel as a sync pulse.

As in the DME, the ASC uses quad-redundant circuits except for the analog gates. The packaging technique is much the same as the DME except that the printed circuit cards are smaller.

### 8.2.3 Analog Sub-Subcommutators

The analog sub-subcommutators (ASSC) are capable of time multiplexing 24 analog signals onto a common output line; their purpose is to increase telemetry channel capacity of the sail and wheel ASC's. The output of each sail ASSC is fed into a channel of the sail ASC and the output of the wheel ASSC is fed into a channel of the wheel ASC. The ASSC's are advanced one channel per ASC subframe.

Each ASSC consists of a buffer amplifier, five flip-flops, a diode matrix, and 24 analog switches (Figure 8-8). The subframe rate pulse from the controlling ASC is fed into the buffer amplifier, which isolates the internal flip-flops from the external data handling system. The output of the buffer amplifier drives the first flip-flop in the count-down circuit. The five flip-flops are connected in a conventional ripple-through counter arrangement with feedback from the fifth to fourth stage that causes the counter to recycle at the count of 24. The outputs from the flip-flops sequentially turn on the analog switches via the diode matrix. The analog switch that is turned on couples the input signal to the common output line with a minimum of signal loss. The input of each switch has an overvoltage protection circuit to prevent an overvoltage condition on any input channel from interfering with the operation of the remaining channels. The sail ASSC sync is generated by applying 0 and 5 volt signals to the inputs of channels 23 and 24, respectively. The wheel ASSC sync is generated the same way but appears in channels 7, 8, 15, 16, 23 and 24. The sail ASSC's are synchronized as described in paragraph 8.2.7.

The analog switches use field effect transistors and have the advantages of simple control circuits, no offset voltage, and excellent long-term stability since small changes in the FET parameters are not critical to the switch operation.





F72-01

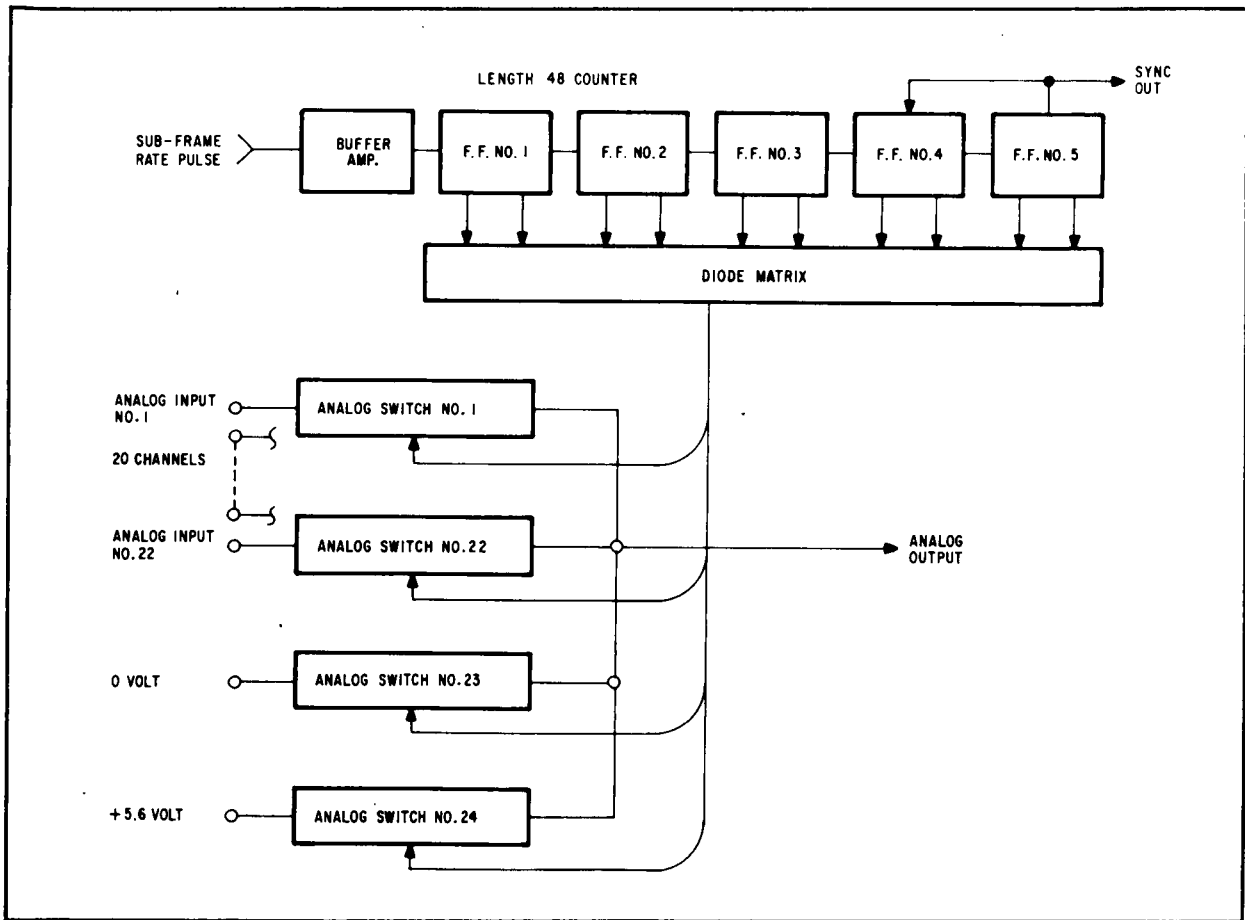


Figure 8-8 ASC Block Diagram

The ASSC's on OSO-7 have been modified to meet colder back sail temperature requirements. The acceptance level temperature range is now  $-35^{\circ}\text{C}$  to  $+35^{\circ}\text{C}$ , while the temperature range on OSO-6 was  $15^{\circ}$  warmer ( $-20^{\circ}\text{C}$  to  $+50^{\circ}\text{C}$ ). Thus, the following modifications were made:

- The 15-volt regulator zener current was doubled, and the zeners were screened to select high voltage units.
- The FET analog switch was changed from a 2N3378 to a 2N5114. This new FET has a lower pinch-off voltage ( $V_p$ ) and lower saturation resistance ( $R_{DS}$ ).
- The switching transistors used in the length 48 counter design were screened to select high beta units.



F72-01

#### 8.2.4 PCM Junction Box

The purpose of the redundant PCM junction-boxes is to provide interconnection and distribution of all data-handling timing signals, provide buffering and conditioning of these signals for proper interface with other data handling equipment, and provide buffering and gating of main frame data. A functional diagram of the PCM junction-box is shown in Figure 8-9.

Format Assignments. All of the word gate signals (generated by the DME) are routed into the junction-boxes where they are interconnected according to the channel assignments for day or night operation. Figures 8-9 and 8-10 show that isolators No. 10 and 11 operate from day power while the remaining isolators operate from launch power. At night, isolators No. 1 and 11 are turned off. These channels are used for aspect sensor assembly data. To ensure proper loading of the DME output circuits, each word gate is applied across a 1 K-ohm load resistor and isolation is provided by a 2 K-ohm series resistor.

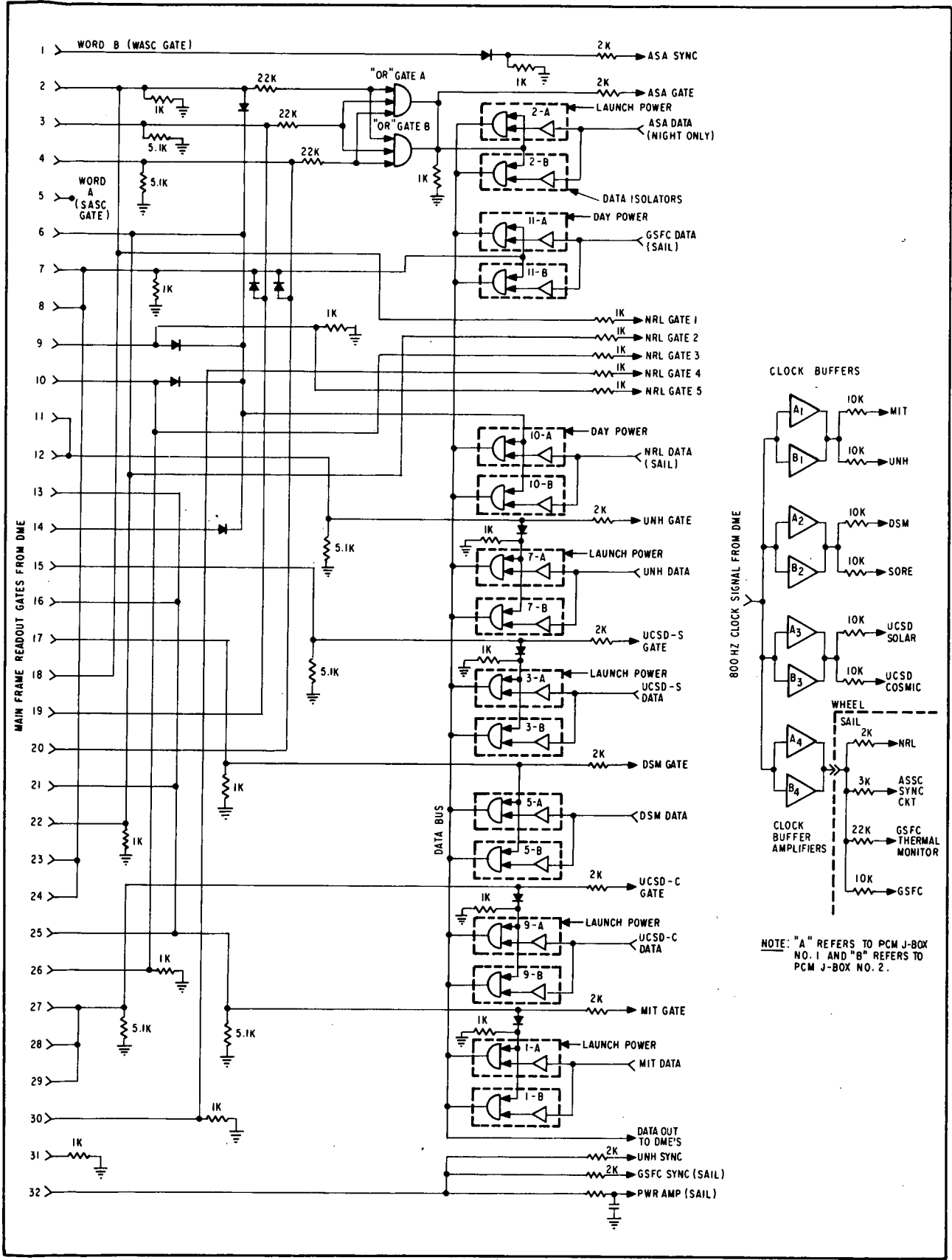
Master Clock Buffer Amplifiers. The 800 Hz master clock is routed from the DME to the junction-boxes where it is distributed to the experiments and other spacecraft assemblies requiring this signal. To prevent loading by one user which might affect the signal characteristics, and to improve overall reliability, the clock signal is routed through parallel buffer amplifiers. Each buffer amplifier is capable of supplying signals to four separate users in such a way that a short circuit can occur on the external signal line without affecting the signal characteristics for the other users. This is accomplished by providing a low output impedance at the amplifier and inserting series isolation resistors in each line.

Data Isolators. Due to the possibility of a circuit failure in one experiment affecting another, all digital data signals are buffered and isolated in the PCM junction-boxes before they are multiplexed. Buffering between the data sources and the data handling equipment is accomplished by connecting each digital data line to a simple buffer amplifier which also provides a compatible interface (such as, impedance matching, gain, etc.) for each data source. The output of each of these amplifiers is connected to a diode AND gate which is enabled by the word gates assigned to the particular data source. Finally, the outputs of the AND gates are connected to a common line which is the signal line to the DME. The spacecraft housekeeping and experiment data from the DSM are gated (multiplexed) by data isolator No. 5 onto the junction-box output data line.

PCM Junction-Box Redundancy. Two PCM junction-boxes have been interconnected on OSO-7 for redundant operation, as shown in Figures 8-1 and 8-10. The operating J-Box is selected by an external power switching relay. Also, both power and ground lines are switched to the clock buffers and Aspect Sensor Assembly (ASA) "OR" gates to protect against grounding failure modes.



F72-01



NOTE: "A" REFERS TO PCM J-BOX NO. 1 AND "B" REFERS TO PCM J-BOX NO. 2.

Figure 8-9 PCM Junction Box Functional Block Diagram



F72-01

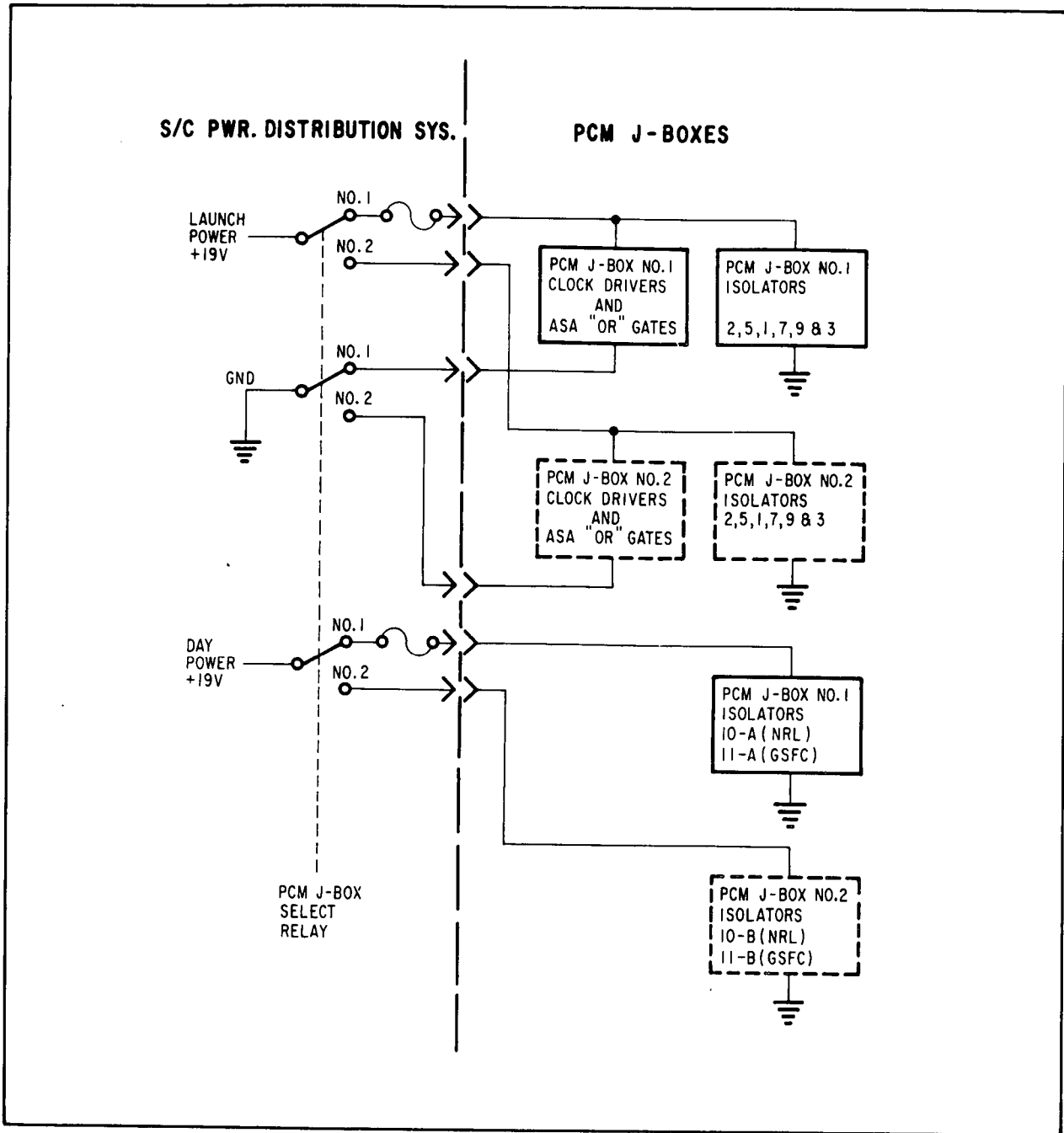


Figure 8-10 PCM Junction Box Power Switching

8.2.6 Digital Submultiplexer and Frame Counter

The digital submultiplexer and frame counter (DSM/FC) performs the following functions:

- Generates sequential gate pulses for readout of digital data.
- Stores and updates a count of the number of digital subframes for a time reference.



F72-01

- Provides a readout of the frame count into the main multiplexer.
- Generates the digital subframe sync code.

Digital Submultiplexer. A functional block diagram of the DSM is shown in Figure 8-11. The synchronization of the DSM is provided by a gate signal from the DME which occurs once per main frame. This signal drives a divide-by-48 counter which establishes the subframe length. A diode matrix then generates 48 sequential gate pulses that are displaced in time from each other by one main frame. These gate signals can be used in the same manner as gate signals from the DME to readout data from external shift registers. Data from external registers are read out directly to the PCM junction-box. Some of these gates are connected internally for readout of the internal shift register. The internal shift register data include all single bit, sync code, and frame count data.

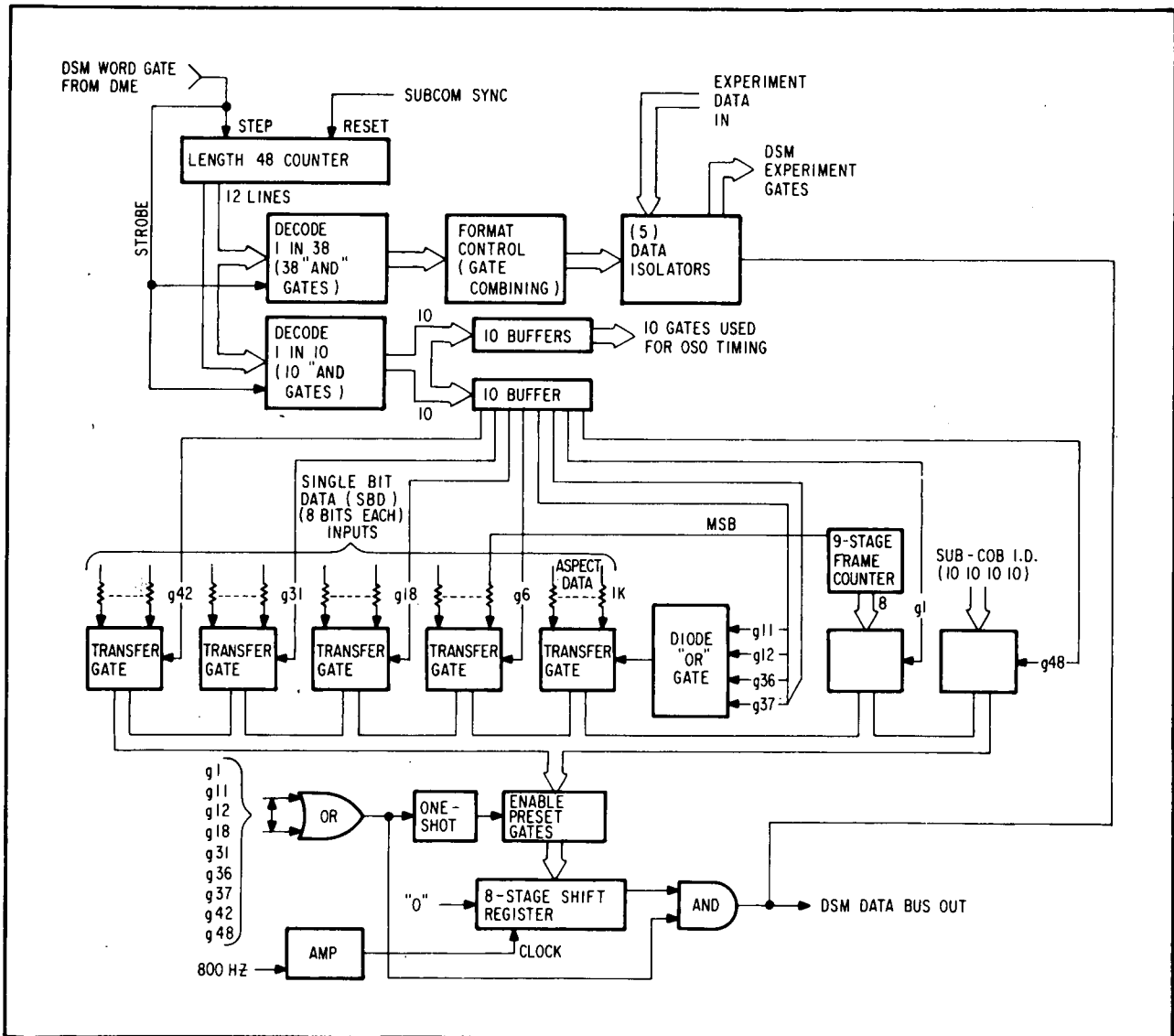


Figure 8-11 Frame Counter and Digital Submultiplexer Functional Block Diagram



F72-01

The 800-Hz master clock is used to transfer the shift register data onto the DSM data bus. Another set of transfer gates is used to transfer a fixed sync code word (085) into the shift register at the beginning of the subframe. The sync code is then shifted into the main multiplex by the 800-Hz clock. Also, transfer gates in the DSM transfer parallel digital data from external sources into the internal shift register.

Frame Counter. A signal from the divide-by-48 counter goes into a nine-stage counter which accumulates a count of the subframes. Transfer gates connected between the eight stages of the counter and the internal shift register are actuated by a selected gate signal to transfer the accumulated frame count into the shift register for readout into the main multiplex. The most significant bit of the 9-stage frame count is read out on a separate single-bit channel. This frame count provides a means of determining time correlation of the playback data over a continuous period of 131 minutes.

Correlation of frame count to time of day is accomplished by:

- Allowing 8 or 10 realtime major frames (about 2 minutes) to elapse and verify sync before playback is commanded (done every orbit).
- The data reduction computer will record a realtime frame count and correlate it with the time of day.
- Playback is then sent, with time correlation established for the playback data.

#### 8.2.7 Tape Recorder/Reproducer

Data collected when the satellite is out of range of ground receiving stations are stored by two redundant magnetic tape recorders. The tape recorders then playback the stored data, upon command, when the satellite is within range of ground stations. The location of ground stations used for OSO establishes the nominal requirement that data be stored for a complete orbit (about 96 minutes). The nominal time required for playback over a ground station is about 6 minutes. This is accomplished with an 18-to-1 playback-to-record ratio and allows ample time on either side of the playback to avoid the marginal transmitting conditions when the satellite is near either horizon.

The OSO-7 magnetic tape recorder uses a continuous loop of magnetic tape to record the biphase signal from the DME. Data are recorded at a rate of 800 bps and are played back at a rate of 14,000 bps. The tape capacity of the recorder is about 324 feet (an increase of about 24 feet over the OSO-6 recorder). At a bit packing density of 1,333 bits per inch, the recorders will store 108 (+1, -2) minutes of data. The OSO-7 tape recorders, like the OSO-6 recorders, use single track recording techniques and are belt driven. The playback timer and the drive electronics are driven by an internally contained clock which is synchronized to the telemetry clock. The tape is erased during playback.



F72-01

Operation. A functional block diagram of the tape recorder/reproducer is shown in Figure 8-12. The biphas data from the DME is amplified and differentiated to produce positive and negative spikes. These spikes are fed to a flip-flop that serves as the record-head driver. The negative pulses are fed to one winding of the record head while the positive pulses are fed to the other winding. The pulses drive the record windings in push-pull so that the tape is driven into saturation in either of two directions.

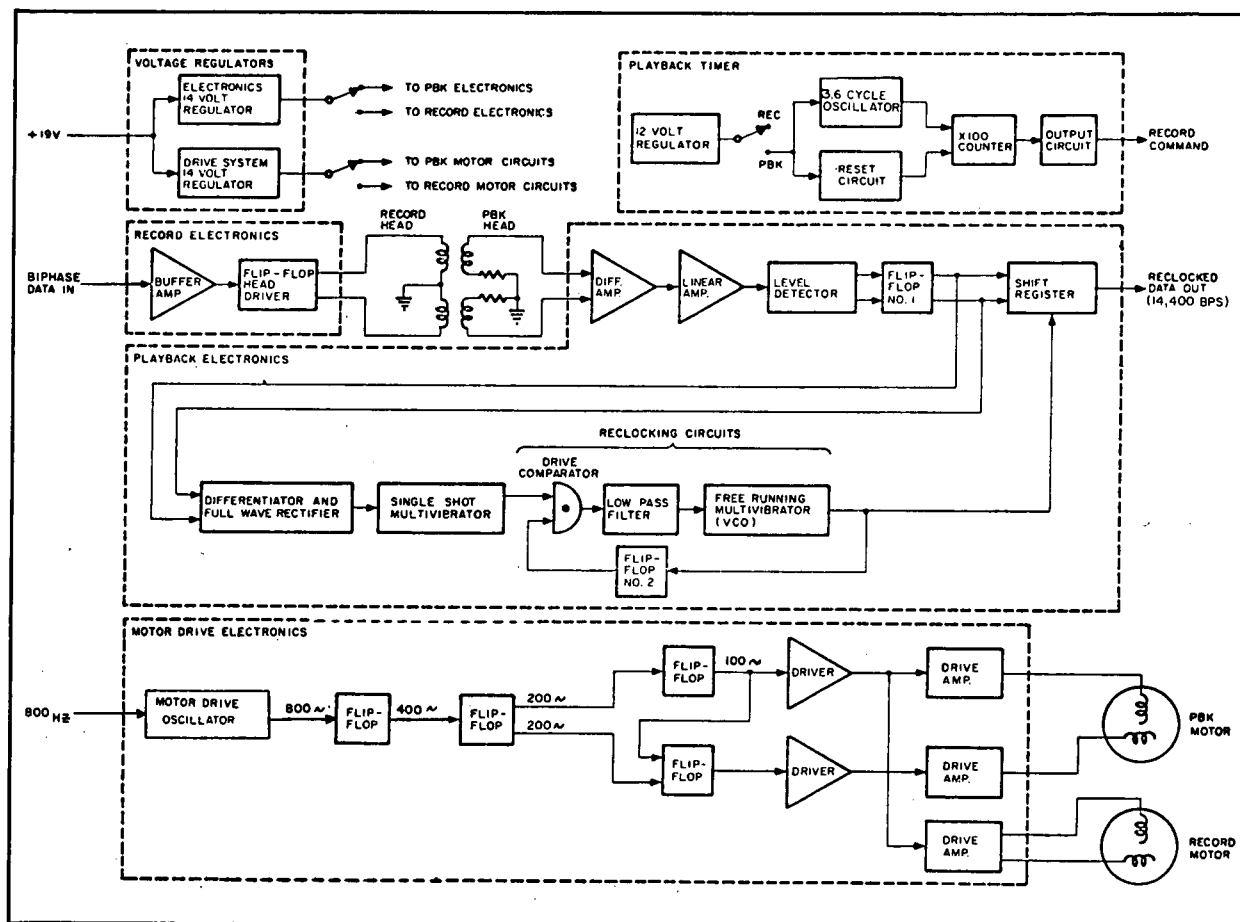


Figure 8-12 Tape Recorder Block Diagram

In the playback mode, the two windings of the playback head develop a pulse that is rounded off and is an approximation of the recorded signal. The playback signal is amplified and clipped by two amplifiers and a level detector. The two squared pulses are then differentiated and are applied to the input of flip-flop No. 1 (FF1). The output of FF1 is the same as the input signal to the recorder, but increased in frequency by the 18-to-1 ratio (reproduce/record speed), is modulated by wow and flutter, and has minor distortion caused by the detection electronics. The signal distortion manifests itself in phase and frequency modulation of the signal and is referred to as jitter.



F72-01

To correct for some of the jitter components, the playback signal is reconditioned by the reclocking circuits. These circuits compare the phase of the flip-flop output with a reference signal obtained from a voltage-controlled oscillator (VCO). The phase difference is then detected and this error signal is filtered and applied to the VCO. The error signal then changes the reference frequency until no error is detected. The filter does not allow high-frequency changes to reach the VCO. Thus, the reference signal is controlled by the average frequency out of FF2. The ac signal from the VCO is used to clock the flip-flop No. 1 output into a one-stage shift register. The output of the shift register then has the same frequency as the FF1 output, with high-frequency jitter components reduced.

Any low-frequency changes (wow) in the playback signal are due mainly to the motors that drive the tape. Thus, very stable synchronous motors are used and are controlled by the 800-Hz telemetry clock to assure stable operating speed. The 800-Hz clock is divided down to 100 Hz in flip-flops and applied to the motor-driver amplifiers. Both motors run at the same speed and drive power is applied to the capstan by a system of pulleys and Mylar belts. Only one motor has power applied to it at any one time. The playback drive mechanism produces a tape speed that is 18 times the record speed.

Tape Recorder Playback Timer. The playback time is governed by a timer in each tape recorder. This timer generates a control pulse at the end of a preset time period which terminates playback and switches the tape recorders back to the record mode.

When a playback command is received, a latching relay is actuated, applying power to an oscillator. This oscillator consists of a unijunction transistor and an RC timing network which establishes the oscillator period of about 3.6 seconds per cycle. The oscillator output is connected to a magnetic counter with a capacity of 100 counts. When power is first applied to the oscillator, the counter is not reset and thus it is important to allow the timer to time-out after each playback command to assure that it starts at the zero state.

After the counter receives 100 counts, (corresponding to  $3.6 \text{ seconds} \times 100 \times 1/60 = 6 \text{ minutes}$ ), it produces an output pulse which triggers a capacitor discharge in the output circuit. The capacitor discharge generates a timer output that switches the recorder back to the record mode, and disconnects power from the oscillator.

The timer is designed to minimize frequency variations over the environmental extremes, assuring that the entire tape will be reproduced under all temperature conditions.

Recorder/Transmitter Interface Circuit. The tape recorders provide a low impedance interface circuit for playback data, with diode isolation. This circuit assures fast rise and fall times and waveform symmetry at the transmitter modulation terminals. Diode isolation permits a direct connection between the two playback signals.





F72-01

Automatic Playback Feature. An automatic playback selection circuit (Figure 8-13) has been added on OSO-7 to simplify tape recorder orbital operation. This circuit automatically selects for playback the tape recorder that was last recording, by sending two commands: "TR1 & 2 Pwr ON" (WH-01) and "Pbk. Auto/Auto Mode Sel." (WH-18). Command WH-01 applies power to both recorders (it is assumed that one recorder was already recording; therefore, this command merely causes the recorder that was off to start recording) and command WH-18 causes the recorder that was on to be played back.

Series Recording. Automatic series operation of the two recorders has been added on OSO-7 (Figure 8-13). This provides data storage capacity for two orbits without ground station commands. In this mode, one recorder operates for 103 minutes during the first orbit, then a timer turns the other recorder on and 15 seconds later turns the first recorder off, providing a 15-second recording overlap. The timer functional diagram is shown in Figure 8-14. It counts the telemetry major frame sync pulses which occur at 15.36 second intervals. The time count is started on receipt of the timer power ON command (WE44). Timer output pulse T1 occurs at 103 minutes, followed 15.36 seconds later by pulse T2. T1 is applied to the power-on circuit of both recorders, starting the idle recorder. T2 is applied 15.36 seconds later to turn off the "filled" recorder. Thus, the total record time is 103 + 108 = 211 minutes. The total playback time is 2 x 6 = 12 minutes.

Tape Recorder Command Functions. The tape recorder command functions are:

<u>Command</u>	<u>Cmmd. No.</u>	<u>Function</u>
TR1 Pwr OFF/Pbk Sel 2	WH-02	<ol style="list-style-type: none"> <li>1. Turns off TR1.</li> <li>2. Selects TR2 for auto playback (i.e., "Pbk Auto" command will be routed to TR2).</li> </ol>
TR2 Pwr OFF/Pbk Sel 1	WH-03	<ol style="list-style-type: none"> <li>1. Turns off TR2.</li> <li>2. Selects TR1 for auto playback (i.e., "Pbk Auto" command will be routed to TR1).</li> </ol>
TR1 ON/Pbk Sel 1/Series Record Timer Enable	HE-36	<ol style="list-style-type: none"> <li>1. Turns on TR1 (in record mode).</li> <li>2. Selects TR1 for auto playback.</li> </ol>
TR2 ON/Pbk Sel 2/Series Record Timer Enable	HE-37	<ol style="list-style-type: none"> <li>1. Turns on TR2 (in record mode).</li> <li>2. Selects TR2 for auto playback.</li> </ol>
TR1 Pbk/Man Mode Sel	WH-04	<ol style="list-style-type: none"> <li>1. Inhibits auto playback function.</li> <li>2. Places TR1 in playback mode.</li> <li>3. Inputs TR playback data to transmitters.</li> <li>4. Enables "T<sub>2</sub>" signal from record timer to turn-off TR2.</li> </ol>
TR2 Pbk/Man Mode Sel	WH-05	<ol style="list-style-type: none"> <li>1. Inhibits auto playback mode.</li> <li>2. Places TR2 in playback mode.</li> <li>3. Inputs TR playback data to transmitters.</li> <li>4. Enables "T<sub>2</sub>" signal from record timer to turn off TR1.</li> </ol>



F72-01

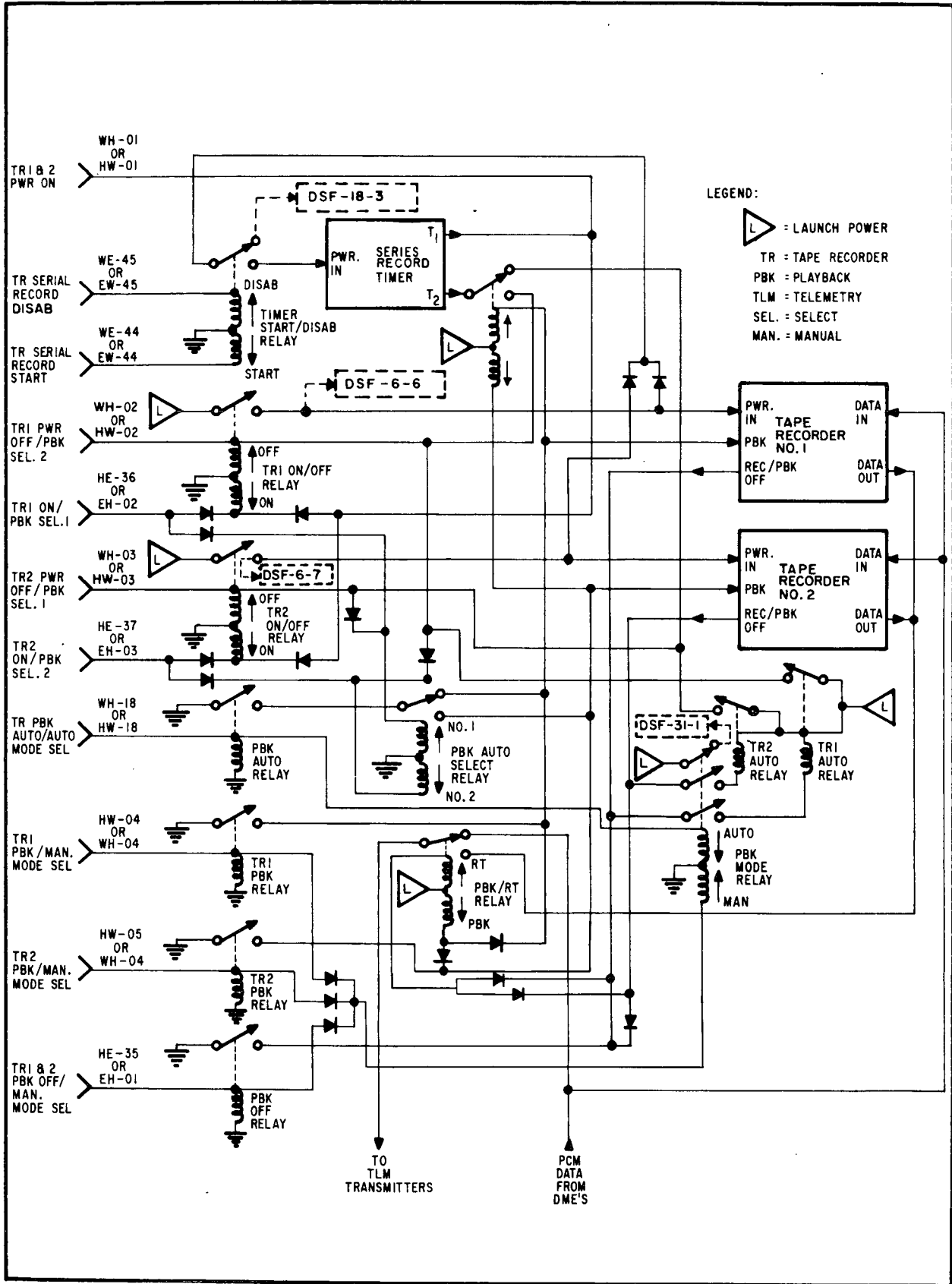


Figure 8-13 Tape Recorder Switching Diagram

C-3



F72-01

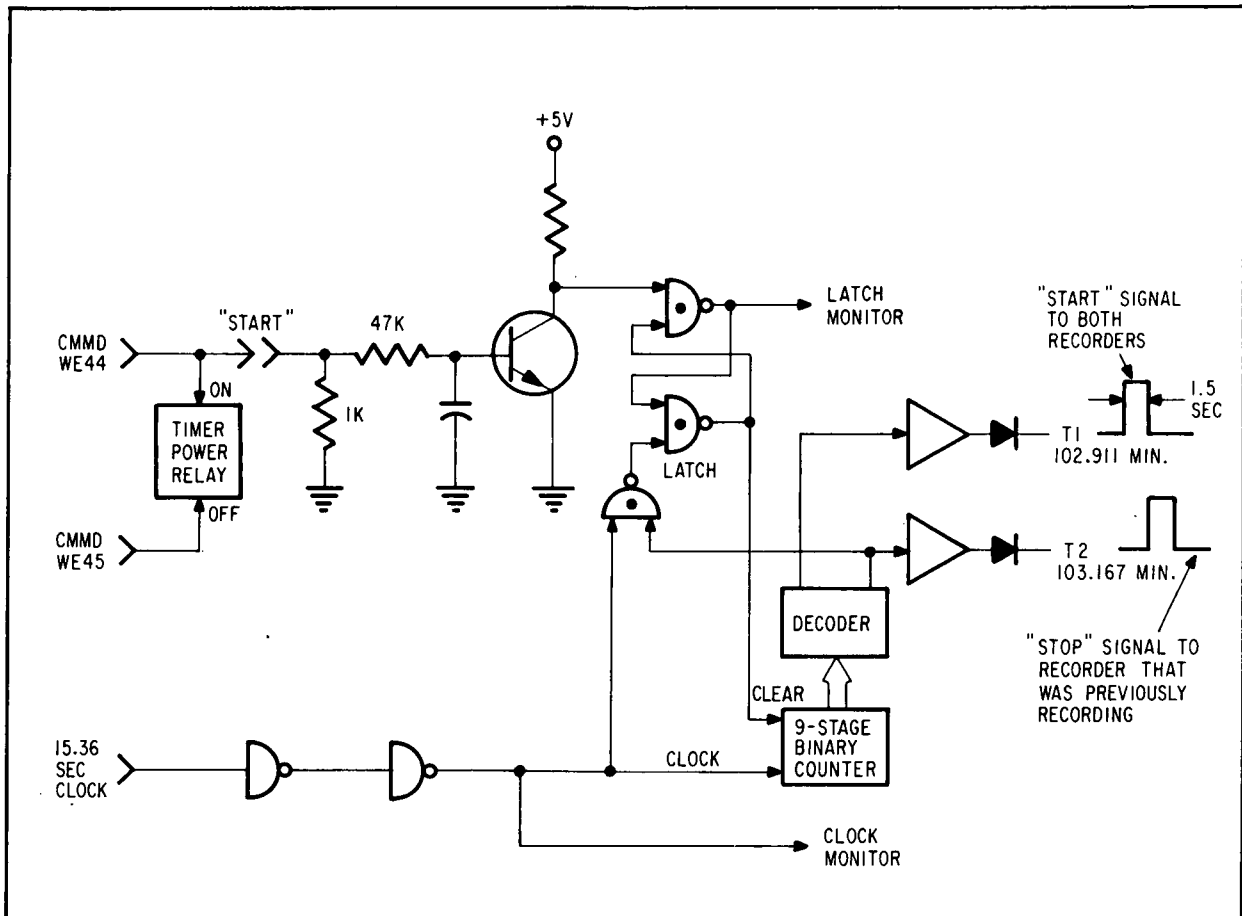


Figure 8-14 Tape Recorder Timer

Command	Cmmd. No.	Function
TR1 & 2 Pwr ON	*WH-01	1. Turns TR1 and TR2 on (in record mode).
Pbk Auto/Auto Mode Sel	*WH-18	1. Places TR1 in playback mode and enables "T <sub>2</sub> " of series record timer to turn off TR2 if "auto pbk" relay is in "No. 1" position.
Pbk OFF signal from TR1	This is not a command; it is a ground signal from the TR internal timer)	<ol style="list-style-type: none"> <li>If auto pbk mode is selected: <ul style="list-style-type: none"> <li>• Turns TR1 OFF</li> <li>• Selects TR2 for auto pbk the next time an "auto pbk" cmmd is sent.</li> <li>• Inputs DME output (realtime data) to transmitters.</li> </ul> </li> <li>If man. pbk mode is selected: <ul style="list-style-type: none"> <li>• Inputs DME output to transmitters.</li> </ul> </li> </ol>

\*These are the only commands normally needed for in-orbit operation.



F72-01

<u>Command</u>	<u>Cmmd. No.</u>	<u>Function</u>
Pbk OFF signal from TR2	This is not a command; it is a ground signal from the internal timer)	<ol style="list-style-type: none"><li>1. Same as above except that TR2 is turned off and TR1 is selected for playback the next time an "auto pbk" command is sent.</li><li>2. Places TR2 in playback mode and enables "T<sub>2</sub>" of record time to turn off TR1 if "auto pbk" relay is in "No. 2" position.</li><li>3. Inputs TR playback data to transmitters.</li></ol>
TR1 & 2 Pbk OFF/Man Mode Sel	HE-35	<ol style="list-style-type: none"><li>1. Inhibits auto playback mode.</li><li>2. Inputs realtime data from DME to transmitters.</li><li>3. Places TR1 and TR2 in record mode.</li></ol>
TR Serial Record Start	WE-44	<ol style="list-style-type: none"><li>1. Applies power to and starts record timer which turns on both recorders at 102.911 minutes (one is already on) via "T<sub>1</sub>", terminal; 15 seconds later, "T<sub>2</sub>" turns off recorder that was previously recording.</li></ol>
TR Serial Record Disable	WE-45	<ol style="list-style-type: none"><li>1. Removes power from record timer.</li></ol>

#### 8.2.8 Sail Junction Box

The sail junction-box serves primarily to distribute power, command, and telemetry signals used by the various sail electronic components and the pointed instruments. It does not perform any multiplexing chores as does the wheel PCM junction-box. The sail junction-box houses the pointed instruments' power control relays, the launch sequence backup relay, the offset pointing control relays, clock isolation resistors, roll coil controls, gyro heater control, and the ASSC synchronization circuit. Finally, it serves as the attach point for the flexible cables that carry the various signals to and from the pointed instruments.

ASSC Sync Circuit. The ASSC synchronization circuit is a new requirement on OSO-7 due to the addition of a second ASSC in the sail. The purpose of this circuit is to keep the two ASSC's in synchronization with each other. The sync circuit, shown in Figure 8-15, makes a continuous waveform comparison of the two ASSC "sync out" signals. If the signals are not synchronized, a fast clock (800 Hz) is supplied to ASSC No. 2, bringing the units back into sync.

#### 8.3 SPACECRAFT HOUSEKEEPING DATA ACQUISITION

Spacecraft housekeeping data, including performance monitors and status monitors, are read out through the DSM, the two analog subcommutators, and the three analog sub-subcommutators.

The input voltages to the analog commutators range from zero to +5 volts. These monitors include temperatures, voltages, current levels, and others which are not readily converted to digital form in the sensing subassemblies. Conversion is done in the DME's.



F72-01

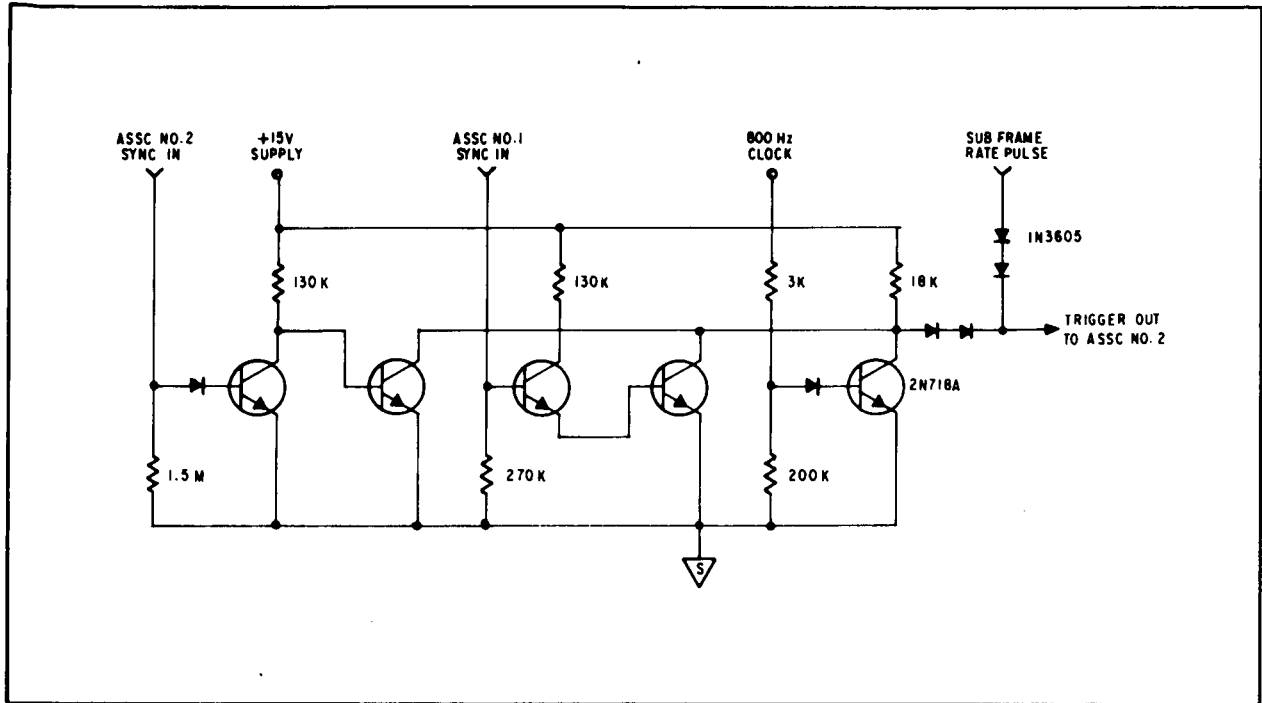


Figure 8-15 ASSC Synchronization Circuit

Single-bit status monitors are used in the digital subframe, so that up to eight status points can be read through a single subframe word. This technique allows more analog channels for experimenter use and simplifies machine interpretation of status-monitor data.

Other spacecraft data read through the digital subframe include the aspect data (SORE, star scanner, and large-angle pitch readout) and the frame count.

#### 8.4 RF SUBSYSTEM

The RF subsystem consists of two redundant telemetry transmitters, a coaxial relay, a diplexer, a hybrid circulator, and an antenna. A block diagram of this subsystem is part of Figure 8-1. The subsystem operates at 136.29 MHz.

The telemetry transmitters provide phase modulation using the biphase-coded input data. Power to the redundant transmitters, both of which operate on the same frequency, is controlled by ground commands. The coaxial relay, which is used to connect the desired transmitter to the diplexer, is also operated by these commands.

The diplexer provides a low-attenuation path between the selected transmitter and antenna at the transmitter carrier frequency while providing high attenuation at the command receiver frequency. Thus, any high-power rf signals originating from the transmitter at the command receiver frequency do not reach the command receivers. Conversely, the diplexer provides low attenuation between the antenna and the receivers.

The hybrid circulator is used as a power divider for the two command receivers while providing high isolation between them. A common antenna is used for transmitting telemetry signals and receiving command signals.



F72-01

### 8.4.1 Transmitters

OSO-7 uses the same BBRC type PSK-600A transmitter that was used on OSO-6. A block diagram of the PSK-600A is shown in Figure 8-16. The electrical and mechanical characteristics of the PSK-600A transmitter are given in Table 8-2.

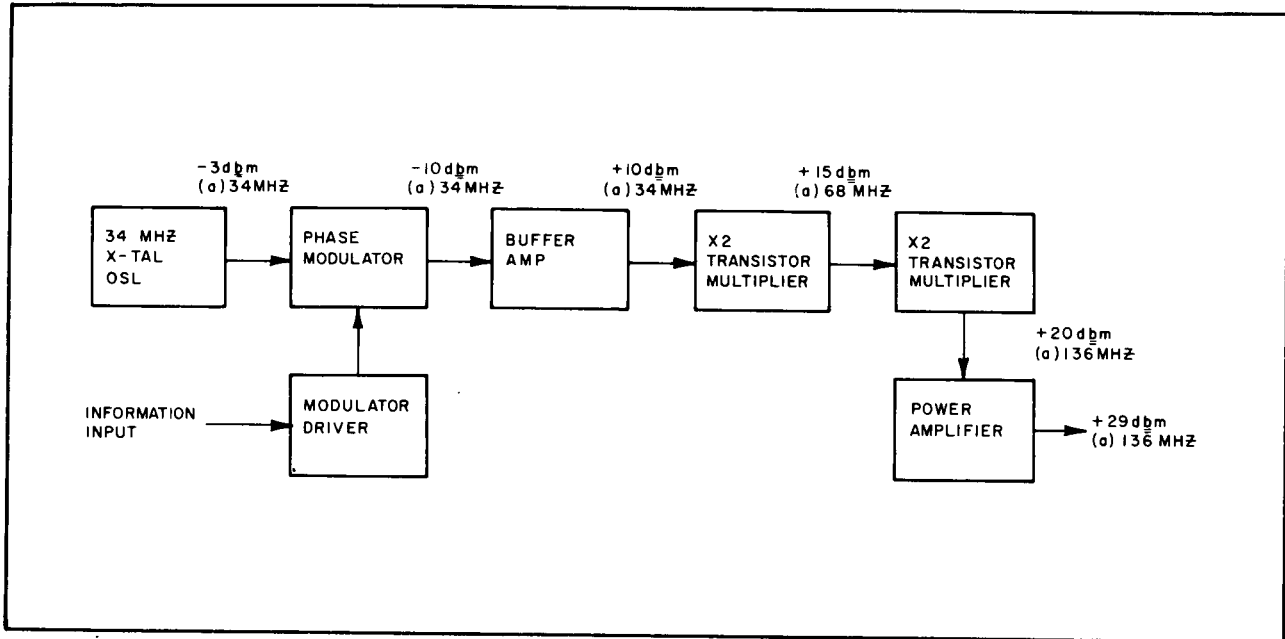


Figure 8-16 Telemetry System (PSK-600A) Block Diagram

Table 8-2

### SPECIFICATIONS FOR THE PSK-600A TELEMETRY TRANSMITTER

#### ELECTRICAL CHARACTERISTICS

- Frequency: 136 to 137 MHz (fixed tuned)
- Frequency Stability  $\pm 0.0037$  percent
- Power Output: 700 mw minimum
- DC/RF Efficiency: 25 percent (minimum)
- Modulation: Phase
- Frequency Response: 400 to 15,000 bps
- Modulation Sensitivity: 1.75 to 6 v peak-to-peak, to cause the specified phase deviation
- Deviation: Selectable from 50 to 90 degrees peak  $\pm 5$  degrees
- Input Impedance: 10,000 ohms
- Coherent Spurious Radiation: All harmonics in the range from 30 to 500 MHz to be at least 40 dB below the carrier
- VSWR: The transmitter can operate into a 2:1 all-phase load with no spurious outputs greater than 60 dB below the carrier and with a maximum power variation of 4 dB. The transmitter can also survive a 5:1 all-phase load without damage.
- Power Supply: 16 to 22 v (19 v nominal)
- Incidental AM: 5 percent maximum
- Incidental FM:  $\pm 5$  degrees for pulse period at 1/Bit rate

#### MECHANICAL CHARACTERISTICS

- Size: 3.125 by 1.75 by 3.25 in.
- Weight: 1 lb maximum



F72-01

Operation. The modulator driver conditions the biphase-coded input data from the tape recorders or DME's and establishes a fixed voltage level. The output of the modulator driver is fed to the phase modulator.

A 34 MHz crystal oscillator is used to establish a stable frequency reference for the transmitter. The output level for this oscillator is -3 dBm. The crystal oscillator is followed by a phase modulator that changes the phase of the reference signal in response to the input data supplied by the modulator driver. Some loss is experienced in the phase modulator, and the output signal level becomes approximately -10 dBm.

A buffer amplifier follows the phase modulator and provides isolation between the modulator and the subsequent multipliers, and raises the signal level to +10 dBm. This level is required to overcome the 0.7-volt base-to-emitter drop of the subsequent multiplier stage and drive this stage into class C operation. Class C operation is necessary for the multiplier to establish a nonlinear waveform on the output of the multiplier so that the second harmonic can be extracted by a bandpass filter.

The output of the first times-2 multiplier is at a +15 dBm level and at a frequency of 68 MHz. This signal drives a second times-2 multiplier that is identical to the first multiplier, but with the output stage tuned to the second harmonic or 136.29 MHz on OSO-7. The signal level at this point in the transmitter is about +20 dBm. The final times-2 multiplier is followed by a power amplifier which raises the 136 MHz signal to about +29 dBm (750 mW), a level suitable for transmission.

Modulation Filter. To limit the bandwidth of the transmitter, a pre-modulation filter is used. This limits the bandwidth of the data signal which in turn limits the bandwidth of the transmitted signal to about 90 MHz during playback.

The pre-modulation filter is an active filter with a cut-off frequency of approximately 35 kHz. Functionally, the filter module consists of a shaping circuit followed by a five-pole active filter. The supply voltages for these circuits are derived from zener-diode supplies. An EMI filter is also used to minimize the amount of conducted 136 MHz on the spacecraft power lines.

The filter module is contained in a separate aluminum case, 4.25 inches by 3.50 inches by 1.00 inch.

#### 8.4.2 Coaxial Relay

The coaxial relay is a single-pole, double-throw magnetic latching relay operated by a +19-volt pulse of 30 milliseconds duration. This relay closes in the position corresponding to the transmitter selected. It has a volume of approximately 1 cubic inch, not including connectors.



F72-01

### 8.4.3 Diplexer

The purpose of the VHF diplexer is to permit simultaneous operation of the telemetry transmitters and command receivers from a common antenna. An M-derived high-pass type filter using lumped constants provides a minimum of 20 dB attenuation of any signal from the transmitter which is at the receiver frequency. At the same time, this filter allows the transmitter frequency to pass with a maximum attenuation of 0.25 dB.

Two low-pass filters, used between the antenna and receiver terminals, provide a minimum of 50 dB of attenuation at the transmitter frequency while allowing the receiver frequency to pass with less than 0.7 dB loss.

### 8.4.4 Hybrid Circulator

The hybrid circulator permits simultaneous operation of two command receivers on the same frequency. A lumped-constant bridge circuit is used to provide over 40 dB isolation between the two receiver terminals. The input signal is divided equally between the two receiver terminals within  $\pm 0.2$  dB with an insertion loss of less than 0.5 dB.

### 8.4.5 Antenna Array

Since the satellite is not stabilized with respect to the earth, nearly-isotropic radiation patterns are required. This nearly-isotropic radiation is accomplished on OSO-7 with a turnstile slot antenna.

Antenna Design. The OSO-7 turnstile slot antenna, illustrated in Figure 8-17, consists of a circumferential slot backed by a cavity approximately a quarter-wavelength in depth (that is, a radial transmission line that is shorted at its innermost point).

This cavity is excited, in progressive phase, at four equally spaced feed points on a constant radius near the circumferential slot end of the radial line. The quarter-wave cavity smooths the feed point excitation so that the slot is excited with an equal-amplitude, progressive-phase electric field of

$$E_{\text{gap}} = E_0 \cos(\phi)$$

Thus producing the required nearly isotropic radiation patterns.

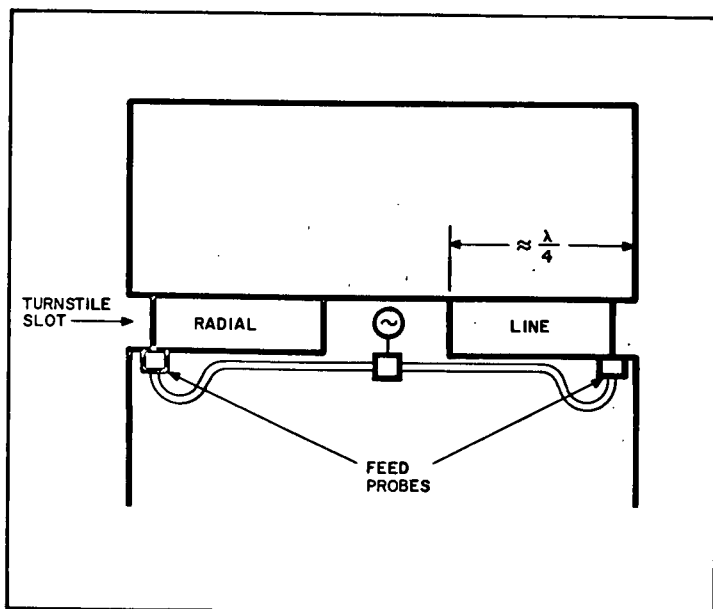


Figure 8-17 Turnstile Slot Antenna





F72-01

The basic characteristics of the turnstile slot antenna are:

Feed Phasing	Po/4 $\angle 0^\circ$ , Po/4 $\angle 90^\circ$ Po/4 $\angle 180^\circ$ , Po/4 $\angle 270^\circ$
Polarization on Axis	RHC/LHC
Polarization at Broadside	$E_\theta$
Power Pattern Coverage	Omni
Roll Pattern Variation	Approaches 0 dB
Roll Polarization Variation	None

Feed Network. The microwave feed network is shown in Figures 8-18 and 8-19. The power,  $P_o$ , from the transmitter is split in quadrature phase at the  $90^\circ$  hybrid,  $P_o/2 \angle 0^\circ$ ,  $P_o/2 \angle 90^\circ$ . These outputs in turn are split in half at tees  $P_o/4 \angle 0^\circ$ ,  $P_o/4 \angle 0^\circ$  and  $P_o/4 \angle 90^\circ$ ,  $P_o/4 \angle 90^\circ$ .

The extra half wavelength (that is, the  $\lambda/2$  portion of the two lines designated " $L + \lambda/2$ " on Figure 8-18) of line from each tee to one feed point produces an additional phase shift of  $180^\circ$  for one output of each tee:  $P_o/4 \angle 0^\circ$ ,  $P_o/4 \angle 180^\circ$  and  $P_o/4 \angle 90^\circ$ ,  $P_o/4 \angle 270^\circ$ . These outputs are routed as shown in Figure 8-18 to get:

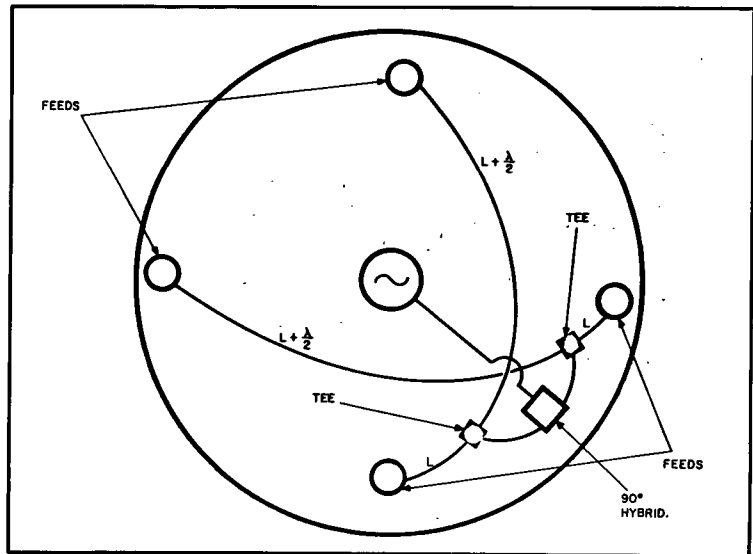


Figure 8-18 Progressive Phase Feed Layout

<u>Power Phase of Feed</u>		<u>Circumferential Feed Location</u>
Po/4 $\angle 0^\circ$	at	$\phi = 0^\circ$
Po/4 $\angle 90^\circ$	at	$\phi = 90^\circ$
Po/4 $\angle 180^\circ$	at	$\phi = 180^\circ$
Po/4 $\angle 270^\circ$	at	$\phi = 270^\circ$

The network schematic is shown in Figure 8-20.



F72-01

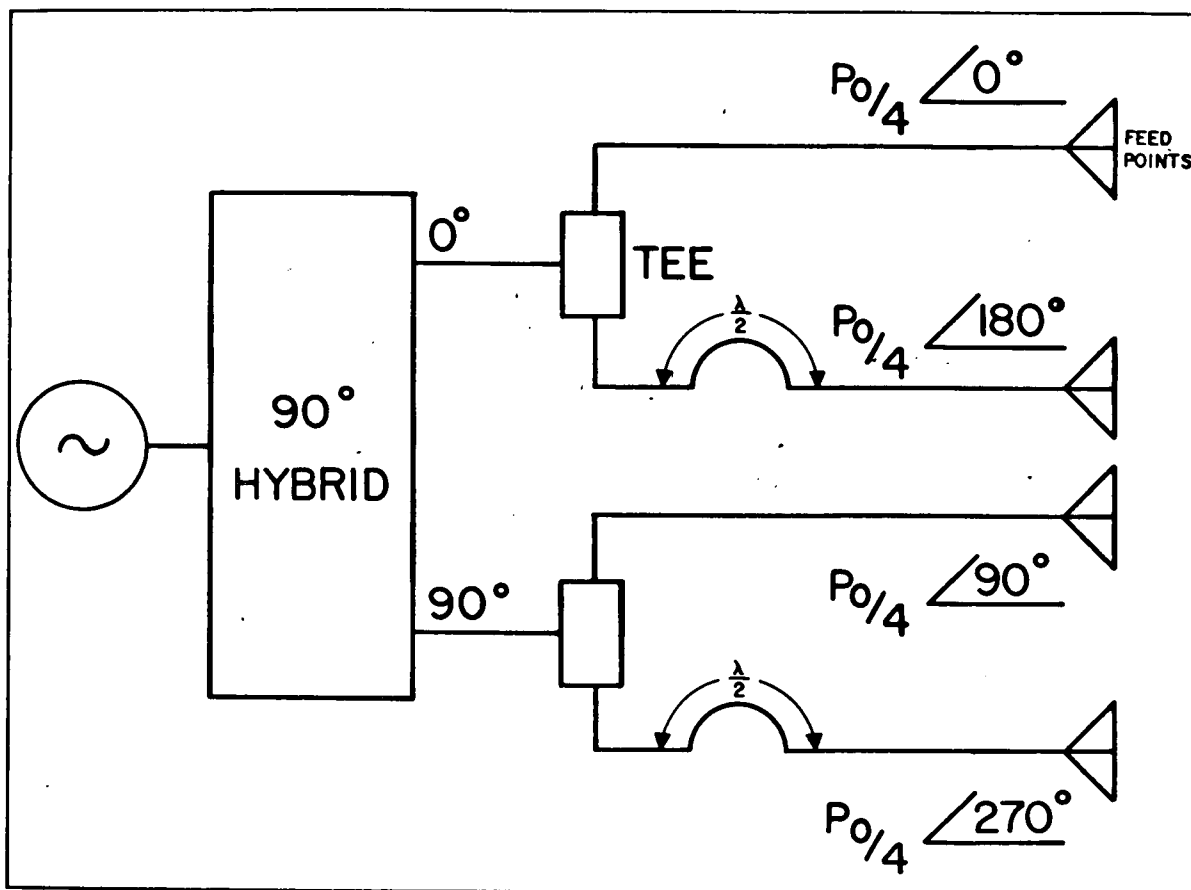


Figure 8-19 Progressive Phase Feed Block Diagram

The network consists of a 90-degree hybrid and two identical systems of transmission lines that include two-wavelength ( $2\lambda$ ) matching stubs, two feed lines which come together at a tee, and short lengths of interconnecting lines. The hybrid is an arrangement of transmission lines of appropriate lengths and impedances in a closed loop circuit which produces two outputs of equal power phased 90 degrees with respect to each other. This entire network is constructed of microstrip on one continuous sheet of teflon-fiberglass laminate.

Antenna Structure. The antenna is comprised of two main structural members, the antenna slot and the antenna skirt. The antenna structure is made from a honeycomb material.

The slot subassembly is a nine-sided polygon with a 56.0-inch diameter circumscribing circle. It consists of a 0.5-inch-thick nylon phenolic core sandwiched between two aluminum face sheets.



F72-01

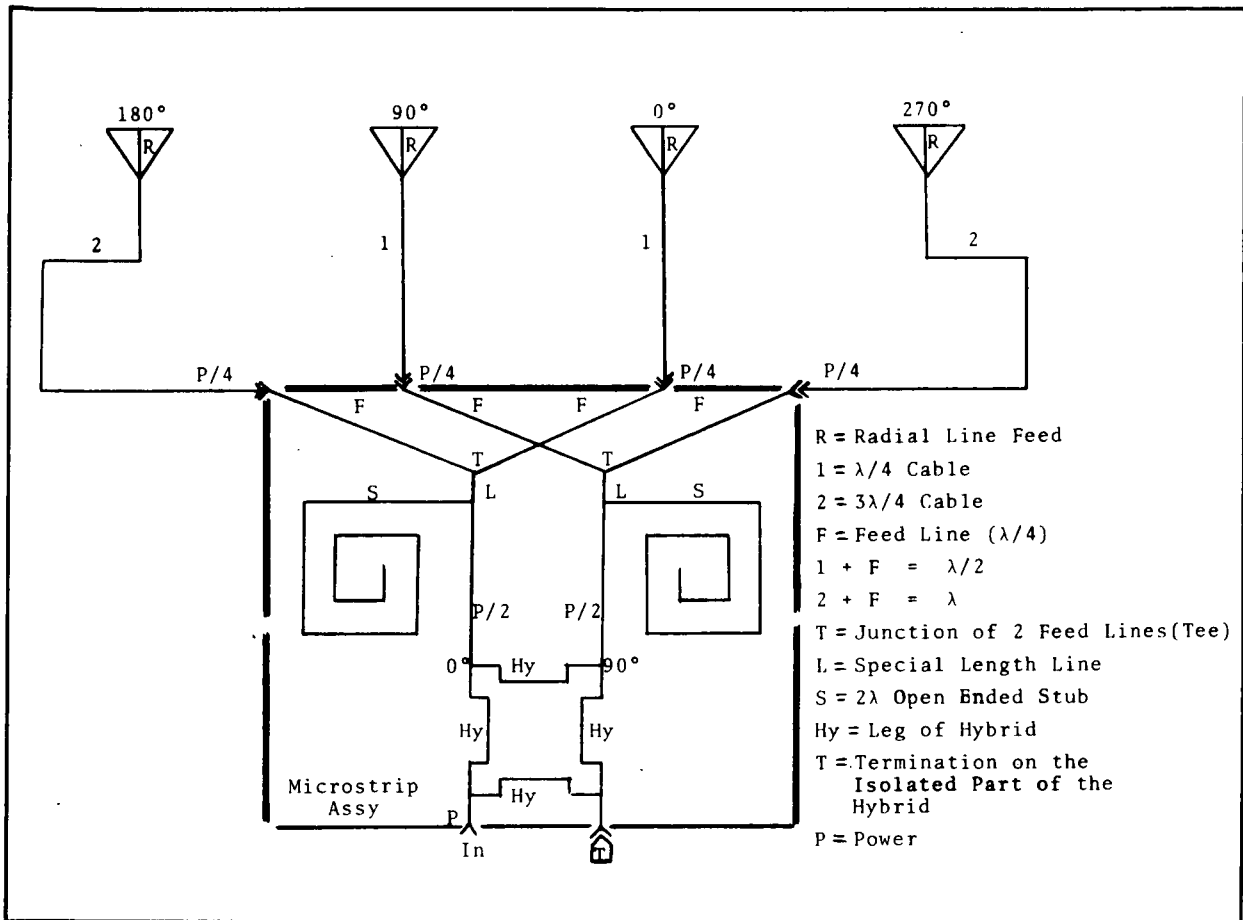


Figure 8-20 Feed Network Schematic

The skirt subassembly also is a nine-sided "polygon" with a circumscribing circle of 56.0 inches diameter, 14 inches high. The skirt is comprised of nine flat honeycomb panels connected by angle extrusions. Each panel is about 19.2 inches wide by 14.0 inches high by 0.25 inch thick.

A "sail extension" assembly (metal tapes) is used to extend the electrical (RF) height of the sail to about 16 inches above the uppermost solar panel. This assembly prevents degradation of the radiation patterns.

Telemetry Frequency Radiation Patterns. When the radiation pattern at 136.5 MHz is measured by two orthogonally-polarized receiving antennas, the field sensed by the vector sum of the antennas is greater than -8 dB for 100 percent of the aspect angles. Field plots of components that may be considered typical of the antenna performance are shown in Figures 8-21 and 8-22, respectively. Figure 8-23 shows the sum of RHC and LHC plots. These RHC and LHC figures are equal-power-contour plots showing the antenna gain with reference to a linear isotropic source. Note that right hand circular (RHC) polarization dominates above the spacecraft (sail side), while left hand circular (LHC) polarization is dominant below the spacecraft.



F72-01

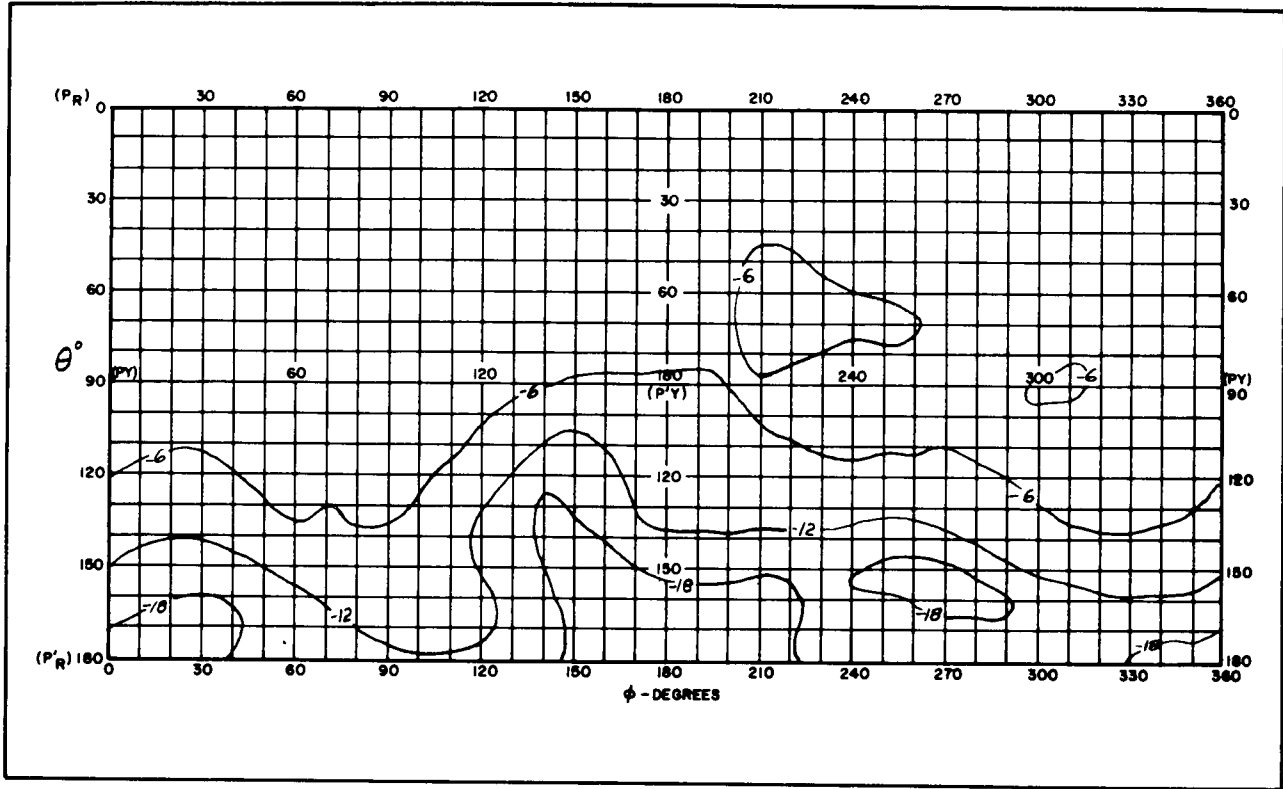


Figure 8-21 Telemetry Frequency Radiation Pattern (RHC Polarized)

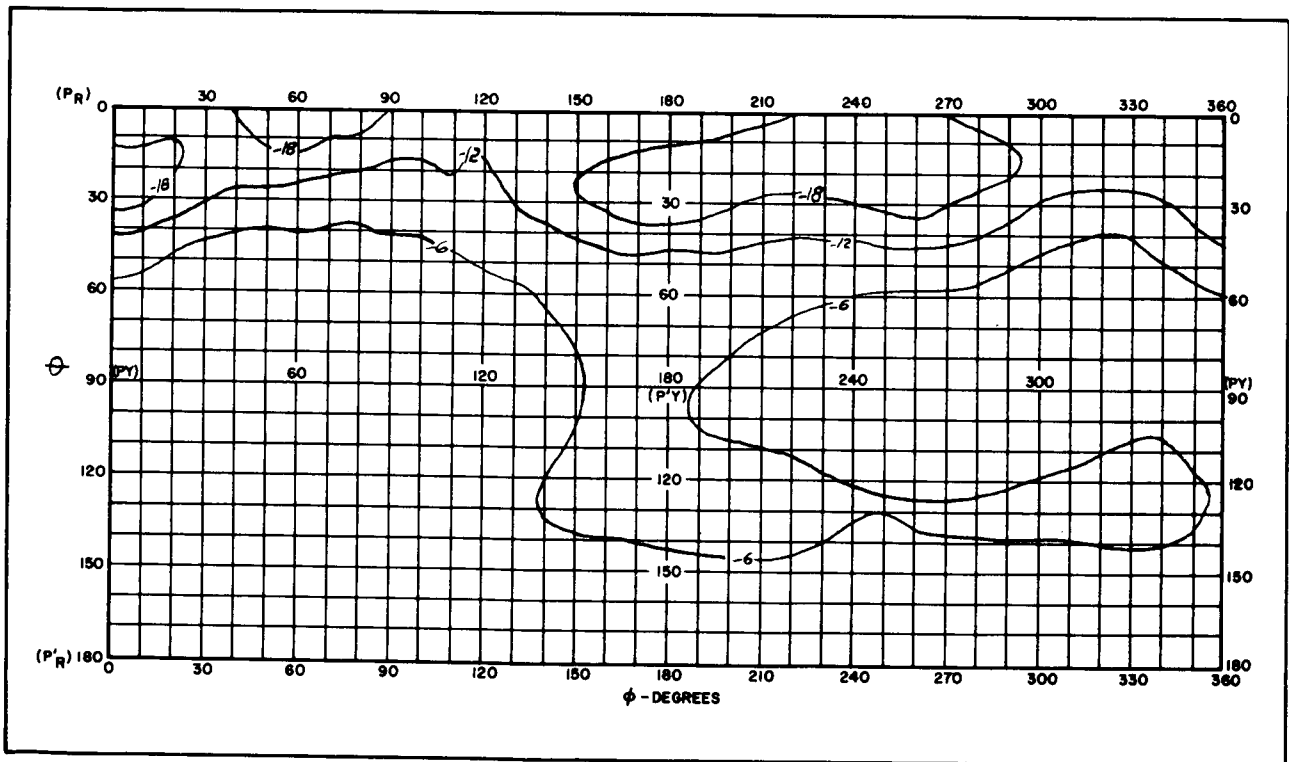


Figure 8-22 Telemetry Frequency Radiation Pattern (LHC Polarized)



F72-01

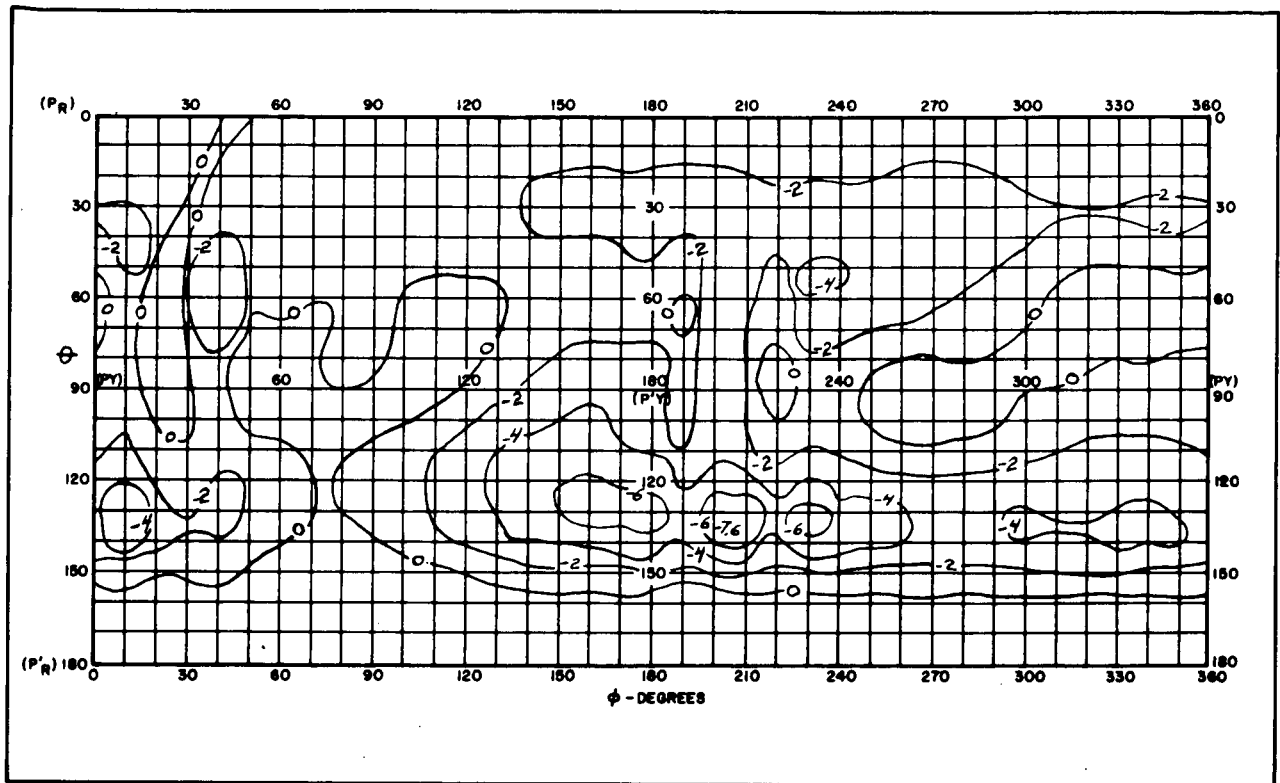


Figure 8-23 Telemetry Frequency Radiation Pattern (Combined RHC and LHC)

Refer to Figure 8-24 for the coordinate definition for all radiation patterns.

Command Frequency Radiation Patterns. The same antenna is used for command reception at approximately 150 MHz; however, the performance characteristics are somewhat different because command transmission is right circularly polarized and radiation field measurements must be sensed with a right circularly polarized antenna. For command reception, the measured gain is greater than -18 dB with respect to a linear isotropic source for 95 percent of the aspect angles. Figure 8-25 is an equal-power contour plot that may be considered typical of the antenna radiation patterns at the receiver frequency of about 150 MHz. The plot reflects the gain with reference to a linear isotropic source. Other characteristics that may be considered typical are gains greater than -27 dB over 99.7 percent and greater than -12 dB over 90 percent of the aspect angles. Nulls below -27 dB are sharp and are offset from the spin axis to permit at least one of two commands to be received outside the null due to observatory spin.



F72-01

### 8.5 TELEMETRY LINK ANALYSIS

The performance of the communications link between OSO and the GSFC Satellite Tracking and Data Acquisition Network (STADAN) is dependent upon both the airborne and the ground equipment. Table 8-3 shows the link analysis for playback transmission of 14,400 bps in a 300 nautical mile equatorial orbit. This table also lists the equipment parameters used to establish the gain margin.

The gain margin at the playback rate is 12 dB nominal, and the margin at the lower realtime data rate improves by 12 dB, for a total margin of 24 dB.

The worst-case link margin is +0.6 dB. On the surface, 0.6 dB is not a suitable margin, but to get it down this low, the following events must happen simultaneously:

- The attitude of the spacecraft must be such that the ground antenna sees only the small area in which -11 dB gain occurs
- The spacecraft must be at maximum range
- The spacecraft and ground station must line up with the galactic pole
- The spacecraft transmitter power must be at its minimum specification value
- The modulation index of the transmitter must be at its minimum specification value.

The probability of all these happening simultaneously is extremely small, so it can be concluded that the link is adequate with -11 dB spacecraft antenna gain.

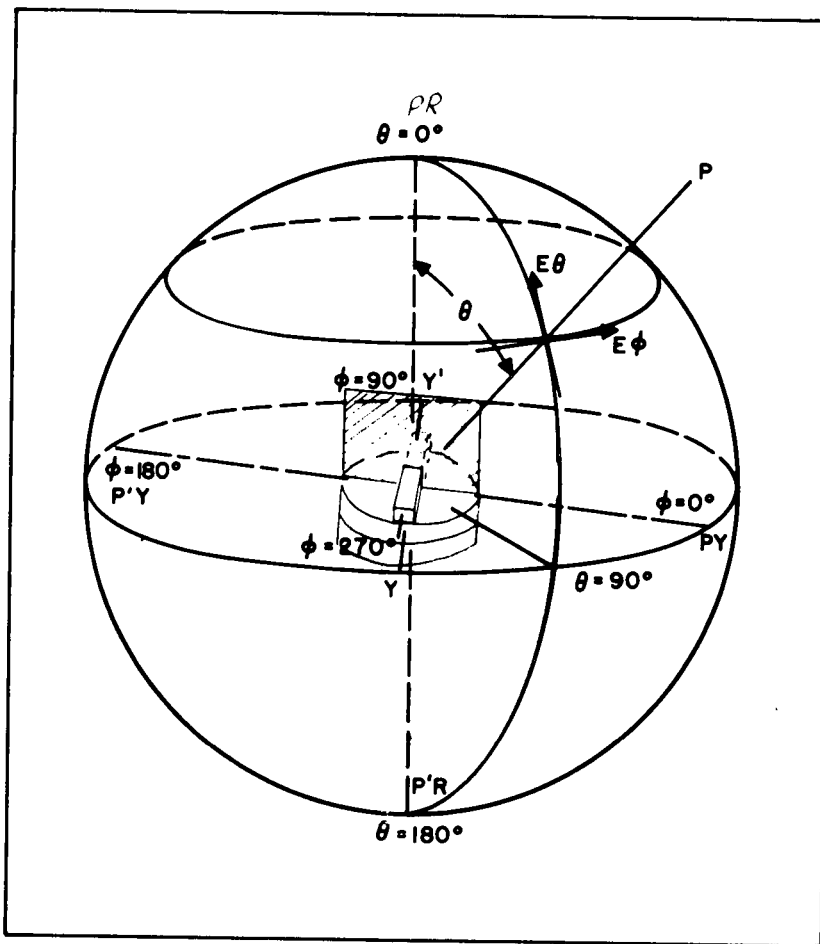


Figure 8-24 Vehicle/Antenna Coordinate System



F72-01

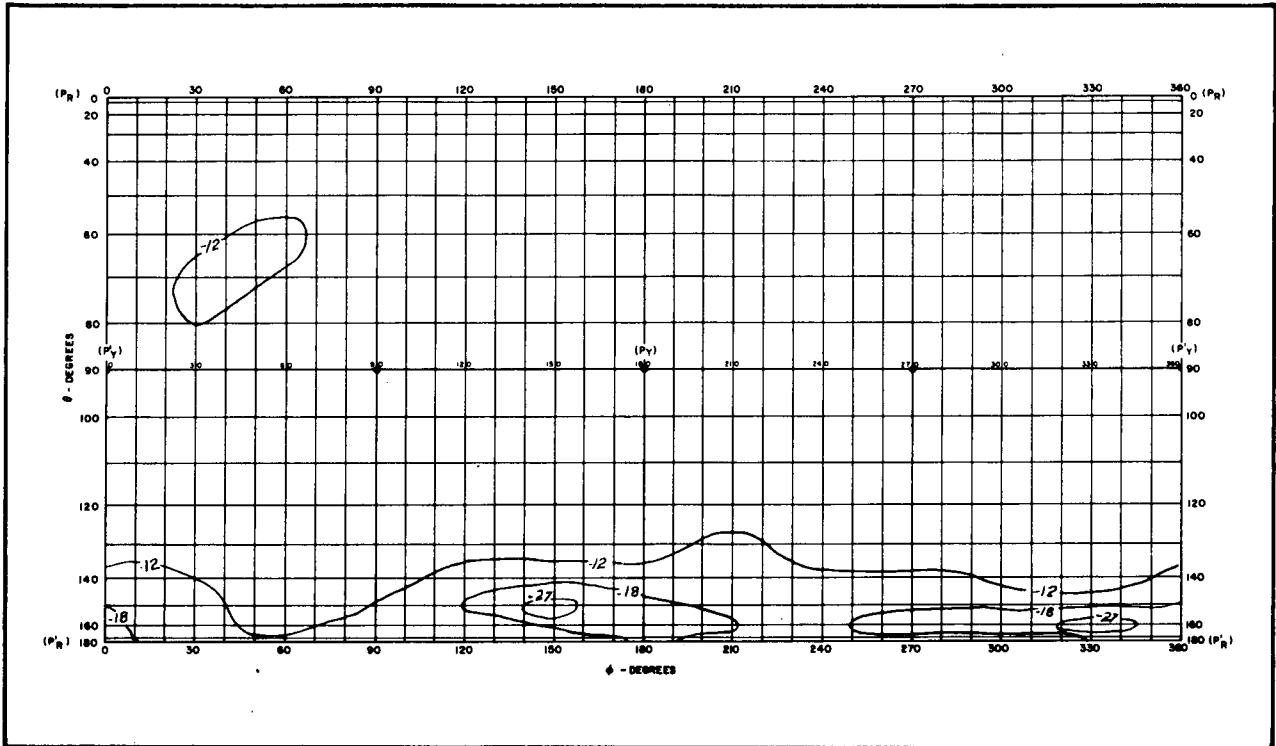


Figure 8-25 Command Frequency Radiation Patterns (RHC Polarized)

Table 8-3  
OSO-7 TELEMETRY LINK ANALYSIS

1. Received Signal Power

<u>Item</u>	<u>Nominal</u>	<u>Worst Case</u>	<u>Units</u>
Transmit Power (Note 1)	-3.0	-4.8	dBW
Spacecraft Antenna Gain	-7.0	-11.0	dB
Polarization Loss	-0.2	-0.3	dB
Path Loss (Note 3)	-140.4	-142.1	dB
Atmospheric Attenuation	0.0	-0.2	dB
Ground Antenna Gain (Note 2)	<u>+22.2</u>	<u>21.0</u>	<u>dB</u>
Received Signal Power	-128.4	-137.4	dBW

2. Signal to Noise Density Ratio (SNDR)

<u>Item</u>	<u>Nominal</u>	<u>Worst Case</u>	<u>Units</u>
System Noise Density (Note 4)	-196.5	-195.2	dBW/Hz
Received Signal Power (Item 1)	<u>-128.4</u>	<u>-137.4</u>	<u>dBW</u>
SNDR	68.1	57.8	dB-Hz



F72-01

Table 8-3 (Cont.)

3. Carrier Loop Signal to Noise Ratio (CLSNR)

<u>Item</u>	<u>Nominal</u>	<u>Worst Case</u>	<u>Units</u>
SNDR (Item 2)	68.1	57.8	dB-Hz
Carrier Modulation Loss	-4.6	-6.4	dB
Carrier Loop Bandwidth (assume 100 Hz)	<u>-14.8</u>	<u>-20.0</u>	<u>dB</u>
CLSNR	48.7	31.4	dB

4. Carrier Loop Margin

<u>Item</u>	<u>Nominal</u>	<u>Worst Case</u>	<u>Units</u>
CLSNR (Item 3)	48.7	31.4	dB
Required CLSNR	<u>-20</u>	<u>-20</u>	<u>dB</u>
Carrier Loop Margin	28.7	11.4	dB

5. Signal to Noise Ratio Per Bit (SNR in 1/T)

<u>Item</u>	<u>Nominal</u>	<u>Worst Case</u>	<u>Units</u>
SNDR (Item 2)	68.1	57.8	dB-Hz
Data Modulation Loss	-2.1	-3.2	dB
Bit Rate (14.4 Kbps)	<u>-41.6</u>	<u>-41.6</u>	<u>dB</u>
SNR in 1/T (Note 5)	24.4	13.0	dB

6. System Margin

<u>Item</u>	<u>Nominal</u>	<u>Worst Case</u>	<u>Units</u>
SNR in 1/T (Item 5)	24.4	13.0	dB
Required SNR in 1/T	<u>-12.4</u>	<u>-12.4</u>	<u>dB</u>
System Margin	12	+0.6	dB

8.5.1 Notes on Link Calculations

Transmitter Power. The worst-case transmitter power is pessimistic. Normal spacecraft bus voltage is at least 19 volts. The transmitter is specified to have an output power of -1.6 dBW (0.7 watts) at this voltage. Spacecraft circuit losses are 1.5 dB resulting in -3.1 dBW delivered to the antenna instead of the worst-case subsystem specification value of -4.8 dBW.

Ground Antenna. The ground antenna used in the calculations is the SATAN 16-Yagi array located at all stations of interest. An older antenna, also located at all stations, is the 9-Yagi array. The 9-Yagi array will not suffice for the worst case condition because it has 3 dB lower gain and is manually tracked. The manual tracking results in additional loss due to tracking error. The 9-Yagi array will suffice for the nominal case.





F72-01

Path Loss. The nominal case is taken at an elevation angle of  $10^\circ$  and the worst case is for  $5^\circ$ . Altitude is assumed to be 300 nautical miles.

Normal operation during a station pass is to take about one minute of real-time data prior to initiating playback. There is no problem with real-time because the lower bit rate adds 12 dB to the margins. During this minute, the slant range to the spacecraft decreases from 1198 to 974 nautical miles with a resulting decrease in path loss of 1.8 dB.

System Noise Density. For the nominal case, the antenna temperature is assumed to be determined by the average galactic noise. A 0.5 dB line loss is assumed and the receiver noise figure is taken as 3.5 dB.

For the worst case, a receiver noise figure of 4 dB was assumed.

SNR in 1/T. This quantity is equal to the ratio of the unit (energy per bit) to the unit of (noise spectral density) and is the fundamental quantity determining bit error rate. The worst case value, 12.4 dB, is derived for a  $10^{-5}$  BER and assumes premodulation filtering at 3/4 bit rate and filter/sample detection. The premod filter for OSO-7 has a cutoff at 1.14 B which will improve the BER slightly.



F72-01

Section 9  
COMMAND SYSTEM

9.1 GENERAL DESCRIPTION

The OSO-7 command system consists of two redundant VHF-AM command receivers, three redundant wheel decoders, two redundant sail decoders, two partially redundant sail decoders, and a receiver switching relay. The seven command decoders with the two command receivers form a versatile airborne command system that enables ground operators to perform various functions in the orbiting observatory. Figure 9-1 is a block diagram of the command system.

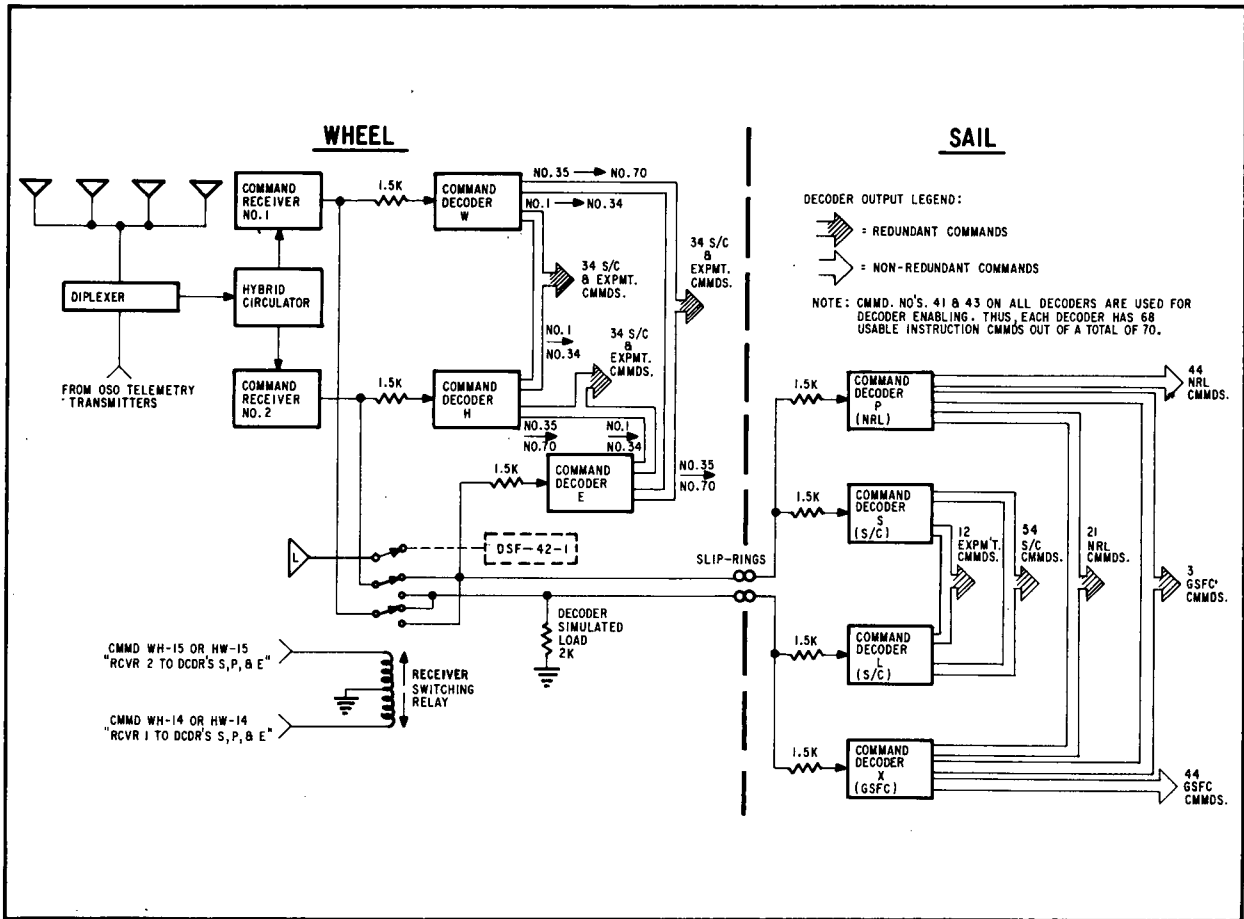


Figure 9-1 OSO-7 Command System Block Diagram

All of the spacecraft wheel and sail commands are obtainable from either receiver through redundancy or by operating the receiver switching relay (see Figure 9-1). All of the wheel experiment commands are likewise redundant, but only about half of the sail experiment commands are redundant. Table 9-1 lists OSO-7 commands.



F72-01

Table 9-1  
OSO-7 COMMAND CHART

WHEEL DECODERS  
W AND H\*

FOR DECODER W - USE WH  
FOR DECODER H - USE HW

01	0015	TR 1 AND 2 PWR ON
02	0107	TR 1 PWR OFF/PBK SEL 2
03	0111	TR 2 PWR OFF/PBK SEL 1
04	0113	TR 1 PBK/MAN MODE SEL
05	0114	TR 2 PBK/MAN MODE SEL
06	0207	XMTR 1 ON
07	0211	XMTR 2 SEL
08	0213	XMTR 2 ENAB
09	0214	XMTR 2 DISAB
10	0303	DME 1 SEL
11	0305	DME 2 SEL
12	0306	PCM J-BOX 1 SEL
13	0309	PCM J-BOX 2 SEL
14	0310	RCVR 1 TO DCDR'S S,P, AND E
15	0312	RCVR 2 TO DCDR'S S,P, AND E
16	0407	TORQUE MTR PWR ON
17	0411	TORQUE MTR PWR OFF
18	0413	TR PBK AUTO/AUTO MODE SEL
19	0414	DL OFF/LOW ADA HEATER ON
20	0503	UVS BYP ENAB
21	0505	UVS BYP CLOSED
22	0506	UVS BYP OPEN/DL LOW LEVEL SEL
23	0509	UVS BYP DISAB/DL HI LEVEL SEL
24	0510	BATT 3 AND 4 ON
25	0512	TIME DELAY RELAY DISAB/UVS AUTO TURN ON DISAB
26	0603	D-N BYP PLSZ/SPIN MAN/ASA DISAB/ASA PWR OFF/ASA PWR DISAB
27	0605	D-N BYP OPEN/ASL ENAB
28	0606	SAIL DAY PWR ENAB
29	0609	SAIL DAY PWR DISAB
30	0610	WH EXPT PWR ENAB
31	0612	WH EXPT PWR ENAB BYP
32	0701	MIT PWR ON
33	0702	MIT PWR OFF/DL SEL
34	0704	UNH PWR ON

WHEEL DECODERS  
W AND E\*

FOR DECODER W - USE WE  
FOR DECODER E - USE EW

35	0708	UNH PWR OFF/DL SEL
36	0807	UCSD - S PWR ON
37	0811	UCSD - S PWR OFF/DL SEL
38	0813	UCSD - C PWR ON
39	0814	UCSD - C PWR OFF/DL SEL
40	0903	MIT/UNH DL ENAB
42	0906	UCSD-S AND UCSD-C DL ENAB
44	0910	TR SERIAL RECORD START
45	0912	TR SERIAL RECORD DISAB
46	1003	ASA PWR ON
47	1005	SPIN AUTO/ASL ENAB
48	1006	SPIN MAN/ASL DISAB
49	1009	SPIN UP/ASL DISAB
50	1010	SPIN DOWN/ASL ENAB
51	1012	PITCH COIL ON
52	1101	PITCH COIL FULL PWR
53	1102	PITCH COIL POS
54	1104	MIT/UNH DL DISAB
55	1108	UCSD-S AND UCSD-C DL DISAB
56	1203	MIT CODE 1
57	1205	MIT CODE 2
58	1206	MIT CODE 3
59	1209	MIT CODE 4
60	1210	MIT CODE 5
61	1212	MIT CMMD SET
62	1301	MIT CMMD CLEAR
63	1302	ADA HEATER ENABLE
64	1304	20W ADA HEATER ON
65	1308	UCSD-C STEP CD HV
66	1401	UCSD-C RESET CD HV
67	1402	UCSD-C STEP ASPECT MODE
68	1404	UCSD-C RESET ASPECT MODE
69	1408	UCSD-C SWITCH SHIELD HV
70	1500	UVS AUTO TURN ON ENABLE

WHEEL DECODERS  
H AND E\*

FOR DECODER H - USE HE WITH NO'S 35 ON  
FOR DECODER E - USE EH WITH NO'S 01 ON

35	0708	TR 1 AND 2 PBK OFF/MAN MODE SEL	01	0015
36	0807	TR 1 ON/PBK SEL 1	02	0107
37	0811	TR 2 ON/PBK SEL 2	03	0111
38	0813	PITCH COIL OFF	04	0113
39	0814	PITCH COIL HALF PWR	05	0114
40	0903	PITCH COIL NEG	06	0207
42	0906	DIG ASPECT SENSOR PWR ON	08	0213
44	0910	ASA THRESHOLD GAIN CHANGE	10	0303
45	0912	ASA PWR ENAB	11	0305
46	1003	ASA THRESHOLD RST	12	0306
47	1005	ASA PWR OFF/ASA PWR DISAB	13	0309
48	1006	ASPECT MODE ALTERNATE	14	0310
49	1009	ASPECT MODE NORM/ASPECT ENCDR PULSE ENAB	15	0312
50	1010	ASPECT ENCDR PULSE DISAB	16	0407
51	1012	UNH QUADRANT CHANGE	17	0411
52	1101	UNH SCAN CHANGE	18	0413
53	1102	UNH MAN CALIB ON/OFF	19	0414
54	1104	UNH GAIN CHANGE	20	0503
55	1108	UNH HV STEP	21	0505
56	1203	UNH CENTRAL HV PWR	22	0506
57	1205	UNH SHIELD HV PWR	23	0509
58	1206	UNH AUTO CALIB ON/OFF	24	0510
59	1209	UNH MAG PULSE ON/OFF	25	0512
60	1210	UCSD - S CODE A1	26	0603
61	1212	UCSD - S CODE A2	27	0605
62	1301	UCSD - S CODE A3	28	0606
63	1302	UCSD - S LOAD 1	29	0609
64	1304	UCSD - S LOAD 0	30	0610
65	1308	BATT 1 ON / BATT 2 ISOLATED	31	0612
66	1401	BATT 4 ON / BATT 3 ISOLATED	32	0701
67	1402	BATT 3 ON / BATT 4 ISOLATED	33	0702
68	1404	BATT 2 ON / BATT 1 ISOLATED	34	0704
69	1408	BATT 1 AND 2 ON	07	0211
70	1500	DIG ASPECT SENSOR PWR OFF/ADA HEATER OFF-DISABLE	09	0214

ABBREVIATIONS:

- |                                       |  |   |
|---------------------------------------|--|---|
| ADA = AZ DRIVE ASSEMBLY               | FIL = FILAMENT   | RCVR = RECEIVER                                       |
| AGC = AUTOMATIC GAIN CONTROL          | FOC = FOCUS  | REF = REFERENCE                                       |
| APTR = APERTURE                       | FRNG = FAIRING   | REG = REGULATOR                                       |
| ASA = ASPECT SENSOR ASSEMBLY          | FW = FILTER WHEEL                                      | REL = RELEASE   |
| ASL = AUTOMATIC SPIN LIMITER          | GEN = GENERATOR  | RO = READOUT  |
| ASSC = ANALOG SUB-SUBCOMMUTATOR       | GSFC = GODDARD SPACE FLIGHT CENTER EXPERIMENT          | RST = RESET   |
| AUTO = AUTOMATIC                      | H-A = HYDROGEN ALPHA                                   | RSTR = RASTER   |
| AZ = AZIMUTH                          | HI = HIGH  | SA = SOLAR ARRAY                                      |
| BATT = BATTERY                        | HTR = HEATER   | SASC = SAIL ANALOG SUBCOMMUTATOR                      |
| BKGRD = BACKGROUND                    | HV = HIGH VOLTAGE                                      | SC = SPACECRAFT                                       |
| BU = BACKUP                           | HVPS = HIGH VOLTAGE POWER SUPPLY                       | SECT = SECTOR   |
| BYP = BYPASS (BYPASSED)               | ID = IDENTIFICATION                                    | SEL = SELECT  |
| CALIB = CALIBRATE                     | I-L = INTERLACED                                       | SEP = SEPARATION                                      |
| CD = CENTRAL DETECTOR                 | LCH = LAUNCH   | SEQ = SEQUENCE  |
| CHRG = CHARGE                         | LG = LARGE   | SHTR = SHUTTER  |
| CKT = CIRCUIT                         | LO = LOW   | SORE = SPIN ORIENTATION AND RATE ELECTRONICS          |
| CLK = CLOCK                           | LSBU = LAUNCH SEQUENCE BACKUP                          | SPECT = SPECTROMETER                                  |
| CLSD = CLOSED                         | LUV = LONG ULTRAVIOLET                                 | SQ = SQUIB  |
| CMMD = COMMAND                        | LV = LOW VOLTAGE                                       | SSC = SUB-SUBCOMMUTATOR                               |
| CMPT = COMPARTMENT                    | LVPS = LOW VOLTAGE POWER SUPPLY                        | ST = STATUS   |
| CNTRL = CONTROL                       | LWR = LOWER  | STG = SETTING   |
| CP = CHARGED PARTICLES                | LXR = LONG X-RAY                                       | SUV = SHORT ULTRAVIOLET                               |
| CR = COUNT RATE                       | MAG = MAGNETOMETER                                     | SW = SWITCH   |
| CTR = COUNTER                         | MAN = MANUAL   | SXR = SHORT X-RAY                                     |
| CUR = CURRENT                         | MIT = MASSACHUSETTS INSTITUTE OF TECHNOLOGY EXPERIMENT | SYNC = SYNCHRONIZATION                                |
| DCDR = DECODER                        | MON = MONITOR  | TEMP = TEMPERATURE                                    |
| DDP = DIGITAL DATA PROCESSOR          | MSB = MOST SIGNIFICANT BIT                             | TMG = TIMING  |
| DEG/SEC = DEGREE PER SEC              | MSP = MISPOINT   | TR = TAPE RECORDER                                    |
| DIG = DIGITAL                         | MTR = MOTOR  | UCSD-C = UNIV. OF CALIF., SAN DIEGO COSMIC EXPERIMENT |
| DISAB = DISABLE                       | MUV = MEDIUM ULTRAVIOLET                               | UCSD-S = UNIV. OF CALIF., SAN DIEGO SOLAR EXPERIMENT  |
| DISCNCT = DISCONNECT                  | NEG = NEGATIVE   | UNH = UNIV. OF NEW HAMPSHIRE EXPERIMENT               |
| DL = DUMMY LOAD                       | NRL = NAVAL RESEARCH LABORATORY EXPERIMENT             | UPR = UPPER   |
| DME = DIGITAL MULTIPLEXER AND ENCODER | NUT = NUTATION   | UV = ULTRAVIOLET                                      |
| DMF = DIGITAL MAIN FRAME              | OFST = OFFSET  | UVS = UNDER VOLTAGE SWITCH                            |
| D-N = DAY-NIGHT                       | OPER = OPERATION                                       | VRNR = VERNIER  |
| DSF = DIGITAL SUB FRAME               | O-R = OVERRIDE   | WASC = WHEEL ANALOG SUBCOMMUTATOR                     |
| ELECT = ELECTRONICS                   | PCM = PULSE CODE MODULATOR                             | WH = WHEEL  |
| EL = ELEVATION                        | PBK = PLAYBACK   | WL = WHITE LIGHT                                      |
| ENAB = ENABLE                         | POLAR = POLARIMETER                                    | XMTR = TRANSMITTER                                    |
| ENCDR = ENCODER                       | POS = POSITIVE   | XR = X-RAY  |
| EUV = EXTREME ULTRA VIOLET            | PT = POINT   | XUV = EXTREME ULTRAVIOLET                             |
| EXCT = EXECUTE                        | PWM = PULSE WIDTH MODULATOR                            |   |
| EXP = EXPOSURE                        | PWR = POWER  |   |
| EXPT = EXPERIMENT                     |  |   |



F72-01

Table 9-1 (Cont.)

SAIL SPACECRAFT DECODERS  
S AND L\*

FOR DECODER S - USE SL  
FOR DECODER L - USE LS

01	0015	GYRO MODE NORM/ACTIVE HTR ENAB
02	0107	GYRO MODE BU
03	0111	GYRO PWR ON/SEL 104°F
04	0113	GYRO PWR OFF/LOW TORQUE DISAB
05	0114	GYRO ACTIVE HTR DISAB/
06	0207	GYRO SEL 116°F
CHG	07	0211 LO TORQUE RATE-BIT A/GYRO TORQUE LEFT
CHG	08	0213 LO TORQUE RATE-BIT B/GYRO TORQUE RIGHT
09	0214	LOW TORQUE RATE - BIT C
10	0303	LOW TORQUE RATE - BIT D
11	0305	LOW TORQUE RATE - BIT E
12	0306	0.33 DEG PER SEC TORQUE ON
13	0309	0.33 DEG PER SEC TORQUE OFF/0.05 DEG STEP
14	0310	LOW TORQUE RATE RST/LOW TORQUE ENAB
15	0312	ROLL COIL 1 AND 2 PWR ON/POS POLARITY
16	0407	ROLL COIL 1 AND 2 NEG POLARITY
17	0411	ROLL COIL 1 AND 2 OFF
18	0413	ROLL COIL 3 AND 4 PWR ON/POS POLARITY
19	0414	ROLL COIL 3 AND 4 NEG POLARITY
20	0503	ROLL COIL 3 AND 4 OFF
CHG	21	0505 LSBU DISAB/LS ENAB
CHG	22	0506 LSBU ENAB/LS DISAB
23	0509	LSBU EXCT
24	0510	SA PANEL ON-UPPER LEFT
25	0512	SA PANEL OFF-UPPER LEFT
26	0603	EL OFST BIT 2 ON
27	0605	EL OFST BIT 3 ON
28	0606	EL OFST BIT 4 ON
29	0609	EL OFST BIT 5 ON
30	0610	EL OFST BIT 6 ON
31	0612	EL OFST BIT 7 ON
32	0701	AZ OFST BIT 2 ON
33	0702	AZ OFST BIT 3 ON
34	0704	AZ OFST BIT 4 ON
35	0708	AZ OFST BIT 5 ON
36	0807	AZ OFST BIT 6 ON
37	0811	AZ OFST BIT 7 ON
CHG	38	0813 OFST GEN STATE 1, 2
CHG	39	0814 EL BIT 1 OFF
CHG	40	0903 AZ BIT 1 ON
42	0906	EL BIT 1 ON/AZ BIT 1 OFF
44	0910	OFST MODE SEL/LG RSTR ON/OFST GEN STATE 1, 2
45	0912	OFST MODE OFF/PT MODE ON
46	1003	OFST PT ON/RSTR'S OFF
47	1005	SMALL RSTR ON/OFST PT ON
48	1006	INTERLACED RSTR ON
49	1009	INTERLACED RSTR OFF
50	1010	PITCH AUTO
51	1012	PITCH MAN
CHG	52	1101 PITCH UP
CHG	53	1102 PITCH DOWN
54	1104	SAIL EXPT DAY PWR ENAB
55	1108	SAIL EXPT DAY PWR ENAB BYP
56	1203	NRL DAY PWR ON
57	1205	NRL WL SEL
58	1206	NRL XUV SEL
59	1209	NRL PWR OFF/DL SEL
60	1210	GSFC DAY & LCH PWR ON
61	1212	GSFC PWR OFF/DL SEL
62	1301	GSFC-NRL DL ENAB/SQ BATT CHRNG DISAB
63	1302	GSFC-NRL DL DISAB/SQ BATT CHRNG ENAB
64	1304	NRL/GSFC SQ FIRE ENAB
65	1308	NRL/GSFC SQ FIRE DISAB
66	1401	SA PANEL ON-UPPER RIGHT
67	1402	SA PANEL OFF-UPPER RIGHT
68	1404	GYRO OFST COMPENSATION ON
69	1408	THERMAL COATING CNTRL MON PWR ON
70	1500	THERMAL COATING CNTRL MON PWR OFF

NRL EXPERIMENT DECODER  
P

FOR DECODER P - USE PX (REDUNDANT)  
- USE PN (NON-REDUNDANT)

PX	01	0015	NRL WL CALIB OFF
PN	02	0107	NRL WL ELECT CALIB ON
PN	03	0111	NRL WL LIGHT CALIB ON
PN	04	0113	NRL WL TIMER B OFF
PN	05	0114	NRL WL TIMER B ON
PN	06	0207	NRL WL SPARE
PN	07	0211	NRL WL FIL/FOC 1
PN	08	0213	NRL WL FIL/FOC 2
PN	09	0214	NRL WL FIL/FOC RESET
PN	10	0303	NRL WL FIL/FOC NO. 3
PN	11	0305	NRL WL FIL/FOC NO. 4
PX	12	0306	NRL WL SPARE
PX	13	0309	NRL WL TIMER A OFF
PX	14	0310	NRL WL TIMER A ON
PN	15	0312	NRL WL CLK/CTR NO. 1
PX	16	0407	NRL WL O-R MSP SENSE
PX	17	0411	NRL WL SHTR IN CONTROL
PN	18	0413	NRL WL CLK/CTR NO. 2
PN	19	0414	NRL WL CLK/CTR NO. 3
PN	20	0503	NRL WL EXP TIME NO.1
PN	21	0505	NRL WL EXP TIME NO. 3
PN	22	0506	NRL WL EXP TIME NO. 2
PN	23	0509	NRL WL EXP TIME NO. 4
PN	24	0510	NRL WL CORRIDOR NO. 1
PX	25	0512	NRL WL CLOSE SHTR/O-R DISAB
PX	26	0603	NRL WL CORRIDOR NO. 2
PX	27	0605	NRL WL CORRIDOR NO. 3
PN	28	0606	NRL WL HV-LV NO. 1
PX	29	0609	NRL WL NORM SCAN/NO SECT
PN	30	0610	NRL WL HV-LV NO. 2
PN	31	0612	NRL WL HV-LV NO. 3
PN	32	0701	NRL WL REVERSE SCAN
PX	33	0702	NRL WL ENAB NORM SEQ
PX	34	0704	NRL WL DISAB NORM SEQ
PN	35	0708	NRL WL SECTOR NO. 1
PN	36	0807	NRL WL SECTOR NO. 2
PN	37	0811	NRL WL SECTOR NO. 3
PX	38	0813	NRL XUV HVPS 1 ON
PX	39	0814	NRL XUV HVPS 1 OFF
PN	40	0903	NRL XUV HVPS 1A ON
PN	42	0906	NRL XUV HVPS 1B ON
PX	44	0910	NRL XUV HVPS 1 STEP
PX	45	0912	NRL XUV HVPS 1 RST
PX	46	1003	NRL XUV HVPS 2 ON
PX	47	1005	NRL XUV HVPS 2 OFF
PN	48	1006	NRL XUV HVPS 2A ON
PN	49	1009	NRL XUV HVPS 2B ON
PN	50	1010	NRL XUV HVPS 2 STEP
PN	51	1012	NRL XUV HVPS 2 RST
PN	52	1101	NRL XUV ELECT CALIB ON
PN	53	1102	NRL XUV ELECT CALIB OFF
PN	54	1104	NRL XUV SOURCE IN
PX	55	1108	NRL XUV SOURCE OUT
PN	56	1203	NRL XUV MIRROR COVER ON
PX	57	1205	NRL XUV MIRROR COVER OFF
PN	58	1206	NRL XUV SASC ON
PN	59	1209	NRL WL SASC ON
PN	60	1210	NRL XUV LVPS 1 ON
PN	61	1212	NRL XUV LVPS 2 ON
PN	62	1301	NRL XUV DDP 1 ON
PN	63	1302	NRL XUV DDP 2 ON
PN	64	1304	NRL XUV NORM AUTO CALIB
PN	65	1308	SPARE
PX	66	1401	NRL EXPT SQ FIRE EXCT
PX	67	1402	GSFC EXPT SQ FIRE EXCT
PX	68	1404	GSFC SXR FW AUTO
PX	69	1408	GSFC LXR FW AUTO
PN	70	1500	NRL SPARE

GSFC EXPERIMENT DECODER  
X

FOR DECODER X - USE XP (REDUNDANT)  
- USE XN (NON-REDUNDANT)

XP	01	0015	NRL WL CALIB OFF
XN	02	0107	SPARE
XN	03	0111	GSFC LXR/SXR FW'S AUTO
XN	04	0113	SPARE
XN	05	0114	GSFC POLAR AND XR HV OFF
XN	06	0207	GSFC LV TO DAY PWR
XN	07	0211	GSFC STEP APTR ONCE
XN	08	0213	GSFC STEP SXR FW
XN	09	0214	GSFC STOP APTR AUTO
XN	10	0303	GSFC SWITCH LINE SEL
XN	11	0305	GSFC RO UV AUTO
XP	12	0306	NRL WL SPARE
XP	13	0309	NRL WL TIMER A OFF
XP	14	0310	NRL WL TIMER A ON
XN	15	0312	GSFC SPECT FAST SCAN
XP	16	0407	NRL WL O-R MSP SENSE
XP	17	0411	NRL WL SHTR IN CONTROL
XN	18	0413	GSFC LXR HV ON
XN	19	0414	GSFC LXR A ONLY
XN	20	0503	GSFC LUV STEP/STOP SCAN
XN	21	0505	GSFC LXR A-B
XN	22	0506	GSFC POLAR HV ON
XN	23	0509	GSFC SPECT TO LUV
XN	24	0510	SPARE
XP	25	0512	NRL WL CLOSE SHTR/O-R DISAB
XP	26	0603	NRL WL CORRIDOR NO. 2
XP	27	0605	NRL WL CORRIDOR NO. 3
XN	28	0606	SPARE
XP	29	0609	NRL WL NORM SCAN/NO SECT
XN	30	0610	SPARE
XN	31	0612	GSFC H-A HV ON
XN	32	0701	GSFC SXR HV ON
XP	33	0702	NRL WL ENAB NORM SEQ
XP	34	0704	NRL WL DISAB NORM SEQ
XN	35	0708	GSFC SXR B ONLY
XN	36	0807	GSFC SXR A-B
XN	37	0811	SPARE
XP	38	0813	NRL XUV HVPS 1 ON
XP	39	0814	NRL XUV HVPS 1 OFF
XN	40	0903	GSFC MUV HV ON
XN	42	0906	SPARE
XP	44	0910	NRL XUV HVPS 1 STEP
XP	45	0912	NRL XUV HVPS 1 RST
XP	46	1003	NRL XUV HVPS 2 ON
XP	47	1005	NRL XUV HVPS 2 OFF
XN	48	1006	GSFC SPECT TO SUV
XN	49	1009	GSFC SUV AND LUV HV ON
XN	50	1010	GSFC EUV AND H-A HV OFF
XN	51	1012	GSFC SUV STEP/STOP SCAN
XN	52	1101	GSFC LXR B ONLY
XN	53	1102	GSFC RO H-A AND SUV
XN	54	1104	SPARE
XP	55	1108	NRL XUV SOURCE OUT
XN	56	1203	GSFC SPECT SLOW SCAN
XP	57	1205	NRL XUV MIRROR COVER OFF
XN	58	1206	GSFC STEP LXR FW
XN	59	1209	SPARE
XN	60	1210	GSFC RO MUV AND LUV
XN	61	1212	GSFC LINE SEL AUTO
XN	62	1301	GSFC APTR TO REF
XN	63	1302	SPARE
XN	64	1304	GSFC SXR A ONLY
XN	65	1308	GSFC STEP APTR AUTO
XP	66	1401	NRL EXPT SQ FIRE EXCT
XP	67	1402	GSFC EXPT SQ FIRE EXCT
XP	68	1404	GSFC SXR FW AUTO
XP	69	1408	GSFC LXR FW AUTO
XN	70	1500	GSFC LV TO LCH PWR

LATEST REV. 6/23/71

CHG - CHANGE MADE



F72-01

The OSO-7 spacecraft, like the OSO-6, uses a STADAN-compatible tone-digital command system. With this system, the command RF signal (149.52 MHz) is 75 percent amplitude modulated by a 7.7 KHz audio tone. This tone is keyed by a coded (pulse duration modulation) command signal. The OSO command system receives, detects, and decodes the command signal and executes the instructions.

The OSO-7 command system has been improved over the OSO-6 system as follows:

- The number of command functions has been increased from 206 to 282 (excluding command enable functions, but including spares).
- All spacecraft command functions are redundant.
- A "command enable" feature has been added for greater security.
- The decoder addresses and subcarrier frequency have been changed to avoid conflicts with other OSO's.
- The RF thresholds have been improved.

The OSO-7 command system provides the following command complement:

62	redundant spacecraft (wheel)
40	redundant experiment (wheel)
54	redundant spacecraft (sail)
38	redundant experiment (sail)
88	non-redundant experiment (sail)
<hr/>	
282	total command (including 14 spares)

The RF input is identical for each receiver since the RF input power is divided equally by a hybrid circulator. Both receivers and the wheel decoders have dc power applied continuously. The sail decoders are powered from the sail launch power bus.

## 9.2 COMMAND AND ADDRESS FORMATS

The STADAN ground station transmits addresses and commands to the OSO by either a punched paper tape mode or a manual mode. The paper tape mode, which is usually used, allows the transmission of as many tone-digital commands in sequence as desired. As the name tone-digital implies, digital information is contained in the pulse duration of the 7.7 KHz tone. This tone is pulse-duration modulated (PDM) so that three distinct tone bursts occur.



F72-01

9.2.1 Command Word Format

A command word consists of 10 bit periods (see Figure 9-2). A bit period is defined as a time duration equal to 72 cycles of the 7.7 KHz carrier tone. A sync pulse is defined as a tone burst of 54 cycles in length. Similarly, tone bursts of 36 and 18 cycles in length define a "one" and "zero", respectively. A word consists of 10 bit periods in the following order: eight information bits of "ones" and "zeros" preceded by a blank bit and a sync pulse. Address words and command words have the same format. They differ only in the combinations of "ones" and "zeros". The arrangement of information bits in an address word is either six "ones" and two "zeros", or six "zeros" and two "ones". The arrangement of information bits in a command word is four "ones" and four "zeros". The period of each 10-bit command or address word is 0.0935 second.

9.2.2 Command Word Encoding

Command and address words are encoded as two serial 4-bit codes and are designated by the decimal equivalent of these 4-bit codes. These codes are given in Table 9-1, and some examples are given below:

Function	Binary Code
Command #2	0001, 0111
Command #10	0011, 0011
Decoder "S"	1110, 1101

Decimal Equivalent

01, 07  
03, 03  
14, 13

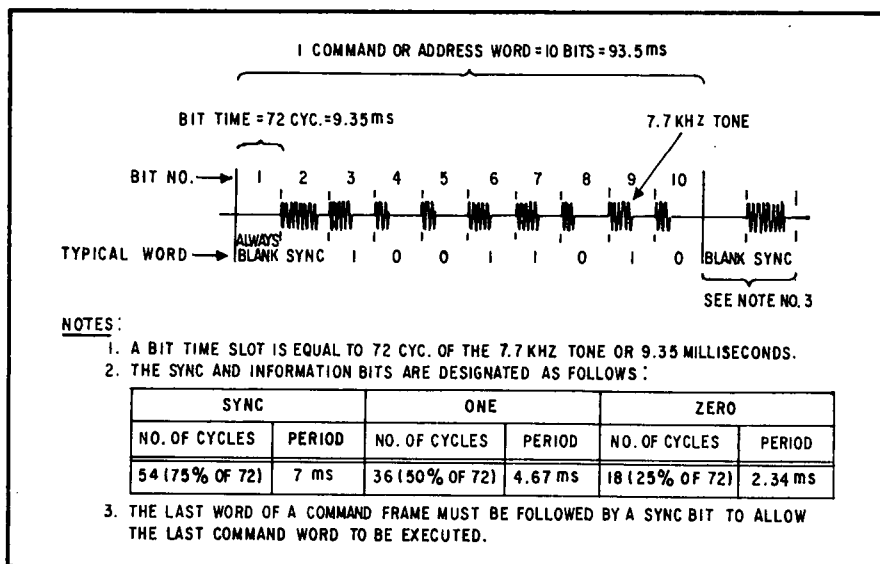


Figure 9-2 Command and Address Word Format

Thus, the output of the STADAN command encoder is a serial train of tone bursts that amplitude-modulate the STADAN command transmitter. The OSO command receivers amplify and detect this serial train of tone bursts and deliver it to the command decoders. The decoder that is addressed is gated "on", decodes the command word, and outputs a pulse on one of its 68 output lines.

9.2.3 Addressing and Command Enabling

The total address of each decoder consists of one of seven externally selected (patched) address codes plus one of two externally patched command enable codes. Reception of a proper address code allows the selected decoder to accept command codes, the first of which will be one of the selected command enable codes.



F72-01

OSO-7 differs from previous OSO command systems in that it contains an additional security feature, the command-enable timer. The command-enable timer is a retriggerable flip-flop (1.5-second timer) that is triggered by each command-enable command. Once the command-enable function has been executed, it allows execution of any of the remaining 68 output commands in the decoder for a nominal period of 1.5 seconds. The address and command enabling codes on OSO-7 are given in Table 9-2.

Table 9-2  
ADDRESS AND COMMAND ENABLE CODES

	<u>Decoder</u>	<u>Drawing 35499 Dash No.</u>	<u>Address Code</u>	<u>Command Enable Code</u>	<u>Command Enable No.</u>
Wheel	W	-1	02, 08	0905	41
	H	-1	04, 01	0909	43
	E	-1	08, 04	0905	41
Sail	S	-1	14, 13	0905	41
	L	-501	11, 07	0909	43
	P (NRL)	-501	01, 02	0905	41
	X (GSFC)	-501	13, 11	0909	43

Each decoder is capable of executing a maximum of 70 commands. However, on OSO-7, two of the command functions (words 41 and 43) are reserved for the command enabling functions.

9.2.4 Command Message Format

A command message is defined as consisting of two command frames and is comprised of all of the addresses and commands needed to execute an individual command function. As mentioned earlier, a command message can be transmitted by either of two formats, manual or punched-tape. These two formats are defined in Figure 9-3.

9.3 DECODER DESCRIPTION

The digital command decoder, manufactured by AVCO Corp., is designed to accept a message in the NASA tone-digital format, process it to determine if the proper address is present, and if so, provide the selected output. The decoder is solid-state throughout and provides 70 separate on or off commands. Two of the 70 commands are used for command enabling and, therefore, are not available for external control functions. All logic circuitry is either transistor-diode or transistor-resistor.

The decoder output and performance characteristics are given in Tables 9-3, and 9-4, respectively.



F72-01

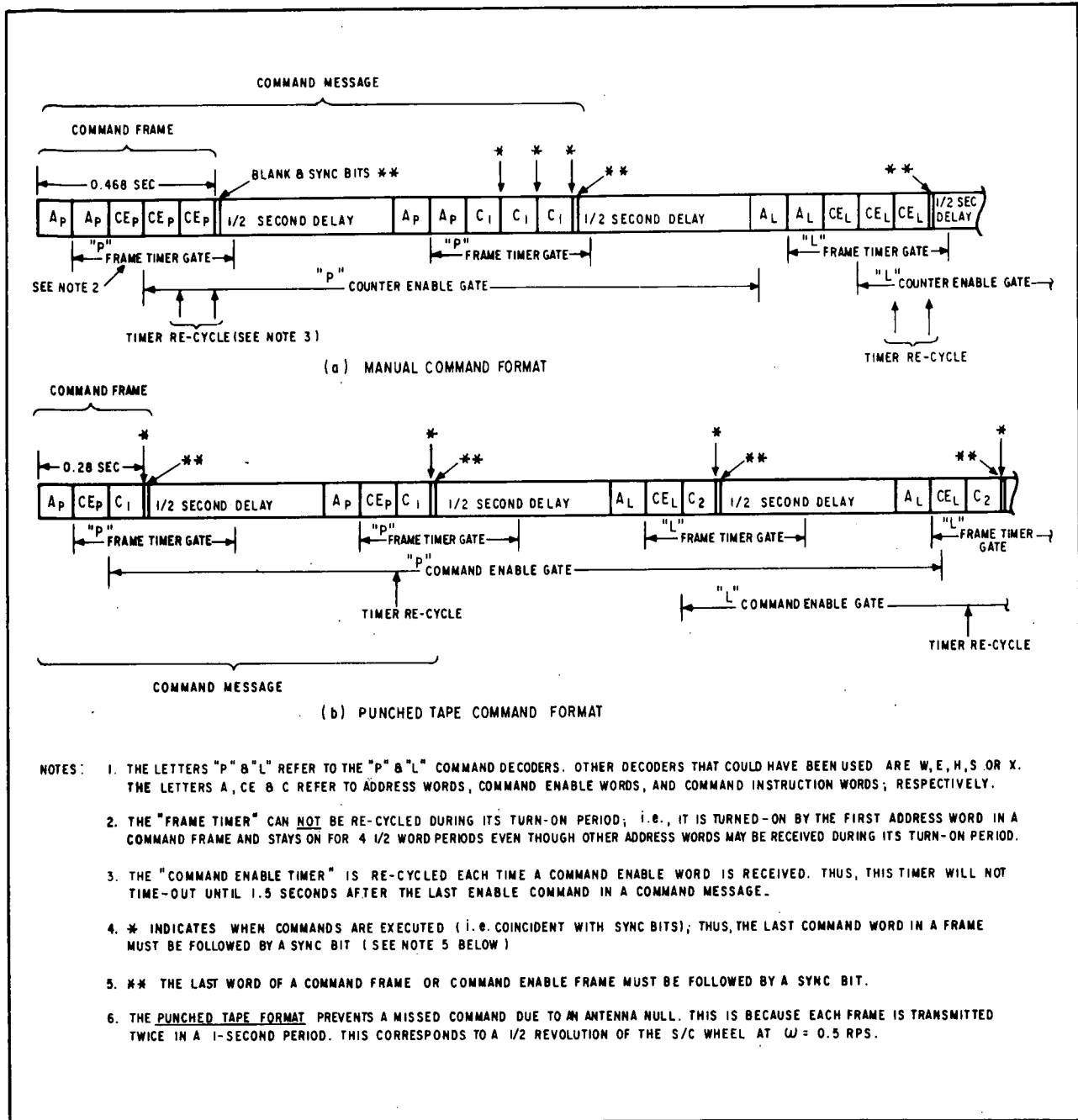


Figure 9-3 Command Frame Timing Formats

9.3.1 Physical Description

Each decoder occupies about 64 cubic inches and weighs about three pounds. The physical configuration permits stacking with other satellite equipment. Mechanical isolation of the decks permits operation of the decoder in vibration environments as high as 55 g without performance degradation.





F72-01

Table 9-3  
OUTPUT CHARACTERISTICS

Number of Outputs (Ext)	68 solid-state switches
Output Pulse Duration	35 ± 5 msec
Output Pulse Amplitude	9 volts (minimum)
Output Current	325 ma (maximum)

Table 9-4  
PERFORMANCE CHARACTERISTICS

Characteristic	Specification
Type	Tone Digital, Single Tone
Modulation Required	PDM, NASA Tone Digital Standard
Frequency	7.7 KHz
Dynamic Range	0.55 VRMS to 8.0 VRMS
Input Impedance	500 ohms, ±20% (2000 ohms including 1.5 K ohm external resistor)
Supply Voltage	19 volts DC, ±3 VDC
Standby Power	6.00 mw maximum
Interrogate Power (Without Leads)	5.00 watts maximum
Bit Error Rate	1 in 10 <sup>5</sup>

Cordwood printed circuit modules are used throughout the decoder. Functional division of circuitry was made to achieve simplicity so that the bit detector circuitry is on the first board, the data converter on the second board, and the output matrix and switches are divided between the top two boards.

After bench testing, the input tone filter is encapsulated in a high stability epoxy casting material. The modules are then assembled to the parent board to which a cable harness is connected. The parent board, with modules attached, is encapsulated in a semi-rigid polyurethane foam. This allows limited repairs to be made if necessary, and provides some vibration isolation.



F72-01

The completed parent boards are mechanically isolated on all sides by a silicone-elastomeric material. Mechanical damping in this material results from the energy dissipated during the cyclic stressing. After assembly in the housing, cover plates having a viscoelastic shear damping mechanism are attached. These cover plates complement the vibration isolation characteristics of the isolating pads to allow hard mounting of the equipment while effectively isolating the interior.

### 9.3.2 Operational Concept

The tone-digital format is first processed by a pulsewidth detector (bit detector) to sense the transmitted "sync", "one", and "zero" information. This detector automatically adjusts the decision threshold to sense the true pulse width accurately regardless of large variations in input signal amplitude. Pulse width detection is accomplished by gating the detection circuits with timing signals which then determine the time periods of the command bits.

The first "sync" pulse out of the bit detector is used to clear the logic circuits and is read into a 9-stage shift register. This pulse also triggers the power switch and regulator that supplies power to the remainder of the decoder. The "one" and "zero" outputs from the bit detector are then loaded into the shift register by means of read-in and shift multi-vibrators.

After all information bits have been loaded into the shift register, a check is made by address and command verification circuits to determine if the word is an address or a command. If it is an address word (as the first word should be), a frame timer is started. This timer stays on for about 4.5 word periods during which command enable and instruction words can be processed. If the word is a command (and was preceded by an address word within 4.5 word periods), a command code matrix will accept the uniquely coded command word and one of 70 command output gates will be enabled. Two of the 70 outputs (commands 41 and 43) are used for enabling the remaining 68 outputs and one of these "enable commands" must precede any of the remaining 68 instruction commands. An "enable command" starts a timer that stays on for about 1.5 seconds during which time an instruction command may be executed. When an instruction command is executed, a 35-millisecond, 18-volt pulse is fed to one of 68 destinations within the spacecraft to perform the desired control function.

### 9.3.3 Detailed Operation

Pulse Detection and Decoder Enabling. The incoming serial train of tone bursts from the command receivers is fed to the command decoders. Here the PWM tone bursts are first passed through a bandpass filter and then to a tone detector where the envelope of the tone bursts is detected and shaped (see Figure 9-4). The decoder remains in the "standby" state (that is, no power is available to most of the logic circuits) until the threshold of the tone detector has been exceeded by the leading edge of the first input pulse. When this happens, the "early" B+ is turned on and the decoder's internal clock, counters, sync bit detector, and reset clamp circuit are activated. The decoder is then in the "ready" state.



F72-01

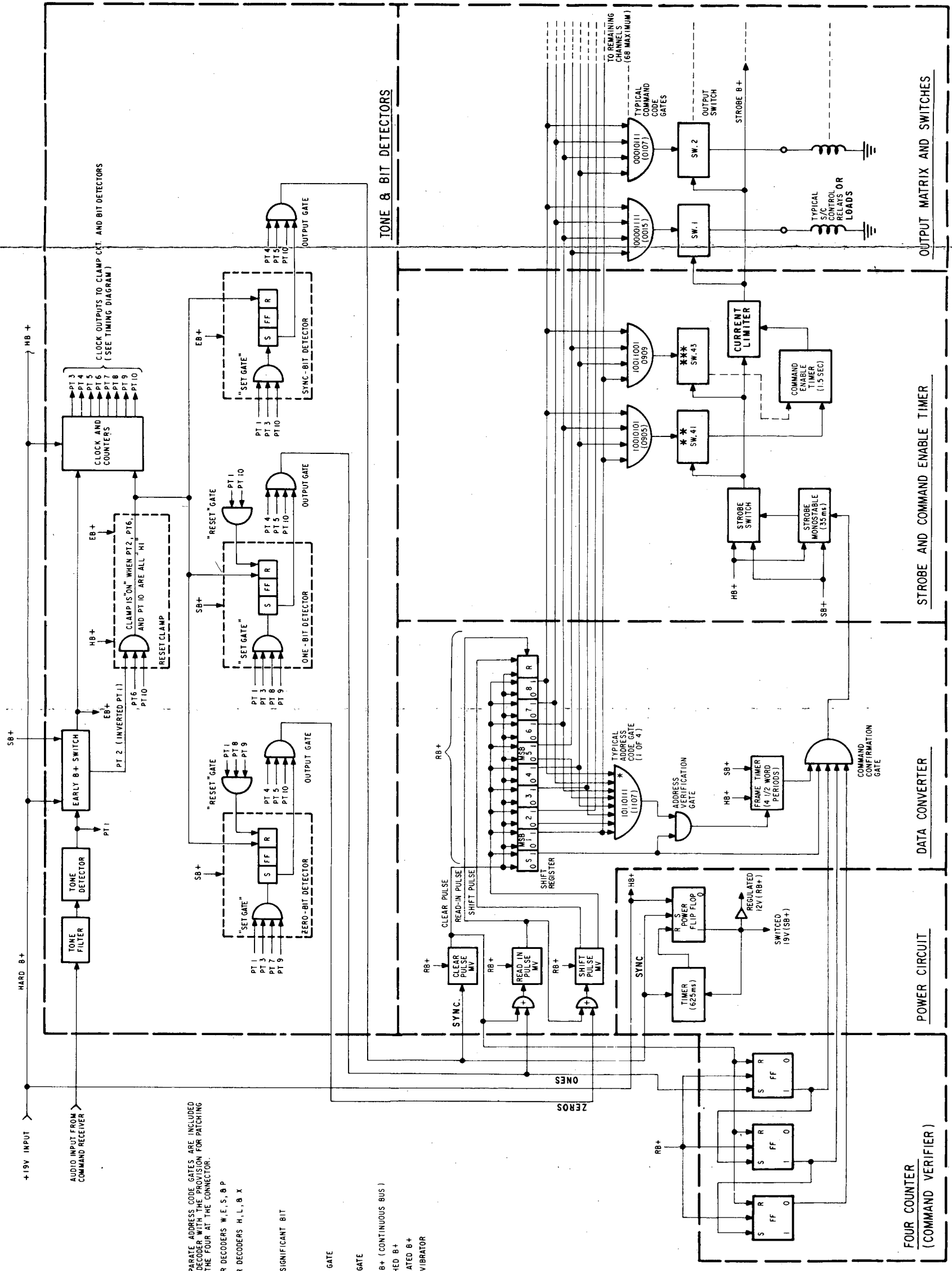


Figure 9-4 Command Decoder Functional Diagram

9-11/9-12

FOLDOUT FRAME 2

FOLDOUT FRAME



F72-01

The early B+ switch (EB+) has positive feedback and latches itself "on" for 10 clock intervals (about 14 milliseconds) and, if this first input pulse is not a sync bit, it will reset itself at the end of this period, thus returning the decoder to the standby state (see Figure 9-5, segment A).

Reset Clamp. The first logic event after the threshold has been detected is the removal of the "reset clamp" from the decoder clock, counter, and bit detector circuits. This is accomplished by routing the inverted command pulse train (PT2 on Figure 9-5, segment B) to the reset clamp AND gate.

Clock and Counter. The removal of the reset clamp allows the internal, free-running clock to start. The frequency of this clock is about five times that of the command word bit frequency (that is, the clock period is about 1.4 milliseconds compared to about 7 milliseconds for a command word bit period). The output of the decoder clock is then counted-down by a 3-stage counter into 1/2, 1/4, and 1/8 clock outputs. These outputs are identified as PT3 through PT10 on Figures 9-4 and 9-5.

Bit Detectors. The appropriate outputs from the clock and counter are then ANDed together with the input command pulse train by the "set gates" of the bit detectors (see Figures 9-4 and 9-5). This ANDing is the means by which the three bit detectors determine the identity (pulse duration) of the command bits.

If the first command bit is a sync bit, the sync bit detector will produce an output as shown in Figure 9-5, segment C; this, in turn, causes SB+ to be applied to the "zero" and "one" bit detectors and latches up the EB+ for 625 milliseconds. After a sync bit has been detected, the "zero" and "one" bits are detected as shown in Figure 9-5, segments D and E, respectively. (Note in Figure 9-4 that power is not applied to the "zero" and "one" bit detectors until after a sync bit has been detected.) In the "zero" and "one" detector timing diagrams, extraneous bits are generated (i.e., the zero bit detector generates an output for all three types of bits). Therefore, reset bits are also generated by these detectors to cancel these unwanted bits. The outputs of the bit detectors are ANDed with counter outputs PT4, PT5, and PT10 (see Figure 9-5, segment F) at the output gates of the detectors. These "sync", "zero", and "one" bits are all routed to the data converter. Also, the "ones" are routed to the "four counter" and the sync bit is routed to the switched B+ power circuit.

Switched B+ Power Circuit. Each time a sync bit is detected, the 625-millisecond timer is started (recycled if it is already on), and the power flip-flop is set to supply "switched" 19-volt unregulated and 12-volt regulated power. These two types of power are used in the remaining decoder circuits (those not powered by "hard" B+ or "early" B+) and their application changes the decoder from the "ready" state to the "active" state.

The power timer resets the power flip-flop at the end of 625 milliseconds. This reverts the decoder to the "ready" state and, if another sync bit is not received, the early B+ will reset itself about 14 milliseconds later and the decoder will revert to the "standby" state.



F72-01

NOTE: \* = BITS INHIBITED BY RESET BITS  
 \*\* = ONLY ONE BIT IS SHIFTED OUT BY THE OUTPUT ENABLING BIT

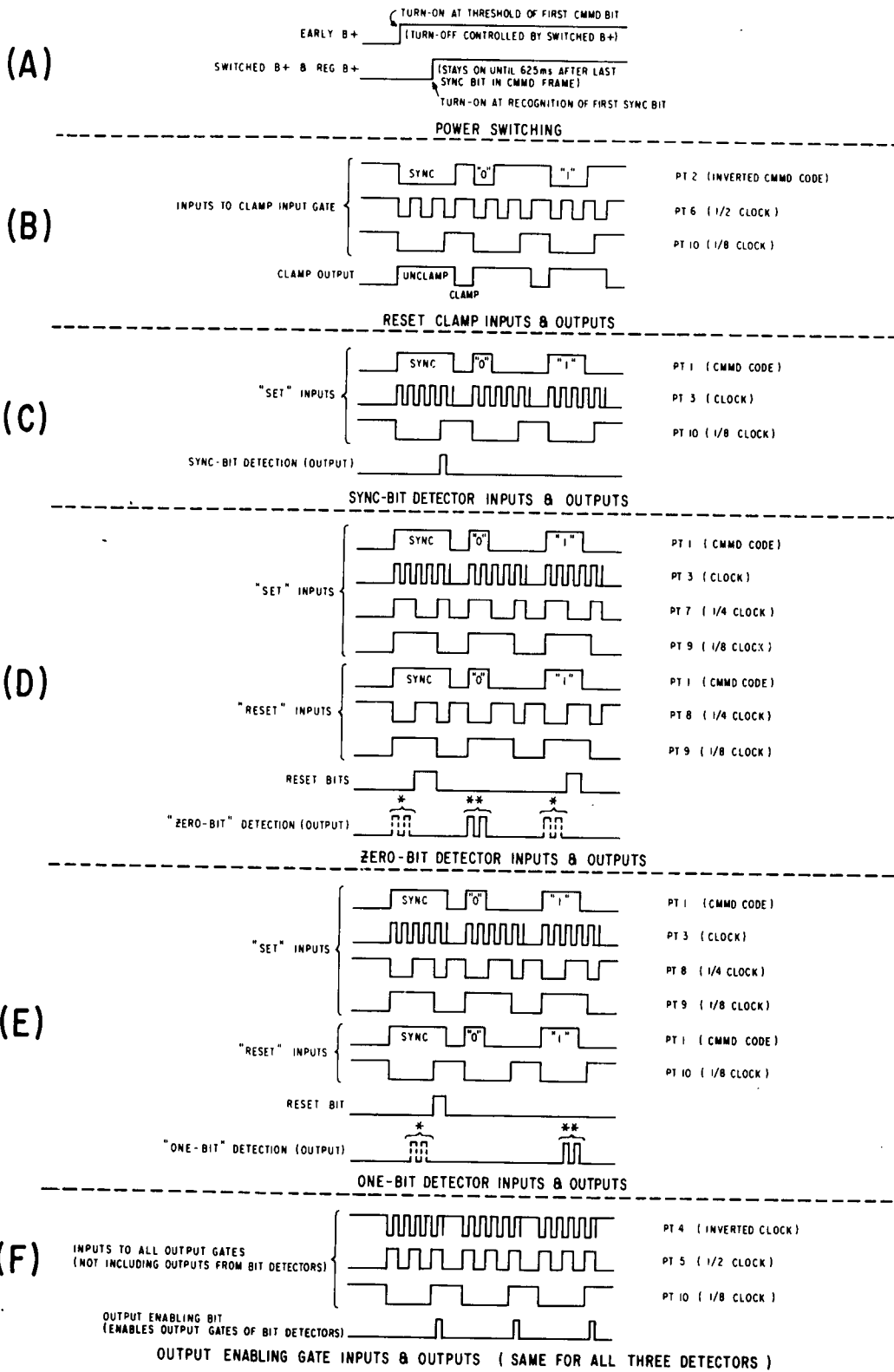


Figure 9-5 Decoder Timing Diagram



F72-01

Data Converter. The output of each bit detector triggers the clear, shift, and read-in pulse multivibrators. These multivibrators convert the pulses from the bit detectors into read-in, clear, and shift pulses to transfer the incoming pulse train into the proper positions of the shift register for further decoding.

When the decoder receives a message, the differentiated signal from the trailing edge of the "sync" pulse triggers the clear pulse multivibrator. This pulse clears the shift register and "four counter" circuits. The "clear" pulse is also applied to the read-in pulse multivibrator with the "one" line from the bit detector. The presence of either a "one" or "sync" pulse, therefore, triggers the read-in pulse generator. The read-in pulse, in turn, sets the input buffer stage (R) in the shift register to the "one" state before being applied, with the "zero" line from the bit detector, to the shift pulse multivibrator. The shift pulse causes the "one" state of any shift register stage to be transferred to the next stage.

After the "sync" pulse is read into the shift register, the process is repeated with the "zeros" and "ones" in the message until all of the eight data bits are read into the shift register. When this occurs, the bit positions of the shift register are in the "on" or "off" state depending on whether they correspond to a "one" or a "zero" in the original word. The shifting of the "sync" bit into its proper position in the shift register (the "S" position) triggers the decoder into the next phase of operation -- address recognition. This is done by an address code and gate connected to the data positions of the shift register.

Address Recognition. If the address word for which the decoder is wired (that is, a unique combination of six "ones" or six "zeros") is presented to the address code gate, the output of this gate is applied with the "sync" position output of the shift register to the address verification gate, which in turn triggers the frame timer. The frame timer provides a period of 4.5 word lengths (about 420 milliseconds) after the receipt of a valid address during which a command word can be accepted. Thus, the turn-on of the frame timer signifies that a valid address has been received, and readies the decoder for command interrogation.

Command Verification. The second type of word transmitted in the standard tone-digital format is a command-enable word (which is actually a command instruction word and differs only in its function). The decoder must recognize that this word is a command word and not an address. This is done by the command word verification circuit ("four counter"). This circuit counts the number of "ones" received in a word and inhibits the command confirmation gate on a count of other than four. Since, by definition, a valid command word contains four "zeros", and four "ones", this circuit inhibits a command output for other than a valid command, assuming that the received command word does not contain compensating transpositions.

Command Enable Timer. The command confirmation gate strobes both of the command enable gates for 35 milliseconds. One of these gates (either gate 41 or 43\*) is patched back into the

---

\*Gate 41 is used in decoders W, E, S, and P and gate 43 is used in decoders H, L, and X.



F72-01

decoder to the command-enable timer which enables a current-limiting circuit in series with the remaining 68 command gates. Thus, when the proper command-enable code has been received, this timer allows current-limited strobe power to be applied to the remaining 68 commands for a period of 1.5 seconds. It is during this time that the instruction commands can be executed.

Execution of Instruction Commands. In a standard message frame, the third type of word is an instruction command. This word is read into the shift register and verified in the same manner as with the command-enable word. When read-in is complete, the "sync" bit again activates the command confirmation gate if:

- The frame timer output is present (indicating that the correct address has been received).
- The command word verification signals are present (indicating that the received word is a valid command; that is, containing four "ones" and four "zeros").

The output of the command confirmation gate again triggers the strobe pulse monostable. This again causes a 35-millisecond turn-on pulse to be applied to the strobe gate, which applies line voltage to the current limiter. At this time, an instruction command will be executed if:

- The command-enable timer output is present (indicating that the proper command-enable code has been received).
- The instruction command code conforms to one of the assigned codes.

Only four inputs are applied to each of the command decoding gates; these inputs are from the "ones" position of the shift register. This is possible because the command verification circuit has already established that the word contains four "one" data bits, thus requiring that the remaining four bits must be "zeros".

Output Switch Characteristics. The output switches operate as complementary symmetry flip-flops so that once triggered on, they remain on until B+ is removed by the strobe gate. If a particular decoder channel is short-circuited by a fault in the load circuitry, no output current flows since the low impedance of the load prevents the output switch from turning on. For this reason, current limiting of the output is not absolutely necessary (although it is provided for additional reliability).

If a valid command word is present, the command code gate corresponding to that word produces an output to trigger the proper output switch, which then applies unregulated B+ (19-volt launch power) to the selected load. The output drive characteristics are:

<u>Drive Voltage</u>	<u>Load Resistance (<math>\Omega</math>)</u>	<u>Current Limit (mA)</u>
12	100	100
11	65	170
9	50	180



F72-01

The command output circuit that interfaces between the decoder and spacecraft subsystems and experiments is shown in Figure 9-6.

#### 9.4 COMMAND RECEIVERS

The OSO command receivers use single conversion super-heterodyning, and are fixed-tuned to the NASA specified frequency of 149.52 MHz. The receivers are solid state, and some of their circuits are connected in series across the power supply to reduce power consumption.

A block diagram of the command receiver is shown in Figure 9-7. Electrical characteristics are listed in Table 9-5.

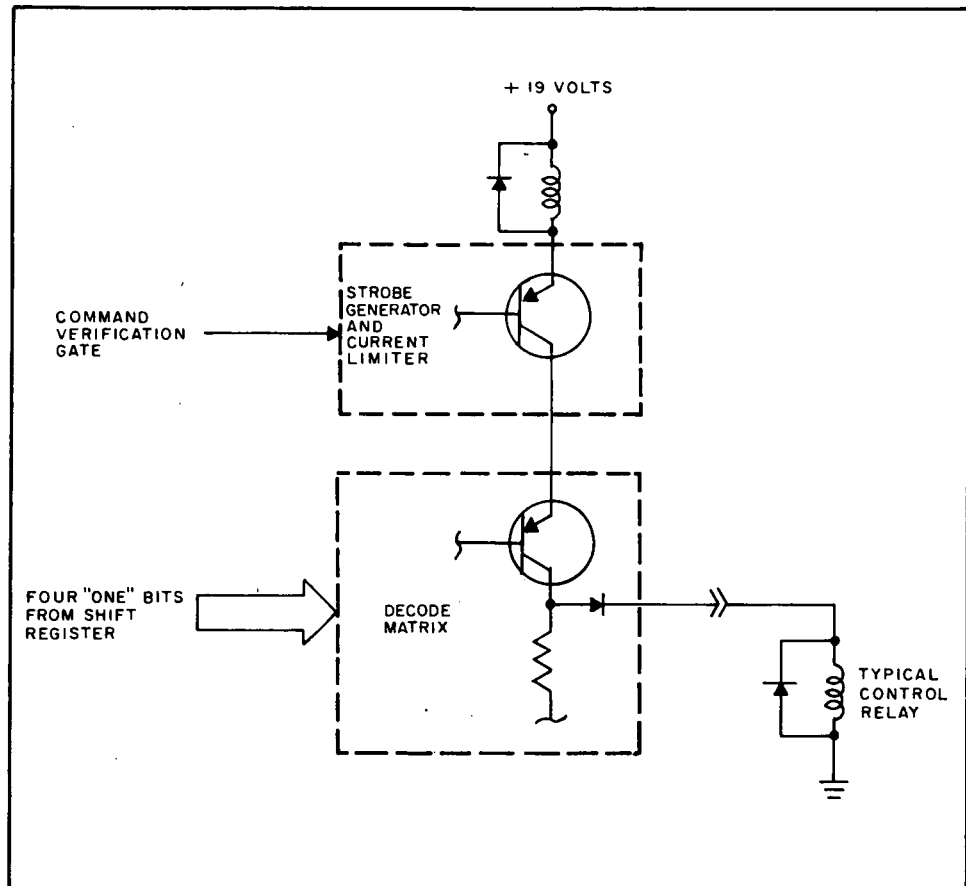


Figure 9-6 Output Switch Configuration

The two redundant command receivers are fed from a common antenna system through a diplexer and a hybrid circulator (see Figure 9-1). The diplexer isolates the OSO telemetry transmitters from the command receivers and permits a common antenna system to be used for both transmitting and receiving. The hybrid circulator provides 40-dB isolation between the command receivers to permit independent operation in case one of the receivers fails.

Each receiver has a single conversion 10.2 MHz IF stage with a bandwidth of 36 KHz. The audio frequency response is  $\pm 1.5$  dB from 5 to 9 KHz. Each receiver has an independent, Automatic Gain Control (AGC) circuit that uses varicap diodes in the interstage coupling circuits. This AGC loop holds the audio output power constant into a 500-ohm load for input voltage levels of 4 microvolts to 1 millivolt (75 percent modulated).

VHF selectivity is obtained by using a triple-tuned preselector followed by an RF amplifier stage and a single-tuned coupling transformer. An image trap is designed into the coupling transformer. Image frequencies are attenuated 50 dB by the preselector and 30 dB by the image trap, resulting in an overall image rejection of 80 dB. A high degree of rejection to spurious signals is obtained by use of a crystal-controlled local oscillator and a crystal filter ahead of the IF amplifier stage.





F72-01

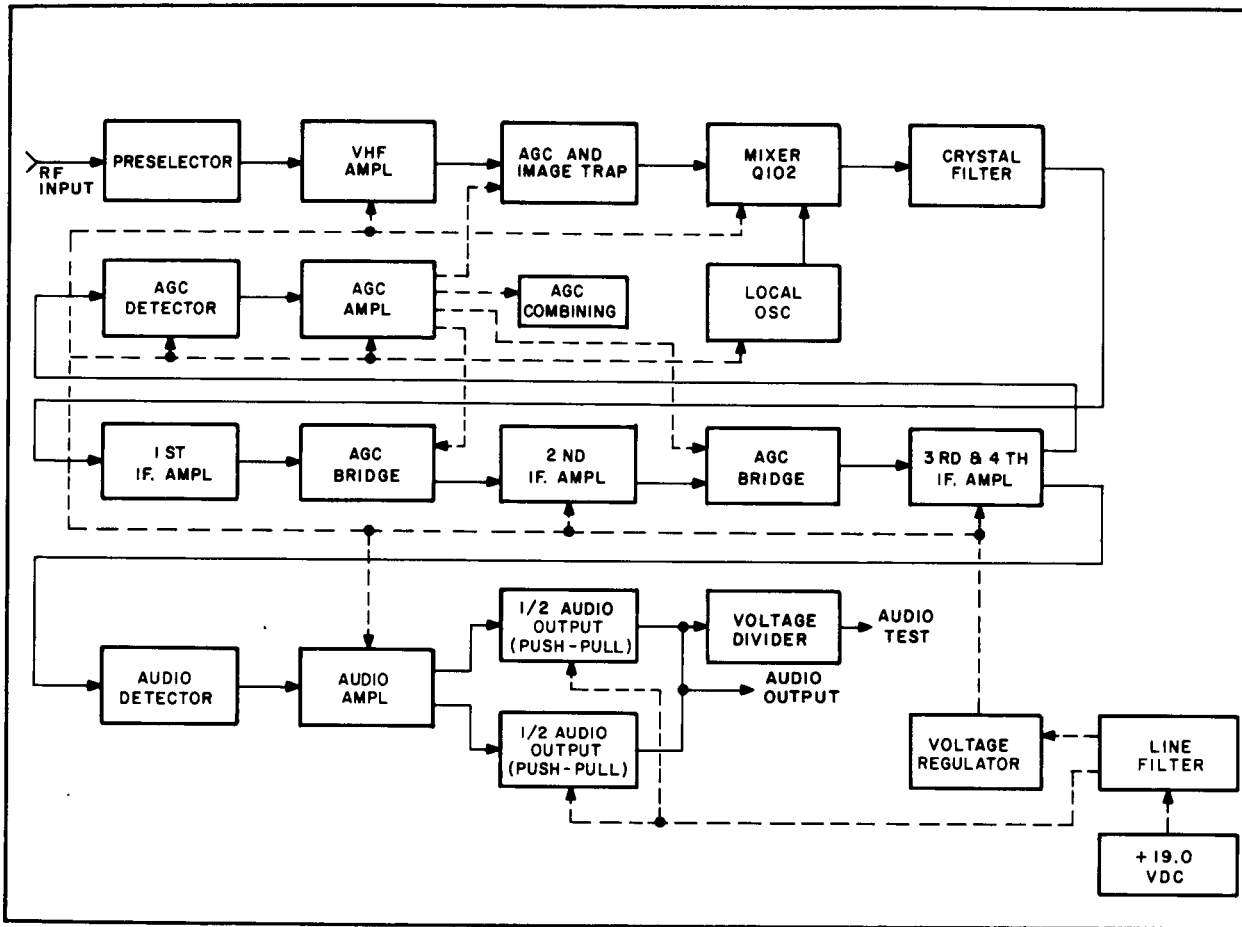


Figure 9-7 VHF Command Receiver Block Diagram

System security has been improved for OSO-7 by improvements in the stability of the system threshold. The no-command threshold level is now -103 dBm minimum, while the 100 percent command threshold level is -98 dBm maximum.

### 9.5 SYSTEM PERFORMANCE REQUIREMENTS

The performance requirement of the OSO command system is to provide reliable command control of OSO from ground-based stations.

The OSO command system design is based on a minimum elevation angle of 5 degrees above the local ground station horizontal and constraints of the existing ground equipment. The ground station equipment consists of a 1000-watt AM transmitter, a right-circularly polarized transmitting antenna having a gain of +23.5 dB, and a command encoder. An RF transmission line loss of 3 dB is assumed for the ground equipment.



F72-01

Table 9-5  
RECEIVER ELECTRICAL CHARACTERISTICS

Characteristic	Specification
Type	Superheterodyne, single conversion, fixed-tuned
Modulation Received	Amplitude modulation (75%)
Command Frequency	149.52 MHz
IF Frequency	10.2 MHz
Local Osc. Frequency and Stability	139.32 MHz $\pm$ 2 KHz
Image Frequency	129.12 MHz
Audio Response Within 1.5 dB	5000 to 9000 Hz
Dynamic Range	4 $\mu$ v to 1mv
Bandwidth: At 6 dB points	35 to 42 KHz
At 60 dB points	104 to 110 KHz maximum
Receiver Local Oscillator Stability	$\pm$ 2 KHz
Undesired Response Rejection:	
Image Frequency	80 dB
136 to 138 MHz	100 dB
Other spurious signals	75 dB
Power Requirements	
Input Voltage	16 to 22 vdc
Standby mode	320 mW maximum
Interrogate mode	700 mW maximum

The OSO-7 command link analysis is shown in Table 9-6. This analysis shows the system margin to be 2.5 dB at the maximum range for 99.7% of aspect angles. At the antenna specification value of -18 dB gain for 95% of aspect angles, the system margin is +11.5 dB. As shown in the antenna patterns of Section 8, receiving antenna gains below -27 dB can occur for short times as the spacecraft spins through off-axis antenna nulls. Normal operating procedure at the ground station (by means of the paper tape format) is to transmit each command twice during a revolution of the wheel. This procedure assures that commanding of the OSO will be executed reliably.



F72-01

Table 9-6  
OSO-7 COMMAND LINK ANALYSIS

Item	dBm or dB	Remarks
Transmit Power	+60 dBm	1000 watts
Transmit Line Loss	-3 dB	Assumed
Transmit Antenna Gain	+23.5 dB	
Polarization Loss	-1 dB	Assumed
Space Loss	-143 dB	300 nm, 5° elevation
S/C Circuit Loss	-5 dB	Including hybrid
S/C Antenna Gain	-27 dB	99.7% coverage
Received Signal Power	-95.5 dBm	
Receiver Sensitivity	-98 dBm	Specification value
System Margin	+2.5 dB	
<hr/>		
S/C Antenna Gain	-18 dB	95% coverage - specification value
Received Signal Power	-86.5 dBm	
System Margin	+11.5 dB	



F72-01

Section 10  
STRUCTURAL, PNEUMATIC AND THERMAL CONTROL DESCRIPTION

10.1 DEVELOPMENT HISTORY OF OSO-7

OSO's 1 through 6 had similar structural, pneumatic and thermal characteristics and capabilities. OSO-7, however, provides increased capabilities and hence has very different characteristics. The OSO-7 structure accommodates three times the experiment volume of OSO-6 while housing both spacecraft equipment and experiments within the same dynamic environmental limits. The design requirements for the OSO-7 wheel were to house 270 pounds of experiments with additional capability of 230 pounds of experiments and 70 pounds of spacecraft components. The OSO-7 sail was to house 180 pounds of pointed experiments with additional capability of 70 pounds of pointed experiments, additional solar array panels, and up to 40 pounds of additional spacecraft equipment.

The OSO-7 solar array area is two and one-half times greater with growth potential to approximately four times greater than OSO-6. To meet the new pneumatic system life requirements, the pitch reservoir size was doubled and the spin reservoir size nearly tripled. The spacecraft equipment and experiments thermal limits are similar to those of OSO-6; certain experiments have even more stringent limitations. At the same time, the observatory could not exceed the 57-inch dynamic envelope of the Delta-N fairing.

10.1.1 Design History

The tall, narrow cylindrical envelope available within the Delta-N fairing and the requirement for solar array surface area were primary constraints on the observatory shape. Furthermore, the observatory must be dynamically "disk" shaped rather than "rod" shaped. With the observatory configured at the full 1900 pound capability, the experiments and equipment outboard in the wheel required sufficiently large moments of inertia to ensure inherent dynamic stability. However, OSO-7 was to have only about one-half the design limit wheel experiment weight, which produced a deficit in wheel spin MOI. Rather than incorporating deployable arms, a ring of ballast weights was added to the wheel rim. Any future use of the structure, with a heavier wheel experiment complement would require only the deletion of a corresponding amount of this ballast ring weight. This design provides a nearly constant structural configuration of the wheel, independent of the wheel payload weight.

The 9-inch observatory/vehicle attach interface used for OSO-6 was not structurally adequate for the heavier OSO-7. The 18-inch cylindrical tube through the center of the OSO-7 wheel provided:

- Safe enclosure of a single spin gas bottle on the spin axis
- Structural enclosure of a modulator azimuth drive assembly
- Common mounting for a flat top deck and simple rectangular radial rib panels



F72-01

- Simplified structural and thermal analytical modeling
- Rapid and inexpensive fabrication and integration techniques
- Easy adaptation to ground testing and checkout hardware
- Use of a radial slot antenna with an improved pattern
- Structurally adequate vehicle interface.

The top deck and radial rib panels were made of honeycomb for maximum stiffness and damping characteristics while maintaining simplicity and interchangeability of parts.

The OSO-6 sail structure was made up of aluminum azimuth and elevation castings and a riveted "eggcrate" matrix which supported the sail equipment and solar array. No castings were used on the OSO-7 sail. This eliminated the long-lead procurement and complex radiographic inspection requirements, the high rejection rate, and the problems of choosing arbitrary "casting factors" to use in the structural analysis. The "eggcrate" approach was eliminated primarily to improve component access during integration and test.

OSO-6 used a single unloaded ABEC-5 radial bearing on either side of the elevation gimbal and a brush-type motor. The OSO-7 uses a preloaded duplex pair of ABEC-7 angular contact bearings on either side of the gimbal and a brushless motor. The pitch gas supply was equally divided into two reservoirs, symmetric about the spin axis, to preserve sail balance as gas was exhausted.

The individual components within the OSO-6 azimuth drive system were separately integrated into the spacecraft. The OSO-7 pitch bottle no longer had to surround the azimuth shaft so a modular azimuth drive assembly (ADA) was used. The modular drive allowed the unit to be acceptance tested prior to integration so that drive units could be interchanged in the observatory with only minimum effort. A 40-circuit, gold-on-gold slip ring assembly replaced the 22 circuit silver assembly previously used. Other improvements in the drive are discussed in Section 10.2.

OSO-7 was designed for passive thermal control as were all six previous OSO's. The OSO-7 thermal control system can make use of active elements such as the gyro heater, the ADA heater, and the power system dummy loads on a contingency basis if required. The new OSO-7 structure and payload required a thermal modeling of conductivities, capacitances, view factors, external fluxes, and internal electrical heat generation. Section 10.6 describes the thermal analysis of OSO-7.

#### 10.1.2 Analysis History

During the development phase the structure was configured and sized for adequate stiffness, damping, and structural integrity. Previously flown components were not to be exposed during launch or structural testing to dynamic environments exceeding their previous qualification levels.



F72-01

Complex spring and mass matrices were developed for computer determination of the first ten cantilevered resonant frequencies and their associated ten mode shapes. After several iterations, the design evolved so that the resonant frequencies were adequately separated and decoupled from known vehicle modes, so that no adverse control system interaction would occur. A simplified three-mass, three-spring model was then generated. This model was equivalent to the complex model in terms of primary resonant frequency, mode shape, MOI, and mass. These simplified spring mass models were combined with the vehicle model to determine launch load factors and angular accelerations of the three masses (wheel, sail, and pointed experiment package) for the critical launch excitation modes.

For the stress analysis, the simplified loads for the most critical launch modes were redistributed by computer program back into the complex observatory model while maintaining equivalent total load and moment at the Delta adapter. Stresses were directly available from computer programs for those items that had been idealized as simple geometric forms (e.g., panels). Stresses were determined for the more complicated structural elements using these redistributed sets of complex loads.

A determination was made of the extent to which the sinusoidal vibration test inputs would have to be reduced at the cantilevered resonances to avoid exceeding the launch loads during vibration testing. This was done using the analytical mode shapes with an estimated overall damping factor, and then solving for the input value which would result in duplication of the maximum primary structural launch loads.

A structural analysis report was prepared approximately eight months prior to launch, when observatory projected weight was 1,370 pounds. The report was updated to include results of the subsequent qualification vibration testing and the launch-phase simulation testing of the OSO-7 Qualification Model including weight factor increases of the final launch configuration weight of 1,415 pounds.

In addition to evaluating qualification vibration dynamic response and launch-phase simulation tests, necessary minor modifications were made in the complex spring and mass matrices. The resultant final resonant frequency and mode shape predictions were nearly identical to those actually observed during test. The simplified spring mass models were then correspondingly modified, flight loads obtained and assessed, and the stress analysis updated.

Thermal analysis also was an iterative process since conductivities, capacitances, view factors, and internal electrical heat generation were evolving early in the program. Absorptivities and emissivities were adjusted to obtain the required heat flux exchange for proper equilibrium temperatures. The thermal analysis was completed approximately nine months prior to launch, after determination that the observatory and its component temperature extremes were within the OSO-6 envelopes. This analysis used a 183-node mathematical thermal model. The analysis also determined the steady state and transient responses for mean solar intensity and mean orbit plane angle, and the appropriate acceptance and qualification test limits for components.



F72-01

A complete 49-node thermal analysis was also performed on the azimuth drive assembly to determine temperature gradients and "hot spots", to assess adequacy of the 0.0015 inch longitudinal thermal expansion clearance, and to assess lubricant migration behavior within the drive.

Pneumatic systems analysis dealt primarily with nozzle sizing; regulator, solenoid, and line pressure drops; thrust and mass flow rate calculations; reservoir sizing; and thermal calculations to assure that icing could not occur.

### 10.1.3 Testing History

OSO-7 was tested according to the environmental test requirements of NASA S-320-G-1. To demonstrate compliance, a Qualification Model observatory was fabricated for a complete qualification program. The Qualification Model used mass simulations of the experiments and several previously flown and separately qualified components.

Structural qualification of OSO-7 (at the spacecraft level) included sinusoidal and random cantilevered vibration in the three mutually perpendicular spacecraft axes; observatory/vehicle attach clamp separation shock; and launch phase simulation.

During the vibration testing, structural dynamics response, component local environment effects, and OSO-7/Delta-N interface integrity were verified. It was determined that the programmed shock test of S-320-G-1 could be replaced by the more severe attach clamp separation shock test. A necessary associated effort was the requalification of the 18-inch interface attachment hardware to formalize qualification status for the 1415 pound payload.

The launch phase simulation tested steady state acceleration along the longitudinal axis, acoustic noise, and ascent pressure decay, all in their real-time launch profiles. Two separate tests were performed, one at "acceptance" levels and another at "qualification" levels. Longitudinal vibration was not performed during this test so the steady state acceleration value was adjusted to envelop both the predicted steady state acceleration and the primary structural response at 17-23 Hz. This approach resulted in a longitudinal qualification level run at 17.9 g's.

Thermal qualification of OSO-7 at the spacecraft level included thermal vacuum and thermal balance tests. Spacecraft performance was verified during thermal vacuum testing at 10°C above and 10°C below the anticipated mean mass in-orbit temperature extremes (+43°C and -10°C). Thermal vacuum testing also verified that corona, launch sequencing, pyrotechnic performance, operational spin and control systems performance, proof pressurization and leak checking, temperature transition operation, cold "start-up" operation, and day-night cycling operation were satisfactory.

The thermal balance tests were performed only on the qualification model sail, since historical prediction accuracy of in-orbit OSO wheel temperatures was excellent. The primary purpose of the thermal balance testing was to verify the predicted subsystem temperatures throughout the range of orbit plane angle, solar intensity, and on-board power dissipation. The equivalent fluxes were adjusted by using adhesive electrical



F72-01

heater sheets on critical surfaces. The sail/wheel thermal interface was duplicated by using a real azimuth drive assembly and a real wheel top deck.

Pneumatic system qualification on OSO-7 verified compliance with all the requirements including those from the Eastern Test Range. The tests included leak rate checks at the spacecraft level, spin and pitch gas mass flow rates, and burst and proof tests at piece part and system levels. Other tests included piece part leak rates, solenoid reliability cycling life tests, system flowing pressure, system mass flow rates, and system tests to show that icing did not occur with extended operation time.

Component level testing on OSO-7 was accomplished to demonstrate compliance to the applicable parts of S-320-G-1. The approach was to incorporate into the qualification model as many of the previously qualified components as was practical and all the new components.

The new or redesigned components included the antenna and its matching network, spin and pitch pneumatic subsystems, azimuth and elevation drive assemblies, gyro and gyro electronics, decoders, star scanner, digital aspect sensor, battery cell monitors, SORE package, tape recorder switching logic, solar arrays, pitch coil, launch sequence subsystem, sail J-Box, and the servo coarse acquisition subsystem. All these components were environmentally qualified while on the qualification model and/or at the component level.

To simplify vendor subcontract negotiations and definitize reliability responsibility, all procured components were functionally and environmentally qualified at the component level prior to delivery. They were then incorporated into the qualification model spacecraft for additional testing.

Numerous "component" tests were performed on the new items that were not specifically required by the general requirements documents. A few of the more important tests were: life tests of azimuth and elevation drive assemblies; flexible cable life test; ADA temperature gradient test; honeycomb thermal conductivity, structural, and leak rate tests; tests to determine that motor arcing was unlikely; extensive parametric testing on bearing friction; ADA springrate and impulse sequence tests; fastener reliability and debris potential tests; adherence tests of thermal paints; soft lock structural tests; pointed experiment alignment hardware development testing; gyro thermal testing; and extensive electro-mechanical servo system tests.

## 10.2 OBSERVATORY STRUCTURE

The OSO-7 observatory structure consists of three major items, the lower section or wheel, the upper section or sail, and the interface structure including the despin or azimuth drive assembly (ADA). The observatory is contained within a cylinder 57 inches in diameter and 80.6 inches high. The launch weight of the observatory is 1415.5 pounds which includes 19 pounds of expendable dry nitrogen.

The observatory structure provides the interfaces for spacecraft equipment, experiments, Delta-N booster, ground handling and testing equipment, and servicing and checkout.





F72-01

The structural interface with the equipment and experiments provides the thermal and mechanical connection to spacecraft and the required alignments, provides for cable harness routing, and protects against harmful contamination. The interface with the Delta-N booster includes the spacecraft-to-launch vehicle mechanical attachment and separation provisions, the electrical connector for the fairing pull-away cable, and the separation-indicating switch assembly. The structure contains the attachment points for lifting and transporting, measuring moments of inertia and center of gravity, dynamic balancing, solar pointing, and for the integration and test stand. The pneumatic system fill ports, the dry nitrogen purge port, and the ground test and checkout electrical interface connectors also are mounted on the spacecraft structure.

### 10.2.1 Wheel Description

The wheel is a 15-inch high nine-sided polyhedron. The nine compartments of the wheel are separated by rib panels radiating from the 18-inch diameter central hub. The upper and lower compartment closures are the flat deck and the three cover segments, respectively. The peripheral closures are nine rim panels. Figure 10-1 shows the wheel structural components. The wheel interfaces with the antenna and Delta-N booster adapter on its lower surface, and the azimuth drive is nested within the upper portion of the central hub.

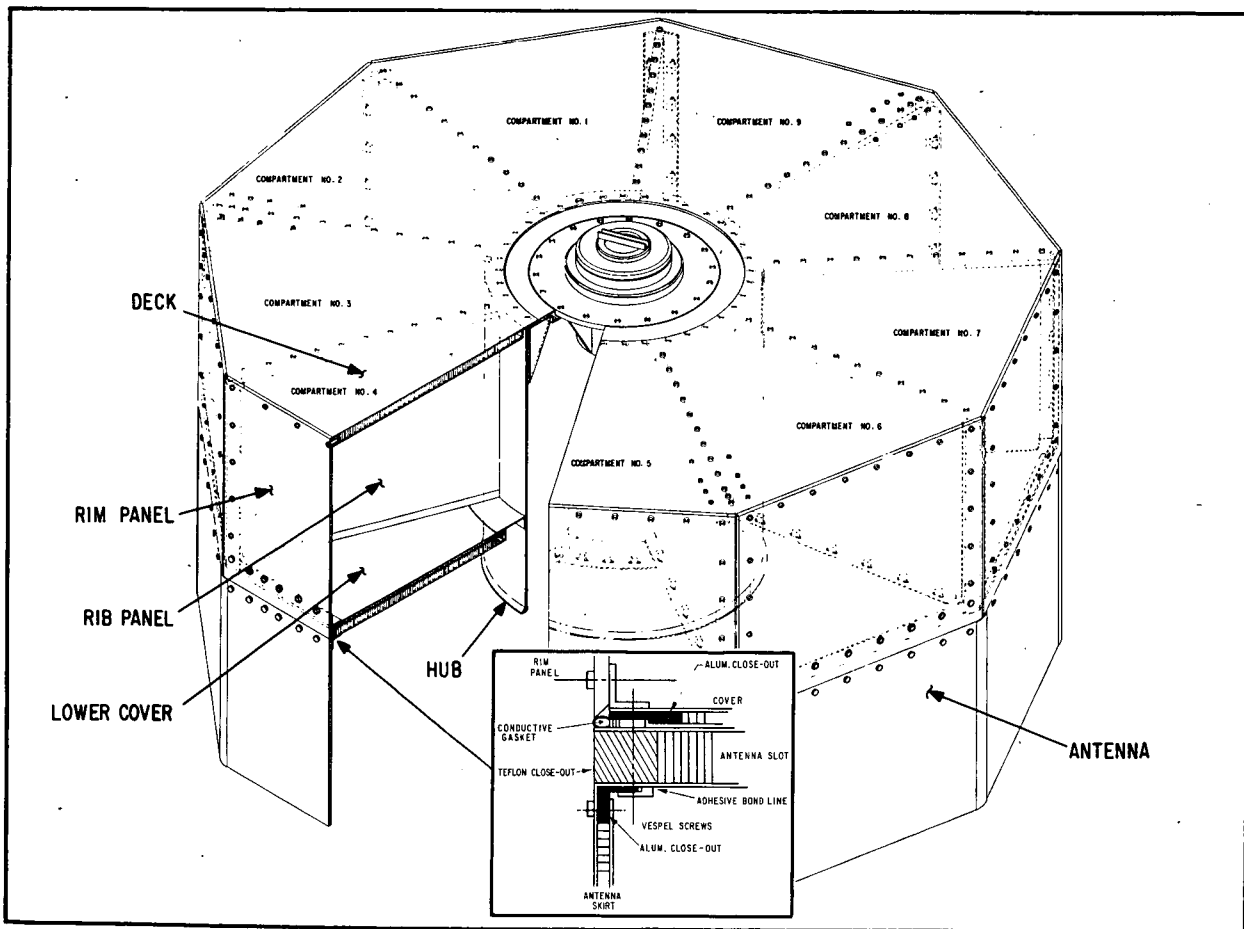


Figure 10-1 Wheel Structural Components



F72-01

Compartments 3, 5, 6, 8, and 9 accommodate experiments and 1, 2, 4, and 7 carry spacecraft equipment. Each 40° compartment has a trapezoidal shape 17.3 inches along the radial and with outer and inner base lengths of 19.3 and 6.2 inches respectively, for a total volume of approximately 3300 cubic inches.

The deck, ribs, and central hub are the primary load carrying members of the wheel structure. Sail loads, via the azimuth drive, are also fed directly into the hub's upper ring. All loads are ultimately reacted at the hub/launch vehicle clamped interface.

The deck, ribs, and lower covers are of honeycomb sandwich construction. The core material, 5056-H39 aluminum-foil honeycomb, is attached to the 2024 aluminum face sheets and 6061 aluminum edge closures with 0.005 inch FM 1000 sheet adhesive. The face sheet thickness is 0.020 inch for the covers, 0.032 inch for the ribs, and 0.032 inch upper and 0.062 inch lower for the deck.

For mechanical attachments the sandwich panels contain 3/4-inch diameter inserts bonded between the face sheets, locally replacing the honeycomb core. The overall thickness of the deck is 0.75 inch, the rib panels are 0.5 inch thick, and the cover panels are 0.25 inch thick. The central hub is machined from a single ring forging of 7075-T652 aluminum. The rim panels are machined from 2024-T351 aluminum sheet and are fitted to the equipment or experiment aperture requirements.

The antenna structure, constructed of sandwich panels, is attached to the lower surface of the wheel structure. It is cylindrical in shape, open on the aft end and closed at the forward end by the feed slot. The vertical members contain 5056-H39 aluminum honeycomb core bonded to 6061 aluminum edge closures and 0.012 inch thick 2024-T3 aluminum face sheets with 0.005 inch FM 1000 sheet adhesive. The nine 19.3 inch by 14.5 inch by 0.25 inch thick vertical members (skirt panels) are riveted together with doublers to form the skirt section. The feed slot or top cover to the antenna skirt is a nine-sided panel, shaped like the deck externally, but 0.56 inch thick. The feed slot contains fiberglass honeycomb core bonded to teflon edge closures and 0.032 inch thick 2024 aluminum face sheets with 0.005 inch FM 1000 sheet adhesive.

The two antenna sections are bonded and screwed together using redundant Vespel screws, to form the antenna assembly.

#### 10.2.2 Sail Description

The sail section is rectangular in shape, 55 inches wide and 50 inches high including the two antenna "ear" extrusions. The sail contains three major subassemblies as shown in Figure 10-2: the beam assembly, the frame assembly and the elevation assembly.

The frame assembly interfaces with the ends of the beam assembly and contains the majority of the sail-mounted equipment. The solar-cell array is attached to the front of the frame, forming shear plates for lateral framework stiffness. The elevation assembly interfaces with the top of beam assembly and contains the remainder of the sail-mounted equipment and the pointed instruments. The beam assembly supports the other sail assemblies and attaches to the azimuth drive on its lower face.



F72-01

The frame assembly consists of a network of vertical struts and lateral shelves. The frame members are fabricated from 2024-T3 and 2024-T351 aluminum to form "I" beams which are riveted together to form the sail frame assembly.

The elevation assembly contains the elevation frame, elevation drive, and elevation frame support members (trunnions). The elevation frame is machined from a 7075-T6 aluminum ring forging, heat treated to the T73 condition. The frame is supported by titanium shafts containing duplex bearing pairs held by the 7075-T73 aluminum trunnions.

The beam assembly is the major load-carrying member of the sail and transmits the frame and elevation loads to the azimuth drive assembly. The beam assembly is machined from 7075-T73 aluminum.

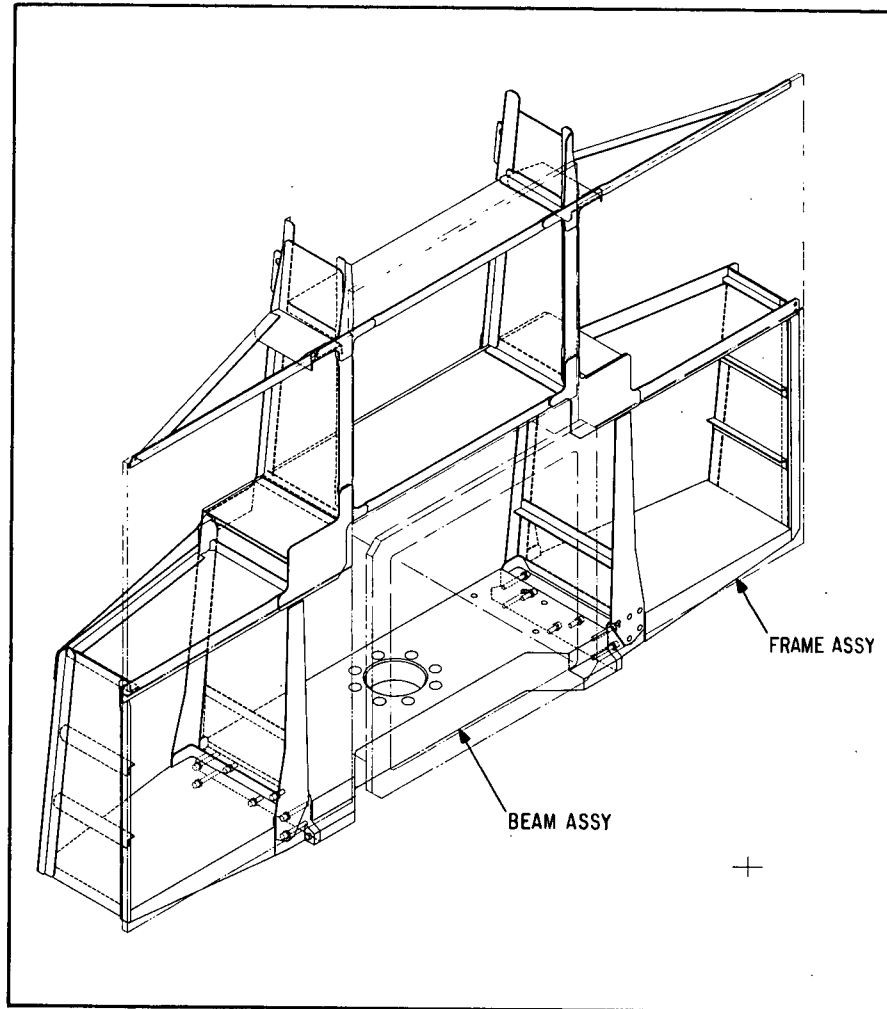


Figure 10-2 Beam and Frame Assemblies

The solar-cell array substrates, which form the shear panels for the sail framework, are 16.3 inch by 18.3 inch by 0.42 inch thick sandwich panels containing 5056-H39 aluminum foil honeycomb core bonded to 6061 aluminum edge closures and 0.020 inch thick 2024-T3 aluminum face sheets with 0.005 inch thick FM 1000 sheet adhesive.

### 10.2.3 Azimuth Drive Assembly (ADA)

The azimuth drive assembly is shown in Figure 10-3. The 6 A1-4V titanium housing flange is bolted to the web ring on the top of the 18 inch hub and the 6A1-4V titanium shaft is bolted to the sail's transverse beam. The ADA contains the duplex pair of angular contact bearings, azimuth motor and filter, slip ring assembly, and magnetic pickup. The sail side



F72-01

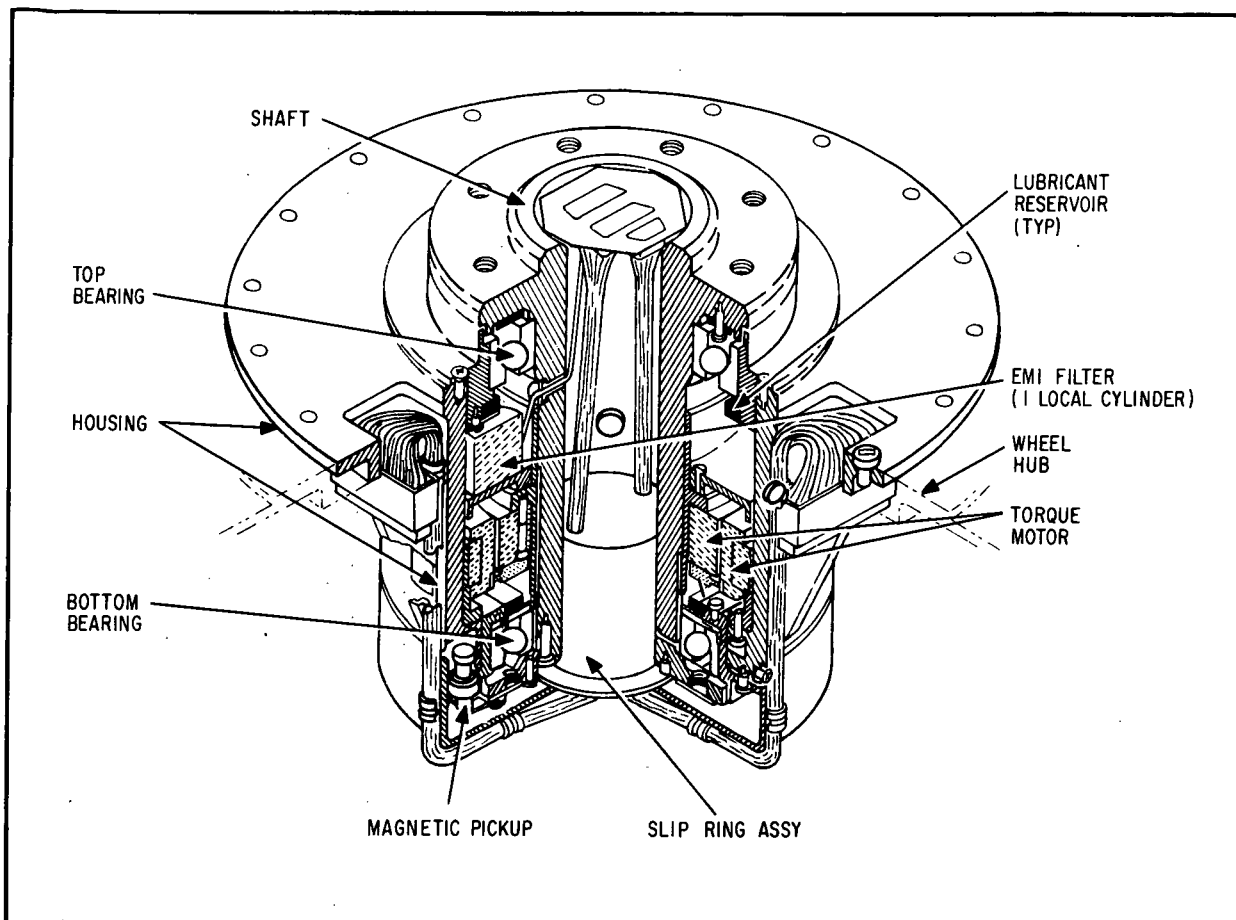


Figure 10-3 Azimuth Drive Assembly

is loaded against the wheel side using axial preload springs across the 0.001 inch to 0.002 inch axial thermal gap. In orbit, this 5 pound total preload is sufficient to remove most of the angular contact bearing "slop", smoothing the rotational friction. The bearings, motor brushes, and 40-circuit slip ring assembly are lubricated using the BBRC-developed liquid Vac Kote process. There are also Vac Kote saturated nylasint reservoirs on either side of each bearing.

### 10.3 PNEUMATIC SYSTEMS

Nitrogen gas pneumatic systems control the spacecraft pitch attitude and add or subtract angular momentum from the wheel. Each system consists of a fill connection, check valve, pressure vessels, manifold, pressure transducer, filters, pressure regulator, solenoid valve, nozzles, and pneumatic lines.



F72-01

The check valves, pressure vessels, pressure transducer, filters, and regulator all are connected to the high pressure manifold. The check valve prevents nitrogen from escaping through the fill line and fitting. The pressure transducer senses the pressure in the vessels and produces a proportional analog voltage which is telemetered to the ground receiving stations. The pressure vessels store the nitrogen gas originally at 3000 psia. The filters prevent particles from entering the pneumatic system downstream from the manifold. The gas then flows to the pressure regulator which reduces the downstream pressure to obtain appropriate system mass flow rates. When a control solenoid is activated, the low pressure gas flows to the appropriate nozzle.

#### 10.3.1 Spin Pneumatics

Most of the spin pneumatics is centrally located within the lower section of the wheel hub, as shown in Figure 10-4.

The nozzles are located at the ends of the ribs between compartments 1 and 2, 4 and 5, and 7 and 8. The nozzles are slanted 20° outward from the tangent to wheel rim to eliminate interference in exhaust plume and to decrease gas density near experiments during bursting. The important parameters of the spin system are shown in Table 10-1.

#### 10.3.2 Pitch Pneumatics

The pitch system is located on the back side of the sail, as shown in Figure 10-5. The two pressure vessels are contained on the bottom two shelves, one on either side of the elevation assembly. The high pressure manifold, check valve, pressure transducer, filters, pressure regulator and solenoid valves are modularly mounted to the outboard section of the left shelf. The nozzles are attached to the upper ends of the vertical sail frame members. The important parameters of the pitch system are shown in Table 10-2.

#### 10.3.3 Leak Rate of Pneumatic Systems

The total allowable leak rate is 35 standard cubic centimeters of nitrogen per hour. This is equivalent to the test condition of a 90-percent nitrogen and 10-percent helium mixture leaking at a rate of 9.3 standard cubic centimeters of helium detected per hour. At nominal in-orbit temperatures, the leak rate is much smaller than this; even at -10°C, the total leak rate is only about 1/2 of this allowable limit.

### 10.4 STRUCTURAL ANALYSIS SUMMARY

#### 10.4.1 Methods of Analysis

To determine internal structural loads, thermal stresses, natural vibration mode shapes, and frequencies, a finite element structural model was developed. This mathematical model was then used for the structural loads and dynamic analysis. A computer-drawn isometric view of the OSO-7 structural model is used as an aid in verifying that the structure has been modeled properly.



F72-01

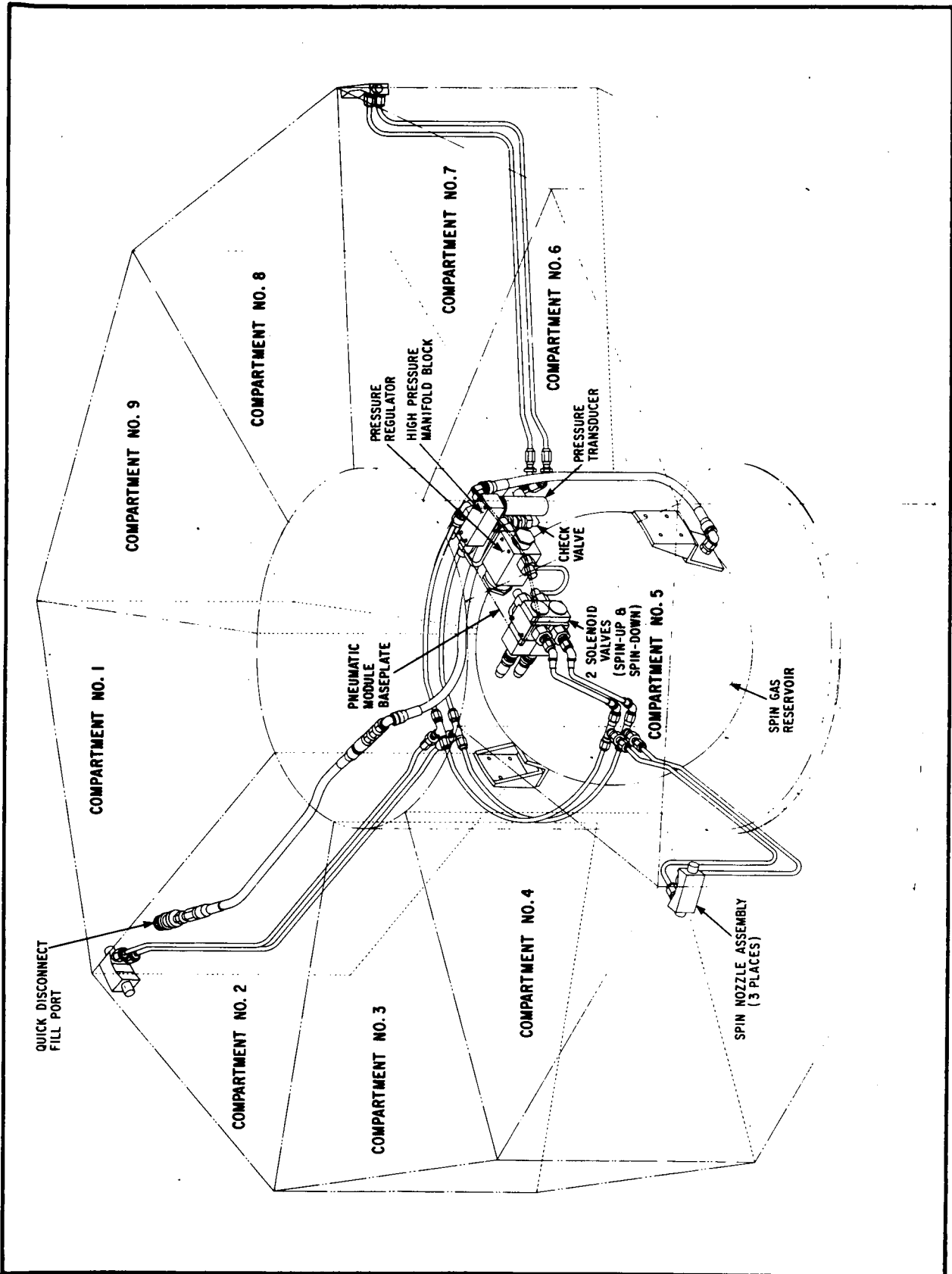


Figure 10-4 Spin Pneumatic System



F72-01

Table 10-1  
SPIN PNEUMATIC PARAMETERS

Nitrogen pressure at launch	3000 psi
Nitrogen weight at launch	10.75 lbs
Weight equivalent for launch sequence	1.42 lbs
Weight equivalent available to orbit	9.33 lbs
Moment arm	2.33 ft
Flowing pressure at nozzles	98 psi
Mass flow rate (total)	0.00744 lb m/sec
Thrust per nozzle	0.183 lbs
Total thrust	0.549 lbs
Angular acceleration of wheel	0.0141 rad/sec <sup>2</sup>
Spin correction per 4 sec. burst	0.009 rev./sec.
Total spin correction available at launch	3.28 rev./sec.
Total spin correction available in orbit	2.85 rev./sec.

All deflections and internal loads for the OSO-7 spacecraft were determined using the "Stiffness Finite Element Method" of structural analysis. All natural vibration mode shapes and frequencies for OSO-7 were determined using matrix iteration on the dynamic matrix; defined as the product of the inverse of the stiffness or spring matrix and the mass matrix. The mass matrix is generated by lumping mass at discrete node points on the complete mathematical model. As nearly as possible within the constraints of lumped masses and inertias, the mass distribution represented by the mass matrix is maintained the same as the actual mass distribution for the observatory. The location of the mass center is also preserved, as is the observatory total mass and mass moments of inertia.

The stiffness or spring matrix is generated by the stiffness finite element method. The analytical model used for determining the spring matrix contains much more detail and many more node points than that used for generating the mass matrix. The spring matrix is reduced by a method compatible in dimension with the mass model.

Design Criteria. The following design criteria were used in the analysis of the spacecraft:

- The structure must withstand application of ultimate loads (1.5 limit loads) in conjunction with associated environmental conditions without failure.
- The structure must withstand application of limit loads in conjunction with associated environmental conditions without yielding.
- Structural deformations under any loading and associated environmental condition must not be detrimental to the mission of the spacecraft.



F72-01

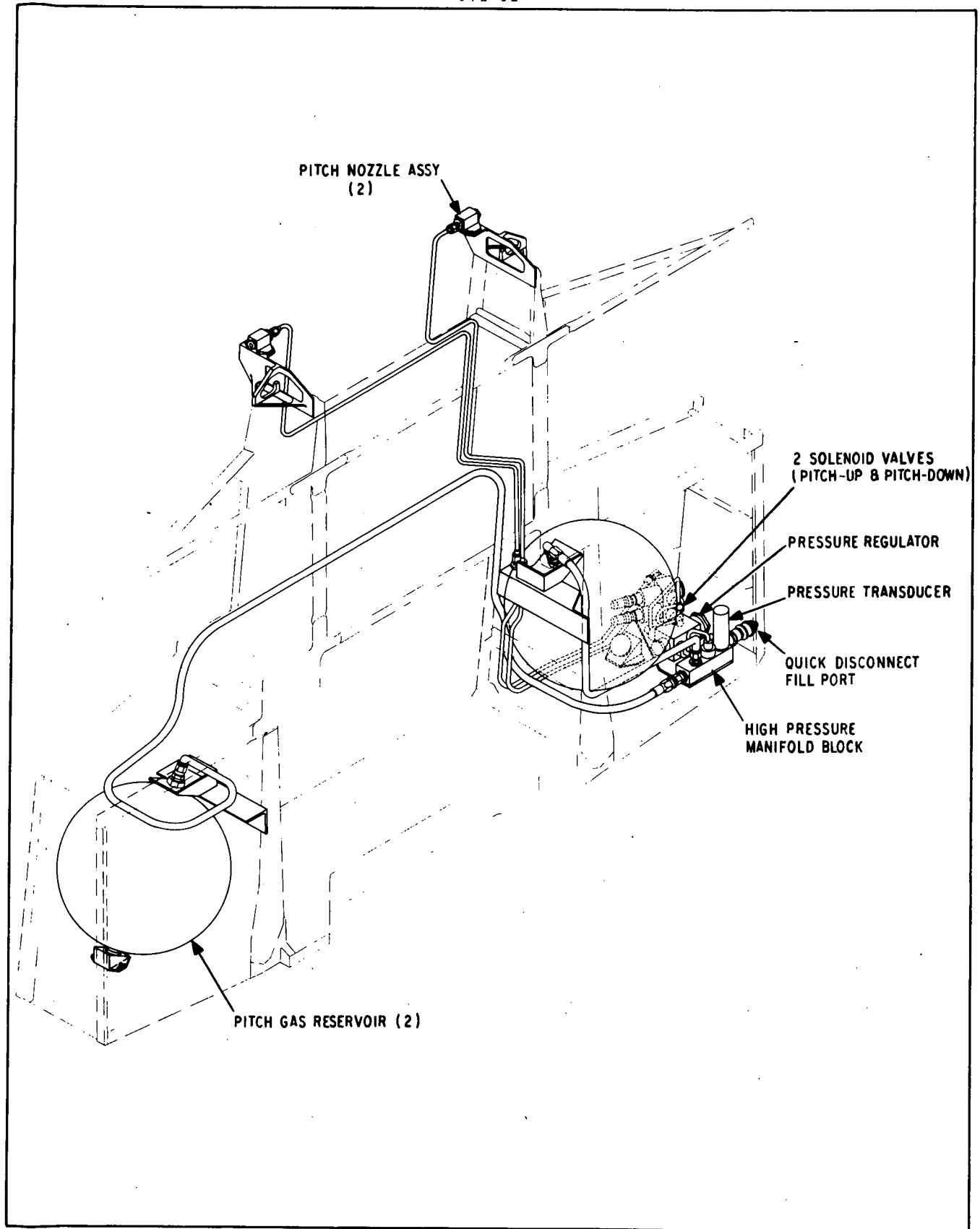


Figure 10-5 Pitch Pneumatic System





F72-01

Table 10-2  
PITCH PNEUMATIC PARAMETERS

Nitrogen pressure at launch	3000 psi
Nitrogen weight at launch	8.22 lbs
Moment arm	3.42 ft
Flowing pressure at nozzles	63 psi
Mass flow rate	0.00149 lb m/sec.
Thrust	0.11 lb
Pitch rate (for wheel spin rate of 0.5 rps)	0.0754°/sec.
Total pitch correction available	208° rps - (416° at 0.5 rps)

- Factors of safety for design of the various structural elements must be consistent with accepted structural design practice, safety, and launch facility requirements.
- Margins of safety shall include the effects of combined loads or stresses (interaction).
- The spacecraft structure must be designed to minimize coupling at fundamental launch vehicle resonances.
- Spacecraft resonances must not couple with control system frequencies.
- Fundamental sail resonances must not couple with fundamental wheel resonances.

#### 10.4.2 Structural Dynamics Analysis

A modal analysis of OSO-7 was performed with the spacecraft cantilever-supported at the base of the eighteen-inch Delta adapter fitting. The purposes of the analysis were:

- To verify that component environments were compatible with qualification and flight levels of existing component designs.
- To compute fundamental resonant frequencies and mode shapes suitable for use in generating a simplified mass-spring model. The simplified model was coupled to the Delta-N launch vehicle so that dynamic load factors and angular accelerations accompanying the predicted flight environment could be computed at the simplified mass points.
- To prove that fundamental cantilever-supported hard-mounted resonances of the spacecraft do not couple strongly with fundamental booster resonances.



F72-01

- To provide assurance that resonances of the structure do not couple strongly with control system frequencies while in the orbit configuration.
- To determine internal structural loads as a function of sinusoidal vibration inputs while cantilever-supported on the vibration machine. These loads were compared to the loads resulting from the predicted flight environment for the purpose of estimating preliminary vibration notches in the spacecraft sinusoidal vibration specification at the fundamental spacecraft resonances.

The results of the modal analysis showed that there was no severe dynamic coupling of the spacecraft with the booster and that the structural resonances did not couple strongly with the control system. The load factors based on a simplified three mass model coupled to the Delta-N launch vehicle were within the structural capability of the spacecraft. The first torsion mode of the sail is 21.5 Hz with the sail restrained at torque motor.

Structural Natural Frequencies and Mode Shape. The primary modes are summarized in Table 10-3, and include the pre-qualification vibration predictions, the actual vibration modes observed, and the final analytical predictions after slight modeling changes were made. The first vibration mode of the pointed experiment rocking against the launch soft lock is approximately 6 Hz and will not couple significantly with any of the cantilever-supported spacecraft fundamental frequencies. It was assumed that the pointed experiment package was free to rotate about the elevation axis, that is, the pitching mass moment of inertia about the elevation axis was zero. Figures 10-6 and 10-7 show the nodal idealization.

Table 10-3  
PRIMARY MODES OF OSO-7

Axis	Resonant Frequencies			
	Original Model	Test Results	Rerun #1	Rerun #2
X Direction	23.2	17.5	20.4	16.8
Y Direction	20.4	15.5	17.9	15.5
First Pogo	76.1	52.0	64.2	60.35
2nd X Direction	45.5	34.0	44.4	35.5
2nd Y Direction	38.2	32.0	38.1	32.3
2nd Pogo	(1)	98.0	131.8	108.4

(1) Only the first 10 modes are analyzed on the original model which did not include the second pogo resonance.



F72-01

### Structural Responses.

Based on previous experience from OSO spacecraft, structural damping factors were estimated and used analytically to derive structural response data. Structural loads for sinusoidal vibration inputs were derived based on the response data to determine preliminary notching of the vibration specification. Low level sweeps in conjunction with strain gauges and accelerometers allowed final notching of the specifications to limit primary structural loads on the spacecraft to match flight load predictions. Component responses were somewhat lower (with very few exceptions) than those on previous OSO's.

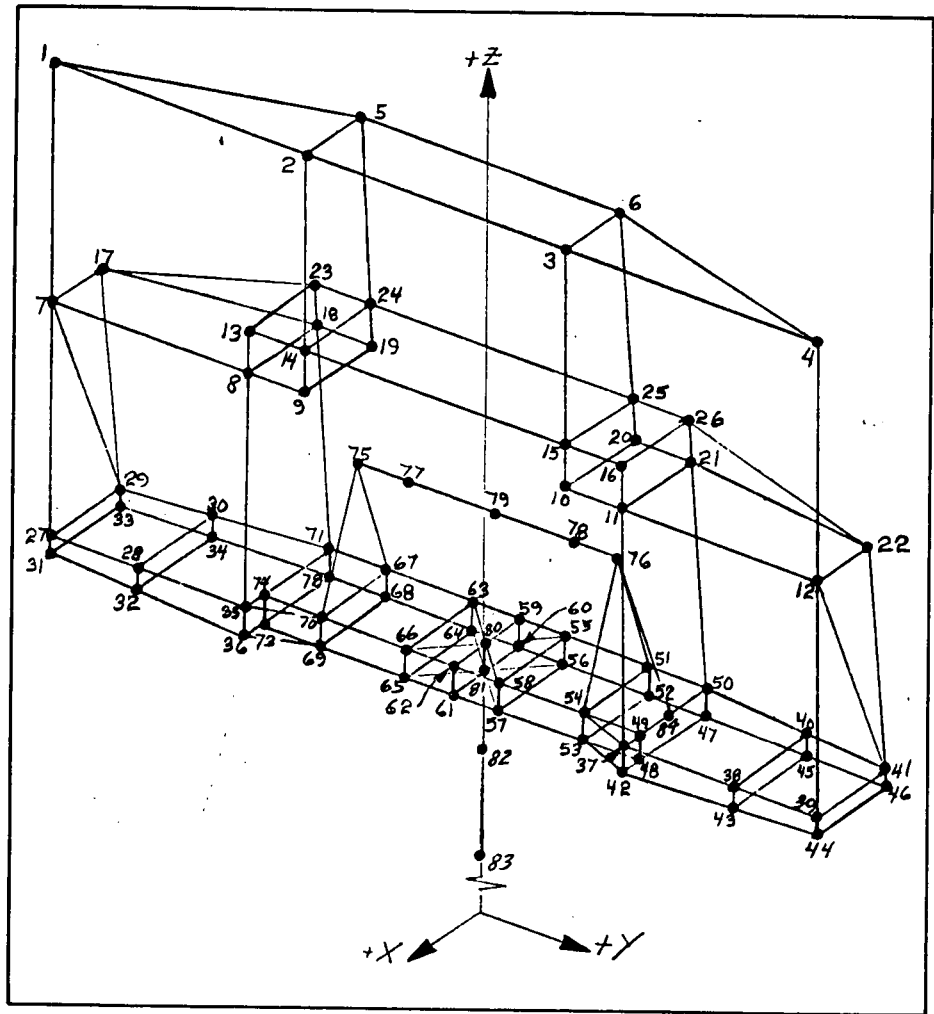


Figure 10-6 Sail Structure Idealization

#### 10.4.3 Stress Analysis

The results of the stress analysis showed that the spacecraft is capable of withstanding all flight and ground handling loads. All computed margins of safety are positive and in general relatively high. The lowest margins of safety are presented in Table 10-4.

#### 10.5 MASS PROPERTIES

The launch weight of OSO-7 is 1415.5 pounds, which includes 19 pounds of expendables. The summary of the measured mass properties is shown in Table 10-5 and the weight breakdown per subsystem is shown in Table 10-6 along with the percent of total observatory weight.



F72-01

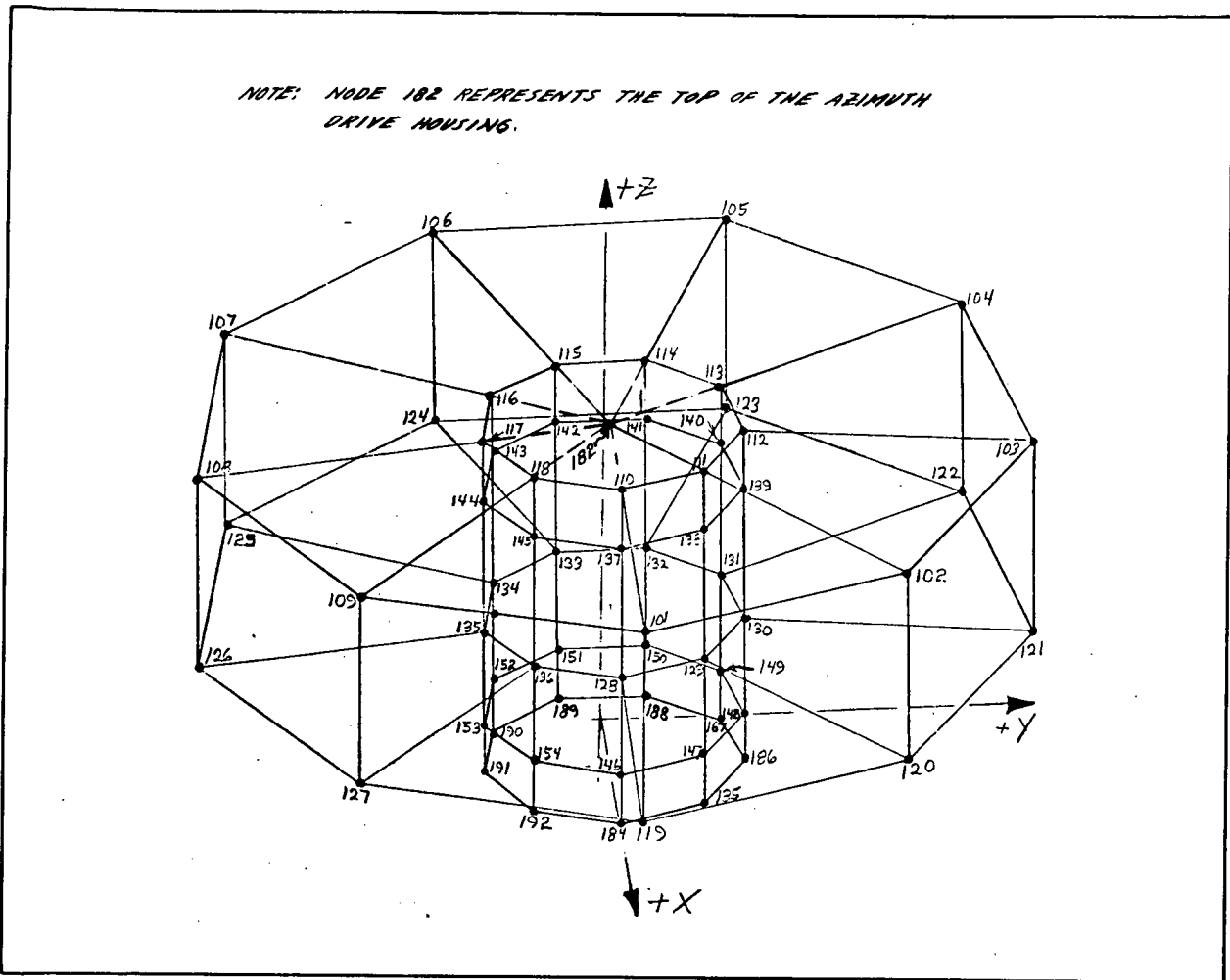


Figure 10-7 Basic Wheel Structure Idealization

Table 10-4  
MINIMUM MARGIN OF SAFETY SUMMARY - OSO-7 SPACECRAFT

<u>Structural Item and Critical Loading Mode</u>	<u>Minimum Margin of Safety</u>
Lower azimuth drive bearing (thrust and radial load)	0.78*
Upper azimuth drive bearing (thrust and radial load)	0.62*
Azimuth shaft to torque box attachments (bolt tension)	0.92
Tube flange for interface with 18-inch adapter (elastic instability due to radial load from V-band tension)	0.14
Torque box lid shear attachments (bolt shear)	0.35
Experiment to deck attachment (bearing in lower face sheet)	0.93
Deck (core shear)	0.46
Deck upper face sheet at edge member (bending and shear)	0.17
Elevation frame bearings (radial load)	0.64*

\*Margins of safety for bearings are based on extreme quiet running allowable loads and worst case bearing parameters. Nominal load margins of safety are much greater than values given.



F72-01

Table 10-4 (Cont.)

<u>Structural Item and Critical Loading Mode</u>	<u>Minimum Margin of Safety</u>
Soft-lock insert (elastomer failure)	0.18
Soft-lock squib support (bearing)	0.36
Soft-lock pin (bending)	0.24
Rib edge member (bending)	0.97
Sail upright-lower section (shear web buckling)	0.99
Upper shelf outrigger (column buckling)	0.57

Table 10-5

OSO-7 LAUNCH MASS PROPERTIES<sup>1</sup>

<u>Property</u>	<u>Launch</u>
Observatory Weight	1415.5 lbs
Observatory CG Above Separation Plane	21.9 in
Observatory Total Spin MOI	112.20 slug-ft <sup>2</sup>
Observatory Transverse MOI About X-Axis	89.65 slug-ft <sup>2</sup>
Observatory Transverse MOI About Y-Axis	87.55 slug-ft <sup>2</sup>
Wheel Weight	954.5 lbs
Wheel CG Above Separation Plane	16.0 in
Wheel Spin MOI	92.8 slug-ft <sup>2</sup>
Wheel Lateral CG Offset From Observatory Centerline <sup>2</sup>	0.050 <sup>3</sup> in
Wheel Principal Axis of Inertia With Respect to Observatory Centerline	0.002 <sup>4</sup> radians
Wheel Transverse MOI About Line Parallel to X-Axis Through Wheel CG	53.65 <sup>5</sup> slug-ft <sup>2</sup>
Wheel Transverse MOI About Line Parallel to Y-Axis Through Wheel CG	53.55 <sup>5</sup> slug-ft <sup>2</sup>
Sail Weight	461.0 lbs
Sail CG Above Separation Plane	32.7 in
Sail Spin MOI	19.6 slug-ft <sup>2</sup>
Sail Lateral CG Offset From Observatory Centerline	0.3206, <sup>8</sup> in
Sail Principal Axis of Inertia With Respect to Observatory Centerline	0.0057, <sup>8</sup> radians
Sail Transverse MOI About Line Parallel to X-Axis Through Sail CG	17.05 slug-ft <sup>2</sup>
Sail Transverse MOI About Line Parallel to Y-Axis Through Sail CG	15.05 slug-ft <sup>2</sup>

<sup>1</sup>These are actual measured properties just prior to shipment of OSO-7 to Cape Kennedy.

<sup>2</sup>Observatory centerline is defined as line perpendicular to observatory/vehicle separation plane and passing through the center of the spacecraft/attach fitting interface diameter.

<sup>3</sup>Wheel CG with respect to bearing axis is aligned during dynamic balance within 0.001" for in-orbit observatory balance about bearing axis. However, due to tolerance build-up between bearing axis and attach fitting, wheel lateral CG shift cannot be guaranteed better than <0.050" from observatory centerline.

<sup>4</sup>Wheel PAI with respect to bearing axis is aligned during dynamic balance within 0.0003 radian, but again cannot be guaranteed better than 0.002 radian from observatory centerline due to bearing axis/observatory centerline misalignment possible.

<sup>5</sup>Transverse MOI's of sail and wheel are not measured, but calculated with an accuracy of 1.0 slug-ft<sup>2</sup>.



F72-01

Table 10-5 (Cont.)

<sup>6</sup>Sail CG with respect to bearing axis is aligned during dynamic balance within 0.004" for in-orbit observatory balance about bearing axis. However, due to bearing axis/observatory misalignment possible plus sail launch unbalance due to NRL pointed instrument CG being 1.16" behind in-orbit position, sail lateral CG shift cannot be guaranteed better than 0.320" from observatory centerline.

<sup>7</sup>Sail PAI with respect to bearing axis is aligned during dynamic balance within 0.0012 radian for in-orbit condition. But due to bearing axis/observatory centerline misalignment possible, and due to 0.002 radian effect of NRL instrument, sail PAI with respect to observatory centerline cannot be guaranteed better than <0.005 radian.

<sup>8</sup>The static and dynamic values discussed in notes 6 and 7 are given because at launch vehicle time 227.450 plus, the sail will be spun to 40 ± 10 rpm.

Table 10-6  
OSO-7 WEIGHT BREAKDOWN BY SUBSYSTEM

Subsystem	Wheel		Sail		Observatory	
	Weight	%	Weight	%	Weight	%
Structure	174.0	18.2	100.8	21.9	274.8	19.4
Data Handling	39.0	4.1	0.6	0.1	39.6	2.8
Command	11.2	1.2	11.6	2.5	22.8	1.6
RF	52.7	5.5	0.2	0.0	52.9	3.7
Power	50.2	5.3	19.2	4.3	69.4	4.9
Electrical Distribution	35.7	3.7	32.3	7.0	68.0	4.8
Experiment	275.0	28.9	185.0	40.1	460.0	32.5
Control	105.5	11.0	90.7	19.7	196.2	13.9
Ballast and Balance	211.2	22.1	20.6	4.5	231.8	16.4
TOTAL	954.5		461.0		1415.5	

10.6 OSO-7 THERMAL SYSTEM DESCRIPTION

Spacecraft thermal control is needed to restrict the range of temperatures in those sections of the observatory that house the experiments and other temperature sensitive components.

Most of the observatory equipment and experiments are designed to operate in the -10 to +35°C temperature range. Exceptions are the solar array, sail structural elements, and the antenna skirt. Minimum orbital temperature variations are desired in optical experiments to prevent thermal distortion of the optical paths.



F72-01

#### 10.6.1 General Concept

Thermal control of the OSO-7 observatory is accomplished passively using thermal control coatings (paints), bare metal or metal treated with chromate conversion coatings. This method of thermal control has proved sufficient for the previous six observatories; but, since the OSO-7 experiment and equipment complement varied in kind and location from previous OSO's, each item was analyzed to determine the required surface finish. The thermal analysis methods employed are discussed in detail in Appendix B.

The mean orbital wheel temperature is controlled primarily by the solar absorptivity and emissivity of the wheel exterior surfaces. Variations in the mean temperature are caused by changes in the orbit plane angle and the annual variation in the solar constant. Changes in the wheel temperature also are caused by changes in the internal power dissipated by wheel-mounted equipment and experiments.

Observatory roll angle changes also cause variations in the intensity and distribution of external heat flux (solar, albedo, and earth radiation) on the observatory. The extent to which flux changes caused by roll angle variations affect the mean observatory temperature has not been analyzed. However, the effect of roll angle on previous observatory temperatures has been negligible and the changes masked by other orbital effects.

The observatory also exhibits a daily (orbit day) variation in temperature caused by the duration of time spent in the sun and in the earth's shadow. The mean value of the temperature and the extreme values are affected by the day/night ratio which is a function of the orbit plane angle.

Solar array and sail-mounted equipment temperatures are affected in nearly the same manner and extent as the wheel by the parameters noted above, with one exception: the solar array maximum temperature and the maximum temperature of other low thermal capacitance components or structural elements is not affected by changes in the orbit plane angle (and the resultant change in day/night ratio). The array and low thermal capacitance components reach steady state conditions on the shortest day. Therefore, no increase in temperature occurs with the longer day.

#### 10.6.2 Expected Performance

Significant parameters affecting observatory temperatures are:

- Orbit plane angle, ( $\beta$ ), variations
- Annual variation in the solar constant
- Electrical power dissipation
- Orbit day/night

Orbit Plane Angle ( $\beta$ ) Variations. Precession of the orbit plane controls the "time-in-sun" and causes the orbit plane to go from edge-lit to illuminated face-on. For evaluating this, it is convenient to define an angle,  $\beta$ , measured between the sun vector and the orbit plane.



F72-01

The  $\beta$  angle is determined by the orbit inclination ( $i$ ), the inclination of the sun and the angle between the sun and the orbit ascending node (orbit plane precession angle). The orbit plane precesses at a rate of about one revolution each 50 days. The standard OSO orbit has an inclination,  $i$ , of 33 degrees and the maximum sun declination is 23.5 degrees. The maximum value of  $\beta$  can occur only at the winter and summer solstices (see Figure 10-8). The maximum  $\beta$  is 56.5 degrees for this orbit and will occur only if the orbit plane precession angle is as shown in the figure. If the orbit is 180 degrees out of phase at the solstice, the  $\beta$  is 9.5 degrees. At the spring and fall equinoxes, the maximum  $\beta$  is 33 degrees. The  $\beta$  angle passes through zero twice each precession revolution (the sun vector lies in the orbit plane). Other plane angles will result in intermediate angles.

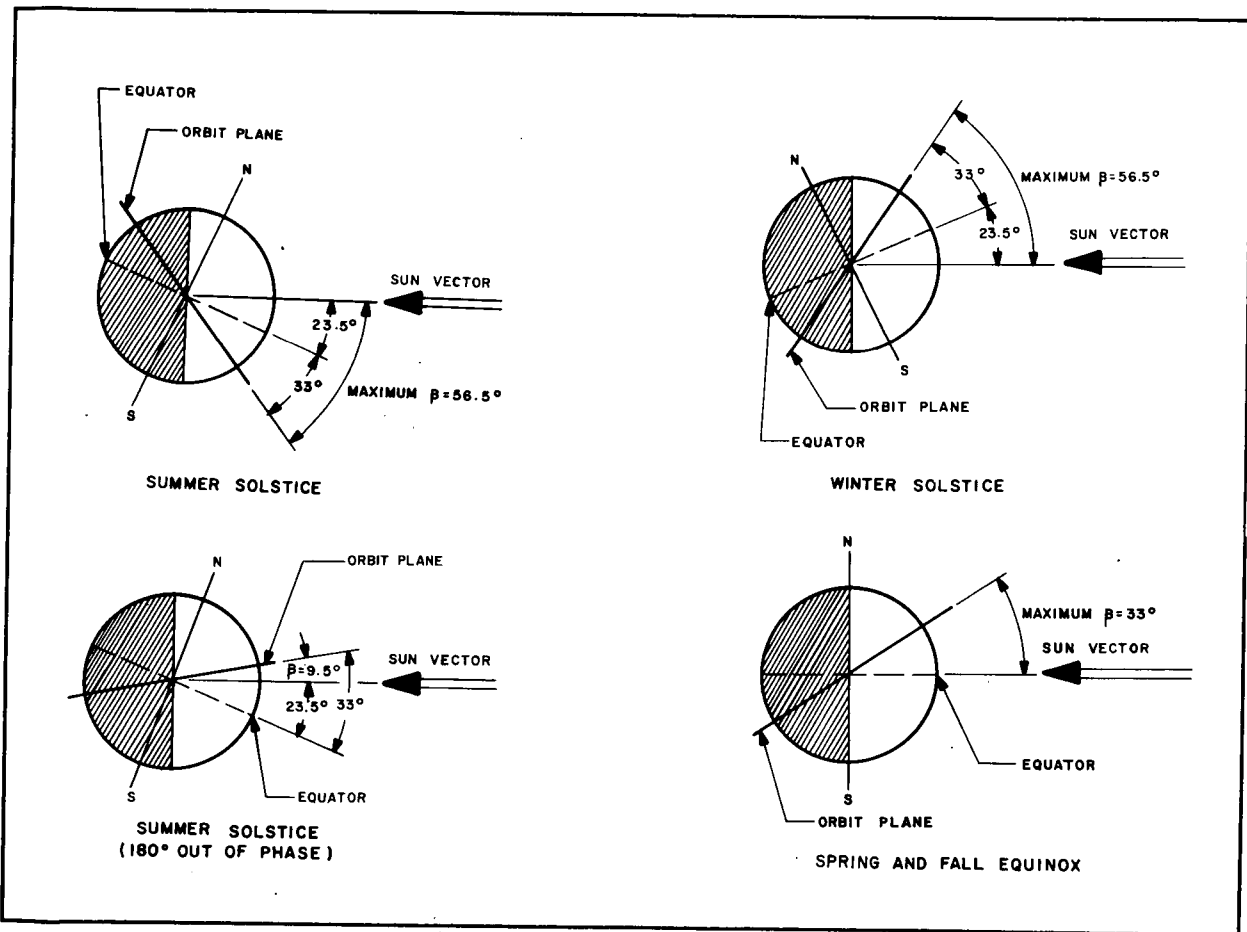


Figure 10-8 Geometry of Maximum  $\beta$  Angle with Time of Year

The observatory is in the earth's shadow longest when  $\beta = 0$  and this produces the coldest mean orbital temperature. The ratio of sun time to orbit period is a function of orbit height and  $\beta$  angle. For the 300 nmi orbit, the spacecraft is sunlit 75.4 percent when  $\beta = 56.5$  degrees. This produces a peak-to-peak difference of  $8^\circ\text{C}$  in the orbital mean temperature of the OSO wheel. For  $\beta = 9.5$  degrees, the sunlit fraction is about 63.2 percent which produces a change of only about  $1^\circ\text{C}$  above the  $\beta = 0$  temperature.





F72-01

A high temperature preceded and followed at a 25-day interval of low temperature is observed near the summer and winter solstices in Figure 10-9. The maximum  $\beta$  that can occur at the fall and spring equinoxes is  $\beta = 33$  degrees producing a sunlit fraction of about 66 percent and a temperature change above  $\beta = 0$  case of about  $3.0^{\circ}\text{C}$ . Two humps of nearly equal size spaced 25 days apart can be observed each side of the fall equinox and also one larger hump at the spring equinox. If the equinox occurs when the sun line is aligned with the ascending node, the humps will be equal. In other words, maximum  $\beta$  varies between 0 and 56.5 degrees near the solstices and only between 0 and 33 degrees near the equinoxes, and this causes the large temperature hump near a solstice and smaller humps near an equinox in Figure 10-9.

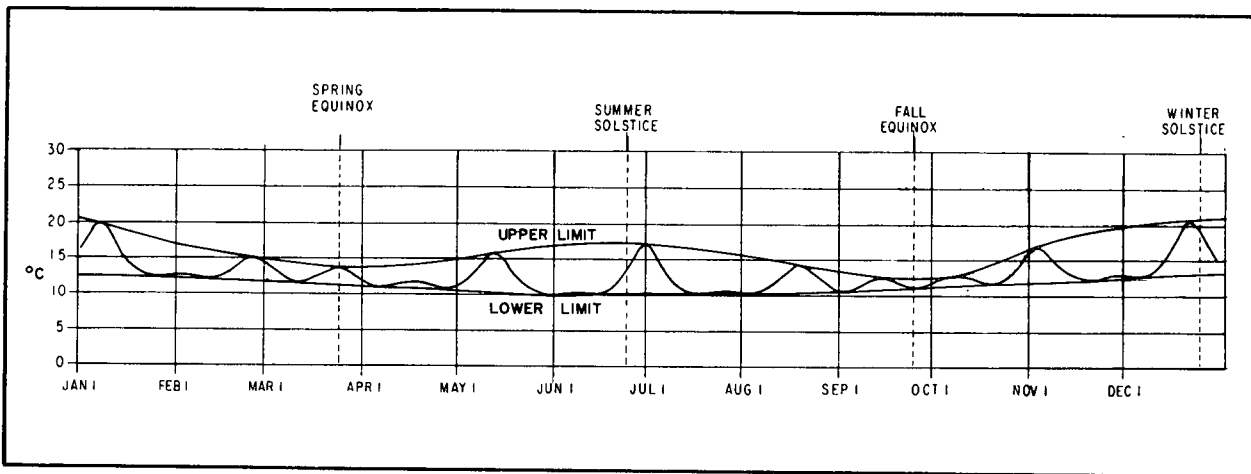


Figure 10-9 Expected Typical Wheel Hub Temperature Variation

Annual Variation of the Solar Constant. The second factor affecting the mean orbital temperature of the OSO wheel is the variation in the solar intensity over the year due to the change in earth-sun distance. The intensity varies about  $\pm 3.25$  percent with the maximum occurring at the perihelion which is about two weeks after the winter solstice. This effect is shown by the lower curve in Figure 10-9 which is the temperature that would occur if the orbit did not precess and  $\beta$  remained zero. This effect produces a peak-to-peak change of  $2.6^{\circ}\text{C}$  in mean orbital temperature.

The combined effects of shadow time ( $\pm 4.0^{\circ}\text{C}$ ) and solar intensity variation ( $\pm 1.3^{\circ}\text{C}$ ) for the standard 300 nmi, 33-degree inclination orbit is therefore  $10.6^{\circ}\text{C}$  (peak-to-peak) for a passively controlled OSO without variations in electrical loads.

Electrical Effects. The mean orbital temperature of the wheel will rise  $0.2^{\circ}\text{C}/\text{watt}$  of change in the orbital average electrical load for passive control near  $15^{\circ}\text{C}$ .

Day to Night Variations. Because of the lack of solar and albedo heating when the spacecraft passes through the shadow of the earth, there will be temperature variations during an orbit. These are small for components with large thermal capacity, but large for isolated components of small thermal capacity located on the outside of the observatory. Therefore, internal wheel equipment has small changes, and the solar array has the largest variation.



F72-01

10.6.3 Thermal Control Coatings

Table 10-7 lists the surface finishes used on the observatory together with the nominal values and permissible range of solar absorptivity and emissivity. Application of these tolerances is dependent upon the location of the structural, experiment or electrical/electronic component, its sensitivity to external heat fluxes, and/or its internal power dissipation. Thermal performance of these finishes was known from extensive test programs and use on previous OSO's. Their selection and application were determined during the thermal analysis.

Table 10-7  
SURFACE FINISHES

<u>Finish</u>	<u>Absorptivity</u>	<u>Emissivity</u>	<u>Tolerance</u>
Spacecraft Finishes			
63W - White Paint	0.26*	0.82*	±0.02
80U - Aluminum Paint	0.42	0.47	
Black CAT-A-LAC	0.95	0.87	
White CAT-A-LAC	0.34	0.80	
Chromicoat	0.42	0.05	
3M Black Velvet	0.95	0.90	
Acid Etch	0.29	0.03	
Aluminum Tape	0.16	0.04	
Gold Plate	0.30*	0.03*	
Polished Aluminum	0.42	0.05	
Shot Peened Titanium	0.77	0.40	±0.02
Experiment Finishes			
D4D Paint (aluminum)	0.30	0.30	
Aluminum Tape	0.16	0.04	
Beryllium	0.70	0.16	
Gold Plate	0.30*	0.03*	
Chromate Conversion Process	0.96	0.44	
Black Paint	0.80	0.80	
Copper Black	0.70	0.87	
Gold Alodine	NA	0.13	
Cleaned Aluminum	0.18	0.08	
Nickel Plate	0.40	0.05	

\*These values were slightly different than those actually measured later in the program.

Figures 10-10, 10-11, and 10-12 are perspective drawings of the wheel exterior and interior, forward sail and aft sail surfaces showing the primary thermal control surfaces and the finish applied to them.



F72-01

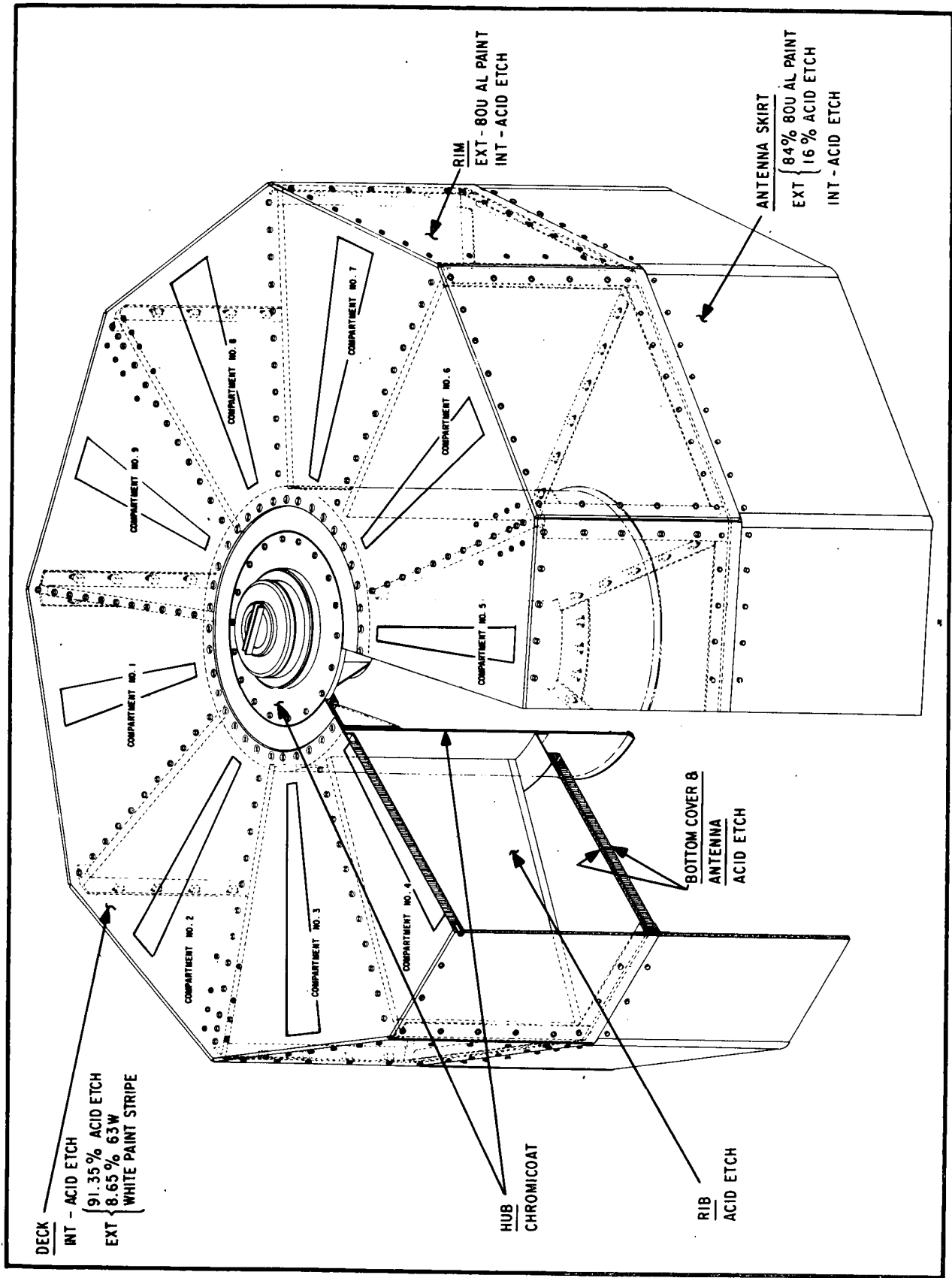


Figure 10-10 Wheel Exterior and Interior Thermal Control Surfaces



F72-01

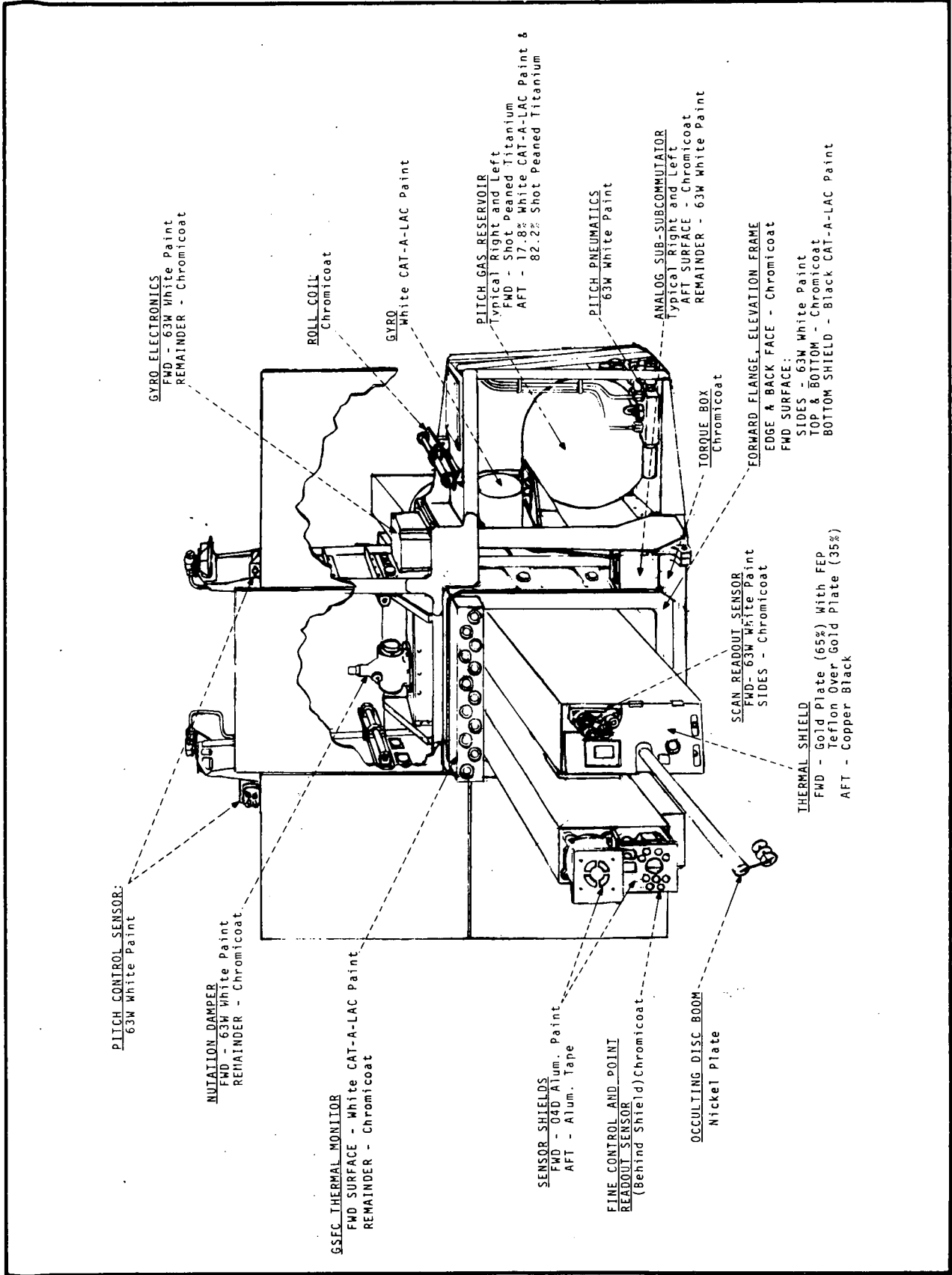


Figure 10-11 Forward Sail Thermal Control Surfaces



F72-01

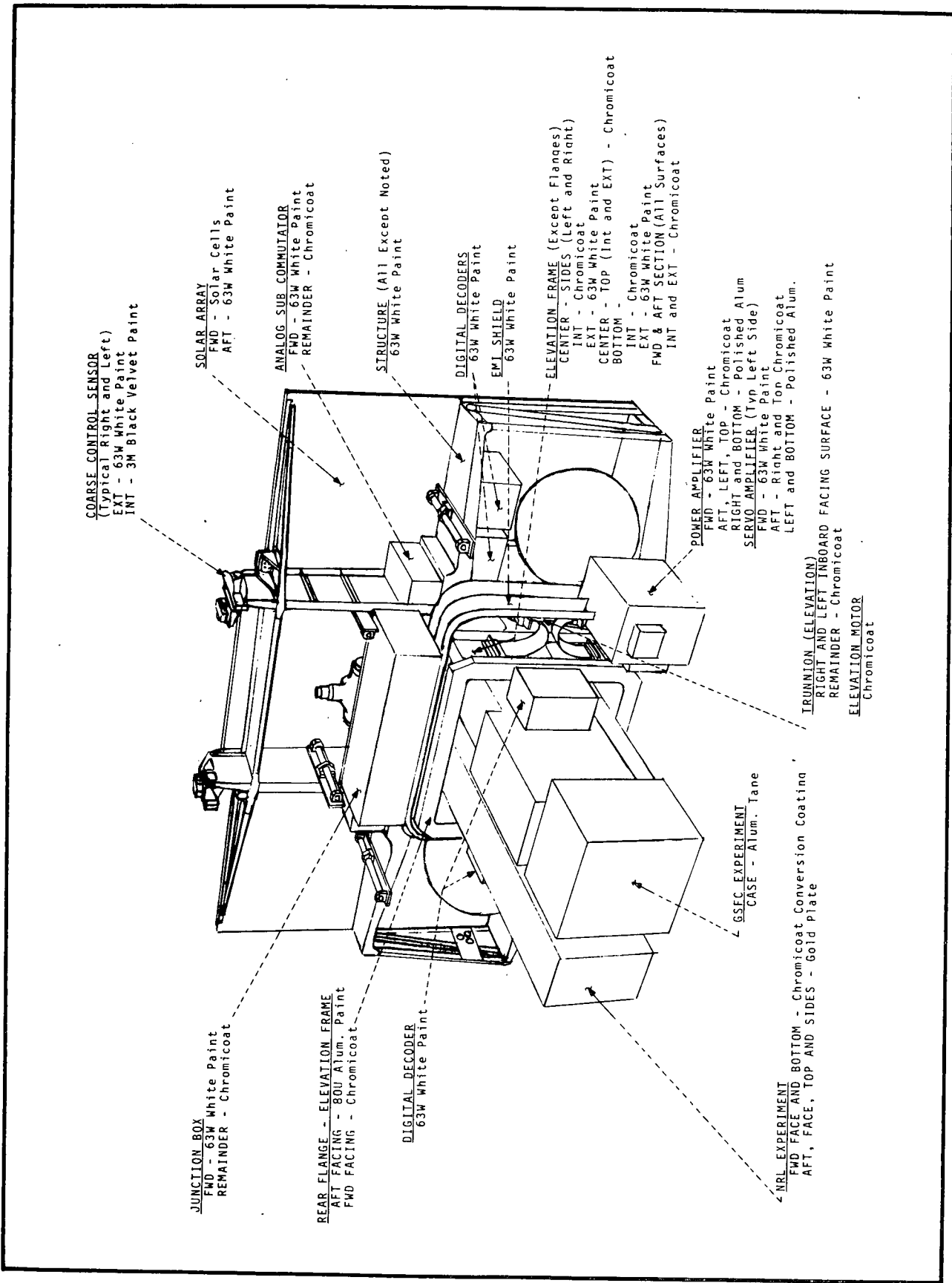


Figure 10-12 Aft Sail Thermal Control Surfaces



F72-01

10.6.4 Predicted Performance

The minimum, maximum, and nominal predicted temperatures for components (and their associated acceptance and qualification levels) are given in Table 10-8. A comparison of the predicted temperatures with those obtained in orbit is given in Section 2. The final predictions compare to the actual in flight temperatures within 5°C (except for a few cases), which is as anticipated.

Table 10-8  
OSO-7 PREDICTED TEMPERATURES

Node No.	Name	Temperatures - °C						
		Predicted			Acceptance		Qual.	
		Max	Nom	Min	Max	Min	Max	Min
1	Despin Drive	15.8	15.6	15.5	26.3	5.0	36.3	-5.0
4	Wheel Hub	12.0	11.6	11.2	22.5	0.7	32.5	-9.3
27	Spin Gas Bottle	10.7	10.7	10.6	21.2	0.1	31.2	-9.9
78	Rib Compartment #7	11.6	10.9	10.2	22.1	-0.3	32.1	-9.7
103	Upper Left Solar Panel	68.8	39.1	-28.3	79.3	-38.8	89.3	-48.8
105	Lower Left Solar Panel	63.1	42.7	0.2	73.6	10.3	83.6	0.3
112	Left Trunnion	18.9	18.2	17.3	29.4	6.8	39.4	-3.2
134	SASC	9.0	2.7	-4.7	19.5	-15.2	29.5	-25.2
135	Power Amplifier	15.4	14.2	12.6	25.9	2.1	35.9	-7.9
136	Servo Amplifier	19.3	18.0	16.3	29.8	5.8	39.8	-4.2
139	NRL Instrument (Fore)	18.7	17.9	16.9	29.2	6.4	39.2	-3.6
140	NRL Instrument (Mid)	17.5	17.1	16.7	28.0	6.2	38.0	-3.8
142	NRL (Eyeblock)	22.5	19.9	16.3	33.0	5.8	43.0	-4.2
143	GSFC Instrument (Fore)	28.4	27.5	26.6	38.9	16.1	48.9	6.1
144	GSFC Instrument (Mid)	26.4	26.1	25.8	36.9	15.3	46.9	5.3
145	GSFC Instrument (Aft)	26.3	26.0	25.6	36.8	15.1	46.8	5.1
150	SASSC (Left)	22.7	19.2	15.3	33.2	4.8	43.2	-5.2
162	GSFC - Thermal Monitor	32.5	28.9	24.5	43.0	14.0	53.0	4.0
331	Pitch Gas Bottle (Right, Aft)	19.3	15.3	11.1	29.8	0.6	39.8	-9.4
505	OIRU (TG Temperature)	37.5	32.9	27.8	48.0	17.3	58.0	7.3
506	OIRU Mounting Flange	29.7	23.4	14.9	40.2	4.4	50.2	-5.6
601	Antenna	11.5	9.5	7.4	22.0	-3.1	32.0	13.1
1012	Batteries Compartment #1	12.9	12.4	12.0	23.4	1.5	33.4	-8.5
3010	MIT Experiment	16.2	15.3	14.4	26.7	3.9	36.7	-6.1
4000	Deck Compartment #4	15.4	15.0	14.7	25.9	4.2	35.9	-5.8
4001	Cover Compt. #4	12.2	11.2	10.4	27.7	-0.1	37.7	-10.1
7000	Deck Compartment #7	12.3	12.1	11.7	22.8	1.2	32.8	-8.8
7003	Rim Compartment #7	16.3	10.7	3.4	26.8	-7.1	36.8	-17.1
8010	UCSD-S Instrument	9.4	9.0	8.5	19.9	-2.0	29.9	-12.0
9010	UNH Instrument	12.2	11.9	11.7	22.7	1.2	32.7	-8.8



F72-01

Appendix A

SORE AND ASA SOFTWARE AND ASPECT COORDINATE SYSTEMS



F72-01

A.1 SORE SOFTWARE

A.1.1 Time Intervals

The basic parameters telemetered in the SORE data are time intervals between the signals into the SORE package. The construction of the counts representing these intervals, and the reconstruction of the intervals on the ground, are illustrated in Figure A-1. The interval indicated by each count is determined by the SORE operating mode, as indicated by the three status bits in Word 37. These may be correlated, along with the day-night monitor in Word 31, with information on Table A-1 to identify the "start" and "stop" signals for the interval.

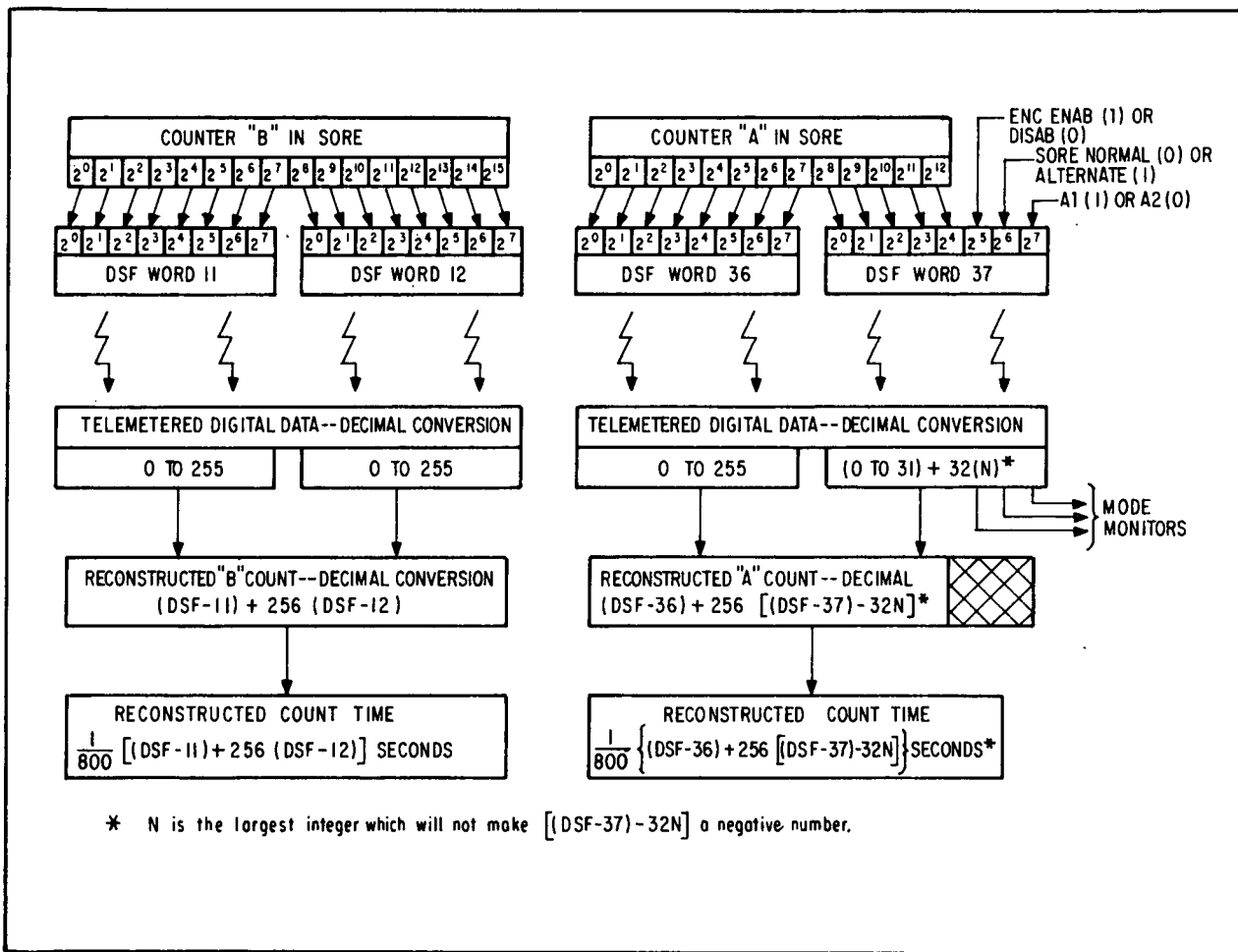


Figure A-1 Reconstructing Telemetered SORE Time

A.1.2 Spin Periods

Where Table A-1 indicates that a count is going from a pulse to the next repetition of the same pulse (Sun to Sun, Mag to Mag, or Enc to Enc), the spin period is the indicated time interval, found by the technique of Figure A-1. The maximum error in spin rates determined





F72-01

Table A-1  
SORE MODES

SORE MODE NAME	DSF-37, Bit 2			DAY OR NIGHT	DSF-11/12 (Count B)	DSF-37, Bit 1 (MSB)	
	DSF-37, Bit 2	DSF-37, Bit 3	DSF-31, Bit 2			DSF-37, Bit 1 (MSB)	DSF-36/37 (Count A)
Normal/Enc Enab	0	1	1	Day	DSF-2 to Sun	1	A1/Sun to Sun
			0	A2/Mag to Sun			
	0	0	0	Night	DSF-2 to Enc (1)	1	A1/Enc to Enc(1)
			0	A2/Mag to Enc(1)			
Normal/Enc Disab	0	0	1	Day	DSF-2 to Sun	1	A1/Sun to Sun
			0	A2/Mag to Sun			
	0	0	0	Night	DSF-2 to Mag	1	A1/Mag to Mag
			0	A2/Mag to Mag			
Alternate/Enc Enab	1	1	1	Day	DSF-2 to Sun	1	A1/Sun to Sun
			0	A2/Enc to Sun(1)			
	0	0	0	Night	DSF-2 to Enc (1)	1	A1/Enc to Enc(1)
			0	A2/Enc to Enc(1)			
Alternate/Enc Disab	1	0	1	Day	DSF-2 to Sun	1	A1/Sun to Sun
			0	A2/Mag to Sun			
	0	0	0	Night	DSF-2 to Mag	1	A1/Mag to Mag
			0	A2/Mag to Mag			

(1) Meaningless unless sail rotation is stopped (gyro on or day mode after solar acquisition)



F72-01

using this technique is estimated to be  $\pm 0.0412$  rps, determined by counter uncertainty and uncertainty in the slope of the SORE input signals. The Enc-to-Enc count offered in the "Alternate/Enc-Enab/Night" mode provides a convenient means of measuring sail spin during the launch sequence, when the wheel is fixed to the launch vehicle.

The spin-period calculation may be further refined using the data in DSF-11/12 (the "B" count). The method, illustrated by Figure A-2, averages the spin period and distributes the inherent errors over a period roughly equivalent to the DSF frame time. The accuracy so achieved is on the order of 0.0043 percent.

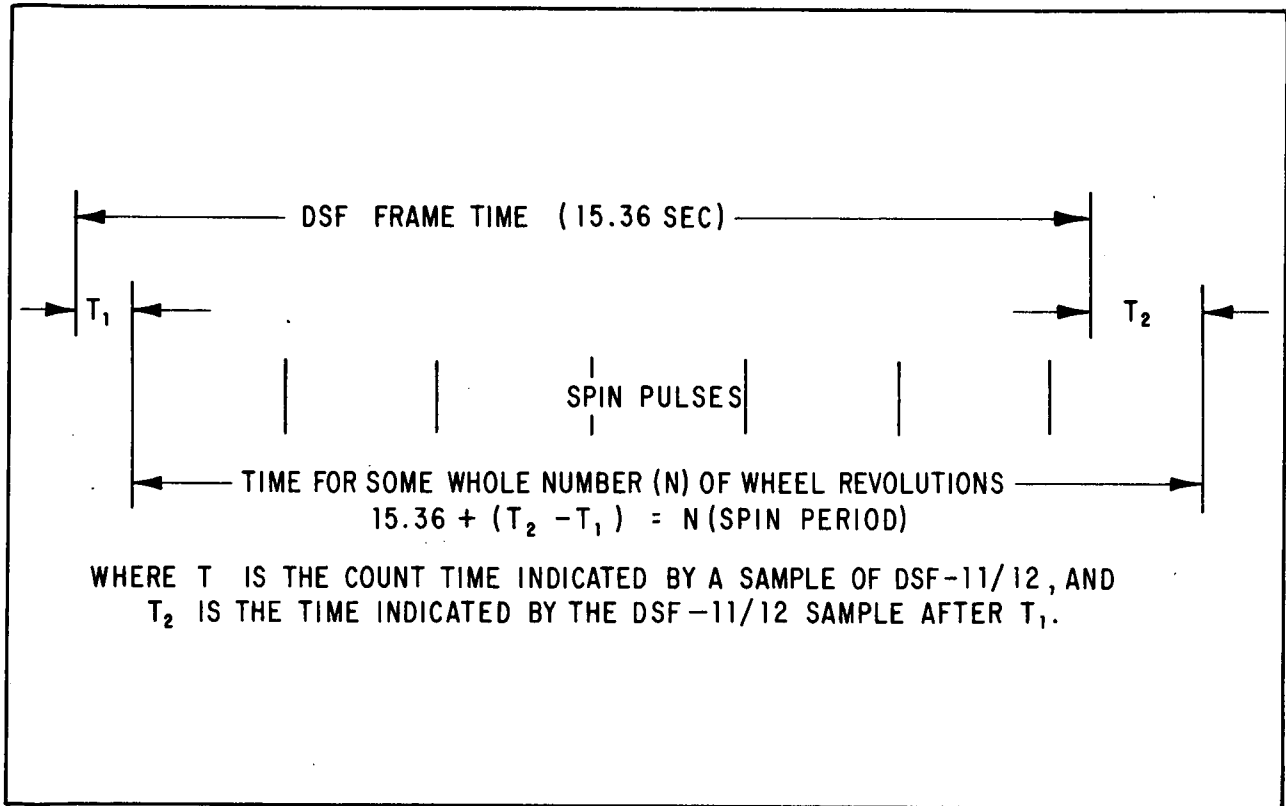


Figure A-2 Spin Period Calculation -- DSF-11/12

Referring to Table A-1, the DSF-11/12 count represents the time from DSF-2 to the next sun pulse, or the next magnetometer or encoder pulse, depending on the SORE operating mode. The operating mode has no effect on the validity of the method, since the total period calculated represents some whole number of revolutions in any case.

$T_1$  and  $T_2$  are calculated by applying the method of Figure A-1 to two consecutive samples of DSF-11/12. Once the calculation of Figure A-2 is done, the operator must know only the number of revolutions to determine the spin period, to the accuracy offered by this method.



F72-01

The value of N can be found from the approximate spin period, which is easily calculated using the A1 count, as described above. Division of the time for N revolutions by the approximate spin period yields a number between the two possible values of N. If  $T_2 > T_1$ , this quotient, increased to the next higher whole number, is N. If  $T_1 > T_2$ , then the quotient must be decreased to its next lower whole number to yield N. Spin period is then:

$$\frac{\text{Time for N Revolutions}}{N}$$

#### A.1.3 Measured Angles

The time intervals between SORE events, as reconstructed by the method of Figure A-1, may be converted to angles of wheel rotation between events by applying the relation

$$\text{Angle (in degrees)} = 360 \left( \frac{\text{interval in seconds}}{\text{spin period in seconds}} \right)$$

using the spin period calculated by the method of Figure A-2. Thus, referring again to Table A-1, we see that SORE data can be made to yield the following angles of wheel rotation:

- Between the magnetometer pulse and the sun pulse. (This angle is used in the calculation of observatory roll orientation.)
- Between the magnetometer pulse and the blipper pulse. (This angle is roughly equivalent to (1) above when the gyro holds the sail in its sun-pointing position during orbit night.)
- Between the blipper pulse and the sun pulse. (This measurement is primarily a check on the preflight coalignment measurement of the sun pulse and blipper pulse, but may also be used to read the position of the sail when the sail is slewed away from the sun in the gyro-controlled point mode.)
- Between the DSF-2 gate and the sun pulse, blipper pulse, or magnetometer pulse. (These are used to establish an azimuth position of the wheel at a particular instant in the telemetry frame.)

#### A.1.4 Roll Attitude

The first step in the calculation of OSO roll attitude is to determine  $\beta$ , which is simply the Mag-to-Sun count from DSF-36/37, converted to an angle using the techniques described above.  $\beta$  is then used, as shown in Figure A-3, to find  $\theta_m$ .

In making the roll calculation, if the flux vector is nearly parallel to the spin axis or the sun line the data is ignored because errors may be significant in such cases. The flux direction changes rapidly, so usable data is available in a minute or two.



F72-01

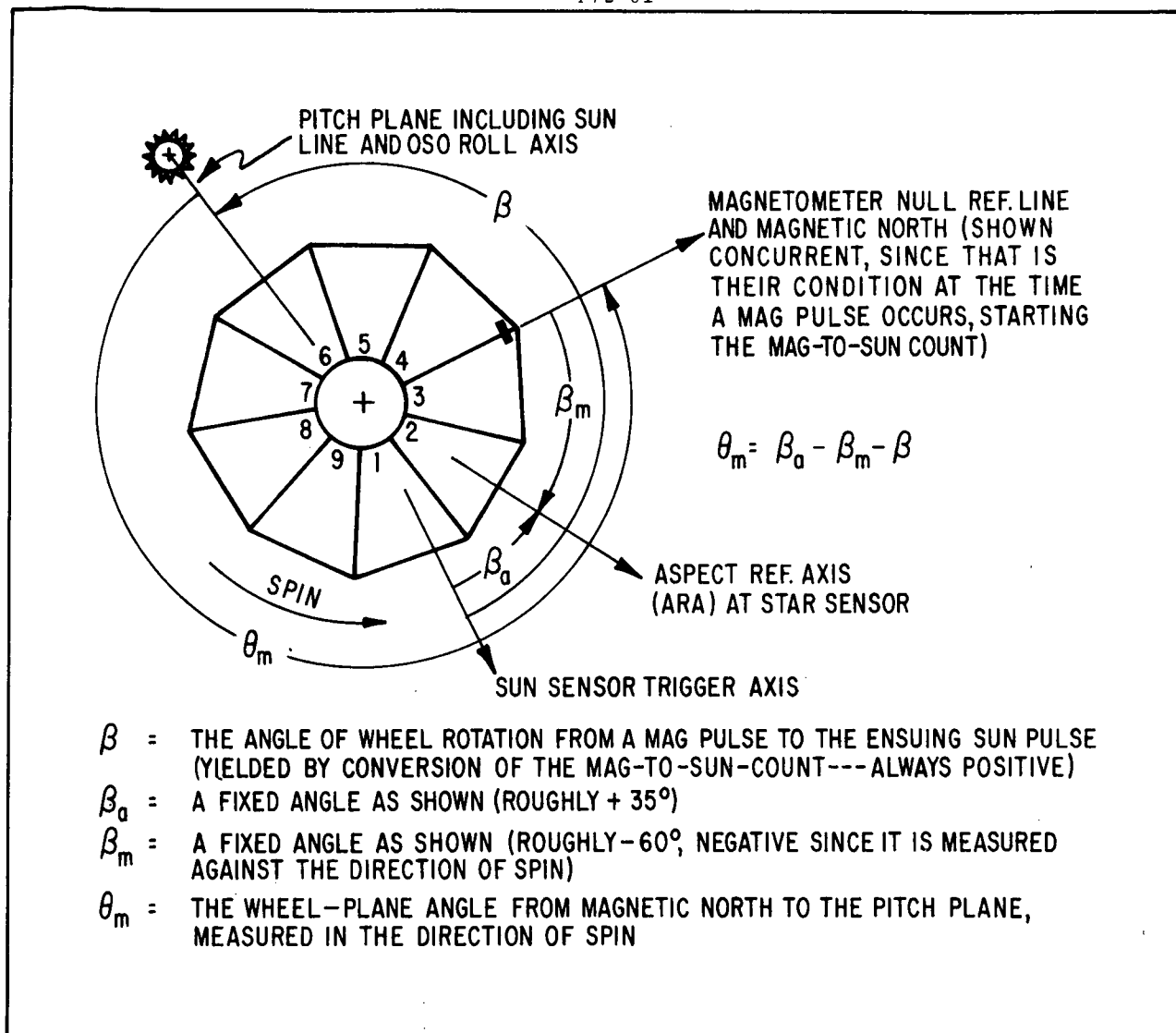


Figure A-3 Definition and Calculation of  $\theta_m$

Imagine a family of planes containing the sun line as shown in Figure A-4. If the field vector is projected into these planes, there are only two such planes where the angle from the field vector to the sun line agrees with the calculated value of  $\theta_m$ . These two are possible approximations of the wheel plane orientation. If a recent solution for roll attitude is available, the plane that agrees with recent history is kept and the other is discarded. If no such historical information is available, the calculation is repeated a few minutes later, and the plane which changes orientation rapidly is discarded. The true solution changes very little at different points in the orbit.

The remaining plane is a true approximation of the wheel plane location. The approximate spin axis orientation is normal to this plane. The positive direction along this spin axis is that direction from which  $\theta_m$  agrees in sign with the measured value.



F72-01

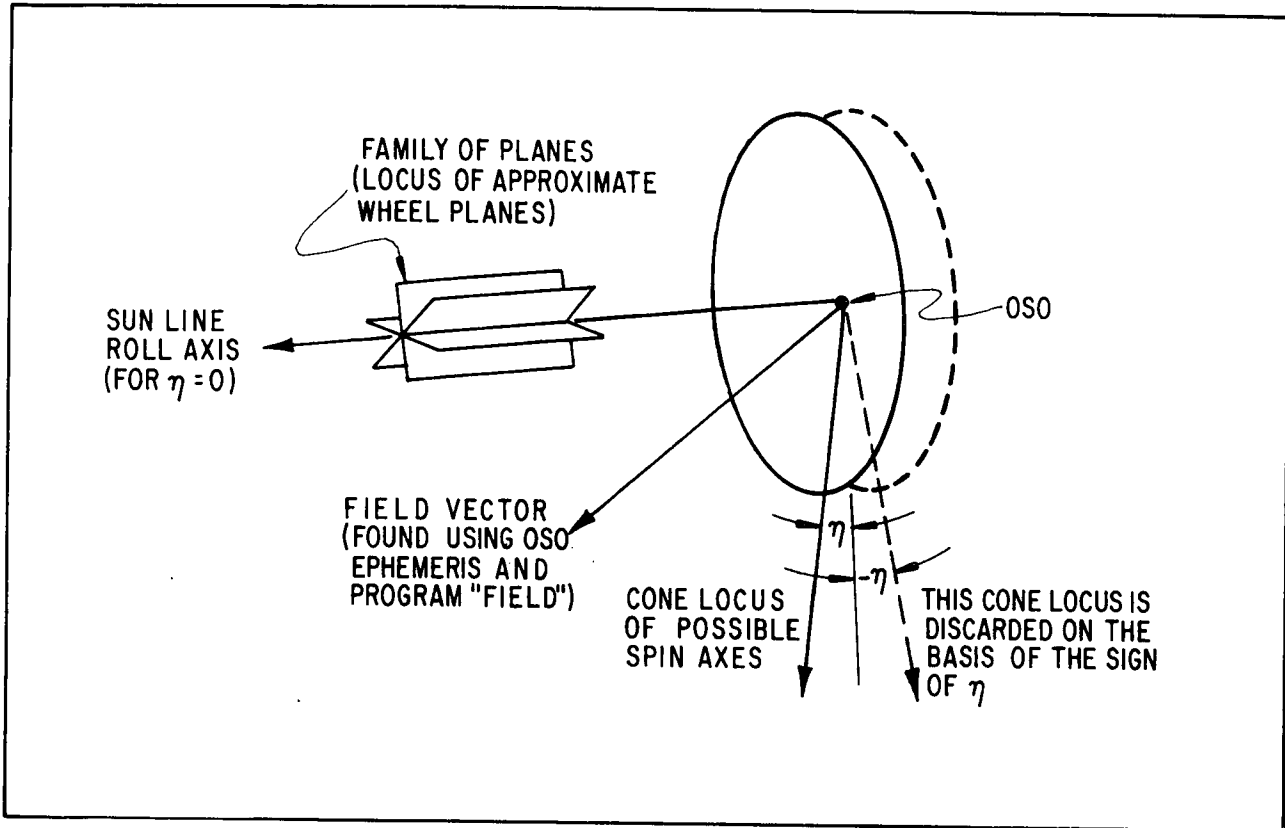


Figure A-4 Roll-Angle Solution Geometry

The intersection the selected approximate wheel plane with the cone defined by  $\eta$  (pitch angle) yields two possible spin axes. The axis which is close to and agrees in sign with the approximate spin axis selected above is the true spin axis orientation. The spacecraft roll angle is expressed as rotation of the spin axis away from the ecliptic pole, about the sun line.

#### A.1.5 Aspect Versus Data Timing

Experimenters with instruments in the wheel of the observatory need to know the parts of the sky their instruments are viewing at any time. To fix the orientation of an instrument's line of sight, we must know the observatory spin axis orientation and the angle ( $\theta_e$ ) between the pitch plane and the instrument line of sight. "Telemetry" (clock) time is used as a basis for  $\theta_e$  measurements.

The aspect reference axis is the line perpendicular to the quartz optical flat on the star sensor assembly. All important azimuth reference lines in the wheel plane are optically surveyed to this line as part of observatory pre-launch calibration tests.

The angles and relationship involved in calculating wheel angular position about the spin axis are shown in Figure A-5. While the SORE measurement is referenced to the fall of the DSF-2 word gate, the angle  $\beta_s$  is referenced to the beginning of the telemetry major frame by addition of 0.49-second. This makes it easier for the experimenter to calculate the position of his instrument at any time in the telemetry frame.



F72-01

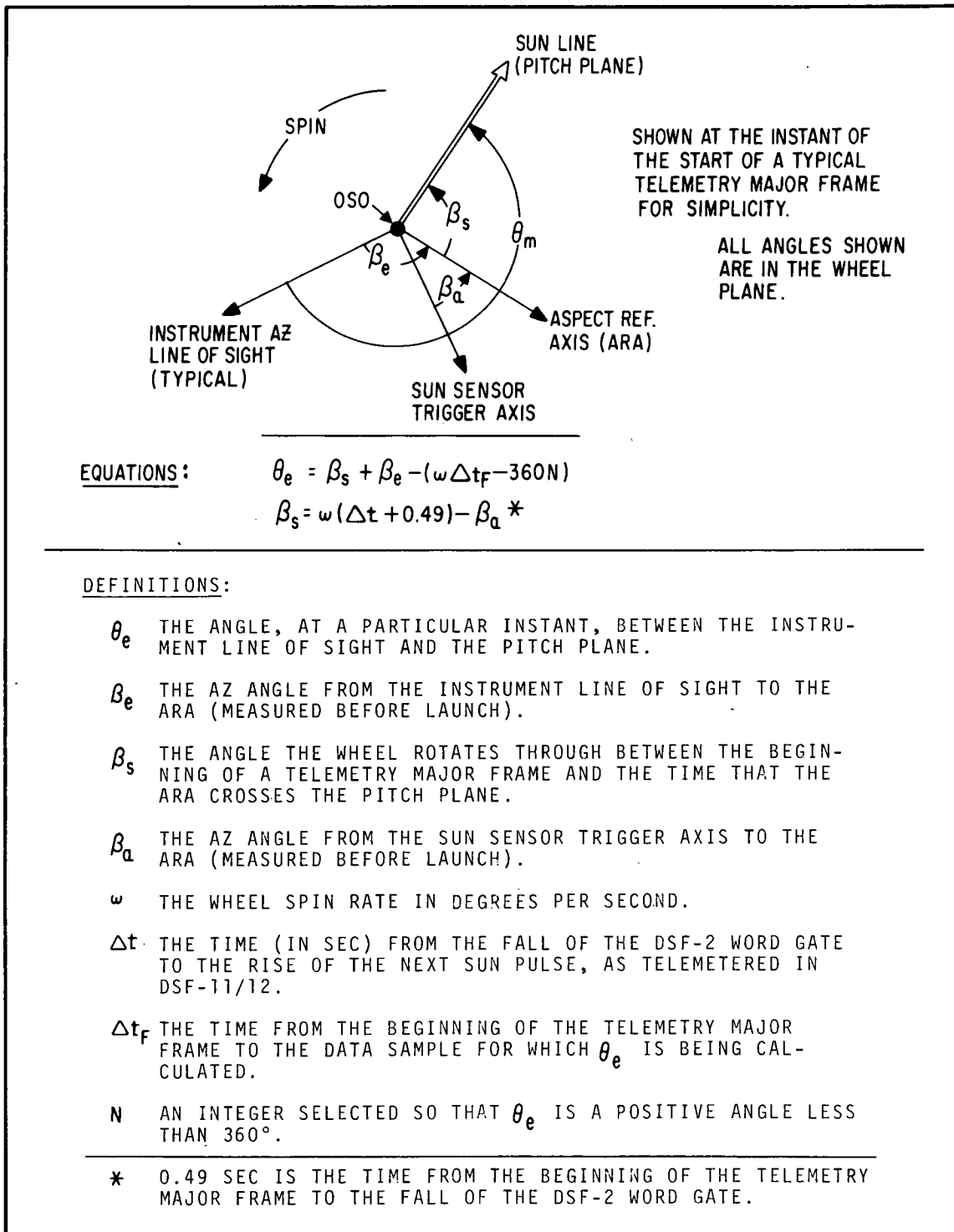


Figure A-5 Daytime Calculation of  $\theta_e$

Other factors not allowed for in Figure A-5 are (1) the "tilt" angle of an experiment, or the angle the instrument's optical axis makes with the wheel plane, and (2) the delay between the observation of a cosmic event by an experiment and the time it is shifted into



F72-01

the telemetry frame. The necessary correction to  $\theta_e$  for these effects must be made in the experimenter's software.

The method is almost identical during orbit night. In the DSF-2-to-Mag mode, the angle  $\beta_m$  (Figure A-3) is substituted for  $\beta_a$ , and  $\theta_m$  is appropriately added to accommodate the substitution of the field reference for the sun-line reference.

In the DSF-2-to-Enc mode, the basic angle remains  $\beta_a$ , but a correction is added to  $\beta_s$  for the time differential between the encoder pulse and the sun pulse if there is an appreciable difference.

## A.2 FINE ASPECT MONITOR SOFTWARE

Using ASA data, OSO attitude (pitch and roll) and the wheel azimuth position can be determined to within  $\pm 0.1$  degree and the wheel spin rate to within  $\pm 1 \times 10^{-5}$  rps.

The fine aspect reduction software consists of a driver program (STARS) and 42 subroutines. The driver manages the program setup and steers the reduction process through consecutive files (major frames) of aspect data. The major frame of telemetry data was chosen as a convenient definition for a file of data. The time duration (15.36 seconds) and the ease with which events may be referred to the telemetry frame make this an appropriate choice. The choice also makes the software package fairly compatible with existing OSO data processing systems.

### A.2.1 Star Sightings

At the observatory nominal spin rate (0.5 rps), the major-frame period includes about seven rotations of the wheel, or seven scans of the band of sky within the ASA field of view. Since there are 48 minor frames in each major frame, and each minor frame may report two star sightings, we may have up to 95 star sightings and the one azimuth index (SORE night) pulse reported in a file of data.

Reducing the data involves rejecting suspected spurious sightings in the data set, identifying the stars associated with the remaining sightings, and calculating the OSO attitude parameters from these remaining sightings.

The computer examines each incoming 24-bit word and determines if that word contains a star-sighting report. If the azimuth and elevation counts in the word are both zero, no star was seen in the time reported by that word. If only the elevation count is zero, then the word is reporting the night SORE azimuth reference, rather than a star. If both azimuth and elevation are non-zero, the report is tabulated as a possible star sighting.

The tabulation includes the following data about each reported possible sighting in the file:

- (1) The reconstructed azimuth count, with 16,384 added in for each reset of the azimuth counter since DSF-48.



F72-01

- (2) The decoded elevation count, found by the software by using a stored table.
- (3) The time interval indicated by the azimuth count (1) above. (This is the time from DSF-48 to the crossing of the azimuth slit.)
- (4) The time interval indicated by the azimuth count (1) plus the elevation count (2). (This is the time from DSF-48 to the crossing of the elevation slit.)
- (5) The time of (3) above reduced by integral multiples of the spin period so that sightings of the same stars have comparable azimuth time references. (This brings all sightings into the first scan, or wheel revolution, after DSF-48.)
- (6) The time of (4) above reduced by integral multiples of the spin period as in (5) above.
- (7) The time between the azimuth and elevation crossings. [Time indicated by (2) above.]
- (8) A flag-code which indicates the results of several validity tests performed on the data.
- (9) An azimuth position reference angle for the star sighted.
- (10) An elevation angle for the star sighted.

The flag code is a three-bit binary code including the following information:

- (1) Hardware Flag -- indicates that the ASA logic circuits received three or more pulses from the discriminator during a 50-millisecond pulse triggered by the first slit crossing. This means that a second star may have stopped the elevation counter before the first star crossed the elevation slit.
- (2) Elevation Flag -- indicates that the elevation count is higher or lower than the limits (with suitable margin) determined by OSO spin rate and the angular separation of the two slits.
- (3) Azimuth Flag -- indicates that the sum of the azimuth and elevation count is not within the nominal measurement period for the data sample. Each sample represents a particular window of time in the telemetry frame, with reference to DSF-48. If the time indicated by the telemetered count does not fall within that window, the sighting is flagged as spurious.





F72-01

### A.2.2 Star Identification

The table of sightings, made by the method described above, serves as input for further data reduction. The program deletes spurious sightings identified by the flag code, and those stars which are only signed once during the major frame being processed.

Many valid sightings are discarded by the software, since enough data remains for a valid attitude solution. Only three stars are needed for an aspect solution, but the program can accept up to eight, for use in a least-squares refinement of the solution.

Stars are identified from a star catalog provided by GSFC. This catalog, which includes position and magnitude parameters for stars that may be seen by the ASA, is programmed into the software package. By using approximate aspect parameters, if known from recent OSO history, the catalog is reduced by the computer routine. In any particular orbit, there is only one band of the sky which will fall within the field of view of the ASA. Stars outside this band are excluded in the calculations. During any particular frame of data, a certain number of stars within the band cannot be seen by OSO, since they are behind the earth. A subroutine accepts OSO ephemeris information, calculates the cone of locus of earth shadow, and excludes stars within it from further consideration. These exclusions, which greatly simplify the identification of stars, are illustrated in Figure A-6.

The final matching of sightings with the stars in the abbreviated catalog may be done by either of two techniques within the STARS program. The first compares the slit-crossing time of each sighting with the predicted crossing times of the stars. If a crossing occurs within some set tolerance of a predicted time, the data point is associated with the catalog star. The second method uses a logical pattern matching, where the angular separation of pairs of observed stars are compared with the separation of pairs of catalog stars.

### A.2.3 Spin Period

Proper star identification requires moderately good knowledge of the OSO spin rate (to within about  $10^{-4}$  radians per second. The program can accept an estimate of spin rate from the SORE, or can derive an estimate by applying the principle of Figure A-2 to the SORE azimuth reference pulse data in the first minor frame (ASA channels) after DSF-48. In any case, using this approximate spin rate and the times of sightings of the stars, a repeating process of spin-rate adjustment is used to form the best match of sightings with catalog stars. It is in this process that knowledge of the spin rate is refined to within  $10^{-4}$  radians per second tolerance.

### A.2.4 Other Attitude Parameters

The full attitude solution includes values for four parameters:

- $\omega_s$  -- spin rate



F72-01

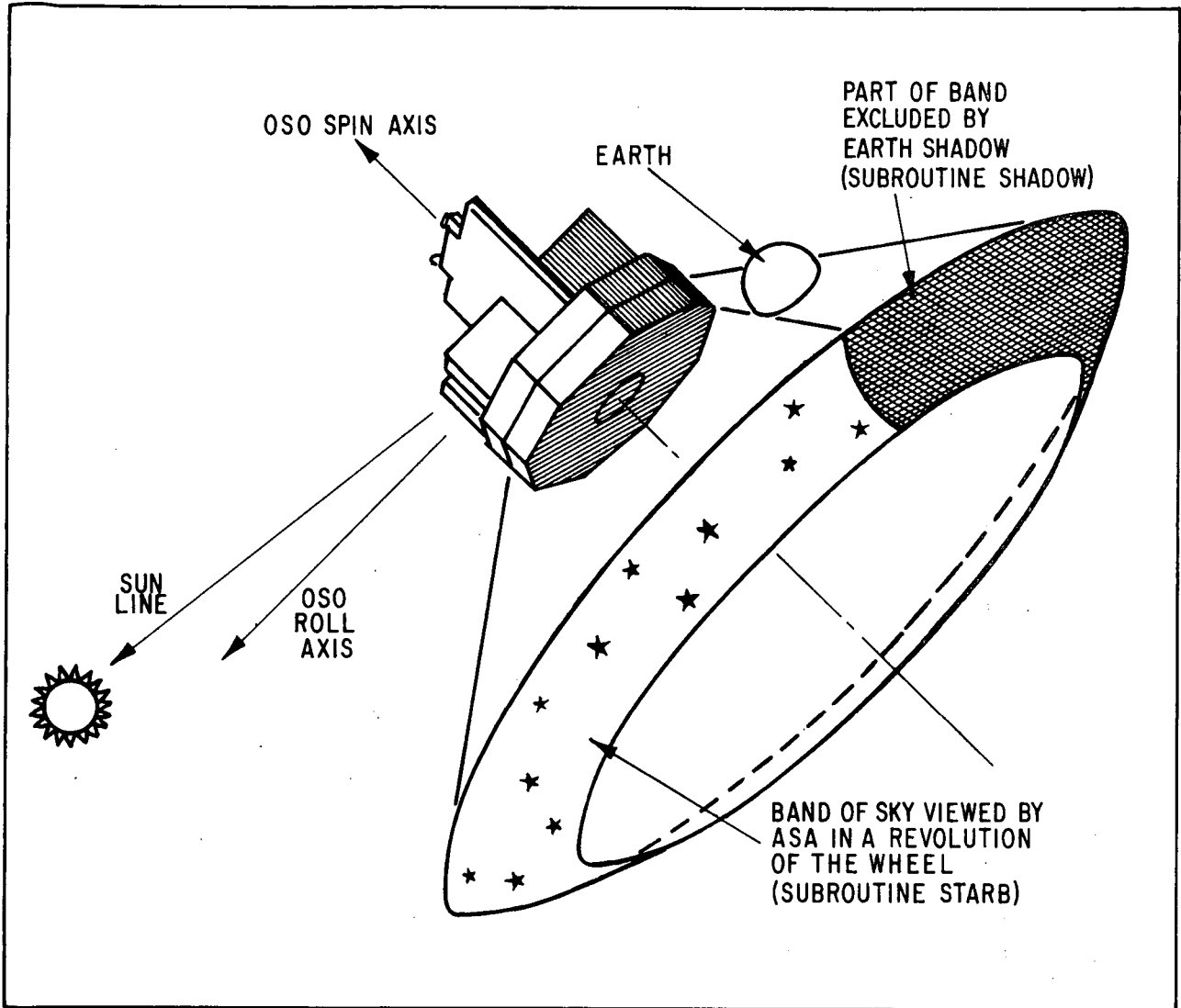


Figure A-6 Reducing the Star Catalog.

- $\eta$  -- pitch angle
- $\phi$  -- roll angle
- $\beta_s$  -- yaw position-time reference angle

These are the same parameters as in our discussion of the SORE. In the aspect software, there are several optional techniques which may be used to solve for each parameter. For purposes of this discussion, it is adequate to see that the ASA fixes known stars in the spacecraft coordinate system, and thereby fixes the spacecraft system in relation to the celestial system.



F72-01

The most-favored approach to the attitude solution is one in which all parameters are solved simultaneously. These are then all adjusted simultaneously by the software in a direction which will reduce inconsistencies in the pattern of star sightings. Crossing times are then predicted on the basis of the adjusted parameters and catalog-star information. These crossing times are compared with the telemetered crossing times to provide a basis for further adjustment of the attitude parameters. This reiterative process is repeated until the attitude parameters are known to the specified accuracy.

#### A.2.5 Experiment Instantaneous Aspect

The calculation of experiment instantaneous viewing direction, in terms of the angle  $\theta_e$ , is almost identical to that used in Figure A-5, which uses a SORE calculation of  $\beta_s$ . The main difference is not in the technique, but in the accuracy of the input parameters.

#### A.2.6 ASA Threshold Setting Predictor

A separate routine, STGAIN, has been developed by BBRC. STGAIN uses spacecraft orbit parameters, approximate attitude parameters, and the star catalog as input. STGAIN may be used to predict the most advantageous discriminator threshold setting for an orbit. This setting may then be commanded into the ASA for that orbit.

### A.3 ASPECT COORDINATE SYSTEMS

The coordinate reference systems commonly used in OSO aspect determination are: Experiment, Spacecraft, Ecliptic, Celestial (Inertial), and Topocentric. These systems are shown in Figure A-7 as they are related to each other. Pairs of coordinate systems are shown with the interrelating aspect angles. The experiment coordinate system is easily related to the spacecraft coordinate reference system; the spacecraft coordinate system is easily related to the ecliptic system, and so on. A definition of each system is given in the following paragraphs.

Experiment Systems. The experiment coordinate systems are defined to provide the simplest mathematical reference available for each experiment. Thus, the X-axis of these systems is always assigned parallel to the instrument optical axis. For convenience, the Y axis of an experiment coordinate reference system always lies parallel to the OSO wheel plane. The Z axis is mutually orthogonal as in a right-hand system.

In this system, then, the direction cosines (Cartesian coordinates) of the unit vector representing the instrument optical axis are (1,0,0).

The aspect parameters that relate the experiment coordinate reference system to the spacecraft coordinate reference system are the azimuth angle ( $\theta_e$ ) and the elevation angle (TILT).  $\theta_e$  is the wheel-plane angle, measured in the direction of spin, from the pitch plane to the instrument optical axis. TILT is positive on the sail structure side of the OSO wheel plane.



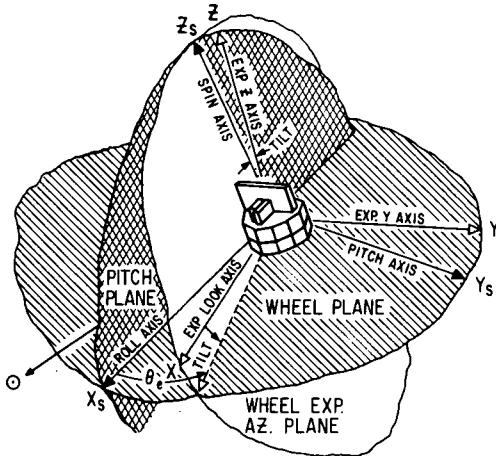
F72-01

EXPERIMENT  
CO-ORDINATE  
REFERENCE  
SYSTEM  $\left\{ \begin{matrix} X \\ Y \\ Z \end{matrix} \right.$

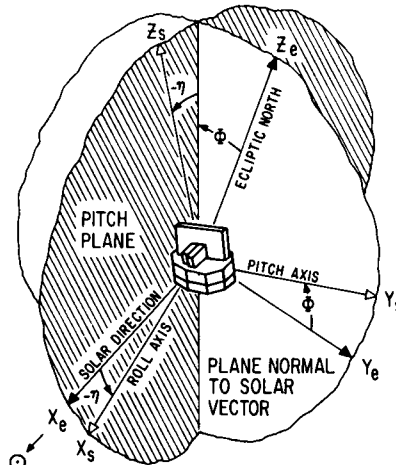
SPACECRAFT  
CO-ORDINATE  
REFERENCE  
SYSTEM  $\left\{ \begin{matrix} X_s \\ Y_s \\ Z_s \end{matrix} \right.$

SPACECRAFT  
CO-ORDINATE  
REFERENCE  
SYSTEM  $\left\{ \begin{matrix} X_s \\ Y_s \\ Z_s \end{matrix} \right.$

ECLIPTIC  
CO-ORDINATE  
REFERENCE  
SYSTEM  $\left\{ \begin{matrix} X_e \\ Y_e \\ Z_e \end{matrix} \right.$



TILT = ANGLE BETWEEN WHEEL PLANE AND WHEEL  
EXPERIMENT LOOK AXIS  
 $\theta_s$  = WHEEL PLANE ANGLE FROM SUN CROSSING  
TO EXPERIMENT POSITION



$\eta$  = PITCH ANGLE  
 $\phi$  = ROLL ANGLE  
 $\hat{z}_s$  = UNIT VECTOR ALONG SPIN AXIS

(1) EXPERIMENT - SPACECRAFT  
CO-ORDINATE REFERENCE SYSTEM

(2) SPACECRAFT - ECLIPTIC  
CO-ORDINATE REFERENCE SYSTEM

(3) ECLIPTIC - CELESTIAL  
CO-ORDINATE REFERENCE SYSTEM

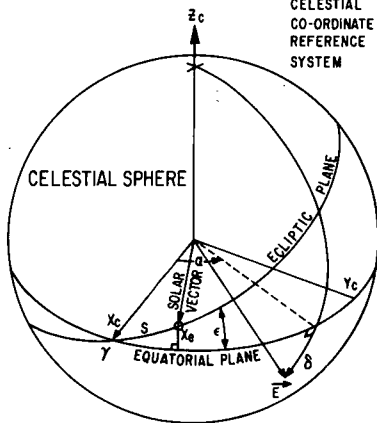
(4) CELESTIAL - TOPOCENTRIC  
CO-ORDINATE REFERENCE SYSTEM

ECLIPTIC  
CO-ORDINATE  
REFERENCE  
SYSTEM  $\left\{ \begin{matrix} X_e \\ Y_e \\ Z_e \end{matrix} \right.$

CELESTIAL  
CO-ORDINATE  
REFERENCE  
SYSTEM  $\left\{ \begin{matrix} X_c \\ Y_c \\ Z_c \end{matrix} \right.$

CELESTIAL  
CO-ORDINATE  
REFERENCE  
SYSTEM  $\left\{ \begin{matrix} X_c \\ Y_c \\ Z_c \end{matrix} \right.$

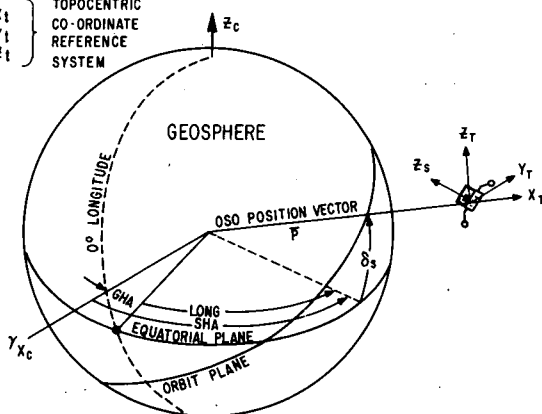
TOPOCENTRIC  
CO-ORDINATE  
REFERENCE  
SYSTEM  $\left\{ \begin{matrix} X_t \\ Y_t \\ Z_t \end{matrix} \right.$



$\vec{E}$  = ANY DIRECTION OF INTEREST  
 $\alpha = \tan^{-1} \frac{Y_c}{X_c}$  = RIGHT ASCENSION  
 $\delta = \sin^{-1} \frac{Z_c}{E}$  = DECLINATION  
T = FIRST POINT OF ARIES  
S = ECLIPTIC ARC OF THE SUN DIRECTION  
(FROM ARIES)  
 $\epsilon$  = ANGLE BETWEEN EQUATORIAL AND ECLIPTIC

CELESTIAL  
CO-ORDINATE  
REFERENCE  
SYSTEM  $\left\{ \begin{matrix} X_c \\ Y_c \\ Z_c \end{matrix} \right.$

TOPOCENTRIC  
CO-ORDINATE  
REFERENCE  
SYSTEM  $\left\{ \begin{matrix} X_t \\ Y_t \\ Z_t \end{matrix} \right.$



GHA = GREENWICH HOUR ANGLE  
SHA = GHA + LONGITUDE = SATELLITE RIGHT ASCENSION OR HOUR ANGLE  
 $\delta_s$  = SATELLITE LATITUDE AND/OR DECLINATION  
LONG = SPACECRAFT LONGITUDE

REV A

Figure A-7 Coordinate Reference Systems



F72-01

Spacecraft System. The spacecraft system Z axis is the OSO spin axis. The plane formed by the Z axis and the line to the sun is the pitch plane. The plane normal to the Z axis, through the center of gravity of the spacecraft, is the wheel plane. The X (or roll) axis lies on the intersection of these two planes. The pitch (Y) axis is perpendicular to the pitch plane and mutually orthogonal to the X and Y axes as in a right-hand system. In this system, the direction cosines of the unit vectors representing the roll, pitch, and spin axes are (1,0,0), (0,1,0), and (0,0,1) respectively.

The aspect parameters that relate the spacecraft coordinate reference frame to the ecliptic coordinate reference system are ROLL ( $\phi$ ) and PITCH ( $\eta$ ). ROLL is measured counterclockwise about the spacecraft roll axis from ecliptic north to the spacecraft spin axis. PITCH is the angle between the spacecraft spin axis and the plane normal to the line to the sun. If the spin axis is pointed away from the sun, pitch is positive (a backwards convention).

Ecliptic System. In the ecliptic system, the X axis points from the center of the spacecraft to the center of the sun. The Z axis is perpendicular to the ecliptic plane. The Y axis lies parallel to the ecliptic plane and mutually orthogonal to the X and Y axes as in a right-hand system.

In this system, the direction cosines of the unit vector representing the line to the center of the sun are (1,0,0).

The parameters that relate the ecliptic to the celestial coordinate reference frame are the angle S, measured in the ecliptic plane from the Vernal Equinox to the earth-sun line, and the fixed angle  $\epsilon$  ( $23^{\circ}26'59''$ ) between the ecliptic plane and the celestial equator.

Celestial System. The celestial (or inertial) coordinate system has the Z axis parallel to the north polar axis of the earth. The X and Y axes lie parallel to the equatorial plane. The X axis is also parallel to the intersection of the ecliptic plane and the earth's equatorial plane. Thus, the X axis points along the earth-sun line at the line of vernal equinox. At the time of vernal equinox (about March 22), the sun moves from a southern declination to a northern declination. This initial reference line points in the general direction of the constellation Aries, and is sometimes called the "Line-of-Aries". It is often represented symbolically as T.

The inertial reference frame is important since the locations of stars and other celestial objects are generally expressed in this frame. The system is also used in making the transformation from ecliptic to topocentric coordinates or from topocentric to ecliptic.

The aspect parameters that relate the celestial coordinate reference system to the topocentric coordinate reference systems are the right ascension and declination of the observatory geographic position. These angles are named SHA and DLAT in BBRC's aspect programs.



F72-01

Spacecraft Topocentric System. The X axis is directed along the OSO local vertical away from the earth. The Y and Z axes are in the OSO's local horizontal plane. The Z axis is local north and the Y axis is local east. A unit vector pointing from the observatory toward the center of the earth has direction cosines (-1,0,0) in this system.

The topocentric coordinate reference system is useful in defining the geometry of OSO's scientific instruments with relation to the earth. It is also important in observatory ground aspect tests and magnetic field definition. The GSFC geomagnetic subroutine, and subroutine FIELD, give the coordinates of the geomagnetic field in the spacecraft topocentric system.

Parallax. The difference in the direction to a distant object from different starting points is called parallax. In the OSO aspect software, the spacecraft is treated as the center of all coordinate systems. This may appear unusual to some readers, since the center of the earth is usually accepted as the center of the celestial and ecliptic systems. However, when viewing celestial or solar phenomena, the distance from earth center to OSO is negligible.



F72-01

Appendix B  
THERMAL ANALYSIS METHODS



F72-01

Appendix B  
THERMAL ANALYSIS METHODS

The thermal analysis is based upon the requirements of an overall heat balance for any component. The heat balance equation states that the time rate of the component's internal energy must equal the difference between the heat gained and the heat lost by the component.

An exact analysis of any structure involves solutions of nonlinear integro-differential equations of extreme complexity. Because a closed-form solution for any complex structure treated as a continuous system is practically impossible, numerical methods must be utilized. The continuous system is replaced by a series of discrete elements that are coupled thermally. Each element is treated as having a constant temperature throughout and differing discontinuously in temperature from the temperatures of the adjacent elements. A further advantage of using a solution by elements is that it permits adding or changing components as a result of design changes.

In a solution of this type, the first step is to break the structure and components into nodes. This forms the thermal model. Then thermal coupling between nodes by radiation and conduction is determined. With this information in hand, along with the heat capacity of each node, and the electrical heat inputs for those nodes representing electrical devices, the temperature-time histories for all of the nodes can be predicted. These temperature-time histories are the result of the simultaneous solution of  $n$  transient equations, where  $n$  is the number of nodes, and each equation describes the temperature-time behavior of a particular node.

Heat Balance Equation. The general form of the transient equation applicable to each node is <sup>(1)</sup>

$$W_n c_{p_n} \frac{dT_n}{d\theta} = \sum_m b_{n,m} \sigma T_m^4 - T_n^4 + \sum_m c_{n,m} (T_m - T_n) + K_n(\theta) + \sum_{i=1} A_{ne} \alpha_{ni} G_{ni}(\theta) - A_{ne} \epsilon_n \sigma T_n^4$$

where

- $W_n$  = mass of node  $n$
- $c_{p_n}$  = specific heat of node  $n$
- $T_m$  = absolute temperature of node  $m$
- $T_n$  = absolute temperature of node  $n$
- $\theta$  = time
- $b_{n,m}$  = radiation exchange factor between node  $n$  and node  $m$
- $\sigma$  = Stefan-Boltzmann constant
- $c_{n,m}$  = Thermal conductance between node  $n$  and node  $m$
- $K_n$  = electrical heating of node  $n$

<sup>(1)</sup> Kreith, Frank, Radiation Heat Transfer for Spacecraft and Solar Power Plant Design, Scranton, Pa., International Textbook Co., 1962, p. 80.





F72-01

- $A_{ne}$  = area of node n that receives flux  $G_{ni}$
- $\alpha_{ni}$  = surface absorptivity of node n
- $G_{ni}$  = radiant heat flux incident upon node n (in general this is an input table of values as a function of time)
- $\epsilon_n$  = emissivity of the surface of node n

The meaning of each term, starting with the left-hand side of the equation, is as follows:

1. The term on the left represents the rate of change of the energy stored in node n.
2. The first term on the right represents the net energy exchange by radiation between all nodes of the system and node n.
3. The second term on the right represents the net energy exchange by conduction between node n and all nodes of the system. This term is zero for all nodes except those in intimate contact with node n.
4. The third term on the right represents the heat input rate into node n from joule heating.
5. The fourth term on the right accounts for the thermal energy that enters a node n due to solar radiation.
6. The fifth term on the right represents the thermal energy lost to space from surface of node n by radiation.

The above equation describes the thermal behavior of a particular node within its own environment. When this environment is composed of other nodes, each with its own thermal environment dependent upon other nodes, the temperature-time history of all nodes must be arrived at simultaneously. Thus, it is necessary to set up one specific equation for each node of the system and to solve all of these equations simultaneously.

Computer Programs. The spacecraft axes defined in Figure B-1 and Figure B-2 is a pictorial representation of the nominal orbit conditions for which the analysis is performed. Figures B-3, B-4 and B-5 are included as typical radiative and conductive heat flow paths (solar array panel, UNH wheel experiment, and the wheel as a whole). Temperatures of the connecting nodes and the steady state heat flows are noted for the mean orbital conditions and a nominal orbit. A flow chart of the thermal analysis computer programs used by BBRC in the thermal analysis is shown in Figure B-6.



F72-01

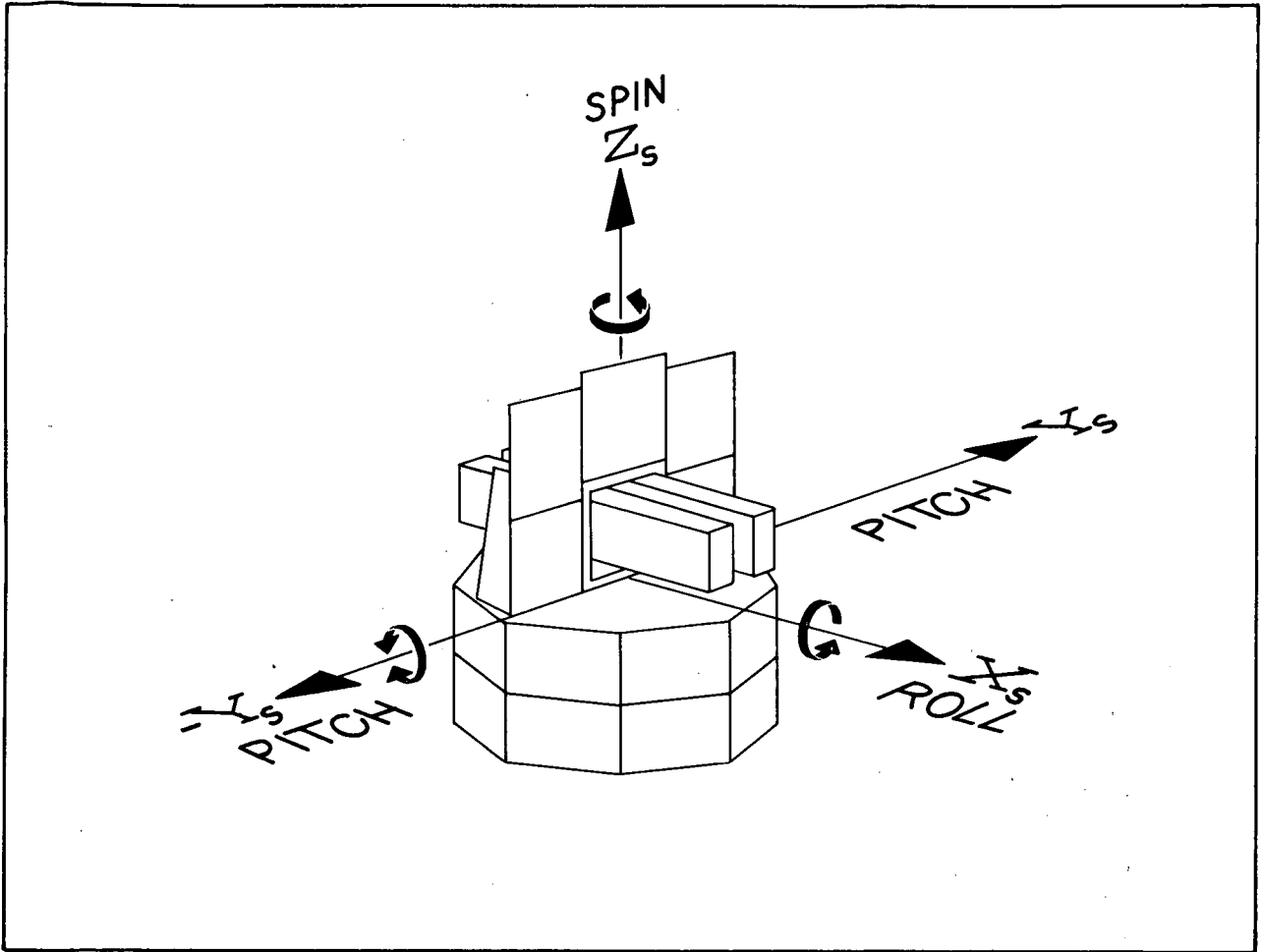


Figure B-1 OSO-7 Observatory Axes



F72-01

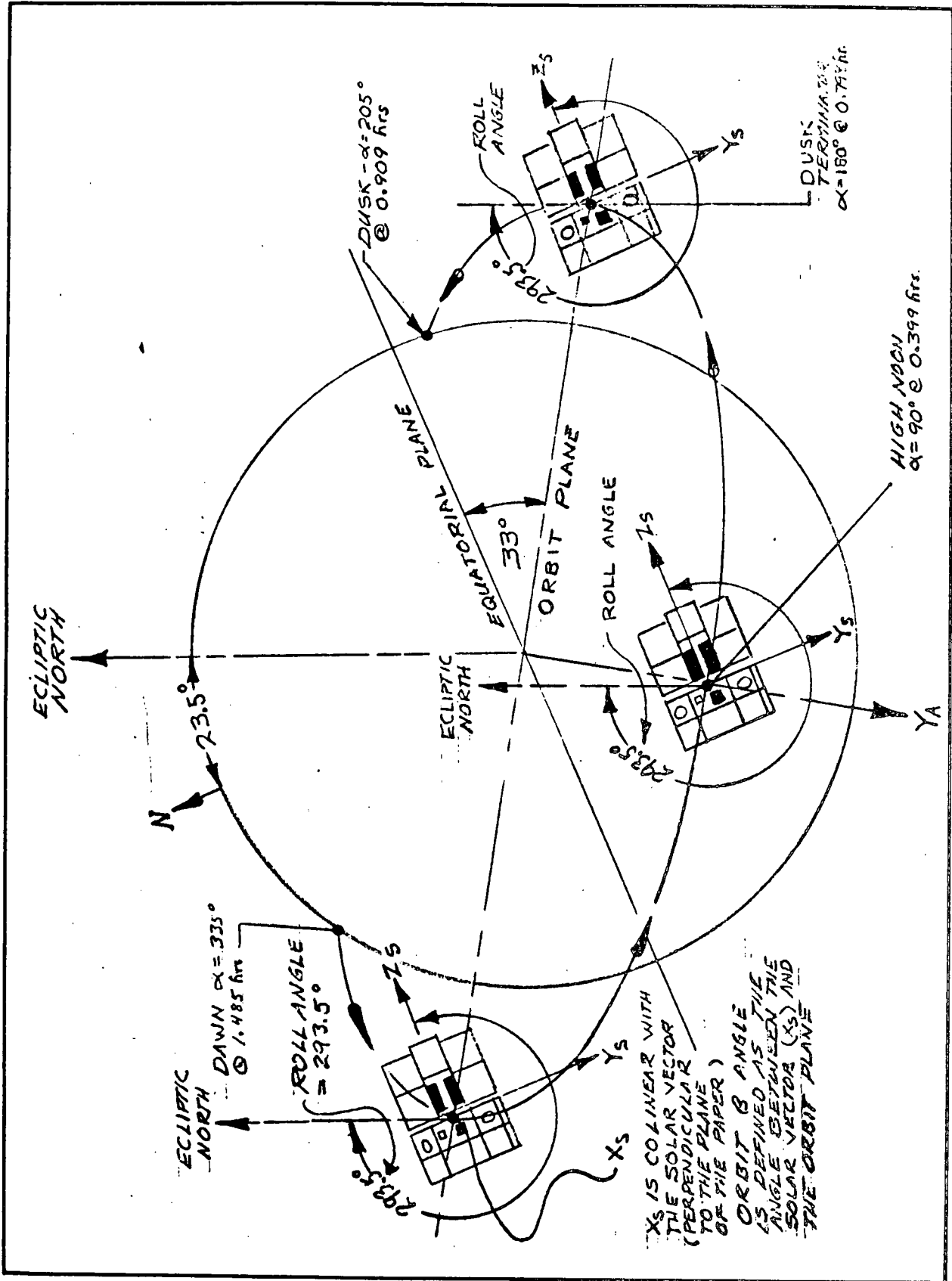


Figure B-2 Solar View of OSO-7 Orbit at Autumnal Equinox and Roll Angle of 293.5 Degrees



F72-01

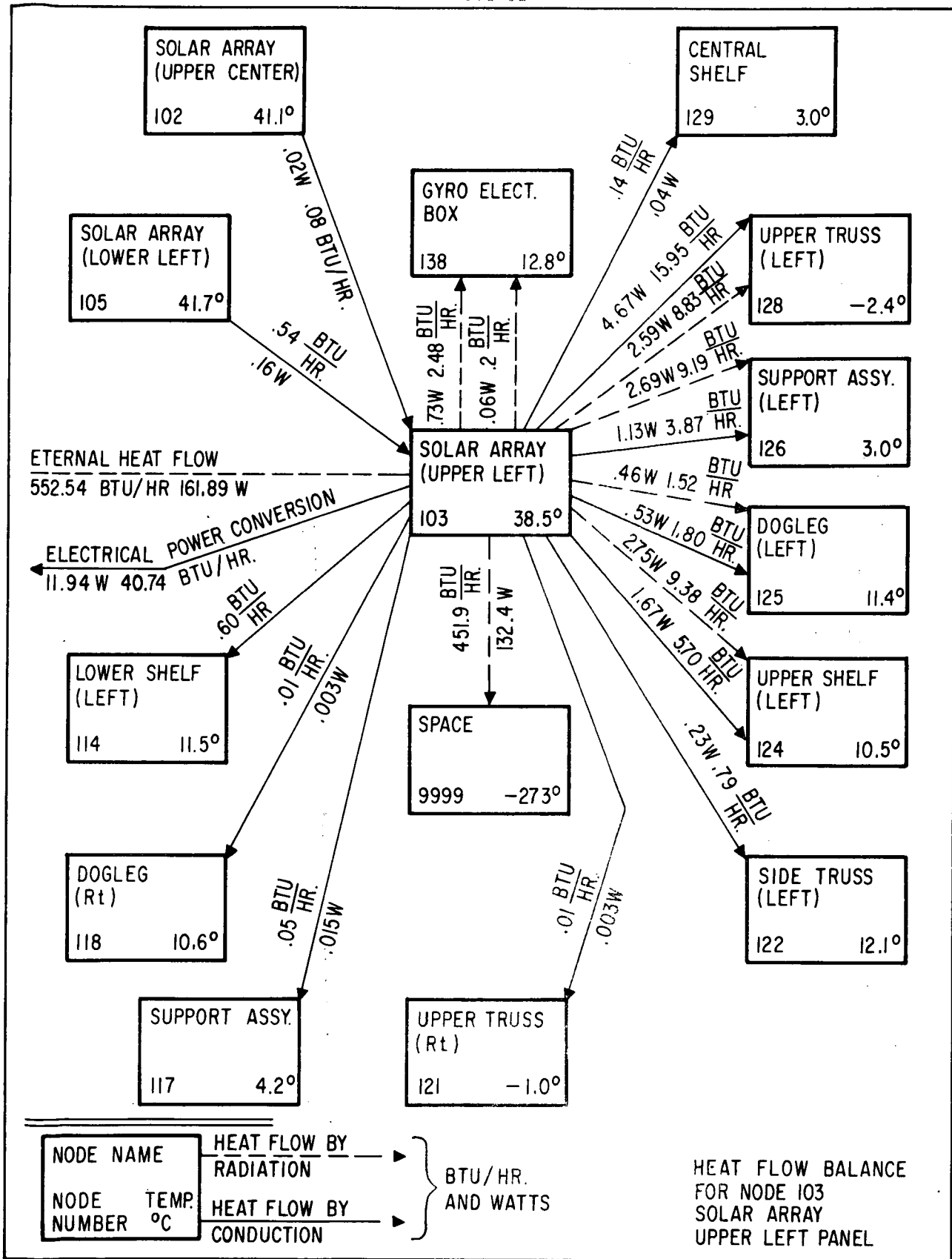


Figure B-3 Solar Array Panel Radiative and Conductive Heat Flow Paths



F72-01

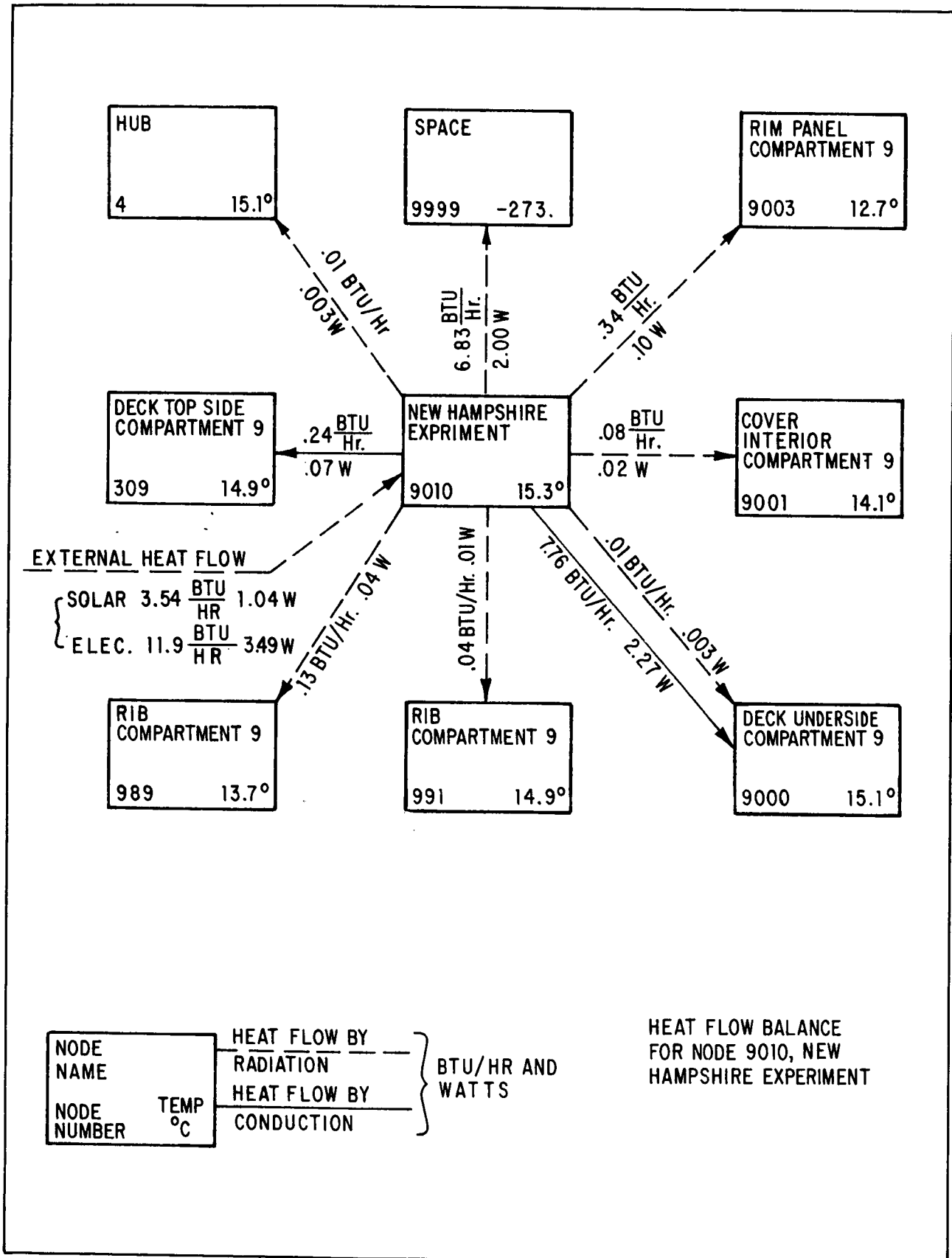


Figure B-4 UNH Experiment Radiative and Conductive Heat Flow Paths



F72-01

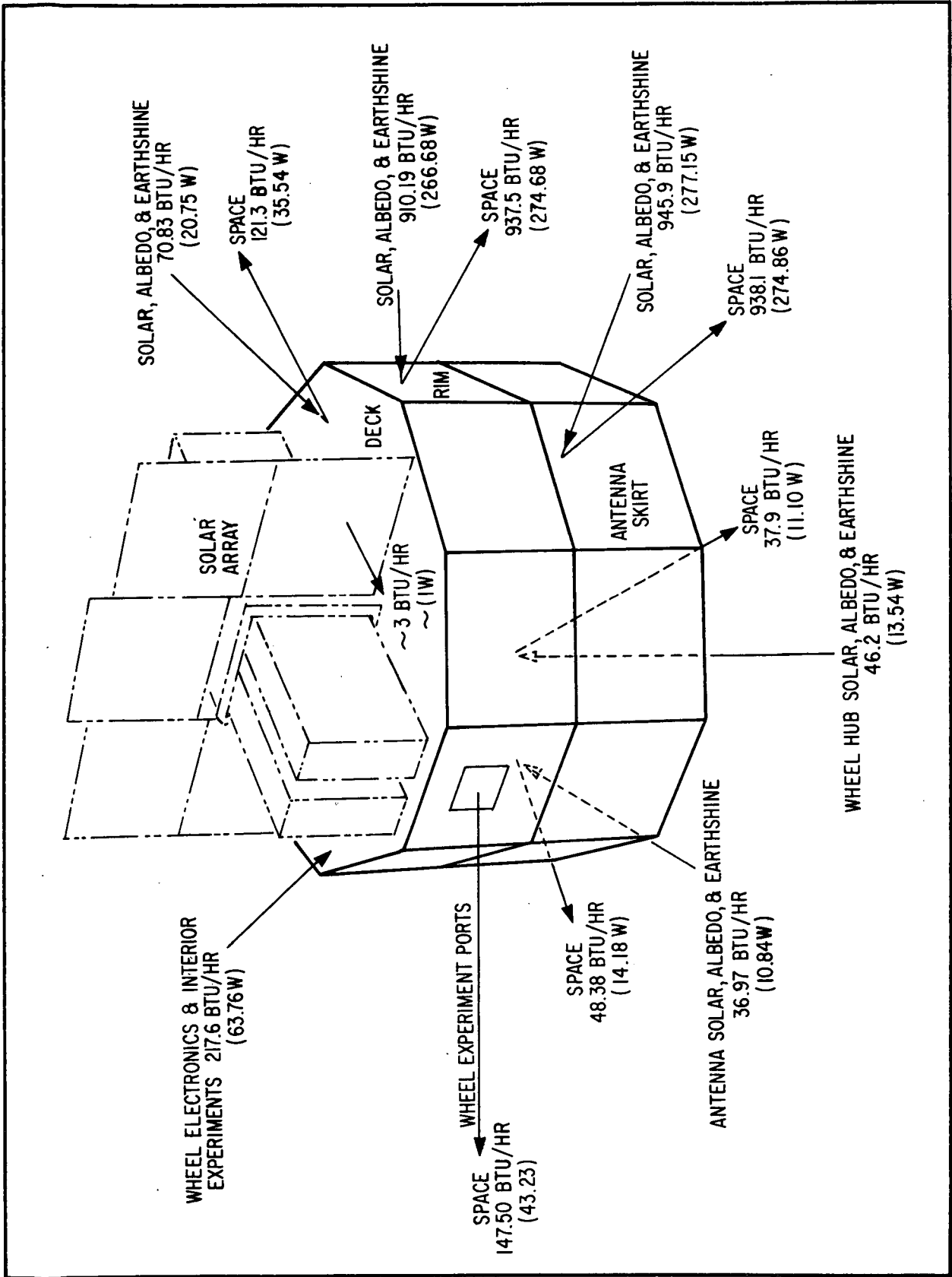


Figure B-5 Wheel Radiative and Conductive Heat Flow Paths



F72-01

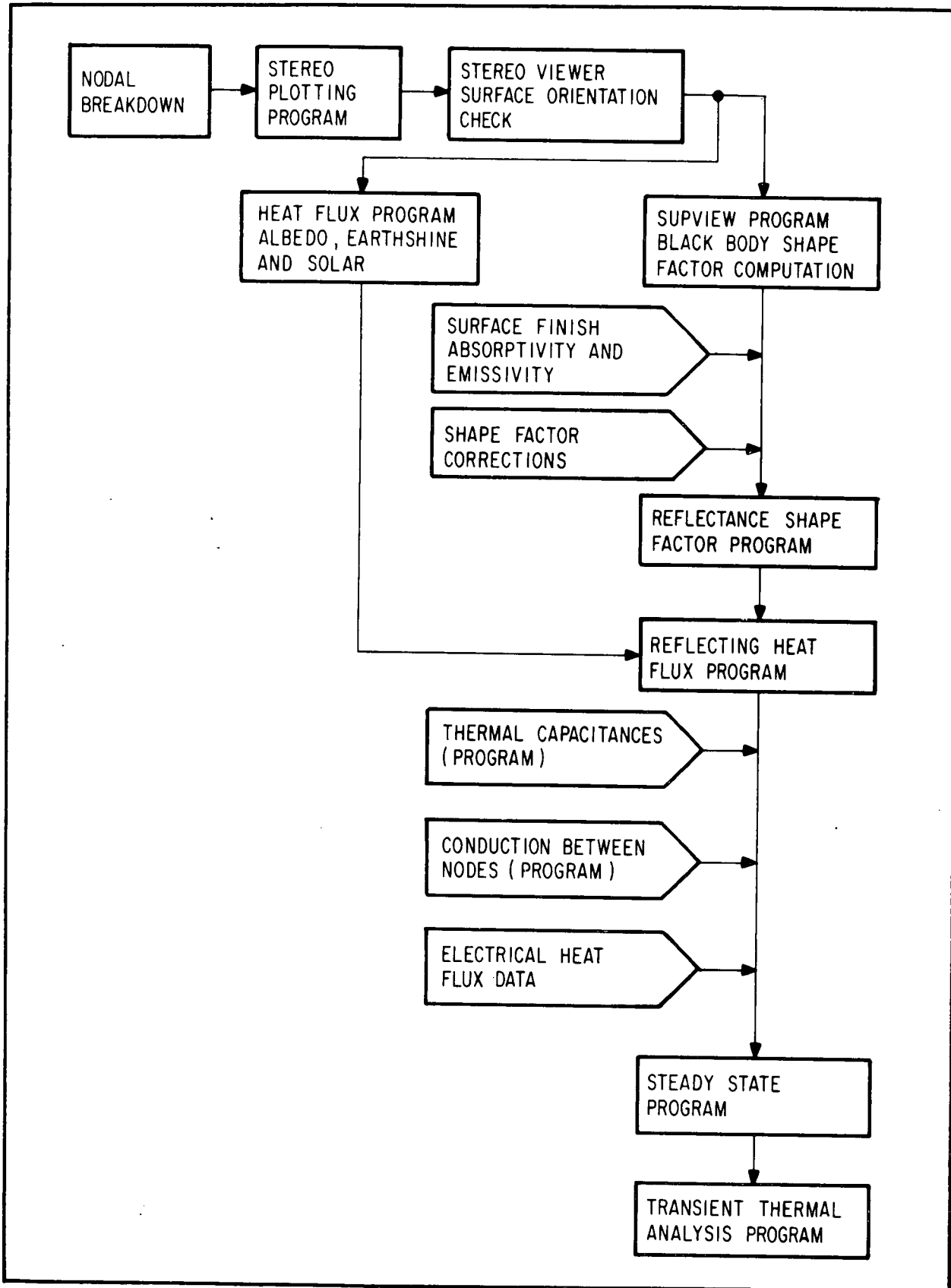


Figure B-6 Thermal Analysis Computer Program Flow Chart